University of Crete, Department of Physics

FORTH, Institute of Electronic Structure and Laser

Structural, magnetic and magnetodielectric behavior of geometrically frustrated manganese oxides

Ioanna Thomai Bakaimi

A thesis submitted for the degree of Doctor of Philosophy

Heraklion, 2014

Structural, magnetic and magnetodielectric behavior of geometrically frustrated manganese oxides

The work described in this thesis was performed in the "Functional Nanocrystals and Quantum Magnetism Laboratory" at the Institute of Electronic Structure and Laser, Foundation of Research and Technology-Hellas, Heraklion, Greece, under the supervision of Dr. Alexandros Lappas.

This research has been co-financed by the European Union and Greek national funds through the Research Funding Program Heracleitus II, Grant number 349309 (WP1.56) and the Institute of Electronic Structure and Laser.

“We are at the very beginning of time for the human race. It is not unreasonable that we grapple with problems. But there are tens of thousands of years in the future. Our responsibility is to do what we can, learn what we can, improve the solutions, and pass them on.”

Richard P.Feynman

To my parents

University of Crete, Department of Physics

Foundation for Research&Technology-Hellas (FORTH)

Institute of Electronic Structure and Laser (IESL)

The Ph.D Thesis of Ioanna's Thomai's Bakaimi was reviewed and approved by the following seven-member committee

Alexandros Lappas

Research Director, Institute of Electronic Structure and Laser, Foundation for Research and Technology-Hellas

Panagiotis Tzanetakis

Professor, Department of Physics, University of Crete

Nikolaos Papanicolaou

Professor, Department of Physics, University of Crete

Antonis Andriotis

Research Director, Institute of Electronic Structure and Laser, Foundation for Research and Technology-Hellas

Alexandros Georgakilas

Professor, Department of Physics, University of Crete

Pantelis Trikalitis

Associate Professor, Department of Chemistry, University of Crete

Eleutherios Iliopoulos

Assistant Professor, Department of Physics, University of Crete

Acknowledgements

I am indebted to many people for the help, discussions and knowledge that I gained during the last years. I had the honor, luck and privilege to interact with excellent scientists and great teachers.

Foremost I would like to thank the Physics Department in the University of Crete, for accepting me as a Ph.D candidate. I am deeply grateful, to my supervisor Dr. Alexandros Lappas who gave me the opportunity to pursue high quality and competitive research as well as for the continuous assistance, invaluable guidance and fruitful discussions he offered me in order to accomplish my goals.

Professor Panagiotis Tzanatekis has provided advices and help especially for the optimization of the magnetodielectric measurements set up, therefore I am grateful for all his contribution.

One of the steepest learning curves and by far one of the most fascinating experiments I had the joy to carry out, were the neutron powder diffraction experiments. I would like to thank Prof. Mark A. Green, for inviting me in the NCNR-NIST and for helping me with this experimental work and the relevant analysis. Dr. Efrain Rodriquez, Dr. Chris Stock, Dr. Craig Brown and Dr. Pawel Zajdel have been very helpful so a great thanks to all of them.

A demanding and time consuming task in my thesis has been the building and the continuous optimization of the magnetodielectric measurements set up. This work did entail a lot of effort, trials, interaction with experts and people with advanced technical skills. For the successful completion of this work, I appreciate the help of Dr. Bohdan Kundys, Giorgos Papadakis, George Goussis and Giannis Koutsaidis, Michalis Viskadourakis and the people in the machine shop. Also, Giannis Tsampos and George Papaioannou for their important help with the construction of the LabView software program.

Concerning the numerous questions that have been insistently feeding my thoughts, I had discussions with many people, which is impossible to acknowledge one by one. I would like to thank for the help, Prof. Nikos Flytzanis, Dr. Andrej Zorko, Dr. Zacharias Viskadourakis, Prof. Liberato Manna and Dr. Rosaria Brescia in the I.I.T of Genova, Dr.Artem M. Abakumov, Dr. Alexander A.Tsirlin, my colleagues in the laboratory Dr. Athanasia Kostopoulou, Kostantinos Brintakis, Dr. Othon Adamopoulos for the former extensive research related with the α-$NaMnO_2$ polymorph, and Eleni Aza for continuing a part of this project.

An enormous support has been offered generously by my friends and family.

I wish to thank my friends Eirini and Lykourgos, for being there.

I am grateful to my husband Antonis, for his endless patience and understanding. For the trust we gained and the things we lost, the three years we spent apart.

I deeply thank my parents Kostas and Mathildi, and my sister Stella, for the love, the support in my decisions and everything that they have been doing for me. (Ευχαριστώ θερμά τους γονείς μου Κώστα και Ματθίλδη, και την αδερφή μου Στέλλα, για την αγάπη, την υποστήριξη και όλα όσα έχουν κάνει για μένα).

Ioanna Bakaimi

Ιωάννα Μπακαΐμη

List of Figures

List of Tables

Abstract

The current trend in materials science is the discovery of smart materials which combine different properties and are controlled by external factors. Magnetoelectrics can be characterized as such, since they exhibit a cooperative response in magnetic and electric fields. In practice that means that the magnetic properties are affected by an electric field and the electric properties can be controlled by an external magnetic field. This is the corner stone property in many multifunctional devices such as spintronics and sensors.

The current thesis reports the finding of two new magnetodielectric compounds the α-$NaMnO_2$ and β-$NaMnO_2$. Spin driven magnetodielectric coupling in β-$NaMnO_2$ is reported for the first time. Neutron powder diffraction data of the β-$NaMnO_2$ reveal a noticeably complex crystal structure and moreover, two magnetic orderings, a commensurate state at high temperature and an incommensurate one with temperature lowering. Distinct dielectric anomalies appear at the temperatures where the magnetic transitions occur, pointing out the coupling between the magnetic and electric degrees of freedom. Surprisingly α-$NaMnO_2$ also exhibits a sharp dielectric anomaly at the same temperature region where β-$NaMnO_2$ develops the incommensurate structure. Transmission electron microscopy studies connect the inhomogenuous microstructure in both polymorphs with the observed physical response. Planar defects appear in both phases. In α-$NaMnO_2$ are generated by the coherent intergrowth of β-$NaMnO_2$, and *vice versa*. However the latter suffers by an increased concentration of such defects. The final outcome of these structure irregularities is the formation of a modulated superstructure which generates the lattice topology of the α-$NaMnO_2$, the β-$NaMnO_2$ and promotes the development of intermediate phases.

The observation of the β-$NaMnO_2$ in the microstructure of α-$NaMnO_2$ relates the dielectric anomaly of the latter with the incommensurate magnetic ordering of the former. The unusual finding of magnetodielectric coupling induced by the microstructure

inhomogeneity opens new perspectives in the field of the magnetodielectric systems and the relevant underlying mechanisms. The role of the nanodomains and the microstructure irregularities on the development and strength of the magnetodielectric coupling are intriguing questions which require extensive analysis and relevant future work.

Περίληψη

Η σύγχρονη τάση στην επιστήμη των υλικών είναι η ανακάλυψη έξυπνων υλικών τα οποία συνδυάζουν διαφορετικές ιδιότητες και μπορούν να ελεγχθούν από εξωτερικούς παράγοντες. Τα μαγνητοηλεκτρικά μπορούν να χαρακτηριστούν ως τέτοια υλικά, αφού ανταπόκρινονται τόσο σε μαγνητικά όσο και σε ηλεκτρικά πεδία. Στην πράξη αυτό σημαίνει οτι οι μαγνητικές ιδιότητες επηρεάζονται από ένα ηλεκτρικό πεδίο και οι μαγνητικές ιδιότητες μπορούν να ελεχθούν από ένα εξωτερικό ηλεκτρικό πεδίο. Αυτό αποτελεί θεμελιώδη ιδιότητα πολλών πολυλειτουργικών συσκευών όπως είναι οι σπιντρονικές διατάξεις και οι αισθητήρες.

Η παρούσα διδακτορική διατριβή αναφέρεται στην εύρεση δύο νέων μαγνητοδιηλεκτρικών χημικών ενώσεων: το α-$NaMnO_2$ και το β-$NaMnO_2$. Για πρώτη φορά γνωστοποιείται μαγνητοδιηλεκτρική σύζευξη υποκινούμενη από τις μαγνητικές ροπές στο β-$NaMnO_2$. Δεδομένα περίθλασης νετρονίων από το πολυκρυσταλλικό β-$NaMnO_2$ αποκαλύπτουν μια αξιοσημείωτα πολύπλοκη κρυσταλλική δομή. Επιπλέον τα πειραματικά αυτά δεδομένα, υποδεικνύουν την ύπαρξη δύο μαγνητικών τάξεων: μίας σύμμετρης μαγνητικής δομής ως προς την κρυσταλλική κυψελίδα που εμφανίζεται σε υψηλή θερμοκρασία και μίας ασύμμετρης σε χαμηλότερες θερμοκρασίες. Ευκρινείς ανωμαλίες στην διηλεκτρική σταθερά ανακύπτουν στις θερμοκρασίες των μαγνητικών μεταβάσεων, επισημαίνοντας τη σύζευξη μεταξύ μαγνητικών και ηλεκτρικών βαθμών ελευθερίας. Απροσδόκητα, και στο οξείδιο α-$NaMnO_2$ παρατηρείται μία έντονη διηλεκτρική ανωμαλία στην ίδια θερμοκρασιακή περιοχή στην οποία το β-$NaMnO_2$ αναπτύσσει την ασύμμετρη μαγνητική τάξη ως προς την κρυσταλλική κυψελίδα. Η μελέτη που διεξήχθη μέσω μικροσκοπίας υψηλής διέλευσης συνδέει την ανομοιογένεια της μικροδομής και στα δύο πολύμορφα με τις παρατηρούμενες φυσικές ιδιότητες. Διεπιφανειακές ατέλειες διακρίνονται και στις δύο $NaMnO_2$ φάσεις. Στο α-$NaMnO_2$ προκύπτουν από την ανάπτυξη του β-$NaMnO_2$ και αντίστροφα. Ωστόσο το β-$NaMnO_2$, χαρακτηρίζεται από αυξημένη συγκέντρωση ατελειών. Το τελικό αποτέλεσμα αυτών των δομικών ανωμαλιών είναι η δημιουργία μιας υπερδομής που ευθύνεται για την τοπολογία

πλέγματος του α-$NaMnO_2$, του β-$NaMnO_2$ και προωθεί τον σχηματισμό ενδιάμεσων φάσεων.

Η παρατήρηση του β-$NaMnO_2$ στην μικροδομή του α-$NaMnO_2$ συσχετίζει την διηλεκτρική ανωμαλία του δεύτερου με την ασύμμετρη μαγνητική τάξη του πρώτου. Το ασυνήθιστο εύρημα της επαγόμενης μαγνητοδιηλετρικής σύζευξης από ανομοιογένειες μικροδομής, δημιουργεί νέες προοπτικές στο πεδίο των μαγνητοδιηλεκτρικών συστημάτων και των σχετικών υπαίτιων μηχανισμών. Ο ρόλος των νανοδομών και των ατελειών της μικροδομής στην ανάπτυξη και ενίσχυση του μαγνητοδιηλεκτρικού φαινομένου, αποτελούν ενδιαφέροντα ερωτήματα που χρήζουν εκτεταμένης ανάλυσης και σχετικής μελλοντικής έρευνας.

Chapter 1:

Introduction-What is already known?

An overview of this thesis

1.1.1 The Goal

The goal of this thesis is to design, synthesize and study new spin driven magnetoelectric manganese oxides. Magnetic ferroelectrics[1, 2] are systems in which ferroelectricity develops as a result of a complex magnetic order. These materials have a tremendous advantage: the magnetoelectric coupling is strong, thus the values of the appeared polarization are high. Recently, it has been reported that complex spin configurations arise when geometric magnetic frustration is lifted over- an ideal mechanism for the appearance of this type of magneto-electric coupling. [3, 4, 5]

Geometric magnetic frustration arises from competing interactions of the magnetic moments in specific types of crystal lattices. The simplest case of frustration is found in the antiferromagnetic alignment of magnetic cations in a trianglular arrangment. The triangular lattice configuration is very common among the ABO_2 (A: alkali, B: transition metal) oxides. We choose to study the $NaMnO_2$ polymoprhs, in order to relate their magnetic frustration with the possible appearance of magnetoelectric coupling.

The driving force behind the present research on spin driven magnetoelectrics is twofold: first, there is the continuously increasing need to discover new materials that will exhibit strong magnetoelectric coupling and could be used in multifunctional devices due to this characteristic property. Second and most important, arises the necessity to understand the mechanisms that connect the magnetoelectric coupling with the geometric magnetic frustration. Unraveling the connection between the crystal structure, the imposed from the lattice topology magnetic frustration and finally the induced magnetoelectric coupling will provide the key answers towards the design of multifunctional devices.

1.1.2 The materials

Since the revival of the magnetoelectric effect, there is a grown interest to discover more magnetoelectrics and especially to find out materials and methods which will point towards an enhanced strength between the coupling of magnetic and electric properties. The recent finding that $CuFeO_2$ is a magneto-electric gave a fascinating perspective to the systems that have similar properties.

The oxides with general chemical type ABO_2 (A: alkali, B: transition metals), are two dimensional layered oxides, in which the transition metal (B^{+3}) maps out on a triangular lattice topology. Among the possible lattice topologies leading to configurations of spins that result in magnetic frustration, the antiferromagnetic arrangement of three magnetic moments in a triangular lattice is by far, the simplest one. As it will be discussed on paragraph 1.5.1 there are numerous examples of ABO_2 oxides which exhibit the magneto-electric coupling as a result of the magnetic frustration resulting from the competing interactions of the spins upon a triangular lattice topology.

The current thesis focuses on the study of the crystal, magnetic and magnetodielectric behavior of the polymorphs α-$NaMnO_2$ and β-$NaMnO_2$, first reported by Parant et al,[6] α-$NaMnO_2$, β-$NaMnO_2$ and the birnessite like oxide $Na_{0.3}MnO_2\times0.2H_2O$ which belong to a vast family of oxides namely the $NaMnO_2$ polymorphs. Much of the research in these oxides has been driven first by the possibility of being host frameworks for intercalation processes and secondly by their potential application as cathode materials in rechargeable batteries. Although there have been reports concerning the variety of the soft chemistry routes applied in $NaMnO_2$ compounds and their possible applications, there has been no reference concerning the appearance of their possible magnetoelectric coupling.

In this work the major goal was to study the crystal and magnetic properties of the β-$NaMnO_2$ and prove that is a magnetoelectric or magnetodielectric compound. This goal has been achieved, which is shown in chapter 4. Previous interesting findings on the magnetoelastic coupling of the 2D antiferromagnet α-$NaMnO_2$ [7, 8] naturally lead to the comparison of the crystal and magnetic structure properties between the β-$NaMnO_2$ and α-$NaMnO_2$ polymoprhs. This comparison was completed by the investigation of the latter as a possible magnetodielectric compound. Surprisingly, α-$NaMnO_2$ has also been found to possess the magnetodielectric coupling, as it is discussed in chapter 3.

Neverthelss, the upper goal on these compounds is to unravel the interplay between the crystal stucture and the magnetic properties. For this reason the hydration of the α-$NaMnO_2$ has been carried out which resulted in the formation of the birnessite like

compound $Na_{0.3}MnO_2 \times 0.2H_2O$. For the first time a birnessite compound is reported to be a canonical spin glass as it is discussed on chapter 5.

1.1.3 The methods

The properties and origin of the magnetoelectric coupling can only be fully understood when we have a good knowledge of the crystal's structure which imposes a specific magnetic order. For that purpose a variety of experimental methods has been used.

The majority of the experiments have been conducted at the Institute of Electronic Structure and Laser-Foundation of Technology and Reasearch-Hellas (IESL-FORTH). The first experimental stage was the synthesis of the bulk compounds and for that, solid state reaction has been the major preparative route. Preliminary characterization has been done by X Rays Powder Diffraction and Thermogravimetric Analysis. The magnetic properties have been studied by a Superconducting Quantum Interface Device (SQUID). In order to measure dielectric permittivity and polarization of the compounds studied in this thesis at the temperature range 5-320 K and under magnetic fields -7 T to 7 T an appropriate set up and a home made probe were developed.

The crystal and magnetic structure on temperatures 4 K-400 K has been studied by Neutron Powder Diffraction Experiments at two neutron facilities: the NIST Center for Neutron Research of the National Institute of Standards and Technology (NCNR-NIST) in Maryland, USA as well as in the ISIS- Rutherford Appleton Laboratory, Oxford, United Kingdom.

Experiments of: a) Electron Diffraction (ED) b) High Resolution Transmission Electron Microscopy (HRTEM), c) EDS Mapping and d) Electron Energy Loss Spectroscopy were carried out using a Jeol JEM 2200FS instrument, equipped with an image aberration corrector, an in-column energy filter and a silicon drift detection system for EDS at the Italian Institute of Technology–Genova, Italy by Dr. Rosaria Brescia under the supervision of Dr. Liberato Manna. ED patterns and HRTEM images were obtained also with a Tecnai

G2 electron microscope operated at 200 kV in EMAT, University of Antwerp, in Belgium by Dr. Artem Abakumov.

1.2 Basic Concepts of Magnetism

"*loadstone attracts iron because it has a soul"*. This statement- first scientific observation of magnetism belongs to the Greek philosopher Thales around 558 B.C. Much later around 1820 Oersted discovered that a magnetic field could be generated with an electric current. During the 20^{th} century the contribution of many great physicists like Maxwell, Curie, Weiss, Anderson, Bloch and Landau has been enormous in the classification of magnetic materials and created the foundations of modern technology. As a result our knowledge towards magnetism, or better, electromagnetism has increased impressively. Nowadays, the applications of magnetic materials are literally everywhere: sensors, laptops, cellphones, quantum devices and data storage devices such as magnetic memories.

The following paragraph summarizes the basic concepts of magnetism essential for an experimental physicist and necessary for understanding the results and the characterization presented in the following chapters.

1.2.1 The origin of Magnetism

A material is characterized as "magnetic" as long as it has magnetic ions, which result from unpaired electrons at partially filled "f" or "d" shells. The magnetic atoms are found in the transition elements with incomplete 3d and 4d- shells, the rare earth and the actinide elements, with incomplete 4f- and 5f- shells respectively. These unpaired electrons have an intrinsic property: the spin angular momentum and due to their periodic motion around a nucleus they also have orbital angular momentum. The sum of spin and orbital angular momentum is the total angular momentum and it is known as magnetic moment or "spin" which is the fundamental unit of magnetism.

1.2.2 Categories of Magnetic Materials

Materials are classified into categories, according to way that their spins respond under the effect of an external magnetic field and interact with each other (Figure 1.1). When spins are randomly oriented the material is called paramagnetic. The ions of paramagnetic field will align under an external magnetic field. On the contrary a diamagnetic material will counteract an applied magnetic field. Parallel and antiparallel alignment of neighboring spins leads to ferromagnetic and antiferromagnetic materials, respectively. Ferrimagnetism arises when the magnetic moments are aligned antiparallel and are unequal, thus a magnetization remains in the material.

In antiferromagnetic structures, there are different ways that the spins may point up or down, which depend on the type of the crystal lattice. An example of four different antiferromagnetic structures of a cubic lattice is shown in Figure 1.2.

Moreover, there are also the non collinear magnetic orderings, which may arise from competing interactions as it will be discussed in paragraph 1.3. In a non collinear magnetic ordering the neighboring spins are neither parallel nor antiparallel, such as canted ferromagnetism, where the magnetic moments are not parrallel but tilted by a small angle. Examples of non collinear structures are the spiral, cycloid and conical magnetic orders, as shown in Figure 1.3.

Moreover, there are also the non collinear magnetic orderings, which may arise from competing interactions as it will be discussed in paragraph 1.3. In a non collinear magnetic ordering the neighboring spins are neither parallel nor antiparallel, such as canted ferromagnetism, where the magnetic moments are not parrallel but tilted by a small angle. Examples of non collinear structures are the spiral, cycloid and conical magnetic orders, as shown in Figure 1.3.

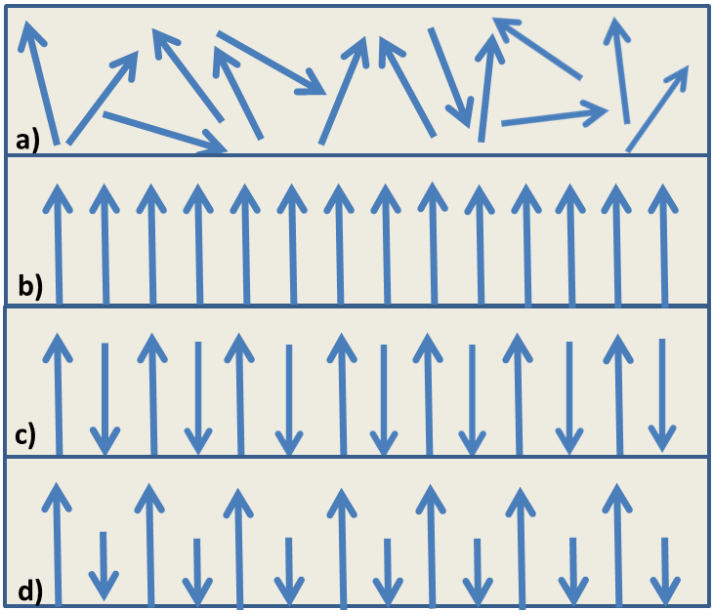

Figure 1.1 Basic types of magnetic materials according to the spins alignment: a) Paramagnets b) Ferromagnets c) Antiferromagnets d) Ferrimagnets

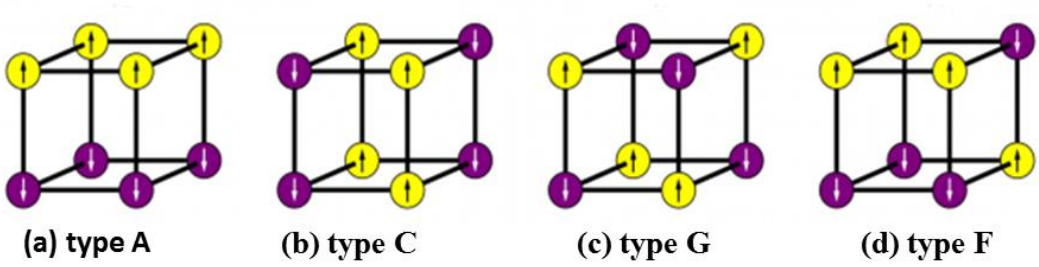

Figure 1.2 Different types of antiferromagnetic ordering on a cubic lattice. Reprinted from webpage http://andrewsteele.co.uk/physics/mmcalc/docs/magneticpropagationvector.

A type of magnetic ordering which is very common among the non collinear structures described above is the "incommensurate magnetic structure". The way that the spin waves are propagated in the lattice depends on the crystal lattice. This happens since the magnetic ions are placed in specific positions determined the crystal (chemical) lattice structure. For example, when the magnetic unit cell can be described as a doubling of the crystal cell in

the three directios x, y, z, then the magnetic structure is "commensurate" to the crystal's cell and the propagation vector of such a magnetic structure will be **k** (½, ½, ½). In cases when the spins are not exactly parallel with each other, but vary slowly by small angular steps, the magnetic cell is not commensurate with the chemical. That results in a propagation vector with at least an irrational number for example **k** (½, 0.43333, 0).

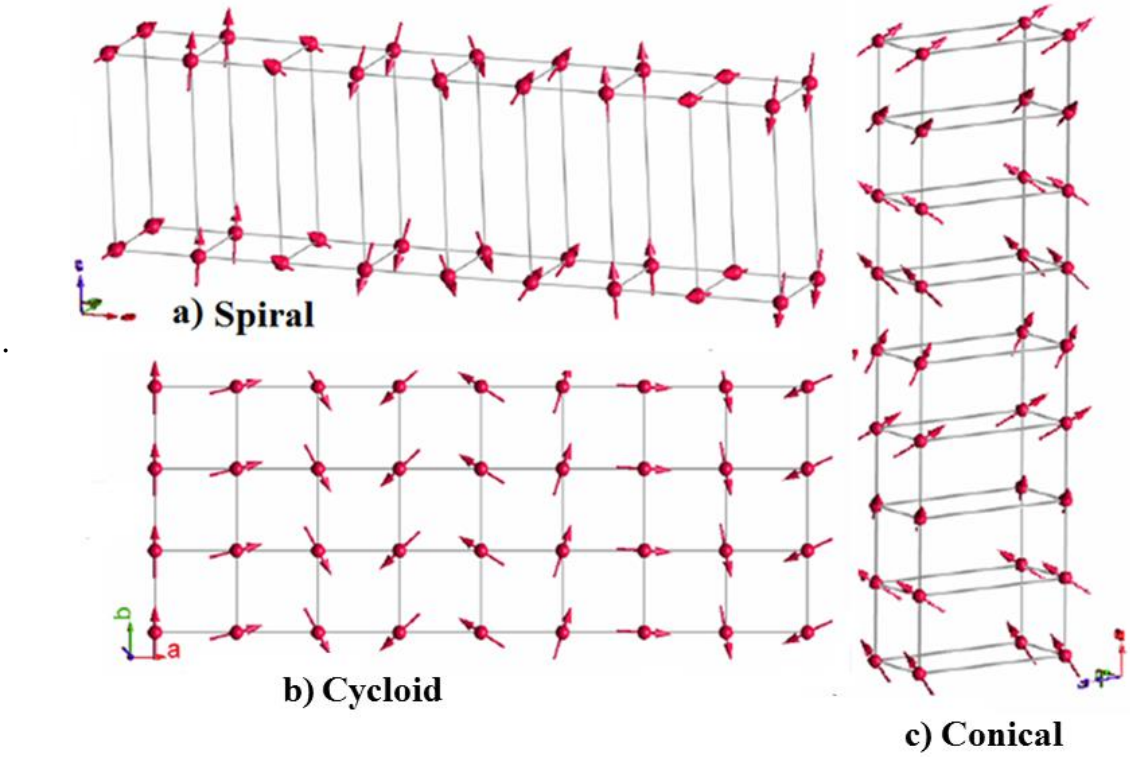

Figure 1.3 Examples of non collinear magnetic orderings (a) Spiral (b) Cycloid and (c) Conical. The magnetic moment for the cycloidal magnetic ordering lies on the plane of the page unlike the spiral and the conical magnetic ordering. Figure reprinted from presentation of Laurent Chapon entitled "Symmetry applied to magnetoelectrics and multiferroics" presented in the European School of Multiferroics in 2010.

1.2.3 Interactions between the magnetic moments (spins)

When the interactions of the neighboring spins are stronger than any other energy in the system, such as thermal energy, then long range magnetic ordering occurs. The transition takes places below the critical temperatures, which is called Curie and Neel Temperature in

the case of ferromagnetic and antiferromagnetic interactions, respectively. The emergence of a magnetic ordering, either ferromagnetic or antiferromagnetic, means that the system reaches its overall minimum energy. The interaction between spin at site i and the spin at site j, of a magnetic material under an external magnetic field H, can be described by the simple Hamiltonian:

$$H=-\sum_{(ij)} J_{ij} Si \bullet Sj + g\mu\beta \sum_j \mathbf{S}_j \bullet H \qquad (\mathbf{1.1})$$

The first term corresponds to the Heisenberg exchange energy, whereas the second term is the Zeeman energy. The J_{ij} is the exchange interaction between the two spins $\mathbf{S_i}$ and $\mathbf{S_j}$.The summation is made in all over bonds (ij). Each bond may have different exchange coupling constant and the spin $\mathbf{S}_i$ and $\mathbf{S}_j$ have values which depend upon the system's properties. When $J_{ij}>0$ then the interactions between the spins are ferromagnetic, whereas when $J_{ij}<0$ the system is antiferromagnetic.

The exchange interactions between the spins of electrons are a result of the magnetic dipolar interaction and the exchange interaction. The magnetic dipolar interaction, results from the spin which behaves as a magnetic dipole, so it creates energy that is proportional to the magnitude of the spin and inversely proportional to distance r ($1/r^3$) where r is the distance between the poles of the dipole (spin). The exchange interactions are dominated by quantum mechanical considerations, such as the Pauli Exclusion Principle and the Hund's rules. These interactions can be of various types, such as direct, superexchange, double and anisotropic (Dzyaloshiinski- Moriya DM) exchange interaction which is discussed in paragraph 1.4.6.1. Direct exchange comes from electrons which interact directly with other. Double exchange can be found in transition metals with mixed valence. More common though, is the superexchange interactions when two non-neighboring magnetic ions interact via a non magnetic ion (such as oxygen) which is situated in between them.

Interactions of Magnetic Moments in Lower Dimensional Magnetism[9]

The study of magnetic systems that refers to the interactions of spins in one (1D) or two (2D) lattice dimensions is referred as "lower dimensional magnetism". The magnetic ions are assumed to interact only with their nearest neighbors at a restricted space. This short range magnetic order eventually becomes long range order at a low temperature. The characteristic experimental signature of the low dimensional magnetism is the broad maxima at high temperatures observed at the curves of the magnetic susceptibility and the specific heat. Some examples of magnetic systems that are characterized by lower dimensional interactions are: the 1D or linear chain systems, the spin ladders, and the Spin-Peirls systems.

Low dimensional magnets show a variety of quantum mechanical effects operating within them. Hereafter we discuss the 1D chains and the spin ladders as they are highly related with the $NaMnO_2$ polymorhs studied in this thesis.

Linear or 1D chains

One of the systems studied in this work was characterized by fits of the magnetic susceptibility as a "1D chain" (Figure 3.6). A 1D chain (Figure 1.4a) can be an Ising, XY or Heisenberg system, meaning that its magnetic moments are aligned along one, two or three axis. The Hamiltonian of a 1D chain, for a Heisenberg system is given by the equation:

$$H=-2J\sum_i \mathbf{S}_{z,i}\mathbf{S}_{z,\,i+1} \qquad \textbf{(1.2)}$$

In a 1D chain, intra and inter chain interactions appear, the later become more dominant as the temperature is lowered. A typical example of these systems is the compound $Cu(NH_3)_4SO_4\cdot H_2O$.

***Spin ladders*[10, 11]**

Spin ladders are low dimensional magnetic quantum systems that are considered as the connection between 1D and 2D magnetic systems. They consist of a specific number of strongly magnetically coupled chains of infinite length and finite width. The exchange couplings J are found along the ladder's "rungs" ($J_{\perp}$) and "steps"($J_{\parallel}$). In an ideal spin ladder the exchange couplings along rungs and legs are very similar, that is $J_{\perp} \approx J_{\parallel}$. To characterize a system as spin ladder, data of the magnetic susceptibility are required (Figure 4.40). The exact nature of their ground state though, is characterized by neutron scattering, nuclear magnetic resonance (NMR) and muon spin resonance (μSR). Examples of two and three legs spin ladders are shown in Figure 1.4.

The Hamiltonian that describes these systems is:

$$H=- J_{\parallel} \sum_{a=1,2} \sum_{i=1}^{L} \mathbf{S}_{i,a} \cdot \mathbf{S}_{i+1,a} - J_{\perp} \sum_{i=1}^{L} \mathbf{S}_{i} \mathbf{S}_{i,2} \qquad \mathbf{(1.3)}$$

Where $S_{i,a}$ is the spin operator in the site i (i = 1, 2…..L) on the leg α (α = 1, 2…) of a ladder with L rungs. $J_{\perp}$ (J perpendicular) and $J_{\parallel}$ (J parallel) denote the intra and inter-rung exchange couplings, respectively.

The magnetic properties of a spin ladder depend on whether it has odd or even number of legs. Spin ladders with even number of legs, exhibit strictly short-range spin interactions along the legs, thus they are characterized by a spin liquid ground state. Even leg spin ladders are characterized by spin singlet pairs and the presence of a finite spin gap. On the contrary odd leg spin ladders behave quite similarly with a 1D antiferromagnetic Heisenberg chain at a low thermal energy showin gapless spin excitations.

Examples of compounds that have been classified as spin ladders are: $SrCu_2O_3$, the two leg spin ladders CaV_2O_5, [12] and the $(LaSr)CuO_{2.5}$[13]

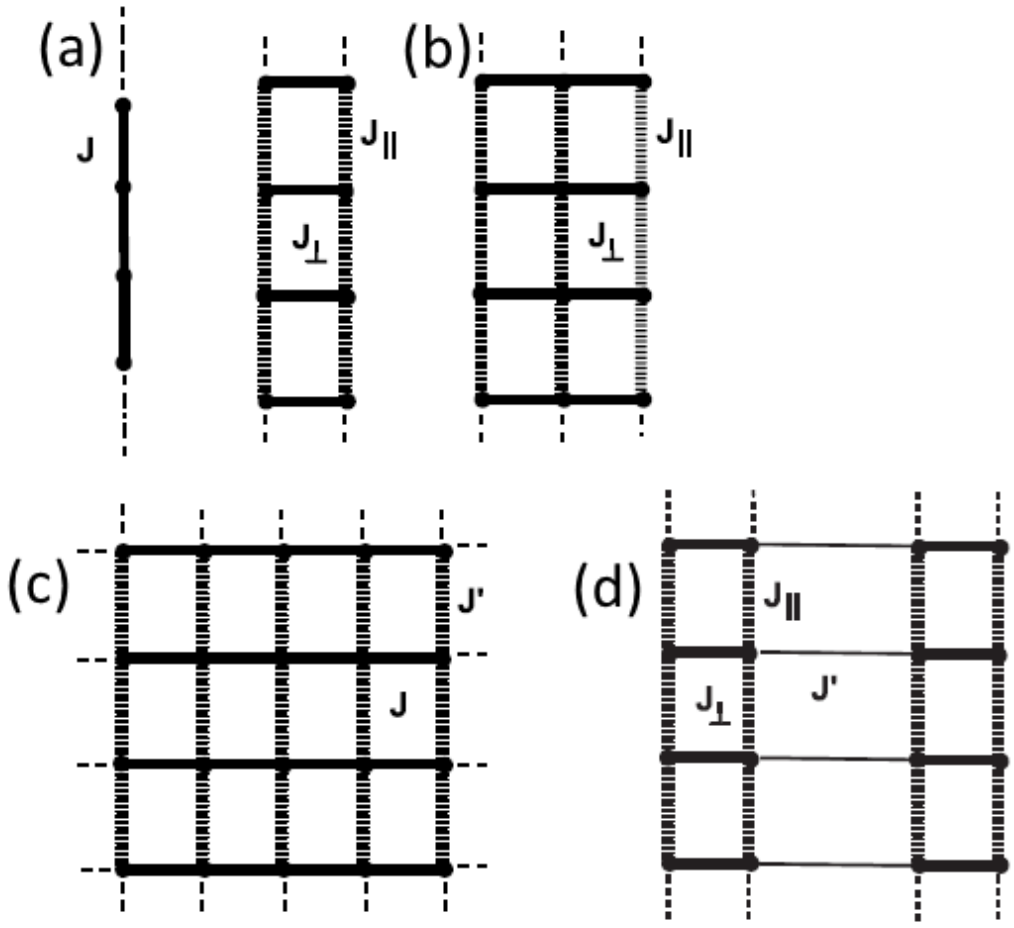

Figure 1.4 Representation of different kinds of low dimensional magnetic systems.a)1D chain b) two leg and three leg spin ladders.$J_{\|}$ and $J_{\perp}$is the coupling along chains and rugs, respectively c) 2D square lattice with exchange coupling costants J and J´.d) Two leg ladder showing intra-ladder ($J_{\|}$ and $J_{\perp}$) and inter-ladder (J´) exchange couplings. Black dots denote spin units whereas continuous and dashed lines represent antiferromagnetic interactions of different strength. Reprinted from Reference 10.

1.2.4 What an experimentalist observes and measures [14, 15, 16]

In order to understand the magnetic behavior of a material one should check how the material behaves under the application of an external magnetic field. The response of a magnetic material to an applied magnetic field **H** is measured by its magnetization **M**. The magnetization **M** is defined as the magnetic moment (m) per unit volume (V)

$$\mathbf{M}= \frac{\mathbf{m}}{V} \text{ (emu/cm}^3\text{)} \qquad (\mathbf{1.4})$$

Magnetization is a property of the material, and depends on the magnetic moments of the spins and the spins interaction and alignment.

In a magnetic solid the relationship between the magnetization **M** and the applied field **H (**A/m**)** is called the magnetic induction (or magnetic flux) and is expressed by:

$$\mathbf{B}=\mu_o (\mathbf{H}+\mathbf{M}) \qquad (\mathbf{1.5})$$

where μo is the permeability of the free space. The unit of B is Tesla (T) or Oersted (Oe) also called as gauss-G, where 1 T=10^4 Oe.

The induction divided with the field is called permeability μ, and corresponds to the amount of the magnetic flux that passes through the material:

$$\mu=\frac{\mathbf{B}}{\mathbf{H}} \text{ (gauss/Oe)} \qquad \mathbf{(1.6)}$$

Dividing the Magnetization with the applied field gives, gives the susceptibility χ:

$$\chi=\frac{\mathbf{M}}{\mathbf{H}} \quad \text{(emu/(cm}^3\text{Oe)} \qquad (\mathbf{1.7})$$

by which one can validate how responsive is the magnetic material under an external magnetic field. It is also common to express the susceptibility χ per unit mass, in that case the units of χ are: (emu/ (grOe)).

Taking into account that

$$\mathbf{M}=N\mu_\beta g\left[\frac{2J+1}{2J}\coth\left(\frac{2J+1}{2J}\alpha\right)-\frac{1}{2J}\coth\left(\frac{\alpha}{2J}\right)\right]=N\mu_\beta gJB_{J(\alpha)} \quad \textbf{(1.8)}$$

Where

μ_β is the Bohr magneton, g is the Lande factor, β is the Boltzman constant, J is the total angular momentum of a single ion, and N is the number of free spins

And $B_{J(\alpha)}=\frac{J+1}{J}\alpha-\frac{[(J+1)^2+J^2](J+1)}{90J^3}+\ldots\ldots$ (where $\alpha=Jg\mu_BH/k_BT$)

is the Brillouin function written as a Taylor series, which is equal to the Langevin in the limit that $J \to \infty$. For small magnetic fields, we keep only the first term in the Taylor expansion, which yields the Curie Law[15]

$$\chi=\frac{\mathbf{M}}{\mathbf{H}}=\mu_\beta^2 g^2 NJ(J+1)/k_\beta 3T=\frac{C}{T} \quad \textbf{(1.9)}$$

1.2.5 Curie and Curie- Weiss Law

The Curie Law supports that the susceptibility of a paramagnet is inversely proportional to its temperature

$$\chi=\frac{C}{T} \quad \textbf{(1.10)}$$

where C equals to $$C=\frac{\mu_\beta^2}{3k_\beta}Ng^2J(J+1) \quad \textbf{(1.11)}$$

and J is the angular momentum quantum number (see equations 1.8-1.9)

In magnetic systems where at a critical temperature below which a ferromagnetic or antiferromagnetic ordering develops, equation 1.10 becomes:

$$\chi=\frac{C}{T-\theta_w} \quad \textbf{(1.12)}$$

Curie's Weiss Law predicts a dependence of the inverse susceptibility χ with the temperature T, for high temperatures and small fields. θ_w is the Curie-Weiss temperature above which the material becomes paramagnetic. When the material develops an

antiferromagnetic order below its T_N (T_{Neel}), then θ has a negative value, hence equation 1.12 becomes

$$\chi = \frac{C}{T-(-\theta_w)} \qquad \textbf{(1.13)}$$

Moreover the Curie-Weiss law is used for the analysis of experimental data, ploteed as the inverse magnetic susceptibility $1/\chi$ (Figure 1.5). A linear fit ($y=a+b\cdot T$) of the $1/\chi$ plot results in the value of the slope and the constant term which are equal to the effective moment ρ and the θ_w respectively, according to the equations:

$$\rho=\sqrt{g^2\, S(S+1)} \qquad \textbf{(1.14)}$$

and

$$\theta_w = 2zJS(S+1)/3k\beta \qquad \textbf{(1.15)}$$

where z is the number per nearest neighbors per spin and J is the effective magnetic interaction with one nearest neighbor.

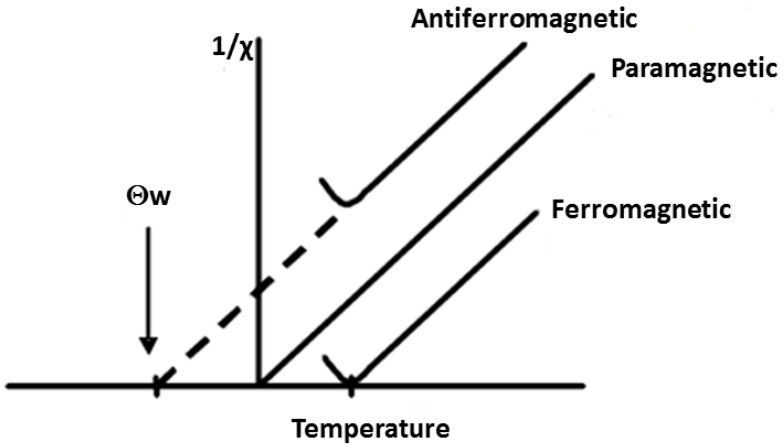

Figure 1.5 The linear fit of the plot $1/\chi$ versus T, yields two values which are essential for the characterization of a magnetic material: a) the effective magnetic moment and b) the Curie temperature θ_w. The above figure shows the θ_w temperature in the case of ferromagnetic ($\theta_w>0$), paramagnetic ($\theta_w=0$) and antiferromagnetic ($\theta_w<0$) ordering.

1.3. Geometric Magnetic Frustration

The basic concept of frustration and its different sources are illustrated in Figure 1.6. [17] In paragraphs 1.3.1-1.3.5 we discuss the relevance of magnetic frustration with this thesis, its origin and the most common frustrated lattices and magnetic systems.

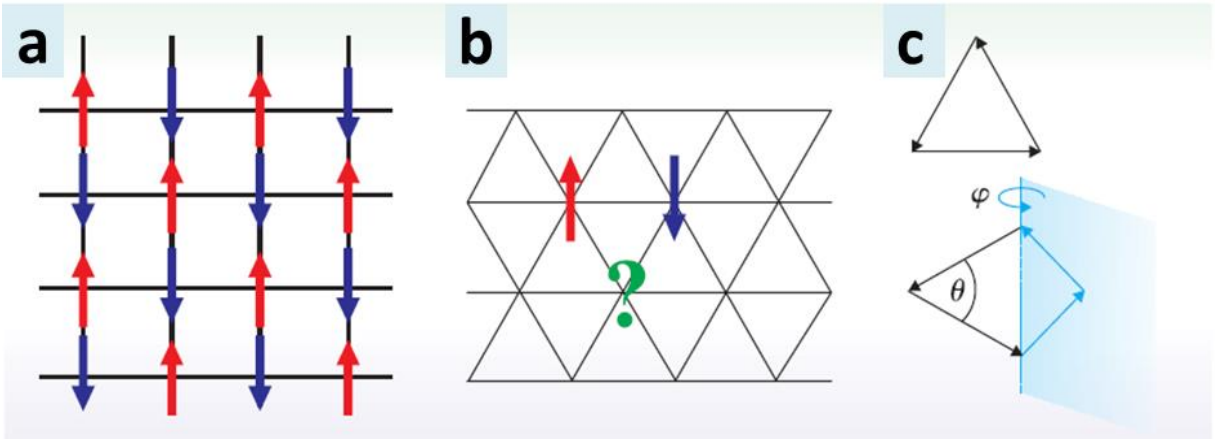

Figure 1.6 A geometrically frustrated system is one in which the geometry precludes the simultaneous minimization of all interactions.(a) In the unfrustrated antiferromagnet on the square lattice each spin can be antialligned with all each neighbors. (b) On a triangular lattice, such a configuration is impossible: Three neigbhoring spins can not be pairwise antialligned, and the system is frustrated. (c) The ground states of a cluster of Heisenberg spins have zero total spin, so the vector sum of an elementary group of spins must add up to zero. A cluster of three spins forms a unique structure, whereas four spins form a family of degenerate ground states, with θ and φ the structure's two degrees of freedom. Reprinted from Reference 17.

1.3.1 Why Geometric Frustration is related to this thesis

In magnetic systems, frustration arises from competing interactions and results in a degenerate ground state. The energy of all pair – wise interactions can not be minimized simultaneously due to the magnetic moments alignment on specific lattice topologies like the triangular topology or the Kagome lattice.[18] The large degeneracy of the ground state leads to excited states and novel physical phenomena related with various phase transitions. Specifically when the magnetic frustration is dictated complex magnetic

structures emerge. Recently it has been found that magnetic frustration plays a key role to the appearance of the magnetoelectric coupling.[1, 5] This new class of magnetoeletrics, often named as induced magnetoelectrics, such as $TbNiO_3$, NiV_3O_8, $CuCrO_2$ is characterized by a magnetic phase transition to a spiral order which promotes ferroelectric order. The aim of this work is to discover new magnetoelectric compounds derivatives of the delafossite structural type in which the magnetoelectric coupling is related with the magnetic frustration.

1.3.2 The origin of Frustration

The ground state of a closed thermodynamic system is the one which is characterized by its minimum overall energy. The minimization of the energy is predicted by the third law of thermodynamics which states that when the temperature of a perfect crystal reaches at 0 K its entropy should also become zero. One could possibly assume that each system is characterized by a unique macroscopic state which leads to the minimization of the energy, hence its ground state. However in 1933[19, 20] calculations on the entropy of water ice molecule showed a difference of $S_0 = 0.82 \pm 0.05$ cal/(mol·K) = 3.4 J/(mol·K) in the values between the calculated entropy and the one predicted by the theoretical model of an ideal gas. If the result of the residual entropy was indeed true, then water ice molecule would seem strangely not to obey the third law of thermodynamics.

The term frustration was introduced by Pauling [20] in order to solve the paradox of the appeared residual entropy in the water ice molecule. Pauling proposed that the disorder in water ice molecules results from the possible distances of the hydrogen bonds between the hydrogen atoms and the oxygens. The bonds are not situated in half way between the O-H distances. Specifically, for each oxygen atom, there are two different positions of a hydrogen atom: two hydrogen atoms are located near and two far from it, according to the so-called, 'ice-rules' originally formulated by Bernal and Fowler.[21] In other words, frustration comes from the different positions of the hydrogen atom in the O-H bond, by which the water molecule maintains its structure and reaches its ground state.

1.3.3 Frustration in Magnetic Systems

Frustration in magnetic systems arises from the incompatibility between the geometry of the spin arrangement and the spin interactions. To illustrate the simple case where there are no competing interactions, hence no frustration, the antiferrmagnetic allignement of the spins in a square lattice is examined. Assume that the spins are constrained on the plane of the page, are represented as vortices and can either point up or down, namely they are "Ising" spins. The square geometry of the lattice and the antiferromagnetic configuration of the magnetic moments are easily combined, thus the system exhibits a long range antiferromagnetic order as shown in Figure 1.7.

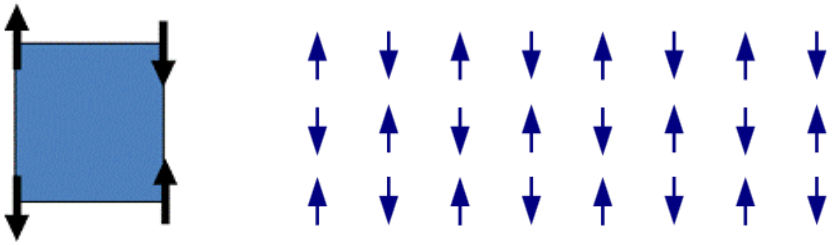

Figure 1.7 Non frustrated interactions: Antiferromagnetic alignment of the spins on a square lattice (left) and the resulting long range antiferromagnetic order (right). Right part of the Figure reprinted from http://en.wikipedia.org/wiki/Antiferromagnetism

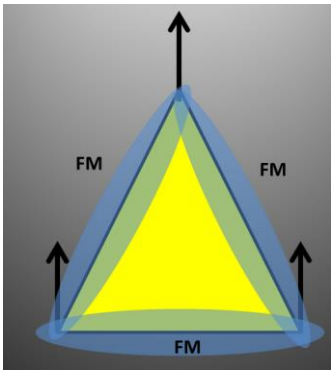

Figure 1.8 Non frustrated interactions: Ferromagnetic alignment of three Ising spins on a equilateral triangle.

Likewise the ferromagnetic arrangement of three Ising spins on an equilateral arrangement leads to the minimization of their bipartite interactions since all of the magnetic moments can simultaneously point at the same direction (Figure 1.8). Thus, there are two possible spin configurations, all spins pointing up or down, which lead to the macroscopic minimization of the overall energy, and finally the system reaches its ground state.

On the contrary the simplest case of geometric magnetic frustration occurs upon the antiferromagnetic configuration of three Ising spins on a triangular lattice. Only the two out of the three spins can simultaneously satisfy the antiferromagnetic interaction. The third spin, for example the one illustrated on Figure 1.9[22] on the bottom right, causes the

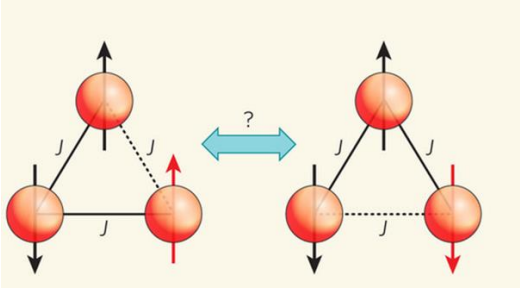

Figure 1.9 Illustration of geometric magnetic frustration on a triangular lattice. Only two of the three spins can be antiferromagnetically aligned minimizing their bipartite interactions. Reprinted from Reference 22

There are six spins configurations resulting [23] in the lowest energies, so in a triangular lattice there are six possible microscopic states leading in the minimum energy of the ground state. Since an antiferromagnetic allignment is not possible for obtaining a long range magnetic order, the best compromise results in the configuration in which neighboring spins are oriented by forming 120˚ deg angles relative with each other. [24] The result is a non collinear long range magnetic order like the helical or cycloidal magnetic structures.

1.3.4 Other Frustrating Lattices

We have highlighted the case where geometric magnetic frustration is caused by the triangular lattice topology, since this topology is related with the materials of this work. However, it is important to note here that there are other types of geometries in a lattice that could yield magnetic frustration and moreover it is not only evidenced in the Ising like spins, but also in the XY[25] (when the spins can move along two axis) and Heisenberg spins [26] (when the spinc can move along three axis). Most common lattices where frustration occurs is the 2D the triangular lattice, such as α-$NaMnO_2$, [7, 8]and the 2D Kagome lattice found for example in the $Ba_2Sn_2Ga_3ZnCr_7O_{22}$. [27] An example of 3D topology is the pyroclore lattice such as $YCaNb_2O_7$. [28]Examples of frustrated lattices are shown in Figure 1.10. [29]

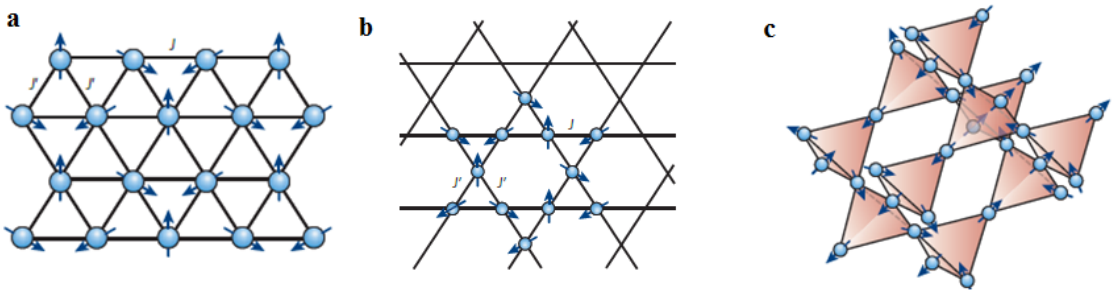

Figure 1.10 Types and examples of systems of frustrating lattices. Reprinted from Reference 29.

1.3.5 Frustration in Spin Glasses

Spin glasses is a fascinating topic of condensed matter physics primarily related with the concept of frustration. The 1970's is characterized by a tremendous interest in this field, evident first by the various theories related to the short range interactions among the frozen spins below the spin glass temperature and second, by the experiments carried out which provided the signatures of the spin glass behavior.

Undoubtedly, one may refer to many interesting observations for the vast and continuously growing subject such as spin glasses. Nevertheless, for the scope of the current thesis, it is useful to focus to the concepts related to frustration and spin glasses which are essential for the understanding of the results in chapter 5 which concern the glassy behavior of the birnessite like compound.

A spin glass is a disordered and frustrated system. Starting by the definition given by Mydosh [30] "*spin glass is a random, mixed, interacting, magnetic system characterized by a random yet co-operative freezing of spins at a well defined temperature T_f below which a highly irreversible, metastable frozen state occurs without the usual long range spatial magnetic order*"

It is critical to shed light on two questions: a) what is the origin of frustration in spin glasses and b) how the short range magnetic order is established below the glass transition.

Frustration in spin glasses arises from site disorder or bond disorder.[30] Site disorder is equivalent to structural disorder, so it occurs when there is a discontinuity in the periodicity of the crystal lattice, as it happens when an atom is dislocated or missing from the lattice. Bond disorder arises when a bipartite magnetic interaction is different from the majority of the rest interactions as illustrated in Figure 1.11 (reprinted from [31]).

In other words, randomness, hence frustration, is the corner stone property of a spin glass. A way to create a spin glass is to dope with magnetic impurities a non magnetic host material. An example of this case can be found in Mydosh's book[30], where the CuMn system is extensively studied as a prototype and canonical spin glass.

To answer the question stated above, i.e how it is possible to have a short range order despite the existence of frustration, it is helpful to visualize that the spin glass, at $T > T_f$, consists of numerous domains or clusters. These domains are separated by large energy barriers which prevent the system to possess one single macroscopic state of minimum energy. Two competing forces define the formation of the domains: the short range exchange interaction between two spins of distance r_{ij}, $J(r_{ij})$ and the thermal fluctuations given by k_BT.

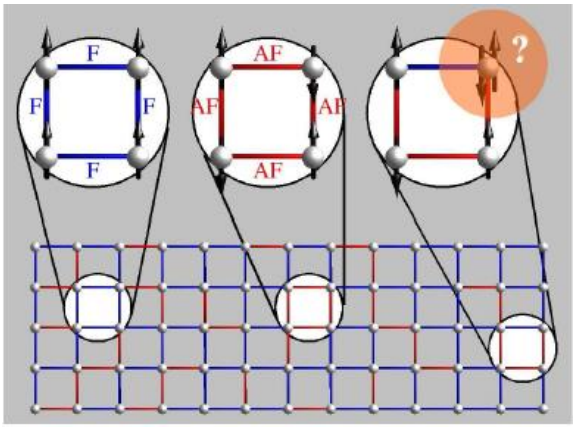

Figure 1.11 Schematic illustration of bond disorder. A cubic lattice where the allignment of spins can be either ferromagnetic (blue bonds on the left) or antiferromagnetic (central disk with the antiferromagnetic bonds shown in red). In these cases the minimization of the energy is possible. On the contrary when a spin does not have a unique orientation (right disk), leading to odd numbers of antiferromagnetic or ferromagnetic interactions, a bond disorder is caused. The competing ferromagnetic and antiferromagnetic interactions can be the basic ingredient of frustration in spin glasses. Reprinted from Reference 31.

When $J(r_{ij}) > k_B T$ a group of spins forms a magnetic cluster. The spins move to random directions, and they slow down only when they join a cluster. The total magnetic moment of the clusters has random orientation, yet it is characterized by a correlation length ξ, which increases as the temperature decreases and reaches close to $T_{f.}$ This procedure results in magnetic clusters of various shapes and different relaxation times. As T reaches T_f preffered orientations, in random directions are established in the crystal. At $T=T_f$ an infinite cluster is formed whose building blocks are smaller clusters frozen in random orientations.

It clear then that the spin glass state is a metastable state, whose dynamics has wide distribution of relaxation times. What is important to define in order to characterize the nature of interactions in a spin glass, is the values of the energy barriers between the

clusters and the relaxation times τ. Dynamic magnetic susceptibility measurements and relevant analysis provides the answers concerning the magnetic interactions of a spin glass.

1.3.6 Experimental Realization of Frustration

An important question that arises here is how the magnetic frustration can be observed experimentally. Magnetic frustration can be probed independently by two experiments: by measuring the heat capacity and the magnetic susceptibility [18, 27]

The fingerprint of frustration is given by plotting the inverse susceptibility $1/\chi$ (mole/emu) versus temperature T (K). The fit obtained by the Curie Weiss law (already discussed in section 1.2.5) yields the Curie Weiss temperature θ_w. For frustrated antiferromagnetic systems an empirical measure of frustration is estimated by the ratio:

$$f=-\frac{\theta_w}{T_N} \qquad \textbf{(1.16)}$$

where T_N is the Neel Temperature. Values of f higher than 1 ($f>1$) indicate frustrated interactions.[18]

Specifically, for the case of spin glasses various experiments can be carried out in order to verify the existence of the glassy state. These are discussed in the next paragraphs.

Generally, the first step to spot a spin glass transition is to observe a peak at the transition temperature. There are three fingerprints of the spin glass behavior:

a) The bifurcation of the static (DC) susceptibility of the ZFC-FC magnetization curves at $T< T_f$ under small external magnetic fields. The sample is first cooled under zero magnetic field (ZFC measurement) and afterwards when cooling the sample under an applied magnetic field (FC measurement). Usually below T_f the ZFC shows a sharp decrease whereas the FC curve is approximately flat. This experiment marks the irreversibility of the ZFC-FC curves, but it is not exclusively related to a spin glass behavior.

b) High magnetic fields (even below 1 T) destroy the spin glass transition. This can be clearly seen in experiments presenting the evolution of the magnetic susceptibility versus T under different external magnetic fields which show a continuous broadening of the spin glass peak and finally the elimination of the peak at the highest applied magnetic field. The

temperature of the maximum shifts towards lower temperatures, which can be described by the Gabay-Toulouse line in case of XY or Heisenberg spins or the Almeida Thoughless line in case of Ising spins. The same experiment can be off course carried out while measuring the dynamic (AC) susceptibility.

c) Aging and rejuvenation experiments. Both of these experiments aim on defining the relaxation processes involved in the spin glass state. In an aging experiment, what is measured is the relaxation times of the magnetization. The sample is cooled under a small field at a $T<T_f$ and after waiting for a specific amount of time (t_w), then the applied field is cut of. Magnetization is then measured as a function of the observation time. Two features correspond to a spin glass behavior: i) the magnetization relaxation is slow and ii) the magnetization is highly depending on the waiting time: the longer the waiting time the slower the relaxation (aging).

Rejuvenation experiments show memory effects, relevant with the spin glass behavior. The first step, which is used as a reference experiment, is to measure the susceptibility M(ref) of a zero field cool (ZFC) protocol under a small magnetic field. Then the following measurements are again carried out on a ZFC mode but upon cooling there is a waiting time t_w, at a $T_w<T_f$. The magnetization is then measured upon heating versus temperature (Mt_w). The memory effect of the glassy state is evidenced by plotting the difference $M_{(t_w)}-M_{(w)}$ which should show a dip of the curve at the temperature T_w of the waiting time.

The aforementioned experiments of magnetometry are the most fundamental in order to probe frustration and the spin glassy state. Other methods, corresponding to shorter relaxation times such neutron spin echo experiments, can be applied but it is beyond the purpose of this thesis to analyze them.

1.4 Multiferroics and Magneto-electrics

1.4.1 The definitions

The term "*multi-ferroic*" is attributed to Schmid in 1994: "*Crystals can be defined as multiferroics when two or more of the primary ferroic properties coexist in the same phase*". [32] Ferroic properties refer to ferroelectricity, ferromagnetism and ferroelasticity. In the ideal case, a multiferroic compound exhibits spontaneous magnetization so it is magnetically polarizable, but at the same phase it shows spontaneous polarization thus it is electrically polarizable. The "coupling" between the electric and magnetic degrees of freedom means that the magnetization can be affected by an electric field [2] and *vice versa*, the polarization can be controlled by a magnetic field. The graphical illustration of the definition is shown in Figure 1.12. The coexistence of at least two types of order is appealing for two reasons: a) it brings out novel physical phenomena and b) it can be used in multifunctional devices. The technological applications of these oxides include magneto-electric sensors, magnetic memories controlled electricalyl such as the highly desirable four-state logic devices (both up and down polarization and both up and down magnetization).

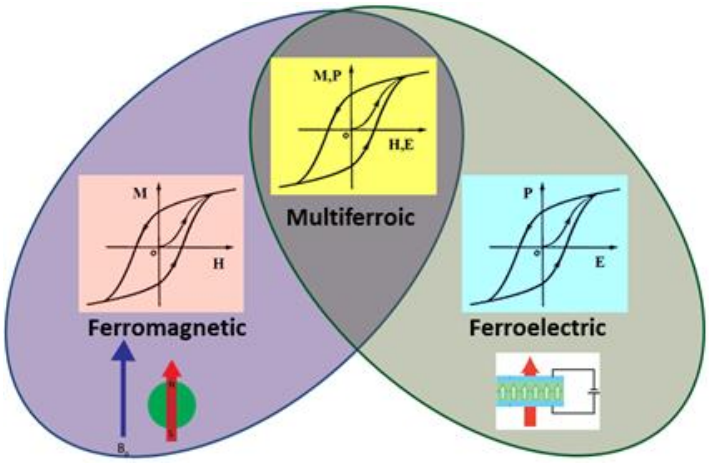

Figure 1.12 Illustration of the definition "multiferroism": Materials that combine ferroelectric and ferromagnetic order at the same phase. This characteristic property allows an external magnetic field to modify the polarization hysteresis loop and similarly an electric field to affect the magnetization loop.

Important to note here, that strictly according to the definition a "multiferroic magnetoelectric" exhibits spontaneous polarization and spontaneous magnetization at the same phase. The case of multiferroic which combines both ferromagnetic and ferroelectric order is very rare, due to restrictions imposed by structural, physical and electronic properties.[33]

In the current trend though, the definition that is widely used is the "magnetoelectrics" which is a broader one and includes more materials.[34] Magnetoelectrics are systems who exhibit the magnetoelectric coupling which is defined as: '*the induction of electric polarization (magnetization) by an external magnetic (electric) field'.*[1] The term magnetoelectrics refers to materials that exhibit any kind of magnetic order including antiferromagnets, spiral magnets, weak ferromagnets, even paramagnetic ferroelectrics.[35] Hereafter, the terms multiferroic or magnetoelectric are going to refer to the coupling of electric and magnetic fields in matter.

1.4.2 The early historical background

Despite the fact that the magnetoeletric effect met a breathtaking revival around the early 1970's, the very first concepts of magnetoelectric coupling are found before the 19th century. It was Maxwell at 1873[36, 37] who predicted the interplay between magnetism and electricity in his groundbreaking equations. The magnetization of a dielectric placed in an electric field was observed by Roetgen, [38] which was followed by the observation of the reverse phenomenon: the polarization of a moving dielectric in a magnetic field.[39] A strong coupling between the magnetic and electric degrees of freedom was observed in an insulator as an intrinsic property of matter, at 1894 by Piere Curie. Curie even then claims that "*it is the symmetry that creates the phenomenon*", recognizing that the magnetic symmetry is the key ingredient for the existence of magnetoelectricity. The term "magnetoelectric" is tracked for the first time by Debye.[40]

The real beginning of the magnetoelectric phenomenon starts in 1959 by Landau and Lisfitz. [41] These the first to realize the concept of the linear magnetoelectric effect. They supported that there could be matetials with specific magnetocrystalline symmetry which would allow a linear coupling between electric and magnetic fields. The same year Dzyaloshinksii[42] predicts and soon after Astrov[43] observes the magnetoelectric coupling in Cr_2O_3 in 1960. Up to now (2014) there have been synthesized and reported more than 100 magnetoelectrics, a number which is continuously increasing.

1.4.3 The linear magnetoelectric effect [34, 44, 45]

The magnetoelectric effect in a single crystal can be described thermodynamically, by the Landau theory, using the expansion of the free energy F. The free energy for a non –ferroic single crystal, with no polarization of magnetization under zero external fields, is given by:

$$F(\vec{\mathbf{E}}, \vec{\mathbf{H}}) = \mathbf{F}_o - \mathbf{P}_i^s\mathbf{E}_i - \mathbf{M}_i^s\mathbf{H}_i - \frac{1}{2}\varepsilon_o\varepsilon_{ij}\mathbf{E}_i\mathbf{E}_j - \frac{1}{2}\mu_o\mu_{ij}\mathbf{H}_i\mathbf{H}_j - \alpha_{ij}\mathbf{E}_i\mathbf{H}_j$$
$$-\frac{1}{2}\beta_{ijk}\mathbf{E}_i\mathbf{H}_j\mathbf{H}_k - \frac{1}{2}\gamma_{ijk}\mathbf{H}_i\mathbf{E}_j\mathbf{E}_k \qquad \textbf{(1.17)}$$

Where F_o is the ground state free energy, **E** is the electric field, **H** is the magnetic field, $\mathbf{P}^s$ is the spontaneous magnetization, and $\mathbf{M}^s$ is the spontaneous magnetization, ε and μ denote the electric and magnetic susceptibilities hence ε_o and μ_o are the electric and magnetic susceptibilities in vacuum. The subscripts (i, k, j) correspond to the spatial coordinates of the three axes (x, y, z).

The term $\alpha_{ij}(T)$ is called the "magnetoelectric coefficient" and corresponds to the linear magnetoelectric coupling, whereas the terms β_{ij} and γ_{ij} represent high order magnetoelectric coefficients.

If the three terms of equation (1.17) give a sum greater than 0, then the following stability condition holds for the magnetoelectric coupling term α_{ij}:

$$\alpha_{ij}^{2} \leq \varepsilon_o\mu_o\varepsilon_{ij}\mu_{ij} \qquad \textbf{(1.18)}$$

Polarization **P** and its dependence from the magnetic field, is given by the differentiation of equation (1.17) with respect to $\mathbf{E}_i$:

$$\mathbf{P}_i(\vec{\mathbf{E}}, \vec{\mathbf{H}}) = \frac{-\partial\mathbf{F}}{\partial\mathbf{E}_i} = \mathbf{P}_i^s + \frac{1}{2}\varepsilon_o\varepsilon_{ij}\mathbf{E}_j + \alpha_{ij}\mathbf{H}_j + \frac{1}{2}\beta_{ijk}\mathbf{H}_j\mathbf{H}_k + \frac{1}{2}\gamma_{ijk}\mathbf{H}_i\mathbf{E}_j\mathbf{E}_k \qquad \textbf{(1.19)}$$

Similarly magnetization **M** is calculated by the differenatition of the the free energy in equation 1.17 with respect to **M**:

$$\mathbf{M}_i\ (\vec{\mathbf{E}},\vec{\mathbf{H}}) = \frac{-\partial F}{\partial \mathbf{M_i}} = \mathbf{M}_i^s + \mu_o\mu_{ij}\mathbf{H}_j + \alpha_{ij}\mathbf{E}_i + \beta_{ijk}\mathbf{E}_i\mathbf{H}_j + \frac{1}{2}\gamma_{ijk}\,\mathbf{H}_i\mathbf{E}_j\mathbf{E}_k \qquad \textbf{(1.20)}$$

It is crucial to underline here that the linear magnetoelectric coupling does not hold for all types of materials. In cases where the dielectric susceptibility or the magnetic susceptibility is too small, the high order terms β_{ij} and γ_{ij} dominate, hence the non linear magnetoeelectric coupling applies. Moreover, when there are effects like magnetostriction, there are more variables in equation (1.17) which correspond to strain and the "indirect coupling" is a more suitable term. Even though the Landau theory provides a qualitavive frame for the magnetoelectric coupling, the differences that may apply in various types of materials and different mechanisms of coupling, can be fully understood and explained only when the magnetic symmetry of the material is known.

1.4.4 Requirements for a magnetic Ferroelectric: The symmetry considerations

There are various restrictions and microscopic phenomena that tend to exclude the mutual existence of magnetism and ferroelectricity in the same compound.

The first one comes from the incompatibility of the partially filled d shells, a necessary condition for the existence of magnetic ordering, as stated in paragraph 1.2.1, and the fully occupied d-shells for the appearance of ferroelectricity.

Most importantly, the second constraint comes from the aspect of symmetry. A multiferroic can exist only when both time reversal and spatial inversion symmetry are broken. Statistically, the co-existence of magnetism and ferroelectricity is possible in only 13 groups out of the 122 Subnikov's magnetic point symmentry groups. Nevertheless, the magnetic materials are not equally distributed among the magnetic point groups, so the 13 groups available for the existence of multiferroism, is definitely a restriction, but does not describe the issue in a complete way.

In a ferroelectric material the presence of electric dipole is allowed only when the spatial space symmetry is broken. That is since an electrical dipole is attributed to the splitting of the negative and positive charges of the unit cell, which leads to the differentiation of the one side of the chemical cell in respect to the other. If the cell is centro-symmetric, this can not happen, so polarization will not build up in the system. In other words, spatial inversion symmetry breaking is the premise of ferroelectricity.

As for the existence of the magnetic ordering, spatial inversion symmetry is not a precondition since the spin acts as a pseudovector, thus the spin's direction remains unchanged under the spatial inversion symmetry. However, the breaking of the time reversal symmetry switches the direction of the spins, i.e the direction of the magnetic ordering. Time reversal symmetry in respect to the spins ordering is the symmetry operation by which spins remain randomly oriented in the paramagnetic state, but their direction can be switched when they are in the magnetically ordered state. Time reversal though, does not affect the direction of the dipole moment. Hence, the existence of a multiferroic is based on both the time reversal and spatial inversion symmetry breaking.

1.4.5 Classification of Multiferroics and Relevant Examples

Mulitiferroics can be classified in three major categories: a) The type one multiferroics in which the ferroelectric transition occurs in temperatures higher than those of the magnetic order, hence, the mechanism of the ferroelectricity does not depend on the magnetic order. b) The type II multiferroics, or the "magnetic multiferroics" in which the ferroelectricity is related to the magnetic order, and thus occurs at the same or at lower temperatures of the magnetic transition. c) The "disordered multiferroics" whose basic characteristic is the disorder (glassy state) and may exist in one or two ferroic orders. [46]

Type I multiferroics

The major advantages of type I multiferroics is that the coexistence of the magnetism and ferroelectricity usually occurs well above room temperature. Unfortunately, their most basic disadvantage is that the magnetoeletric coupling is weak. Examples of the type I, or

the "old multiferroics" as they are named, include mostly perovskites such as the $BiFeO_3$, which is probably the best well known multiferroic. Hexagonal manganites such as the the $YMnO_3$ [47, 48] is also classified in this category. Specifically, in $YMnO_3$ ferroelectricity is not attributed to the mangetic cations Mn^{+3}, but it is caused by the tilting of the MnO_5 block.

Type II multiferroics

The properties of type-II multiferroics are exactly the opposite: the coupling is strong but it occurs in rather low temperatures. Clearly, the holy grail of multiferroics is a material with strong magnetoelectric coupling in room temperature. Usually, ferroelectricity appears as an effect of a spiral or cycloid magnetic order. In this category belong the following oxides: $TbMnO_3$ [3] $TbMn_2O_5$[48], $Ni_3V_2O_{8,}$[49] the, $CuFeO_2$, $ACrO_2$ [50]and $AgFeO_2$[51] as well as the $CaMn_7O_{12}$[52] with the recently discovered giant polarization.

Type III multiferroics

Type III multiferoics are common among spin glasses such as the $PbFe_{0.5}Nb_{0.5}O_3$ [53] or the $Sr_{0.98}Mn_{0.02}TiO_3$.[54] The magnetoelectric coupling depends on the nature of the dynamic component, in other words, the cause of the disorder.

The materials of this thesis belong to the second category, since the magnetic frustration and the complex magnetic structures generate the magneto-electric coupling.

1.4.6 Magnetoelectric coupling and Mechanisms in type II-multiferroics

This paragraph refers to two of the basic mechanisms that been proposed for the appearance of the magnetoelectric coupling in type II-multiferroics. It is of outmost importance to clarify here that each compound which exhibits the magnetoelectric coupling should be and has been studied separately on the basis of symmetry considerations. The intention is not to generalize or oversimplify a complex phenomenon,

rather than to categorize some of the most frequent mechanisms that have been proposed for the magnetic ferroelectrics.

The first one refers to the Inverse Dzyaloshinksii Moriya (DM) interaction. This mechanism holds for the induced polarization which is perpendicular to the propagation vector of the spins. The second one, is the spin orbit interaction and it is valid for the induced polarization whose direction is parallel to the propagation vector of the magnetic ordering.

1.4.6.1 The Inverse Dzyaloshinskii Moriya Interaction

The first mechanism usually called "*the inverse Dzyaloshinskii-Moriya interaction*[55, 56] or the "spin current model" as proposed by Katsura for cycloid magnets,[57] suggests that canted spins moments on two neighboring magnetic sites $\mathbf{S_i}$ and $\mathbf{S_j}$ induce polarization which is given by the equation:

$$\mathbf{P}=A\ \mathbf{e}_{ij}\times(\mathbf{S}_i\times\mathbf{S}_j) \qquad (\mathbf{1.21})$$

Where A is the coupling constant related to the spin-orbit coupling and the spin exchange interaction, $\mathbf{e_{ij}}$ denotes the unit vector along the direction from site i to j (Figure 1.13[57]). This mechanism is based on the following concept: The Dzyaloshinskii-Moriya (DM) interaction between two magnetic ions refers to the anisotropic interaction between the excited state of the one magnetic cation and the ground state of the other. It results in the canting of the two interacting spins, this means that the spins are not parallel to each other but rotated by a small angle. The canted spins, produce a spiral state, which can displace the ion in between them, i.e the oxygen, through magnetoelastic effects. The atomic shifts generate the Dzyaloshinskii-Moriya (DM) vector or the ferroelectric polarization. The DM interaction explains successfully the ferroelectricity observed in $TbMnO_3$,[3] $DyMnO_3$[58] $Ni_3V_2O_8$,[49] $CoCr_2O_4$[59] and $MnWO_4$.[60]

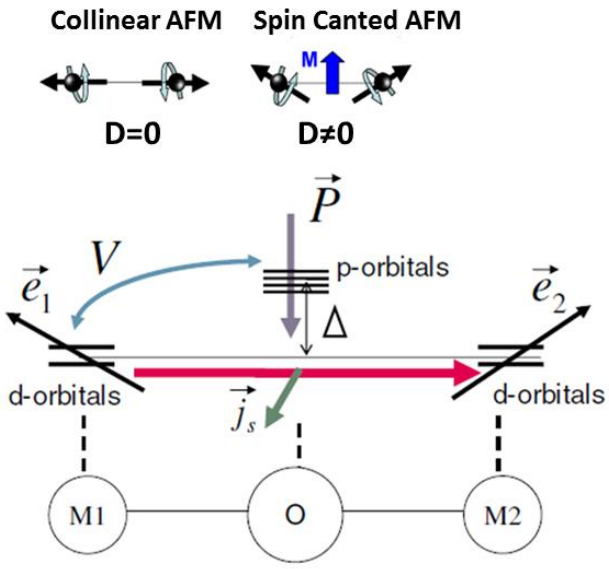

Figure 1.13 The result of the Dzyaloshinskii Moriya interaction between two magnetic ions leads to the DM vector (D≠0) and the canting of the spins. M_1 and M_2 denote the magnetic ions, and O is the atom of oxygen in between them. The canted spin directions $\mathbf{e_1}$ and $\mathbf{e_2}$ produce the spin current $\mathbf{j_s} \propto \mathbf{e_1} \times \mathbf{e_2}$ between M_1 and M_2. The direction of the spin polarization is that of the spin current $\mathbf{j_s}$ and it is given by $\mathbf{P} \propto \mathbf{e_1} \times \mathbf{j_s}$. Reprinted from Reference 57.

1.4.6.2 Spin Orbit Interaction of the d-p hybridization Mechanism

By definition the term "spin orbit coupling" refers to the interaction of the electron's magnetic moment with the magnetic field from its orbital motion. The magnetic moment is a result of the spin's electron, whereas the electron's orbital angular momentum, creates its magnetic moment which is associated with a magnetic field.

The mechanism based on the spin orbit coupling, has been proposed for the ferroelectric polarization of the ABO_2 compounds (A: alkali, B: transition metal) by Arima in 2007.[61]

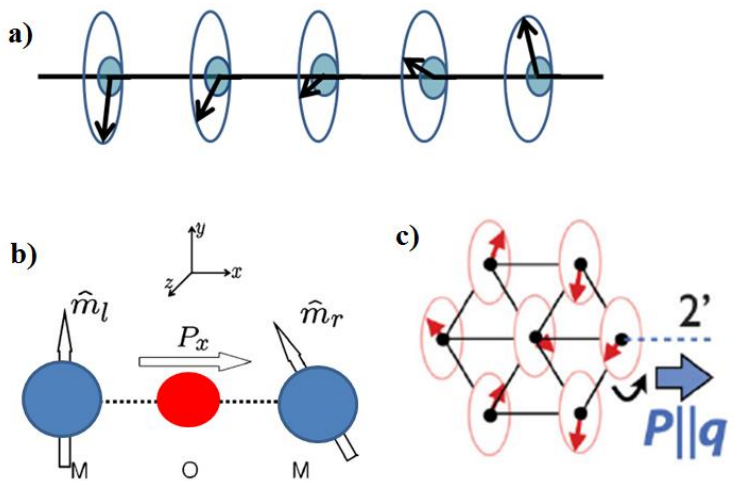

Figure 1.14 (a) Proper screw axis magnetic ordering (b) The arrangment of two magnetic ions, reprented with blue spheres and the a oxygen ion represented with a red sphere. The magnetic moment orientations are pointed with $\hat{m}_l$ and $\hat{m}_r$, whereas the direction of the polarization $\mathbf{P}_x$ is parrallel to the x axis. (c) Proper screw magnetic order on a delafossite crystal lattice. The direction of the induced polarization is parallel to the direction of the helicity of the spiral **q**.(b) and (c) parts of figure were reprinted from references 62 and 63, respectively.

The inverse DM interaction, in a proper screw magnet fails to explain the induced polarization, since the $\mathbf{e_{ij}}$ is parallel to the $\mathbf{S}_i \times \mathbf{S}_j$, in average. In a proper screw magnetic orderding, the spin rotation axis is parallel to the magnetic modulation vector **q**, thus the product of the DM interaction $\mathbf{e_{ij}} \times (\mathbf{S}_i \times \mathbf{S}_j)$ equals zero.

Arima, based on the analysis of Jia[62] for the induced ferroelectric polarization, suggests that polarization in crystals with low symmetry, i.e triclinic, monoclinic and rhombohedral symmetry, is induced by proper screw axis magnetic ordering through the spin orbit interaction (Figure 1.14[62, 63]). The sign of polarization is governed by the spin helicity (the vector of the spin chirality).

The microscopic origin of the mechanism is based on the variation of the hybridization between the 3d magnetic ions (Fe, Cr) and 2p ligand ion (oxygen). This mechanism has

explained successfully the ferroelectric polarization of the oxides $CuFeO_2$, $CuCrO_2$[50, 63], $AgFeO_2$[51] and $AgCrO_2$[50, 63] and the $Ba_2XGe_2O_7$ [64]

Specifically, the polarization at the center of a cluster which is composed of two magnetic ions (Figure 1.14c[63]) is given by the equation:

$$\Delta\mathbf{P}_{\mathbf{l+e/2}} = \mathbf{P}^{ms}(\mathbf{m}_l \cdot \mathbf{m}_r)\mathbf{e} + \mathbf{P}^{sp}\mathbf{e}^{\times}(\mathbf{m}_l{}^{\times}\mathbf{m}_r) + \mathbf{P}^{orb}[(\mathbf{e}\cdot\mathbf{m}_l)\cdot\mathbf{m}_l - (\mathbf{e}\cdot\mathbf{m}_r)\mathbf{m}_r] \qquad \mathbf{(1.22)}$$

Where m_l and m_r are the local magnetic moments, at the sites m and l, with distance e in between them, and l+e/2 is the middle in the e distance between the m and l sites. In equation 1.22 there are the three terms which correspond to the three different mechanisms of the induced polarization. The first term corresponds to the magnetostriction, which is the deformation of material under an external magnetic field. Magnetostriction has been proposed for the explanation of the magnetoelectric effect in Cr_2O_3 and the $RMnO_3$ (R=Ho,Tm).[65, 66] The second term corresponds to the inverse DM interaction, which has been discussed in the previous paragraph. The third term corresponds to the spin orbit interaction mediated modulation of the d-p hybridization and dominates in the systems where proper screw magnetic ordering develops.

1.4.7 Probing the magnetoelectric coupling experimentally

Experiments that shed light on the existence of the magnetoelectric coupling include measurements of the magnetic susceptibility, the dielectric constant, the polarization, magnetostriction versus temperature and external fields (electric and/or magnetic). All the results of the aforementioned experiments are interpreted based on the crystal and magnetic structure analysis of the material, studied by X-Ray diffraction, neutron diffraction and when needed, transmission electron microscopy.

Magnetization measurements usually carried out by SQUID, will indicate possible magnetic transitions. In the case of spin driven magnetoelectricity, it is highly likely that dielectric anomalies will be observed at the magnetic transition temperatures. An example is presented of these measurements is presented in Figure 1.15[50]

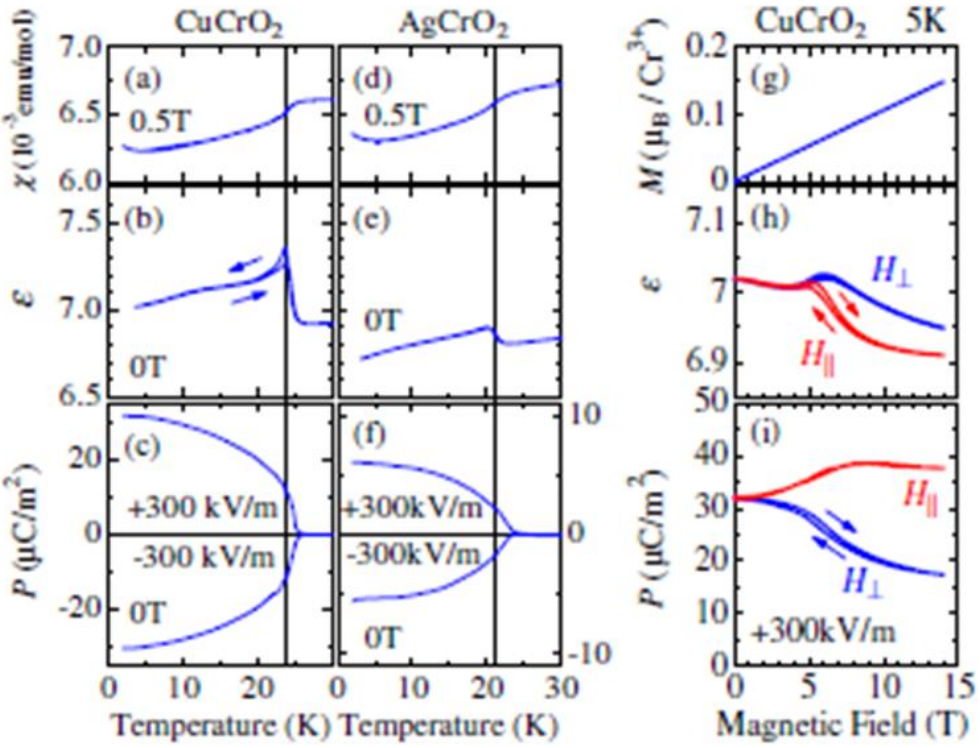

Figure 1.15 Plots of the magnetic susceptibility, the dielectric constant and the polarization of the delafossite compounds $CuCrO_2$ and $AgCrO_2$ without (plots on the left) and under the application of an external magnetic field (plots on the right).Reprinted from Reference 50.

Dielectric constant (ε_r) anomalies correspond to fluctuations of the polarization (P) since

$$\mathbf{P}=\varepsilon_o(\varepsilon_r-1)\mathbf{E} \qquad \textbf{(1.23)}$$

Where ε_o is the dielectric permittivity of vacuum and E is the applied electric field. Measurements of polarization (charge) versus temperature show the existence of pyroelectric current. Experiments of polarization versus an applied electric field prove the ferroelectricity of the system since it shows the characteristic signature of the ferroelectric materials: inversion of the electric dipoles by 180° when reverse electric field is applied (±V, ie electric voltage of different sign). In the ideal case of a multtiferroic which is

ferroelectric and ferromagnetic, it is expected, at least theoretically, that the polarization loop can be controlled by the magnetization and *vice versa* (the magnetoelectric coupling).

In practice, carrying out all the aforementioned experiments is not always possible. The major problem, is that the physical quantities measured are quite small, in addition there leakage currents, that affect greatly the signal of the sample. Moreover, additional complexity is added when the sample is ceramic: grain size effects, aging and internal bias fields, stress effects from external applied fields affect the microstructure and thus the final result of the dielectric and ferroelectric measurements. [67]

1.5 Magnetodielectric Coupling

The term **"***magnetodielectric coupling"* was introduced firstly by Lawes et al [68] to describe materials that show a coupling between the dielectric properties and the magnetization. The term magnetodielectric excludes the requirement of the spontaneous polarization or the symmetry constraints which are essential for linear magnetoelectrics and multiferroics. Magnetodielectrics exhibit a change in the dielectric constant at the magnetic ordering temperature or show finite magnetocapacitance. However, ferroelectricity does not appear below the temperature of the dielectric anomaly. In this thesis, ferroelectricity has not yet been proven. Moreover the magnetic structure analysis and in turn, the examination of the magnetic symmetry is under progress. According to the experimental data and the relevant analysis, we are going to refer to the $NaMnO_2$ polymorphs as magnetodielectrics.

Examples of magnetodielectrics are MnO,[69] Mn_3O_4,[70] $TmFeO_3$,[71] $Dy_2Ti_2O_7$,[72] $Tb_2Ti_2O_7$,[73] $Tb_3Fe_5O_{12}$,[74] and $ZnFe_2O_4$.[75] Two mechanisms have been reported to contribute to the appearance of the magnetodielectric coupling: magnetic frustration and magnetostriction. Specifically, frustration has played the key role in the coupling between the dielectric and magnetic properties in the following: $Dy_2Ti_2O_7$, $Tb_2Ti_2O_7$ and $ZnFe_2O_4$. In this class of materials, external magnetic fields affect the dielectric constant and apart from the dielectric constant experiments, magnetocapacitance measurements are also critical. Interesting to mention here, that in the aforementioned magnets, the magnetic frustration

has not led to spiral magnetic orderings, which is the usual case for many magnetoelectrics. In the second group of magnetodielectris, magnetostriction is the underlying mechanism behind the magnetodielectric coupling. Examples of this group are the MnF_2, [76] $TmFeO_3$, $Tb_3Fe_5O_{12}$ and $Co_3V_2O_8$.[77] In these materials dielectric anomalies are noticed at the temperatures of the magnetic ordering. It has also been reported that the magnetic field dependence indicates a negative magnetocapacitance which is proportional to the magnetic susceptibility. This strongly suggests a magnetostrictive origin for the influence of the magnetic field on the magnetocapacitance and the magnetic susceptibility.

1.5.1 Magnetodielectric Coupling in ABO_2 systems

The current thesis is focused on the magnetodielectric coupling of two ABO_2 compounds: the α-$NaMnO_2$ and β-$NaMnO_2$. Therefore, it is quite useful to discuss some examples of the most well studied ABO_2 compounds who exhibit the magnetodielectric coupling.

ABO_2 are ternary oxides with the general chemical formula $A^{+1}B^{+3}O_2$, where A is an alkali like Cu, Na, Li, Pt, Pb and B is the magnetic cation, usually a 3d transition metal such as Mn, Fe, Al, Cr, Co, Ga, Rh, In. These materials are widely known for the variety of the physical and chemical properties including their use as host frameworks for intercalation and deintercalation processes,[78, 79] the possibility of synthesizing new compounds by soft chemistry routes [80, 81] as well as their possible technological applications. ABO_2 are promising materials as cathode materials in rechargeable batteries like the $LiMnO_2$, [82, 83] for their integration into transparent electronic devices,[84] and as semiconductors for thermoelectric conversion.[85] To a large extent, the interest for the ABO_2 oxides arises from the frustrated magnetic interactions in a triangular lattice.[86, 87]

Their structure is characterized by layers of stacking of BO_6 edge-shared octahedral which are linked by linearly coordinated A atoms. Two polytypes exist, the rhombohedral 3R and the hexagonal 2H with space group symmetry $R\bar{3}m$ and P63/mmc, respectively (Figure 1.16[88]). Their difference is attributed in the orientation of the oxygen in the BO_6 octahedra.[88, 89] Regardless of the structure polytype, the important factor is the arrangement

of the magnetic cation in the triangular lattice topology. As discussed in paragraph 1.3 a phenomenon closely related to the triangular arrangement of spins, is the magnetic frustration of the B cations which has recently been proved to promote the magneto-dielectric coupling.

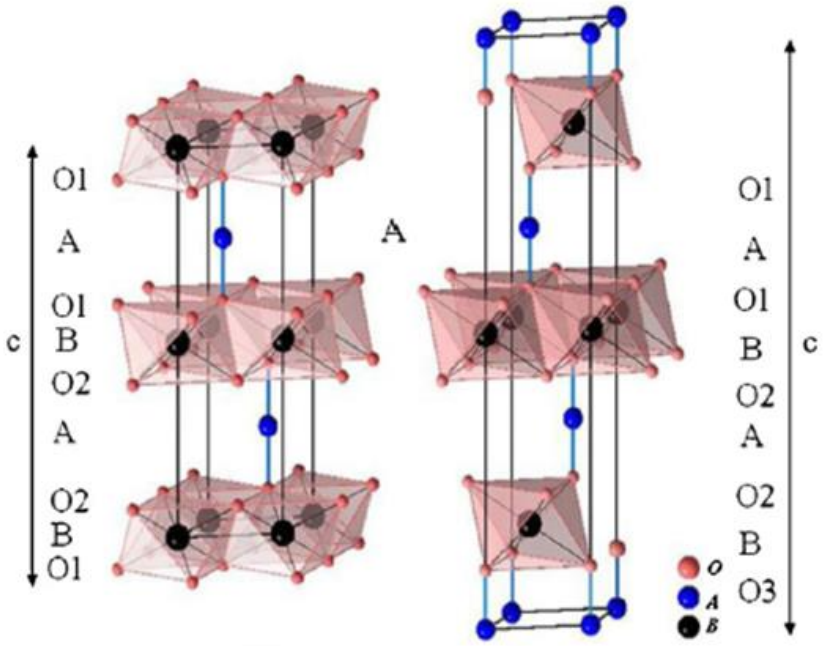

Figure 1.16 The two polytypes of the ABO_2 structure. Reprinted from Reference 88.

Examples of the magnetoelectric ABO_2 oxides are the

a) the $AFeO_2$, with the recently discovered $AgFeO_2$ [51] and the compound of the $CuFeO_2$

b) $ACrO_2$ [50] (A: Cu, Ag, Li, or Na) such as the $CuCrO_2$

Although the aforementioned systems present many similarities which arise from the similar lattice topology, the origin of the microscopic mechanism for the induced magnetoelectric coupling and the polarization is examined separately for each case under the frame of symmetry analysis.

1.5.2 The case of $CuFeO_2$

$CuFeO_2$ [90] is the most extensively studied magnetoelectric ABO_2 compound.[90] Since the discovery of the spiral spin induced polarization of the $CuFeO_2$ by Kimura et al, a vast amount of research has been triggered towards the ABO_2 oxides as excellent candidates for magnetoelectric coupling. New magnetoelectric compounds have been synthesized by the substitution of Fe^{+3} with various trivalent metals. Partial substitution of Fe, with Mn, Al, and Rh, resulted in the magnetoelectrics, $CuFe_{1-x}Al_xO_2$, [91] $CuFe_{1-x}Mn_xO_2$[92] and $CuFe_{1-x}Rh_xO_2$.[93] Kimura's results suggest a strong interplay between non-collinear incommensurate structures, the inversion symmetry breaking and the induced polarization. The most critical findings of this work, can be summarized in the following:

a) $CuFeO_2$ crystallizes in the delafossite structure with a centrosymmetric space group $R\bar{3}m$ at room temperature. The magnetic moment arises from the Fe^{3+} ions with S=5/2, which can cause frustration due to the triangular arrangement. $CuFeO_2$ undergoes a series of magnetic transitions. The zero field ground state, is a commensurate magnetic structure with wave vector (1/4, 1/4, 0). At 11 K a collinear (the magnetic moments of the nearest neighboring moments are parallel) incommensurate phase emerges until 14 K where the system becomes paramagnetic. A striking characteristic, is the rich magnetic phase diagram when the magnetic field is applied along c axis (B//c). At temperatures between 5 K -11 K and at fields between 7 T-13 T, a non collinear magnetic phase develops (Figure 1.17).

b) Magnetoelectric coupling is evidenced by the appearance of the polarization only at the non collinear magnetic phase, with a value of P=100 $\mu C/m^2$, which is comparable to those observed in known multiferroics with long-wavelength magnetic structures.[94, 3, 49] The fact that inversion symmetry is broken at an incommensurate phase, strongly suggests that non collinear helical magnetic structure is of fundamental importance for the breaking the inversion symmetry of $CuFeO_2$.

c) Kimura compares his results with the multiferoics $TbMnO_3$ and $Ni_3V_2O_8$ where inverse Dzyaloshinskii Moriya interaction or as it is called "the spin current model" in helical

magnets,[57] explains successfully the mechanism responsible for the magnetoelectric coupling.

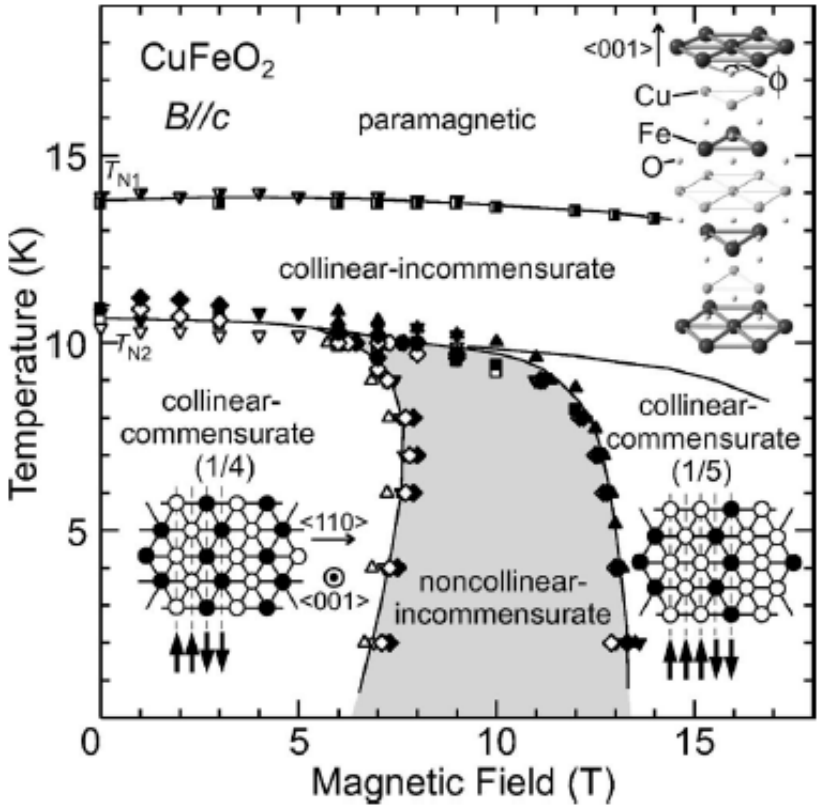

Figure 1.17 Magnetic and temperature phase diagram of $CuFeO_2$, reprinted from reference 88. Measurements of magnetization, dielectric constant, electric polarization and magnetostriction are represented with diamond, square, triangle and inverse triangle respectively. Open and filled symbols correspond to the data points taken upon cooling or magnetic field decreasing and warming or magnetic field increasing respectively.Worth noticing that the polarization emerges at the grey area where the non collinear magnetic structure develops. Reprinted from Reference 90.

However, Arima and Tokura[63] prove that the electric polarization, is not explained on the frame of the spin current model, but results from the spin-orbit interaction. The polarization depends on the spin helicity and is explained from the viewpoint of symmetry analysis.

Furthermore, the research of the $CuFeO_2$ by Kimura, has been expanded by studies concerning it's crystal and magnetic structure in zero,[95, 96, 97] and high magnetic fields,[98] to further investigate the coupling between the polarization and the helical magnetic order.

Important to note here, that the compounds $CuCrO_2$, $AgFeO_2$, $LiCrO_2$ and $NaCrO_2$, that also belong to the delafossite's family, have been primarily studied by Seki et al [44] in 2008. The proposed microscopic mechanism for the ferroelectric polarization is the same as $CuFeO_2$, i.e the spin orbit interaction for the proper screw magnetic order.

Chapter 2: Experimental Techniques

Introduction

The purpose of this chapter is to refer to the experimental techniques that have been used for the study of the compounds. The working principle of each technique and a generic layout of the instruments that have been used are presented. Especially, section 2.4 analyzes the construction of the magnetodielectric measurements setup and the relevant preparation of the polycrystalline samples for these experiments. The reason for the detailed explanation is to describe the methods that have been developed for overcoming the various and complex technical difficulties that these experiments entail.

2.1 Solid State Synthesis

All the compounds studied in this thesis have been prepared by solid state synthesis, in the Functional Nanocrystals Lab in IESL-FORTH.

The solid state synthesis is the most simple and common way to prepare a bulk material. In this method the final product is obtained because the starting materials react with each other when heated at high temperutares (500°C-2000°C). The first step is to find the appropriate starting materials that should be used in order to obtain the final desired product.

Initially, one has to weight the stoichiometric amounts of the reactants, grind them in a pestle and mortar to improve the homogeneity of the mixture and to obtain uniform particle size. The pelletizing of the mixture under some pressure applied by a hydraulic press (usually 1-5 tones) also improves the direct contact of the crystallites faces. The pellet is heated with a specific heating rate and possibly under special atmospheres (such as inert gas or oxygen) in a furnace for hours or even several days. When the heating is completed the cooling can be done by quenching inside the furnace, in atmosphere or in liquid nitrogen.

The basic principle behind the solid state synthesis lies on the fact the high temperature enables the reaction since it increases the diffusion rate between the ions of the reactants. The driving force of the cations is the thermal energy that they absorb and enables them to

overcome the lattice energy, and move from their initial lattice position so that diffusion and reaction can occur. Even though the heating occurs in high temperatures, still the temperature is raised well below the melting point, so the reaction takes place on the solid state. The reaction occurs at the interfaces of the solids. Once the interface has reacted then the reactants diffuse from the bulk to the interface.[99] Usually during the heating the pellet is cooled, removed, crushed, re-grinded and re-pelletized. This is to ensure that fresh surfaces are brought in contact and the reaction speeds up.

Despite the fact that solid state synthesis is very simple, there are many drawbacks that could cause problems and faults in the quality of the final products. The most important of all is that the compounds synthesized at high temperatures could be unstable and decompose, or may even contain secondary phases that are formed in lower temperatures. For instance while trying to obtain α-$NaFeO_2$ phase, it is quite common to end up with a final product that will also contain β-$NaFeO_2$, which has the same stoichiometry but different crystal structure. Apart from that unreacted traces of the starting materials can be found due to limited diffusion of the ions during the reaction.

A number of factors can be modified in order to optimize the synthesis conditions. These include the heating rate, the dwelling time at the final temperature, the number of intermediate regrindings, the special atmosphere or the amounts of reactants.

2.2 Characterization

2.2.1 X- Ray Powder Diffraction (XRPD) [100, 101, 102, 103]

X Ray Powder Diffraction has been used for every compound that has been synthesized in this thesis. Actually it was the first experiment conducted for preliminary characterization, since an XRPD pattern is the fingerprint of each compound. The importance of this non-destructive technique lies on the identification of the phase (or phases if any secondary ones are present) and provides the first information about the quality and crystallization of the compound. Apart from the phase identification and the quantative phase analysis, when

analyzing an XRD pattern it is possible to refine the unit cell parameters, estimate the crystallite size and microstrain and check if there is any preferred orientation in the sample.

X rays is an electromagnetic radiation of wavelength ~0.1 to ~100 A°, a range which is located after the ultraviolet and before the γ-rays. In order to probe the crystal structure of the materials, the wavelengths most commonly used are between 0.5 Å and 2.5 Å which are of the same order of magnitude as the shortest interatomic distances observed in both organic and inorganic materials.

Generation of X Rays

Electromagnetic radiation is generated when electrons accelerate or decelerate. There are two sources that produce X Rays: a) The Conventional X-Ray Source (X- Ray tube) and b) The Synchrotron. In this paragraph the conventional X-Ray Source is going to be described briefly. X Rays are generated in the so called X Ray tube. The cathode, which is usually an electrically heated filament, such as tungsten, emits electrons that are accelerated inside a high vacuum tube by a high potential difference (20-50 kV) towards the anode. The high energy electrons strike the water cooled anode which emits the X rays spectrum. Typical metals used for anode materials are copper Cu and Mo in powder and in single crystal diffractometers, respectively. The X-Ray spectrum generated as described above, consists of three intense peaks (spectral lines) which are imposed on a continuous background, known as white radiation or bremsstrahlung, as shown in Figure 2.1 The bremsstrahlung radiation, a highly undesirable characteristic of X Ray emission spectrum, is caused by the electrons which are scattered by the electric field near the nuclei.

The characteristic spectral lines $K_{\alpha 1}$, $K_{\alpha 2}$, and K_{β} are attributed to the interaction of high energy (E_1) electrons heat the target and kick off an orbital electron from the outer shells. The electron vacancy will be filled by a higher energy level electron (E_2). The difference of the above energies: $\Delta E=E_2-E_1$ corresponds to an emitted photon with the energy hv thus:

$$\Delta E = h\nu = \frac{hc}{\lambda} \qquad \textbf{(2.1)}$$

Where h: the Planck's constant $6.626 \cdot 10^{-34}$ Js, v: the frequency, c: the speed of light in a vacuum ($2.998 \cdot 10^{8}$ m/s), λ the wavelength of the wave associated with the energy of the photon .

Specifically the K_α intense line stands for the transition of an electron from the L shell to K shell, whereas the K_β radiation is attributed to the transition from L to M shell. The K_α radiation consists of two components the $K_{\alpha 1}$ and $K_{\alpha 2}$, which correspond to the transitions $2p_{1/2}$ to $1s_{1/2}$ and $2p_{3/2}$ to $1s_{1/2}$, where p and s are the orbitals and the subscripts 1/2 and 3/2 is the total angular momentum j. K_α and K_β are determined by the target metal of the anode in each diffractometer.

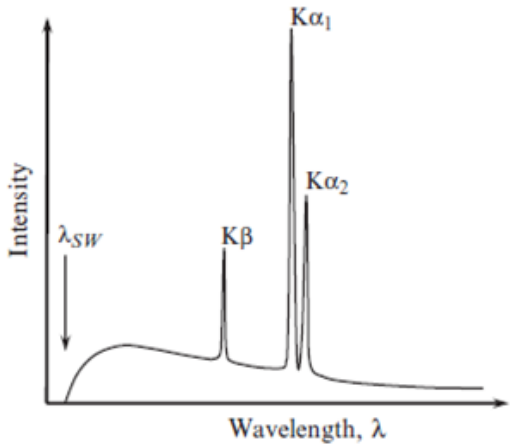

Fig 2.1 Typical emission X-Ray spectrum

Bragg's Law

The basic principle behind the X-rays diffraction and the X Rays analysis patterns is the Bragg's law. Each crystal is composed by a periodic structure characterized by a lattice. The building block of a lattice is a parallelepiped, called the unit cell. The construction of the lattice is described by the propagation of the unit cell and its arrangement in the lattice planes.

Bragg (1912), taking into account that the crystalline state can be described by a periodic arrangement of atoms in crystal planes, has treated mathematically the diffraction as reflections from the diffracting crystal planes. Thus the constructive interference can be simply described in the following equation- the Bragg's law:

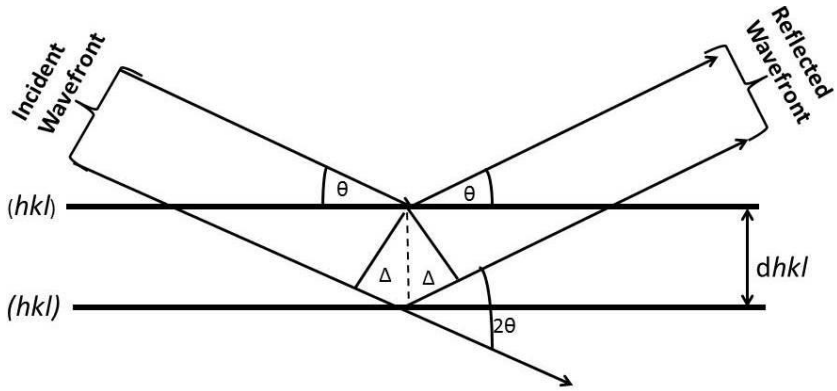

Figure 2.2 The Bragg's law.θ, 2θ are the Bragg angles, $2\Delta=2d_{hkl}\sin\theta$ the path difference and $2\Delta=n\lambda$ the constructive interference.

$$n\lambda=2d_{hkl}\sin\theta \qquad \textbf{(2.2)}$$

n: the order of diffraction, i.e if we apply from equation 2.2 to the 111 lattice plane for

n=1: $1\lambda=2d_{111}\sin\theta_1$ and

n=2 $2\lambda=2\,d_{111}\sin\theta_2$

However, n is usually incorporated into the lattice plane symbol, that is:

$$\lambda=2(d_{hkl}/n)\sin\theta=2d_{nh}d_{nk}d_{nl}\sin\theta \qquad \textbf{(2.3)}$$

The Powder Diffractometer

Powder X-ray diffraction experiments (XRPD), have been carried out on a Rigaku D/MAX-2000H rotating anode diffractometer. This diffractometer uses the Bragg Bretano Geometry (θ-2θ) which is shown in Figure 2.3. The angle θ is the one between the sample's surface and the incident x-ray beam and 2θ is the angle between the incident beam and the receiving slit-detector

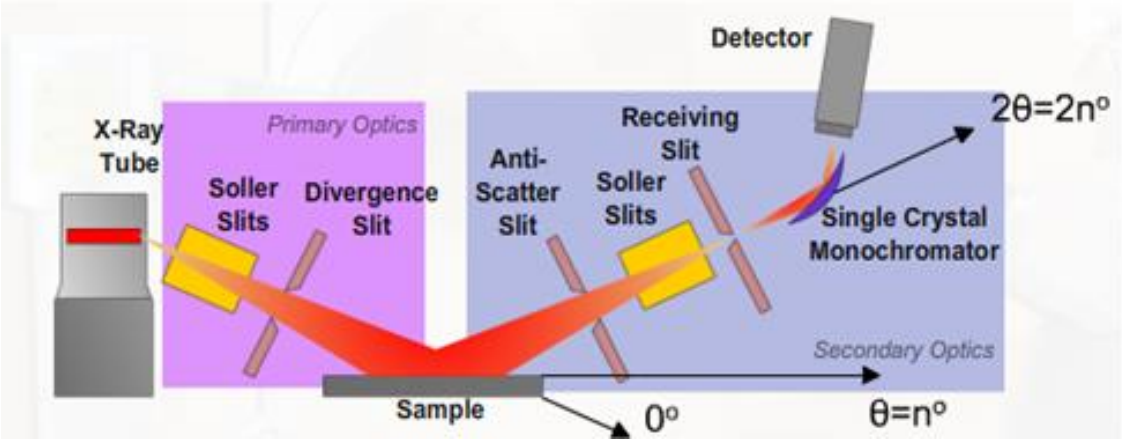

Figure 2.3 Schematic Illustration of the Bragg- Bretano Geometry. Reprinted from http://www.ammrf.org.au/myscope/xrd/background/machine

The basic parts of a diffractometer are:

a) The X Ray tube (F) which is the X rays source, b) The goniometer: the platform that holds and moves the sample, optics, detector, and/or tube, c) the sample holder (S), d) The detector: counts the number of X Rays- counts (counts/sec) scattered by the sample, e) slits

- Divergence slits (DS): fitted in the incident beam path to control the divergence of the incident beam, and thus, the amount (length) of the sample that is irradiated by the incident X-Ray beam.
- soller slits (SS, "SS1" on "tube" side, "SS2" on detector side), a series of closely spaced parallel plates, designed to: limit the axial divergence of the incident and diffracted X Rays beam, improve the peaks' shape and
- Receiving slit (RS): Placed before the detector to improve the resolution.

The diffractometer Rigaku D/MAX-2000H has Cu as target metal whose K_α and K_β is at 1.5418 Å and 0.7107 Å respectively.

Preparation of the Samples for the XRD Measurement

In order to perform an X-Ray measurement the sample (either powder or pellet) was placed in a homemade holder, specifically designed to protect the sample from contact with air and moisture. The holder consists of 3 parts, the magnetic round base which is attached on the goniometer, an aluminum square part with concentric dips where the sample is mounted and the top cover which has a round hole. At the cover of the holder a part of mylar was glued with GE-Varnish, to allow X rays to penetrate but at the same time to prevent any insertion of air or moisture during the measurement. An adequate amount of powder (150-200 mg) was mounted in the holder shown in Figure 2.4 inside the Ar filled MBraun (LAB master 130) glove box and then the cover was screwed tightly with 8 screws on the base of the holder.

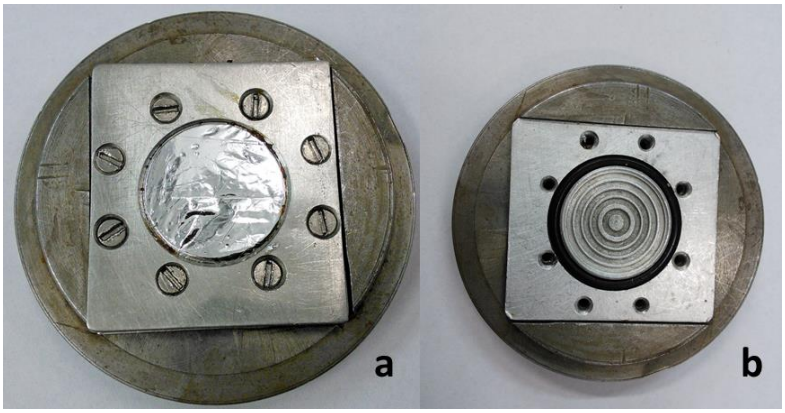

Figure 2.4 The air sensitive sample's XRD holder: (a) with the mylar attached on the top cover (b)The base aluminum part where the sample is placed

This holder then as one piece is attached on the goniometer of the XRD. The mylar tape, which is a kind of aluminum foil, gives a few (four) extra peaks in the X Ray pattern, which are easily recognizable and thus are not taken into account in the sample's characterization.

2.2.2 Inductive Coupled Plasma Optical Emission Spectroscopy (ICP-OES) [104, 105]

Inductive Coupled Plasma Optical Emission Spectroscopy is very sensitive analytical technique used for the identification and quantification of the chemical elements in a sample. It is a spectroscopic technique, which identifies the elements according to the emission of their characteristic wavelengths and intensities that are converted into concentration information for the analyst.

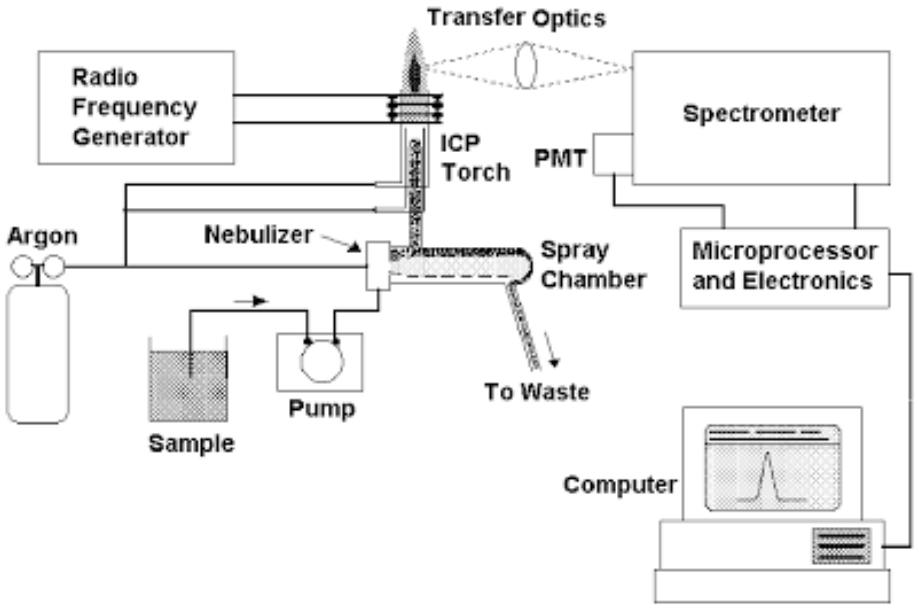

Figure 2.5 Basic concept of ICP-OES analysis for aqueous samples. Reprinted from Reference 104.

More specifically, the sample whose elements need to be traced is diluted in aqua. This aqueous sample is converted to aerosols with the use of a nebulizer. The aerosols pass through the inductive coupled plasma (Argon) at the high temperature range of 8.000-10.000°C. Due to the heat the sample is desolvated, vaporized, atomized and excited to different states. Depending on the atomic or ionic state of the excitation, characteristic optical emissions are produced. The emissions occur at characteristic wavelengths and their intensities are proportional to the concentrations of the analytes in the sample. The light emitted is detected, measured in a spectrometer yielding an intensity measurement that is turned into electronic signals into an elemental concentration by comparison with

calibration standards. Detection limits typically range from parts per million (ppm) to parts per billion (ppb), although depending on the element and instrument, sometimes less than ppb detection is achieved. Worth mentioning here that the elements which can not be detected by the ICP-OES method are the: C, H, O, N and the halogens. The basic components of an ICP-OES are shown in Figure 2.5.

2.2.3 Thermogravimetric Analysis (TGA) and Differential Scanning Calorimetry (DSC) [99]

Thermogravimetric analysis measures the changes on the weight of a sample as a function of: a) temperature while heated up on a constant heating rate and b) of time while dwelling on a specific temperature, under inert atmosphere (usually Argon gas). At the same time, it is also possible to measure the amount of heat released by the sample or as it is known the differential heat flow - a technique known as Differential Scanning Calorimetry (DSC).

The instrument that was used was a SDT-Q600 from TA instruments which supports simultaneous TGA and DSC measurements from room temperature to 1500°C. This instrument features a matched Platinum / Platinum-Rhodium thermocouple pair within the ceramic beams and provides direct sample, reference, and differential temperature measurements. A few mgs of the powder samples were placed on an alumina pan, whereas the reference pan remained empty. The thermobalance is situated on a horizontal furnace that can be heated at a constant rate varying from 1-20 °C/min. In most of the experiments the average rate of 10 °C/min was used. A purge gas system provides sufficient gas flow (100 ml/min Ar, O_2) to the sample resulting in the elimination of back diffusion and the removal of decomposition products from the sample. Due to the temperature increase, various physical and chemical phenomena might occur. The data recorded show the changes in the weight (% mg) and the heat flow (W/g) of the sample, usually presented in the same graph.

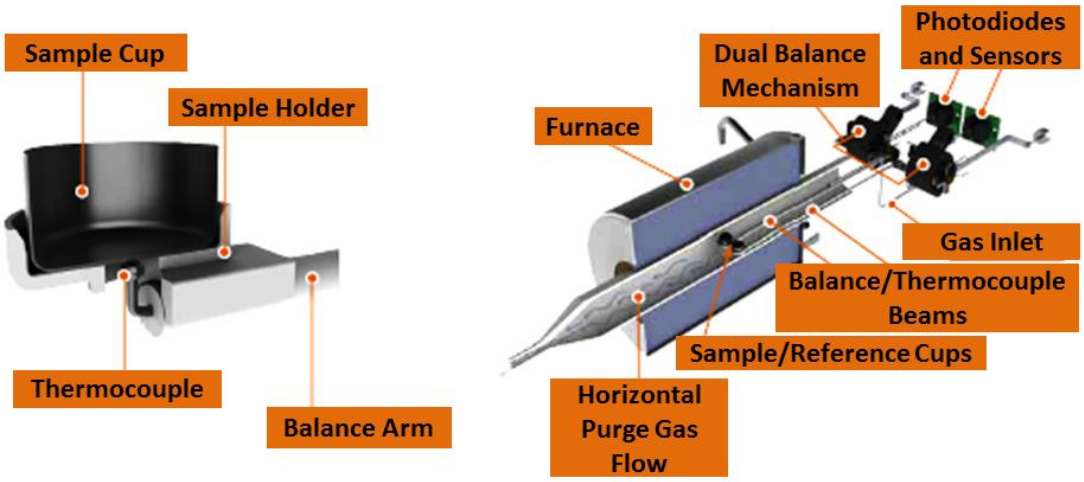

Figure 2.6 Left: A detail of the sample cup. Right: Schematic illustration of the simultaneous TGA/DSC instrument lay out. Specifically the model of the above figure shows the SDT Q600. Reprinted from the website http://www.tainstruments.com/pdf/brochure/sdt.pdf of TA's instruments.

2.3 Magnetic Measurements

2.3.1 The SQUID Magnetometer

A critical part of this work is based on the measurement of magnetization at the temperatures 5-320 K. All the samples which were found to be single phase have been measured with a comercially available equipment of Quantum Design Inc, the Magnetic Property Measurement System (MPMS) rf SQUID magnetometer.[106] The acronym SQUID stands for Superconducting Quantum Interface Design. This magnetometry is based on the conversion of the magnetic flux into current and finally electric voltage. At the moment it is the most sensitive, accurate and reliable method for measuring incredibly small magnetizations.

The basic working principle of SQUID

SQUID could be simply described as a superconducting ring separated by one (RF SQUID) or two (DC SQUID) Josephson junctions. The Joshephson junction, also described as weak link [107] is an insulating barrier between two superconductors. Josephson effect postulates that Cooper pairs can tunnel from one superconducting layer to the other and the superconducting current (Is) can also pass through the resistive barrier without any voltage drop. The use of the Josepshon Junctions in a SQUID, is it to link the phase difference of the wave functions $\Delta\varphi$ of the Cooper pairs, with the total magnetic flux. The total magnetic flux penetrates the superconducting loop and it is a quantized quantity.

How a measurement is performed on SQUID.

The MPMS-XL RF SQUID that we used was equiped with a superconducting magnet that can apply up to 7 T fields on the sample chamber. The sample is placed on the sample chamber inside a long cylindrical insert known as the probe. The sample chamber is maintened in vacuum (0.001Torr) and temperatures can reach from 2-350 K, by controlling the impedances and heaters, also placed inside the probe. The sample is inserted in the sample chamber through an airlock connected with the He bath.

The majority of the samples measured in this work were air/moisture sensitive, so initially an amount of powder about 50-80 mg was placed in a gelatin capsule inside an Ar filled M Braun Glove Box. The gelatin capsule was mounted inside a straw. Important to note here, that both capsule and straw, have negligible magnetic signals in comparison to the signal of the powder specimen (10^{-4} emu, where 1emu=1electromagnetic unit=1erg/G). The straw was then attached to the brass (also non magnetic) end of a rod, commercially available from Quantum Design Inc. Then the rod is inserted to the sample chamber through the airlock chamber and it can move vertically since it is anchored on a stepper motor.

The sample moves smoothly between four loops of wire as shown in Figure 2.7 while a DC magnetic field is applied. The upper and lower wire loop are wounded in the same direction, whereas the two loops in the middle are wounded in the opposite direction

forming in this way a second order gradiometer. As the sample moves vertically within the 3 cm distance of the loops it induces a change in the magnetic flux $\Delta\varphi$. Any change in the magnetic flux $\Delta\Phi$, caused by the sample's magnetic moment, is being sensed by the detection or signal coil (Figure 2.8) which the wires sense it as an induced voltage or current ΔI. The relationship between the change in the total magnetic flux $\Delta\Phi$ and the current induced[106] is expressed in the following equation:

$$\Delta\Phi = N \cdot A \cdot \Delta B = (L_{coil} + L_{input}) \cdot \Delta I \qquad \textbf{(2.4)}$$

Where: ΔB is the change in applied field, N, A, and L coil are the number of turns, area, and inductance of the detection coil, respectively, L input is the inductance of the SQUID input coil; and ΔI is the change in current in the superconducting circuit.

The detection coil will further convert the flux changes into electric current ΔI. The resulting current changes the magnetic flux of the input coil which is connected to the SQUID sensor. SQUID is connected with a feedback circuit which provides a magnetic field to compensate for the change that the sample's magnetic flux has created. This magnetic flux will be converted through a resistor to an output voltage which will be stored in the data storage system. This method can detect changes in the magnetic flux ranging from 10^{-7} emu and higher.

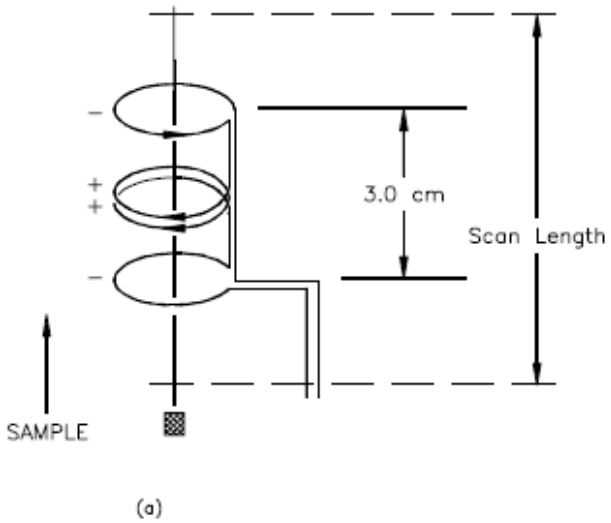

Figure 2.7 Schematic diagram of the SQUID operation.Reprinted from Reference 106.

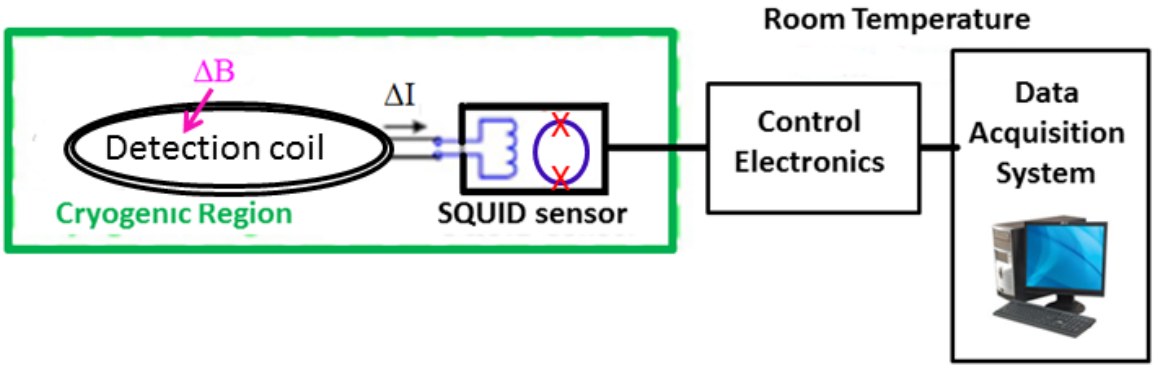

Figure 2.8 A schematic diagram of the SQUID magnetometer. Reprinted from Reference 106.

2.3.2 Static Magnetic Susceptibility

The most common way to study the magnetic properties, is to apply a static DC magnetic field on a sample and measure the magnetic susceptibility χ. As the word static implies, all the phenomena observed in these experiments, are time-independent. It is commonly called DC magnetic susceptibility. As an external field H is applied to the sample under study, an internal magnetic field in the sample B is going to be produced given by:

$$\mathbf{B}=\mu\mathbf{H}=\mu_o[1+\chi(H)]\,\mathbf{H} \qquad \textbf{(2.5)}$$

Where: μ_o is the vacuum permeability, $\mu_o=4\pi\cdot10^{-7}$ H/m, whereas the product of the susceptibility χ(H) with the external field H, χ(H)·H, stands for the magnetization M of the material, i.e

$$\mathbf{M}=\chi(H)\cdot\mathbf{H} \qquad \textbf{(2.6)}$$

Which gives for the susceptibility $\chi=dM/dH$ **(2.7)**

There are two types of measurement usually performed in SQUID by applying a DC field.

a) The first one aims to measure the susceptibility $\chi_H(T)$ versus increasing temperature under an external magnetic field. The sample is being cooled from a high temperature to 5 K or in general a very low temperature. In low temperatures the thermal energy of the magnetic moments is minimized. This is necessary to estimate if they possess the

necessary energy to form an ordered magnetic state. Afterwards a magnetic field is applied and its magnetization is being recorded as the temperature increases at a specified rate and step. It is possible to follow two protocols while cooling the sample. The first one is known as Zero Field Cool (ZFC) according to which the sample is being cooled without applying any magnetic field. The second one is the so called Field Cool (FC), in which the sample is being cooled while an external magnetic field is applied from a high temperature, well above the temperature where a phase transition might occur. The plots of susceptibility $\chi(T)$ and the inverse susceptibility $1/\chi(T)$ might show peaks, or cusps, which possibly reveal the critical temperatures, if any. A rather good approach is to check for any peaks in the graph provided from the calculation of the first derivative of the susceptibility in respect with the temperature, the $d\chi/dT$. Most of the samples in this thesis have been measured using the ZFC protocol.

b) Another method applied, is to measure isothermally the magnetization versus the applied magnetic field H. If the sample is ferromagnetic or possess a ferromagnetic component, a hysteresis loop $\chi_T(H)$ will be observed. Information can be extracted by the area of the loop, the coercive field and the remnant magnetization.

2.3.3 Dynamic Magnetic Susceptibility

The Dynamic Susceptibility is measured by the AC (alternating current) magnetometry in which a small AC drive magnetic field is superimposed on the DC field, causing a time-dependent moment in the sample.[108] This method is preferred when very small changes of the susceptibility need to be detected. When measuring on high frequencies the sample's magnetization may lag behind the drive field by a phase difference φ. The phase difference results in two measurable quantities: the in phase or real part of the susceptibility χ' and out of phase or the imaginary part χ'', thus the total susceptibility is given by:

$$\chi=\chi'+i\chi'' =\chi\cos\varphi +\chi\sin\varphi \quad \textbf{(2.8)}$$

and $$\varphi= \arctan (\chi''/\chi') \quad \textbf{(2.9)}$$

Both χ' and χ'' are very sensitive to thermodynamic changes, so they are used to detect magnetic phase transitions. χ' represents the slope of the curve dM/dH whereas the χ'' points towards the existence of dissipative phenomena such as Eddy currents. In spin glasses the analysis of the frequency dependent susceptibility versus temperature is useful for the idententification of the type of interaction between the magnetic moments and thus the classification of the spin glass.

2.4 Magnetodielectric Measurements [109, 110]

2.4.1 The Construction of the Magnetodielectric Measurements Set Up.

As mentioned previously the goal of this work is to discover new magnetoelectric compounds and unravel the interplay between the crystal, magnetic and magnetodielectric properties. The investigation of the magnetoelectric coupling, can be done by measuring the dielectric constant and polarization versus temperature and magnetic field. For this purpose an experimental set up (Figure 2.9) was constructed and modified to achieve the optimum conditions for measuring capacitance as low as 10^{-12} F (pF or less) and 10^{-9} A (nanoAmps or less). The experiment was controlled through LabView Software, with a program specifically designed for the needs of these measurements (see Appendix B).

The basic tools that have been used throughout these measurements were:

1. Agilent 4284 LCR Capacitance Bridge with frequencies on the range 20 Hz-1 MHz, for measuring the capacitance and the dielectric loss of the samples.
2. Janis research supertran_VP cryostat system which is controlled by a 332 LakeShore Temperature Controller, supplied with liquid Nitrogen for the cooling down of the system up to Temperatures of 77 K.
3. A 7 Tesla cryogen-free superconducting solenoid magnet system cooled by a Cryomech pulse tube cryocooler, Model PT410 with remote motor, and Model CP2800 water cooled compressor commercially available by the American Magnetics Instruments (AMI). The superconducting magnet is controlled by the AMI 420 programmer and a compatible four quadrant power supply.

4. 6517 Keithley electrometer for measuring the polarization and DC quasi static ferroelectric measurements.

5. Home built probe to measure the capacitance and polarization of the samples at low temperatures. The probe is inserted in the cryostat, carries a heater- a resistance of 40 Ohm which provides heating to the sample space and a temperature sensor- a Cernox for measuring the temperature at the sample space

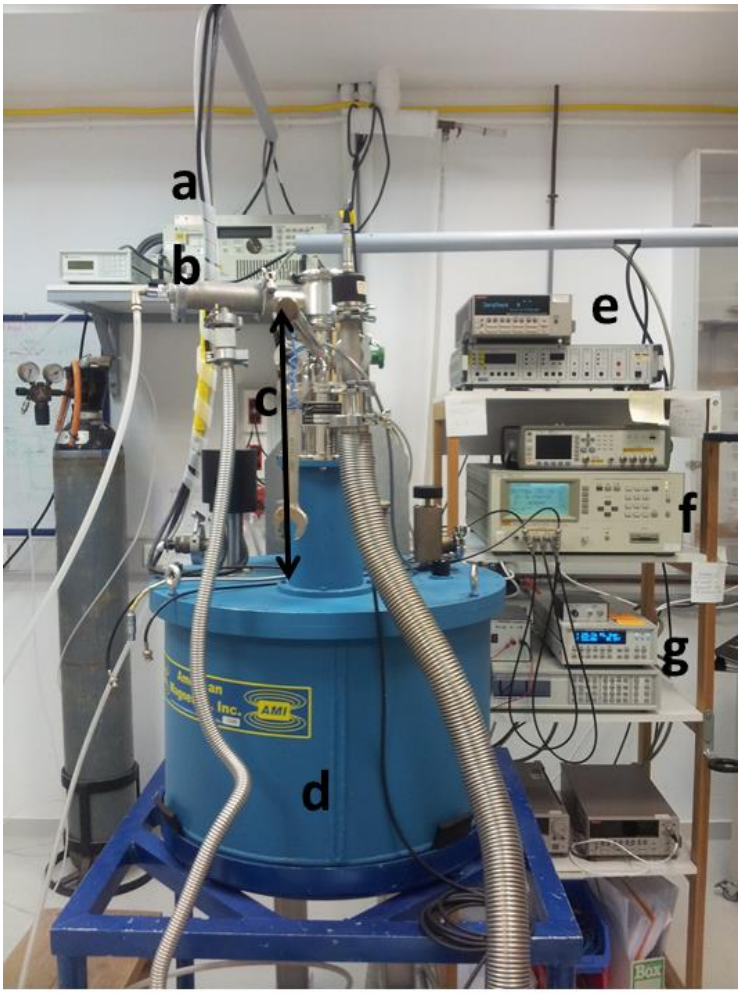

Figure 2.9 The home made 7 Tesla low temperature measurements set up. Some its basic parts are a) superconducting magnetic controller b) superconducting magnet voltage supply c) The Janis cryostat d) The 7 T superconducting magnet e) Keithley Electrometer f) LCR bridge g) Temperature Controller Lakeshore 332.

Description of the Holder Probe

The probe was constructed using a carbon fiber tube (Figure 2.10). On the top end of the carbon fiber tube an aluminum flange is placed. At the bottom end of the tube there is a heater made of manganin wire corresponding to a total resistance of 40 Ohms covered with stycast epoxy to ensure electric insulation (Figure 2.10 b) and the sample sandwich like brass holder. A Cernox sensor is attached on the brass holder, a few mm (<5mm) away from the sample's position, to measure its exact temperature. Two point measurements were carried out with this probe, so two female bnc (Bayonet Neill-Concelman) connectors are connected with copper coaxial cables of low resistance. The copper wires are connected with the two the bnc connectors of the top flange, and are inserted to the internal of the carbon tube. The end of each wire is soldered to one of the plaques of the sandwich holder. The top flange is equipped with a limo connector which connects the heater of the probe and the Cernox sensor with the output voltage of temperature controller. This flange has a total of eight male bnc connectors for the possibility of modification for other types of measurement using this probe. The shields of the bnc connectors are not isolated with each other, in order to have one common potential which is connected to the ground.

Mounting and stabilizing the sample has been based on the design of a sandwich like holder (Figure 2.10 c). It consists of two pieces of brass (Figure 2.10 b and Figure 2.10 d) so the sample is placed in the space in between them. In each plaque of brass a gamma shaped (Γ) printed circuit board (pcb) is attached (Figure 2.10 d) which has copper pad printed on it. Both pcbs are placed on pieces of sapphire, which is glued with GE-Varnish on the bronze plaques, in order to isolate electrically the signal coming from the sample and to minimize the leakage currents. Each copper pad is a 3mm diameter circle .The sample is placed so that each surface of the sample (upper and lower surface) adjoins one copper pad. The copper wires are connected with the pads by a copper line.

Since the mechanical strain induced to the sample from the holder could affect the measurements and could cause cracks on the surface of the sample, extra care had to be taken to the pressure applied from the brass plaques. To ensure that the sample will be well mounted among the brass plaques, not loosely but not very tight also, the brass bottom

plaque has a small mechanism with non magnetic steel spring, attached on a Teflon screw. The user can modify the distance between the two plaques by adjusting the Teflon screw, depending on the thickness of the sample.

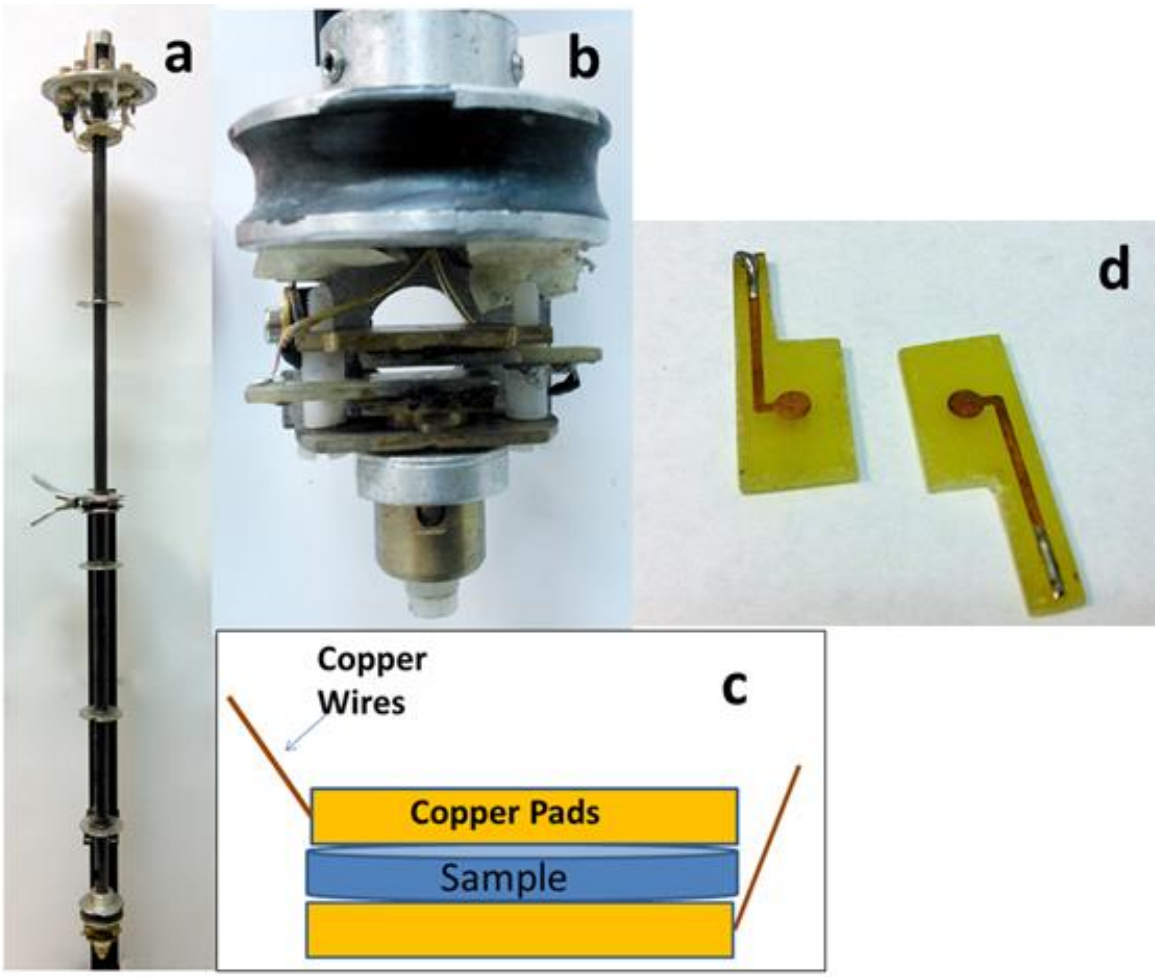

Figure 2.10 The Magnetodielectric measurements probe. a) A photo of the entire probe b) The base of the probe: The brass base in which is attached the sandwich like holder c) An illustration of the sketch by which the holder has been designed d) a view of the pcb piece with the copper pad on it.

Preparation of the samples

The samples used in the magnetodielectric measurements were 5 mm diameter pellets of thickness from 1-1.5 mm approximately. The fact that the materials were air sensitive powders introduced a number of factors that had to be taken into account when pelletizing the sample in the glove box, mounting the sample on the probe and while measuring it in the cryostat. The specimens used, were initially in powder form, so in order to apply silver paste contacts and place them as solid piece at the holder, they had to be pressed in small pellets using a home made alloy steel press of 5 mm diameter (Figure 2.11) and a torque key in the Ar filled glove box. An average pressure around $4.7 \cdot 10^8$ Pa applied on the powder was sufficient to produce a firm, stable pellet. To obtain a parallel plate capacitor, silver paste (purchased by DuPont (U.K) Limited Coldharbour Lane, Bristol) was applied on both circular parallel surfaces of the sample. After the silver paste contacts had dried, the pellet was taken out of the glove box and immediately placed in the sandwich like holder of the probe (Figure 2.10 (b), (c)). Worth mentioning here that Indium contacts deposited with an ultrasonic soldering have also been tested as option, however it turned out an aggressive technique since the pellets could obtain cracks or could easily break while Indium was applied on their surface.

Figure 2.11 Left: The 5mm home made steel press. Also shown part of the torque key that was used to apply specific values of pressure. Right: A 5 mm diameter pellet of β-$NaMnO_2$ pelletized with the press as seen from the stereoscope.

2.4.2 Dielectric Constant Measurements [111, 112, 113]

As discussed earlier the magnetodielectric coupling is revealed when the magnetic field or the intrinsic magnetic order affects the dielectric constant or the polarization.

In practice, measuring the dielectric constant is accomplished by measuring the capacitance C (F) of the sample versus temperature upon heating and cooling. A dielectric material of parallel plate geometry has capacitance

$$C=\varepsilon_o\varepsilon_r \frac{A}{d} \qquad \textbf{(2.10)}$$

where A is the conductive area of the plates and d is the distance between them (in other words d is the thickness of the sample). The capacitance expresses the amount of charge that can be stored in the dielectric material of a capacitor at a certain voltage. Thus, high capacitance suggests preferable qualifications for the electric device that could possibly be obtained from the material under study. However the capacitance and subsequently the dielectric constant are strongly affected by the specimen's age and history as well as the temperature and the frequency used in the experiment.

The complex permittivity or dielectric constant is defined as:

$$\varepsilon=\varepsilon'-i\varepsilon'' \qquad \textbf{(2.11)}$$

where ε' and ε" the real and imaginary part of dielectric constant respectively is connected through the Kramers Kroning relations. [114] Both of the ε' and ε" have physical meanings significantly important for the qualification of a capacitor. A capacitor whose plates are separated by a dielectric material, has a real capacitance ε' times greater than would have a capacitor with the same electrodes in vacuum. The ε" is a measure of the energy dissipation per period and for this reason it is known as dissipation factor or dielectric loss. In an ideal capacitor ε" is zero. Since real capacitors have parasitic effects, such as unwanted resistance and inductance it is essential to know the values of d for the proper qualification of the capacitor.

In order to carry out a dielectric constant measurement, an Agilent 4284 LCR bridge is used which measures simultaneously both the real and the imaginary part of the complex

dielectric constant. The principle behind the measurement is simple (Figure 2.12, reprinted from Reference 111). An AC voltage is applied to the specimen or DUT (device under test), which causes an AC current to flow through it. The LCR computes the impedance Z (measured in Ω) by using Ohms law:

$$Z=\frac{V}{I} \qquad \textbf{(2.12)}$$

and also calculates the admittance Y, where Y=1/Z. To have the capacitance measured and displayed on the instruments screen, the appropriate internal circuit (parallel or in series) has to be selected which is based on the sample's resistance. The compounds studied in this work usually had a capacitance at the range of some pF, so for these values the "Parallel Resistance Circuit" is selected. This enables the LCR bridge to calculate the Cp (Capacitance) and D (dissipation Factor). The selection of this function and circuit is based on the fact that low capacitance values ($C<10^{-6}$ F) yield large reactance, which implies that the effect of the parallel resistance (R_p) has relatively more significance than that of series resistance (R_s).

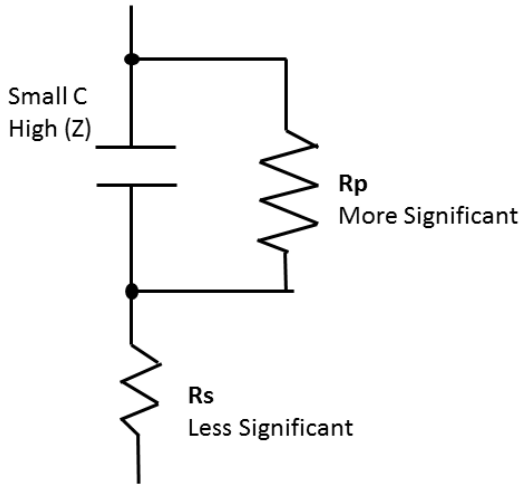

Figure 2.12 A simple circuit which shows the principle behind the capacitance (Cp-D) measurement with the LCR bridge. Reprinted from Reference 111.

In an electric circuit which is driven by the DC current there is no distinction between the impendace and the resistance. On the contrary, in AC circuits there are two additional impending mechanisms: the capacitance (C) and the inductance (L). The total impendance

caused by these two mechanisms yields the imaginary part of the impendance, which is also known as reactance. The resistance forms the real part.

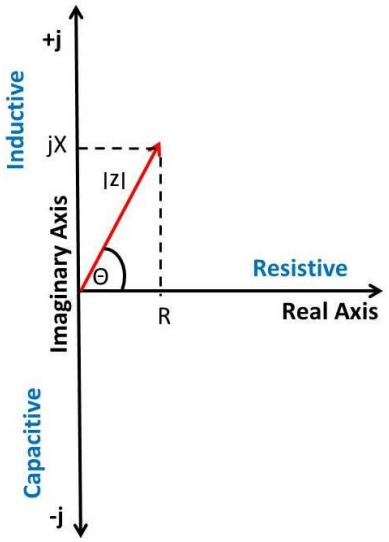

Figure 2.13 A representation of the impedance measurement plane. Reprinted from Reference 111.

To understand the calculation of the capacitance through the impendance Z, the vector representation of impedance is presented in Figure 2.13. The angle θ is the phase of the impendance: the more ideal a capacitor the less resitive it would be so θ would take values close to -90 deg. The equations that relate the impendance-Z, the Resistance-R and the Reactance-X are:

$$Z=R+jX \tag{2.13}$$

$$Y=\frac{1}{|Z|} \tag{2.14}$$

Where $Y=\sqrt{G^2+B^2}=1/|Z|$

and $\varphi=\arctan(|B|/G)=-\theta$

where G is the conductance (S), $B=2\pi fC$ is the susceptance (S).

2.4.3 I-V and Polarization Loop Measurements [115, 116, 117]

Attempts have been done to measure currents versus voltage (I-V) and P-V loops (polarization versus voltage) using a Keithley electrometer 6517A in β-$NaMnO_2$ and α-$NaMnO_2$ samples. The aim in these experiments was to reveal possible ferroelectricity below the temperature where the dielectric changes appear.

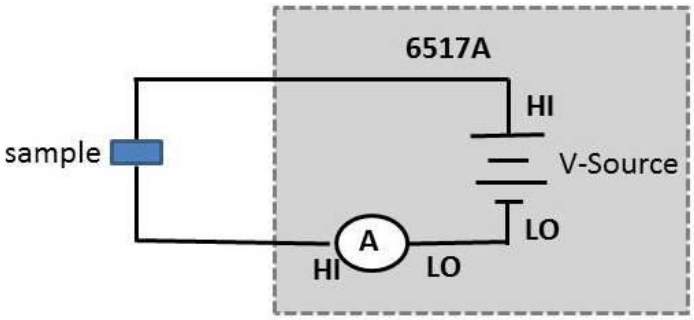

Figure 2.14 The circuit by which the I-V is measured with the help of the Keithley 6517A electrometer. Reprinted from Reference 116.

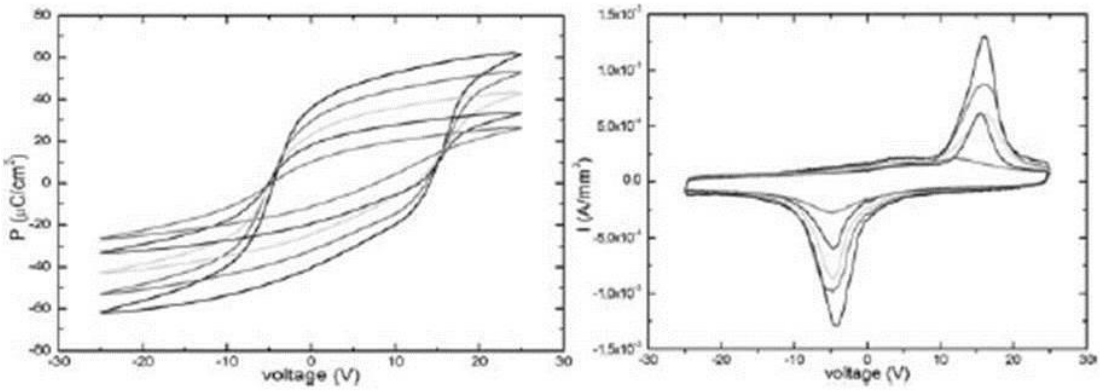

Figure 2.15 Polarization loops for a number of $PbTiO_3$ /$SrTiO_3$ samples. On the right part of the figure: the corresponding I-V loops for ferroelectric materials. Reprinted from Reference 117.

The sample is connected with a Keithley electrometer, through a triax cable as shown in Figure 2.14. The Lo-voltage and the Lo- of the Ammeter (pointed as "A" in Figure 2.14) are connected internally through a specific setting of the electrometer. The experiment takes place on a stable temperature. During the measurement, voltage is applied at the sample and current is being measured.

The expected I-V (right panel of Figure 2.15) graph of a ferroelectric material, displays two symmetric peaks of the current, one in the positive applied voltage and the other on the negative voltage. Between the peaks the current should be zero, if no leakage current appears in the measurement set up. A peak of current represents the movement of the charges towards the same direction revealing that polarization builds up in the compound. When the voltage is further increased no current is expected since the sample is already polarized. The symmetric peaks on both positive and negative voltages, strongly suggest that the direction of the electric dipoles (polarization) can be reversed by 180°.

The P-E is loop is calculated by using the same data of the I-V graphs. Specifically, the integration of the current (I) in respect with the time (t) gives the charge (Q), according to the equation:

$$Q=\int I dt \qquad \textbf{(2.15)}$$

The calculation of the polarization is accomplished by dividing the charge with the conductive area of the sample (S), since P=Q/S. The units of polarization are C/m^2. Nevertheless, it is more common to express polarization in $\mu C/cm^2$ for magnetoelectrics since it is more suitable for the quantities of charge that are measured. Converting the voltage to electric field is done by simply diving the voltage with the thickness of the sample (E=V/d).

In practice, measuring polarization, or equivalently current or charge proves to be a rather complicated task since there are many factors that affect the signal and total outcome of such measurements. First, the experimental set up consists of some components such as the wires, which carry a signal. The current that is driven through these components, may affect significantly the outcome of the measurement. Parasitic capacitance and leakage

currents are the most common reasons behind a distorted I-V measurement. If this is the case, the current values will be shifted (I≠0) along x and y axis due to the parasitic capacitance and leakage current, respectively. Secondly, the applied voltage on the sample should be below the breakdown voltage threshold of the material under study. If this occurs, then the output values of current or charge are not trustworthy. A third factor that is of outmost importance in these measurements is the previous experiments that have been carried out in the specific sample, in other words, the history of the sample. Prior application of electric of magnetic fields, will lead to different results of I-V graphs in comparison with a sample that has not been treated under any kind of field. Moreover, the temperature in which the current is being measured affects all the aforementioned factors. As a rule of thumb, if the temperature is well below the critical temperature of the possible ferroelectric transition the peaks in the I-V graph will be more pronounced and thus the P-V(or P-E) loop will be more open (the coercive field will be higher). [118]

2.5 Neutron Powder Diffraction (NPD) [16, 119, 120, 121, 122, 123, 124, 125, 126]

Neutron Powder Diffraction is a powerful technique for studying the structure and dynamics of condensed matter. It has provided crucial data for the compounds studied in this work. There are two types of neutrons sources a) the reactors such as nuclear fusion or fision and b) the spallation neutron sources in which a heavy nucleus is hit by a high energy proton and as a result emits a large number of nucleons. Most of the experiments done in this work were carried out on the BT1 diffractometer of the NCNR (NIST) center. In the NCNR neutrons are generated by a 20 MW water cooled and moderator reactor. Access has been gained by the admittance of peered reviewed proposals into two large neutron facilities the: NCNR-NIST (NIST Center for Neutron Research of the National Institute of Standards-and Technology) USA and the ISIS- RAL (UK) and at the ISIS-RAL, a spallation neutron source of 800 MeV.

Ever since the discovery of the neutron scattering phenomenon by Shull and Smart from MnO in 1949[127] a great amount of experimental research has been reported, resulting in a

continuously growing understanding of the phenomenon most of which is accessible in excellent books.[111-119] The following paragraphs, present a brief description of the neutron scattering techniques which are essential in order to understand the neutron experiments of this work.

Various properties of neutrons impose their use in condensed matter physics. Neutrons can behave as particles or as waves. They have a mass (m_n=1.674928(1)·10^{-24} gr) so they are scattered by the nucleus resulting in the so called nuclear neutron scattering. They also have a spin 1/2, thus they can interact and be scattered by the unpaired electrons of atoms - this corresponds to the magnetic neutron scattering. Furthermore, neutrons set particles into motion as they recoil from them, thus spin dynamics information can also be obtained. Having no charge, a negligible electric dipole moment and a small size (10^{-4} the size of an atom) they are far more penetrative in comparison with other charged particles. Neutrons can travel through most of the materials over long distances without being absorbed due to the fact that they interact with atoms via the nucleous.

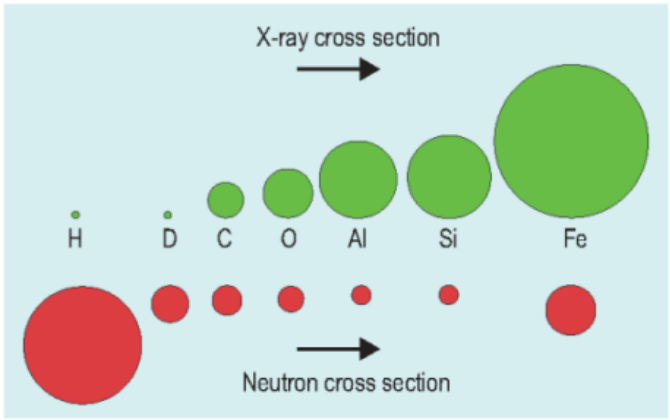

Figure 2.16 Comparison for the scattering cross sections of Neutrons (red) and X Rays (green) by some elements. Note that neutrons have a stable cross section independent of the atomic number of each element, yet are scattered rather strongly by H.

Unlike X- Rays where scattering cross section varies with the atomic number Z as Z^2, neutron scattering cross section shows little systematic variation with the atomic nucleus. Therefore neutrons are very sensitive to the scattering of light atoms such as hydrogen and

helium. A schematic representation of the difference between the scattering cross sections of elements for neutrons and X Rays is shown in Figure 2.16

The basic working principle of Neutron Powder Diffraction

Neutron scattering experiments measure the flux (Φ) of neutrons scattered by a sample into a detector as a function of the change in neutron wave vector (Q) and energy (hω). The scattering of neutrons can be described in terms of the momentum (Q), the energy (E) and the scattered flux (Φ).

Neutron scattering techniques are divided in two major categories depending on the energy of the scattered neutron beam: a) The Elastic Scattering, where the energy of the incident beam equals with the energy of the scattered beam and b) The Inelastic Scattering where some energy of the incident beam is gained or lost through the sample, so the scattered beam has a different energy from the incident (Figure 2.17). Regardless of the type of scattering, the laws that hold for all the diffraction and scattering experiments are

Momentum Conservation $\mathbf{Q}=\mathbf{k}-\mathbf{k}'$ or $\frac{h}{2\pi}\ \mathbf{Q}=\frac{h}{2\pi}(\mathbf{k}-\mathbf{k}')$ **(2.16)**

Energy Conservation: $\hbar\cdot\omega=E-E_f$ **(2.17)**

Where:

k is the neutron's wave vector of magnitude $k=\frac{2\pi}{\lambda}$ **(2.18)**

pointing along the neutron's trajectory, **k** and E is the wave vector and energy of the incident, whereas $\mathbf{k}'$ and $\mathbf{E_f}$, is the wave vector and energy of scattered neutrons respectively, and *h* is Planck's Constant.

Elastic neutron powder diffraction refers to the scattering that is done by polycrystalline samples, or samples which are composed of many crystals. Referring to terms of wave vector of the neutron, elastic scattering is the one in which the direction of the vectors does change but its magnitude remains the same.

The neutron's wave vector **k** is collinear with its velocity **v** and related by the equation:

$$\hbar\cdot\mathbf{k}=m\mathbf{v} \qquad \textbf{(2.19)}$$

The basic principle of this type of scattering can be depicted in the scattering triangle shown in figure 2.17a. The triangle shows how the vectors of momentum Q is depending on the incident and scattered wave vectors through the scattering angle 2θ. Elastic scattering occurs when k=k', whereas in inelastic k≠k'. In the triangle of Figure 2.17a taking into account that k=k' and it is derived that

$$Q=4\pi\frac{\sin\theta}{\lambda} \qquad \textbf{(2.20)}$$

When neutrons are scattered from a lattice of regularly spaced scattering centers constructive interference occurs. The condition for constructive interference between two adjacent planes which are separated by a distance d, is that Q must be perpendicular to the two scattering planes:

$$\mathbf{Q}(\mathbf{r_j}-\mathbf{r_k})=\mathbf{Q}d=2\pi n \qquad \textbf{(2.21)}$$

Where $|\boldsymbol{r_j}-\boldsymbol{r_k}|$ =d is the d spacing: d=2π/q and n is an integer (Figure 2.17c).

The combination of the equations **(2.20)** and **(2.21)** yields the Bragg law: nλ=2dsinθ.

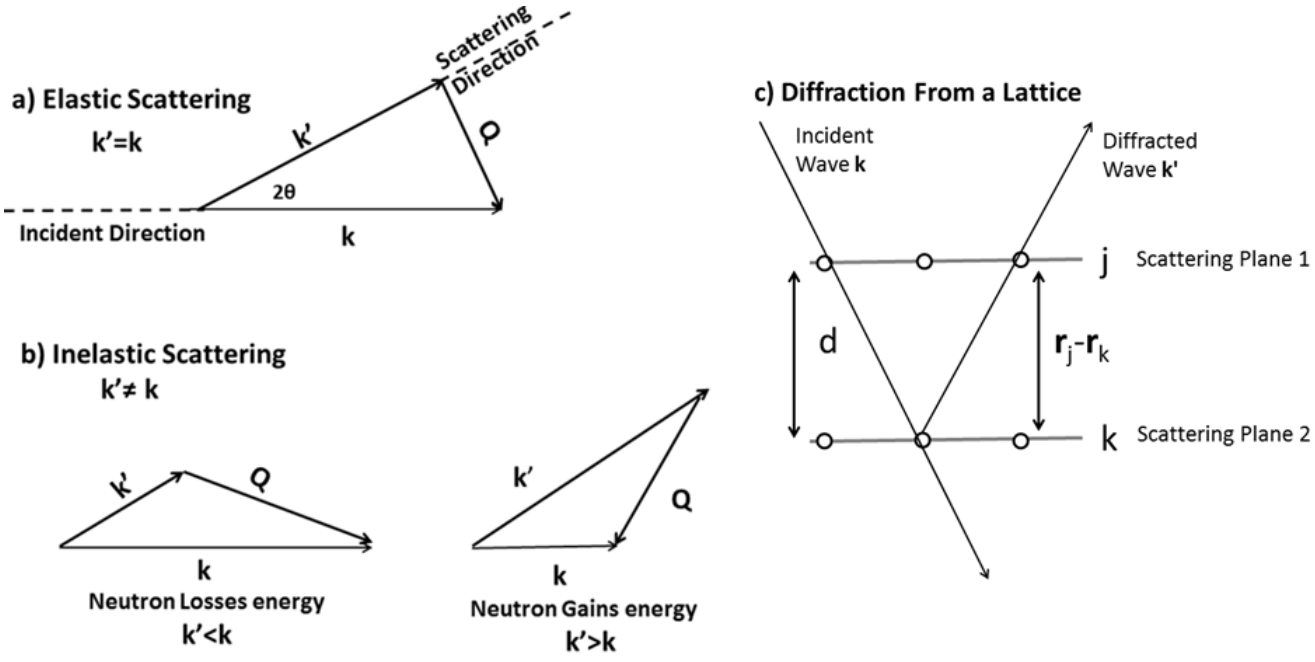

Figure 2.17 Scattering triangle in a) Elastic and b) Inelastic Scattering c) Diffraction from a Lattice.

The scattering triangle for the case of inelastic scattering is shown in Figure 2.17 (b).In this work two scattering techniques have been used the Constant Wavelength abbreviated hereafter as CW, in which the wavelength is fixed and the scattering angle varies and the Time of Flight (TOF) in which the angle θ is fixed. These methods will be discussed further, on the next paragraphs.

2.5.1 Constant Wavelength (CW)

In order to carry out a neutron scattering experiment the following are needed: a) a source of neutrons b) a way to prescribe the wavevector of the neutrons incident on the sample c) a sample, if powder preferably large (3grs and more) d) a method to determine the wavelength of the scattered by the sample neutrons and e) a detector.

CW are the most common type of powder diffractometers. As stated before they operate by using a fixed wavelength λ. Generally λ could take values among 0.7 Å to 2.5 Å. A generic layout of a CW diffractometer is shown in Figure 2.18 which is reprinted from reference.[120] Each part of the instrument is shown with a number (1-8). Neutrons are produced by a reactor (1). They pass through a shielded path (2) without suffering from intensity loss and then via a primary collimator (3) that narrows the beam. They are incident to a monochromator (4) that selects a single wavelength (monochromatic) beam. Neutrons are then guided to the secondary collimator (5) and scattered by the sample (6). Detectors are placed in an arc arrangement (7) and finally the beam is absorbed by a beam stop (8).

All the samples of this work have been studied in the high resolution diffractometer BT1 of the NCNR NIST whose layout is shown in the Figure 2.19. BT1 can be used with Ge(311), Ge(733) or Cu(311) collimators. In the experiments that will be discussed in chapters 3, 4, and 5, Ge(311) and Cu(311) with corresponding wavelengths 1.54 Å and 2.079 Å have been used.

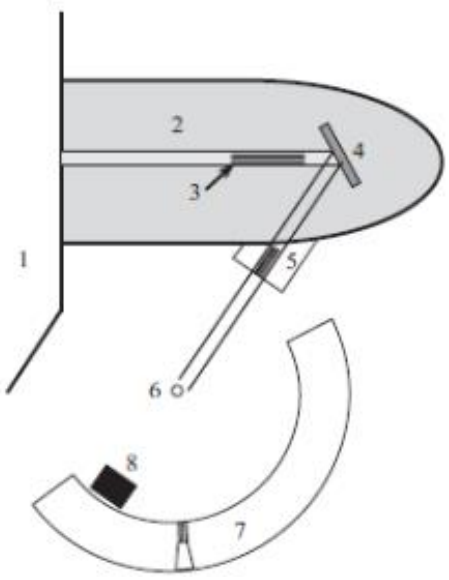

Figure 2.18 Generic layout of a CW neutron diffractometer. Numbers represent specific parts of the instrument which are explained in the text.Reprinted from Reference 120.

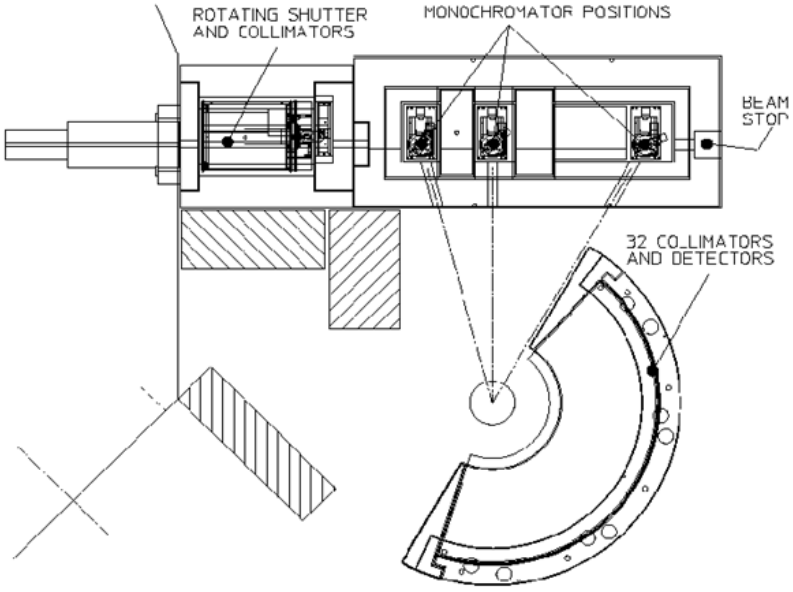

Figure 2.19 Layout of the BT1diffractometer. Reprinted from the BT1's home page: (http://www.ncnr.nist.gov/instruments/bt1/bt1_plan.html)

2.5.2 Time of Flight

In TOF technique not a single wavelength of the neutron beam, but a broad spectrum of wavelengths and therefore energies is used. The incident neutrons are monochromatized using choppers. It is important to highlight here that the independent variable is the time of flight and not the scattering angle as it happens for the constant wavelength technique. Therefore what is measured is the time required for the beam to travel from the source to the detectors of fixed scattering angles.

β-$NaMnO_2$ has been studied on the TOF diffractometer WISH (Wide angle on a single Histogram) in Target Station 2, at ISIS of Rutherford Appleton Laboratory. The general layout of TOF diffractometer is presented in Figure 2.20.

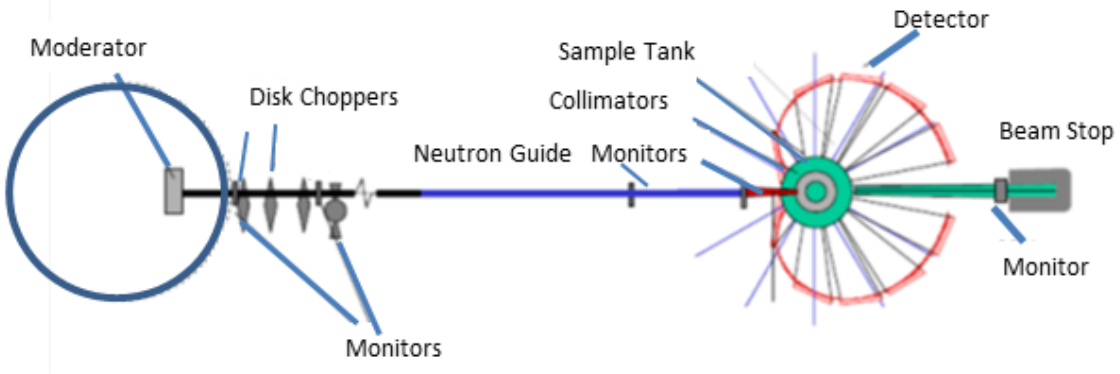

Figure 2.20 Graphic representation of a TOF diffractometer. Worth noticing the arrangement of the detectors (pointed with red lines) that correspond to different d-spacings. Reprinted from the website http://www-llb.cea.fr/SOLEIL-LLB/DiffractionPoudres/PDF/P.Radaelli.pdf

WISH is a new long wavelength magnetic diffractometer suitable for the study of magnetic or large unit cell compounds. One of its remarkable characteristics is that the wavelengths vary from 1.5 Å to 15 Å (or d-spacing 0.7 Å -50 Å). Neutrons travel towards the sample with a velocity v, through a guide of total length L (for the WISH instrument L=50 m). The time of flight (t) for neutrons is related to the wavelength (λ) by De Broglie equation:

$$\lambda = \frac{h}{p} = \frac{ht}{mL} \quad \textbf{(2.22)}$$

For the case of TOF diffractometer Bragg's law can be re-written as

$$\lambda_{hkl} = 2d_{hkl}\sin\theta \quad \textbf{(2.23)}$$

where θ is the fixed detector angle and each interplanar spacing d_{hkl} corresponds to a distinct wavelength λ_{hkl}.

The substitution of the wavelength in equation (2.22) with its equivalent from equation (2.23) yields for the interplanar spacinng

$$d_{hkl} = \frac{ht}{2mL\sin\theta} = \frac{t}{505.554L\sin\theta} \quad \textbf{(2.24)}$$

Data presented in the form of number of neutrons as a function of time of flight (in microseconds) are collected from different detectors (or "banks" as they are usually called) which are placed circularly with respect to the sample covering different d-spacing regions. Backscattering detectors also exist, which in the case of WISH produces the data with the highest resolution. At this point it is useful to clarify that there is no golden rule on which is the best method to choose, TOF or CW. Each technique has both advantages and disadvantages, so it all depends on the specific requirements of each experiment and compound under study.

2.5.3 Data Processing of Neutron Powder Diffraction Patterns [100, 120, 128, 129, 130, 131, 132]

A Neutron Powder Diffraction (NPD) Pattern is the result of Bragg scattering of neutrons from the powder specimen, which consists of a large assembly of crystalline grains with random orientations. Analysis of a NPD pattern leads to the knowledge of the crystal and the magnetic structure parameters of the specimen under study.

The NPD pattern represents the one dimensional projection of a three dimensional lattice. A Bragg reflection of perfectly crystalline material measured on an ideal diffractometer would have a Dirac peak profile, meaning a δ function located at the 2θ angle predicted by the Bragg law. Nevertheless, neither perfect crystals exist nor ideal instruments. As a result, the characteristics of the Bragg reflections depend on a number of factors which are

primarily related to the specimen's crystal and magnetic properties. Moreover the diffractometer's technique (CW, TOF) and the instrumental specifications have a tremendous effect on the shape of the peaks, the width, the symmetry, the resolution and other desicive factors for the formation and the quality of the pattern.

Diffraction from an infinite number of crystallites is attributed to the construction of the Ewald's sphere in the reciprocal space. Since the incident beam is scattered by a number of crystallites, diffraction occurs by continuum of diffracted beams all forming a 2θ angle with the transmitted beam. The diffracted beams form concentric cones, known as Debye Sherrer cones, which are centered on the incident beam. The diffraction fingerprint of each specimen is a set of Debye Serrer cones in all directions from each d_{hkl} spacing of the crystal. The detector's plane is perpendicular to the direction of the incident beam and the Debye Sherrer cones.

A diffraction pattern is represented by the scattered intensity at Y-axis as a function of the independent variable the 2θ Bragg angle. Alternatively, the X–axis can be the interplanar distance d, the so called d-spacing, a representation which is used in patterns resulting from time of flight experiments. The analysis of the neutron diffraction data has been done by using the software "FullProf Suite".

Le Bail Method and Rietveld Refinement

In the following chapters (3, 4, 5) there are going to be presented neutron diffraction patterns, which have been analyzed with the Le Bail method. This method is based on the so called Rietveld code. A few of the basic concepts of these methods are presented in the following pages, which are helpful for the understanding of the patterns presented in the experimental part.

Both methods rely on the matching of the observed pattern (the experimental diffraction data) with the calculated one using the least squares method. In this work mostly the LeBail method has been used.

Prior to any further analysis of the neutrons powder pattern, Le Bail method is the first step to carry out. This technique, first introduced by Pawley on 1981, is used to determine the Bragg peak integrated intensities and it also yields a refined unit cell. A Le Bail fit is also called "pattern matching" and "Cell Constrained Refinement", as it results in refined unit cell. A good LeBail fit, works using a constant scale factor, and provides good values which can be used in the Rietveld refinement, such as the zero shift, the background and unit cell, the peak's shape and width. More importantly, no structural model is needed. The only constrain is that the angular positions of the reflections should be consistent with the unit cell parameters. The programs that have been used were mostly the DICVOL, and the TREOR in the FullProf suite, in which some soft constraints are required, such at the crystal system and the volume of the unit cell.

Data reduction

The method that is being used for the extraction of the integrated intensities, is the least squares method. In the Rietveld algorithm, used on the LeBail fit, the quantity that is being minimized is the weighted sum of squared differences between the observed ($Y_{o,i}$)and computed intensity ($Y_{c,i}$) :

$$\chi^2 = \sum_i w_i \, (y_{C,i} - y_{O,i})^2 \qquad \textbf{(2.25)}$$

Where:

$y_{O,i}$ represents the intensity of the observed value and i indicates the intensity was measured at 2θ angle for the value 2θi and $y_{C,i}$ stands for the calculated intensity, which is estimated by the model. In any Rietveld or LeBail analysis, there is an estimated uncertainty in the observed intensity $y_{O,i,}$ which is expressed as σ[yO, i] and it is called the estimated standard deviation (esd), or the standard uncertainty (s.u). The term w_i in equation 2.25 represents the weight which is:

$$w_i = \frac{1}{\sigma[YO,i]^2} \qquad \textbf{(2.26)}$$

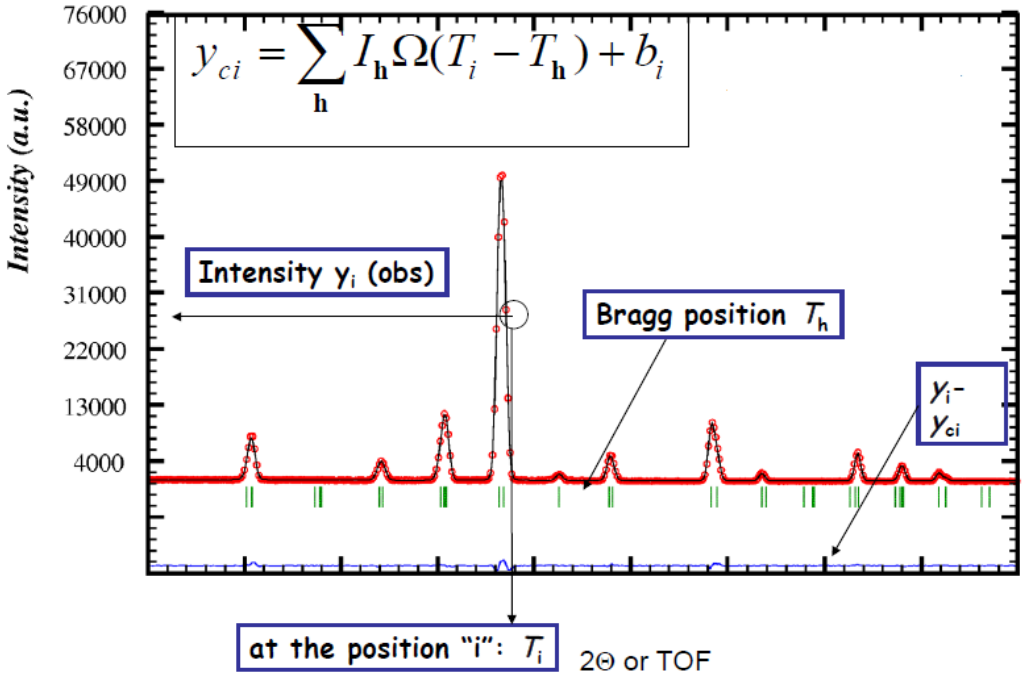

Figure 2.21 Plotted output of a Le Bail fit from the neutron diffraction pattern of $Pr_{0.66}Ca_{0.33}MnO_3$ (G42, LLB, France).The red and black line correspond to the experimental data and theoretical model,respectively, whereas the blue line shows the difference between them (y_i-y_{ci}) indicating the goodness of the fit. Reprinted from the presentation:"Powder Diffraction Patterns" of A.Daoud Aladine provided in FullProf School 2011.

A typical LeBail fit, looks like the one in Figure 2.21. The green tick marks along the x-axis, below each reflection represent the Bragg peaks of one phase Φ, as predicted by the model. In cases where magnetic phases or secondary phases are added in the theoretical model, there are also other lines with tick marks which correspond to the different phases added. The dotted red line represents the experimental data and the black line shows the intensity which is calculated by the model. The calculated intensity at each pattern point is given by:

$$y_{ci} = y_{bi} + \sum_{\varphi=1} S_{\varphi} \cdot \sum_{k_1}^{k_2} I\Phi_k \Omega_{i\varphi k} \qquad \textbf{(2.27)}$$

where:

y_{bi}: the background intensity at each pattern point I,

$\Omega_{i\varphi k}$ profile function for reflection k of phase Φ calculated at pattern point I, S_φ the scale factor for the phase Φ.

The integrated intensities I_k are the variables of the refinement which are calculated using:

$$I_{k(n+1)} = \sum_k I_k(n)\Omega_{ik} \frac{y_{i(n+1)} - y_{bi(n)}}{y_{ci(n)} - y_{bi(n)}} \quad \textbf{(2.28)}$$

The Rietveld refinement, is based on the peak positions and widths and the extracted intensities as calculated by the LeBail fit, but also requires as input the positions of the atoms in the cell. The calculated intensity at each pattern point is a complicated function which depends upon a number of different factors and is given by the equation

$$y_{ci} = y_{bi} + \sum_{\varphi=1}^{N} S\varphi \sum_{k=k1}^{k2} j\varphi k \cdot Lp_{\varphi k} \cdot O\varphi k \cdot M \; |F_{\varphi k}|^2 \cdot \Omega_{i\varphi k} \quad \textbf{(2.29)}$$

Where: the index Φ refers to the sample phases and

k refers to the index of reflections contributing at the pattern point i,

j_k represents the multiplicity of reflection k,

L_{pk} the Lorentz polarization factor,

O_k is the preferred orientation for reflection k,

M is the absorption correction,

Ω_{ik} is the profile function for reflection k of phase Φ calculated at pattern point i, and the $|F\varphi k|$ is the structure factor of reflection k for phase Φ expressed by the equation :

$$F_{hkl} = \sum_{n=1}^{N} f_n \exp 2\pi i (hu_n + kv_n + lw_n) \quad \textbf{(2.30)}$$

f_n is the scattering factor,

hkl are the Miller indices and their subscript indicates the matrix transposition.

The agreement factors

In any LeBail or Rietveld refinement there are the agreement factors which estimate the convolution between the theoretical model and the experimental data and measure in this way the goodness of the fit. The most common factors used to describe the quality a Rietveld analysis are:

The profile fitting R-profile: $$R_p=100\ \frac{\sum i\ |Yo,i-Yc,i|}{\sum i\ |Yo,i|} \quad \textbf{(2.31)}$$

the R-weighted profile: $$R_{wp}=100\ \left[\frac{\sum wi\ |Yo,i-Yc,i|^2}{\sum_i wi\ |Yo,i|^2}\right] \quad \textbf{(2.32)}$$

the R-expected: $$R_{exp}=\left[\frac{N-P}{\sum_i w_i Y^2_{o,i}}\right]^{1/2} \quad \textbf{(2.33)}$$

and the goodness of fit, known as $$\chi^2=\left(\frac{R_{wp}}{R_{exp}}\right)^2=\frac{\sum wi(Y_{o,i}-Y_{c,i})^2}{N-P} \quad \textbf{(2.34)}$$

where: N is the total number of data points,

P is the number of parameters adjusted

The ideal Rietveld or LeBail refinement is characterized by $\chi^2= 1$.

2.6 Transmission Electron Microscopy (TEM)[133,134]

2.6.1 Introduction

TEM experiments have been carried out in Jeol JEM 2200FS instrument, equipped with an image aberration corrector, an in-column energy filter and a silicon drift detection system for EDS at the Italian Institute of Technology –Genova, Italy by Dr. Rosaria Brescia under the supervision of Dr.Liberato Manna. ED patterns and HRTEM images were obtained also with a Tecnai G2 electron microscope operated at 200 kV in EMAT, University of Antwerp, in Belgium by Dr. Artem Abakumov.

Trasmission eletron microscopy is a technique in which a beam of electrons interacts and passes through a sample to produce an image of it. Electrons in TEMs that have been accelerated by potentials of 200 kV have a de Broglie wavelength of 2.7 pm. This small wavelength, actually smaller than a diameter of an atom, is the reason behind the TEM capability for obtaining significantly higher resolution images when compared to the ones of a conventional optical microscope.

TEM microscopy results have played the leading role in unraveling the origin of the magnetodielectric coupling of β-$NaMnO_2$ and α-$NaMnO_2$. In polycrystalline materials TEM yields valuable information related to the existence of secondary phases, the morphology and size of the crystallites and any possible orientation of the crystallites in respect to the electrons beam.

2.6.2 The layout of TEM

The basic components for conducting transmission electron microscopy (Figure 2.22) are an electron gun which emits electrons, a column containing a series of magnetic lens in order to focus the electrons, the sample holder and the imaging system.

A monochromatic beam of electrons is emitted by the point source of an electron gun, which is usually a V shaped filament, of LaB_6 or W, surrounded by an electrode- the Welnet Cup. A high voltage potential is applied to the electrons which are accelerated in high vacuum (10^{-7} Torr). The electron beam is confined by the condenser lens, passes through the condenser aperture and then hits the sample. The transmitted beam passes through the objective lens which forms the image display. Finally the beam is directed to the magnifying system, which consists of three lenses, the first and second intermediated lens which control the magnification of the system and the projector lens. The magnified image is shown on a viewing screen in monitor (or both). The produced image is a 2D map of the material's density.

One of the basic requirements and constraints imposed by TEM function is the thickness of the specimen under study. The thickness of the sample affects both the transmission of the

incident beam but also the brightness and intensity of the formed image. Thick areas of the specimen allow fewer transmitted electrons so these areas appear darker. Generally, thickness of 1000 Å and less are acceptable, since the electrons should be able to interact and pass through the sample.

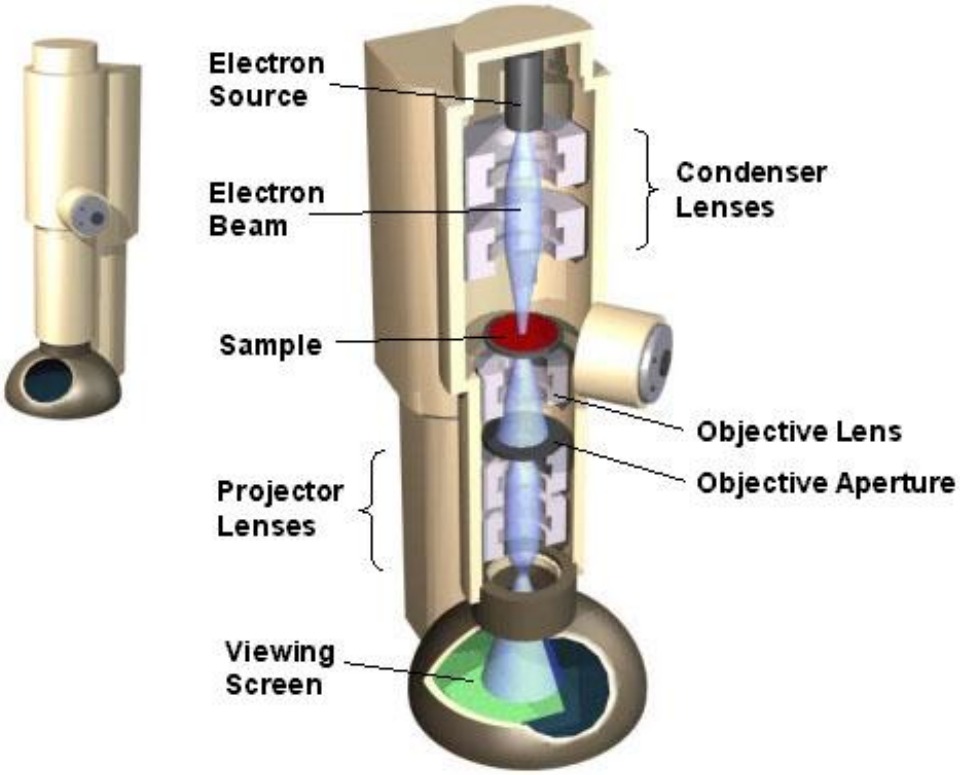

Figure 2.22 The basic parts and the geometry of a TEM microscope (reprinted from the website *http://www.hk-phy.org/atomic_world/tem/tem02_e.html*)

Three possible interactions between the sample and the electrons beam can occur (Figure 2.23); inelastically scattered electrons, elastically scattered electrons (the diffracted beam) and unscattered electrons (the transmitted beam). Depending on the energy of the scattered electrons, TEM has the possibility to apply a variety of techniques which give different information about the sample.

The elastically scattered electrons maintain the initial energy of the incident beam ($E_{f=}E_i$).They are used in electron diffraction techniques such as conventional imaging

(bright field and dark field of TEM), phase contrast imaging (high resolution TEM, known as HRTEM) and energy dispersive spectroscopy (EDS). Conversely, the inelastically scattered electrons that loose some energy after interacting with the sample ($E_f<E_i$), are used in the technique known as Energy Electron Loss Spectroscopy (EELS).

The experimental part contains results obtained from different modes of TEM. When observing a specimen in TEM, these techniques are easily accessible by switching from one mode to another. Their basic principles are discussed in the following paragraphs.

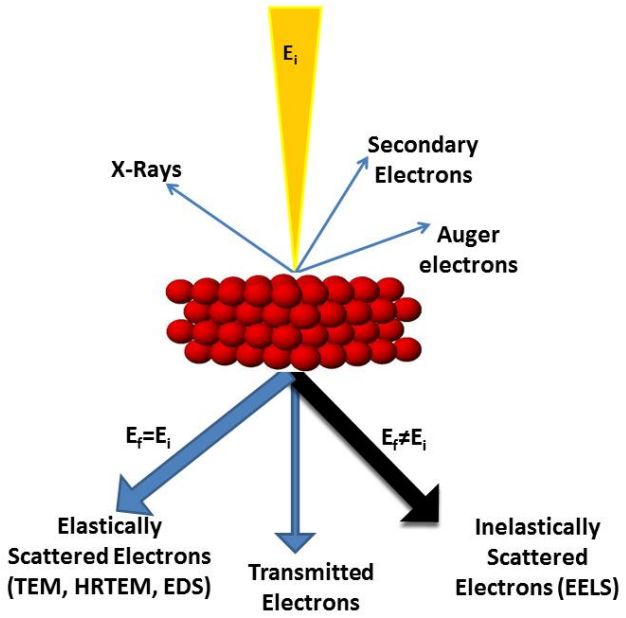

Figure 2.23 The possible interactions of the incident electrons beam (Ei) with the sample in TEM.

2.6.3 Different Modes of TEM

2.6.3.1 Electron Diffraction

Strong diffraction occurs, when electrons of wavelength λ, will be coherently scattered by a crystal lattice of d-spacing. The diffracted beam occurs only in 2θ angles which obey the Bragg law equation: $\lambda=2d\sin\theta$

(by convention n is regarded equal to 1)

Hence, electron diffraction uses the same principle as X-Rays. The difference lies in one important advantage over X-Rays: they can be focused easily.

The diffraction pattern can be imaged by the use of subsequent lens. Two images are formed: the diffracted image is formed in the so called reciprocal space, whereas the magnified image is formed in the real space. The real space can be transformed mathematically to the reciprocal space, and *vice versa*, with the use of a Fourier transformation.

By placing an intermediate aperture in the image plane, a small area of the sample is selected known as the "selected area diffraction" (SAD). A number of crystal structure properties can be obtained: grain morphology and size, lattice symmetry and parameters, existence of secondary phases and orientation of the specimen or of individual grains with respect to the electrons beam.

2.6.3.2 High Resolution Transmission Microscopy (HRTEM)

The HRTEM images reveals columns of atoms, intergrowth of different phases and the existence of planar defects, as observed in the polymorphs α-$NaMnO_2$ and β-$NaMnO_2$.

This technique is based in contrast microscopy. The image formation in HRTEM is an interference phenomenon. Carried out with the use of a large objective aperture the contrast image is formed combining the phase and intensities of diffracted and transmitted beams. When an electron wave passes through the sample, the incident electron wave is scattered at the potentials of the atoms, and thereby the phase of the electron wave is changed. The electron beam also interacts with the periodic arrangement of the atomic columns leading to Bragg diffraction. At the exit surface of the specimen the object wave is formed, which carries important structural information of the sample. The magnification of the object wave adds additional phase shifts due to imperfect lenses (aberrations). Finally, the image recorded is an interference pattern of the electron wave with itself.

2.6.3.3 Energy Dispersive X- Ray Spectroscopy (EDS)

An analytical transmission electron microscopy method used to quantify chemical concentrations. After background removal, the intensities of peaks of the X-Rays, with energies varying from 10^2 eV to 10^4 eV are being measured. Each element gives peaks of different intensity; hence chemical analysis can be carried out.

2.6.3.4 Scanning Transmission Electron Microscopy- High Angle Annular Dark Field (STEM-HAADF)

STEM results in a "chemical map" of the sample where the density distribution of each chemical element is shown. A vertical column of atoms is displayed by STEM as a sharp object. This method is capable of sub Angstrom spatial resolution by using a narrow beam (1 -10 Å) of incoherent elastically scattered electrons. The dark field image is provided by an annular detector which collects a large fraction of the intensity of the scattered electrons at high angles.

2.6.3.5. Energy Electron Loss Spectroscopy (EELS)

The spectrum of energy loss of electrons can be useful for identifying the elemental components of the specimen. EELS is also a powerful tool also for distinguishing between different oxidation states of an element.

Some electrons while interacting with the specimen loose energy to plasmons or inner shell ionizations. The lower energy of the inelastically scattered electrons results in lower values of velocity, which is the criterion for distinguishing and collecting them with a magnetic sensor. EELS results in a spectrum of intensity (counts) versus energy loss (eV), in which the elements and oxidation numbers are located from identifying the peaks according to their energy loss.

Chapter 3:

Crystal, Magnetic and Magnetodielectric Behavior of the Frustrated Antiferromagnet α-$NaMnO_2$

3.1 Introduction

The transition metal oxide α-$NaMnO_2$ has been reported around 1970,[6, 135] and has been the subject of intensive research for various reasons. Its layered crystal structure, provides the ideal host framework system for the synthesis of numerous of compounds by soft chemistry reactions such as intercalation and deintercalation processes.[136, 137, 138] The fact that α-$NaMnO_2$ is isostructural with α-$LiMnO_2$,[82, 139] well-known for its applications as cathode material in the rechargeable batteries, has boosted the structural and electrochemical studies of α-$NaMnO_2$ [7, 140, 141] as an alternative and significantly less expensive option of $LiMnO_2$, as Li is rare while Na is not.

However, little had been known about its magnetic properties until 2007, when M.Giot [7] et al, showed that, the α-$NaMnO_2$ (Mn^{+3}, $3d^4$, S=2) is a system of competing magnetic interactions which are dictated by magneto-elastic coupling at T_N=45 K. At this temperature a structural distortion lifts the magnetic frustration and results in antiferromagnetic ordering with the propagation vector **k** (0, ½, ½). The crystal and magnetic structure, as well as the spin dynamics have already been studied and are discussed briefly in the following paragraphs.

In this work, for the first time, we shed light on the magnetodielectric properties of the α-$NaMnO_2$. Surprisingly the α-$NaMnO_2$ displays a sharp dielectric anomaly around 95 K, well above the temperature where it becomes antiferromagnetic. This excludes the scenario of spin driven magnetoelectricity. Furthermore, the dielectric anomaly is importantly enhanced under external magnetic fields, a phenomenon consistent with the appearance of the magnetodielectric coupling.

To address the origin of the magneto-electric coupling in the α-$NaMnO_2$, transmission electron microscopy (TEM) experiments took place. The TEM studies, also carried out for the first time in α-$NaMnO_2$, showed the existence of planar defects attributed to the presence of the β-$NaMnO_2$. β-$NaMnO_2$ displays anomaly on its dielectric constant around 90 K, which is attributed to the emergence of the incommensurate magnetic structure –a subject analyzed in chapter 4. The realization that a secondary phase in the α-$NaMnO_2$ is

related with the material's magnetodielectric response brings out the role of the nanodomains and the inhomogeneity of a compound's microstructure in the coupling between the electric and magnetic degrees of freedom.

Crystal Structure

The crystal structure of α-$NaMnO_2$ at room temperature is of the prototype α-$NaFeO_2$ type. However α-$NaMnO_2$ does not belong neither at the hexagonal nor at the rhombohedral systems as it expected for the majority of the systems with the ABO_2 stoichiometry, but crystallizes in the monoclinic system, at the C2/m space group with cell parameters: a= 5.67 Å, b= 2.86 Å, c= 5.80 Å, β=113.14 deg. The deviation of α-$NaMnO_2$ from the prototype rombohedral stucture is attributed to the distortion of the MnO_6 octahedra along the z-axis, caused by the Jahn Teller active Mn^{+3} ions (t_{2g}^3 e_g^1).

The crystal structure of the α-$NaMnO_2$ is represented in Figure 3.1, where the manganese, oxygen and sodium atoms are represented with grey, red and purple spheres respectively. α-$NaMnO_2$ is considered as derivative of the rock-salt structure where all octahedral interstices are filled with the A and B cations.[142] The structure is composed by sheets of edge sharing MnO_6 octahedra which are separated by a one dimensional layer of Na cations. Cubic close packing (ABCABC) occurs for the oxygen ions. As shown in Figure 3.2, the Mn^{+3} (represented with the dark grey spheres) are arranged on a triangular lattice, which is a common characteristic for the magnetic cations of the compounds with general chemical formula ABO_2.

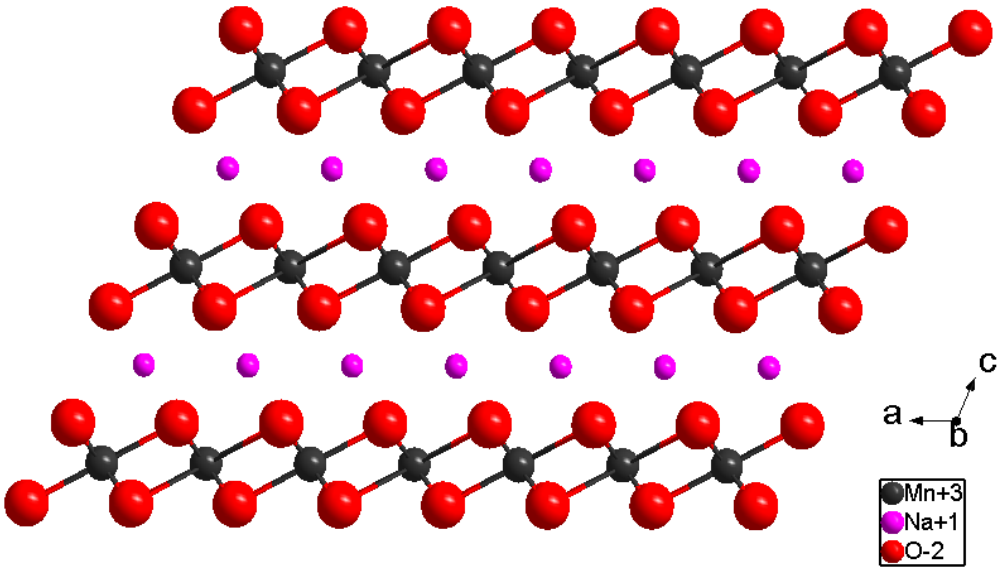

Figure 3.1 The layered structure of the α-$NaMnO_2$. The magnanese (Mn^{+3}), oxygen (O^{-2}) and sodium (Na^{+1}) ions are represented with the grey, red and purple spheres, respectively.

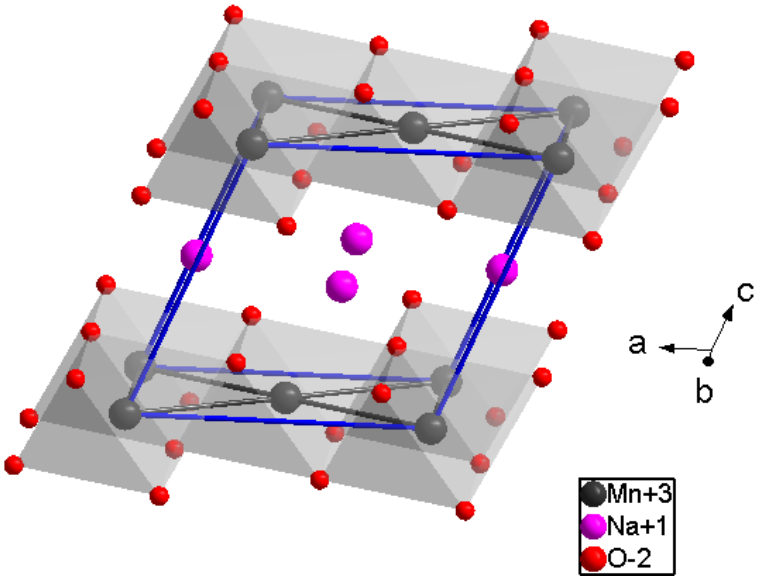

Figure 3.2 A detail of the α-$NaMnO_2$ showing the triangular arrangment of the Mn cations on a flat layer. The cell edges are those indicated with the blue lines.

Studies on the Magnetic Structure

The magnetism of α-$NaMnO_2$ has been investigated by early studies on neutron powder diffraction (NPD) experiments,[7] and recent electronic structure calculations, backed up by numerical simulations.[143]

Neutron Powder Diffraction patterns were obtained at the high resolution diffractometer BT1 (NIST, USA) with the constant wavelength (λ=2.0782 Å). The analysis of the NPD patterns was accomplished with the software FullProf Suite.

According to the NPD data, α-$NaMnO_2$ becomes antiferromagnet below 45 K. The magnetic transition occurs simultaneously with a structural distortion from the room temperature monoclinic structure (C2/m) to the triclinic ($P\bar{1}$) below 45 K. This structural transition results in the dictation of the competing magnetic interactions which are present in the monoclinic structure.

Specifically, the magnetic frustration arises due to the triangular arrangement of the Mn^{+3}, shown in Figure 3.3a. The magnetic interactions, J_1 and J_2 are pointed with the green and blue lines, respectively (J_1, J_2<0, J_1/J_2 small). However, as it is more clear in Figure 3.3b, J_2 in the monoclinic cell (blue cell lines with the indications $a_m b_m$) is both ferromagnetic and antiferromagnetic, pointed with the plus (+) and minus (-) sign, respectively. When the α-$NaMnO_2$ adopts the triclinic structure (blue cell pointed with the a_t b_t indications in Figure 3.3b) the frustration is relieved and the system develops a long range antiferromagnetic order.

The structural distortion at 45 K results in the crystallization of α-$NaMnO_2$ in the triclinic structure. Figure 3.4 shows the Rietveld refinement carried out for the 4 K pattern, in which the calculated profile refers to the triclinic cell (χ^2 = 3.82, R_{Bragg} = 1:56%, $R(F^2)$= 1.19%, R_{magn} = 5.63 %). The new cell parameters, are a_t= 3.1677(7) Å, b_t= 3.16046(7) Å, c_t= 5.78217(6) Å, α_t= 110.465(2)°, β_t = 110.415(2)°, γ_t= 53.6173(8)° where the subscript t refers to the triclinic unit cell.

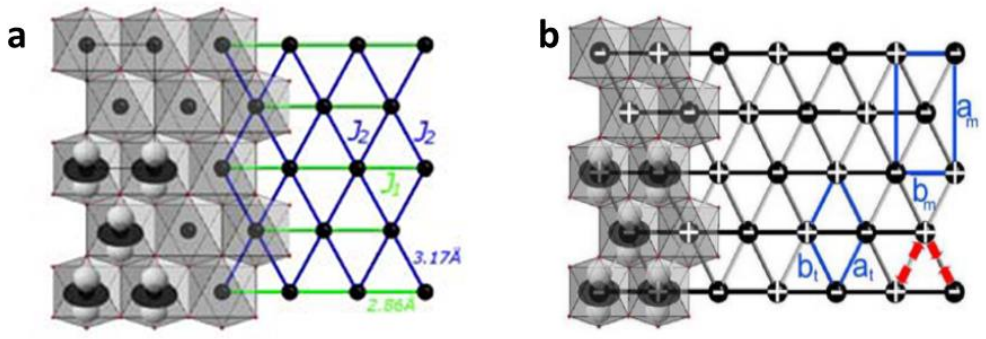

Figure 3.3 (a) Crystal structure in the a_mb_m plane at room temperature. The subscript m refers to the monoclinic system. Mn and O atoms are represented as large black and small red spheres, respectively. J_1 and J_2 are magnetic inequivalent magnetic interactions along bm and $[110]_m$ represented with green and blue lines, respectively. (b) The magnetic order in the ab plane for α-$NaMnO_2$. The monoclinic (T>45 K) and triclinic (T<45 K) unit cells are shown with the blue marks pointed out as a_mb_m and a_tb_t, respectively. Red arrows show the strain directions, whereas the + and – signs indicate the up and down directions of the magnetic moments. Reprinted from Reference 7.

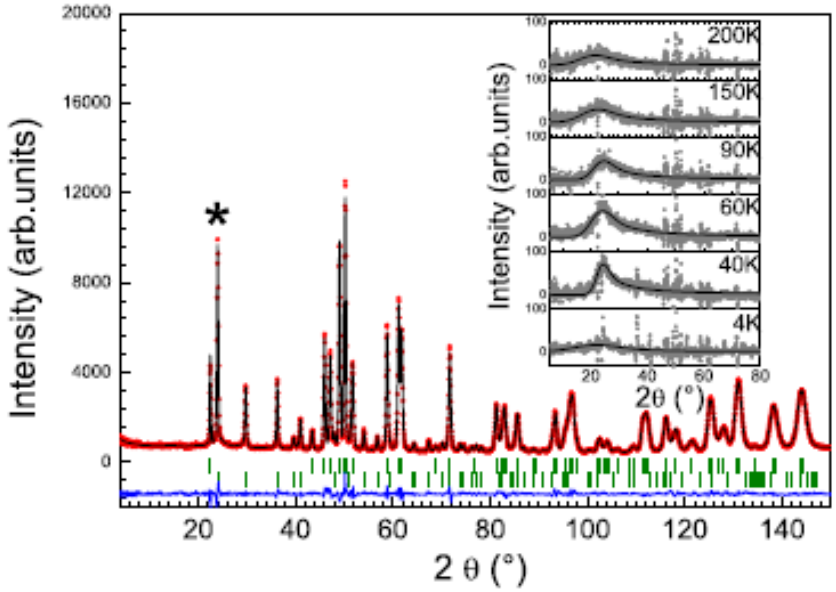

Figure 3.4 Rietveld Refinement of the NPD data obtained at 4 K at the BT1 diffractometer with the reliability factors: χ^2=3.82, R_{Bragg} =1.56%, $R(F^2)$ =1.19%, R_{magn} = 5.63%. The red black line represents the experimental data and the calculated profile, respectively, whereas the blue line shows the difference in between them. The first row of vertical green ticks at the bottom shows the Bragg reflections of the nuclear structure, whereas the second raw indicates the positions of the magnetic peaks. Reprinted from Reference 7.

The inset of Figure 3.4 shows that diffuse magnetic scattering appears already at 200 K. This type of scattering is evident by the broad asymmetric peaks with a long tail on the high 2θ side, widely known as Waren peaks, [144] indicating a 2D magnetic arrangement. Upon further cooling the Waren peaks are eliminated and the 3D magnetic ordering takes place.

The magnetic propagation vector **k** in the triclinic setting becomes $(0, ½, 0)_t$. The neutron powder diffraction studies of α-$NaMnO_2$ manifest the dictation of the magnetic frustration by the magneto-elastic coupling. The coupling is evident by the structural distortion which occurs at the same temperature where the long range magnetic ordering occurs.

Electronic structure calculations.

The Electronic structure of α-$NaMnO_2$ was calculated within the framework of density-functional theory (DFT) in the VASP code.[145 146 147]

The calculations were done with experimental lattice parameters after a full relaxation of atomic positions. The Heisenberg model

$$\hat{H} = \sum_{<ij>} J_{ij} \mathbf{S}_i \mathbf{S}_j \qquad \textbf{(3.1)}$$

was used to map out the total energies of the individual exchange couplings. The summation is over all bonds <ij> between the Mn^{+3} ions.

Figure 3.5 shows the 2D triangular spin lattice of the magnetic interactions in α-$NaMnO_2$. The experimental values of the interactions J_1 and J_2 were found to be 73 K and 29 K, respectively.[7, 148] According to the calculations of the electronic structure, a strong AFM exchange J_1=72 K was found along the b direction and weaker diagonal exchanges J_2=23 K (Figure 3.5). The difference between J_1 and J_2[143]can be attributed to the Mn-Mn distances of 2.86 Å and 3.17 Å (shown in Figure 3.3a). Since $J_1 >> J_2$ the nature of the spin correlations is 1D in agreement with earlier results of the inelastic neutron scattering. [8]

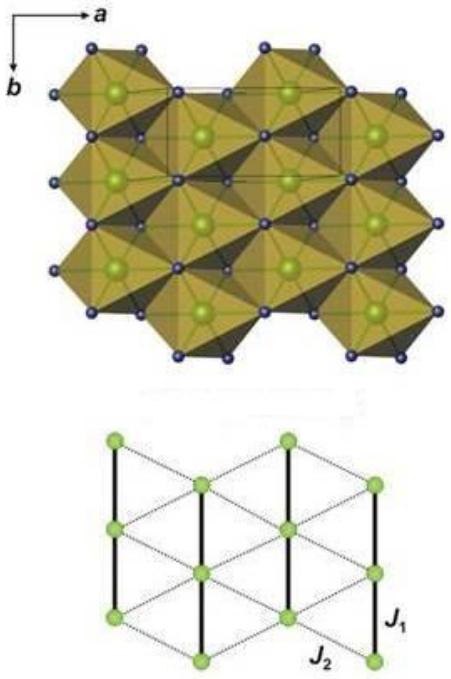

Figure 3.5 Structures of [MnO_2] layers and relevant topologies of magnetic interactions in α-$NaMnO_2$. Reprinted from Reference 143.

Numerical simulations.

The magnetism of α-$NaMnO_2$ polymoprh was further studied by numerical simulations .[143]Magnetic susceptibilities of different spin models are obtained from quantum Monte-Carlo (QMC) simulations performed in the looper code [149] of the ALPS simulation package.[150] Finite lattices with 16 sites (1D) or 16×16 sites (2D) with periodic boundary conditions were used. Finite-size effects are negligible within the temperature range of interest.

The static magnetic susceptibility of α-$NaMnO_2$ measured on a ZFC mode under 200 Oe, is presented in Figure 3.6. The broad maximum observed at high temperatures is typical of low dimensional magnets. [151] The experimental data of Figure 3.6 have been fitted with the equation $\chi=\chi_{int}+C/(T+\theta)$. The term χ_{int} is calculated by the QMC calculations and for

the α-$NaMnO_2$ is the susceptibility of a quantum spin chain.[143] The ratio of C/(T+θ) accounts for the paramagnetic tail noticed at the susceptibility curve at low temperatures. The fit yields J_1=65 K, C=0.013 emu K/mol and θ=0 K.

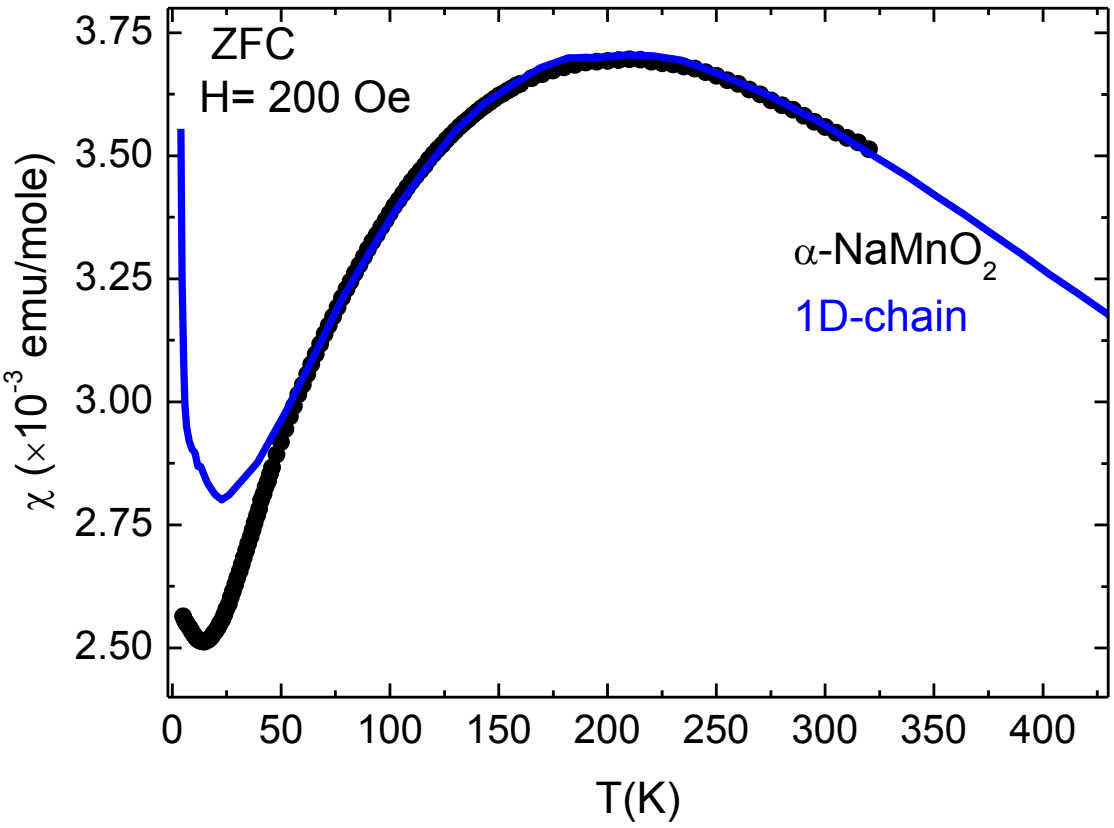

Figure 3.6 The static magnetic susceptibility of the α-$NaMnO_2$ measured on a ZFC mode under 200 Oe magnetic field, shown with the black points. The model description of the α-polymorph presented with the continuous blue line indicates a uniform spin chain.

In detail, the zero field susceptibilities have been derived by Fisher.[9] For an Ising 1D chain is expressed in the following equations:

$$\chi_{\parallel} = \frac{N g_{\parallel}^2 \mu_B^2}{2J} \frac{J}{2kT} e^{\frac{J}{kT}} \quad \textbf{(3.2)}$$

and

$$\chi_{\perp} = \frac{N g_{\parallel}^2 \mu_B^2}{4J} [(\tanh \frac{J}{2kT}) + \left(\frac{J}{2kT}\right) \mathrm{sech}^2(\frac{J}{2kT})] \quad \textbf{(3.3)}$$

where $\chi_{\parallel}$ and $\chi_{\perp}$stand for the parallel and perpendicular susceptibility, respectively. Since $\chi_{\parallel}$is an odd function and $\chi_{\perp}$ is an even one, the sign of the exchange constant in an Ising system can only be determined from the parallel susceptibility $\chi_{\parallel}$.

3.2 Synthesis of α-$NaMnO_2$.

Polycrystalline powder specimens of α-$NaMnO_2$ have been synthesized by high temperature solid state reaction at 750°C. Na_2CO_3 (Aldrich, 99.5+%) and Mn_2O_3 (Aldrich, 99%) have been used as starting materials according to the following chemical reaction:

$$Na_2CO_3 + Mn_2O_3 \longrightarrow 2\ \alpha\text{-}NaMnO_2 + CO_{2(g)} \qquad \textbf{(3.4)}$$

Taking into account the % purity each reactant, 0.4822 gr and 0.718 gr of Na_2CO_3 and Mn_2O_3, respectively have been used in order to synthesize one (1) gr of α-$NaMnO_2$. The starting materials were stored in a drying cabinet of average temperature 60°C-70°C. The reactants were mixed and grounded in an agate mortar for approximately 35 min. Afterwards the powder mixture was placed into 13 mm die, which is inserted into a hydraulic press. Four (4) tons of pressure, which are equivalent with $2.94 \cdot 10^8$ Pa for the specific die, were applied for twenty (20) minutes. The pellet formed has a greyish- black color (due to the white and black color of the Na_2CO_3 and Mn_2O_3, respectively). The heating protocol is shown in Figure 3.7: the synthesis started from room temperature and reached 750°C with a constant heating rate of 3 °C/min. After having dwelled in 750°C, for a total of 60 hrs under continuous Argon flow, the pellet was quenched at room temperature. Its final color was brown. Quenching is accomplished by opening the one end of the furnace and keeping the pellet there, while it remains under Ar flow, for about 10 minutes. From this point, precautions of the air and moisture sensitive compounds are strictly followed, since the Mn^{+3} of the α-$NaMnO_2$ can be oxidized to Mn^{+4} when exposing the sample in the atmosphere. Therefore, the sample was stored in an Ar-filled glove box.

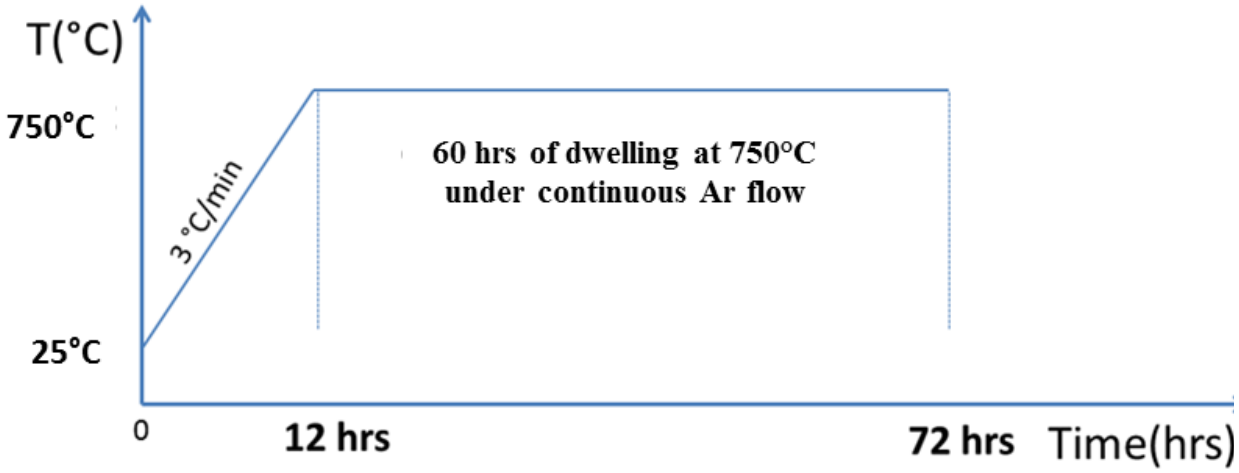

Figure 3.7 The heating protocol that has been followed for the solid state synthesis of the polycrystalline powder α-$NaMnO_2$

3.3 Characterization of α-$NaMnO_2$

3.3.1 X –Ray Powder Diffraction

X Ray powder diffraction (XRPD) using the wavelength λ=1.5406 Å has been carried out to all the α-$NaMnO_2$ the samples synthesized with the protocol which is described in paragraph 3.2. Prior to the X-Rays experiment, the sample was sealed with the mylar film under argon atmosphere (inside the glove box) in order to prevent contact with moisture and air.

The graph obtained by the XRPD is shown in Figure 3.8. The Bragg reflections obtained from the α-$NaMnO_2$ show a perfect matching with the reflections obtained from the database ICSD_16270. Therefore, the room temperature structure of the α-$NaMnO_2$ can be successfully indexed upon the monoclinic structure (C2/m) with cell parameters: a= 5.67 Å, b= 2.85 Å, c= 5.80 Å, β=113.2 deg. Nevertheless, there is one reflection at 14.11 deg pointed with a red arrow in the pattern. This peak corresponds to 001 reflection of the β-

$NaMnO_2$ -a near equivalent in energy polymorph of the α-$NaMnO_2$. This observation is nicely combined with the magnetodielectric experiment's results and it discussed further on the basis of electron diffraction and high resolution electron microscopy images in paragraphs 3.5.1 and 3.5.2.

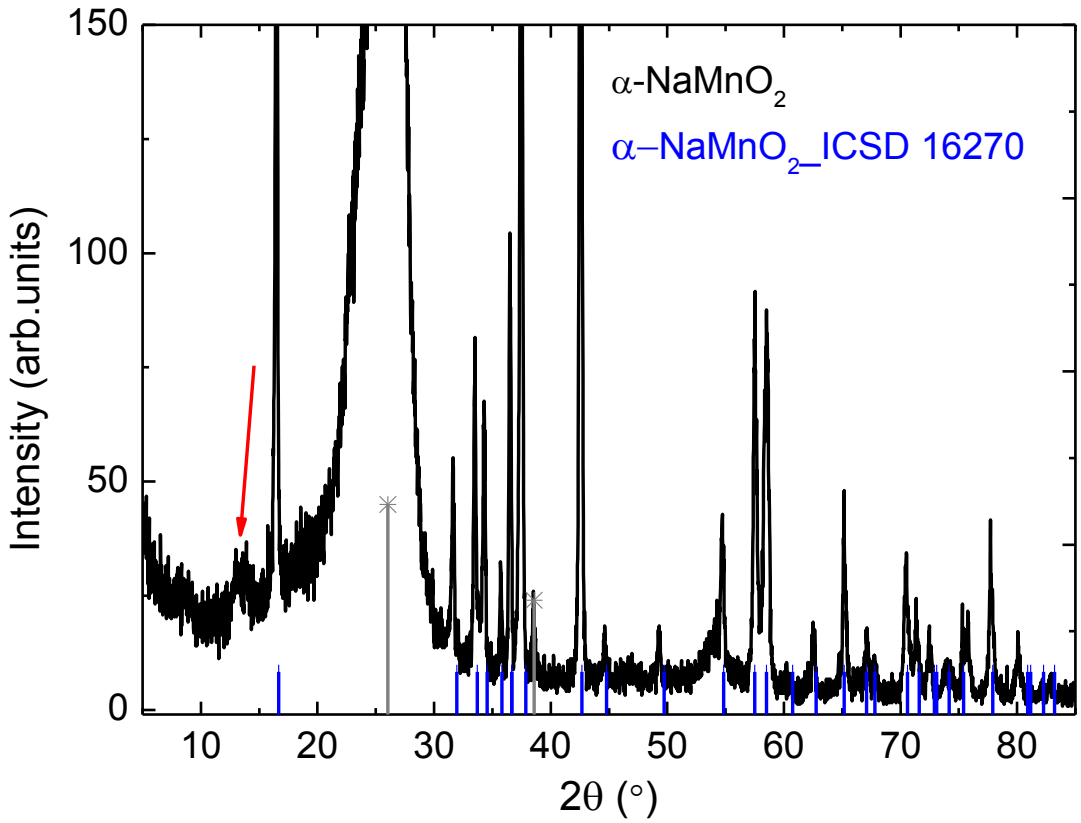

Figure 3.8 X-ray powder diffraction of a polycrystalline sample of α-$NaMnO_2$ (black continuous line). The indexing of the Bragg reflections has been done according to the data base ICSD_16270, which corresponds to the blue vertical ticks. The grey ticks around 26 deg and 38 deg are attributed to reflections of the mylar film. Note the red arrow at 14.11 deg shows a reflection which is attributed to the 001 peak of the β-$NaMnO_2$.

3.3.2 Inductive Coupled Plasma Optical Emission Spectroscopy (ICP-OES)

The purpose of the experiment that has been carried out in the ICP-OES was to determine the Na/Mn ratio in the α-$NaMnO_2$ sample. The ratio was found to be Na/Mn=0.826. This means the amount of Na is less than expected, since based on the stoichiometry of the equation 3.4 the ratio Na/Mn should be 1/1. The reduced amounts of Na in the final product can be explained by the sodium loss at higher temperatures. Sodium carbonate decomposition and sodium loss occurs at temperatures higher than 400°C. However, since solid state reaction is based on the diffusion between the atoms of the reactants, it is not always a straightforward procedure to predict the amount of the Na that will be lost. Transmission electron microscopy (EDS mapping, EELS see next paragraph) were used as analytical techniques for the determination of the elements ratio in the α-$NaMnO_2$ compound.

3.3.3 Energy Electron Loss Spectroscopy (EELS)

EELS results were carried out in Instituto Italiano di Technologia in Genova, Italy. The transition metal $L_{2,3}$ energy loss spectra of the α-$NaMnO_2$ was recorded and carefully analyzed based on the white line ratio method. According to this method, the integral intensity ratio of the L_3 and L_2 excitation peaks of a transition metal is correlated to its formal oxidation state.[152,153] The oxidation state of the Mn ions of the α-$NaMnO_2$ was calculated to 3.2. The expected oxidation state is of the Mn^{+3} in the α-$NaMnO_2$ is 3, so the small deviation that is observed could be related with a small percentage of Mn^{+4} impurities, or a small paramagnetic impurity evident by the contribution of the paramagnetic tail on the magnetic susceptibility of the α-$NaMnO_2$ at low ($T<20$ K) temperatures (see Figure 3.6).

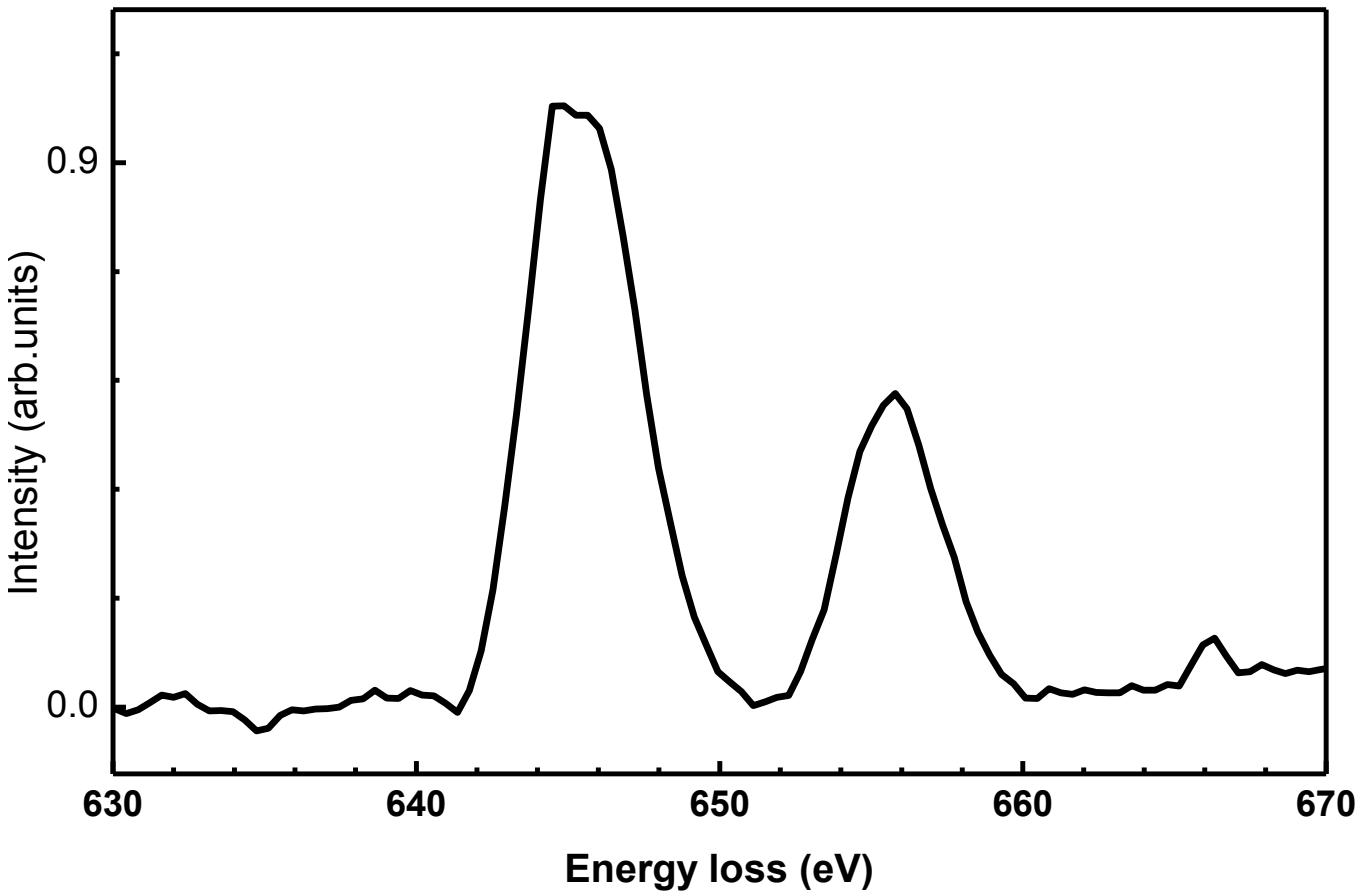

Figure 3.9 L edge energy-loss near-edge structures for the determination of the oxidation state of Mn in the α-$NaMnO_2$.

3.4 Magnetodielectric Measurements

In order to check the possible magnetodielectric coupling in the α-$NaMnO_2$ compound measurements of the dielectric constant (ε') and dielectric loss (ε"or tanδ) versus temperature and under various magnetic fields, have been carried out. The aim is to check for any possible dielectric anomalies.

Sample's Code	**Diameter (mm)**	**Thickness (mm)**	**Electric Field Applied (kV/m)**	**Time between: sample's synthesis and MD experiments**
ib168	5	1.33	751	1 week
oa113_1	5	1.63	613	4 years
oa113_2	5	1.26	793	4 years
spins	5	1.45	689	7 years

Table 3.1 Different α-$NaMnO_2$ samples that have been measured in the magnetodielectric experiments.

Table 3.1 presents the α-$NaMnO_2$ samples which come from 3 different batches (with the sample codes: ib168, oa113, spins) all synthesized with the same protocol as described in 3.2 section. The same magnetodielectric measurements were carried out in the samples of table 3.1, to check the reliability and repeatability of the obtained results. All the samples measured showed good repeatability. Minor differences such as the small deviations in the value of the dielectric constant can be attributed to the differences in the grain size of each sample. In section 3.4 we present the results from two samples: the ib168 and the oa113_1, named as sample 1 and sample 2, respectively.

3.4.1 Magnetodielectric Measurements Under Zero Magnetic field

First, the dielectric constant versus temperature was measured in various frequencies. The reason for measuring at least with two frequencies is to check for possible frequency dependence of the dielectric anomalies. Next in order, magnetic fields (1.5 T-6 T) have been applied.

One of the major concerns when measuring ceramic samples under the effect of electric and magnetic fields is the repeatability of the obtained results. Apart from the external applied fields there are many factors that possibly affect the outcome of each measurement. Examples of these parameters are: the mechanical stress applied from the sample's holder, the quality of the silver paste contacts, as well as the multiple cooling and heating cycles in a large temperature range and the magnetic history of the sample.[154]

To test the repeatability of the results, identical measurements on the same sample have been carried within two days. An α-$NaMnO_2$ pellet (sample's code ib168, see Table 3.1) of 5 mm diameter and thickness t=1.33 mm was measured under the same conditions: the sample is cooled from room temperature to 77 K without applying electric field (ZFC). The temperature is stabilized at 80 K and then V_{rms}=750 V/m is applied from the LCR bridge. The voltage "V_{rms}" stands for the effective value of the sine wave of the test frequency from the LCR's internall oscillator. Measurements of capacitance and dielectric loss are recorded every 0.5 K upon heating at the temperature range 80 K-300 K, under zero magnetic field. When a measurement is completed, the electric field is removed, the sample is then cooled again to 77 K, and the next measurement is programmed.

The results obtained at the first day of the measurements are shown in Figure 3.10. As an overall tendency both ε' and tanδ do not increase their values from 80 K-200 K. Above 200 K the ε' and tanδ measured under 96 kHz start to increase with temperature. A broad peak with maximum at 290 K appears for the first heating at 96 kHz, which vanishes at the next heating of 500 kHz

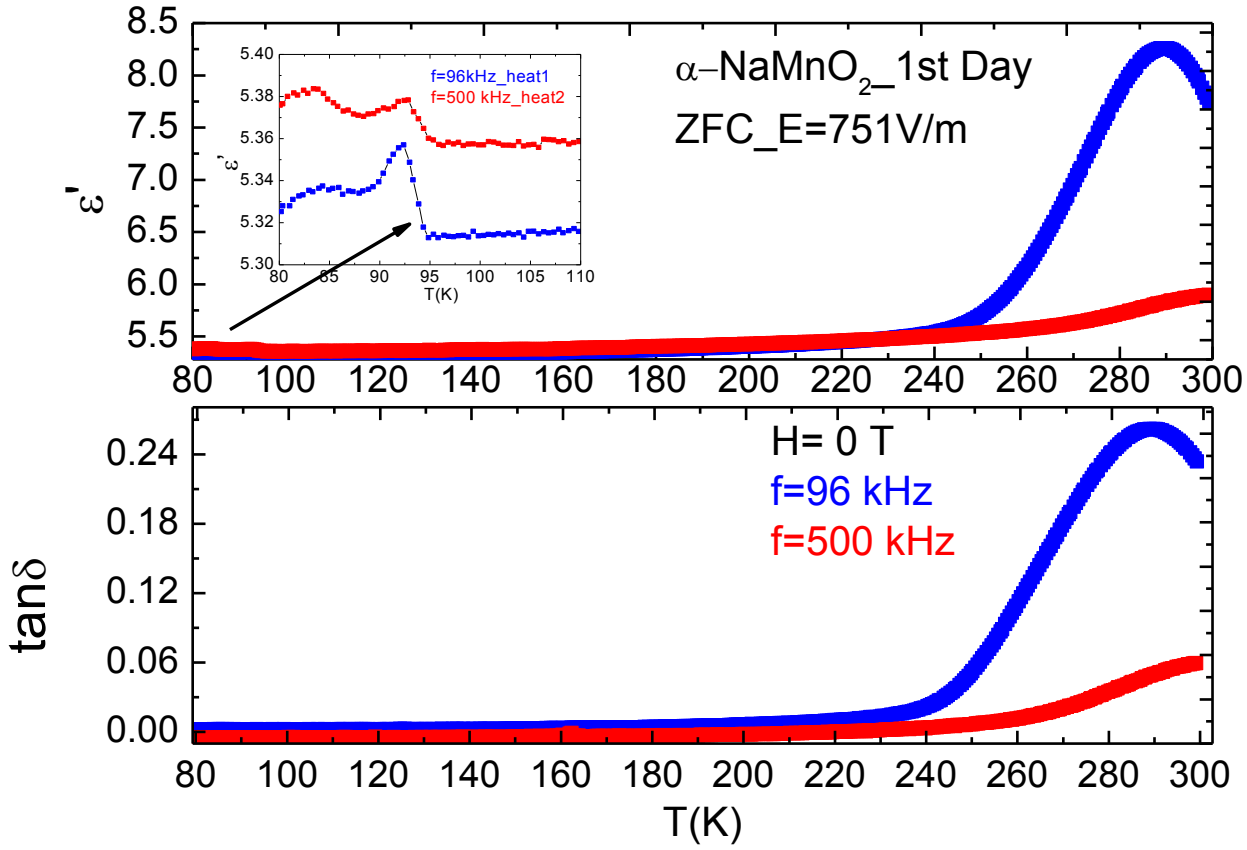

Figure 3.10 Dielectric constant (e') and dielectric loss (tanδ) versus temperature measured with 96 kHz (blue line) and 500 kHz (red line).

After the sample remained under inert atmosphere overnight, the same measurements were repeated as shown in Figure 3.11. Clearly, the graphs taken in both frequencies do not differ. The dielectric anomaly at 95 K still emerges, thus it is an intrinsic property of the α-$NaMnO_2$ sample which can be observed repeatedly.

There are two distinct features. The first one is the dielectric anomaly at 95 K which is shown more clearly in the insets of Figures 3.10 and 3.11. The second characteristic is the peak at 290 K which causes a deviation in the values of ε' and tanδ, between the runs of 96 kHz and 500 kHz. Most probably the difference is not attributed on the frequencies of the

two continuous runs, but on the aging effects between the first (96 kHz) and the second (500 kHz) run.

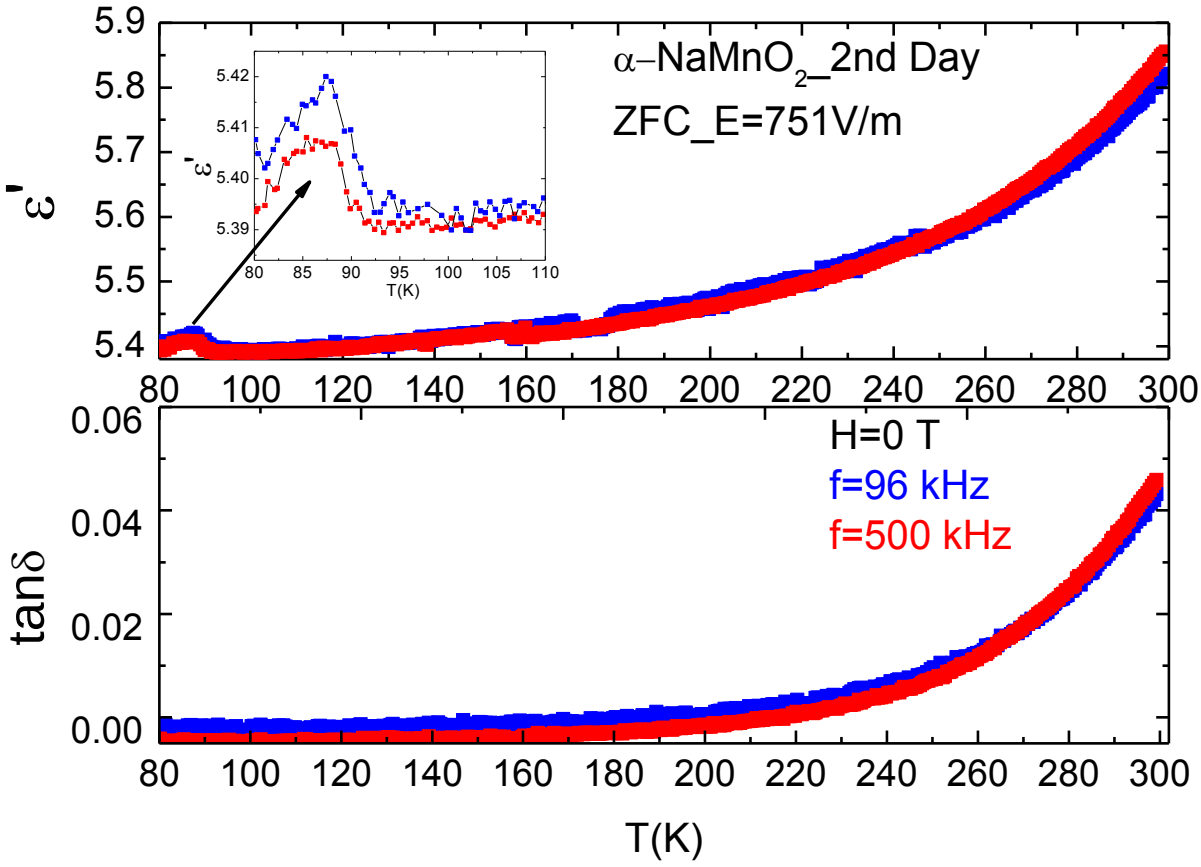

Figure 3.11 A second measurement that repeats the one presented in Figure 3.10. Dielectric constant (ε') and dielectric loss (tanδ) versus temperature measured with 96 kHz (blue line) and 500 kHz (red line)

It is interesting to note on Figure 3.11 the results that were obtained on the next set of runs (2^{nd} day) under the same conditions. The broad peak at 290 K observed in the first set of runs does not appear anymore. The two runs obtained at 96 kHz and 500 kHz are similar.

Dielectric constant and loss increase with temperature, with values that range from 5.4-5.9 and 0.0-0.06, respectively.

The most distinct feature is the dielectric anomaly at 95 K which is shown more clearly in the inset of Figures 3.10 and 3.11. The origin of the dielectric anomaly at 95 K is puzzling. As discussed in the introduction of this chapter, α-$NaMnO_2$ becomes antiferromagnetic just below 45 K. This means that the α-$NaMnO_2$ is paramagnetic at 95 K. Taking this into consideration, the hypothesis that the dielectric anomaly of 95 K is driven by a possible magnetic transition should be ruled out. The appearance of the dielectric anomaly may be justified if one considers the high resolution transmission microscopy studies in combination with the magnetodielectric measurements of the β-$NaMnO_2$ compound (see sections 4.5 and 4.6).

3.4.2 Dielectric Constant Measurements under Different Magnetic Fields

After verifying the existence and the repeatability of the dielectric anomaly at 95 K, the next step was to test the influence of the magnetic field in the dielectric properties of the α-$NaMnO_2$. The measurement of the capacitance and the dielectric loss versus temperature is carried out as described on the previous paragraph. The only difference is the magnetic field which is applied when the temperature has already stabilized at 80 K. When the temperature had reached 300 K, both electric and magnetic fields were removed and then the sample was cooled down for the next measurement.

The measurements of ε' and tanδ at 500 kHz under magnetic fields at the temperature range 5-300 K are shown in Figure 3.12. The effect of the magnetic fieldon the strength of the dielectric anomaly is remarkable: it is clearly enhanced and shifted towards higher temperatures (see also the inset of Figure 3.12). The effect of the magnetic fields on the dielectric constant has been observed for other magnetoelectric compounds.[155, 156, 157] It is important to note that the strength of the magnetodielectric coupling, the shift of the

critical temperature towards higher or lower temperatures and the driving mechanism of the coupling between the electric and the magnetic degrees of freedom is examined separately for each system. Worth mentioning that the values of tanδ appear close to zero but negative. This is probably due to parasitic capacitance and noise in the measurement of the imaginary part of the dielectric constant ε".

The increase and shift of the dielectric constant versus magnetic field is more clearly presented in Figure 3.13 (a). To further reveal this correspondence the relative change in the dielectric constant (Magnetoelectric Effect noted as "ME") is shown is Figure 3.13 (b), where the ratio $\Delta\varepsilon'/\varepsilon'_0$ stands for the

$$\Delta\varepsilon'/\varepsilon'_0 = [\varepsilon'_H - \varepsilon'_0]/\varepsilon'_0 \quad \textbf{(3.5)}$$

In equation 3.5, ε'_0 and ε'_H is the dielectric constant measured under zero and a stable magnetic field, respectively. One can observe that the ε' increases by 14 % for 1.5 T, whereas for the rest of the fields applied (3 T, 4.5 T and 6 T) the increase varies between 11-12%. Thus, the largest enhancement of the dielectric constant is observed for the 1.5 T field, and reduces equally for the 3 T and 4.5 T to finally get the smaller change in $\Delta\varepsilon'/\varepsilon'_0$ the for the 6 T.

It is interesting to point out that the decrease in the dielectric constant shows a step like behavior as seen for example in the ε' graph taken under 1.5 T in Figure 3.13(a). As the sample is heated there is a very small decrease in the ε' ($\Delta\varepsilon$=0.065) around 93 K shown with the first blue arrow from the left. Between the temperatures 93 K-98 K there is a plateau in the ε' value, until 100 K where there is a sharp drop in the dielectric constant pointed with the mark T_1. The transition points obtained when the dielectric constant drops show a smooth shoulder which is clearer for the graphs of 3 T and 6 T. The dielectric constant continues to decrease until a final temperature (T_2) where it takes the minimum value and stabilizes at 115 K. Above this point the overall tendency is a gradual smooth increase of ε' with temperature.

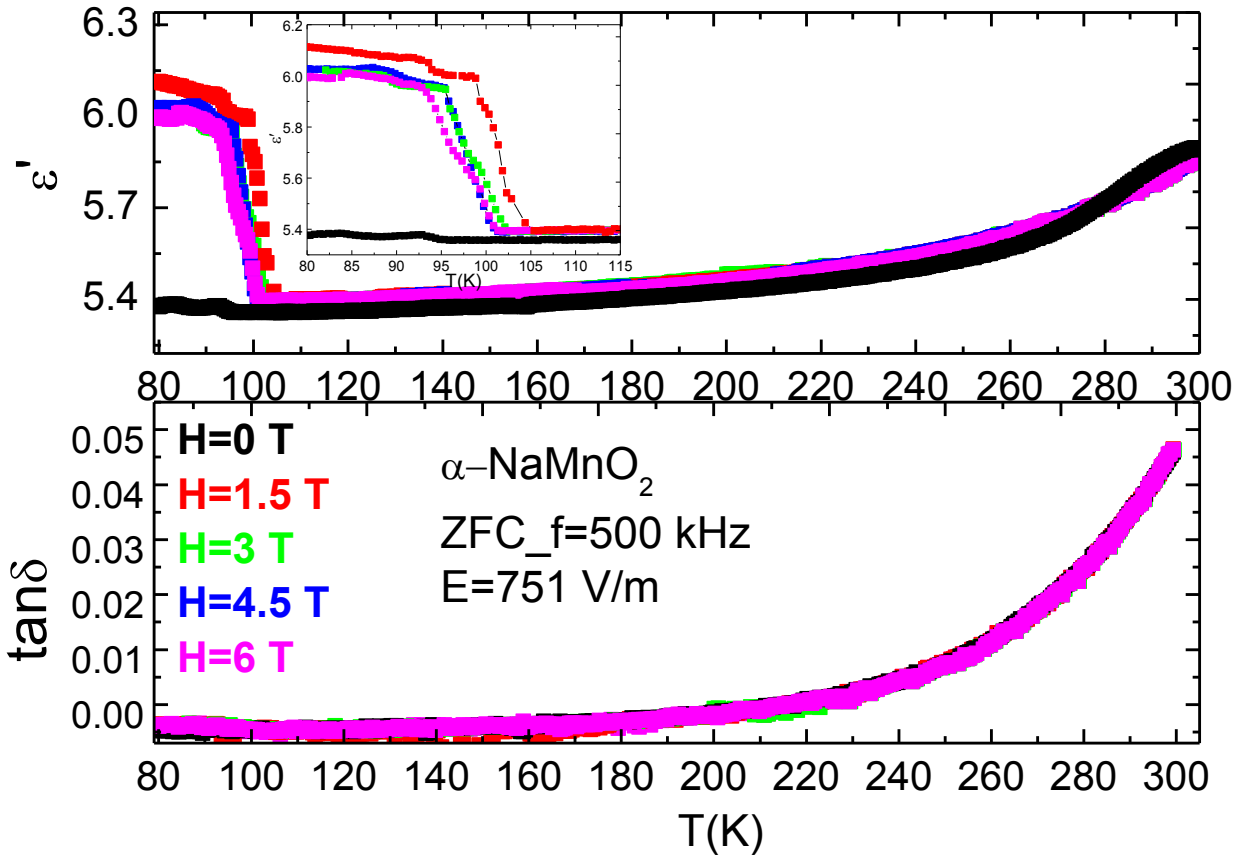

Figure 3.12 Graphs showing the real (ε') and imaginary part (tanδ) of the dielectric constant versus temperature under the magnetic fields: 0 T, 1.5 T, 3 T, 4.5 T and 6 T.

Another characteristic feature shown in Figure 3.13 is that the dielectric constant does not shift linearly to higher temperatures with increasing magnetic fields. Figure 3.14 shows the shift of the temperatures T_1 and T_2 versus the applied magnetic field. As it can be seen in Figure 3.13 (a) T_1 is the temperature where the dielectric constant starts to drop and at T_2 it takes its minimum value and stabilizes. The sample is polarized by an external magnetic field, for the first time when 1.5 T are applied. This is probably why the largest shift in the critical temperatures of the dielectric anomaly is observed between the graphs of 0 T and 1.5 T.

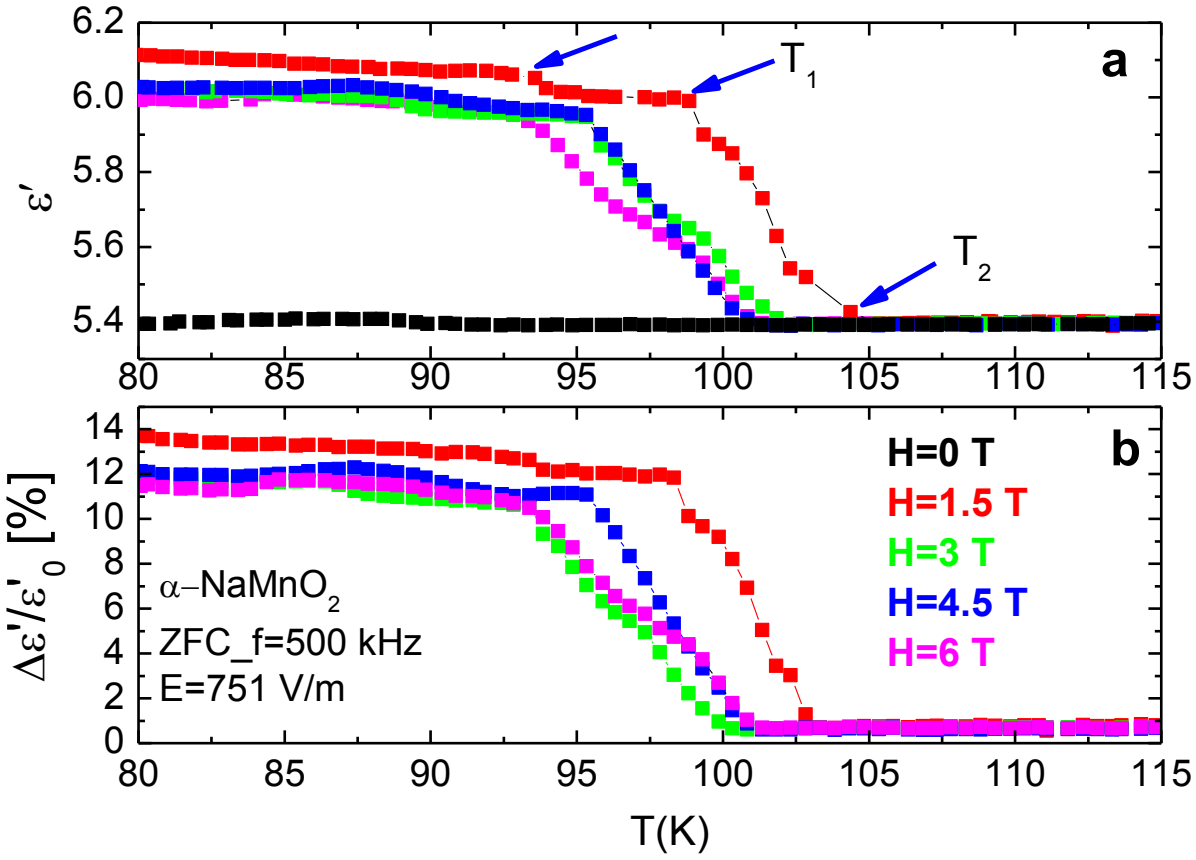

Figure 3.13 (a) A detail of the Figure 3.12 showing the temperature region between 80 K-115 K.(b) ME effect as a function of temperature at 500 kHz under several magnetic fields.

Figure 3.14 shows the dependence of the temperatures T_1 and T_2 from the applied magnetic field. The largest temperature shift is observed for the 1.5 T which is the first magnetic field that polarizes the sample.

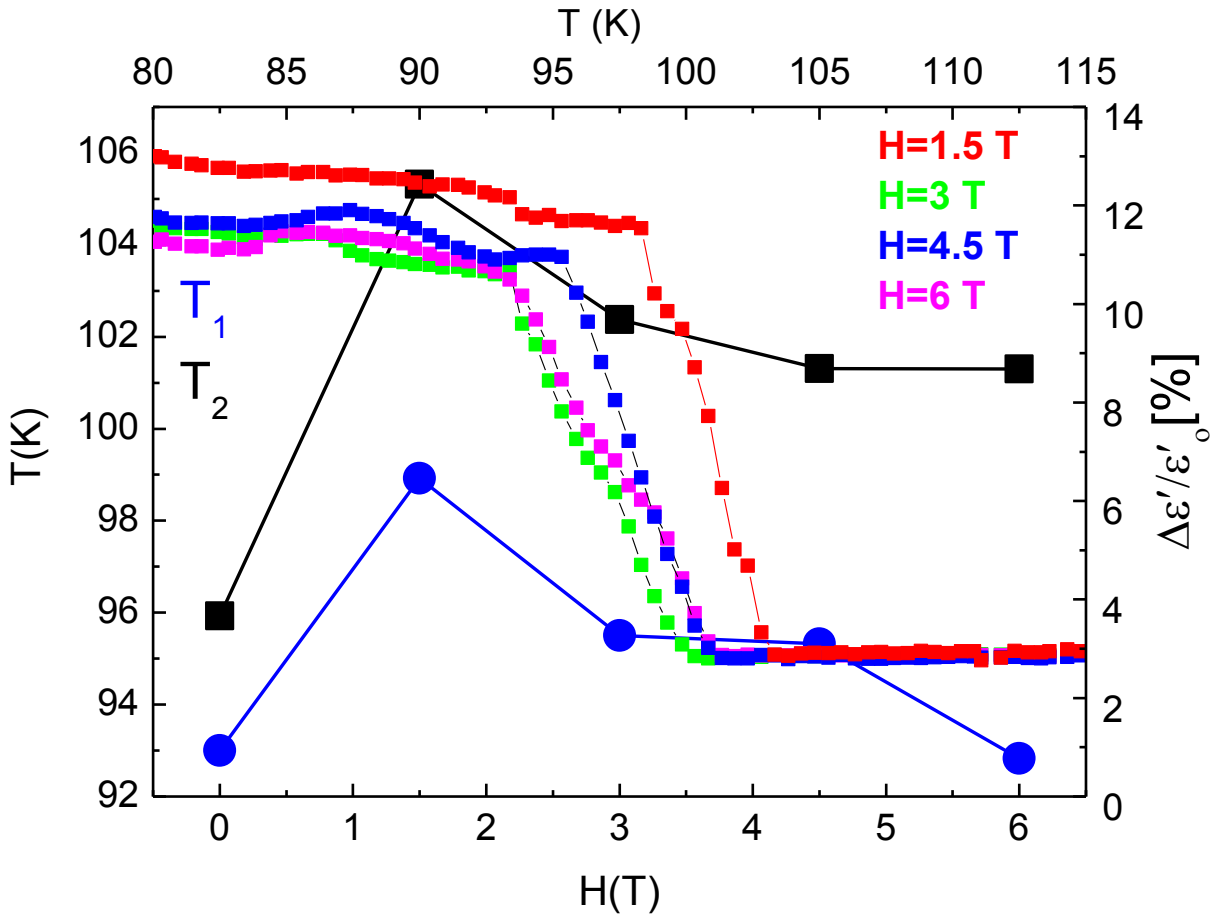

Figure 3.14 A graph that shows the shift of the critical temperatures T_1 and T_2 with respect to the applied magnetic fields (left axis). T_1 and T_2 refer to the temperature where the dielectric constant begins to drop and has taken the final minimum value, respectively. On the right axis the percentage of magnetoelectric effect (ME) is displayed versus temperature, for various magnetic fields.

It is worth mentioning here that another common measurement and way to estimate the strength of the magnetodielectric coupling is by measuring the values of the capacitance versus applied magnetic field, as shown in Figure 3.13 (magnetocapacitance). This results in the calculation of the relative change in the dielectric constant versus magnetic field. The giant magnetocapacitance of 500 % has been observed for the $DyMn_2O_5$ [157] and the

$DyMnO_3$ [158] whereas smaller values of relative change $\Delta\varepsilon'/\varepsilon'_0$ have been measured in the the Mn_3O_4 ($\Delta\varepsilon'/\varepsilon'_0$~0.06%). [70] The same quantity has been calculated for various magnetoelectrics, some examples of which are: the $Ca_3CO_2O_6$ [155] the $BaMnO_{3-\delta}$ [159] and the $CdCr_2S_4$. [160] Interestingly, the values of $\Delta\varepsilon'/\varepsilon'_0$ vary from 5% for example in the polycrystalline frustrated antiferromagnet of $Ca_3Co_2O_6$ and the $Bi_6Fe_2Ti_3O_{18}$ films [161] up to the collosal change of 500% for the single crystal relaxor ferroelectric $CdCr_2S_4$. The strength of the magnetodielectric coupling depends primarily on the driving mechanism of the effect. Other factors which can contribute also to the differentiation of the $\Delta\varepsilon'/\varepsilon'_0$ could be the nature of the sample, meaning whether it is single crystal, powder of thin film.

Apart from the magnetocapacitance, the second feature depicted in Figure 3.13 is the gradual decrease in the dielectric constant. The dielectric constant may decrease abruptly, exhibiting a change almost perpendicular to the Temperature-axis as it has been observed for the cases of $FeVO_4$ [162]and the delafossites $CuCrO_2$ and $AgCrO_2$. [163] More common though, is the smooth decrease of the dielectric constant observed in compounds such as the $DyMn_2O_5$, [157] FeT_2O_5Br,[156] $DyMnO_3$[158] and $CdCr_2S_4$[160] and the step like change of ε' of $Ca_3Co_2O_6$. [155] In these cases, the temperature of the dielectric anomaly starts to drop at a temperature T_1 and stabilizes at a temperature T_2 where $T_1<T_2$. The temperature of the dielectric anomaly is regarded as the one in which the dielectric constant starts to drop, meaning the one noted as T_1 in Figures 3.13 and 3.14. The evolution of the critical temperature (T_1) for the compound α-$NaMnO_2$ versus the applied magnetic field shown in Figure 3.14 shows a maximum for a certain magnetic field (1.5 T) and then decreases at higher fields. Similar behavior has also been noted for the polycrystalline magnetoelectric $FeVO_4$.

3.4.3 Complementary measurements

Experiments on α-$NaMnO_2$ - sample 2 (sample's code oa113)

The observation of the magnetodielectric coupling at 95 K on the α-$NaMnO_2$ was remarkably surprising, since it could not be attributed to its magnetic properties for this temperature region. A first assumption would be that the sample checked for magnetodielectric coupling could have impurities, related with the dielectric anomaly at 95 K. To clear out any concern related with the properties of the specific sample that has been measured, we have performed a series of the same magnetodielectric measurements on different α-$NaMnO_2$ samples.

Therefore, to reach a safe conclusion about the repeatability of the magnetodielectric properties of α-$NaMnO_2$ various samples of different batches have been tested (see Table 3.1). All the samples have been synthesized by the protocol of paragraph 3.2, so in principle, all their properties should be the same. In practice, some changes might be observed in ceramic samples, which are affected by the grain size, the history of the sample including the type of experiments that have been carried out on it.

To present the repeatability on the observation of magnetodielectric phenomenon in the α-$NaMnO_2$, experiments on a second α-$NaMnO_2$ sample are shown in the following graphs. The major difference between sample 2 (sample's code oa113) and the one shown in the previous paragraphs, is that sample 2, was synthesized four years before the specific magnetodielectric experiments took place. On the contrary, sample 1 (ib168) has been synthesized and characterized within the same week. Apart from that, the preparation of both pellets, their XRPD patterns, and the method of the magnetodielectric experiments are identical.

As the following graphs prove, the second sample that is presented also exhibits the dielectric anomaly at 95 K. The magnetic fields affect the dielectric's anomaly strength. However the relative % change in the dielectric constant ($\Delta\varepsilon'/\varepsilon'_0$) varies between 4% -8%, which is smaller than the 10%-12% found for the sample 1.

The small deviations noticed in the strength of the magnetodielectric effect (ME) $\Delta\varepsilon'/\varepsilon'_0$ is probably originated by the differences in the grain size of the two ceramics. A discussion of the similarities and differences on the results obtained from each α-$NaMnO_2$ sample are discussed on the following section 3.4.4.

Dielectric Constant under different frequencies on α-$NaMnO_2$-sample 2 (sample's code oa113)

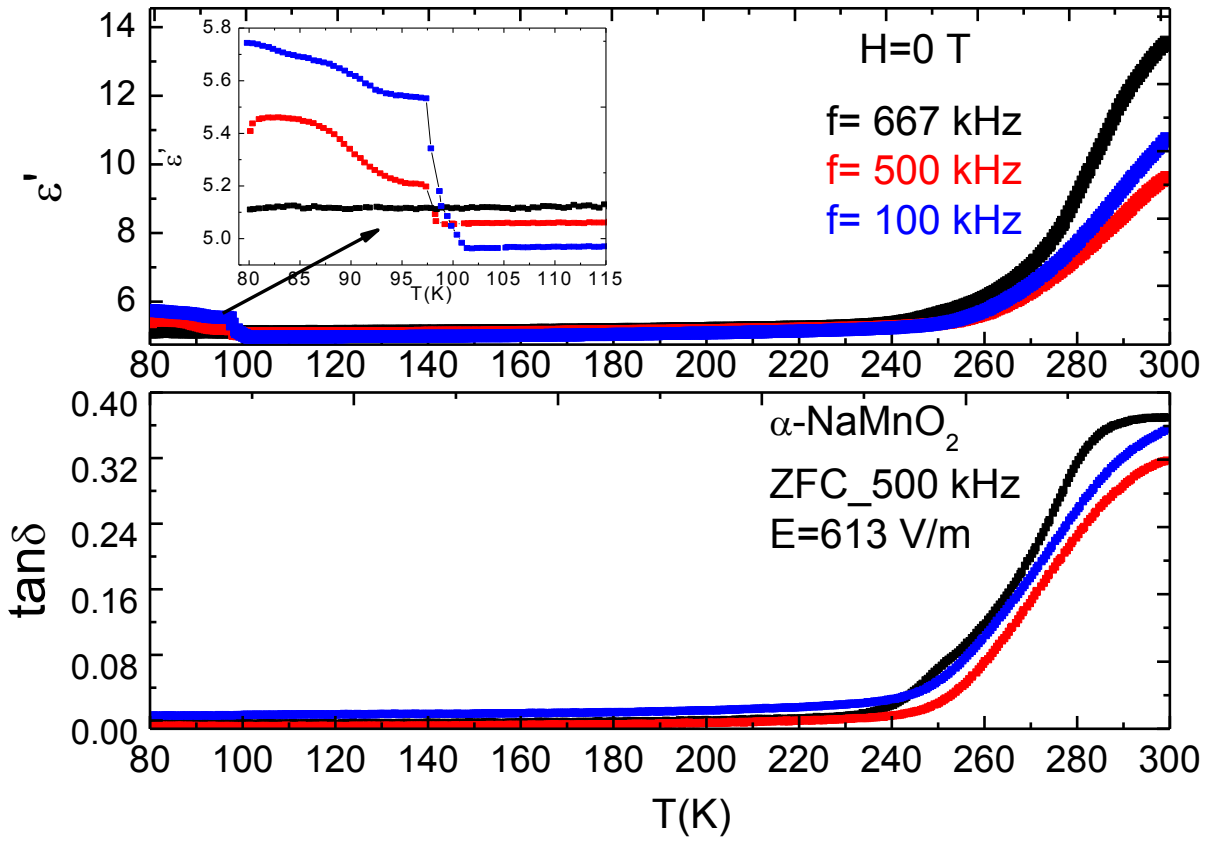

Figure 3.15 Dielectric constant (ε') and dielectric loss (tanδ) versus temperature measured with 100 kHz (blue line) and 500 kHz (red line) and 667 kHz (red line) under zero magnetic field.

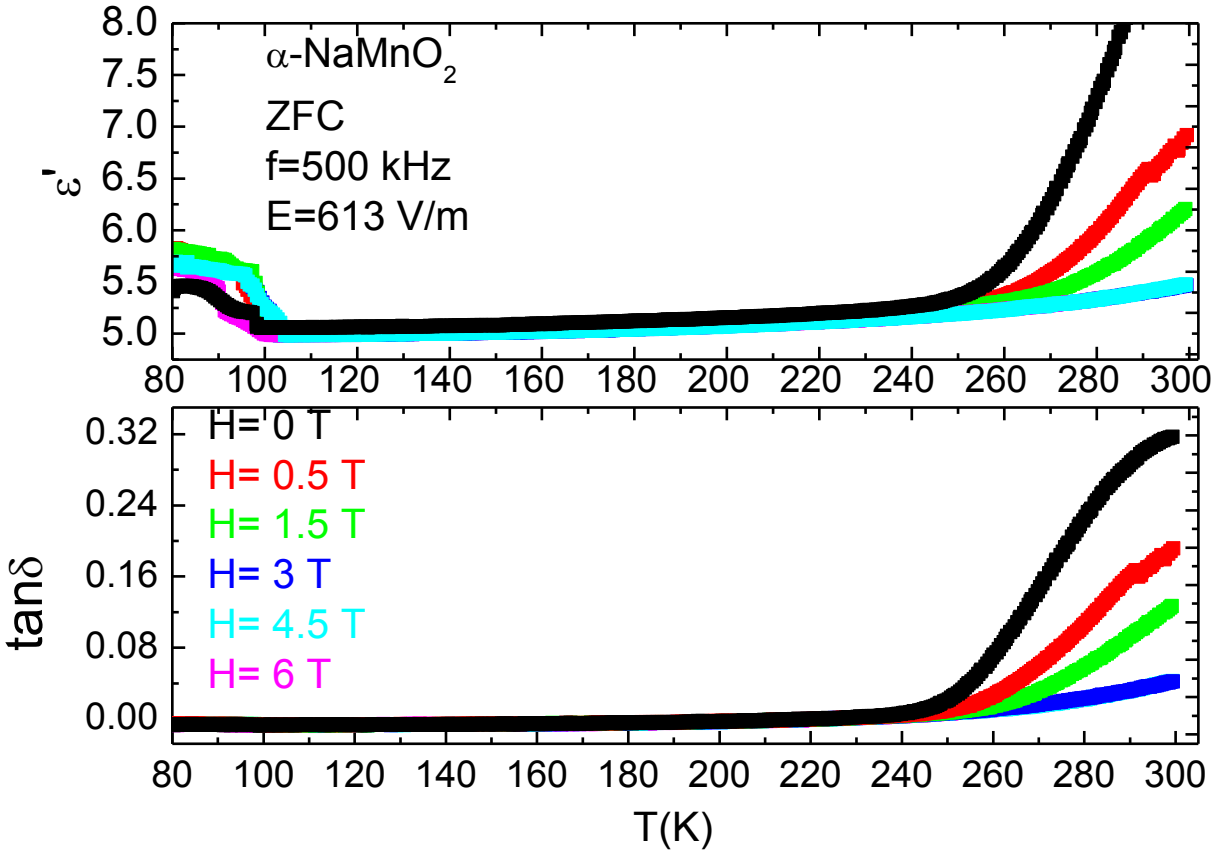

Figure 3.16 Graphs showing the real (ε') and imag inary part (tanδ) of the dielectric permittivity versus temperature under the magnetic fields of: 0 T, 0.5 T, 1.5 T, 3 T, 4.5 T and 6 T on α-$NaMnO_2$ sample 2.

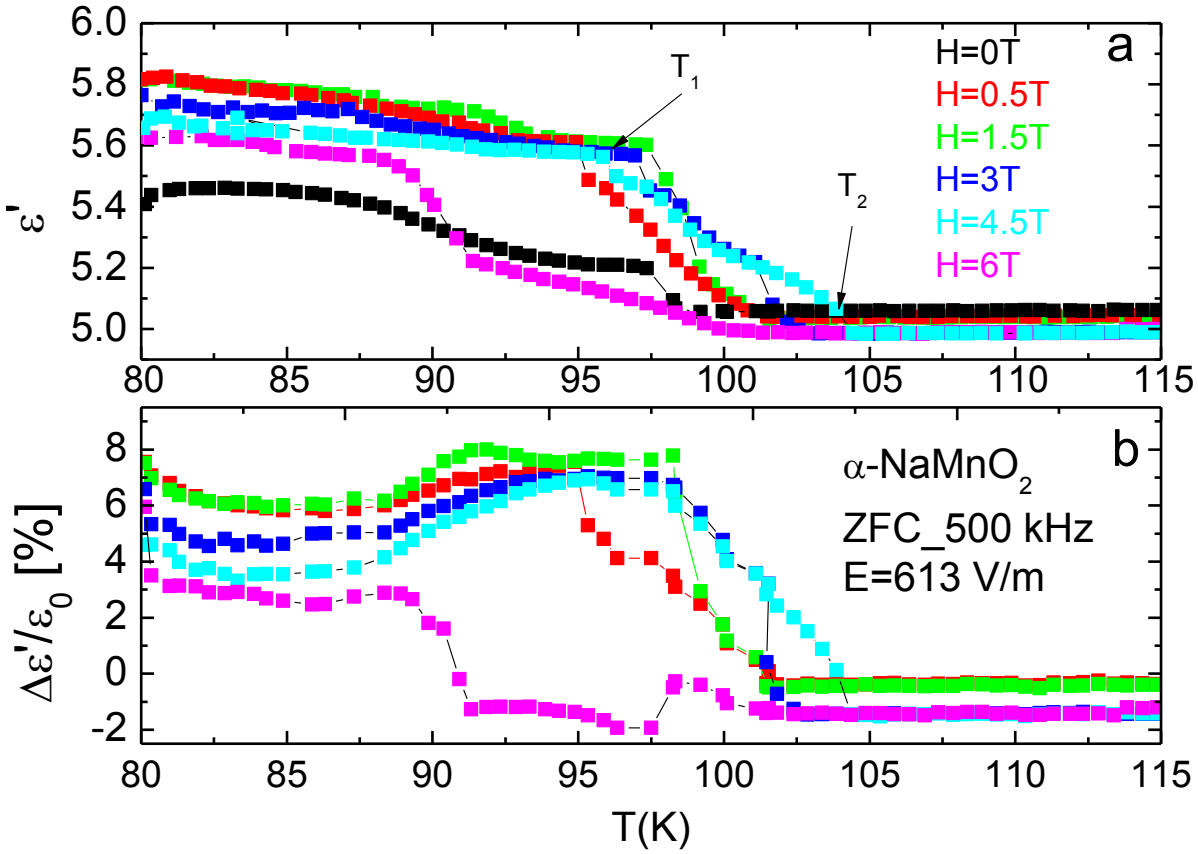

Figure 3.17 (a) A detail of the Figure 3.16 showing the temperature region between 80 K-115 K.(b) ME effect as a function of temperature at 500 kHz under several magnetic fields on α-$NaMnO_2$ sample 2.

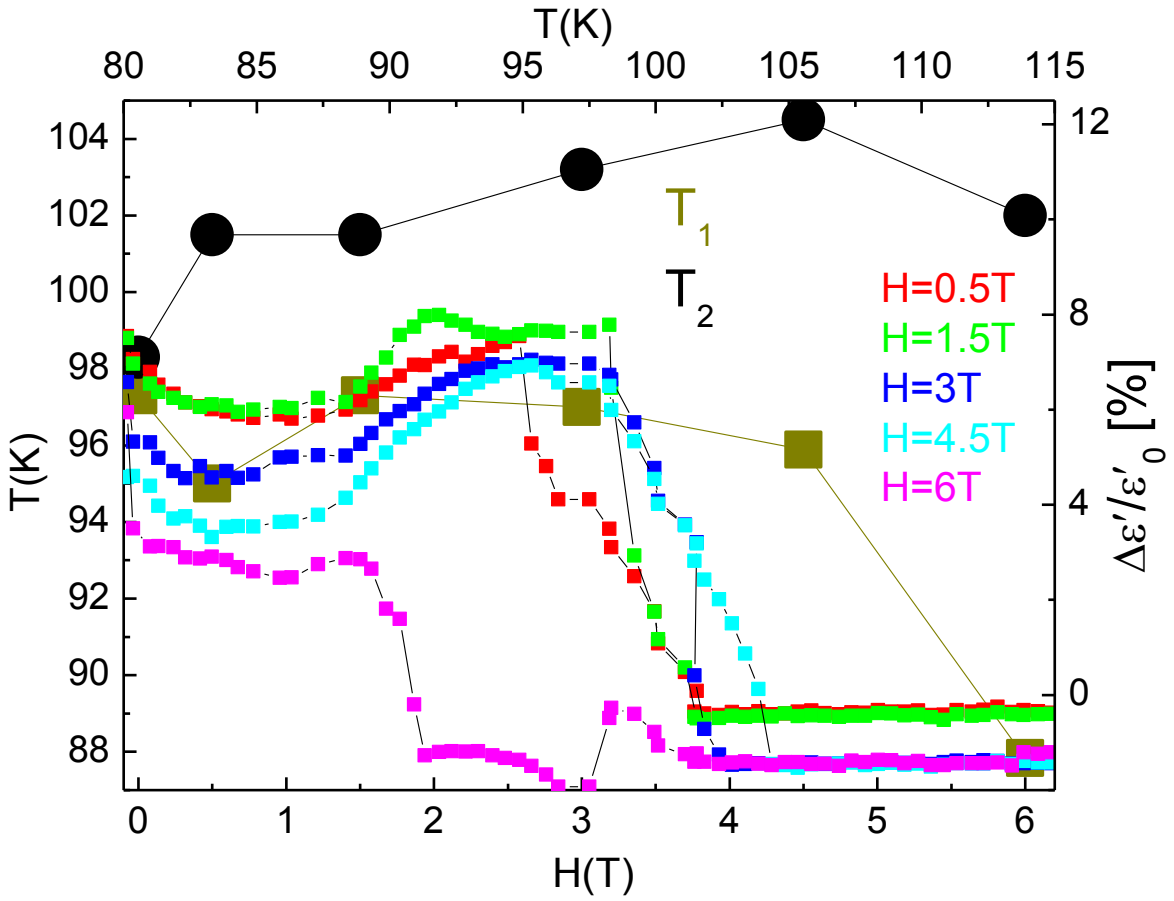

Figure 3.18 A graph that shows: on the left axis the shift of the critical temperatures T_1 and T_2 with respect to the applied magnetic fields. T_1 and T_2 refer to the temperatures where the dielectric constant begins to drop and has taken the final minimum value, respectively. At the right axis the magnetoelectric effect versus temperature for different magnetic fields is presented.

3.4.4. Comparison of the results obtained by different α-$NaMnO_2$ samples, as presented in 3.4.2 and 3.4.3 sections.

At this point it is useful to compare the results obtained from two different samples of α-$NaMnO_2$ presented in paragraphs 3.4.2 and 3.4.3. First we refer on the similarities noticed on the measurements of the two samples: i) the dielectric constant and loss increase smoothly as the temperature increases ii) at zero magnetic field and under the frequency of 500 kHz both samples show a dielectric anomaly at the temperature region between 93 K-97 K. iii) if we compare the values of the dielectric constant for H=0 T at a specific temperature, for instance at 90 K, for the first sample (ib168) ε'=5.37 and for the second one (oa113) ε'=5.31, iv) the dielectric anomalies are enchanched when external magnetic field is applied.

There are also two differences observed when one compares the dielectric behavior of the two samples measured. The first one refers to the critical temperature of the dielectric anomaly (T_1) since for the first sample it is noticed at 93 K whereas for the second sample the anomaly occurs at 97 K (Figure 3.19). The second difference is related with the strength of the magnetodielectric coupling, as for the first sample the MD~14% whereas for the second one MD~8 % as seen in Figures 3.13 and 3.17, respectively.

To the best of our knowledge a comparison on the strength of the magnetodielectric coupling and dielectric constant obtained from different batches of the same ceramic compound is not yet reported in the literature. Still though, there are references which emphasize on the role of different factors that can affect the result of the dielectric measurements. We discuss these factors on the basis of the findings related with one of the most well studied ferroelectrics, the $BaTiO_3$.

It has been reported that the grain size does affect the values of the dielectric properties.[164, 165, 166, 167] The general trend is that the dielectric constant values increase as the grain size decreases.[168] For example pure $BaTiO_3$ with grain sizes ranging between 20-50 μm exhibits dielectric constant of ε'~1500-2000 at room temperature, whereas the ε' reaches 3500-4000 for fine grained (1 μm) $BaTiO_3$ ceramics. The grain size is associated with the

internal stress, for which it has been reported that it gives rise to the increase of ε' .[169, 170] Although the grain size has not been determined for each batch of our ceramic α-$NaMnO_2$ samples, the first assumption is that the grain size should play a major role in the dielectric properties according to what has been reported for other ceramic samples in the literature.

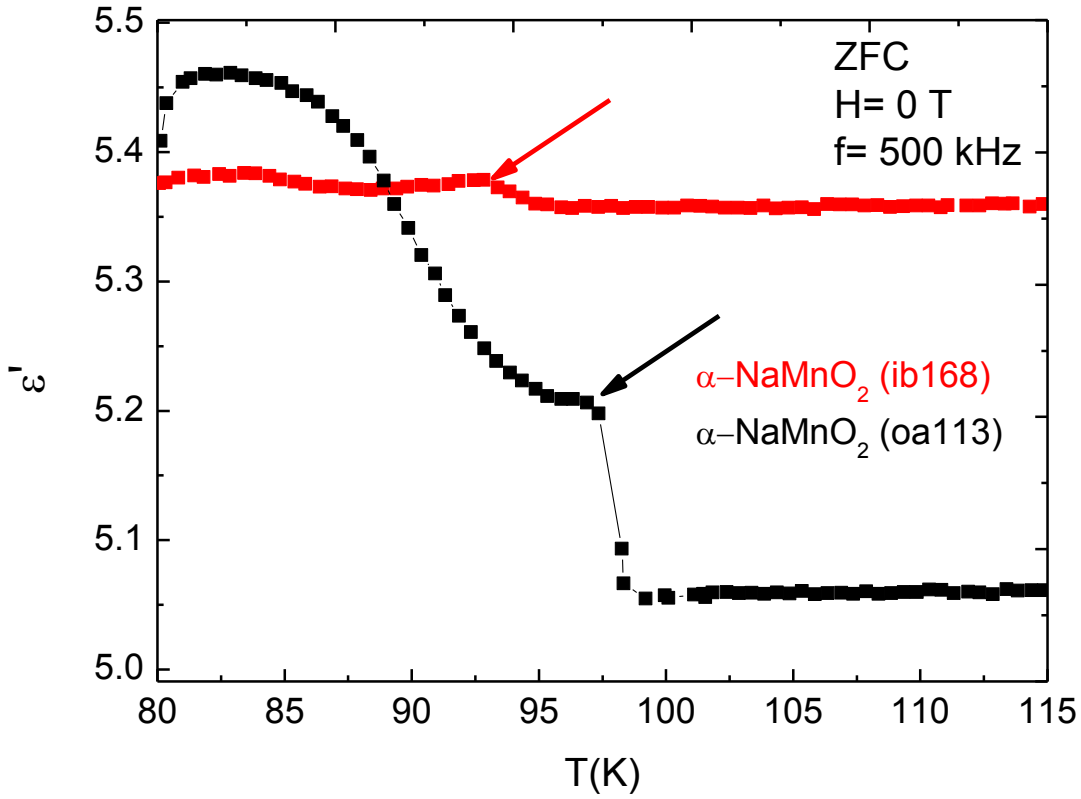

Figure 3.19 Comparison of the dielectric constant measured under zero magnetic field and frequency of 500 kHz of the two different α-$NaMnO_2$ samples whose results are analytically presented in sections 3.4.2 and 3.4.3.

Moreover another parameter which influences the dielectric response of the samples measured is the aging effects which are usually evident by the gradual decrease of the dielectric and piezoelectric parameters. Aging has been reported to originate by defects, boundary or volume effects of the ferroelectric domains.[171, 172, 173, 174, 175, 176, 177] An

example of aging effect in $BaTiO_3$ ceramics has been reported to cause the shift of the temperature of the dielectric transition since the critical temperature shifted towards higher temperatures for the aged sample in comparison with the freshly made one.[171]

It is interesting to note that in the α-$NaMnO_2$ samples the value of the dielectric constants obtained are comparable (5.37 and 5.31). What changes is the strength of the dielectric anomaly and magnetodielectric coupling. As it will be discussed in the next section of TEM studies, the magnetodielectric coupling of α-$NaMnO_2$ is attributed to planar defects caused by the intergrowth of the β-$NaMnO_2$ phase. Thus, a detailed explanation on the differences observed in the strenght of the dielectric transitions and the magnetodielectric coupling in the α-$NaMnO_2$ phase should include also the comparison of the TEM studies obtained for each α-$NaMnO_2$ batch.

Here we also discuss the dielectric behavior of the α-$NaMnO_2$ in respect with other multiferroic ABO_2 systems such as the polycrystalline $CuCr_{0.5}V_{0.5}O_2$ and $CuFe_{0.5}V_{0.5}O_2$.[163] Due to the mixed character of the B site attributed to the presence of Fe^{3+} (S=5/2) and V^{3+} (S=1/2) these compounds demonstrate a disordered magnetic situation manifested by their spin glass transition below 19.9 K and 10.9 K for $CuFe_{0.5}V_{0.5}O_2$ and $CuCr_{0.5}V_{0.5}O_2$, respectively. Both $CuFe_{0.5}V_{0.5}O_2$ and $CuCr_{0.5}V_{0.5}O_2$ exhibit broad humps at their dielectric constants which are frequency dependent, pointing towards relaxor ferroelectricity. Interesting to mention that the values of the dielectric constant are comparable with those of α-$NaMnO_2$ (ε'(T)~4-5) as they range from 7.6-8.2 and 9-16 for $CuFe_{0.5}V_{0.5}O_2$ and $CuCr_{0.5}V_{0.5}O_2$, respectively. Moreover, the dielectric behavior of the $CuFe_{0.5}V_{0.5}O_2$ and $CuCr_{0.5}V_{0.5}O_2$ compounds is not generated by their magnetic transitions ("type I" multiferroics, see section 1.4.5) as the temperature range of the dielectric anomalies (T>30 K) is well above the temperature of the magnetic spin glass state, similarly with the case of α-$NaMnO_2$. Another interesting characteristic of these multiferroic copper oxides is the presence of planar defects (such as low angle boundaries along the c-axis between lamellas and twinned structure along c-axis) in their microstructure as seen by TEM studies.[163] This observation is in consistency with the TEM observations of α-$NaMnO_2$ as it will be discussed in section 3.5.

Various multiferroic powder ABO_2 compounds have been reported with similar values of dielectric constant with that of α-$NaMnO_2$, but the mechanism of the ferroelectricity differs in each case. For the recently discovered rombohedral ($R\bar{3}m$) multiferroic $AgFeO_2$[51] in which ε'(T) is 26-29, the magnetoelectric coupling is driven by the inverse Dzyaloshinskii Moriya effect. It is worth to mention that $AgFeO_2$ shows two incommensurate magnetic transitions (ICM1~15 K and ICM2~9 K) which are accompanied by successive magnetostructural transitions, similarly with the structural transition of α-$NaMnO_2$ at the temperature of the antiferromagnetic order at T_N=45 K.[7] The magnetic transitions are related with the dielectric anomalies ("type II" multiferroics,) and moreover the low temperature magnetic transition (9 K) induces a polarization in $AgFeO_2$ of 300 μC/cm^2.

Similarly in the delafossites $ACrO_2$ [50, 63](A= Li, Na, Cu, Ag) the polarization appears at the temperature of the magnetic transitions. These compounds also crystallize in the $R\bar{3}m$ space group. The ε'(T) values of the $ACrO_2$ compounds are comparable with that of α-$NaMnO_2$ as they range from 6-8. Nevertheless, the generating mechanism of the magnetoelectric coupling is attributed to a simple proper screw order, in contrast with the previously mentioned $AgFeO_2$. Specifically, the origin of polarization and thus the generating mechanism of the magnetoelectric coupling have been proposed by Arima[63] as the modulation of the π-bonding of Cr (or Fe) interactions and O anions with the spin orbit interaction. This mechanism has also been proposed for the $CuFeO_2$ ($R\bar{3}m$) magnetoelectric[63, 90].

The interrelation between noncollinear spin ordering and the ferroelectric polarization has been also demonstrated recently on the rombohedral α-$NaFeO_2$.[178] Interestingly, the α-$NaMnO_2$ resembles the α-$NaFeO_2$ as these two ABO_2 compounds have in common the same ordered rock-salt crystal structure. Since the A cations are Na^+ in both systems, it is interesting to discuss how the B cations, namely Mn and Fe affect their magnetodielectric properties.

The first difference is attributed to the Jahn-Teller active Mn^{+3} cation, which causes a distortion of the MnO_6 octahedra[7, 148] resulting in the monoclinic α-$NaMnO_2$ crystal

structure in contrast with the original rombohedral structure of the α-$NaFeO_2$. Moreover, α-$NaFeO_2$ undergoes two magnetic transitions at 10 K and 5 K. Polarization appears below 7.5 K revealing a connection between the magnetic ordering of 10 K and the induced ferroelectricity. Thus, α-$NaFeO_2$ appears to be a "type II" multiferroic where the responsible mechanism for the appearance of the ferroelectric polarization is the inverse Dzyaloshinskii Moriya interaction. On the contrary, in α-$NaMnO_2$ the magnetic ordering is not relevant with the appearance of the magnetodielectric coupling.

An interesting research has been recently (2014) carried out which reveals the effect of the substitution of the B-site cation at the polycrystalline spin driven magnetoelectric $CuFeO_2$.[179] Ca and Mg cations were used to doped the $CuFeO_2$ delafossite resulting in two types of compounds: the $CuFe_{1-x}Ca_xO_2$ and the $CuFe_{1-x}Mg_xO_2$, $0 \leq x \leq 0.04$. We refer to these compounds since dielectric anomaly has been observed at the temperatures of the magnetic transitions indicating magnetoelectric coupling. The anomaly in the dielectric constant of the $CuFe_{1-x}Mg_xO_2$ is associated with the non collinear antiferromagnetic phase in analogy to previous reports for the Al doped $CuFeO_2$[91] where the proper helical magnetic ordering induced spontaneous electric polarization. All the aforementioned systems are typical examples of magnetoelectric where the magnetic state induces a dielectric anomaly and the appearance of polarization.

The above discussion aimed to show different cases of the magnetoelectric coupling in the most well known ABO_2 compounds, as α-$NaMnO_2$ belongs to them. Although the many of them of them exhibit a connection between the magnetic and the dielectric properties classifying them as magnetoelectrics or "type II" multiferroics, this does not hold for the α-$NaMnO_2$. The origin of the magnetodielectric coupling in α-$NaMnO_2$ is discussed in the next section.

3.5 TEM Studies

Now, we discuss the most important findings from the TEM investigation of α-$NaMnO_2$. ED and HRTEM results were obtained at the Electron Microscopy for Materials Science (EMAT) in University of Antwerp, Belgium by Dr. A.Abakumov. The observation of planar defects in the building blocks of α-$NaMnO_2$, shed light to the role of phase inhomogeneity in a chemical homogeneous system.[143, 180] In general, planar defects refer to grain boundaries, stacking faults or antiphase boundaries. The structure irregularities and the observed disorder are promoted by the small energetic difference between the polymorphs α-$NaMnO_2$ and β-$NaMnO_2$.

ED and HRTEM experiments: Specimens for transmission electron microscopy (TEM) investigation were prepared in an Ar-filled glove box by crushing the crystals in a mortar under anhydrous ethanol or n-hexane and depositing drops of suspension onto holey carbon grids. The specimens were transported and inserted into the microscope under dry Ar, completely excluding contact with air. Electron diffraction (ED) patterns and high resolution transmission electron microscopy (HRTEM) images were obtained with a Tecnai G2 electron microscope operated at 200 kV. High angle annular dark field scanning transmission electron microscopy (HAADF-STEM) images were recorded with a Titan G3 microscope equipped with a probe aberration corrector and operated at 300 kV.

3.5.1. Electron Diffraction (ED) Patterns[143]

Electron Diffraction patterns of α-$NaMnO_2$ are presented in Figures 3.20 and 3.21. The dominant characteristic is the difference between the bright intense and the weaker spots, observed in all the patterns, regardless of the zone axis. The brighetest spots correspond to the C-centered monoclinic unit cell with: a=5.66 Å, b=2.86 Å, c=5.80 Å, β=113 deg. These structural parameters are in agreement with the ones extracted from the neutron diffraction patterns.[11] In Figure 3.20 on the bottom left the [010] ED pattern as well as the $[\bar{1}01]$ and the $[\bar{1}21]$ in Figure 3.21, show characteristic signs of planar defects, evident by the faint

diffuse intensity lines. The diffuse intensity lines intersect the Ewald sphere at the *hk0, h+k≠2n* positions in the [001] pattern, pointed out with the arrowheads in Figure 3.20.

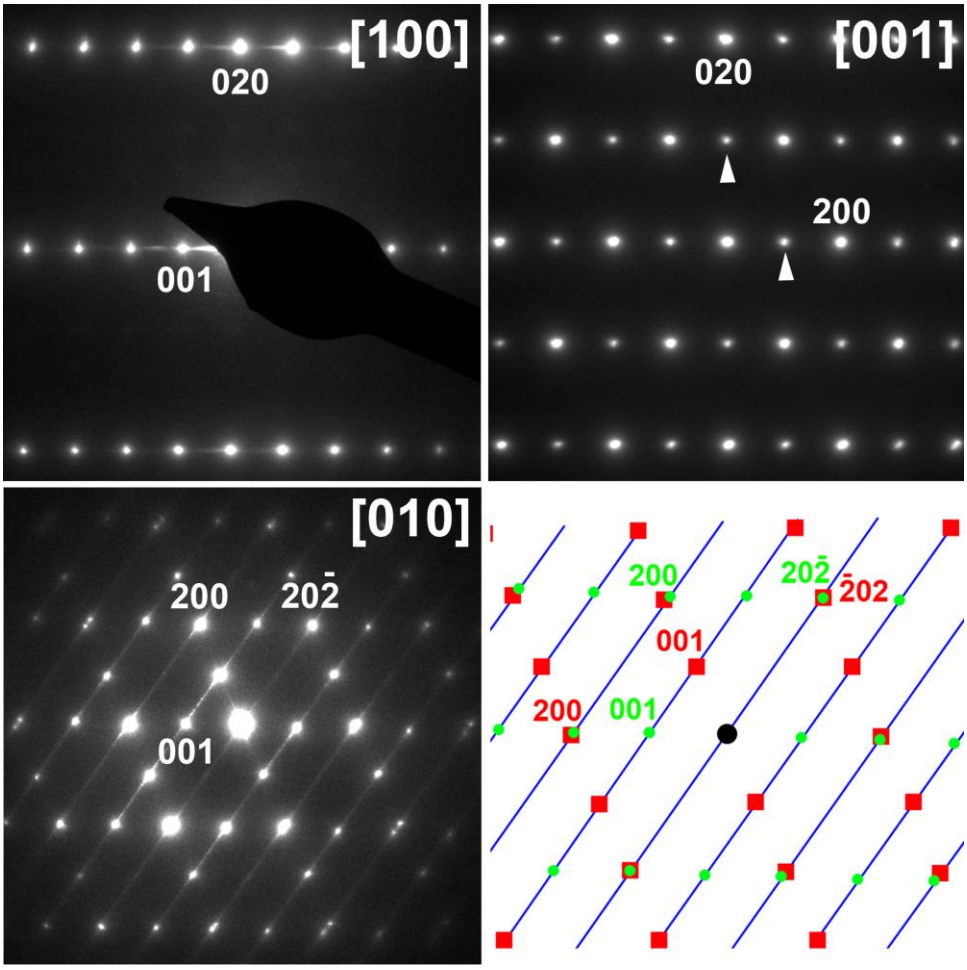

Figure 3.20 Main electron diffraction patterns obtained from the α-$NaMnO_2$. Clockwise: ED patterns along main zone axis.The arrowheads mark the spots which are forbidden by the C-centered unit cell of α-$NaMnO_2$ (see text). Bottom left: presence of weak diffuse intensity lines. In the figure at the bottom right, the red and green lines correspond to the decomposition of the pattern into contributions from two mirror-related domains whereas the diffuse intensity lines are shown in blue.

ED patterns of α-$NaMnO_2$ show characteristic signs of mirror twins such as the split reflections observed with the $(10\bar{1})$ plane. Furter investigation of the structure irregularities of α-$NaMnO_2$ was carried out by HRTEM.

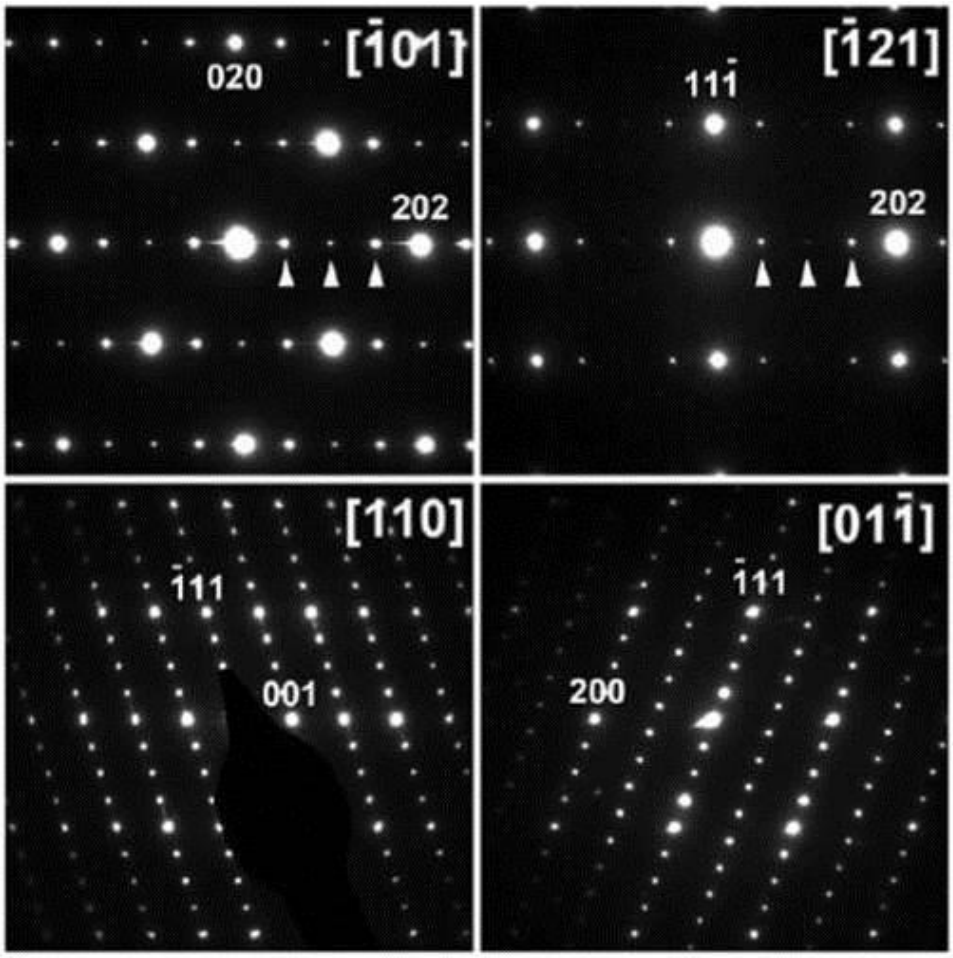

Figure 3.21 Electron diffraction patterns of the α-$NaMnO_2$ obtained from different zone axis. The arrowheads mark the spots which originate from twins and intersection of the Ewald sphere. The spots with the increased size and intensity indicate the presence of regular superlattice k=1/4[$\bar{1}$11] reflections.

3.5.2 High Resolution Transmission Electron Microscopy (HRTEM) Images [143]

The HRTEM image (Figure 3.22) shows clearly patterns of atomic layers which correspond to the rows of bright dots. However, these patterns are not continuous since planar defects act as twin planes causing the mirroring of the atomic columns, on both

sides of the twin plane. This is pointed out by the single arrowheads in Figure 3.22. In addition, two adjacent twin planes which do not alter the orientation of the atomic layers but generate their lateral displacement, act as a stacking fault. This is marked in Figure 3.22 with the double arrowheads.

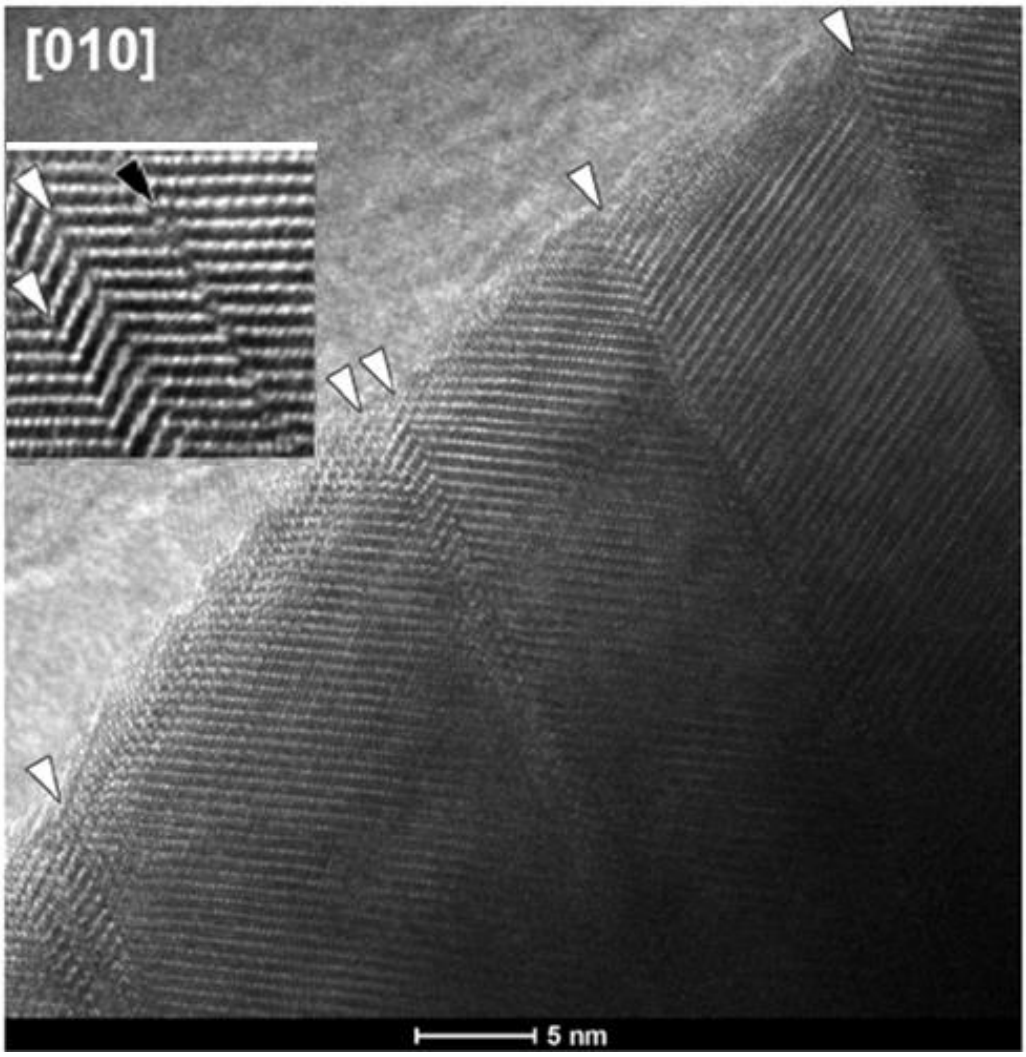

Figure 3.22 The [010] HRTEM image (5 nm magnification) of α-$NaMnO_2$ showing planar defects which are marked with arrowheads. The white arrowheads mark the twin planes whereas the black arrowheads (inset in the left of the figure) point out the antiphase boundaries.

To enlighten the nature of the planar defects in α-$NaMnO_2$ the [010] HAADF-STEM image was taken (Figure 3.23). This image shows projections of the Mn atomic columns, since the Mn atoms have the highest atomic number in the $NaMnO_2$ structure. The twin planes form an angle of 60° in respect to the layers of the MnO_6 edge-sharing octahedra.

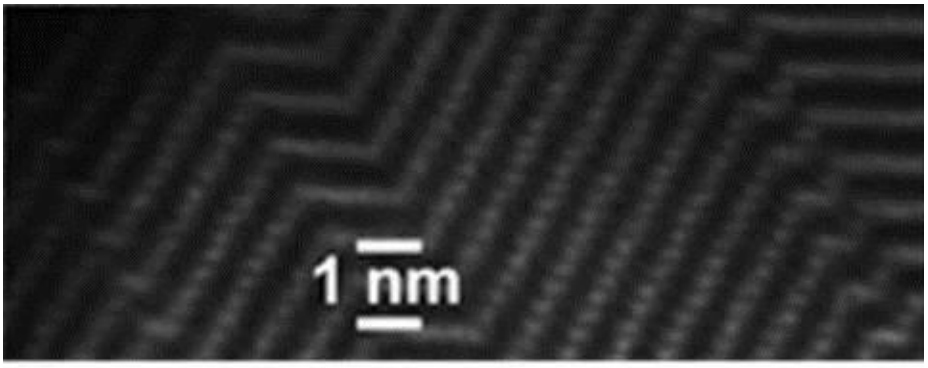

Figure 3.23 The [010] HAADF-STEM image showing the projections of the Mn atomic columns.

According to the above observations, there are two possible models that would explain the planar defects for the monoclinic α-$NaMnO_2$.The first one accounts for the twin planes (Figure 3.24 a) whereas the second one, is the stacking fault model shown in Figure 3.24 b.

TEM observations have been explained on the basis of a superspace model,[181] [182] according to which the $NaMnO_2$ polymoprhs (both the α- and β-phase) crystallize on the (3+1)D superspace.[183, 184] This analysis entails the structure of pure α-$NaMnO_2$, pure β-$NaMnO_2$ and the intermediate phases in which high concentration of planar defects are found. The superspace model[143] (see section 4.6.3) predicts that the $NaMnO_2$ structures crystallize in the monoclinic superspace group with the symmetry elements X*2/m*(α0γ) and the modulation vector q=1/2**a*** +γ**c***.[143] The value of the component γ determines the final structure of the polymorph, since γ=0 results in the pure β-$NaMnO_2$ phase, γ=½ corresponds to the α-$NaMnO_2$ phase. Values of γ between 0 and ½ account for intermediate structures between the α and β phase[143].

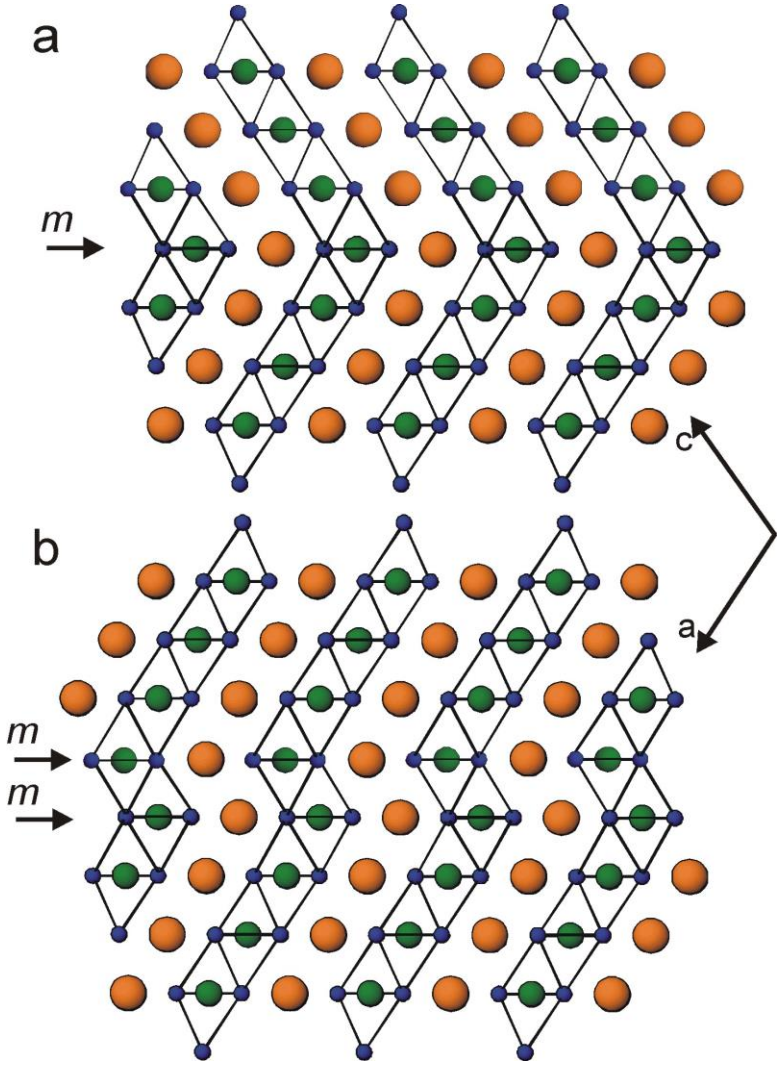

Figure 3.24 Possible models explaining the complex crystal structure of the α-$NaMnO_2$: a) the twin boundary model and b) the antiphase boundary. The Mn, O and Na atoms are shown as green, blue and orange spheres, respectively.

3.6 Results and Discussion

Although the crystal and magnetic properties of α-$NaMnO_2$ have been extensively studied during the recent years,[7, 8, 148, 180] the magnetodielectric properties and the microstructure have not been examined up to now. In the current thesis we have examined the possible

magnetodielectric character of α-$NaMnO_2$ which is explained by its inhomogeneous microstructure as pointed out by TEM.

Quite surprisingly, α-$NaMnO_2$ shows a distinct dielectric anomaly at 95 K. The dielectric anomaly is present under 0 Tesla magnetic field and is well enchanced by 14 % when 1.5 T are applied. The dielectric anomaly also shifts at higher temperatures under the effect of external magnetic fields. The value of the dielectric constant ε' is low (<10) in comparison with the well known dielectrics (for example that of $BaTiO_3$) but still comparable with the values reported for other polycrystalline ABO_2 samples.[50, 163] For example the values of ε' under zero magnetic field have been found to be: for $LiCrO_2$ ε' ~8, for $CuCrO_2$ ε' ~ 7 whereas for $AgCrO_2$ and $NaCrO_2$ ε' ~ 6.5, [50] and for the dipolar glass $CuFe_{0.5}V_{0.5}O_2$ ε' ~7.6-8.2[185]. The repeatability of the measurements has been checked, and although the samples show signs of fatigue and aging, the dielectric anomaly appears after many cycles of heating and cooling the sample.

The origin of dieletric anomaly at 95 K would have remained vague if TEM investigation had not been carried out. In this temperature region α-$NaMnO_2$ is still paramagnetic since it adopts its antiferromagnetic ordering only below 45 K. The 2D diffuse magnetic scattering between 50 K -200 K, evident by the Warren peaks in the NPD patterns can not account for the abrupt change in the dielectric constant. Thus, any correlation of the dielectric behavior with the intrinsic magnetic properties of α-$NaMnO_2$ would not be substantial.

The question related with the cause of the dielectric anomaly in the α-$NaMnO_2$ was resolved through an extensive study of the compound with high resolution transmission electron microscopy. ED diffraction patterns revealed planar defects which were attributed to the presence of the β-$NaMnO_2$ phase. Although the density of the planar defects is significantly less when compared to those of β-$NaMnO_2$, they prove to be enough for affecting the magnetodielectric properties of the α-$NaMnO_2$ compound. In other words, the existence of the β-$NaMnO_2$ in the α-$NaMnO_2$ phase is responsible for the dielectric anomaly at 95 K.

Worth mentioning, that only one of the two dielectric anomalies of β-$NaMnO_2$ (relevant results of the β-$NaMnO_2$ are shown on section 4.5) is present in the dielectric constant of α-$NaMnO_2$. The broad hump at 200 K which appears in the ε'(T) of β-$NaMnO_2$ is missing from the α-$NaMnO_2$. This is probably related with the difference in the strength of each anomaly as well the type of the magnetic interactions between the Mn^{+3} cations that develop in each magnetic transition. Moreover, there is a difference of about 5 K in the low temperature dielectric anomaly, since for β-$NaMnO_2$ the sharp drop of ε' occurs at 90 K whereas for α-$NaMnO_2$ at 95 K.

Although the research in multiferroics, magnetoelectrics and magnetodielectrics traditionally began in single phase crystals and ceramics, this trend is no longer common. On the one hand single phase magnetoelectrics are rare, and on the other hand the coupling is usually weak. Recently, different routes have been proposed for the coupling between the electric and magnetic degrees of freedom. Heteroepitaxially grown thin films [186, 187] such as the well studied $BaTiO_3$-$CoFe_2O_4$[188] or the $BiFeO_3$-$CoFe_2O_4$ nanostructures,[189] disordered multiferroics[46, 190] compositionally modulated multiferroics[191] and composite nanostructure systems[192] provide new routes for the growth of the magnetoelectric materials and the enhancement of the magnetoelectric coupling.

Here, the case of α-$NaMnO_2$ refers to an inhomeogenuous microstructure of a chemical homogeneuous system.[180] The twin and antiphase boundaries (see Figures 3.22 and 3.24), caused by the presence of the β-$NaMnO_2$ phase and overall the complexity of the superstructure are promoting the magnetodielectric coupling in the α-$NaMnO_2$ phase. For example the large magnetodielectric effect in the nanocrystalline double Y_2FeCrO_6 perovskite [193] has been supported by the existence of the antiphase boundaries. Specifically, the large magnetodielectric coefficient is explained by a model in which the spin-polarized electrons hopping through the antiphase boundary contribute higher electrical conductivity to the system when a magnetic field is applied. Furthermore, the effect of the direction of the antiphase boundaries has been reported for the $Ba_{0.5}Sr_{0.5}TiO_3$ films grown on MgO substrates. [194]

A reasonable thought regards the crucial role of the planar defects in the inhomeogeneous microstructure of α-$NaMnO_2$. Undoubtedly, a better understanding of the mechanism that generates the magnetodielectric coupling at 95 K in α-$NaMnO_2$ would require first the knowledge of the microstructure at this tempeture region and second, the effects of this structure on the magnetic properties of the system. This would entail the investigation of the α-$NaMnO_2$ structure by electron diffraction and HRTEM at low temperatures (T<100 K), a fairly challenging task on its own.

The ED patterns revealed and HRTEM figures confirmed the existence of the β-$NaMnO_2$ phase evident by the appearance of planar defects.[143] The planar defects can be considered as forming quasi-periodic sequences which introduce modulations in the arrangenment of the $NaMnO_2$ layers. These defects act as mirror twin planes (Figure 3.22) in the microstructure α-$NaMnO_2$. The existence of two adjacent twin planes (marked with black arrowheads in inserts in Figure 3.22) is equivalent to a stacking fault: they do not change the orientation of the atomic layers and cause their lateral displacement only. The twin planes affect only the arrangement of the Na^+ and Mn^{+3} cations over the octahedral interstices whereas they leave the positions of the oxygen atoms intact. The relative position of the twin planes, determines the formation of the antiphase boundaries. Specifically, when two or any even number of twin planes are adjacent to each other an antiphase boundary is formed due to the exchange of the Na^+ and Mn^{+3} positions (see Figure 3.24b). Quite recently, it has been proposed[195] that antiphase boundaries may possess ferroelectricity in an antiferroelectric system as it has been proved for the lead zirconate (PZ) system. This conclusion points out that domain walls can possess diffenent properties than the domains themselves.

In the case of α-$NaMnO_2$ the structure irregularities appear as a result of two competing phases: α and β-$NaMnO_2$. The competition of the two phases yields the formation of domains which are separated by domain walls. It is interesting to mention how the domains affect the functionality and the macroscopic properties the systems. The thickness δ of the domain walls is[196] given by Kittel's law

$$\frac{\delta}{w}=\sqrt{\frac{\delta}{\mathrm{Gd}}} \qquad \textbf{(3.6)}$$

where w and d is the domain width and thickness, respectively and G is an adimensional parameter. The physical meaning behind Kittel's law is that the density of domain walls, expressed by the fraction δ/w is increasing, when d is decreasing. In other words, the properties of a material which depend on the density of the nanodomains is strictly related with the thickness of the domain walls. Some typical examples where the domain walls have proved to play the key role in the functionality of the materials, include ferroelectrics[197], relaxors[198] with electrostriction, multiferroics [199]and systems which display colossal magnetoresistance.[200]

The structural complexity of the α-$NaMnO_2$ phase is explained on the basis of a superstructure for the $NaMnO_2$ polymorphs. The α-$NaMnO_2$, β-$NaMnO_2$ and the intermediate phases are considered as modulated superstructures in the (3+1)D superspace. The altering of formation between the α- and β-$NaMnO_2$ phases is driven by the Jahn-Teller distorted environment of the Mn^{+3} cations. In pure α-$NaMnO_2$ three Mn^{+3} ions form bonds with the neighboring oxygen atoms, whereas on the twin plane the bonds between the Mn^{+3} and the oxygen atoms are four. If there was no Jahn-Teller distortion, this would result in a modification of the bond valence strengths. However, due to the Jahn-Teller distorted MnO_6 octahedra the structure of the polymoprhs adopts different Mn-O lengths, namely four short (1.95 Å) and two long (2.42 Å) Mn-O configurations.

The formation of the β-$NaMnO_2$ and intermediate phases into the matrix of α-$NaMnO_2$ is supported by the low energy cost, since the $NaMnO_2$ polymorphs have comparable energies, which differ only about $\Delta E \sim 0.2$ (mRy/at) .[201]

3.7 Conclusions

To conclude, the crystal, magnetic and dielectric behavior of the α-$NaMnO_2$ polymorph has been studied. The complex oxide α-$NaMnO_2$ exhibits dielectric anomaly at 95 K. The magnetic fields applied upon the measurement of the dielectric constant enchance the magnetodielectric coupling and shift the critical temperature of the dielectric anomaly to higher temperatures. Similar behavior has been reported for other magnetoelectric systems such as the $DyMn_2O_5$,[157] $DyMnO_3$,[158] Mn_3O_4[70] and $Ni_3V_2O_8$.[202]

The origin of the coupling between the electric and magnetic degrees of freedom is not related with the magnetic ordering of α-$NaMnO_2$, as the oxide remains paramagnetic in this temperature region. Quite notably, the anomaly in the ε'(T) of α-$NaMnO_2$ is attributed on the existence of the β-$NaMnO_2$ phase, evident in the electron diffraction patterns by the appearance of planar defects and other structure irregularities in α-$NaMnO_2$ microstructure.

The novelty and importance of this result lies on the effects of polymorphism in the dielectric response of systems with competing interactions. The observation of the magnetodielectric coupling in α-$NaMnO_2$ at a temperature area where the system does not exhibit long range magnetic order provides a new perspective in the mechanisms of the induced coupling between the electric and magnetic degrees of freedom. The existence of planar defects (in this case twin planes and antiphase boundaries) does not only affect the microstructure of a system but surely has a great impact on its macroscopic properties, such as the magnetodielectric coupling.

The rock salt derivative crystal structure of α-$NaMnO_2$ is dominated by the Jahn Teller distortion of the MnO_6 octahedra caused by the Mn^{+3} cations. The interchange between the Na and Mn atoms positions, leads to a modulated incommensurate structure, in which intermediate phases between the pure α-$NaMnO_2$ and β-$NaMnO_2$ exist. The coherent intergrowth of the β-phase in the matrix of α-phase, as well as the tendency of the polymoprhs to form intermediate structures is encouraged by the energetic proximity of the α and β-$NaMnO_2$ structures.

Chapter 4:

Crystal, Magnetic and Magnetodielectric Behavior of the 2D Antiferromagnet β-$NaMnO_2$

4.1 Introduction

The layered oxide β-$NaMnO_2$, is a member of the Na_xMnO_2 oxides family and has been reported at the same study with α-$NaMnO_2$ by Parant on 1971. [6] The growth of single crystals of β-$NaMnO_2$ and other Na_xMnO_2 (x<1) oxides has only been attempted by Jansen and Hope around 1973.[135, 203] A Few years later Hirano et al, reported the hydrothermal synthesis of Na_xMnO_2 single crystals without including in their results the synthesis protocol of β-$NaMnO_2$.[204]

Thereafter, the studies that have been carried out in respect with the β-$NaMnO_2$ compound are very few in comparison to the research that involved studies of the α-$NaMnO_2$ polymoprh. There are two reasons for this. The first one is attributed to the 2D layered crystal structure of β-$NaMnO_2$. Due to the corrugated arrangement of the Na cations the β-$NaMnO_2$ is not favorable for intercalation and deintercalation processes and as such, has not been used as a precursor for the synthesis of other compounds. The second reason arises from the difficulties entailed in the synthesis of a pure phase β-$NaMnO_2$. The β-$NaMnO_2$ solid state synthesis is accomplished at 950°C. However at lower temperatures other Na_xMnO_2 oxides are formed, for example the $Na_{0.7}MnO_2$ at 660°C and both α-$NaMnO_2$ and $Na_{0.7}MnO_2$ at 750°C. Thus, the most common problem in solid state synthesis is to achieve a pure phase sample of fair crystallinity and to avoid the appearance of secondary phases.

In this chapter, studies on the crystal, magnetic and magnetodielectric properties of the β-$NaMnO_2$ are reported for the first time. The β-$NaMnO_2$ exhibits a compex crystal structure which has been studied by neutron powder diffraction data and analyzed by high resolution electron microscopy. The observations of its microstructure are combined with the neutron scattering results as well as the magnetodielectric response.

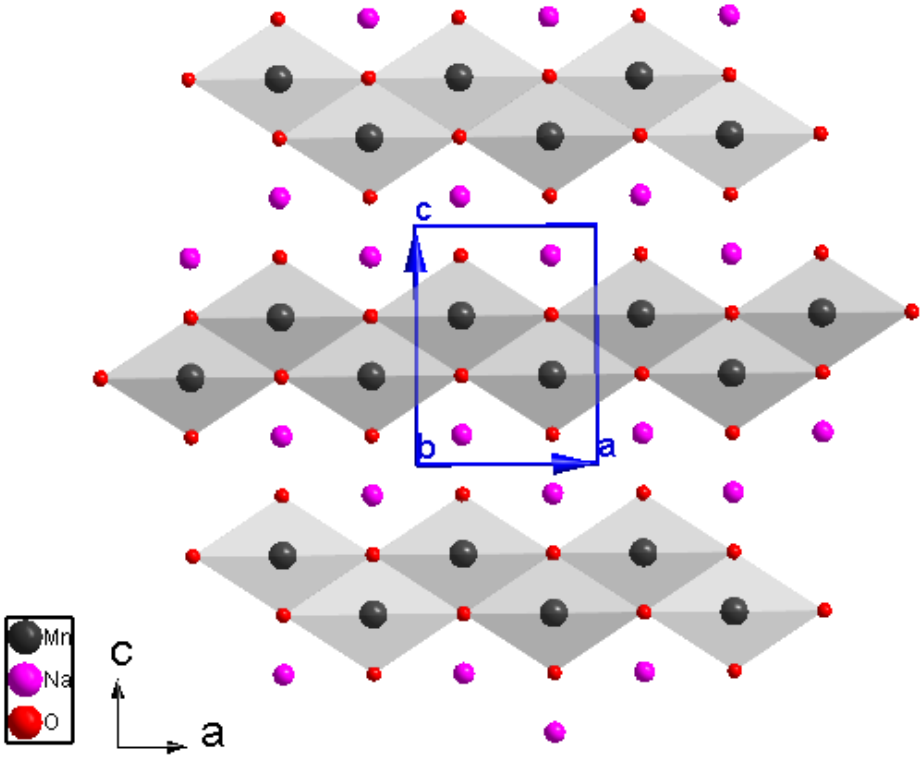

Figure 4.1 The crystal structure at room temperature of β-$NaMnO_2$. Mn, Na and O atoms are represented with dark grey, purple and red spheres, respectively. Cell edges are shown with blue color.

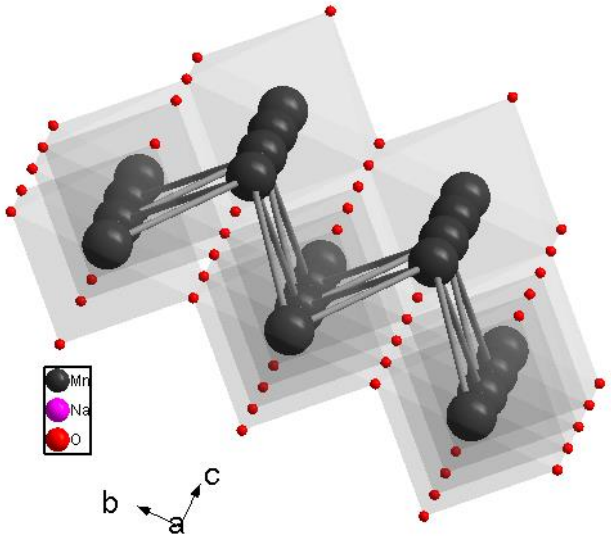

Figure 4.2 A detail of the crystal structure of β-$NaMnO_2$ showing the 2D triangular arrangement of the Mn^{+3} ions.

Crystal Structure and Magnetic Interactions of β-$NaMnO_2$

Although the stoichiometry is the same with the α-$NaMnO_2$ phase, there is a remarkable difference in the structure. At room temperature β-$NaMnO_2$ crystallizes in the orthorhombic cell, at the space group Pmmn, with the cell parameters a=4.77 Å, b=2.85 Å, c=6.33 Å. The Na cations form a 2D corrugated layer which separates the MnO_2 sheets. The crystal structure of β-$NaMnO_2$ is built up of the corrugated zig-zag layers of the edge sharing MnO_6 octahedra, which are distorted due to the Janh-Teller active Mn^{+3}. In the interlayer distance there are two sheets of Na atoms (Figure 4.1) in the octahedral interstices between the MnO_2 sheets. The Mn^{+3} ions map out on a corrugated 2D triangular lattice (Figure 4.2). The specific lattice topology supports geometric magnetic frustration, as it was proved for the case of α-$NaMnO_2$ polymorph.

The magnetic properties of the polymorph β-$NaMnO_2$ have been studied by different methods. Preliminary data obtained by measurements of the static magnetic suscpeptibility on a Superconducting Quantum Interference Device (SQUID) magnetometer (Quantum Design MPMS-XL5.

According to the electronic structure calculations, [143]strong AFM couplings appear, namely the J_1=70 K along the b and J_3=57 K along the a direction. J_1 is the interaction between the Mn cations that are separated by the distance of 2.86 Å, whereas the J_2 corresponds to the 3.21 Å distance of Mn-Mn. J_1 and J_2 form two interpenetrating lattices which are coupled by a weaker frustrated interaction, J_2=13 K. J_3 is a strong AFM superexchange caused by the Mn-O-Mn pathway with the connecting angle of ~167 deg The pure β-$NaMnO_2$ in which J_1 is very close to the J_3 should be regarded as a quasi 2D magnet.

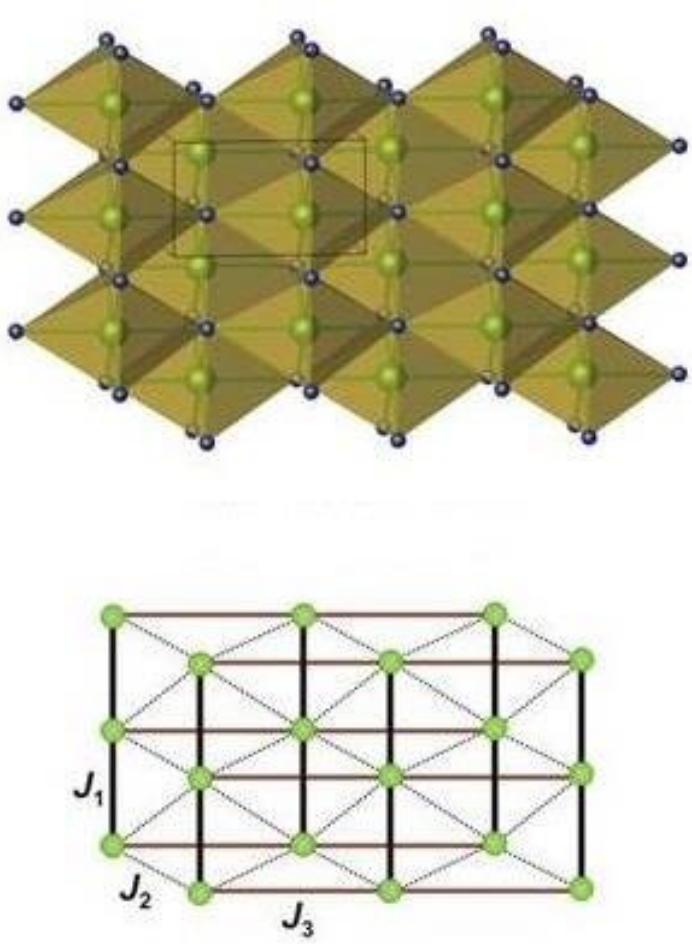

Figure 4.3 Structures of [MnO_2] layers and relevant topologies of magnetic interactions in the β-$NaMnO_2$ polymorph. The Mn and O atoms are shown with the green and blue spheres, respectively. MnO_6 octahedra are shown in transparent green.

4.2 Synthesis of β-$NaMnO_2$

Polycrystalline powder specimens of β-$NaMnO_2$ have been synthesized by high temperature solid state reaction. The synthesis is based on the protocol reported by Parant[6] and includes slight modifications. The first step is the weighting of stoichiometric amounts of Na_2CO_3 (Aldrich, 99.5%) and Mn_2O_3 (Aldrich, 99%), which are stored in a drying cabinet at 60-70°C. The starting materials were mixed, grounded, pelletized (using a 13

mm die under 0.5 ton pressure) and heated from 25°C to 950°C with a slow heating rate (0.4 °C /min) under continuous oxygen flow. A 10% excess of Na_2CO_3 was added in the first grinding to compensate for the loss of sodium. Taking into account the 10 % addition of the Na_2CO_3 and the purity of each reactant, the starting materials that have been used were:

$$Na_2CO_3 + Mn_2O_3 \longrightarrow 2\ \beta\text{-}NaMnO_2 + CO_{2(g)} \qquad \textbf{(4.1)}$$

0.54 gr+0.725 gr 1 gr

The dwelling time at 950°C was 24 hrs. Afterwards, the pellet was quenched at room temperature while it remained under oxygen flow. The quenching lasts ten minutes and from this point the sample is treated as moisture sensitive. A second grinding was carried out in an Ar-filled MBRAUN anaerobic glove-box. The sample is then introduced into a 13 mm evacuable pellet die and pressed at 0.5 ton outside the box. The pellet was taken out immediately from the die and placed in the furnace at the temperature of 950°C for 24 hrs. This step was repeated twice. After the third dwelling at 950°C is over, the pellet is kept in the glove box, where all the preparation for the possible measurements (XRD, SQUID) took place.

Worth mentioning that many attempts took place in order to achieve a pure phase with good crystallinity β-$NaMnO_2$. These attempts included the modification of the synthesis protocol. For example some efforts included: increasing the final sintering temperature (1000°C), changing the heating rate, increasing or decreasing the total heatings of the reaction, quenching the sample in liquid N_2. However these changes resulted in specimens with lower crystallinity and secondary phases mostly attributed to the $Na_{0.7}MnO_2$ and α-$NaMnO_2$ compounds. Similar results showing the existence of secondary phases in the XRPD pattern were obtained when the second and third heating started from lower temperatures (550°C) instead of 950°C.

The efforts for optimization of the synthesis protocol are summarized in Table 4.1. The reagents used in each synthesis were the same (0.54 gr of Na_2CO_3 and 0.725 of Mn_2O_3) and the pelletizing conditions identical. The basic modifications applied in each synthesis

effort are noted in the Table 4.1 and the XRPD pattern of each sample is shown in section 4.3.

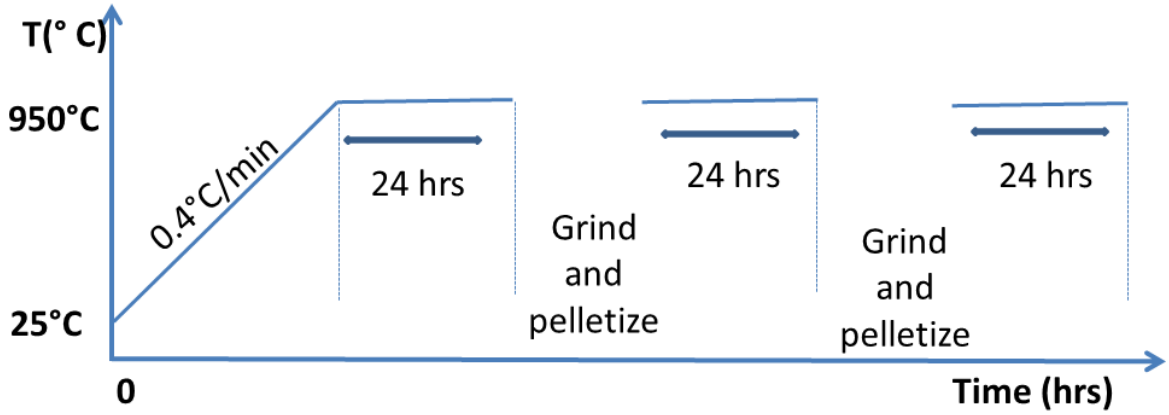

Figure 4.4 A schematic representation of the β-$NaMnO_2$ solid state synthesis. The first heating starts at room temperature and almost 38.5 hrs are required in order to reach the final dwelling temperature at 950°C. The second and third heating started at 950°C.

β-$NaMnO_2$ Sample's Code	**Remarks-Modifications on Synthesis**	**Remarks on XRPD pattern**
ib4	✓ 4 heatings ✓ 2nd and 3rd heating start at 550°C ✓ Quenching in liquid N_2 from the final temperature of 950°C for about 15-20 min ✓ Reduced O_2 flow	Impurity peak at 21 deg
ib6	✓ the reaction includes 3 heatings ✓ Quenching in N_2 for about 15-20 min	001 peaks of α-$NaMnO_2$ and $Na_{0.7}MnO_2$
ib7	✓ 4 heatings ✓ Quenching in air at the edge of the furnace with enhanced O_2 flow ✓ at the 3rd heating dwelling on 750°C for 1.30 hr	$Na_{0.7}MnO_2$ 001 peak
ib8	✓ includes 3 heatings under O_2 flow ✓ the reagents were dried before ✓ Quenching in air with high O_2 flow	001 peaks of α-$NaMnO_2$ and $Na_{0.7}MnO_2$
ib10	✓ Reaction includes 3 heatings ✓ Second and third heating start at 950°C ✓ Quenching in air with high O_2 flow	α-$NaMnO_2$ 001 peak
ib12	✓ Final T=1000°C, ✓ 2nd and 3rd heating start from 1000°C (O_2 flow)	$Na_{0.7}MnO_2$ 001 peak
ib15	✓ Reaction includes only one heating (O_2 flow) ✓ Basic change: at the 1st heating I apply a rate of 25-600°C: 0.5 °C/min 600-950°C: 2 °C/min	001 peaks of α-$NaMnO_2$ and $Na_{0.7}MnO_2$
ib17	✓ 25-600°C:0.5C/min, 600-950°C, 2 °C/min (O_2 flow) ✓ 1st heating: After dwelling for 12 hrs in 950°C, I quench it in air, regrind it in the glove box, pelletize it and put it back to the furnace at 950°C ✓ 2nd and 3rd heating directly at 950°C for 24 hrs	001 peaks of α-$NaMnO_2$ and $Na_{0.7}MnO_2$
ib18	✓ Two heatings at 950°C for 24 hrs ✓ 1st heating 25-950°C: 0.4 °C/min	

Table 4.1 Examples of synthesis protocols applied for the preparation of β-$NaMnO_2$. The protocol that was finally followed is the one which refers to the sample's code "ib10".

4.3 Characterization of β-$NaMnO_2$

4.3.1 X Rays Powder Diffraction (XRPD)

The purity and crystallinity of the β-$NaMnO_2$ phase has been checked by X-Ray diffraction on a Rigaku D/MAX-2000H rotating Cu anode diffractometer (λ=1.5406 Å). The sample is placed on the holder and sealed with a mylar foil in the glove box, so that it is not exposed in the atmosphere during the X-Rays experiment. The synthesized compound is a phase-pure β-$NaMnO_2$ which crystallizes in the orthorhombic Pmnm symmetry (a=2.852 Å, b=6.33 Å, c=4.77 Å, 90 deg, 90 deg, 90 deg).

Figure 4.5 shows the XRPD pattern of the polycrystalline β-$NaMnO_2$ and the indexing of the Bragg peaks according to the 16271 cif file of the crystallographic database ICSD (Inorganic Crystallographic Database) which is pointed with the red ticks. The grey ticks correspond to the reflections attributed to the mylar film. As noticed, there is a very good agreement between the Bragg reflections obtained from the β-$NaMnO_2$ sample and the ones expected from the ICSD database.

Nevertheless, there are two characteristics in the XRPD pattern which yield the necessity of further investigation on the β-$NaMnO_2$ structure. The first one is the blue tick around 16.6 deg which stands for the 001 reflection of the α-$NaMnO_2$ phase, pointed also with the blue arrow. Worth reminding here, that also in the XRPD of the α-$NaMnO_2$ the 001 reflection of the β-$NaMnO_2$ was present. To observe better the presence of the α-$NaMnO_2$ phase, the XRPD of a α-$NaMnO_2$ sample (purple graph) and the blue tick marks which correspond to the predicted Bragg peaks are also shown in Figure 4.5. The second one, which is a rather unusual characteristic, is the broadening of the peaks at 38-40 deg and more clearly at 55 deg. Since a conventional X-Ray diffractometer has limited resolution, neutron powder and electron diffraction studies were carried out to further explore the crystal structure of the β-$NaMnO_2$.

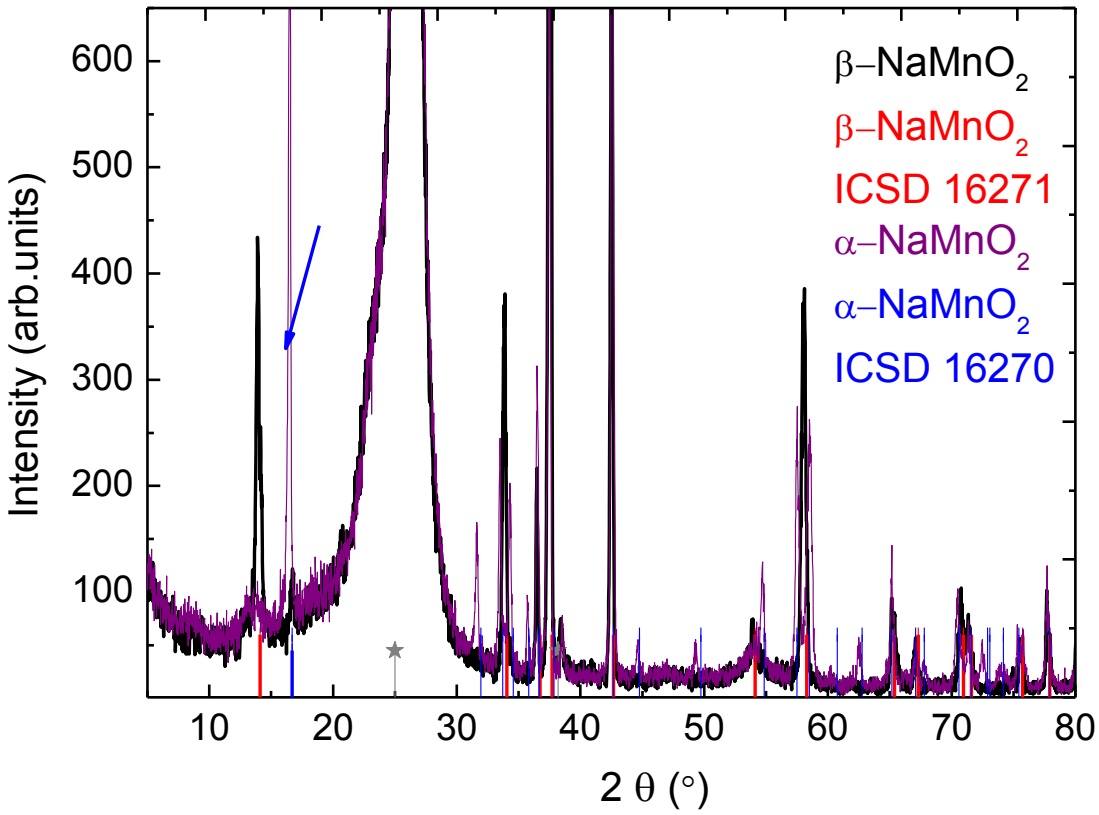

Figure 4.5 X Ray Powder Diffraction pattern of the polycrystalline β-$NaMnO_2$ at room temperature. The red ticks correspond to the orthorhombic cell indexed upon the database of ICSD 16271. The grey ticks represent the reflections of the mylar film. The blue tick is attributed to the 001 reflection of the α-$NaMnO_2$

XRPD patterns of samples that have been synthesized with modified protocols

Figures 4. 6 and 4.7 present the XRPD patterns at the 2θ area of 10-22 deg of the β-$NaMnO_2$ synthesized with modified protocols. The modifications applied for each sample are shown in table 4.1. The specific 2θ area is presented since the major problem of the β-$NaMnO_2$ was the appearance of secondary phases evident by the 001 peaks of $Na_{0.7}MnO_2$ (Crystallographic Data Base and relevant code for $Na_{0.7}MnO_2$: CRYSTMET 485956) at 15.78 deg and α-$NaMnO_2$ at 16.6 deg.

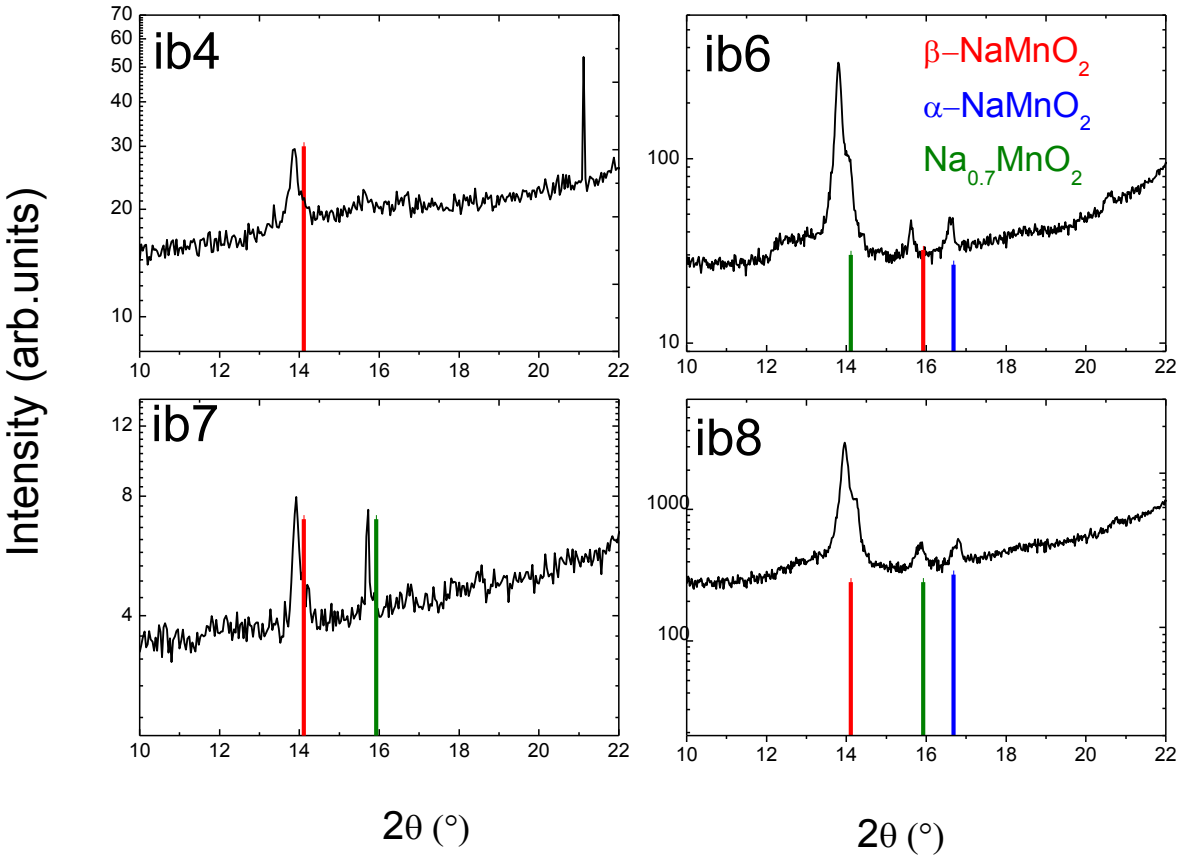

Figure 4.6 Examples of β-$NaMnO_2$ samples that have been prepared by changing a few parameters (see Table 4.1) in order to prepare β-$NaMnO_2$. Note in the presence of the 001 Bragg reflections of $Na_{0.7}MnO_2$ and α-$NaMnO_2$ which appear as secondary phases.

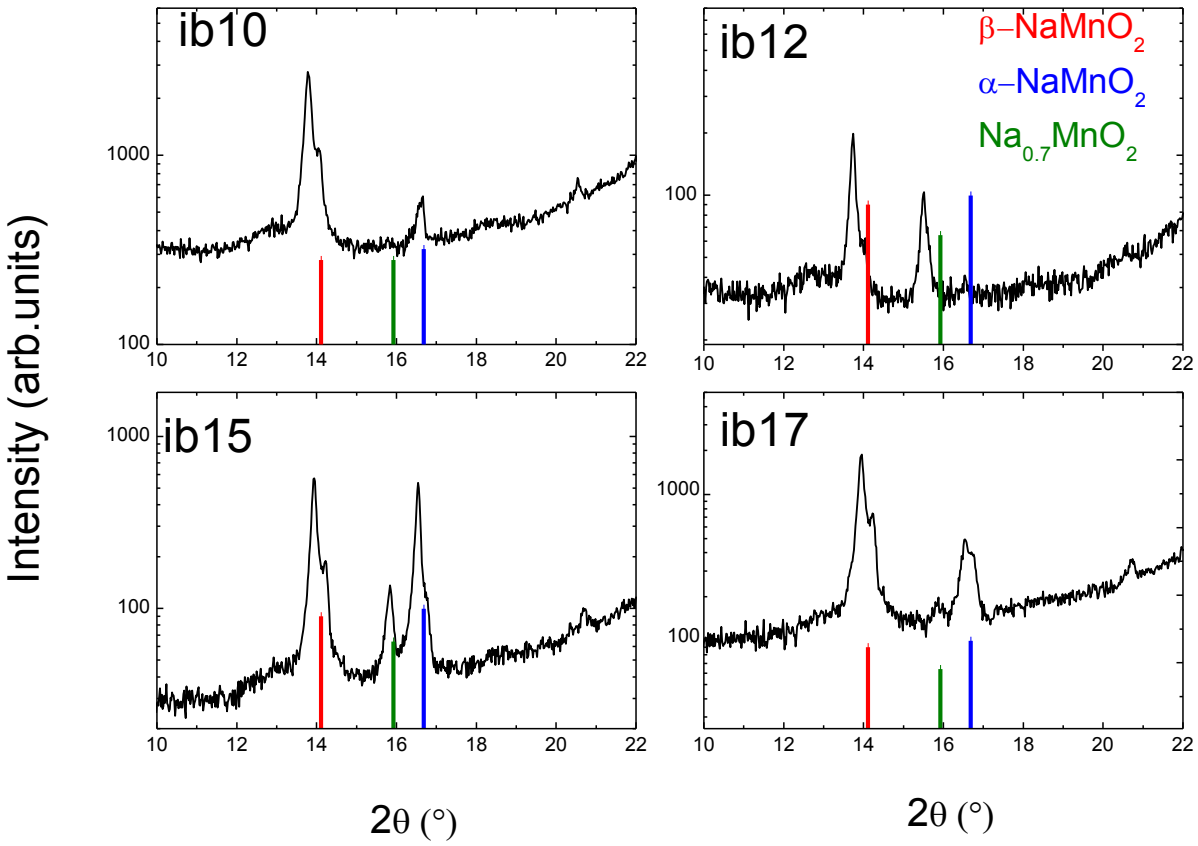

Figure 4.7 β-$NaMnO_2$ samples prepared by applying different modifications (see table 4.1 for details) on the synthesis protocol. The 001 peaks of 001 Bragg reflections of $Na_{0.7}MnO_2$ and α-$NaMnO_2$ appear whereas at the ib12 sample (final sintering temperature 1000°C) there is also problem with the stoichiometry of the β-$NaMnO_2$ phase.

XRPD of the annealed β-$NaMnO_2$ samples

Annealed β-$NaMnO_2$ under O2 flow

For the purposes of the magnetodielectric measurements some β-$NaMnO_2$ samples have been annealed at 300°C for 6 hrs under oxygen flow. A critical issue that needs to be examined is whether the annealing of a β-$NaMnO_2$ sample affects its crystal structure of For this reason XRPD experiments were carried out on the β-$NaMnO_2$ before and after the annealing procedure. The results are presented in Figure 4.8.

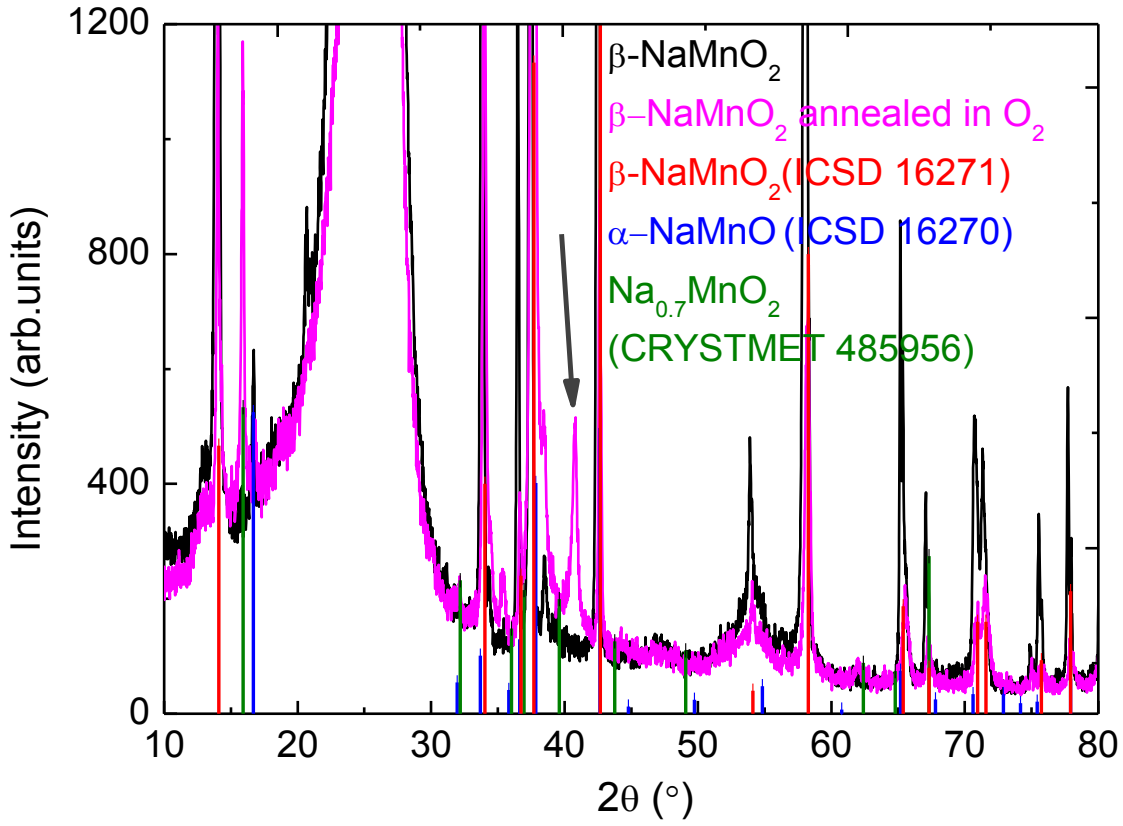

Figure 4.8 XRPD comparing the patterns obtained from the β-$NaMnO_2$ samples represented with the black line with the β-$NaMnO_2$ samples that have been annealed in O_2 shown with the purple line.

Figure 4.8 compares the XRPD patterns of a β-$NaMnO_2$ sample presented in black and the β-$NaMnO_2$ that has been annealed-the graph shown in purple. The patterns have been indexed upon the β-$NaMnO_2$ as well as the α-$NaMnO_2$ and the $Na_{0.7}MnO_2$ oxides which are expected as possible secondary phases. The β-$NaMnO_2$, α-$NaMnO_2$ and $Na_{0.7}MnO_2$ [204] phases are pointed with the blue, red and green tick marks, respectively. The annealed β-$NaMnO_2$ sample shows all the expected Bragg peaks of the β-$NaMnO_2$. Nevertheless, around 41 deg there is one peak pointed with the arrow, which could not be indexed upon the known Na_xMnO_2 or Mn_xO_y oxides.

Most importantly, the annealed sample has the 001 peaks of $Na_{0.7}MnO_2$ and α-$NaMnO_2$ at 15.9 deg and 16.67 deg, respectively, as it is presented in detail in Figure 4.9. The relative intensity of the 001 reflection of the $Na_{0.7}MnO_2$ is comparable with the 001 of the β-$NaMnO_2$ around 14.1 deg. Moreover, the XRPD pattern of the β-$NaMnO_2$ sample, (before the annealing) already shows the 001 peak of α-$NaMnO_2$, an observation which is confirmed by the HRTEM analysis (see section 4.6.2). The co-existence of the $NaMnO_2$ polymorphs is explained upon their small energetic difference.[143]

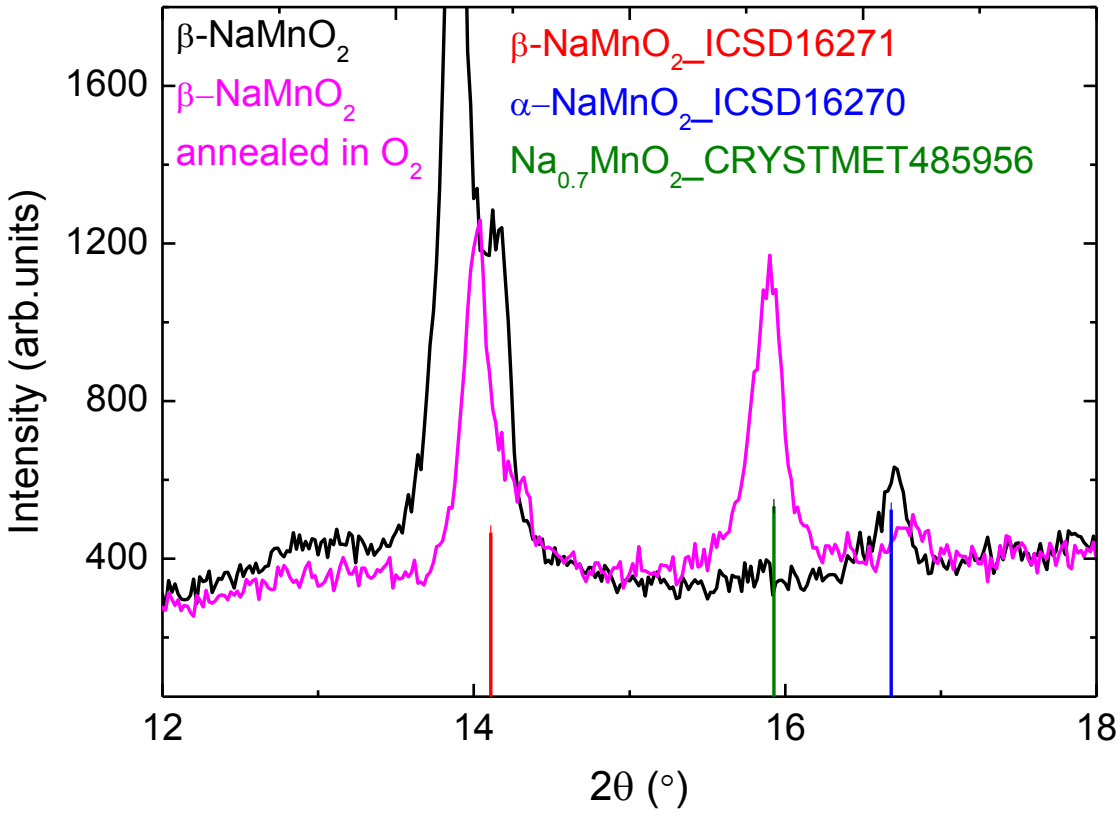

Figure 4.9 A detail of Figure 4.8 showing the 2 theta area between 12-18 deg. Note the Bragg peaks that correspond to the $Na_{0.7}MnO_2$ and α-$NaMnO_2$ shown with the green and blue ticks, respectively.

Annealed β-$NaMnO_2$ samples in air

Annealing at 300°C for 6 hrs under atmospheric air (without having O_2 flow or any inert gas) was also carried out, as a possible option for the optimization of the β-$NaMnO_2$ which would be used for the magnetodielectric measurements. However, this annealing resulted in samples with impurities mostly attributed to the $Na_{0.7}MnO_2$ phase, as it can be seen in Figure 4.10. The relative intensity of the 001 peak of $Na_{0.7}MnO_2$ (15.9 deg) in respect with the 001 reflection of β-$NaMnO_2$ (14.11 deg) shows that the annealing results in a two phase compound. This affects also the magnetic properties of the annealed sample as shown in section 4.4, Figure 4.19.

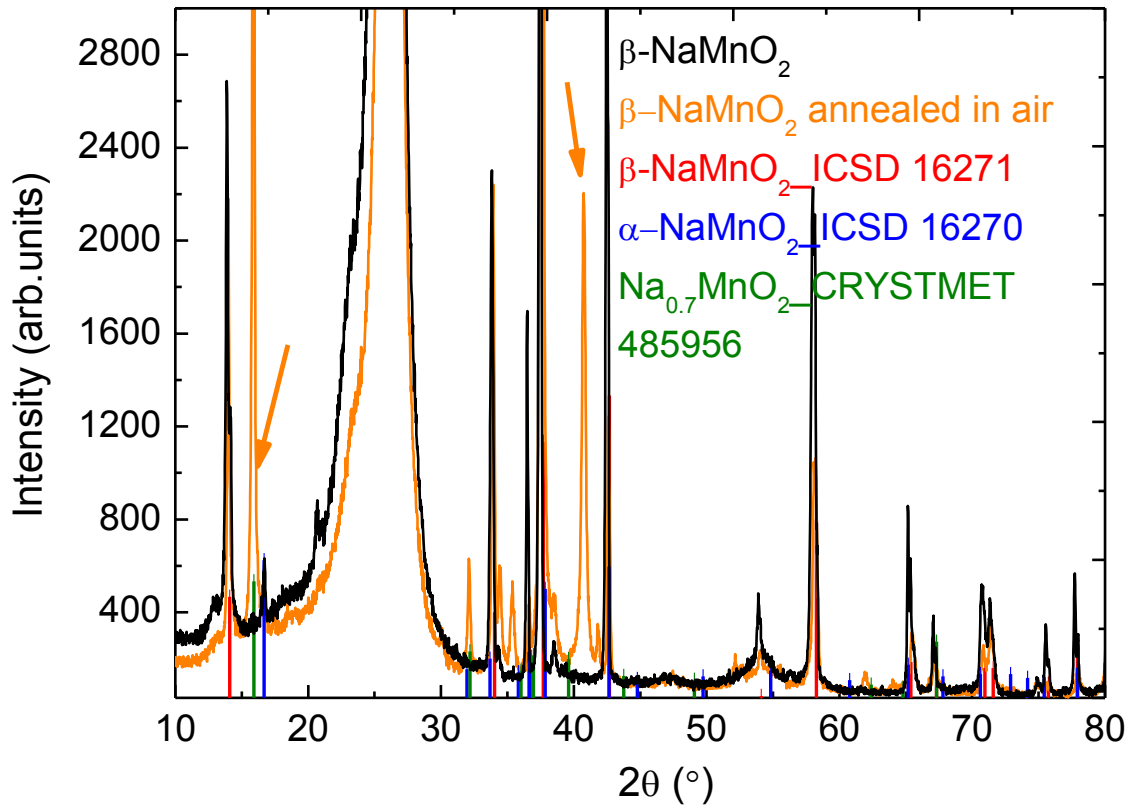

Figure 4.10 XRPD of the β-$NaMnO_2$ sample in comparison with the annealed in air, shown in black and orange line, respectively.

A sample whose polarization versus temperature has been measured (section 4.5.5) was the ib18, which had undergone the procedure of annealing in air at 300°C for 6 hrs. The synthesis of the sample is described in Table 4.1 and the XRPD pattern before and after the annealing is presented in Figure 4.11. The difference of ib18 in comparison with the rest β-$NaMnO_2$ samples is that its synthesis protocol included two heatings instead of three. The annealed sample shows that the peak of 001 of $Na_{0.7}MnO_2$ has higher intensity in comparison with the 001 of β-$NaMnO_2$. The procedure of annealing resulted in a two phase compound (β-$NaMnO_2$ and $Na_{0.7}MnO_2$).

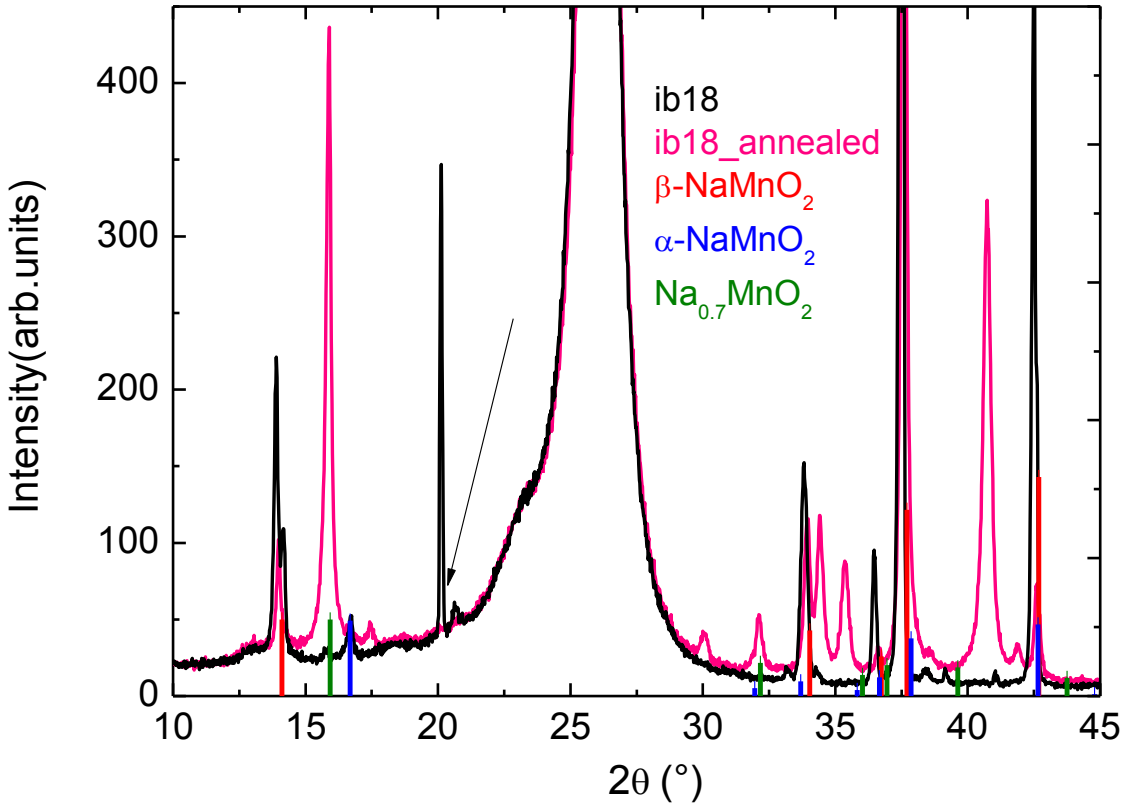

Figure 4.11 XRPD of the sample ib18 before and after the annealing procedure. The sample before the annealing shows peaks of β-$NaMnO_2$, $Na_{0.7}MnO_2$, α-$NaMnO_2$ and a strong peak at 2θ=21 deg which does not belong to any of the known Mn oxides. The annealing seems to enchance the presence of the $Na_{0.7}MnO_2$.

4.3.2 Inductive Coupled Plasma Optical Emission Spectroscopy (ICP-OES)

According to the stoichiometry of the β-$NaMnO_2$ the Na/Mn ratio should be around 1. ICP-OES on powder of β-$NaMnO_2$ has resulted in the Na/Mn ratio of 0.865. Similarly with the result of α-$NaMnO_2$ (Na/Mn= 0.826) the Na quantity is less than expected. As already discussed in the ICP-OES paragraph for α-$NaMnO_2$, Na is quite volatile in high

temperatures which results in Na loss. However for the β-$NaMnO_2$ the amount of Na found is by 4.5% higher than in the α-$NaMnO_2$. This can be explained by the addition of 10% excess of Na_2CO_3 in the first grinding.

4.3.3 Thermogravimetric Analysis

In order to evaluate the stability of the β-$NaMnO_2$ phase in respect with the temperature, thermogravimetric measurements were carried out in the temperature range between 25°C and 1000°C (Figure 4.12). The experiment was carried out using a constant heating rate of 10 °C/min under continuous Argon flow. The initial weight decrease of less than 1.5% around 100°C is attributed to the evaporation of water, which could be absorbed by the pores of the sample's surface while transferring the sample out of the glove box and placing it to the alumina pan of the SDT-Q600. The chemical composition of the sample remains stable at the temperatures 100°C - 500°C, whereas the 16% weight loss noticed between 500°C – 800°C is mostly attributed to the loss of sodium which occurs at temperatures higher than 400°C. Small amounts of unreacted Na_2CO_3, which has been used as a starting material, may also contribute to the weight loss in this temperature region.

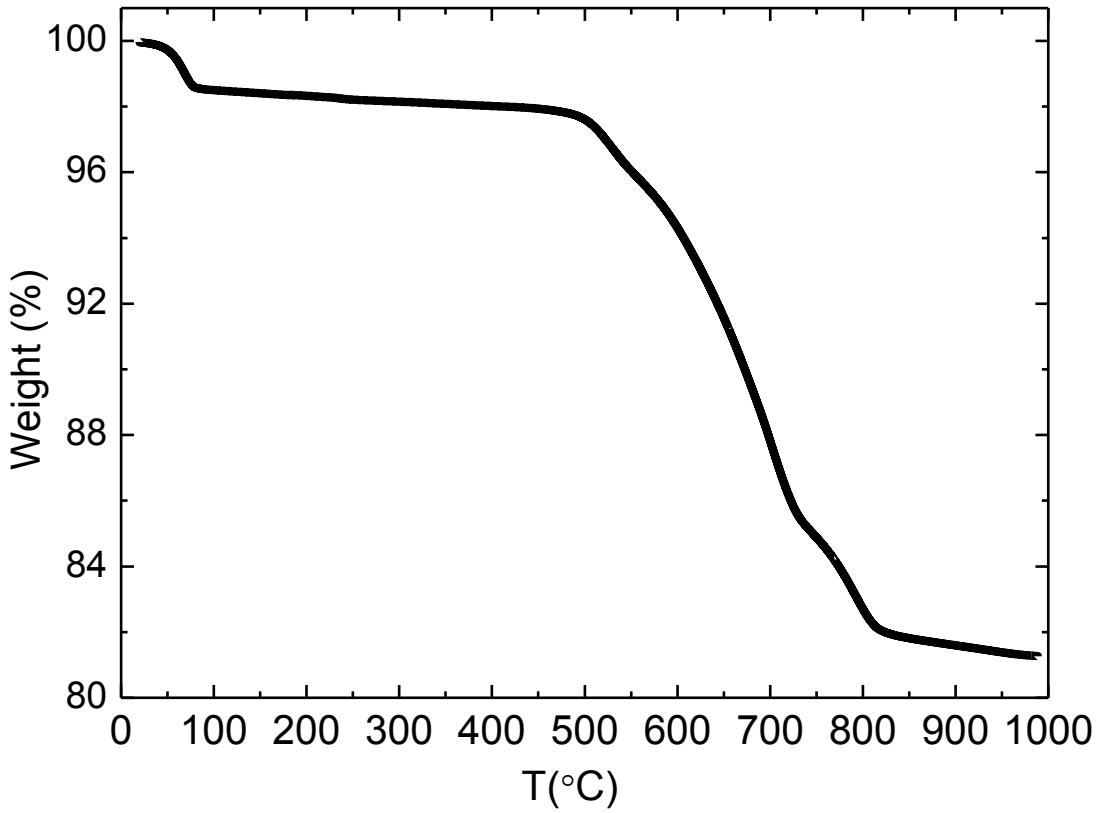

Figure 4.12 The graph obtained by the DCS experiment on polycrystalline powder of β-$NaMnO_2$ which shows the % weight change of the sample versus temperature.

4.3.4 HADFF-EDS mapping of β-$NaMnO_2$

The HADFF-EDS investigation provides a "chemical map" of the distribution each element's present in the compound. Due to the high sensitivity of the method in the atomic number contrast, the images provided are very reliable.

The β-$NaMnO_2$ sample was stored in a N_2-filled glove box. For TEM analyses, the specimen was prepared inside the glove box by crushing the crystals in a mortar in

anhydrous toluene. Few drops of suspension were deposited onto a holey carbon grid inside the glove box before the insertion of the sample in the microscope. HADFF and EELS analyses were carried out using a Jeol JEM 2200FS instrument, equipped with an image aberration corrector.

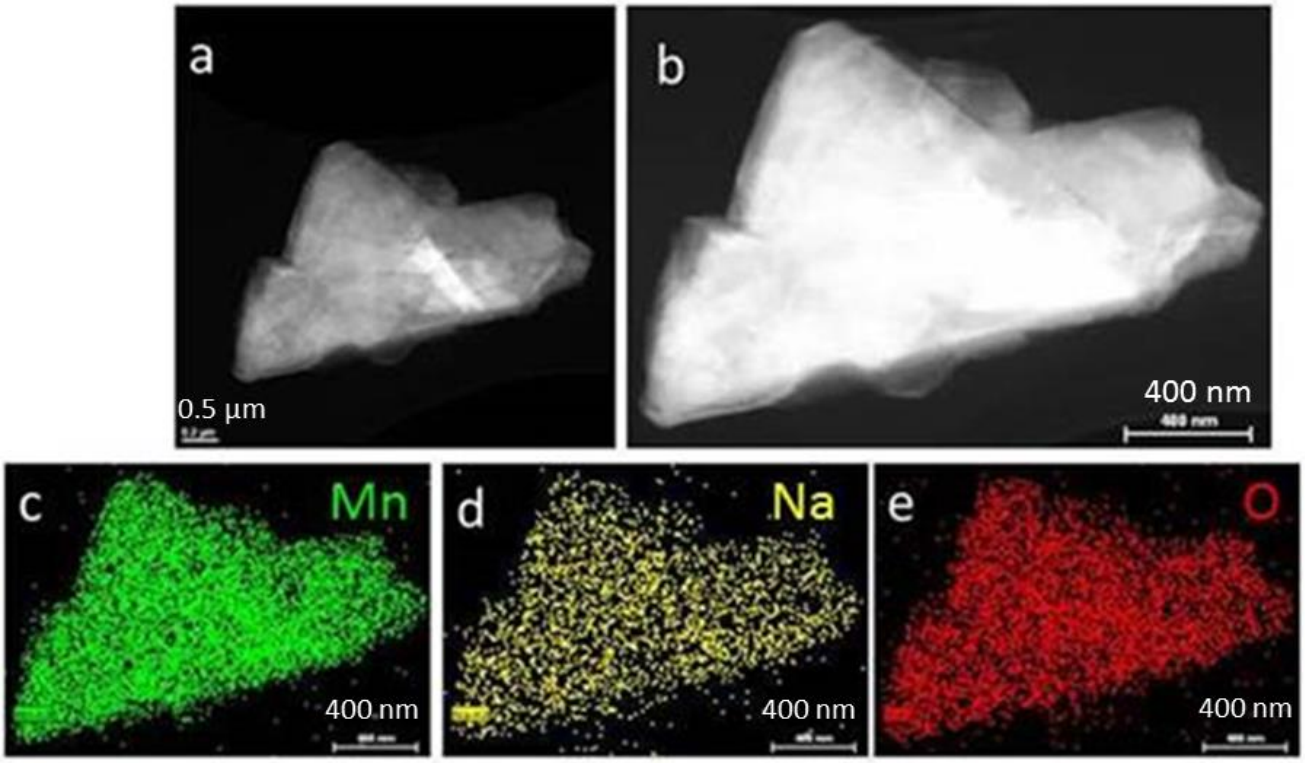

Figure 4.13 A β-$NaMnO_2$ crystal as observed with the HADFF in 0.2 µm (Figure 4.13 (a))and 400 nm magnification (Figure 4.13(b)). Na, Mn and O atoms are represented in Figures 4.13 (c), (d), and with the green, yellow and red colors, respectively. The figures strongly suggest that the Na, Mn and O are distributed homogeneously within the crystals.

Figure 4.13 shows a β-$NaMnO_2$ crystal of a triangular shape with approximate dimensions (a, b, c= 2000 nm, 1200 nm, 1500 nm) where "a" is the base of the triangle. Figures 4.13 a and 4.13 b correspond to 0.2 µm and 400 nm, respectively. The distribution of Mn, Na and O atoms as shown with Figures 4.13 (c), 4.13 (d) and 4.13 (e) appears to be homogeneous upon the entire surface of the β-$NaMnO_2$ crystal.

4.3.5 Electron Energy Loss Spectroscopy (EELS)

The oxidation state of the Mn cations in the β-$NaMnO_2$ compound was checked by electron energy loss spectroscopy. Specifically, the transition metal $L_{2,3}$ energy loss spectra was recorded and analyzed according to the white line ratio method, [152] similarly to the method that was used for the Mn oxidation state in the α-$NaMnO_2$. The EELS spectra for the $L_{2,3}$ of β-$NaMnO_2$ is shown in Figure 4.14. The value obtained for the Mn oxidation state was 3.2. This value, the same as one obtained for the α-$NaMnO_2$, is slightly higher than the 3, which is expected for a pure compound of β-$NaMnO_2$.

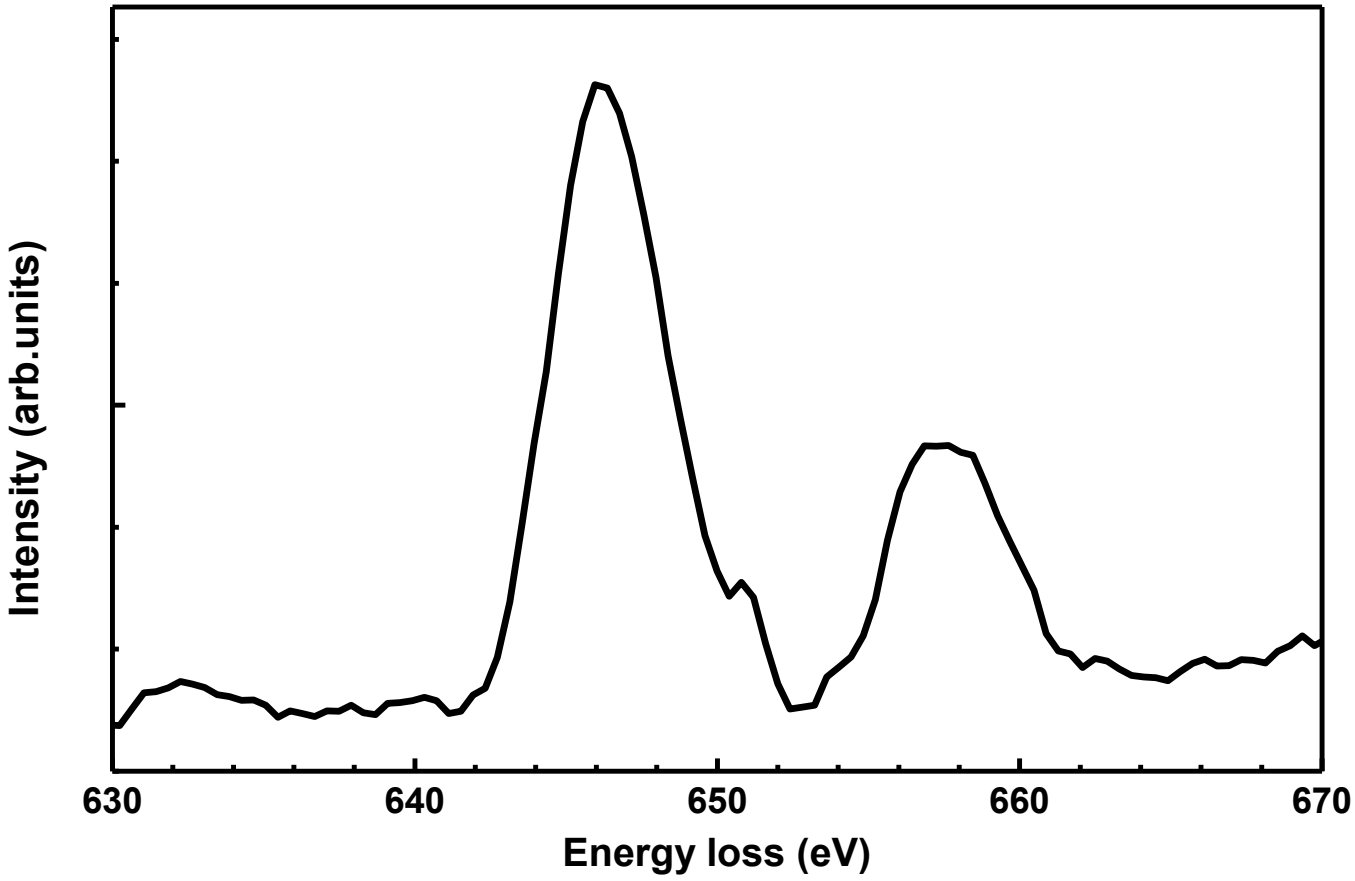

Figure 4.14 L edge energy-loss near-edge structures for the determination of the oxidation state of Mn in the β-$NaMnO_2$ compound.

4.4 Magnetic Properties of β-$NaMnO_2$.

4.4.1 Static Susceptibility

Magnetic susceptibility (χ) of the β-$NaMnO_2$ was measured on a SQUID magnetometer using ZFC-DC mode at 200 Oe magnetic field in the temperature range of 5 K-300 K. First we present the magnetic susceptibility (Figure 4.15) obtained from different batches of β-$NaMnO_2$ which have been synthesized with the protocol described in section 4.2 (Figure 4.4.). Although small deviations may be observed in the value of the magnetic susceptibility χ(T) from different samples, all the χ(T) curves share similar characteristics such as paramagnetic tail at low temperatures and the broad hump at high temperatures.

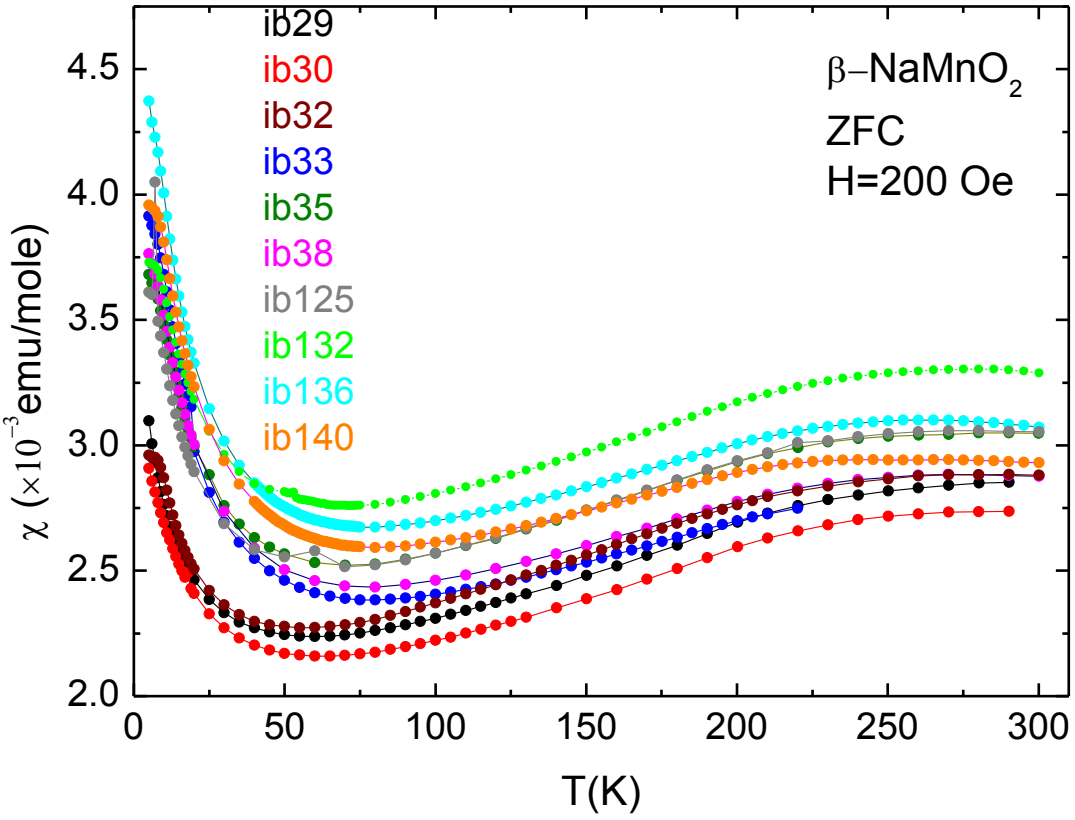

Figure 4.15 Magnetic susceptibilities of different β-$NaMnO_2$ samples measured on DC mode at a ZFC protocol under 200 Oe magnetic field.

The magnetic susceptibility of β-$NaMnO_2$ presented in the graph of Figure 4.15 shows no obvious magnetic magnetic transitions. At low temperatures there is a paramagnetic contribution which results in the paramagnetic tail (T<25 K). Quite clearly, the dominant characteristic of the β-$NaMnO_2$ magnetic susceptibility, is the broad hump at high temperatures of maximum χ(T) around 275 K, a hump which becomes negligible below 80 K. The susceptibility of β-$NaMnO_2$ resembles to the one observed for α-$NaMnO_2$ [143] whose broad hump of χ(T) obtains the maximum values around 200 K, which is presented in the comparative Figure 4.16. This hump is indicative of low dimensional antiferromagnetic spin correlations and has also been observed at the copper II compounds such as the diaquatetra-μ-acetato-dicopper (II) ($CU_2(CH_3COO)_4(H_2O)_2$). [151]

The inset of Figure 4.16 shows the derivative of the χ(T) in which no magnetic transitions can be detected. This does not necessarily mean that the β-$NaMnO_2$ is magnetically frustrated in the entire range of 5-300 K and has no magnetic order.

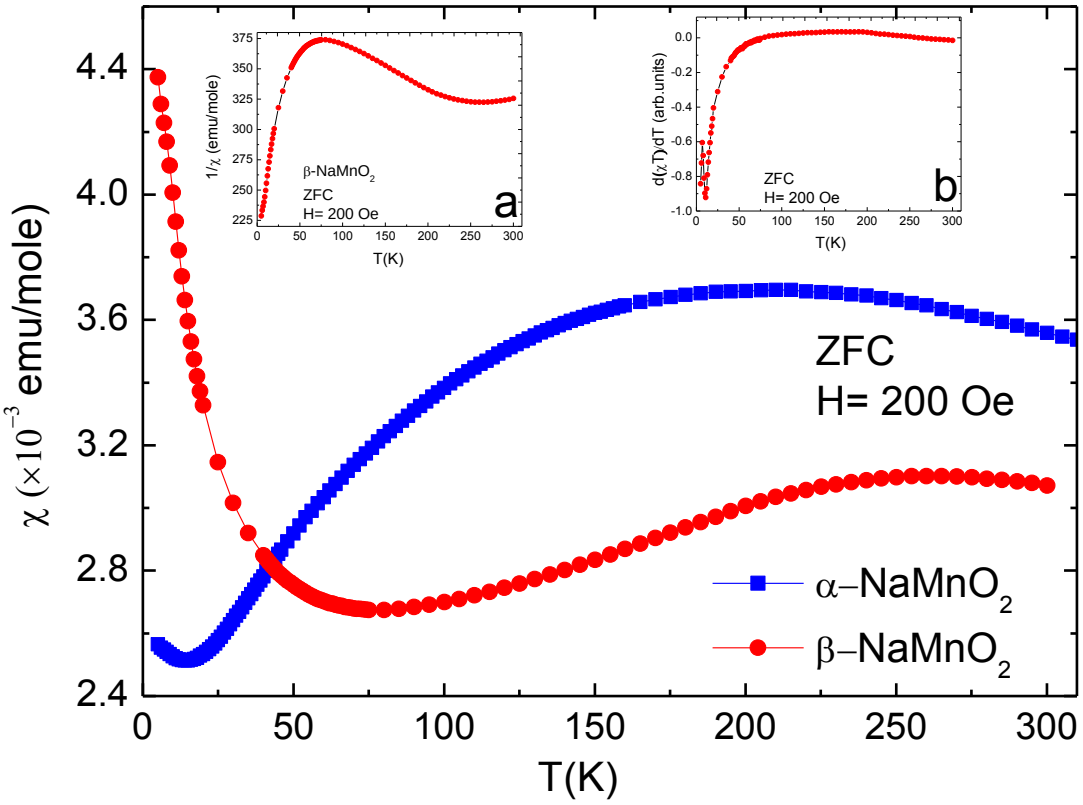

Figure 4.16 A comparative plot of the magnetic susceptibities obtained on DC mode at a ZFC protocol under H=200 Oe, from α-$NaMnO_2$ and β-$NaMnO_2$ polymoprhs, shown with the blue and red graphs, respectively. Inset (a) on the left shows the inverse magnetic susceptibility of β-$NaMnO_2$, whereas inset (b) shows the derivative of the susceptibility with respect to temperature d(χT)/dT of the β-$NaMnO_2$.

Susceptibility of β-$NaMnO_2$ measured in different magnetic fields

To evaluate the magnetic behavior of β-$NaMnO_2$ the χ (T) has been measured in two more different fields, the 0.2 T (2 kOe) and 1 T (10 kOe) as shown in Figure 4.17. The susceptibility curve remains the same in both fields tested, and more importantly no magnetic transition is detected in none of the fields. The inset of the Figure 4.17 shows the second derivative of the susceptibility in respect with the temperature for the measurement of 0.2 T and 1 T shown with the blue and black graph, respectively. We notice a small kink around 50 K, which is clear for the 1 T graph. According to neutron powder diffraction data at 50 K the intensity of the magnetic satellite peaks is saturated (see also Figures 4.20, 4.52 and 4.54) indicating that the incommensurate structure is fully developed.

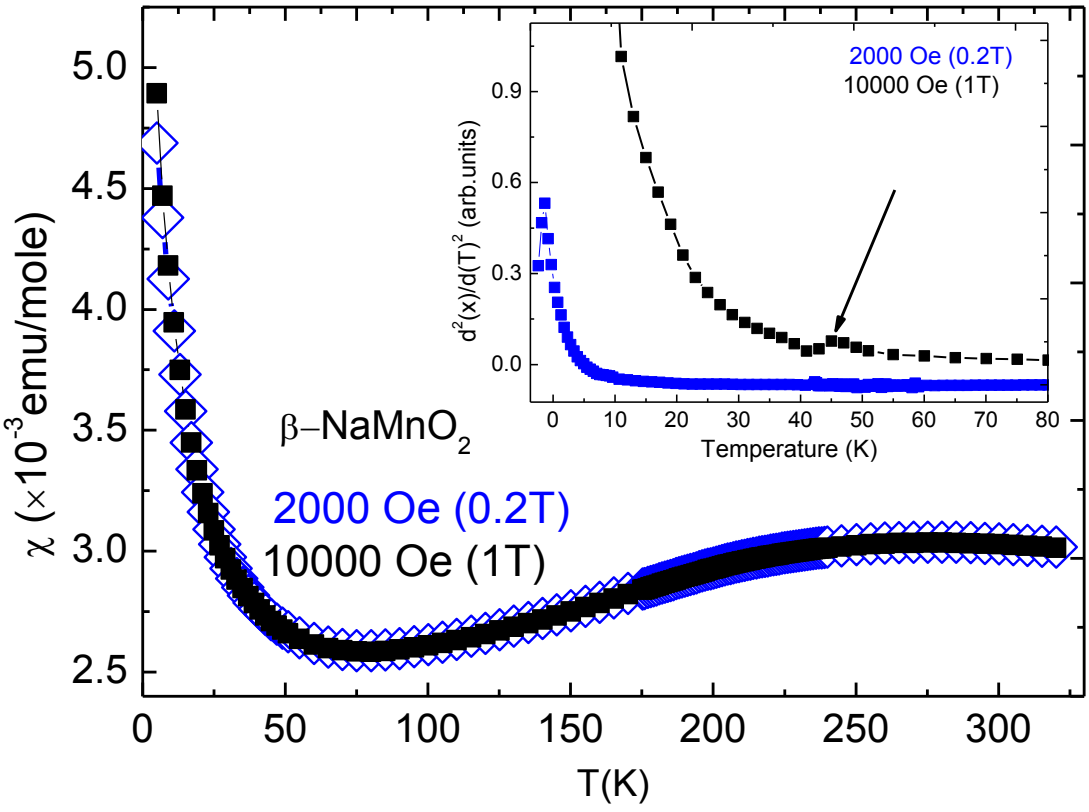

Figure 4.17 χ versus T plot of β-$NaMnO_2$ obtained on a DC- ZFC mode at 2 kOe and 10 kOe shown with graphs in the blue and black marks, respectively. The inset presents the second derivative of the magnetic susceptibility versus temperature where a small hump is observed at 45-50 K for the graph of 1 T.

Magnetization versus Magnetic Field M(H) of β-$NaMnO_2$

The magnetization of β-$NaMnO_2$ versus magnetic fields up to 5 T, has been measured at three different temperatures: 5 K, 50 K and 300 K as presented in Figure 4.18. This measurement is carried out to check for possible ferromagnetic contributions, which would result in the observation of a M(H) loop. However, the magnetization of β-$NaMnO_2$ does not show saturation up to 5 T, at none of the temperatures tested.

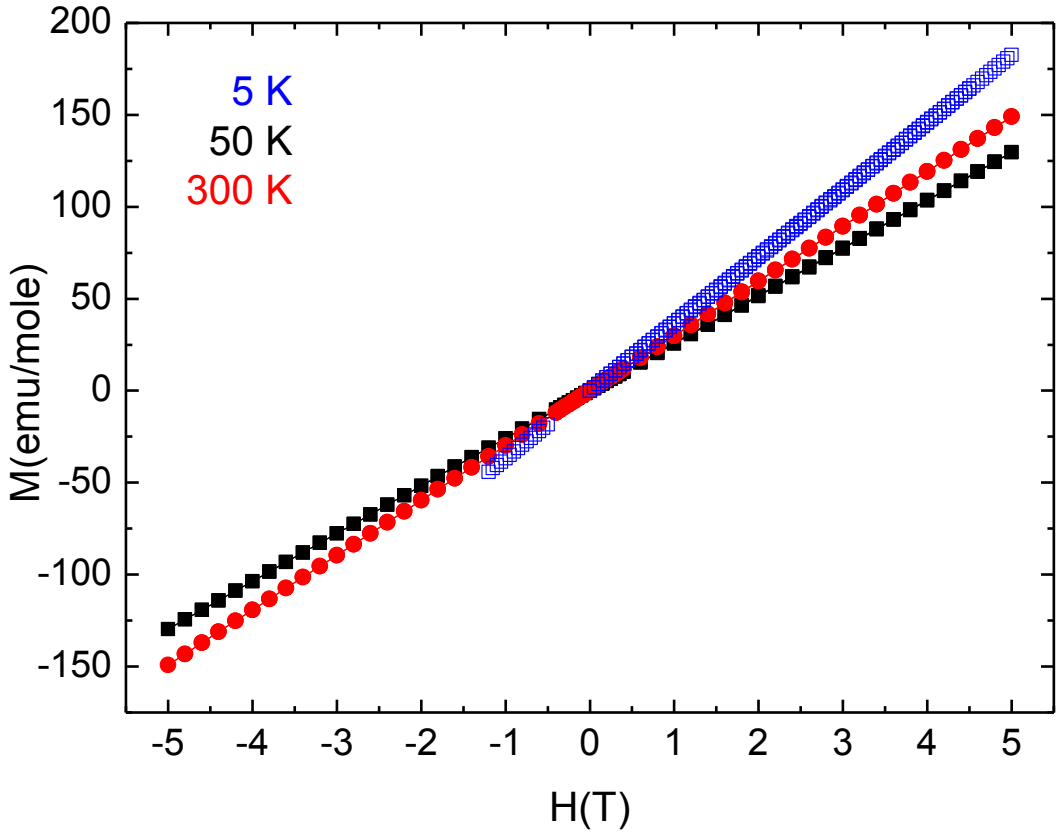

Figure 4.18 Magnetization (M) versus magnetic field (H) at three different temperatures 5 K, 50 K, 300 K represented with the blue, black and red curve, respectively.

Magnetic Susceptibility of annealed β-$NaMnO_2$ samples

As mentioned in section 4.3.1 in "*Annealed β-$NaMnO_2$ samples in air*" the annealing of β-$NaMnO_2$ samples at 300°C for 6 hrs in air resulted in a two phase compound, since intense Bragg peaks of the $Na_{0.7}MnO_2$ phase appeared in the XRPD pattern (Figure 4.10). In Figure 4.19 we show the magnetic susceptibility of the same β-$NaMnO_2$ sample: before (blue line) and after the annealing was carried out (black line). There are two major differences. First the paramagnetic tail at low temperatures has increased in the annealed sample. Second, the slope of χ(T) has changed above 70 K-75 K: the susceptibility of the annealed β-$NaMnO_2$ sample is decreasing whereas in the β-$NaMnO_2$ that has not been annealed the magnetic susceptibility starts to increase at 75 K before it reaches a broad hump at high temperatures (T>250 K).

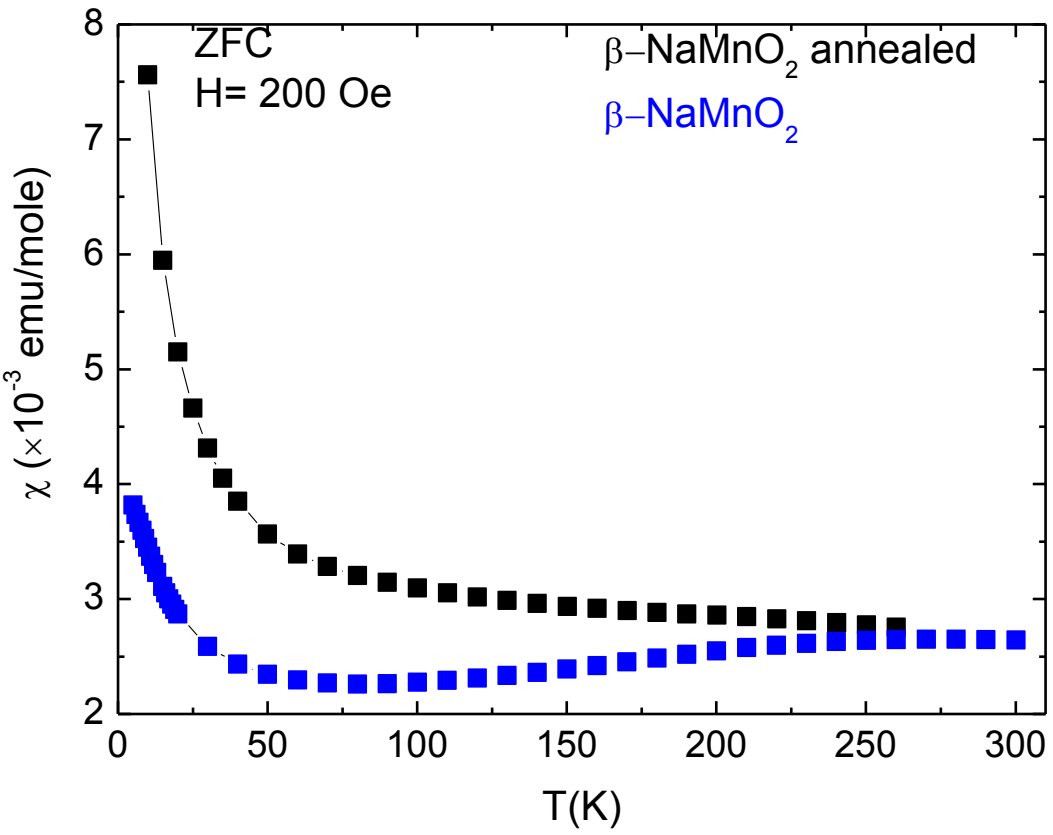

Figure 4.19 Comparison of a β-$NaMnO_2$ sample prepared with the usual synthesis protocol and an β-$NaMnO_2$ annealed one (see text for details) shown in blue and black lines, respectively.

Dynamic (AC) susceptibility measurements have been carried out on a β-$NaMnO_2$ sample of total mass m=263.5 mg. The goal was to detect any magnetic transitions that were not revelead with the static (DC) measurements. The DC applied field was 0 Oe whereas the AC drive field was 3 Oe. All the measurements have been carried out on zero field cooling mode and then upon heating the AC drive field was applied. Measurements were taken on a "settle mode" meaning that the temperature is stabilized in each point and then the value of the long moment (m') is recorded.

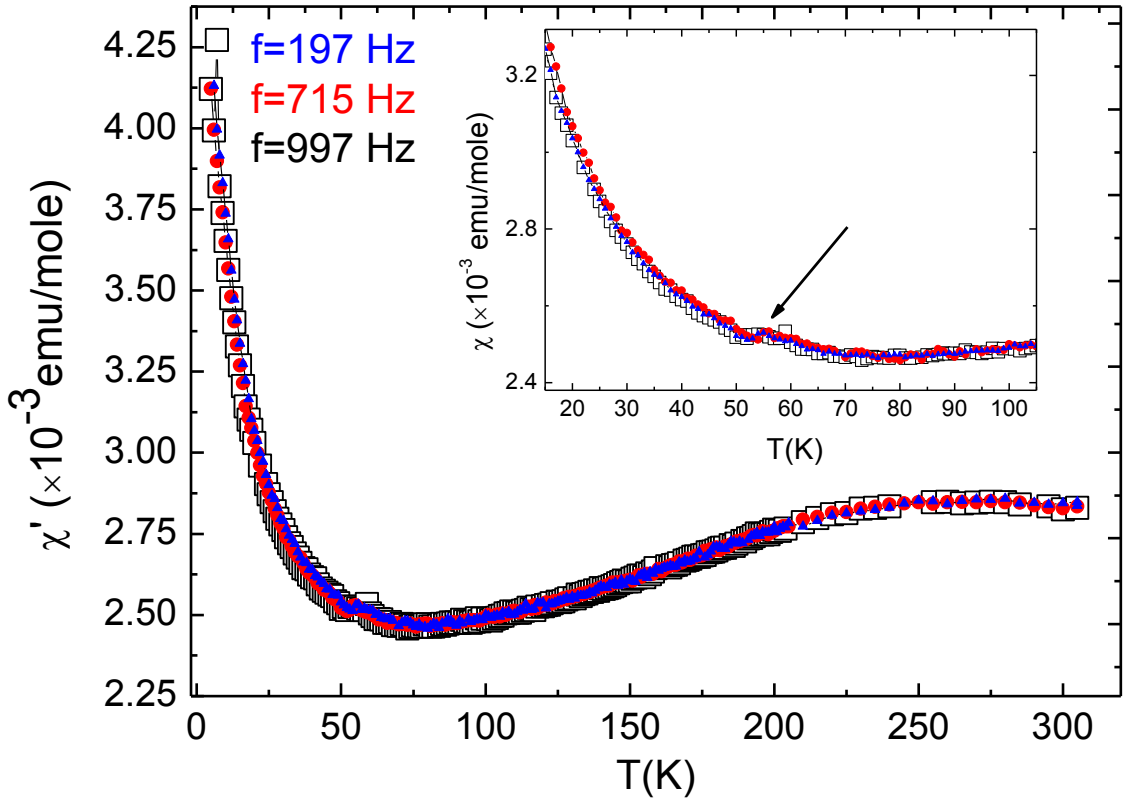

Figure 4.20 The real part of the ac magnetic susceptibility measured upon three different frequencies: f= 197 Hz, f= 715 Hz, and f= 997 Hz and under H_{dc}=0 Oe, represented with the blue, red and black graphs, respectively.

Figure 4.20 presents the real part of the magnetic susceptibility denoted as χ' versus temperature measured upon three frequencies: 197 Hz, 715 Hz and 997 Hz represented with the blue, red and black graphs, respectively. The χ'(T) does not differ much from the χ(T) of the static susceptibility (Figures 4.15-4.17). A closer look however (see inset of Figure 4.20) reveals a small kink around 55 K, which appears in all frequencies. According to neutron powder diffraction data between 50 K-60 K the intensity of the magnetic satellite peaks is saturated (see Figures 4.52 and 4.54) thus the incommensurate structure is fully developed.

The imaginary part of the magnetic susceptibility (χ'') gave noisy measurement which are not shown here.

4.5 Magnetodielectric Measurements

The dielectric behavior of β-$NaMnO_2$ is discussed in the following paragraphs. The 4.5 paragraph is divided into four parts: on the 4.5.1 results refer to β-$NaMnO_2$ samples which have been synthesized with the protocol as described in 4.2 section. After the synthesis was completed these samples were pelletized in the glove box and then used for the magnetodielectric measurements. These samples are usually named as pure or "as made" ones, since no further treatment was carried out on them. On the contrary, the 4.5.2 part refers to samples that have been synthesized as all the β-$NaMnO_2$, pelletized and furthermore had an extra annealing at 300°C for 6 hours under oxygen atmosphere. The annealing at 300°C resulted in more firm and stable pellets. However the major and critical drawback of the annealed pellets was the appearance of secondary phases, especially those of the $Na_{0.7}MnO_2$ and in smaller percentage the α-$NaMnO_2$ phases, evident by their characteristic Bragg peaks in the XRPD patterns. It is of outmost importance to mention that both, the as made and the annealed samples did exhibit the magnetodielectric coupling. The difference in the results between the as made samples and the annealed ones is discussed in the 4.5.3 paragraph. In the 4.5.4 section, efforts of measuring isothermal polarization loops are presented.

4.5.1 Magnetodielectric Measurements on pure β-$NaMnO_2$ samples

4.5.1.1 Measurements of Dielectric Constant Under Zero Magnetic Field

The magnetodielectric measurements on β-$NaMnO_2$ pellets have been carried out with the same way which has been described in paragraph 3.4, for the similar experiments on α-$NaMnO_2$. Again, the ZFC protocol has been applied, meaning that the sample is cooled from room temperature to 77 K with zero magnetic and electric field. Afterwards, specific voltage is applied and the values of the capacitance and dielectric loss were recorded upon heating every 0.5 K. The repeatability of each measurement, the possible frequency dependence and the effects of the increased electric and magnetic field were investigated.

Figure 4.21 presents the dielectric constant and the dielectric loss a β-$NaMnO_2$ sample (Ø 5 mm, and thickness t=1.40 mm) measured with 500 kHz and 714 V/m. The overall tendency is the slow increase of both dielectric constant and loss with temperature. The obvious characteristic of this ε'(T) is the broad hump at 200 K. However, there is also a weak dielectric anomaly around 95 K which is better presented in the inset of Figure 4.21.

Although the values of dielectric constant may slightly vary depending on different β-$NaMnO_2$ sample batch, the value of β-$NaMnO_2$ which is around 6 at f=500 kHz, is comparable to that of α-$NaMnO_2$ measured at the same frequency and with similar applied voltage (Figures 3.10 and 3.11) .

At this point it is useful to refer to values of the dielectric constant in other ABO_2 compounds, in order to compare and evaluate the quantities that have been measured. A comparative study leads to the observation that similar dielectric anomaly with comparable values of ε' has been measured for the powder compounds $CuCrO_2$ and $AgCrO_2$ [50] (for both compounds ε'~7 for H=0 T and f=100 kHz). On the contrary ABO_2 compounds which have Fe as the magnetic cation present some diversity in the measured values of the dielectric constant, ranging from ε'~26-27 for the $AgFeO_2$ [51] to that of ε'~7.5 for the spin glass $CuFe_{0.5}V_{0.5}O_2$. [185] For both α-$NaMnO_2$ and β-$NaMnO_2$ the dielectric constant at H=0 T and f=500 kHz, is around ε'~4-5.

Moreover, since these materials are treated as capacitors we mention the values of their capacitance from which the dielectric constant is calculated. For instance, the dielectric constant shown in Figure 4.21, has been calculated from a pellet whose distance between its parallel plates is 1.4 mm their area is $19.625 \cdot 10^{-6}$ m^2 and for the measurement of the 500 kHz the capacitance (C) ranges from 0.72 pF to 0.9 pF at 80 K and 300 K, respectively.

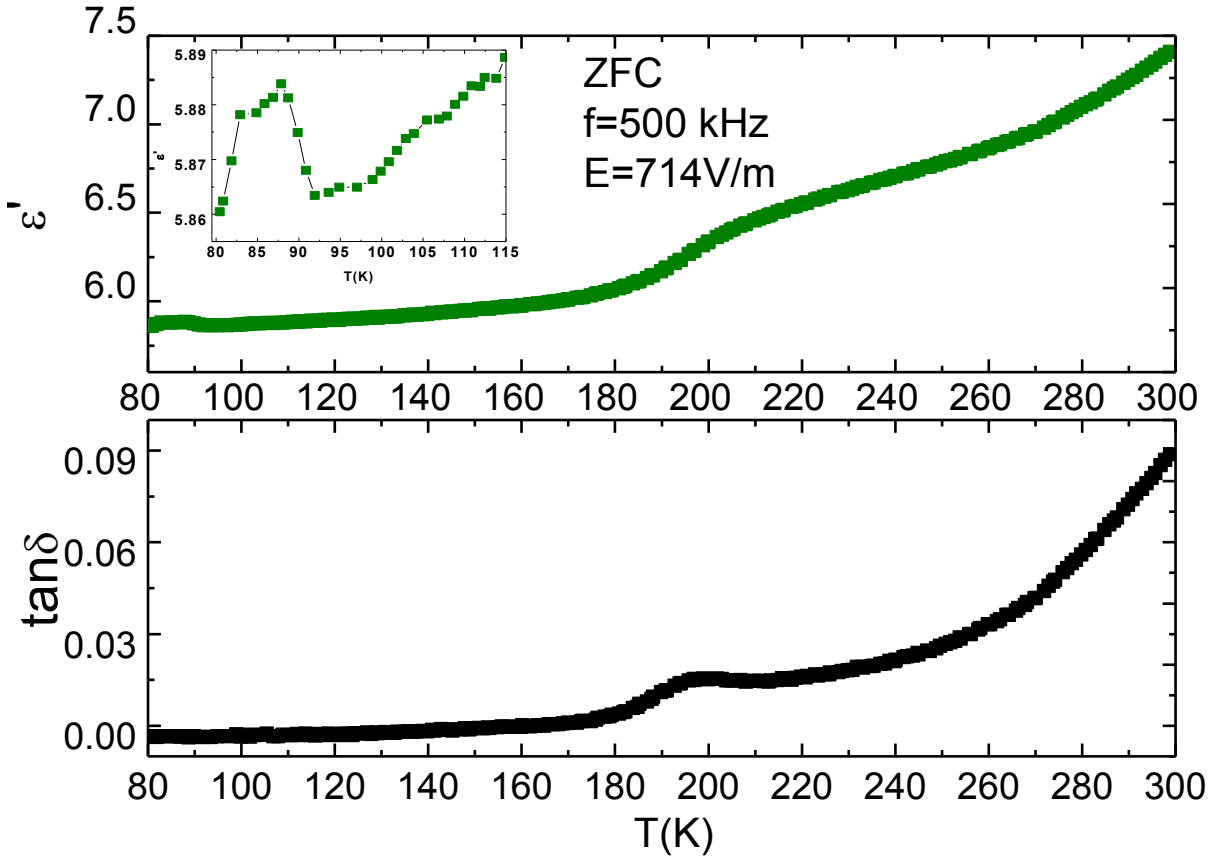

Figure 4.21 Dielectric constant (ε') and dielectric loss (tanδ) of β-$NaMnO_2$ measured with a ZFC protocol at 500 kHz, applying 751 V/m upon heating. The inset on the ε' (T) shows the dielectric anomaly observed at 90 K.

These values are comparable with the lowest capacitance range of the commercial ceramic capacitors, as the available capacitors in the market range from some fractions of pF up to mF. The value of tanδ multiplied by 100, shows the % losses of the sample if it was treated as a capacitor, which is below 10% in the β-$NaMnO_2$ case, and thus of acceptable behavior.

In the general case, dielectric anomalies mark the possible onset of polarization. Both of them appear to be spin driven, since magnetic transitions appear at 200 K and 90 K according to neutron diffraction data (section 4.7.2.2.).

The next chapters present the study of the dielectric anomalies, measured under different frequencies, applied electric and magnetic fields.

4.5.1.1.1 Dielectric Constant Measured under Different Electric Fields

As it has been proved for the case of α-$NaMnO_2$ the dielectric anomaly observed at 95 K, was enhanced by 14% when 1.5 T magnetic field was applied. Similar effect has been observed in the β-$NaMnO_2$ by applying higher external electric field. Applying electric fields, instead of magnetic fields is easier to achieve experimentally and moreover it is more practical for applications in small devices.

Figure 4.22 shows three runs all measured at 100 kHz frequency on a β-$NaMnO_2$ pellet. All the measurements were carried out on the same pellet of thickness t=1.36 mm (Ø 5 mm). The first heating, shown with the blue line, corresponds to the dielectric constant measured under 685 V/m. At 90 K there is a weak hump, at 180 K the dielectric constant raises rapidly up to 210 K and the increasing continues up to 300 K but with a smaller rate. Nevertheless, when the electric field is doubled, the effect on the dielectric anomaly of 90 K is striking: an enhancement of 15% is noticed as it can be seen by the plot in Figure 4.23.

The issue of repeatability in the dielectric measurements has also been checked for the β-$NaMnO_2$. Figure 4.22 shows two experiments on the same β-$NaMnO_2$ pellet carried out under identical circumstances: heating 2 and 3 represented with dark yellow and purple

color, respectively. The only difference between those two experiments is that they took place on two consecutive days, meaning that there is a time difference of approximately 10 hrs between them. During this time, the sample remained in the cryostat at 300 K without applying any electric or magnetic field, under continuous nitrogen flow. Clearly, the results obtained are not identical. The dominant difference is the elimination of the broad hump at around 200 K at the third heating. The drop of ε'(T) at 90 K remains intact, since it still appears, however in this run, it is more sharp and shows a step like behavior.

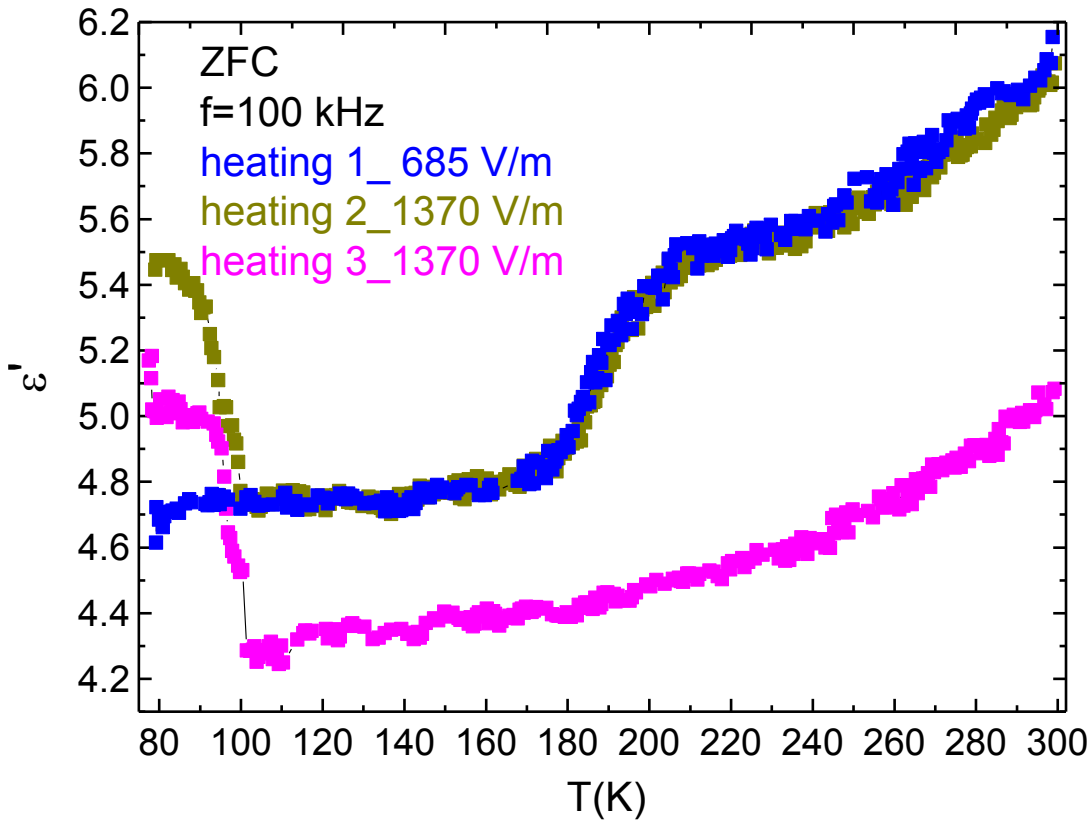

Figure 4.22 Dielectric constant (ε') of β-$NaMnO_2$ measured with 100 kHz, under 685 V/m (blue graph), under 1370 V/m (dark yellow and purple graphs). Note the striking enchantment of the dielectric anomaly below 100 K when the electric field is doubled. The hump at 200 K disappears on the last run (purple graph) due to aging effects.

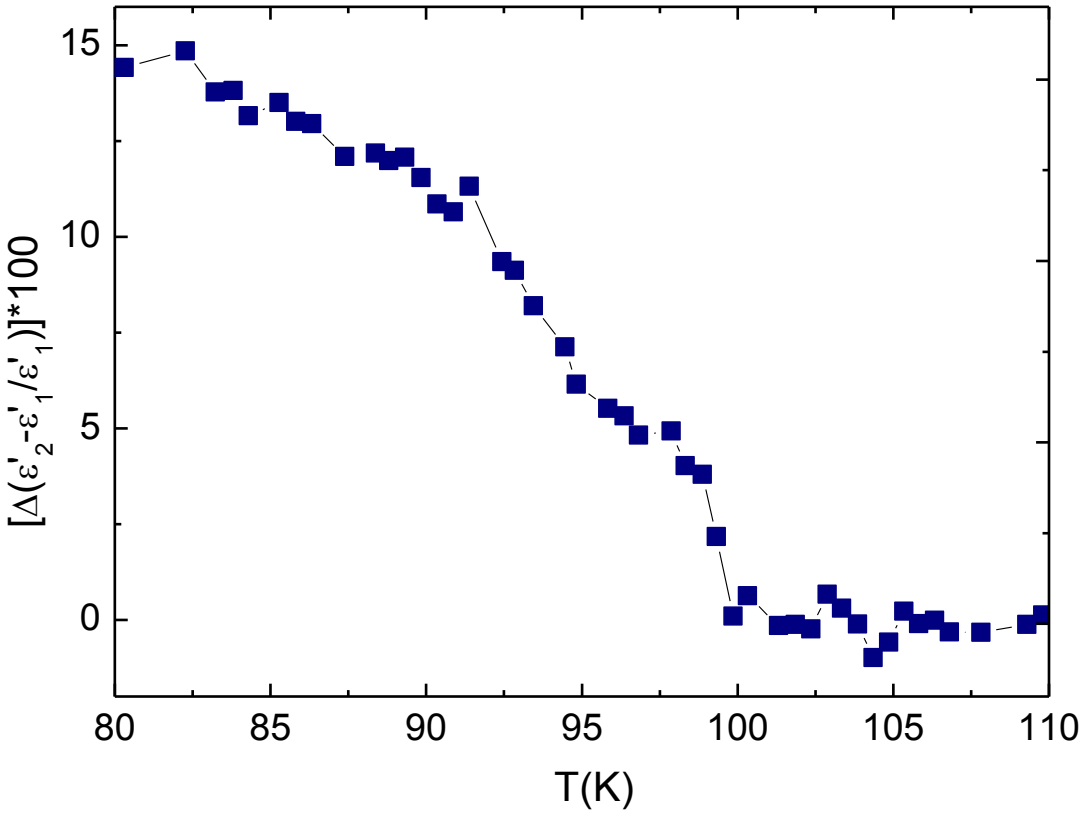

Figure 4.23 A graph showing the % change $\Delta(\varepsilon'_2-\varepsilon'_1)/\varepsilon'_1$ between the dielectric constant measured at 1370 V/m (ε'_2) obtained upon the second heating and 670 V/m (ε'_1) measured upon the first heating. At the temperature range where the dielectric anomaly occurs the % change ranges between 10-15 %.

The elimination of the dielectric anomaly of 200 K after a few consecutive experiments (zero field cooling and measuring upon heating) has also been observed in other as made β-$NaMnO_2$ samples that have been checked in the same conditions. This indicates probably disimilar driving mechanisms, associated with the two different magnetic states that drive the dielectric properties at each temperature. Another assumption behind the dielectric

transition at 200 K and 90 K, could be the different response to the aging phenomena resulting from the continuous cooling and heating of the sample.

4.5.1.1.2 Dielectric Constant measured at Different Frequencies

In dielectric measurements is essential to check whether the phenomenon observed, is frequency dependent. In other words, observing the phenomenon, only at a specific frequency would raise questions about the reliability of the results since it could be attributed to artifacts or effects of the frequency tested. For this reason at least three experiments have been conducted in which the frequencies were different, whereas the rest experimental conditions remained the same.

Figure 4.24 shows the ε'(T) of β-$NaMnO_2$ sample measured at 50 kHz, 100 kHz and 200 kHz. As the frequency increases ε' is expected to decrease, if we take into account the equation:

$$C=\frac{1}{2\pi f X_c} \qquad \textbf{(4.2)}$$

Where C is the Capacitance (F), f is the frequency (Hz) and X_c (Ω) is the reactance. Equation 4.2 states that as f increases, C decreases. According to equation 2.10 ($C=\varepsilon_o\varepsilon_r \frac{A}{d}$) capacitance and ε' ($\varepsilon_r$) are proportional physical quantities, thus any as f increases ε' will also decrease.

This behavior is noticed in Figure 4.24 as the 200 kHz graph is well below the 50 kHz and 100 kHz graph. Examples of magnetoelectric systems where similar dependence of ε' versus frequency has been reported is the $FeVO_4$[205] and the $Co_4Nb_2O_9$.[206] The existence of the dielectric anomaly of 90 K upon three different frequencies undoubtebly yields the conclusion that this feature is an intrinsic phenomenon of the β-$NaMnO_2$, and it is not related with a specific frequency.

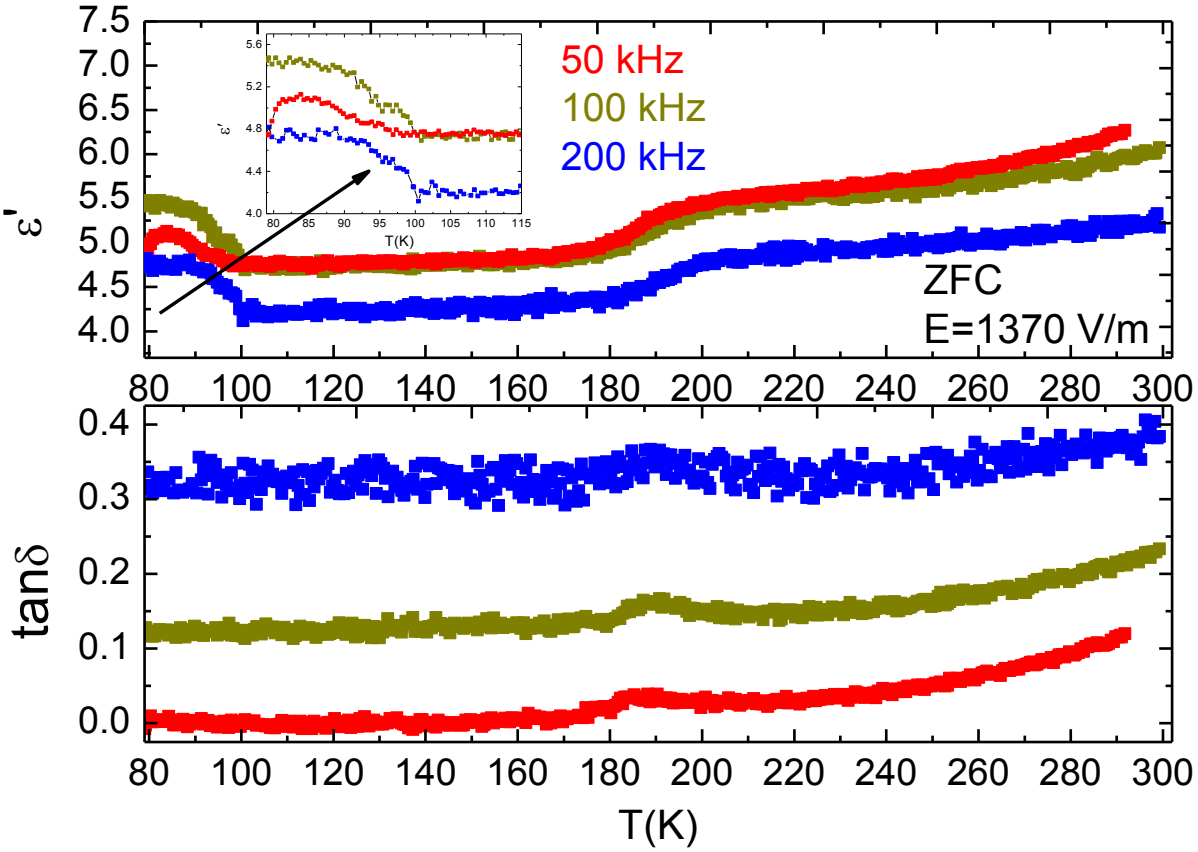

Figure 4.24 Dielectric constant and dielectric loss of β-$NaMnO_2$ measured at three different frequencies: 50 kHz, 100 kHz and 200 kHz shown with the red, dark yellow and blue graph, respectively.

Comparison of the 50 kHz graph with the 100 kHz, shows that both measurements give the same values of ε' at the temperatures 100 K< T <200 K whereas at the temperature region of the dielectric anomaly and at T>200 K the 50 kHz graph resulted in slightly higher values of ε'. Similar phenomenon has been observed for the spin chain relaxor ferroelectric $Ca_3Co_2O_6$ where the dielectric constant of 100 kHz shows a weak upturn above a T_c so that ε' (100 kHz)> ε' (10kHz) and also ε' (100 kHz)>ε' (30 kHz) in the

contrary to what is expected according equation 4.2. [207] The relaxor ferroelectricity of $Ca_3Co_2O_6$ is assumed to be affected by multiple features, such as the formation of microphases, or the possible role of grain boundaries which could result in a sensitive dielectric behavior. To conlude about possible relaxor ferroelectrity in a dielectric compound extensive studies concerning the frequency dependence of the dielectric response are required over a wide range of frequencies.[160] A conclusion about the small variations ε'(T) with frequency of β-$NaMnO_2$ would require many measurements at different frequencies. Similarly, the inconsistency noticed between the two graphs of ε'(T) at 50 kHz and 100 kHz, should also be observed systematically in respect with the applied frequency and the obtained values of ε', in order to reach a safe conclusion. We have not continued with the frequency dependent measurements, in order to avoid possible aging of the sample. Instead we have proceeded with the electric and magnetic field dependence measurements shown in Figures 4.21 and 4.25.

In respect with tanδ presented in Figure 4.24, we expect that as frequency increases tanδ' will increase also since the equations that hold are the:

$$\tan\delta=\varepsilon''/\varepsilon' \qquad \textbf{(4.3)}$$

as well as the 4.2 and 2.10.

The ε' and ε'' of equation 4.3 are the real and imaginary part of the dielectric constant, respectively.

This is also observed in Figure 4.24, since tanδ of β-$NaMnO_2$ clearly increases as the frequency f decreases. More precisely $\varepsilon'(T)_{200\ kHz} > \varepsilon'(T)_{100\ kHz} > \varepsilon'(T)_{50\ kHz}$. This linear behavior though of tanδ upon different frequencies is not observed in all the magnetoelectric systems.[155, 208]

4.5.1.1.3 Memory effect in β-$NaMnO_2$

A question that arises concerns the possibility of shifting the dielectric anomaly to different temperatures upon the application of electric fields. To check this, high DC electric field has been applied. The sample has been zero field cooled from 300 K to 150 K. At 150 K electric field of 180 kV/m has been applied using a 6517 A Keithley electrometer. At 77 K the 180 kV/m is removed and the only field applied is the V_{rms} (735 V/m) from the LCR bridge. Values of the ε' and tanδ values every 0.5 K at 500 kHz are recorded upon heating.

Figure 4.25 shows the dielectric constant measured upon heating just after the electric field has been removed. The curve of the dielectric constant is noticeably different from the ones obtained with the ZFC protocol in the entire temperature range of 77 K- 300 K. The tendency of ε' and tanδ to increase with the temperature, the dielectric anomaly at 90 K and the broad hump at 200 K are eliminated. On the contrary, at the temperature range of 90 K-145 K there is a plateau where the dielectric constant's value is stable around ε'~2.5. The dielectric constant is is decreased when compared to the values of ε'(T) from presented in Figure 4.21, where only voltage apllied is the V_{rms}. This difference is most likely attributed to the effect of the electric field (180 kV/m) upon the dielectric constant values. Interestingly, at 150 K, the temperature where the electric field was applied upon cooling, there is a pronounced increase on the ε' which becomes ε'~3.75. The dielectric constant increases abruptly since a sharp peak feature appears in the ε´ and tanδ. Between 150 K - 300 K, ε' remains stable.

The above experiment demonstrates the effect of the external electric field on the temperature where the dielectric anomaly appears. We notice that below the temperature where the electric field was applied (150 K) as the sample was cooled there is a sharp drop of the ε'(T) value, which resulted in a well pronounced dielectric anomaly. This probably indicates a "memory effect" since the system seems to recognize the temperature upon which the electric field cooling had been applied.

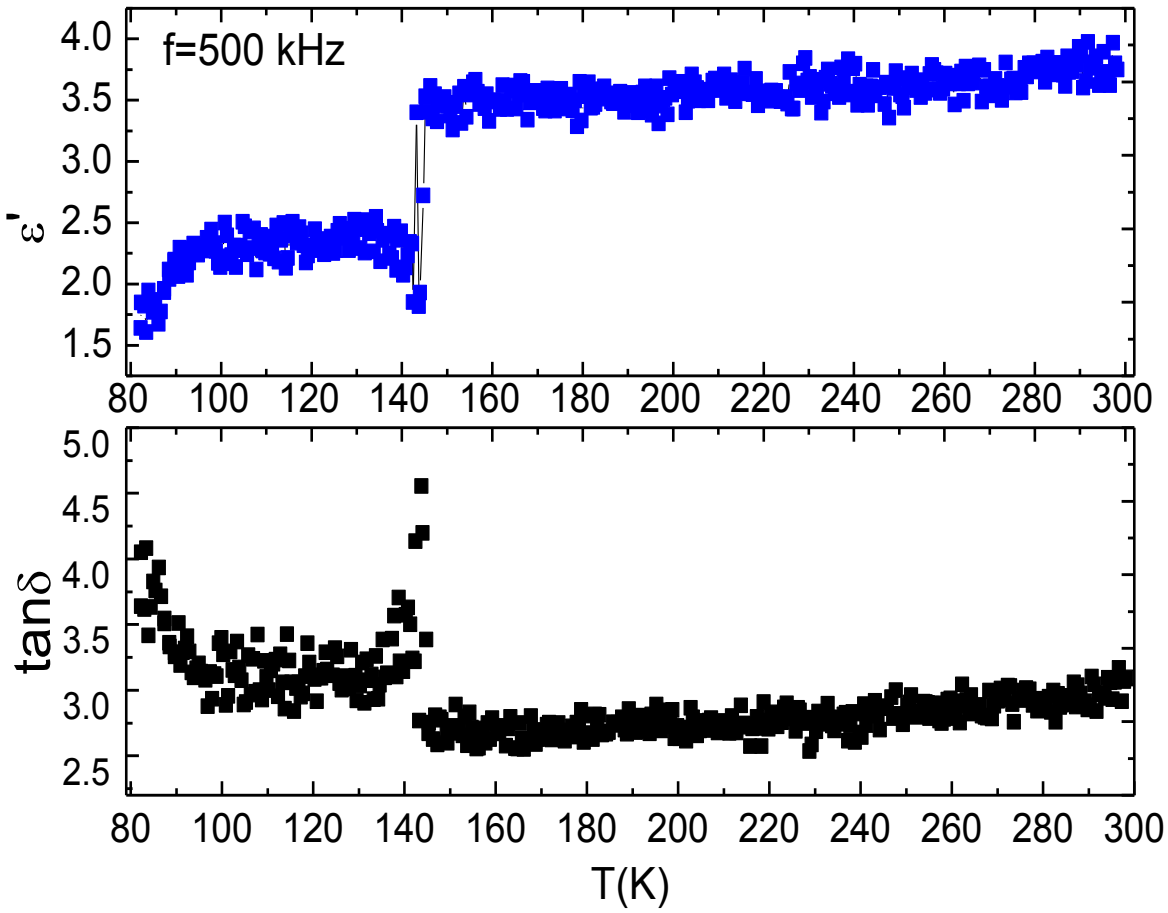

Figure 4.25 Dielectric constant of β-$NaMnO_2$ measured at 500 kHz after having applied electric field of 180 kV below 150 K upon cooling. The electric field is removed at 77 K, but the dielectric constant recorded upon heating shows a sharp increase in the dielectric constant's value around 150K-the temperature where electric field was applied.

4.5.1.2 Dielectric Constant Measurements Under Various Magnetic Fields

The dielectric constant of as made β-$NaMnO_2$ samples has been measured under various magnetic fields, at 100 kHz. The results are presented in Figure 4.26. The sample is the same that has been used in the experiments presented in Figures 4.22-4.24.

As it is clear from Figure 4.26, the dielectric anomaly at 90 K is slightly enhanced when external magnetic fields are applied, as the values of the ε'(T) under zero and various magnetic fields do not differ much. This is attributed to the fact that the dipoles have initially been polarized (excited) on a higher energy level due to the high applied electric field (Figure 4.22). Unfortunately, the data obtained from the pure β-$NaMnO_2$ are noisy, and this excludes any further analysis, such as calculating the relative change in the dielectric constant according to the equation 3.5 (relevant Figures 3.13 and 3.17 for the α-$NaMnO_2$) compound.

Nevertheless, there are two basic features in Figure 4.26, which is useful to discuss here. These are the small enchancement of the ε'(T) and the shift of the dielectric anomaly towards lower temperatures. Examples of other magnetoelectric systems in which the magnetic field does not affect importantly the value of the dielectric constant is the $FeTe_2O_5Br$, [156] in which the external magnetic fields leave the value of ε'(T) intact but shift the temperature of the dielectric anomaly to lower temperatures. The effect of magnetic field in FeT_2O_5Br is related with a transition to a low temperature incommensurate magnetic state. The small shift of the dielectric anomaly upon the application of external magnetic field towards lower temperatures has been observed in various magnetodielectrics such as: the $NdCrTiO_5$, [209] $MnTiO_3$, [210] $FeVO_4$, [205] Cr_2WO_6. [211] So far there has not been proposed a unified phenomenological model, concerning the shift of the dielectric anomaly in lower or higher temperatures when magnetic fields are applied. The phenomenon is related with the specific magnetic symmetry or ordering of each compound at the temperature of the dielectric transition. For example for the polycrystalline samples of $NdCrTiO_5$, the shift of the critical temperature of the ε'(T) is regarded to originate from its antiferromagnetic ordering. More precisely, T_N decreases

with the magnetic field in an antiferromagnet, the magnetic ordering is gradually suppressed and the peak in the dielectric transition shifts also to lower temperatures.

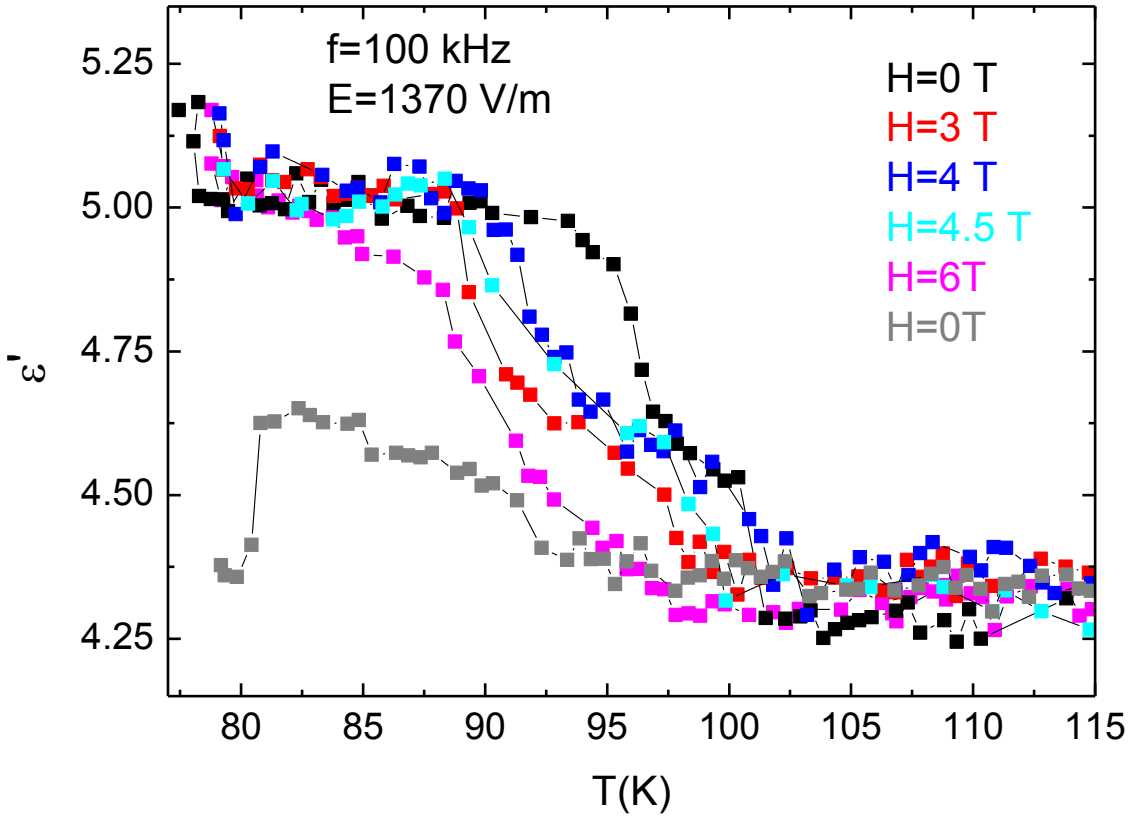

Figure 4.26 Dielectric constant of ε´(T) of β-$NaMnO_2$, measured upon heating at 100 kHz under various magnetic fields:3 T, 4T, 4.5 T and 6 T represented with the red, blue, cyan and purple plots, respectively. The measurement under zero (0 T) magnetic field was carried out twice: first before the application of the magnetic fields, represented with the black plot and second, after the magnetic fields have been applied, shown with the grey plot.

4.5.2 Magnetodielectric Measurements on Annealed β-$NaMnO_2$ samples.

One of the technical problems related to the magnetodielectric measurements was that the β-$NaMnO_2$ pellets appeared to be brittle after remaining for many hours in the cryostat under continuous N_2 flow. As an effect, the samples showed some cracks in the surface when taken out of the cryostat. Proving to be too unstable to handle, they could not be used again for other magnetodielectric measurements.

In order to solve this problem, the effect of extra annealing of the β-$NaMnO_2$ samples was tested. An amount of β-$NaMnO_2$ powder was pelletized in the glove box, and then the pellet (Ø 5 mm, thickmess t= 1.62 mm) was annealed at 300°C, for 6 hrs under continuous oxygen flow. The following results (Figures 4.27-4.29) refer to a sample that has undergone this treatment and afterwards was measured at 500 kHz, according to ZFC protocol.

Figure 4.27 shows the dielectric constant and loss measured at 500 kHz under different external magnetic fields of an annealed β-$NaMnO_2$ sample. The overall tendency of the graph is the smooth increase of the ε΄and tanδ with the temperature in the entire temperature range 80 K-300 K. The ε' value appears to be around 4.42. The samples that were not annealed had ε' (T) at 80 K around 6. The small deviation may be attributed to the annealing and the effect it has on the dipoles. Two dielectric anomalies appear at the expected temperatures: the sharp one at the 90 K and the broad one at 200 K. The low temperature dielectric anomaly is shifted and importantly enhanced upon the application of external magnetic fields, whereas the 200 K hump remains intact. The change of ε'(T) at 200 K disappeared in the measurement where 6.5 T are applied (the one shown with the aqua line).

The effect of different magnetic fields applied in the 90 K dielectric anomaly, is presented in detail in Figure 4.28 (a) and 4.28 (b). Due to the shape in the decrease of the ε', two temperatures are pointed out, T_1 where the ε' starts to drop and T_2 where the ε' starts to stabilize. Important to clarify here that when the dielectric anomaly is not a sharp like peak but occurs over a wide range of temperatures forming a wide peak [157] or a gradual

decrease like in the case of β-$NaMnO_2$, the temperature of the dielectric anomaly is regarded as the one the transition begins, i.e the T_1.

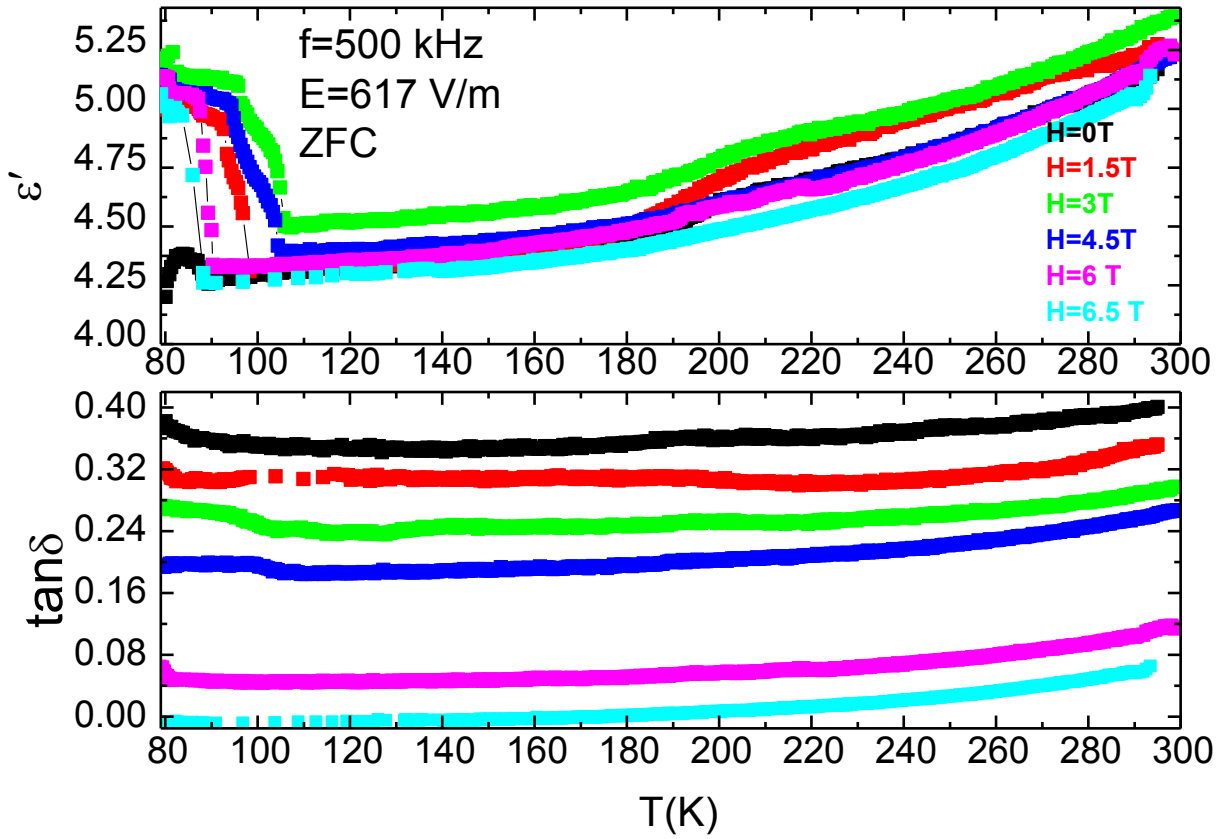

Figure 4.27 Graphs showing the real (ε') and imaginary part (tanδ) of the dielectric constant versus temperature under the magnetic fields of: 0 T, 1.5 T, 3 T, 4.5 T ,6 T and 6.5 T.

The overall effect of the magnetic fields is to shift the anomaly to higher temperatures as shown in Figures 4.27 and 4.28. Among the various magnetic fields applied (1.5 T, 3 T, 4.5 T, 6 T and 6.5 T), the maximum temperature shift is observed for the 3 T. The shift is not linearly increased with the magnetic field, as the measurements of 4.5 T, 6 T and 6.5 T show smaller effect in changing the critical temperature. This is also clear in Figure

4.29 where both T_1 and T_2 increase with the magnetic field up to 4 T, and then decrease for fields H>4 T. Examples of other magnetoelectric systems in which the dependence of the dielectric constant changes above a specific value of magnetic field are the $MnTiO_3$[210], $SrNdFeO_4$[212]. The phenomenon usually denotes a spin flop transition. In order to assure that a spin flop transition occurs in β-$NaMnO_2$ magnetization and capacitance measurements are required (see chapter 6).[210, 212]

A detail of Figure 4.27 is presented in Figure 4.28 (a). Here we show the change of dielectric constant with the magnetic field at the temperature range of 80 K-115 K. The results have no noise and the magnetoelectric effect (ME), given by the ratio $\Delta\varepsilon'/\varepsilon_o'=[\varepsilon'_H-\varepsilon'_0]/\varepsilon'_0$ can be safely calculated and presented in Figure 4.28 (b). Remarkably, the ME effect is around 20% for 3 T, meaning that the application of the specific magnetic field increases the dielectric anomaly about 20%.

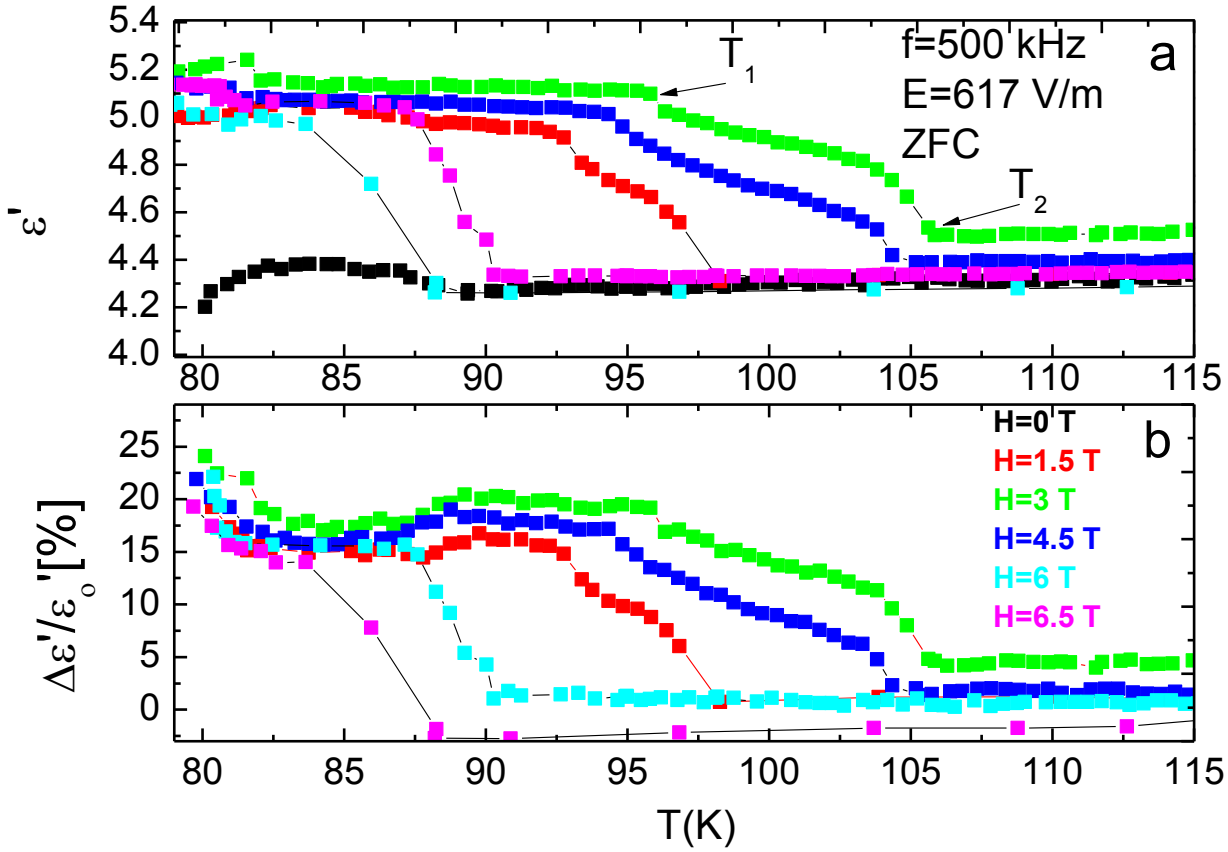

Figure 4.28 (a) A detail of the Figure 4.27 showing the temperature region between 80 K-115 K. b) ME effect as a function of temperature at 500 kHz under several magnetic fields.

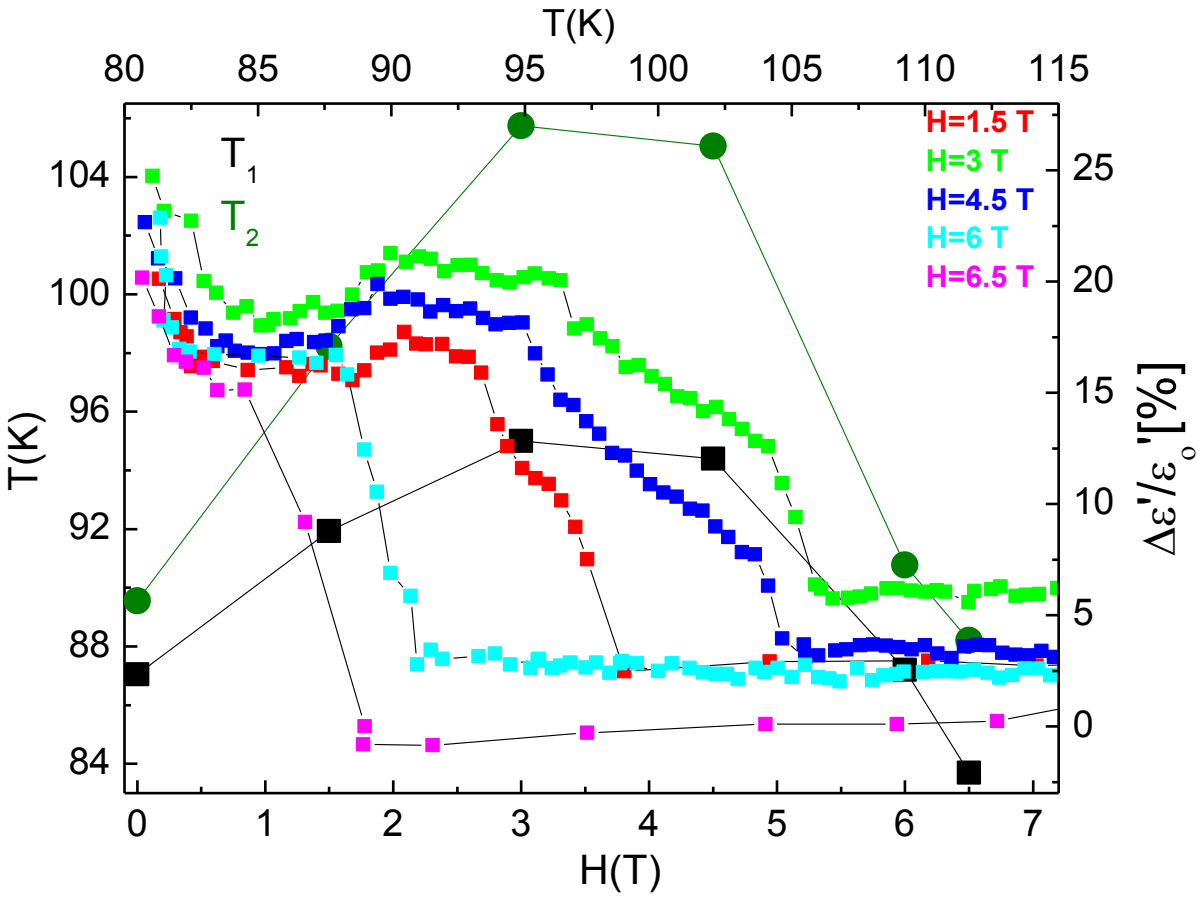

Figure 4.29 Left axis: shift of the critical temperatures T_1 and T_2 with respect to the applied magnetic fields. T_1 and T_2 refer to the temperature where the dielectric constant begins to drop and has taken the final minimum value, respectively. Right axis: ME effect as a function of temperature at 500 kHz (also presented in Figure 4.28 (b))

4.5.3 Comparison of the Dielectric Constant of α-$NaMnO_2$, β-$NaMnO_2$ and the Annealed β-$NaMnO_2$

At this point it is useful to compare the dielectric constant on the three types of manganese oxides that we have already presented: the α-$NaMnO_2$, the β-$NaMnO_2$ and the annealed β-$NaMnO_2$ (details on each sample are presented in Table 4.2) The samples have been

measured with the same way, zero field cooling from room temperature to 78 K. The capacitance values are recorded upon heating from 80 K-300 K, at 500 kHz and zero magnetic field, by applying comparable values of electric field. The results obtained are shown in Figure 4.30.

Compound	**Code**	**Ø(Diameter of Pellet)(mm)**	**Thickness (mm)**	**V_{rms}(V)**	**Electric Field Applied (V/m)**
β-$NaMnO_2$	wish7	5	1.40	1	714
β-$NaMnO_2$ annealed	wish13	5	1.62	1	617
α-$NaMnO_2$	ib168	5	1.33	1	689

Table 4.2 Details of the samples used in the magnetodielectric experiments presented in Figure 4.30.

Obviously, the most distinct dielectric anomaly appears for the annealed sample at 90 K as shown for the measurement represented with the purple color. When presented in the same scale as in Figure 4.30, the dielectric changes in the β-$NaMnO_2$ at 90 K and the α-$NaMnO_2$ at 95 K appear weak in comparison with the one of the annealed β-$NaMnO_2$ sample.

The difference of the annealed sample as seen on the XRPD patterns (Figures 4.6-4.7) when compared to that of the β-$NaMnO_2$ and α-$NaMnO_2$ that did not undergo any further treatment, is the presence of the secondary phases. In the XRPD pattern apart from the expected β-$NaMnO_2$ Bragg peaks, 001 reflection of the $Na_{0.7}MnO_2$ and the α-$NaMnO_2$ are present. The reflection of the $Na_{0.7}MnO_2$ has strongest intensity than that of the α-$NaMnO_2$.

Currently, we have no available information regarding the magneto-dielectric properties of the $Na_{0.7}MnO_2$ which would enlighten the effect of the $Na_{0.7}MnO_2$ in the dielectric properties of β-$NaMnO_2$. However, factors which could relate the strong dielectric anomaly of the annealed sample β-$NaMnO_2$ with the presence of the secondary phases are

the morphology of the samples microstrure, their homogeneity and the density of the planar defects. To address this, extensive research is required and observation of the annealed samples with TEM microscopy. Even though the outcome of a strong dielectric anomaly is quite appealing, the possibility of having a sample which is chemically a two phase material is a critical drawback for the continuation of the specific investigation.

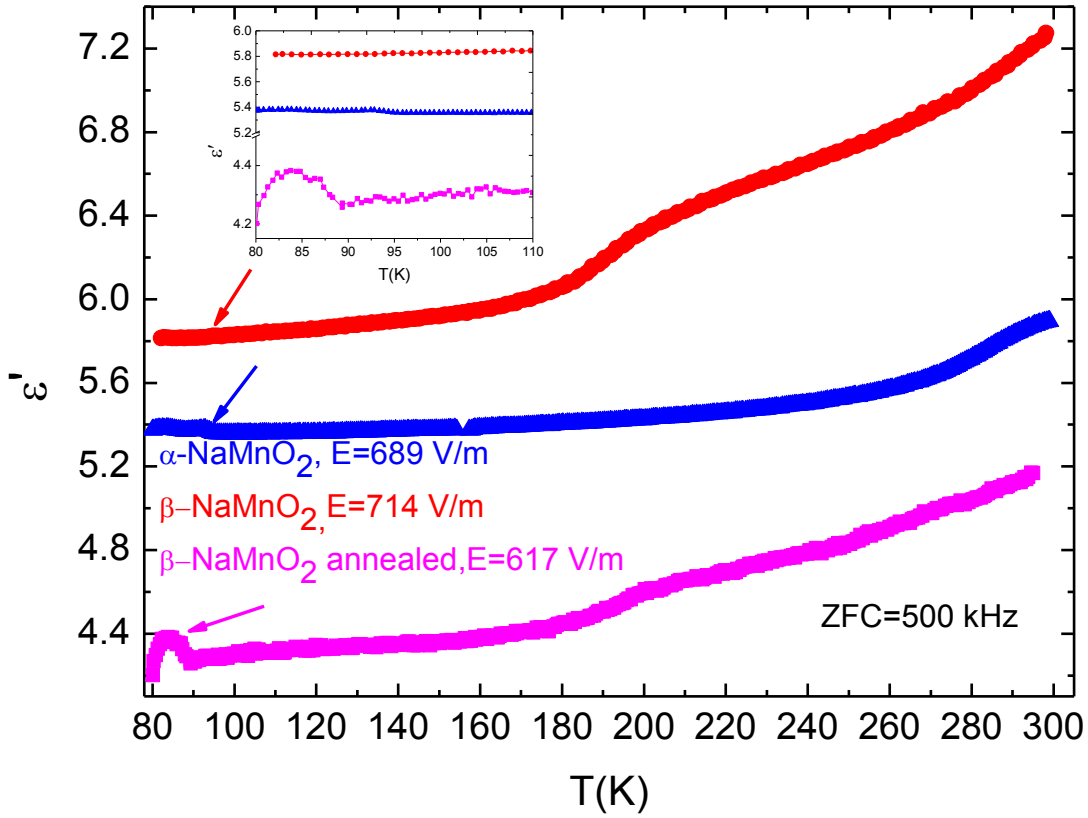

Figure 4.30 Dielectric Constant ε' versus temperature, of the oxides α-$NaMnO_2$, β-$NaMnO_2$ and β-$NaMnO_2$ sample that has been annealed in O_2 presented with the blue, red and purple graphs, respectively. The graph shows that the sharpest dielectric anomaly is observed for the annealed β-$NaMnO_2$ samples. The inset of the figure shows the critical temperature region (80-110 K) of the dielectric anomalies of the three compounds.

4.5.4 Isothermal Polarization Loop Tests on β-$NaMnO_2$

Various efforts took place to prove the possible ferroelectricity in β-$NaMnO_2$. Usually the existence of anomalies in the dielectric constant is generated by a rearrangement of the electric dipoles indicating that polarization builds up in the compound. The existence of polarization strongly suggests that the electric dipoles are oriented in one direction. In that case, the material is characterized as polar. If the direction of the electric dipoles can be reversed by 180 deg when electric field is cycled, then the sample is characterized as ferroelectric and displays the characteristic polarization loops.

In this paragraph we present an I-V test carried out on a β-$NaMnO_2$ sample (Ø 5 mm, thickness t= 1.57 mm). The sample is cooled from room temperature to 77 K with zero electric and magnetic field. After heating up to 80 K, the temperature is stabilized. The dielectric constant exhibits a sharp change at 90 K, so if there is a ferroelectric transition, it should appear at the I-V of 80 K. The sample is connected to a Keithley 6517A electrometer which applies voltage from 0 V to 360 V, 360 V to the -360 V and back to positive voltages, with steps specified by the user. In this experiment, the electrometer is set to apply voltage and measure current. The results are shown in Figures 4.31 and 4.32.

Figure 4.31 shows the graph of current versus electric field (I(E)). The electric field is calculated by dividing the voltage (V) with the thickness of the sample. There is a well pronounced peak around 130 kV/m which states the movement of the charges and thus, the appearance of polarization. However there are two noticeable characteristics in the graph of Figure 4.31. The first one is the absence of a current peak at the negative voltage (at-130 kV/m) and the second is the noise or random values of current. It is likely that this is leakage current. The fact that the peak at -130 kV/m does not appear, possibly implies that the reversing the electric dipoles by 180 deg is not possible. Consequently, the material is not ferroelectric but is likely polar. The noise and appearance of leakage current, could be attributed to parasitic signal coming from the wires and components of the experimental set up.

The P-E graph in Figure 4.32 is a result of integration of the current values of Figure 4.31 according to the equation 2.15. Although there seems to be a lossy loop, due to the poor quality of I-V data and the existence of the current peak only at 130 kV/m, the P-E loop is not the expected one for a ferroelectric system. Still though, the graph of Figure 4.31 provides an indication about the polar character of the β-$NaMnO_2$

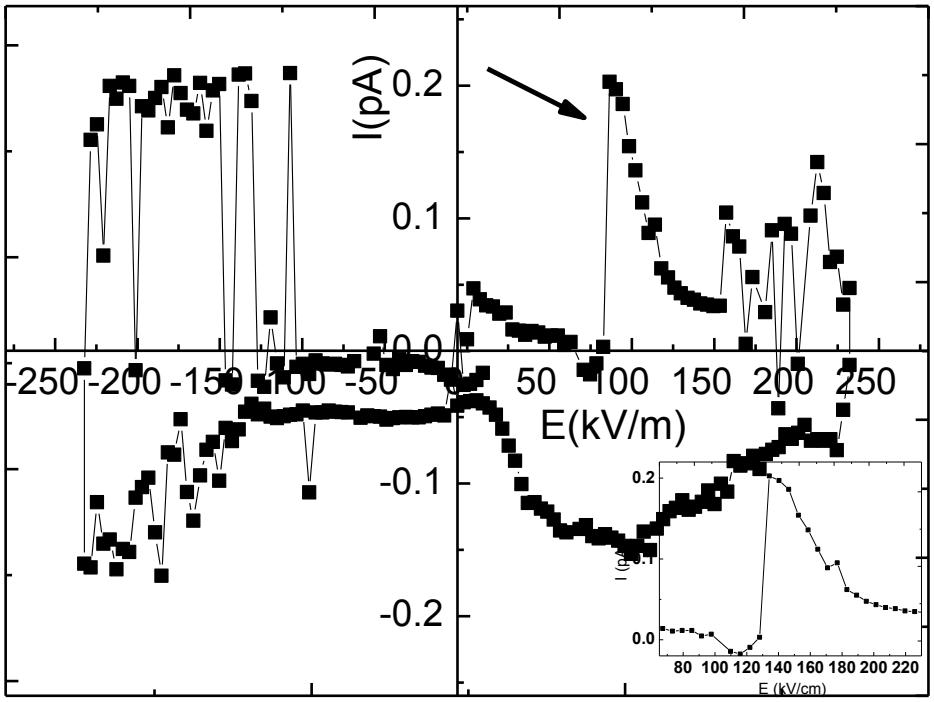

Figure 4.31 I-E (current versus electric field) graph of β-$NaMnO_2$ measured at 80 K and under zero magnetic field. The voltage has been converted to electric field E, by dividing the applied voltage with the thickness of the sample under measurement. The inset of the figure shows a detail from the peak noticed at 130 kV/cm

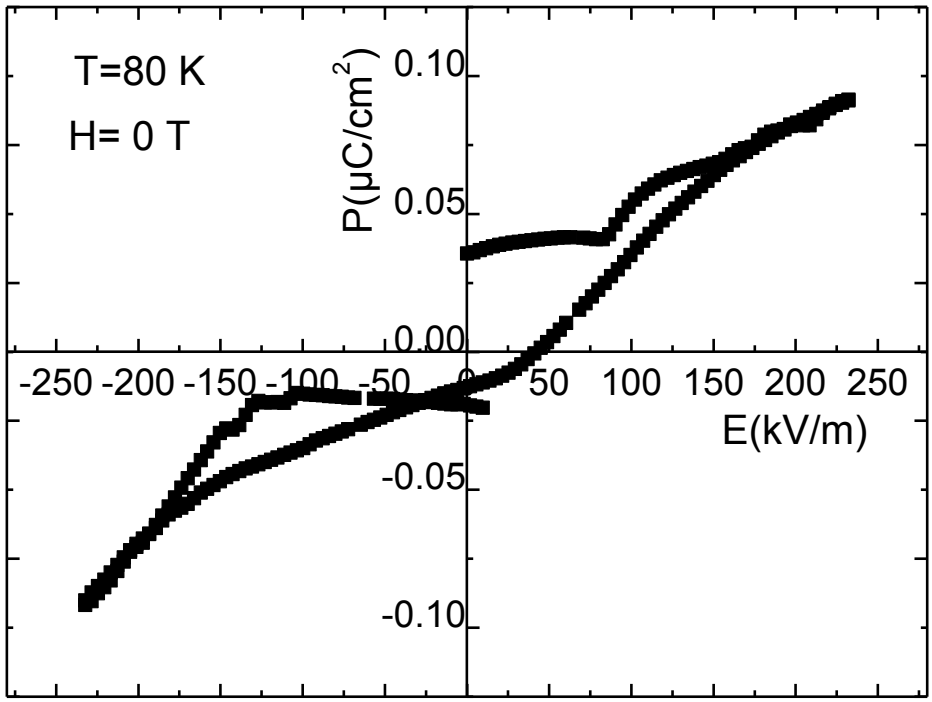

Figure 4.32 P-E (polarization versus electric field) for the β-$NaMnO_2$ at 80 K, calculated from the I-E data of Figure 4.31.

4.5.5 Polarization versus Temperature of an Annealed in Air β-$NaMnO_2$ sample

At this point it is useful to present preliminary data of polarization versus temperature (P(T)) measured on an annealed β-$NaMnO_2$ sample of thickness t= 1 mm and area A= $9.63 \cdot 10^{-6}$ m^2. The β-$NaMnO_2$ synthesis was completed with two heatings at 950°C (sample's code ib18 -see Table 4.1) instead of the usual 3 heatings, and then it was

annealed at 300°C for 6 hrs in air. XRPD of the sample obtained after the annealing (Figure 4.11) showed a two phase material (β-$NaMnO_2$/$Na_{0.7}MnO_2$).

The polarization of the sample was measured upon heating (Figure 4.33). The sample was cooled from 250 K to 40 K by applying electric field of 240 kV/m. The sample's temperature was stabilized at 40 K, the electric field was removed and charge versus temperature was measured upon heating. Dividing the charge with the conductive area of the sample yields the polarization P. The result is shown in Figure 4.33, where an abrupt change of polarization occurs at 70 K.

The inset of Figure 4.33 shows the dielectric constant ε'(T) measured upon heating of an annealed β-$NaMnO_2$ sample of the same batch, measured upon zero magnetic field (0 T-shown with the blue line) and also upon 3 T (presented with the red line). It is clear that two dielectric anomalies exist, at 210 K and 65 K. The dielectric anomalies are shifted towards lower temperatures upon the application of 3 T magnetic field.

A reasonable question regards the shift of the dielectric anomalies at 65 K and 210 K and the appearance of the polarization at 70 K. The explanation lies on the particular β-$NaMnO_2$ sample (ib18) which had $Na_{0.7}MnO_2$ as secondary phase (Figure 4.11). Apparently, the existence of secondary phases has significant impact on the temperature of the dielectric anomalies and polarization. This observation could be supported further if we had Neutron Diffraction Patterns from the specific two phase material sample, which would reveal the temperature of the magnetic transitions. However NPD patterns were taken from batches which consisted from pure β-$NaMnO_2$ samples.

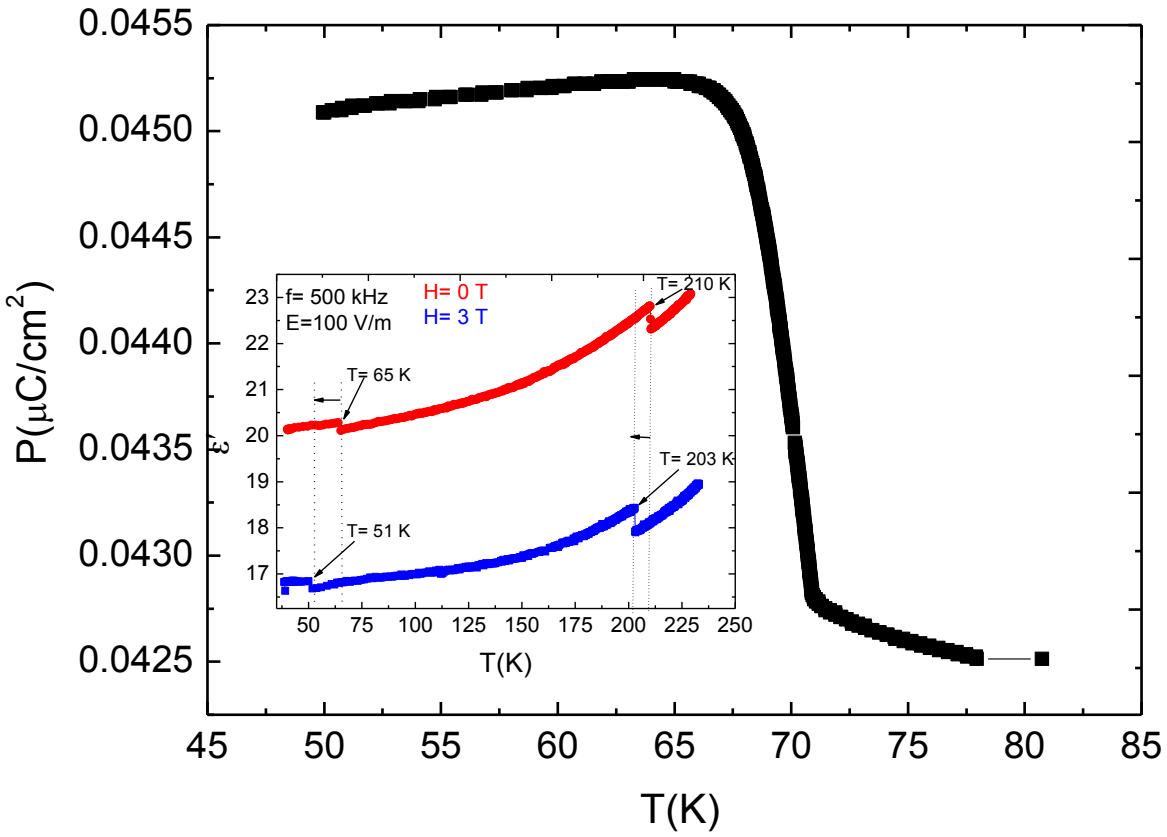

Figure 4.33 Polarization versus temperature measured upon heating an annealed β-$NaMnO_2$ showing abrupt change in the polarization at 70 K.

One comment should be added in respect to the polarization values of Figure 4.30. The transition to a polar or ferroelelectric state is marked by the change of polarization from zero to a finite polarization. As one can observe, in Figure 4.30 there is an offset at the y-axis around 0.0425(μC/cm^2) from where the polarization is increased up to 0.045 (μC/cm^2). Therefore, the correct value of the P is 0.0025 (μC/cm^2) as the offset value of 0.0425 (μC/cm^2) most probably corresponds to leakage current from the components of the experimental setup.

4.6 TEM Studies [143]

In order to further investigate the β-$NaMnO_2$ compound neutron powder diffraction (section 4.7) and TEM experiments took place. Critical answers concerning the crystal structure of β-$NaMnO_2$ were provided by TEM, which is discussed in the following paragraphs. Neutron powder diffraction patterns revealed a rather complex crystal structure which could not be completed with a Rietveld refinement due to the almost complete overlap of the main reflections. This can be explained by the fact that a neutron powder diffraction pattern results from an infinite number of crystallites oriented at random directions. Thus, the observed Bragg reflections, is the overall result which is attributed to all the crystallites of the powder specimen. In cases where the crystal structure shows a high degree of complexity [213, 214, 215]evident by overlapping peaks or stacking faults, electron diffraction combined with HRTEM images provide an essential tool for the investigation of further and complete structural analysis.

The following paragraphs describe the research that has been carried out on the transmission electron microscopy on the β-$NaMnO_2$ compound. Electron diffraction (ED), high resolution transmission electron microscopy (HRTEM), experiments took place in University of Antwerp in Belgium.

4.6.1 Electron Diffraction[143]

Specimens for transmission electron microscopy (TEM) investigation were prepared in an Ar-filled glove box by crushing the crystals in a mortar under anhydrous ethanol or n-hexane and depositing drops of suspension onto holey carbon grids. The specimens were transported and inserted into the microscope under dry Ar, completely excluding contact with air. Electron diffraction (ED) patterns and high resolution transmission electron microscopy (HRTEM) images were obtained with a Tecnai G2 electron microscope operated at 200 kV.

Figure 4.34 shows a series of the ED patterns obtained by tilting a crystallite of β-$NaMnO_2$ around the [100] axis. Figure 4.35 demostrates ED patterns of the β-$NaMnO_2$ taken around different zone axis.

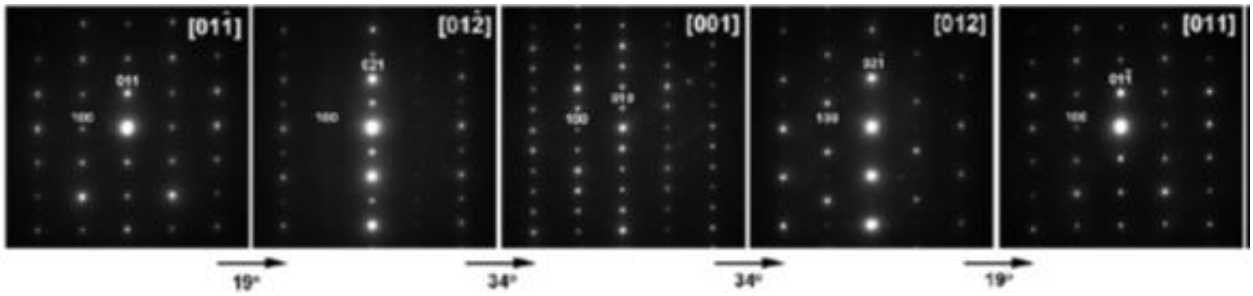

Figure 4.34 Tilt series of the ED patterns of β-$NaMnO_2$

In both Figures, brightest and weaker spots are present. The brightest spots are indexed upon the orthorhombic cell Pnmm of the β-$NaMnO_2$ with $\alpha_o \approx 6.34$ Å, $b_o \approx 2.86$ Å, $c_o = 4.79$ Å (although the structure was given in the Pmnm setting in the original publication, the Pnmm setting was used in the ED and HRTEM analysis). The bottom left in Figure 4.35 of the [010] pattern shows reflections that are positioned according to the orthorombic unit cell. These patterns were denoted as $[010]_\beta$. However, these reflections are very diffuse and streaked with diffuse intensity line parallel to the c* axis. The bottom right of Figure 4.35 shows another type of diffuse reflections. Surprisingly, these reflections are not indexed upon the orthorhombic unit cell of β-$NaMnO_2$ but are positioned according to the monoclinic cell of the α-$NaMnO_2$. These patterns were denoted as $[010]_{\alpha..}$ ED patterns strongly suggest the concentration of stacking faults and intergrowth of the α- and β-phases.

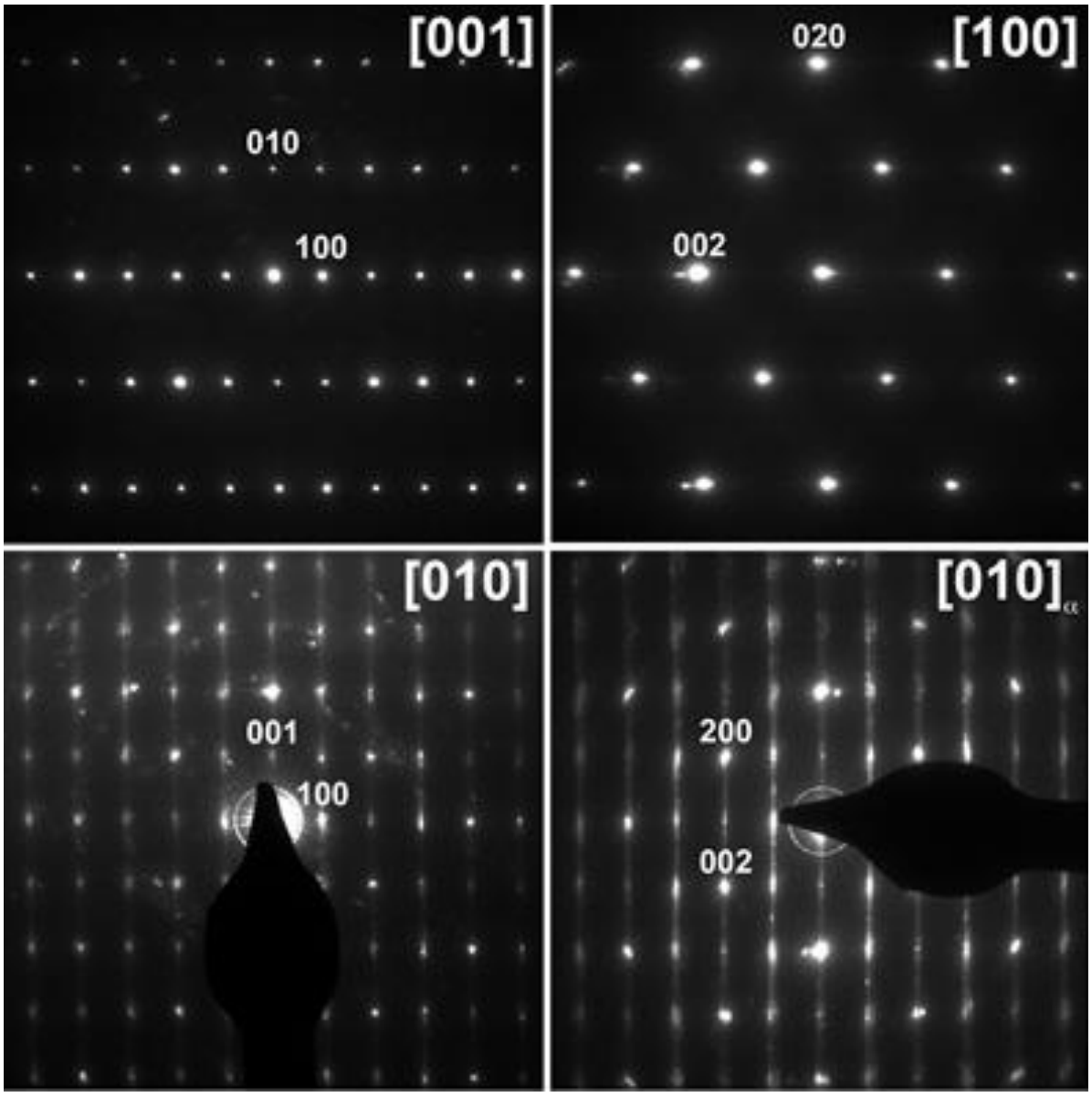

Figure 4.35 The $[100]_\beta$ and $[100]_\alpha$ patterns. The $[100]_\alpha$ pattern is indexed with the unit cell of the α-$NaMnO_2$ phase.

4.6.2 High Resolution Electron Transmission Microscopy [143]

The results of the ED patterns were further confirmed by the HRTEM images, shown in Figure 4.36. The dominant characteristic of these images is the high density of the planar defects. The atomic columns are easily recognized by the rows of the white dots. However a detailed examination of the image reveals two types of atomic arrangements. The first one shows a flat arrangement of atomic columns which corresponds to the α-$NaMnO_2$ phase and is marked with the black arrowheads. The second type shows a corrugated arrangement of atomic columns which resembles the zig-zag structure of the β-phase. These domains are pointed out with the white arrowheads. The coherently intergrown domains present the thickness of a few unit cells.

Apart from these domains, more complex long-period sequences can be observed, an example of whose is marked with the bracket in Figure 4.36 (a). These areas are characterized by thin lamellas of the β-$NaMnO_2$ which are quasi-periodically separated by the fault planes. As an effect there are lateral shifts or of the lamellas along the b-axis.

In order to describe the complex structure of the β-$NaMnO_2$ as seen with the HRTEM images, a Fourier transform has been used (Figure 4.37). The proposed modulated structure can be indexed upon the (3+1)-dimensional approach [182] with an average body centered unit cell with: $\alpha_{av}=1/2a_o$, $b_{av}=b_o$ and $c_{av}=c_o$ where the subscript o in the cell parameters refers to the Pnmm cell values ($\alpha_o\approx6.34$ Å, $b_o\approx2.86$ Å, $c_o=4.79$ Å). The modulation vector for this superstructure is $q=1/2a^*+\gamma c^*$. The modulated structure can be described by the monoclinic (3+1)D superspace group X2/m(α0γ)00, where X=[½, ½,½, ½] is a non standard centering vector. Details on the superspace model are presented in the following section 4.6.3. Based on this description, the planar defects are characterized by quasi-periodic sequences which generated modulations in the layered structure of the β-$NaMnO_2$.

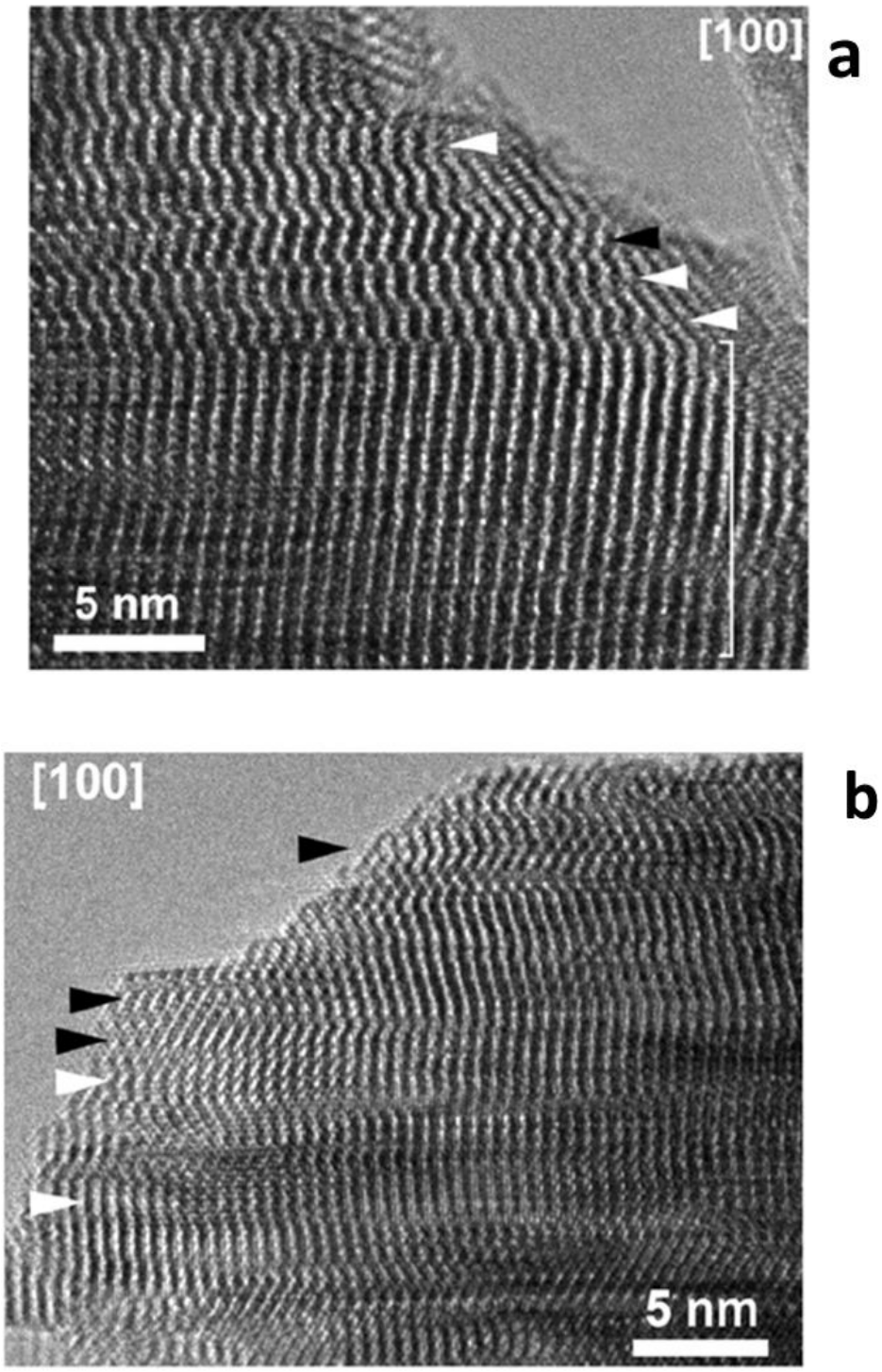

Figure 4.36 HRTEM images showing high concentration of stacking faults. The domains of the α-and β-phases are marked with black and white arrows, respectively. (b) The area where thin lamellas ofthe α-phase are quasi-periodically separated by the faults planes causing lateral shifts is marked with the bracket.

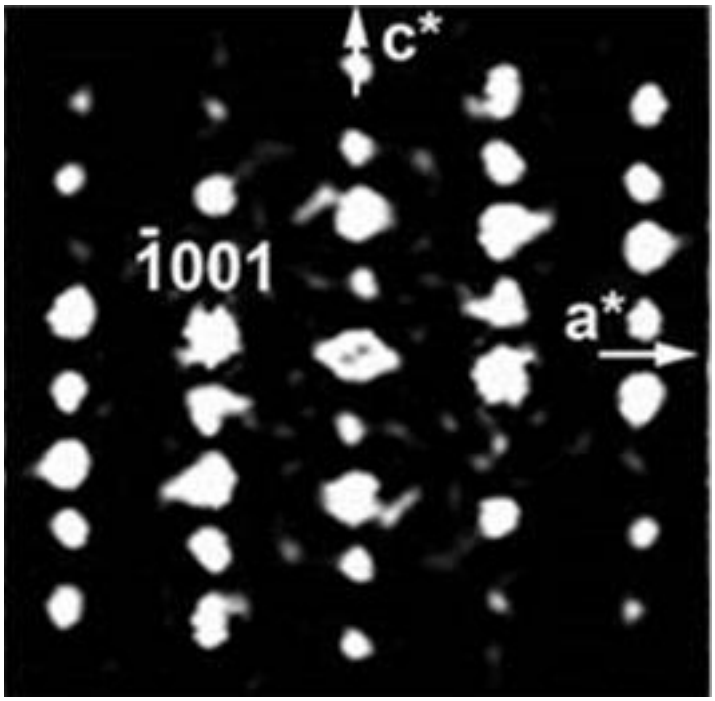

Figure 4.37 Fourier transform of the area marked with bracket in Figure 4.36 (a).

4.6.3 Interpretation of the ED-HRTEM results-The Superspace Model[143]

In this paragraph we discuss the possible models to interpet the results obtained from the ED patterns and the HRTEM images. The goal is to find a common model which describes the stacking sequences of the $NaMnO_2$ polymorphs, namely in both β-$NaMnO_2$ and α-$NaMnO_2$ in the (3D+1) superspace.

Basic Characteristics of an incommensurate crystal structure

To understand the model proposed, it is essential to simplify a few critical meanings of the term "incommensurate crystal structure". An incommensurate structure[182, 183] can be described by a non dirstorted arrangment that is the basic structure, and a wave function which induces the modulation. The wave functions $u(x_4)$ are periodic functions

$$\mathbf{u}^{\mu}(\bar{x}_4 + 1) = \mathbf{u}_{\mu}(\bar{x}_4) \qquad \textbf{(4.4)}$$

The displacement of an atom μ, out of the basic structure of the position x is then given by the equation:

$$\mathbf{u}_{\mu}(\bar{x}_4)=\mathbf{u}_{\mu}(\bar{x}_4)\mathbf{a_1}+\mathbf{u}_{\mu}(\bar{x}_4)\mathbf{a_2}+\mathbf{u}_{\mu}(\bar{x}_4)\mathbf{a_3} \quad \textbf{(4.5)}$$

Where $\mathbf{a_1}$, $\mathbf{a_2}$, $\mathbf{a_3}$, are the basis vectors which define the position of an atom μ with respect to the origin of the unit cell according to the equation:

$$x_{\mu}^{0}=x_1^0(\mu)\mathbf{a}_1+x_2^0(\mu)\mathbf{a}_2+x_3^0(\mu)\mathbf{a}_3 \quad \textbf{(4.6)}$$

and $(x_1^0(\mu), x_2^0(\mu), x_3^0(\mu))$ are relative coordinates with respect to the basis vectors $\mathbf{a}_1$, $\mathbf{a}_2$, $\mathbf{a}_3$.

Investigation of the polymorphism of the $NaMnO_2$ structures

As it has been mentioned earlier the structure of the β-$NaMnO_2$ is described as incommensurate modulated structure with the modulation vector $q=1/2\mathbf{a}^*+\gamma\mathbf{c}^*$. The formation of the planar defects suggests a displacement of each successive ($NaMnO_2$) layer by either $\frac{1}{2}[111]_{av}$ or by $\frac{1}{2}[\bar{1}11]_{av,}$ demonstrated in Figure 4.38 (a). The choise of one of these displacements in a randomly chosen $NaMnO_2$ layer, results in the transfer of oxygen atoms from the selected to the adjacent layer. Depending on the stacking of the layers there could be two possible outcomes: the first case is Na^+ tranfered to Na^+ positions, or equivalent Mn^+ to Mn^+, or the second possibility is that the positions of the Na and Mn are interchanged.

A diffraction pattern is a representation of the reciprocal lattice. Figure 4.38 (b), (c) and (d) shows arrays of spots which correspond to the calculated Laue patterns, each one accounts for different $NaMnO_2$ polymorphs. The distribution of intensity in the spots yields valuable information about the symmetry and orientation of the crystal but also shows characteristics related with certain defects and internal deformation. The Laue patterns have been evaluated to result in the model of structures that are assigned to each $NaMnO_2$ polymorph. The polymorphs of the $NaMnO_2$ are derived by changing the value of the component γ in the modulation vector $q=1/2\mathbf{a}^*+\gamma\mathbf{c}^*$: γ=0 corresponds to the pure β-$NaMnO_2$ structure, γ=1/2 results in the α-$NaMnO_2$ phase, whereas γ=1/6 gives an intermediate structure shown in Figures 4.38 (b), (c), (d), respectively.

The models for the crystal structures of the three polymorphs are shown in Figure 4.39. Each value of the component γ corresponds to a different ordering sequence of the Na and Mn cations along the $[111]_{av}$ direction. In detail, the sequence Na-Na-Mn-Mn refers to the orthorhombic β-$NaMnO_2$ structure, whereas the Na-Mn-Na-Mn sequence is correlated with the α-$NaMnO_2$ phase

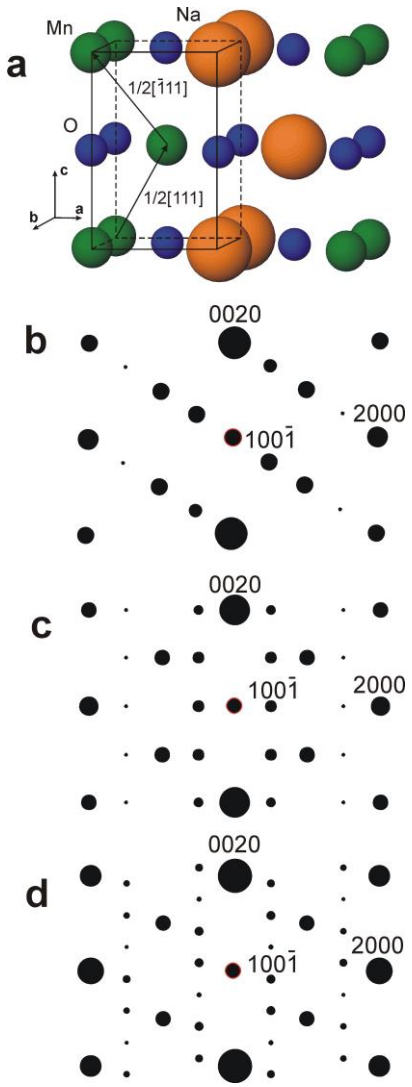

Figure 4.38 The stacking sequence of the ($NaMnO_2$) layers in the β-$NaMnO_2$ structure (a). The average a_{av}= 1/2ao, b_{av}=b_o, c_{av} = c_o unit cell is outlined and the displacement vectors connecting the ($NaMnO_2$) layers are shown. The [010] sections of the reciprocal space for the stacking sequences corresponding to the γ = 1/2 (b, α-$NaMnO_2$ structure), γ = 0 (c, β-$NaMnO_2$ structure) and γ = 1/6 (d) cases.

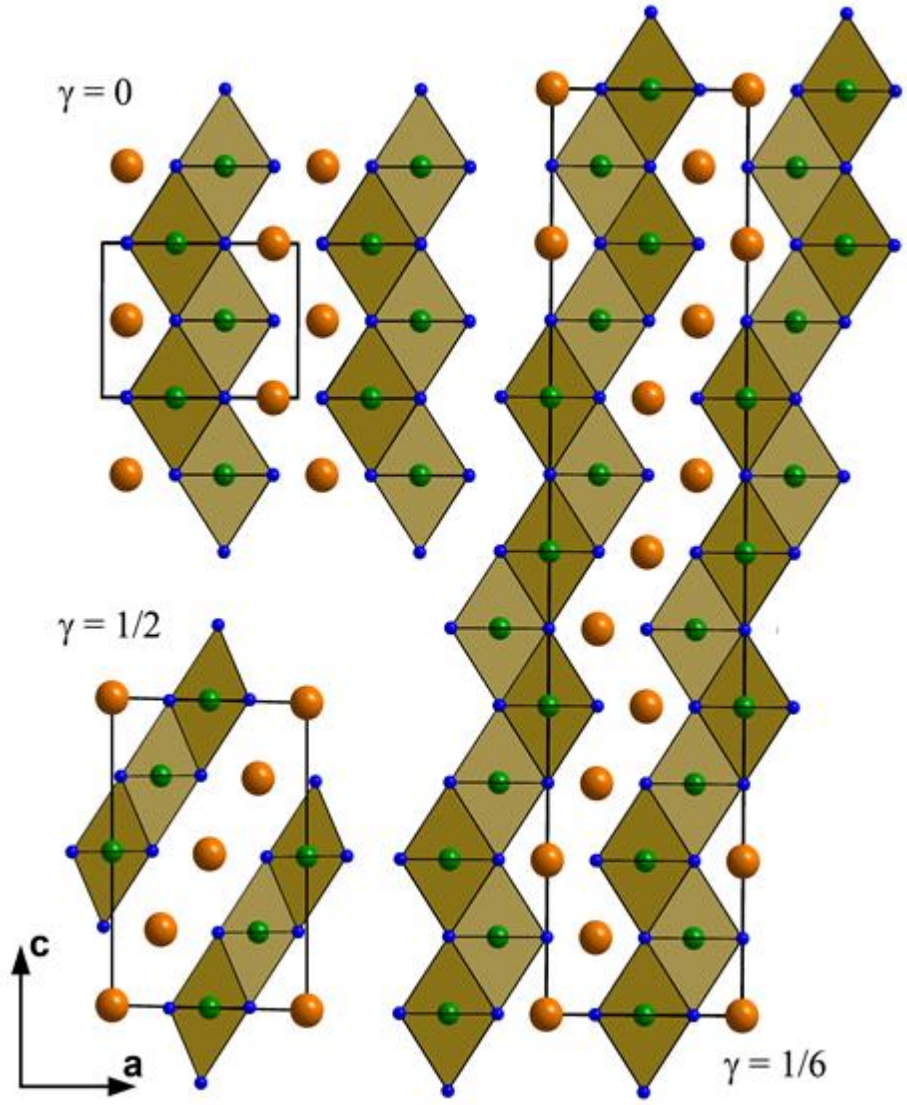

Figure 4.39 The crystal structures of the $NaMnO_2$ polymorphs corresponding to the γ = 1/2 (α-$NaMnO_2$ structure), γ= 0 (β-$NaMnO_2$ structure) and the intermediate structure with γ= 1/6

Combining the HRTEM analysis with X-Rays synchrotron Data[143]

The validity of the superspace model proposed for the $NaMnO_2$ polymorphs has been checked by refinements of the α-$NaMnO_2$ and β-$NaMnO_2$ structures using neutron and synchrotron XRD data. The α-$NaMnO_2$ is best described as (3D+1) commensurately modulated structure. The refinement of the structure (Figure 4.40) based on the NPD data (BT1, NCNR-NIST, λ=2.0787 Å) by means of the superspace model reveals refined parameters and interatomic distances of the Na-O and Mn-O in perfect agreement with those obtained from the corresponding Rietveld analysis.

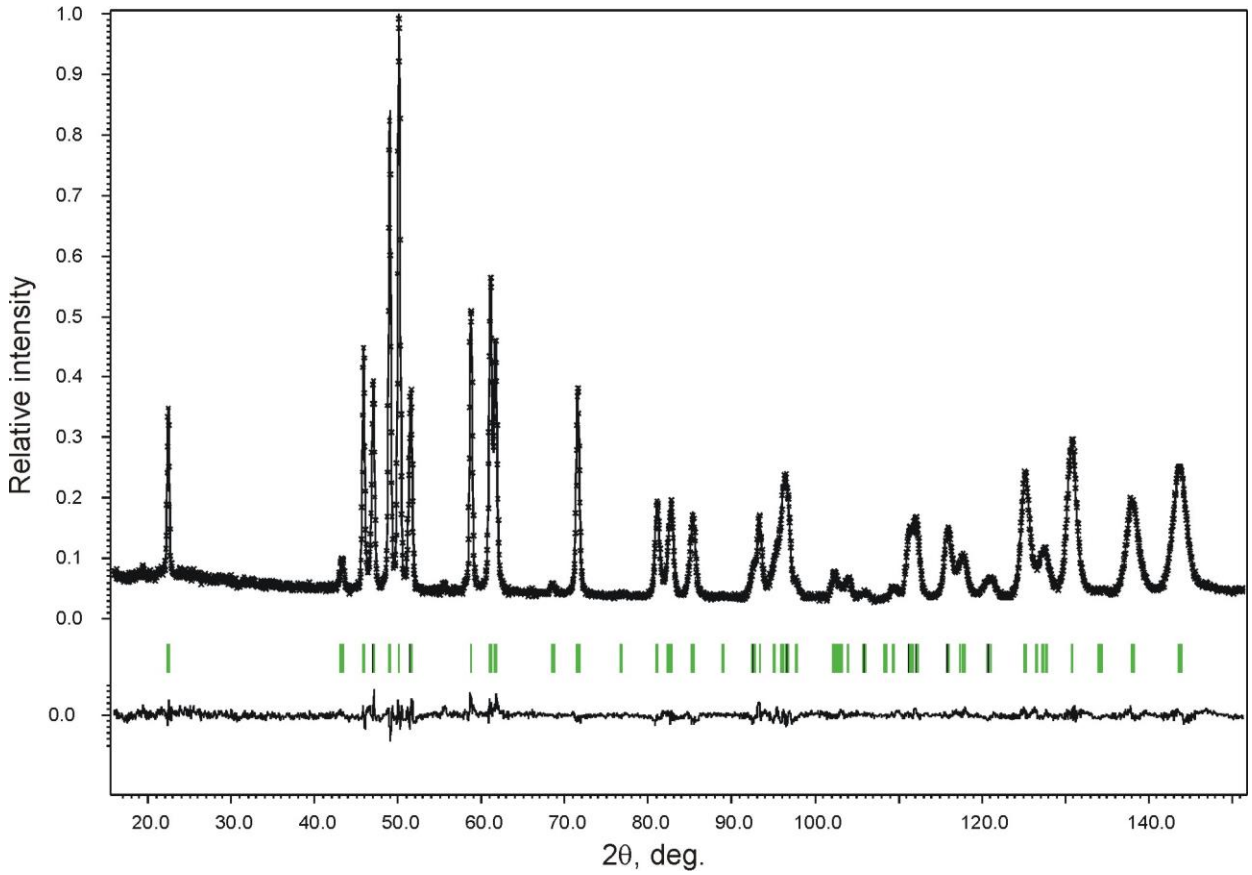

Figure 4.40 Experimental, calculated and difference NPD profiles after the Rietveld refinement of α-$NaMnO_2$ as a (3+1)D *commensurately* modulated structure. Black and green bars mark the positions of the main reflections and first order satellites, respectively.

The crystallographic parameters which are related with the Rietveld refinement of Figure 4.40 are presented in Tables 4.3-4.5

Space group	*X*2/*m*(α0γ)00, *X* = [1/2, 1/2, 1/2, 1/2]	*C*2/*m*
a, Å	3.15607(9)	5.7947(2)
b, Å	2.85532(9)	2.8553(1)
c, Å	4.7804(5)	5.6614(3)
β, deg.	91.452(2)	113.143(2)
q-vector	1/2**a*** + 1/2**c***	-
Cell volume, $Å^3$	43.066(4)	86.133(8)
t-section	*t* = 0	-
Radiation	Neutrons, λ = 2.0787Å	
Temperature, K	200	
Parameters to refine	6	6
R_P, R_{wP}	0.051, 0.063	0.053, 0.067
R_F (main reflections)	0.020	-
R_F (1^{st} order satellites)	0.012	-
R_F (all)	0.016	0.020
GOF	1.22	1.27

Table 4.3 Crystallographic data for the α-$NaMnO_2$ structure refined as a (3+1)D *commensurately* modulated structure and a conventional 3D structure.

Atom	x_1, x_2, x_3	x_4^0	Δ	Displacive modulation	U_{iso}, Å^2
Na	0, 0, 0	0	1/2	-	0.0124(6)
Mn	0, 0, 0	1/2	1/2	-	0.0062(5)
O*	0, 0, 1/2	0	1	$u_{0,x}$ = -0.1751(6), $u_{0,y} = u_{0,z} = 0$	0.0030(3)
				$A_x = A_y = 0$, A_z = 0.0019(2)	

Table 4.4 Atomic parameters for the α-$NaMnO_2$ structure refined as a (3+1)D *commensurately* modulated structure.

The displacement modulation is defined as a combination of the sawtooth function $\mathbf{u}(x_4) = 2\mathbf{u}_0\left[\left(x_4 - x_4^0\right)/\Delta\right]$ and harmonic function $\mathbf{u}(x_4) = \mathbf{A}\sin(2\pi x_4)$. [182]

Distance	(3+1)D	3D
Na - O	2.4222(8) ×2, 2.3405(4) ×4	2.4256(12) ×2, 2.3422(6) ×4
Mn - O	2.3901(8) ×2, 1.9319(4) ×4	2.3873(12) ×2, 1.9304(5) ×4

Table 4.5 Main interatomic distances for the α-$NaMnO_2$ structure refined as a (3+1)D *commensurately* modulated structure and a conventional 3D structure (Å).

Concerning the reliability of the superspace model for the β-$NaMnO_2$, a two phase LeBail fit of the synchrotron data obtained at the ID31 (ESRF-Grenoble,France) presented in Figure 4.41 proves that the β-phase is characterized as an inhomogeneous microstructure. The two phases that were used in order to account for the Bragg reflections in the synchrotron X-Ray powder diffraction pattern (SXPD), were: the orthorhombic Pnmm (a = 6.32995(6) Å, b = 2.85725(2) Å, c = 4.78627(5) Å) and the incommensurately modulated monoclinic phase (a_{av} = 3.16498(2) Å, b_{av} = 2.85761(1) Å, c_{av} = 4.78553(2) Å, , with the modulation vector q = 0.50126(5)a* + 0.1695(3)c*. Worth noticing that the value of the component γ is almost equal to the γ=1/6=0.1666 obtained by the superspace model analysis. Moreover, weak satellite reflections can be indexed according to the modulation

vector q=1/2a*+0.4928(5) c*. This value of γ ~ 0.493 is very close to the γ=1/2 which corresponds to the modulation vector of the α-$NaMnO_2$ phase.

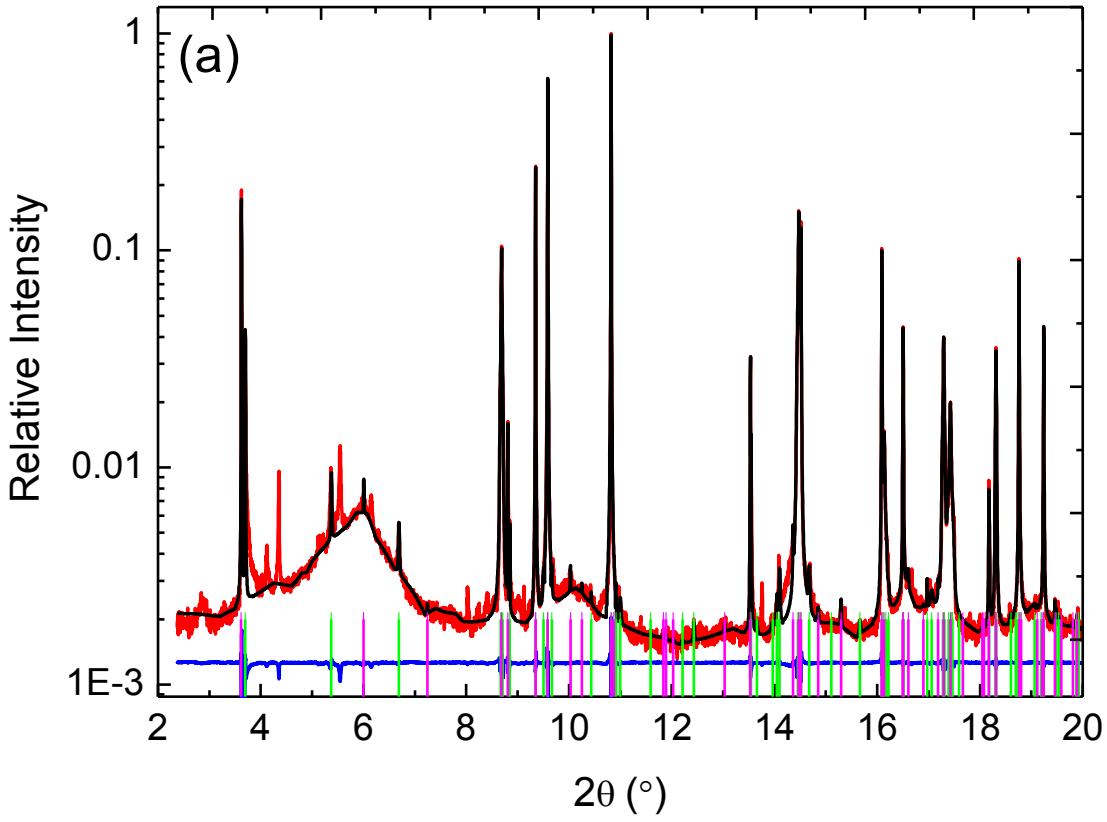

Figure 4.41 (a) Le Bail fit of the synchrotron X-ray powder diffraction pattern of the β-$NaMnO_2$ sample. The purple tick row of bars stands for the reflections of the orthorhombic *Pnmm* β-$NaMnO_2$ phase, the green row of bars mark the reflection positions of the incommensurately modulated monoclinic phase.

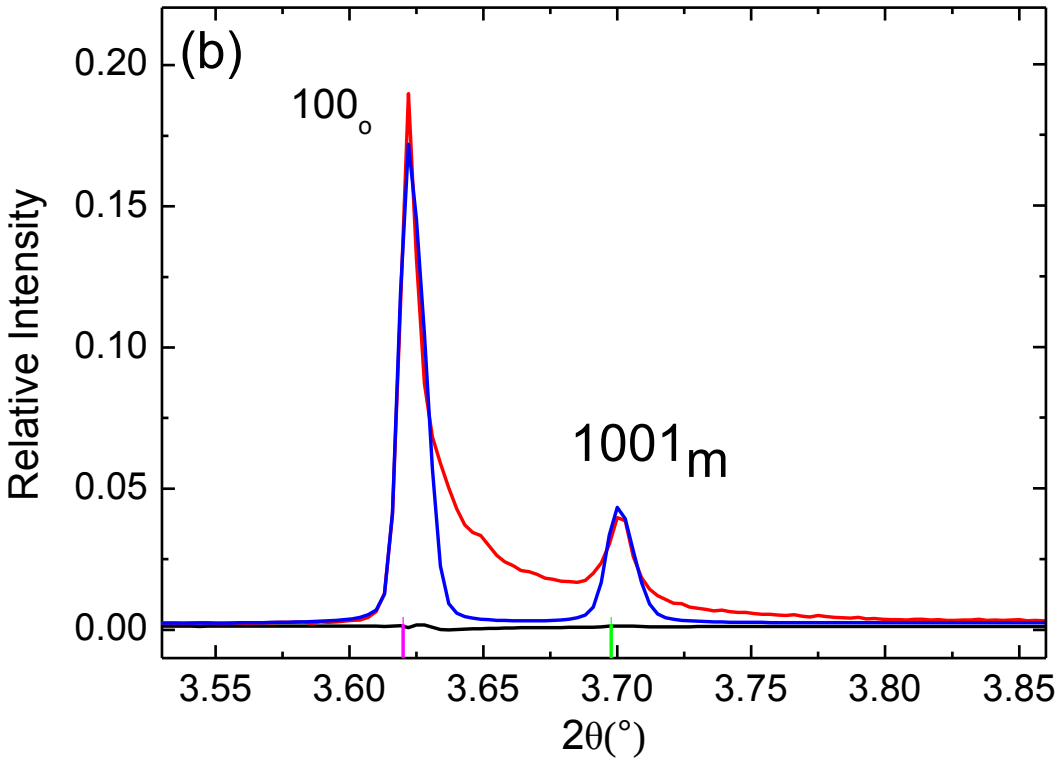

Figure 4.41 (b) A detail of Figure 4.41 (a) which shows lowest-angle satellite reflections from the two phases (100_o reflection of the *Pnmm* phase in a 3D indexing corresponds to the $100\bar{1}$ satellite in a (3+1)D indexing). Note the diffuse intensity between these two reflections indicating a presence of the short-range ordered regions with $0 < \gamma < 1/6$.

Atom	**x**	**y**	**z**
α-$NaMnO_2$:*C*2/*m*, *a* = 5.662 Å, *b* = 2.86 Å, *c* = 5.799 Å, β = 113.1°			
Na	0.5	0	0.5
Mn	0	0	0

O	0.29347	0	0.79147
β-$NaMnO_2$: *Pmmn*, *a* = 2.859 Å, *b* = 4.785 Å, *c* = 6.338 Å			
Na	0.25	0.25	0.12373
Mn	0.25	0.25	0.62628
O1	0.25	0.75	0.16855
O2	0.25	0.75	0.58253
γ = 1/3: $P2_1/m$, *a* = 6.34 Å, *b* = 2.86 Å, *c* = 14.37 Å, β = 90°			
Na1	0.37504	0.75	0.91677
Na2	0.87398	0.75	0.25018
Na3	0.87718	0.75	0.58294
Mn1	0.37566	0.75	0.58416
Mn2	0.87544	0.75	0.91662
Mn3	0.37365	0.75	0.24931
O1	0.33154	0.75	0.08183
O2	0.82959	0.75	0.41621
O3	0.41938	0.75	0.75155
O4	0.91785	0.75	0.08465
O5	0.41596	0.75	0.41645
O6	0.83304	0.75	0.74933

Table 4.6: Relaxed atomic positions in the crystal structures of $NaMnO_2$ polymorphs with γ = 0 (α-$NaMnO_2$), γ = ½ (β-$NaMnO_2$), and γ = 1/3.

4.6.4 Assesment of the Magnetic Interactions According to the HRTEM data [143]

In this praragraph we discuss the magnetic interactions of the β-$NaMnO_2$ based on the elaborate TEM observations. It has been mentioned in the introduction that the ideal β-$NaMnO_2$ is a quasi 2D magnet (Figure 4.3). However, in reality it is extremely challenging to prepare a planar defect free (pure) β-$NaMnO_2$. On the contrary, the samples that have been observed in the TEM are better described as intermediate phases. These phases have high conctentration of twin planes and planar defects from both α and β-$NaMnO_2$ polymorphs and their modulation vector γ takes values such as γ=1/3 or γ=1/6, in contrast with the γ=0 which corresponds to the defect-free and pure phase of β-$NaMnO_2$.

Fitting on the experimental data of the magnetic susceptibility χ(T) shown in Figure 4.42 were carried out for β-$NaMnO_2$. According to the superstructure model, β-$NaMnO_2$ is the polymorph whose structure corresponds to the modulation vector with γ=1/3. The data are fitted with the equation $\chi=\chi_{int}+C/(T+\theta)$: χ_{int} is the intrinsic magnetic susceptibility from the quantum Monte Carlo simulations and the term $C/(T+\theta)$ corresponds to a weak impurity contribution evident by the paramagnetic tail of the susceptibility at low temperatures.

The analysis which gave the best agreement between the fitted and the experimental data was provided for the J_1-J_3 spin ladder: J_1 = 65 K, J_3 = 52 K, C = 0.033 emu K/mol, θ = 3 K, for the polymorph which correspobds to the structure with γ=1/3. The topology between the magnetic interactions J_1, J_3 and J_2 as well as the structures of the MnO_2 layers are shown in Figure 4.43.

The two leg ladder model was developed by Barnes and Riera and is given by the following equation [10]:

$$\chi_{ladder}=\frac{c_1}{T}\left[1+\left(\frac{T}{c_2}\right)^{c_3}\left(e^{\frac{c_4}{T}}-1\right)\right]^{-1}\left[1+\left(\frac{c_5}{T}\right)^{c_6}\right]^{-1} \qquad \textbf{(4.7)}$$

where c_1, c_2, c_3, c_4, c_5, c_6, depend on the $J_{\parallel}$ and $J_{\perp}$ values (see equation 1.3)

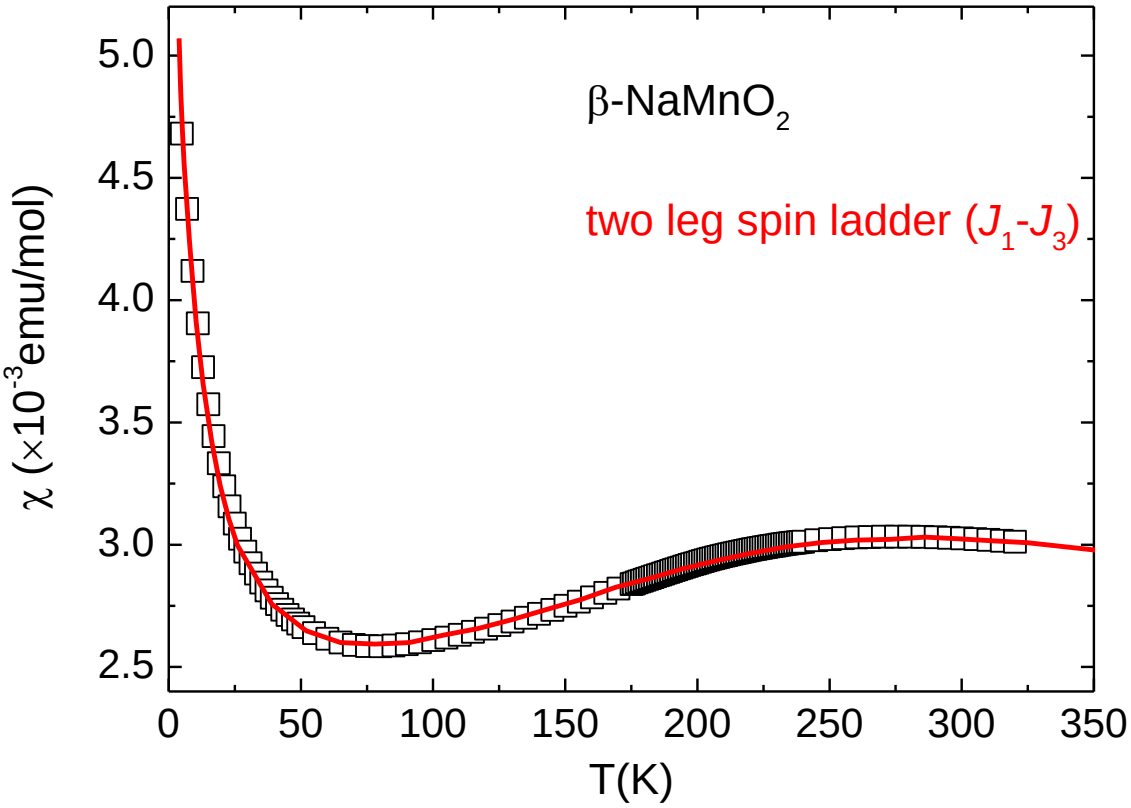

Figure 4.42 Magnetic susceptibility of β-$NaMnO_2$ measured on a DC ZFC mode under 1000 Oe field.The fittings are done according to the the spin ladder corresponding to the γ=1/3 structure. The spin ladder topology leads to the best description for β-$NaMnO_2$.

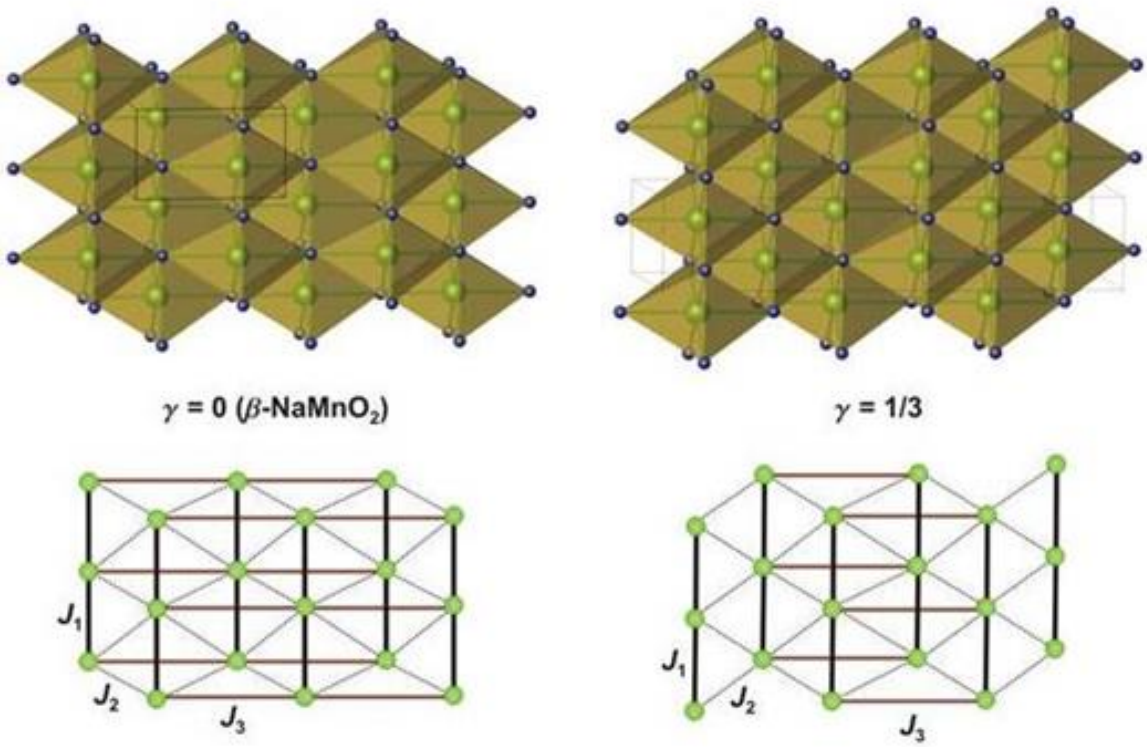

Figure 4.43 Structures of [MnO_2] layers and relevant topologies of magnetic interactions in the pure β-$NaMnO_2$ (γ=0) and the polymorph with γ=1/3; spin ladder type of structures are envisaged.

4.7 Neutron Powder Diffraction (NPD) Data

4.7.1 Costant Wavelength Data

4.7.1.1Crystal Structure at 300 K-Le Bail fits

The first neutron diffraction data of β-$NaMnO_2$ have been obtained from the diffractometer BT1, of the NCNR-NIST neutron center in Maryland, USA. The constant wavelength used was λ=2.0782 Å at temperatures ranging from 4 K-400 K. The mass of the sample that has been used was 7.3 gr and the sample was sealed in a vanadium can (Ø 10.8 mm) using indium wire under He atmosphere inside the glove box. Initially, the crystal structure at 300 K is discussed. Figure 4.44 (a) presents the full pattern at 300 K. As it will be presented in the following pages from the patterns obtained at lower temperatures, no

magnetic transition occurs at 300 K, so all the Bragg reflections correspond to the nuclear (chemical) crystal structure. Prior to any further analysis, there are many characteristics in this NPD pattern which signal the existence of a rather complex crystal structure. The massive broadening of the peaks, the satellite and asymmetric peaks as well as the overlap, evident in some of them all imply structure irregularities. Figure 4.44 (b) shows a detail of the 300 K pattern in which the aforementioned characteristics are clearly presented. The reason of these structure irregularities is the polymorphism of $NaMnO_2$ compounds and the formation of the intermediate phases, already discussed in section 4.6.

A usual introductory approach in the NPD is the Le Bail refinement, a method presented in chapter 2. The first approach was done by indexing the 300 K NPD pattern, using only the β-$NaMnO_2$ phase (Figure 4.44). In Figure 4.44 the red line corresponds to the intensity of the experimental data ("Yobs"), the black line shows the calculated intensity ("Ycalc") according to the theoretical model, and the blue line underneath the graph shows the difference between those two. The vertical blue ticks show the calculated Bragg positions.

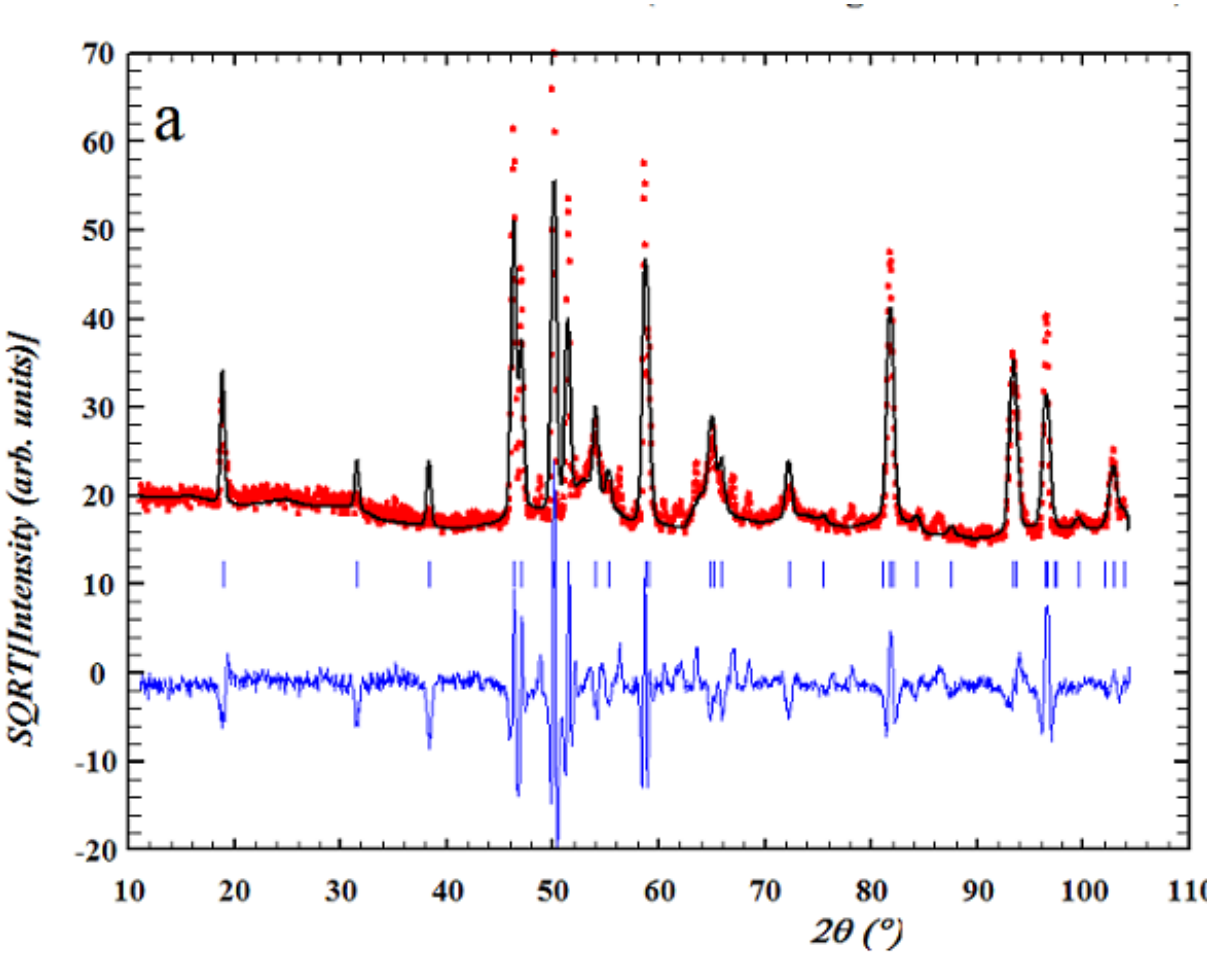

Figure 4.44 NPD obtained at the BT1 diffractometer at room temperature for β-$NaMnO_2$.a) Le Bail analysis of the pattern using the orthorhombic Pmmn β-$NaMnO_2$ phase. b) A detail of the pattern showing clearly massive peak broadening, satellite peaks, asymmetric and peaks with significant overlap.

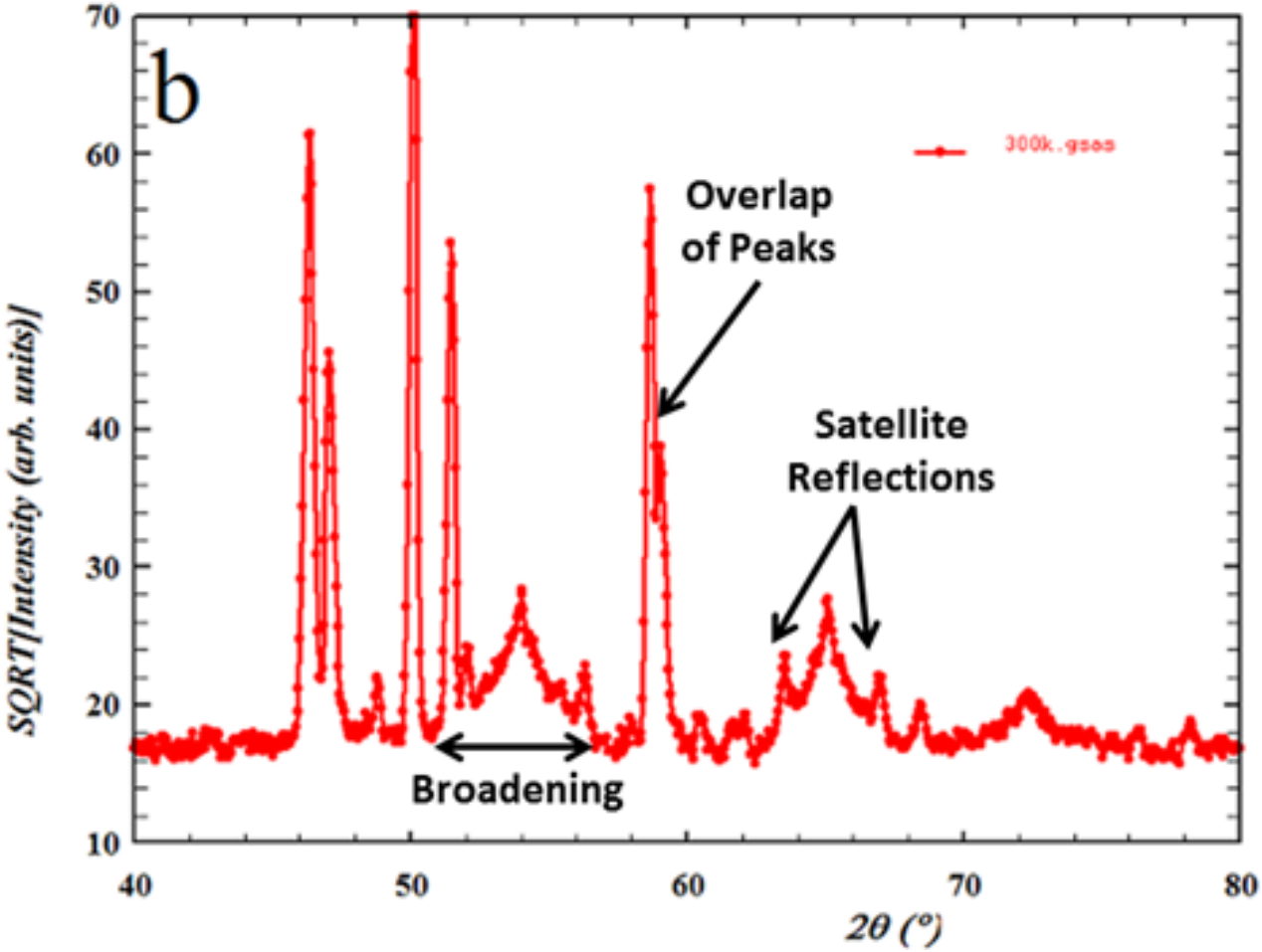

Figure 4.44 (b) NPD obtained at the BT1 diffractometer at room temperature for β-$NaMnO_2$. A detail of the pattern showing clearly massive peak broadening, satellite peaks, asymmetric and peaks with significant overlap.

The indexing of the NPD-300 K pattern according to the orthorhombic Pmmn resulted in the following cell parameters: a=4.793(2) Å, b=2.85372(3) Å, c=6.32105 (2) Å (α=β=γ=90 deg) with the reliability factors: R_{wp}=61.1 % and χ^2=28.6. The quality of the fit is poor since it does not successfully index all the observed Bragg peaks. In order to improve the reliability of the fitting a different approach has been tested.

Two phase Le Bail refinement

A two phase Le Bail refinement was carried out, meaning that the Bragg peaks were indexed upon the expected Bragg positions of the β-$NaMnO_2$ and the α-$NaMnO_2$ (Figure 4.45) which was used as a possible secondary phase. The choice of α-$NaMnO_2$ has been done for the following reasons. Preliminary data obtained from the XRPD patterns of the β-$NaMnO_2$ samples revealed that the 001 α-$NaMnO_2$ peak of low intensity appeared. Moreover, the coexistence of the two phases, α-$NaMnO_2$ and β-$NaMnO_2$ has been observed in the β-$NaMnO_2$ in the TEM experiments. This observation can be related to the fact that the one phase Le Bail refinement fails to predict all the observed reflections from the β-$NaMnO_2$ powder. The energetic proximity of the two phases suggests that intermediate structures of $NaMnO_2$ phases would form with a low energy cost. [143] This observation which can be used in NPD analysis for using two phases or intermediate ones between the α and β polymorphs.

The fit of the observed data using as first phase the β-$NaMnO_2$ and second the α-$NaMnO_2$ is shown in Figure 4.45. More of the observed reflections can be indexed with the addition of α-$NaMnO_2$ as a secondary phase. The two phase Le Bail fit converges to the following parameters: for the otrhorombic β-$NaMnO_2$ phase with space group Pmmn and the cell parameters a=4.813(2) Å, b=2.853(3) Å and c=6.321(1) Å. Fot the second phase, the monoclinic α-$NaMnO_2$ phase of the C2/m space group, the unit cell parameters were a=5.676(1) Å, b=2.821(8) Å, c=5.795(1) Å. The reliability factors are χ^2=24.7 and R_{wp}=56.8 %. The addition of the second phase seems to improve the quality of the fit, yet the final result is not suitable for a safe structural analysis.

The question that arises concerns the quality of analysis that one could do with neutron data, when dealing with such a complicated structure. The anisotropic broadening, the satellite peaks most probably imply the existence of microscopic inhomogeneities. The overlapping of many peaks could be possibly resolved by observing the β-$NaMnO_2$ with long wavelength neutron diffraction data by which the peaks could seem more distinct. For

this reason the neutron powder diffraction experimements were undertaken with the long wavelength WISH diffractometer, which is discussed in 4.7.2 paragraph.

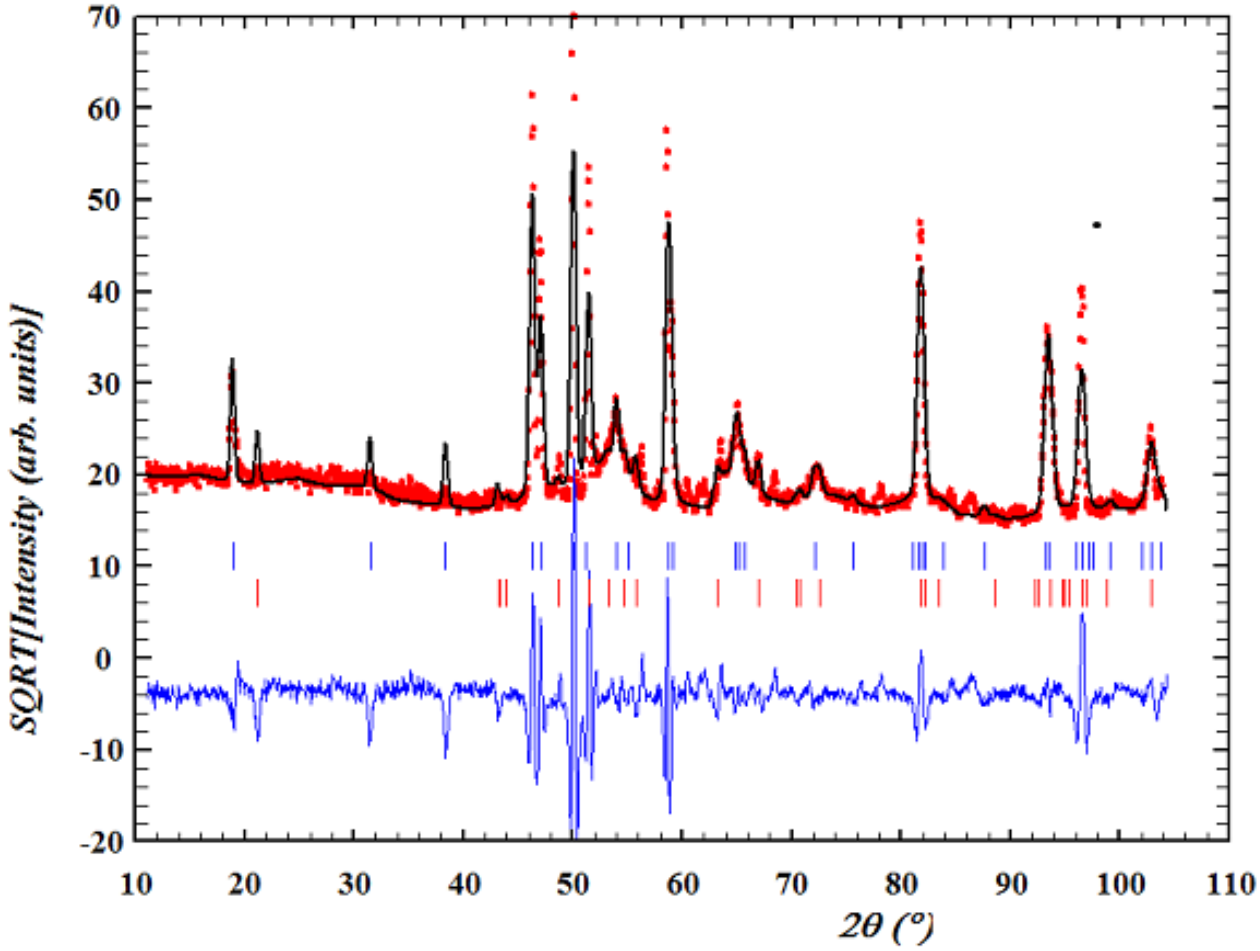

Figure 4.45 NPD obtained at the BT1 diffractometer at room temperature for β-$NaMnO_2$. Analysis of the pattern has been done according to a two phase Le Bail refinement. The first set of tick marks (blue ones) corresponds to the expected reflections of the orthorhombic β-$NaMnO_2$ and the lower (red) set of tick marks shows the theortical Bragg peaks from the monoclinic C2/m α-$NaMnO_2$ phase.

4.7.1.2 Magnetic Ordering of β-$NaMnO_2$ According to the NPD.

NPD patterns obtained at lower temperatures revealed the existence of two magnetic orderings shown in Figures 4.46 and 4.47. The first magnetic peaks appear at 200 K at 2θ ~26 deg and 38 deg (Figure 4.46) which is equivalent with the d-spacing of 3.2 Å and 4.59 Å, respectively (Figure 4.47). The intensity of both peaks is saturated at 100 K, since no increase of the peak's intensity is noticed by further reducing of the temperature. One common characteristic of both magnetic peaks is that they are remarkably broad. The peaks at the d-spacings of 3.2 Å and 4.59 Å, possibly mark the onset of a commensurate magnetic order.

As the temperature is further cooled down to 80 K, satellite peaks appear. Specifically, for the peak of 3.2 Å satellites appear at 3.15 Å and 3.25 Å, whereas the peak of 4.59 Å has its satellites around 4.38 Å and 4.73 Å. The appearance of satellite peaks usually [216, 217, 218] denotes the emergence of an incommensurate magnetic structure. Both magnetic peaks are unusually broad. Regarding the satellites, the one that appears at the low 2θ (high d-spacing) angle has higher intensity than the one that emerges at the high 2θ angle (low d-spacing). The intensity of the satellites is already saturated at the scan of 50 K, as there is no difference on the intensity between the scan of 50 K and the one of the lowest temperature the 4 K.

Figures 4.48a and 4.48b show the magnetic peak of 2θ~26 deg in 3D and 2D plots, respectively. Further discussion on the evolution of the intensity of the magnetic peaks versus temperature is carried out on the paragraph 4.7.2.2 regarding the data from the WISH diffractometer.

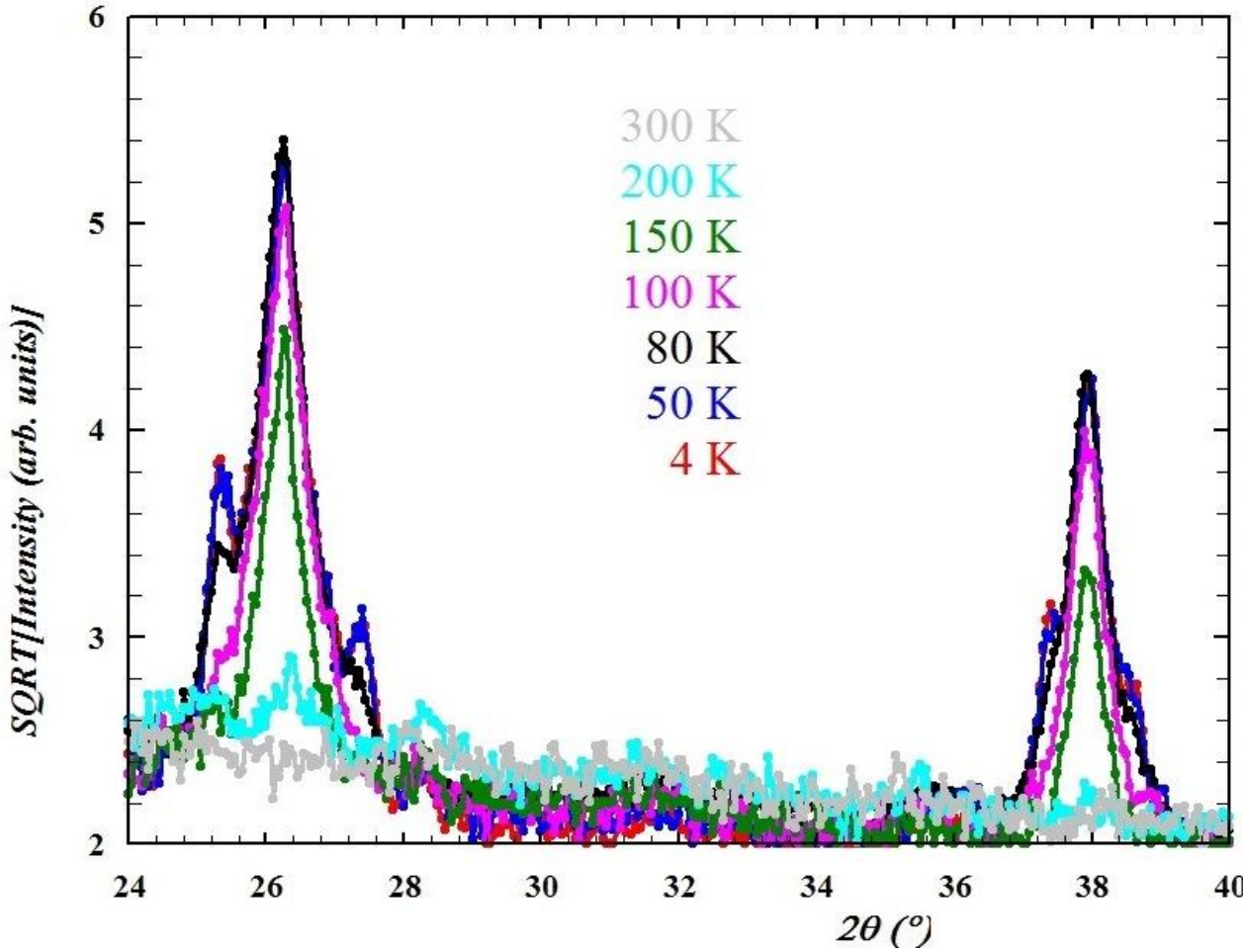

Figure 4.46 NPD patterns showing the temperature evolution of the magnetic Bragg peaks. These peaks are pointing the emergence of two magnetic orderings for the β-$NaMnO_2$: the first one appears at 200 K and the second one, evident by the satellites around 80 K.

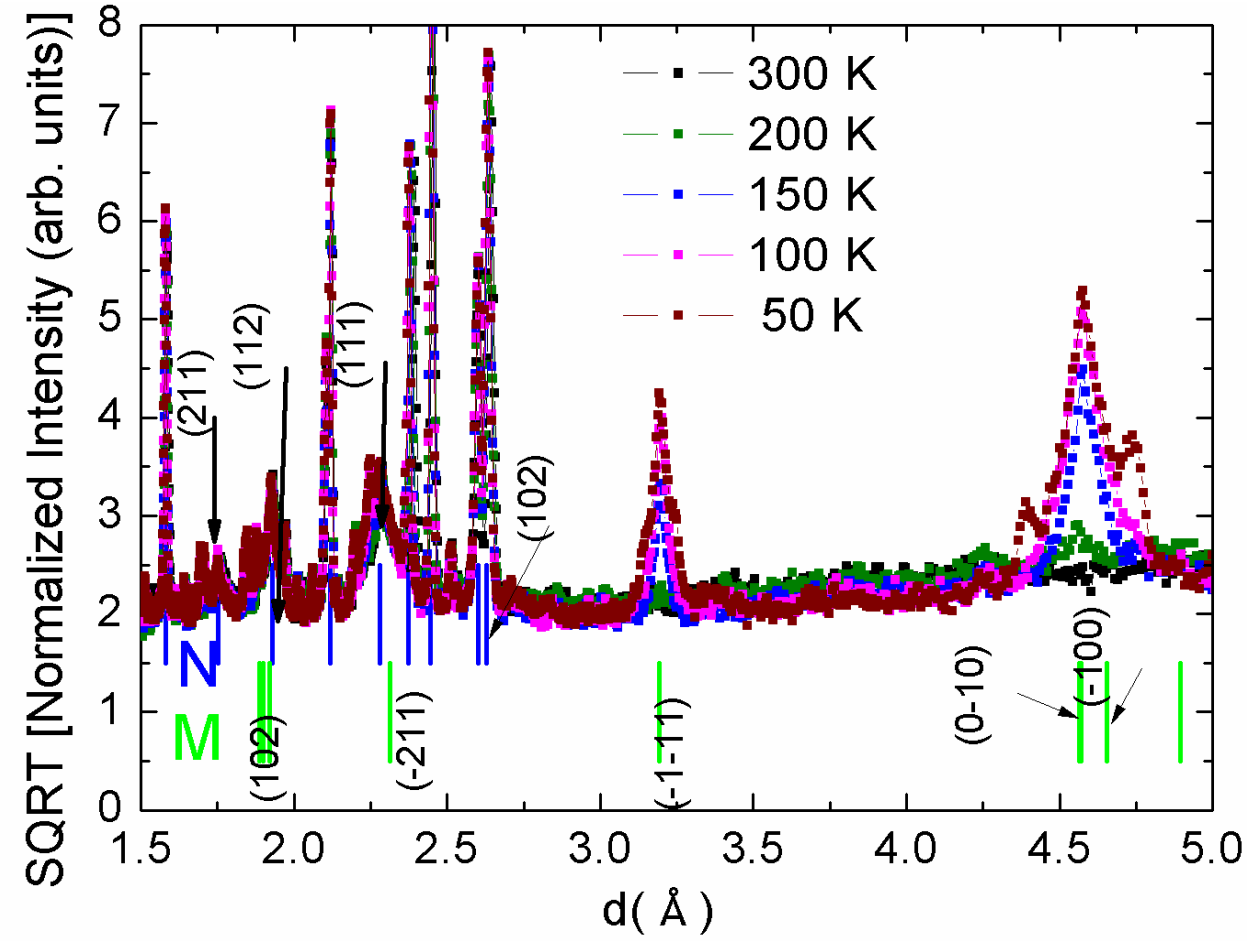

Figure 4.47 NPD pattern showing the square root of the intensity along y-axis and d-spacing along x-axis. Indexing of the nuclear and magnetic peaks is shown with the blue and green ticks, respectively.

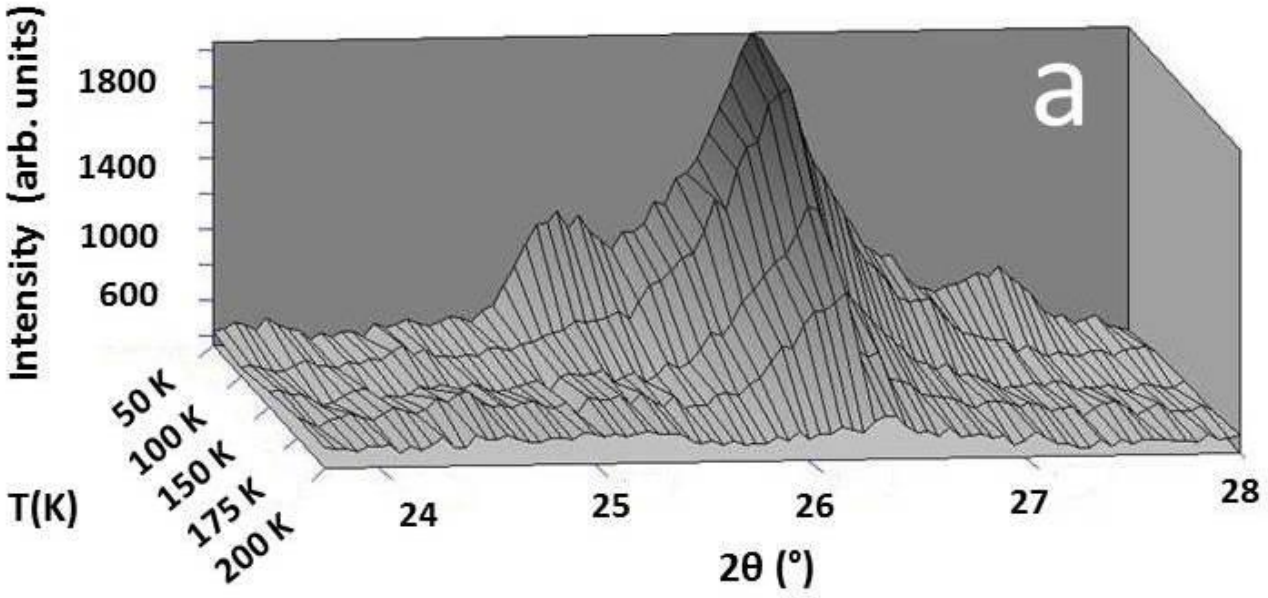

Figure 4.48 (a) A 3D plot of the 2θ=26 deg (4.59 Å) magnetic peak and it satellites on the temperature scans of 200 K, 175 K, 150 K, 100 K and 50 K.

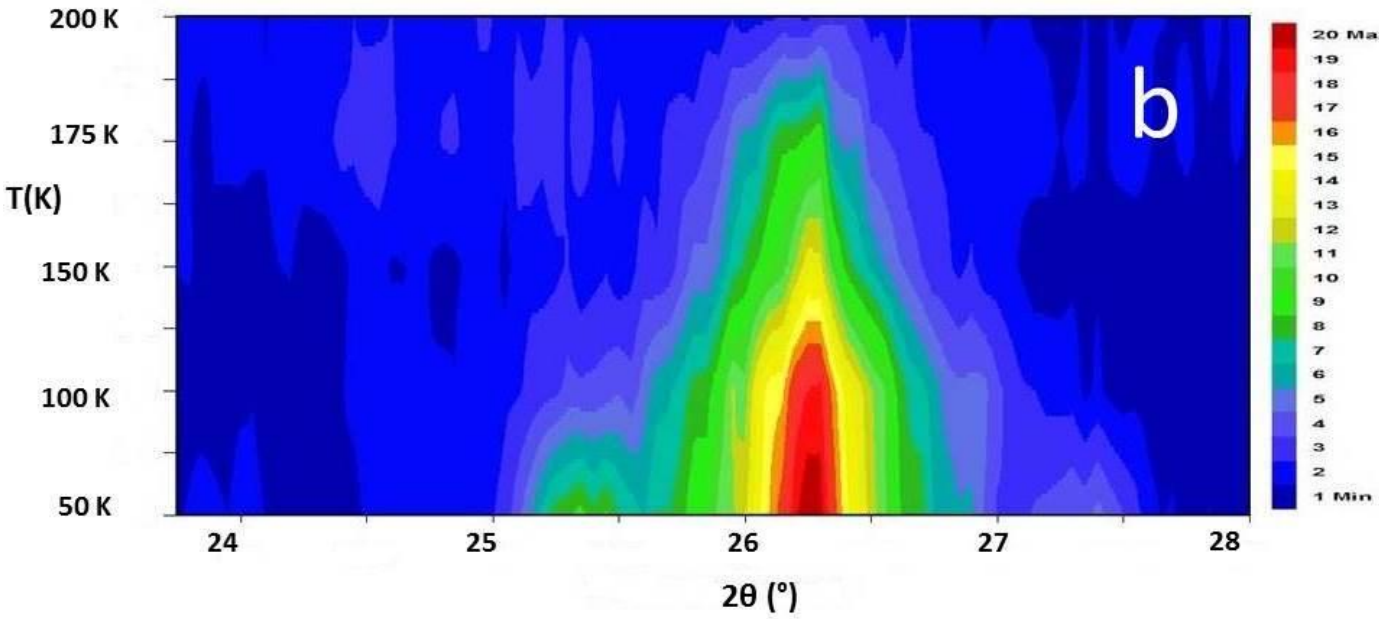

Figure 4.48 (b) The magnetic peak of the 2θ=26 deg (4.59 Å) and its satellites plotted in a two dimensional (2D) contour map

4.7.2 Time of Flight (TOF) Neutron Diffraction Data of β-$NaMnO_2$ obtained at the WISH diffractometer

Neutron powder diffraction data have been obtained using a 2.7 gr sample of polycrystalline powder of β-$NaMnO_2$ sealed on a vanadium can of internal diameter 8 mm (Ø 8 mm). The experiment was carried out on the WISH diffractometer, at target station 2 in the Rutherford Appleton lab (ISIS-RAL) in United Kingdom. The main advantage of the WISH is the higher resolution in comparison with other neutron diffractometers.[219]

The purpose of the neutron's experiment on WISH was twofold. First the data obtained from BT1 (Figure 4.44 (a) and 4.44 (b)), showed excessive broadening, overlapping peaks, and asymmetric satellites reflections at long d-spacings, which yield the necessity of higher resolution neutron diffraction data. The second goal was to investigate the exact temperature of the magnetic transitions which occurred at the temperature regions around 200 K and 80-100 K according to the BT1 data (Figures 4.46 and 4.47). For this reason temperature scans of small steps were carried out. The main aim was to relate the neutron powder diffraction results with a possible symmetry breaking mechanism based on the time reversal and space inversion analysis of the crystal and magnetic structures. This correlation would offer a great insight on the magnetodielectric properties that have been observed at 90 K and 200 K for the β-$NaMnO_2$.

4.7.2.1 Three Phase Le Bail Analysis

4.7.2.1.1 Pattern obtained at 300 K

The first priority was to analyze the pattern obtained at 300 K to figure out the structural behavior. As seen already from the 300 K pattern of the BT1, the two phase Le Bail analysis (Figure 4.45) resulted in an improved indexing since it could predict more of the observed reflections, in comparison with the one phase Le Bail analysis (Figure 4.44). Taking into account that the energies of the two polymorphs are nearly equivalent [201] the formation of intermediate structures at a rather low energetic cost seems rather possible.

Based on this assumption, a third phase was added in the theoretical model in order to account for the reflections that could not be indexed neither by the β-$NaMnO_2$ phase nor the α-$NaMnO_2$. The third phase that was added resembled to that of α-$NaMnO_2$ but the c-cell parameter was same to that of the β-$NaMnO_2$, namely c= 6.323 Å, and the angle b=102.8 deg. The addition of α-$NaMnO_2$ as a third phase with the c-parameter of β-$NaMnO_2$ is not arbitary. It is based on the thought of the possible elongation of the α-$NaMnO_2$ c-parameter (~5.85 Å) along the c-axis due to the coexistence of the α phase with the β-$NaMnO_2$.

The result of the Le Bail fit is demonstrated in Figure 4.49. The reflections predicted for each phase is shown with tick marks of different colours. The fit with three phases, has an overall better result in comparison with the equivalent analysis that were carried out with only one (β-$NaMnO_2$, Figure 4.44 (a) or two phases (β-$NaMnO_2$ and α-$NaMnO_2$, Figure 4.45). This improvement is also presented in Table 4.7. The addition of the α-$NaMnO_2$ phase with the c-parameter of β-$NaMnO_2$ (6.3 Å) results in the indexing of experimental reflections that were not predicted otherwise, such as the asymmetric peak at 6.2 Å.

A better view of the fit is presented in Figure 4.50, showing a detail of the d-spacing between 1.3 Å and 3.3 Å. A quick way to estimate the goodness of the fit is the blue line, which does not show intense ups and downs, meaning that the position and the intensity of the calculated and the experimental reflections are in good agreement. Although the shape of the experimental peaks with those predicted by the theoretical model does not match perfectly (the peak shape was the "T.O.F pseudo-Voigt from the FullProf Suite), the broadening of the reflections is fairly well described. Still though, the complete overllaping of some nuclear peaks still remains, thus the quality of this fit is not adequate in order to perform a Rietveld Refinement for the solution of the crystal structure.

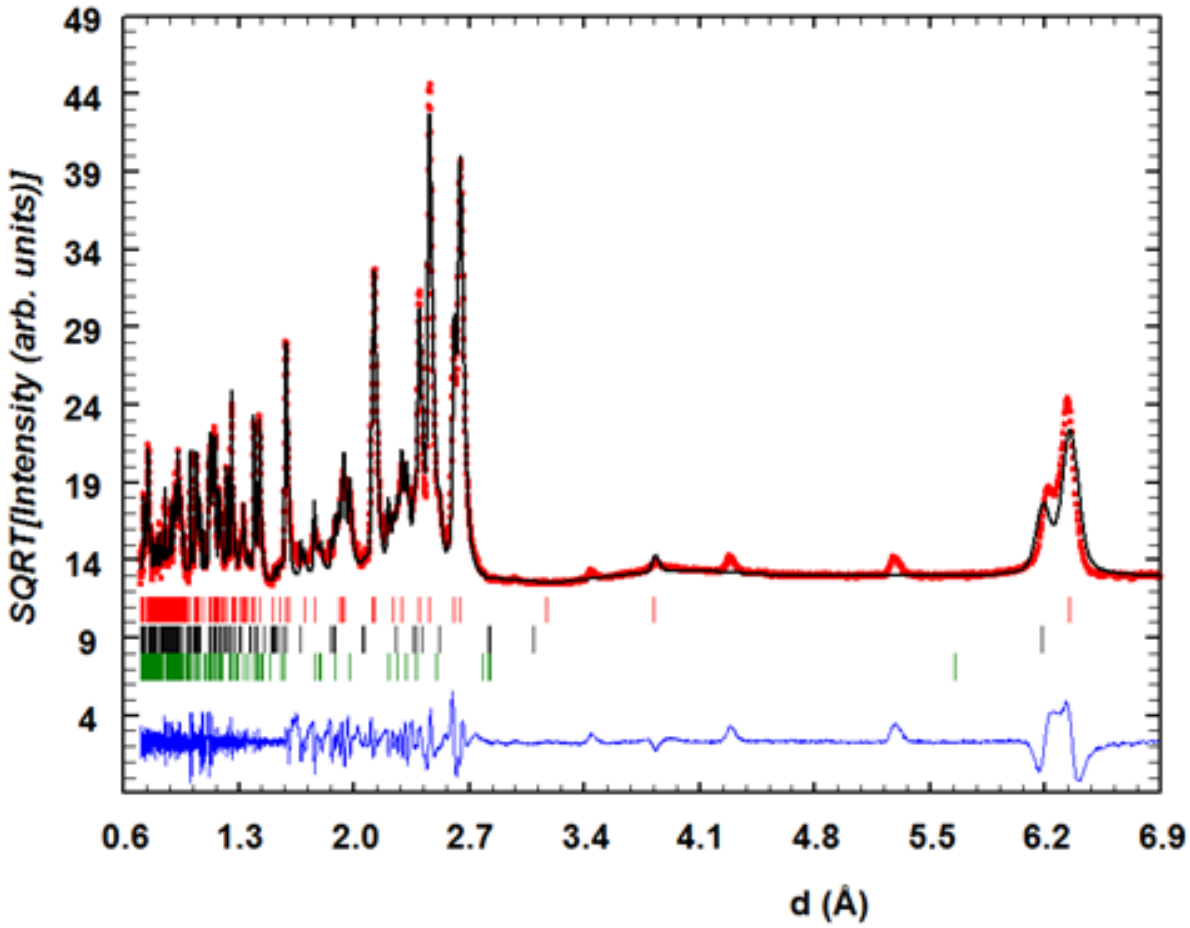

Figure 4.49 NPD pattern of the WISH diffractometer analyzed according to a three phase LeBail refinement. The experimental data are displayed with the red spots and calclulated profile is shown with the continuous black line. The red, black and green tick marks show the predicted reflections from three following phases.

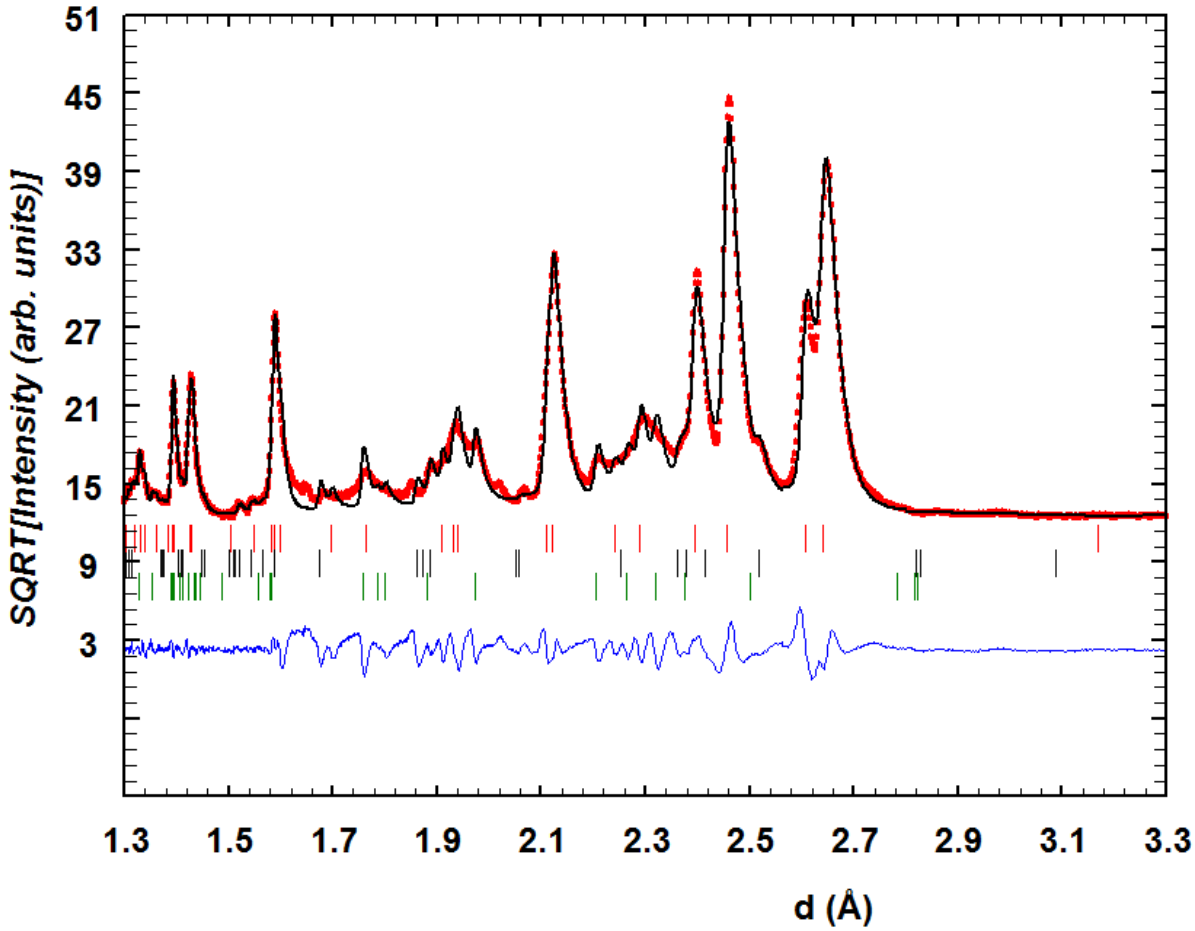

Figure 4.50 A detail of Figure 4.49 showing the d-spacing between 1.3- 3.3 Å. The majority of the peaks can be indexed with the three phases of the Le Bail fitting. The broadening of the peaks predicted by the theoretical model is in good agreement with the observed experimental data.

Comparison Le Bail fits with the use of one, two and three phases at 300 K.

In order to present the improvement obtained from the addition of the second and third phase in the Le Bail analysis of the β-$NaMnO_2$ we have compared the results obtained from the one, two and three phase fits. We present the Figure 4.51 in which the red line corresponds to the experimental data and the black line to the Le Bail fit. The upper panels of Figure 4.51 (i.e Figure 4.51 (a) and (b)) show two critical areas of the fits obtained by

the use of only one phase (β-$NaMnO_2$). The same Q-areas are presented in the lower panels (Figure 4.51 (c) and (d)) which have been obtained from the three phase Le Bail fit. Comparison of the a and c panel of Figure 4.51 shows that the indexing of the shoulder-like peak at Q= 1.01 $Å^{-1}$ has been achieved due to the addition of α-$NaMnO_2$ as second phase. Similarly, panels b and d compare the Q-area between 3 and 4.2 $Å^{-1}$ where it is obvious that the addition of the second and third phase describes well the wide and overlapping peaks at q between 3.2 $Å^{-1}$ and 3.8 $Å^{-1}$.

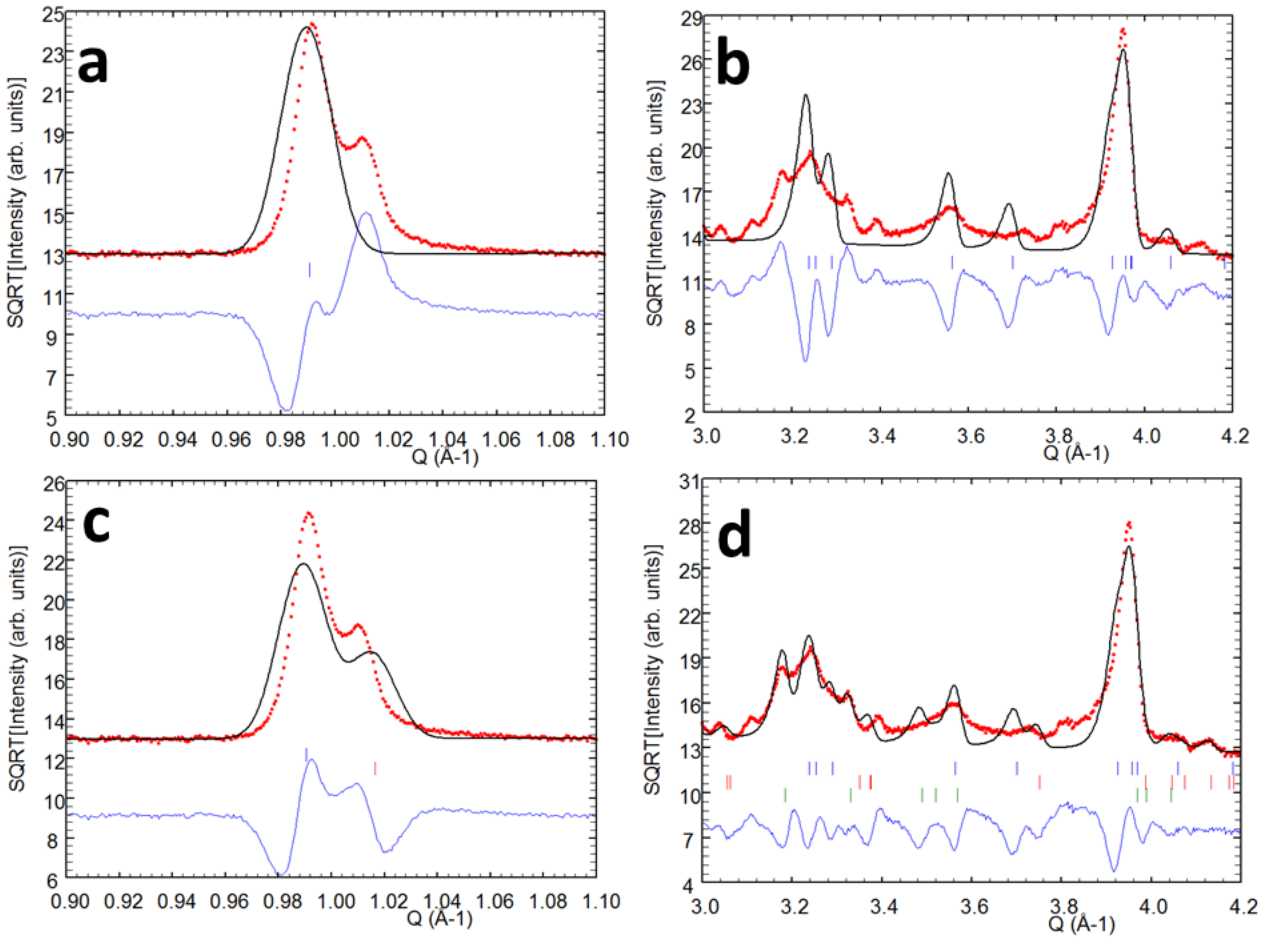

Figure 4.51 Comparison of the Le Bail fits obtained by the use of one phase (β-$NaMnO_2$) in panels (a) and (b) and three phases (β-$NaMnO_2$, α-$NaMnO_2$ and α-$NaMnO_2$ with the same c-parameter as β-$NaMnO_2$) in panels (c) and (d). Two critical Q areas are shown the 0.90-1.10 $Å^{-1}$ and the 3.0-4.2 $Å^{-1}$.

T=300 K					
1 phase	**1st phase orthorhombic β-$NaMnO_2$**				
a	4.7854(5)				
b	2.8572 (3)				
c	6.3269(7)				
V	86.511(1)				
R_{wp}	30.1%				
R_{exp}	2.16%				
χ^2	194				
2 phases	**1st orthorhombic β-$NaMnO_2$**		**2nd phase. αNaMnO$_2$ C$_{2/m}$ (same c)**		
a (Å)	4.7860(5)		5.76267(2)		
b(Å)	2.85746(2)		2.81706(8)		
c(Å)	6.32742(6)		6.32181(6)		
V (Å^3)	86.538(1)		100.088(4)		
		β(°)	102.7727		
R_{wp}	23.0 %				
R_{exp}	2.16%				
χ^2	114				
3 phases	**1st orthorhombic β-$NaMnO_2$**		**2nd phase –αNaMnO$_2$ C$_{2/m}$(same c)**		**3-phase αNaMnO$_2$-C2/m(different C)**
a	4.78695(4)		5.71910(2)		5.75932 (1)
b	2.85734(2)		2.81593(7)		2.78385 (6)
c	6.32747(5)		6.31956(5)		5.80635 (1)
V	86.547(1)		99.292(5)		90.699(3)
		β(°)	102.67945		103.02283
R_{wp}	17.8 %				
R_{exp}	2.16%				
χ^2	67.9				

Table 4.7 Structural parameters and reliability factors of the Le Bail fits obtained from the analysis of the neutron diffraction data at 300 K of β-$NaMnO_2$ with the use of one, two and three phases.

The variation of the most critical parameters in the three different Le Bail fits is shown in Table 4.7. If we compare the quality factor χ^2 of the three fits, we see that the one which a more reliable result, corresponds to the three phase LeBail fit ($\chi^{2\sim}$68, whereas for the one and two phase fits χ^2~194 and χ^2~114, respectively.

4.7.2.1.2 Neutron Diffraction Pattern obtained at 5 K

The same procedure has been followed for the analysis of the 5 K pattern obtainded from the WISH diffractometer.

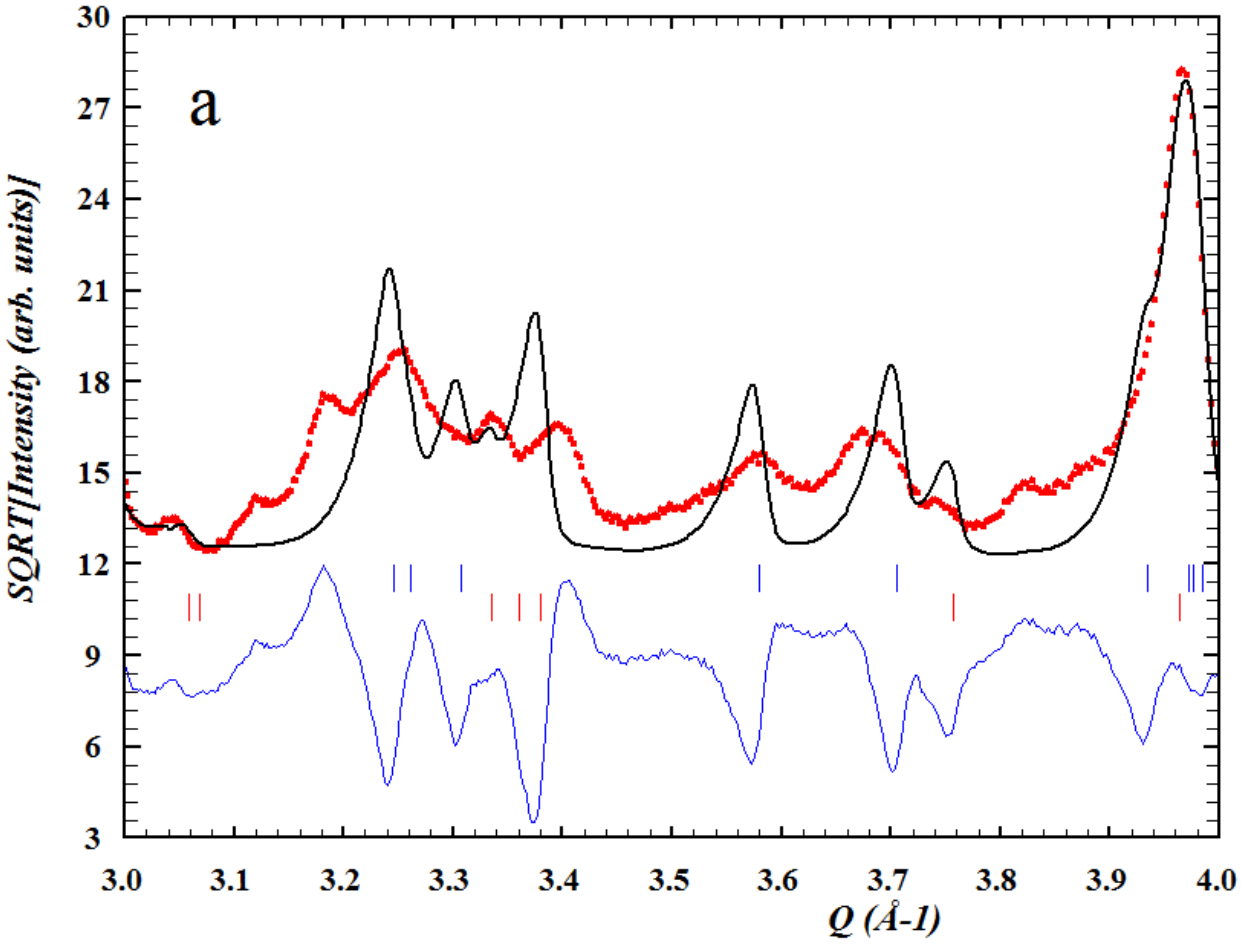

Figure 4.52 (a) Comparison of the Le Bail analysis of the 5 K NPD pattern Panel (a) with the use of two phases

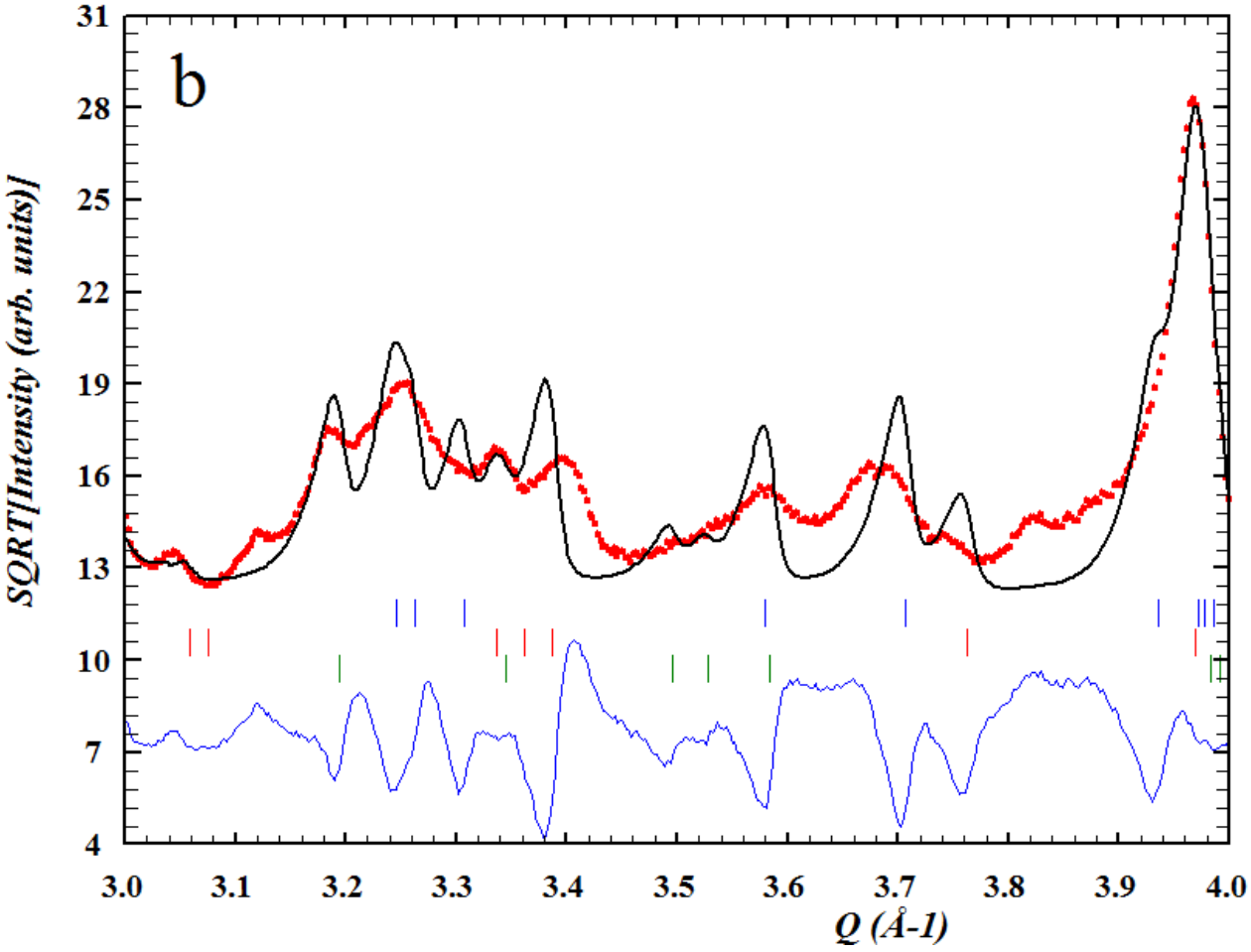

Figure 4.52 Comparison of the Le Bail analysis of the 5 K NPD pattern. Panel (b) with the use of three phases showing the improvement obtained in the three phase analysis.

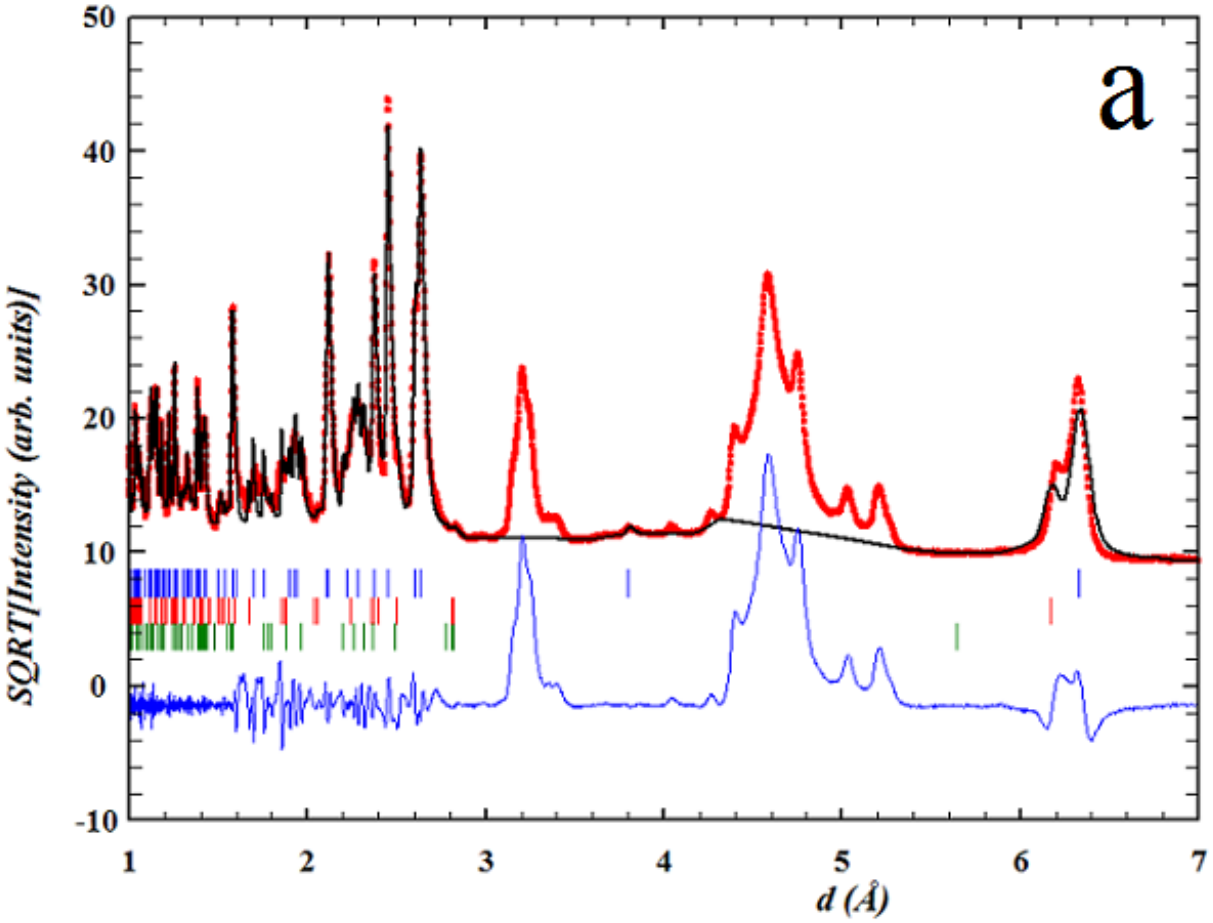

Figure 4.53 (a) Le Bail fit of the neutron data at 5 K with the use of three phases: β-$NaMnO_2$, α-$NaMnO_2$ with the same c-parameter as β-$NaMnO_2$ and α-$NaMnO_2$ shown whose indexing corresponds to the blue, red and green tick marks, respectively. Panel (a) shows the d-spacing in which the magnetic peaks appear.

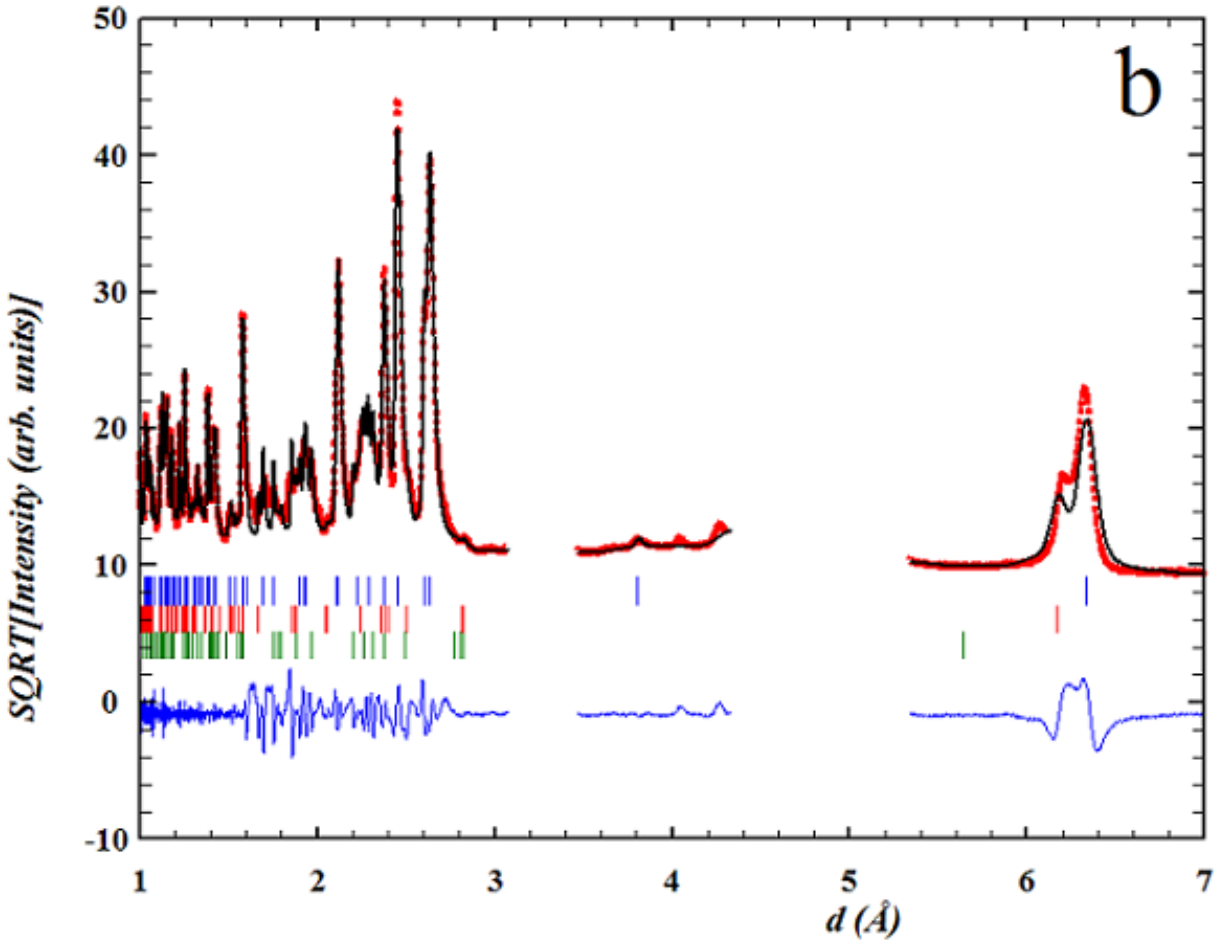

Figure 4.53(b) Le Bail fit of the neutron data at 5 K with the use of three phases: β-$NaMnO_2$, α-$NaMnO_2$ with the same c-parameter as β-$NaMnO_2$ and α-$NaMnO_2$ shown whose indexing corresponds to the blue, red and green tick marks, respectively (b) the regions in which the magnetic peaks appear have been excluded from the analysis.

T=5 K					
1 phase	**1st phase orthorhombic β-$NaMnO_2$**				
a	4.7454(5)				
b	2.8550(3)				
c	6.3169(8)				
V	85.585(1)				
R_{wp}	29.9%				
R_{exp}	1.59%				
χ^2	356				
2 phases	**1st orthorhombic β-$NaMnO_2$**		**2nd phase. α-$NaMnO_2$ $C_{2/m}$ (same c)**		
a (Å)	4.7517(7)		5.7839(9)		
b(Å)	2.8544(3)		2.8011(6)		
c(Å)	6.3160(7)		6.31544(7)		
V ($Å^3$)	85.668(1)		99.778(3)		
		β(°)	102.8046		
R_{wp}	21.5%				
R_{exp}	1.64%				
χ^2	171				
3 phases	**1st orthorhombic β-$NaMnO_2$**		**2nd phase α-$NaMnO_2$ $C_{2/m}$(same c)**		**3-phase α-$NaMnO_2$ C2/m(different C)**
a	4.7517(6)		5.7840(9)		5.7557(3)
b	2.8543(2)		2.7896(6)		2.7826(6)
c	6.3156(5)		6.3151(6)		5.7785(2)
V	85.661(1)		99.362(3)		90.192(3)
		β(°)	102.8040		102.9581
R_{wp}	15.8%				
R_{exp}	0.99%				
χ^2	78.1				

Table 4.8 A comparative table which shows structural parameters and some of the reliability factors from the Le Bail analyses which have been carried out using one, two and three phases.

Similarly the analysis begun with the use of β-$NaMnO_2$ as one phase and then we continued with the addition of α-$NaMnO_2$ with the same c-parameter as a second phase and the α-$NaMnO_2$ as the third phase. Figure 4.52 shows a detail (Q-area from 3.0-4.0 $Å^{-1}$) which presents the analysis obtained from the use of two (β-$NaMnO_2$ and α-$NaMnO_2$ with the same c parameter as β) and the addition of the third phase the α-$NaMnO_2$. As it has

been observed for the 300 K, the theoretical model of the three phases describes better the wide overlapping peaks. The entire d spacing- area of the 5 K NPD pattern is presented in Figure 4.53: panel (a) contains the areas in which the magnetic peaks emerged. On the contrary the areas of the magnetic peaks have been excluded from Figure 4.53 (b).

Comparison of the crystallographic parameters on the phases that have been used for the Le Bail analysis and the quality factors of each fit are displayed in Table 4.8. Here we see an impressive improvement regarding the goodness of fit χ^2 which was reduced from 356% of the one phase to 79% of the three phase analysis.

4.7.2.2 Temperature Evolution of the Magnetic Bragg Scattering

The temperature evolution of the magnetic Bragg peaks observed at the q ($Å^{-1}$) areas of 1.374 $Å^{-1}$ and 1.96 $Å^{-1}$ is demonstrated in the Figure 4.54 (a) and 4.54 (b). The progression of these peaks is presented with the temperature scans of 300 K, 200 K, 195K, 170 K, 130 K, 100 K, 90 K, 80 K, 71 K, 56 K, 5 K. During the experiment more scans were taken, which are not demonstrated in the figure for reasons of clarity.

The commensurate magnetic order marked by single but broad reflection emerges at 200 K. The intensity of this peak is saturated at 150 K. Both peaks, namely at 1.374 $Å^{-1}$ and 1.96 $Å^{-1}$ are profoundly broad. The incommensurate structure emerges at 90 K, since the satellite reflections at Q=1.374± δ where δ≅0.053 first appear at 90 K. The first satellite at 1.326 $Å^{-1}$ is already visible at 90 K whereas the second one at 1.433 $Å^{-1}$ is clearly observed at 80 K. The satellite reflections, rise very close to the main peaks, overlaping with each other. Moreover, magnetic Bragg peaks of smaller intensity shown in Figure 4.55 appear at the Q- vicinity of 1.21 $Å^{-1}$ and and 1.253 $Å^{-1}$ below 90 K. These weak magnetic peaks which were visible only with the high flux and good resolution of the WISH diffractometer at long d-spacings, are probably part of the incommensurate magnetic order not resolved before by BT1.

It is interesting to point out that the transition to the incommensurate magnetic order seems to have an effect to the T-evolution of the lattice volume. This can be observed in Figure 4.56 (derived using the FullProf Suite in the Sequential Analysis option) which shows a negative T-expansion of the orthorhombic β-$NaMnO_2$ cell.

The temperature evolution of the magnetic Bragg peaks of the Q= 1.374 $Å^{-1}$ (main peak) and Q= 1.326 $Å^{-1}$ and 1.433 $Å^{-1}$ (left and right satellite, respectively) is displayed in Figure 4.57. The upper panel (a) of Figure 4.57 shows the Normalized Intensity versus temperature for the main and the satellite peaks (the normalization was done with respect to the highest value of the main peak's intensity). In order estimate the temperature evolution for the intensity of the magnetic peaks, good quality fits of the peaks shown in Figure 4.52 were required. The analysis of the data was done using the program DAVE downloaded from the NCNR's webpage. [220] The magnetic reflections were fitted with Lorentzian functions. More information for the methodology used with the DAVE software is provided in the C Appendix.

Panel (b) of Figure 4.54 shows the dependence of the center of the peaks (Q ($Å^{-1}$)) with the temperature evolution. The intensity of the satellite reflections saturates below 80 K whereas the saturation point for the main peak is around 100 K. The reflection at 1.326 $Å^{-1}$ shows higher intensity in comparison with the one at 1.433 $Å^{-1}$, as already seen by the asymmetry observed in the two peaks in Figure 4.54. The current analysis showed no significant T dependence for the position (Q) of the main peak for the paramagnetic (PM), commensurate (CM) and incommensurate phase (ICM). On the contrary the satellite reflections shift further from the main peak at the temperature range of 80 K-90 K whereas their position remains stable at below 80 K.

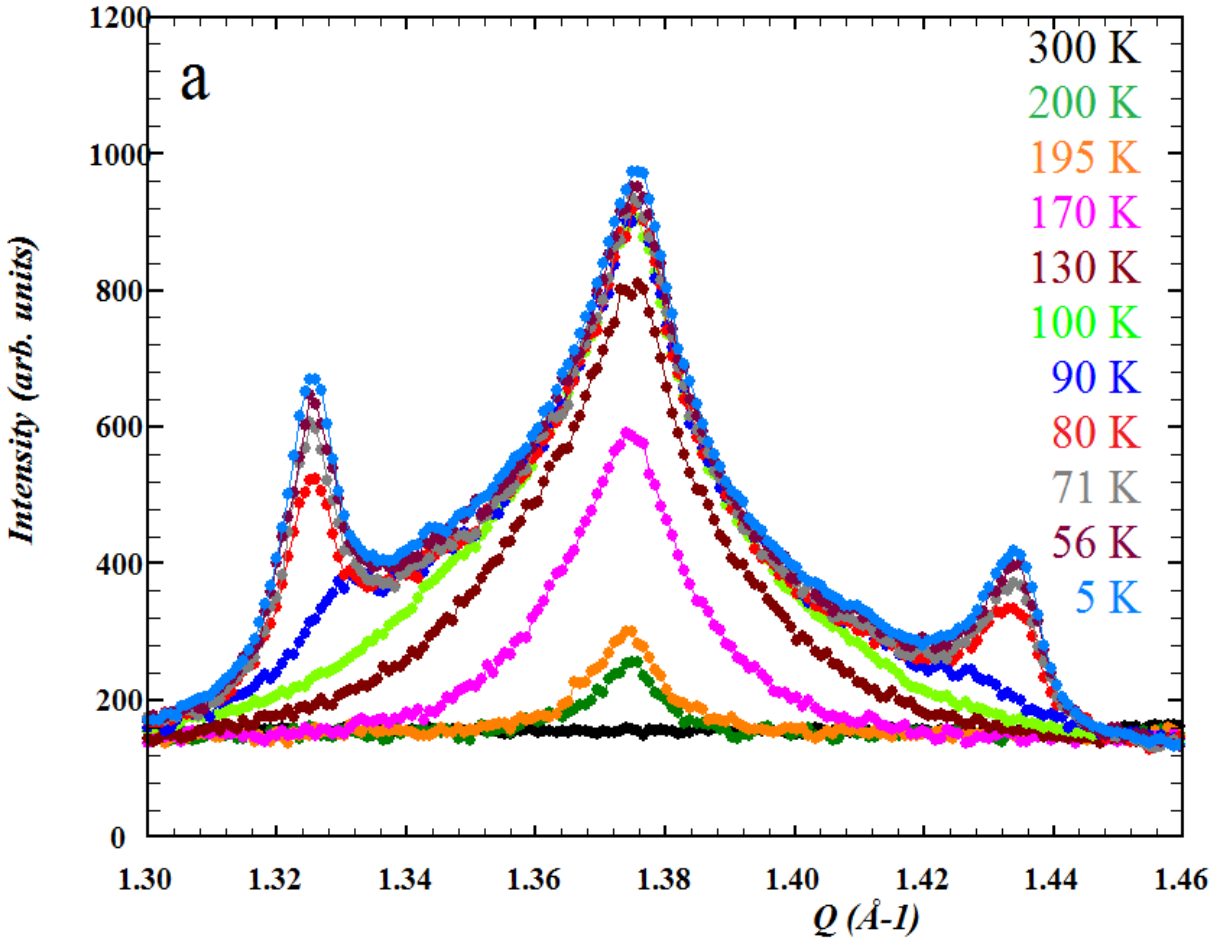

Figure 4.54 (a) Temperature evolution of the magnetic reflections and their satellites at a) Q= 1.374 $Å^{-1}$.

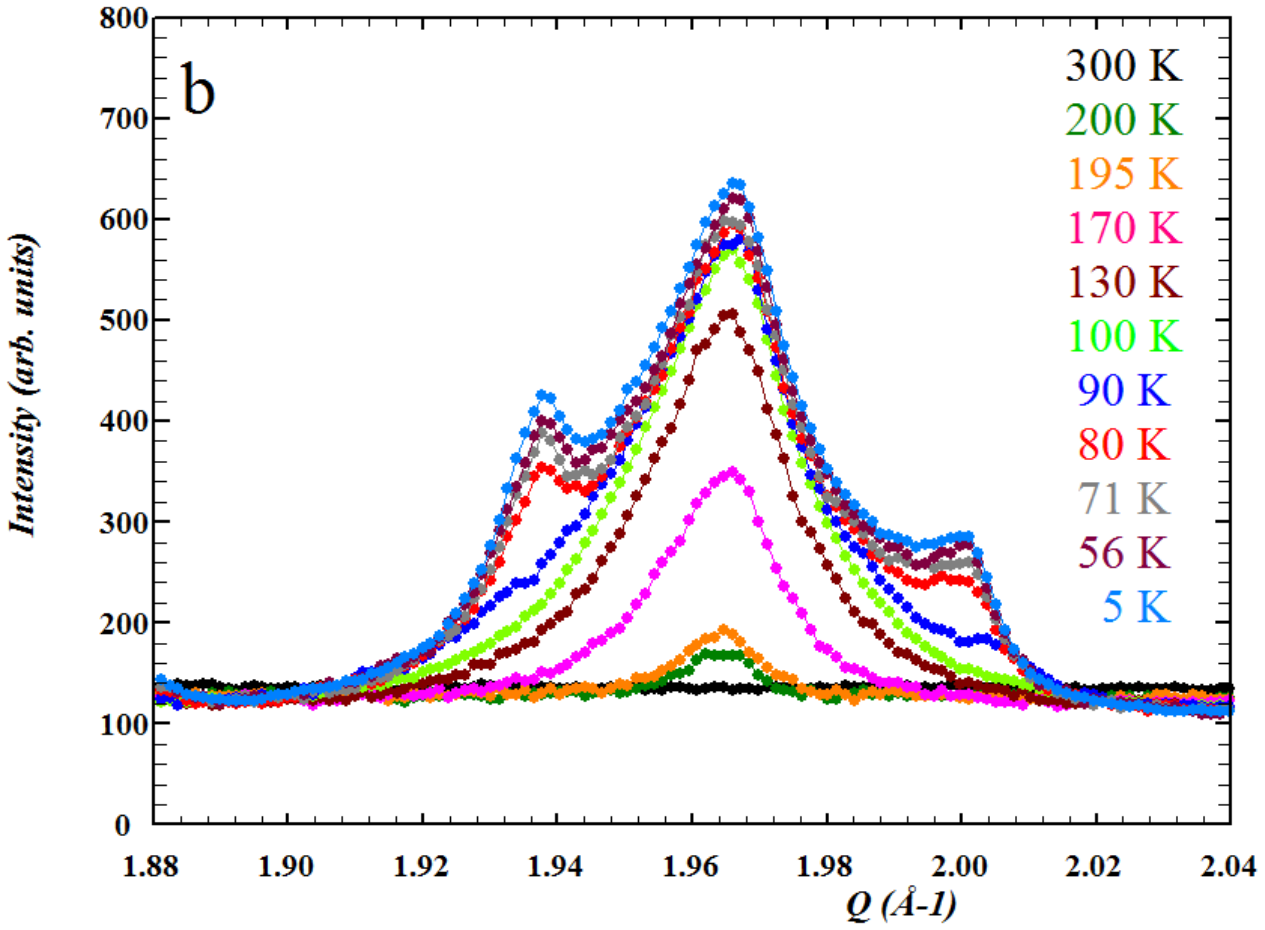

Figure 4.54 (b) Temperature evolution of the magnetic reflections and their satellites at Q= 1.96 $Å^{-1}$.

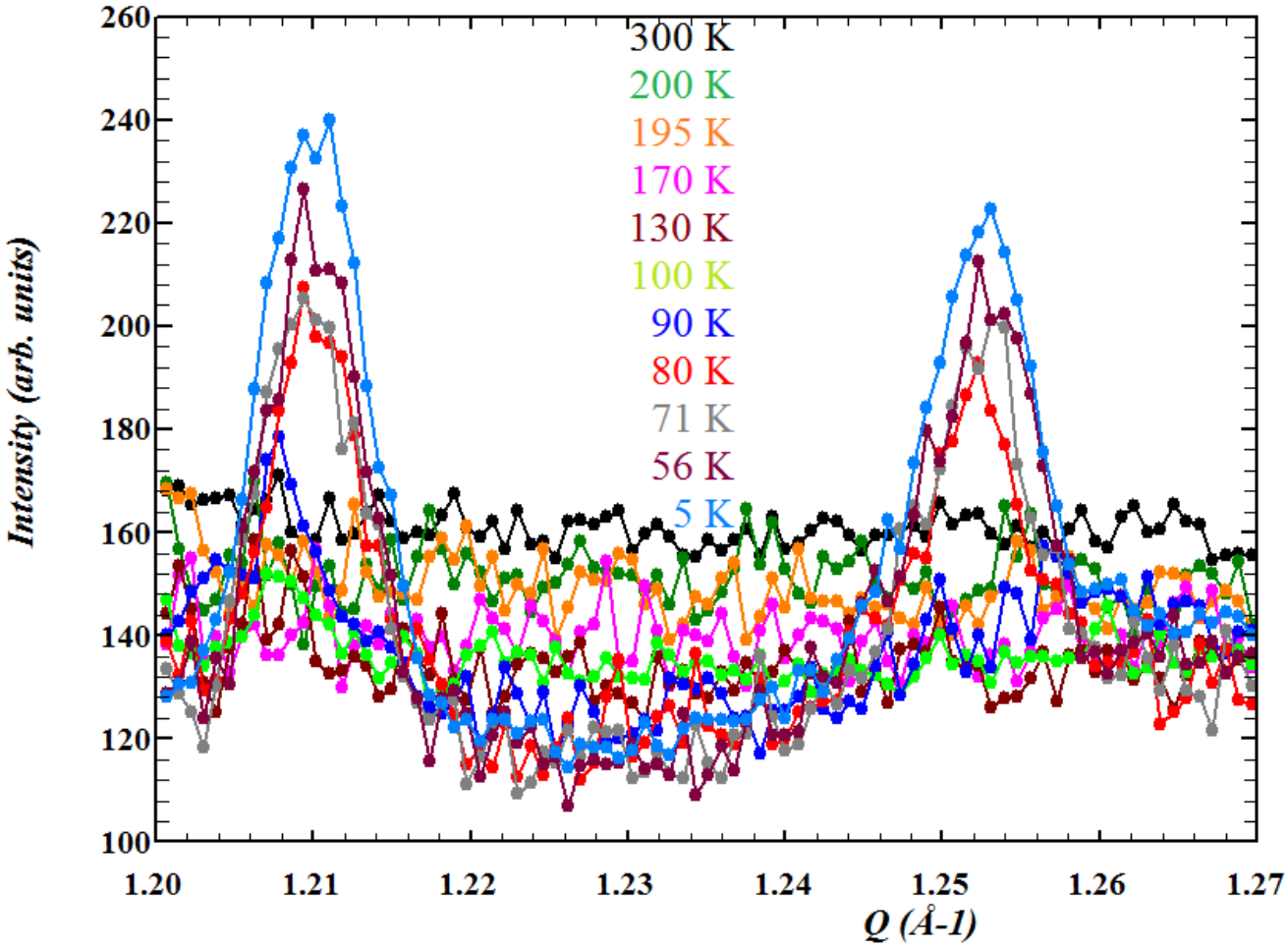

Figure 4.55 Temperature evolution of the magnetic reflections Q= 1.21 $Å^{-1}$ and b) Q= 1.25 $Å^{-1}$ which emerge below 90 K.

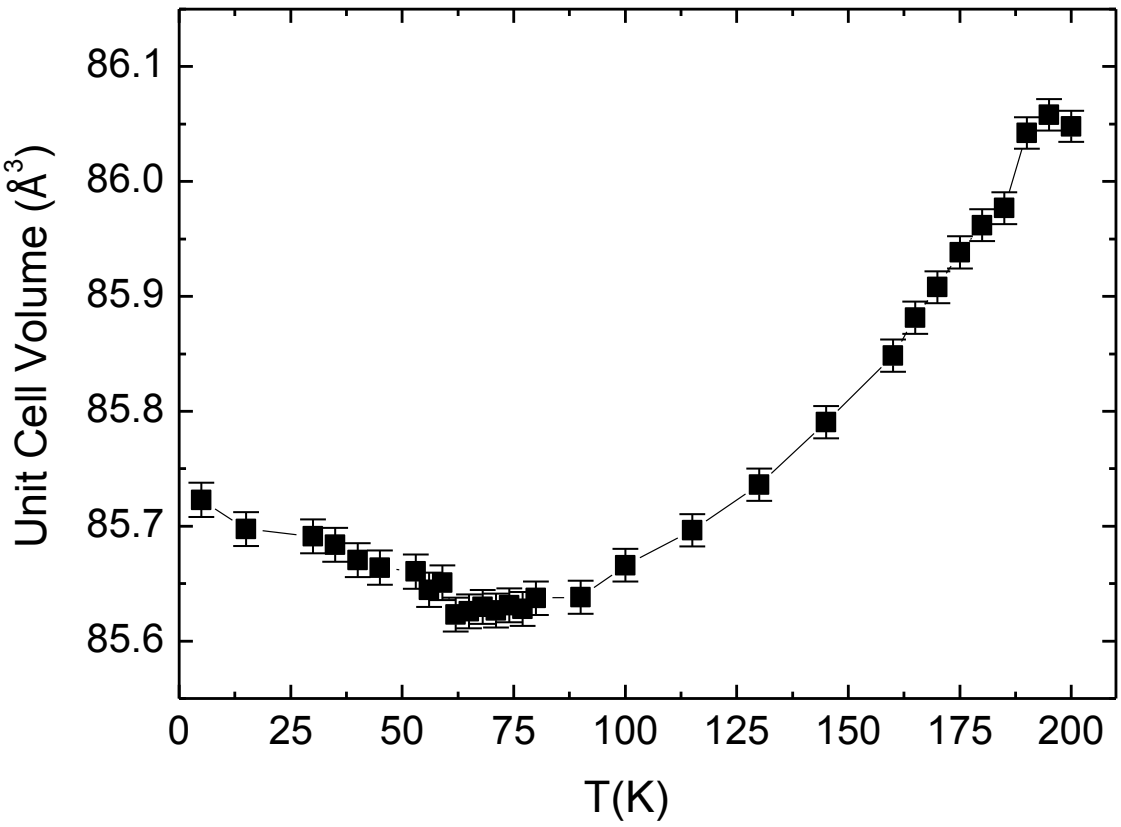

Figure 4.56 Unit cell volume of β-$NaMnO_2$ versus temperature: Negative thermal expansion of the nuclear cell volume at the commensurate to incommensurate transition of 90 K

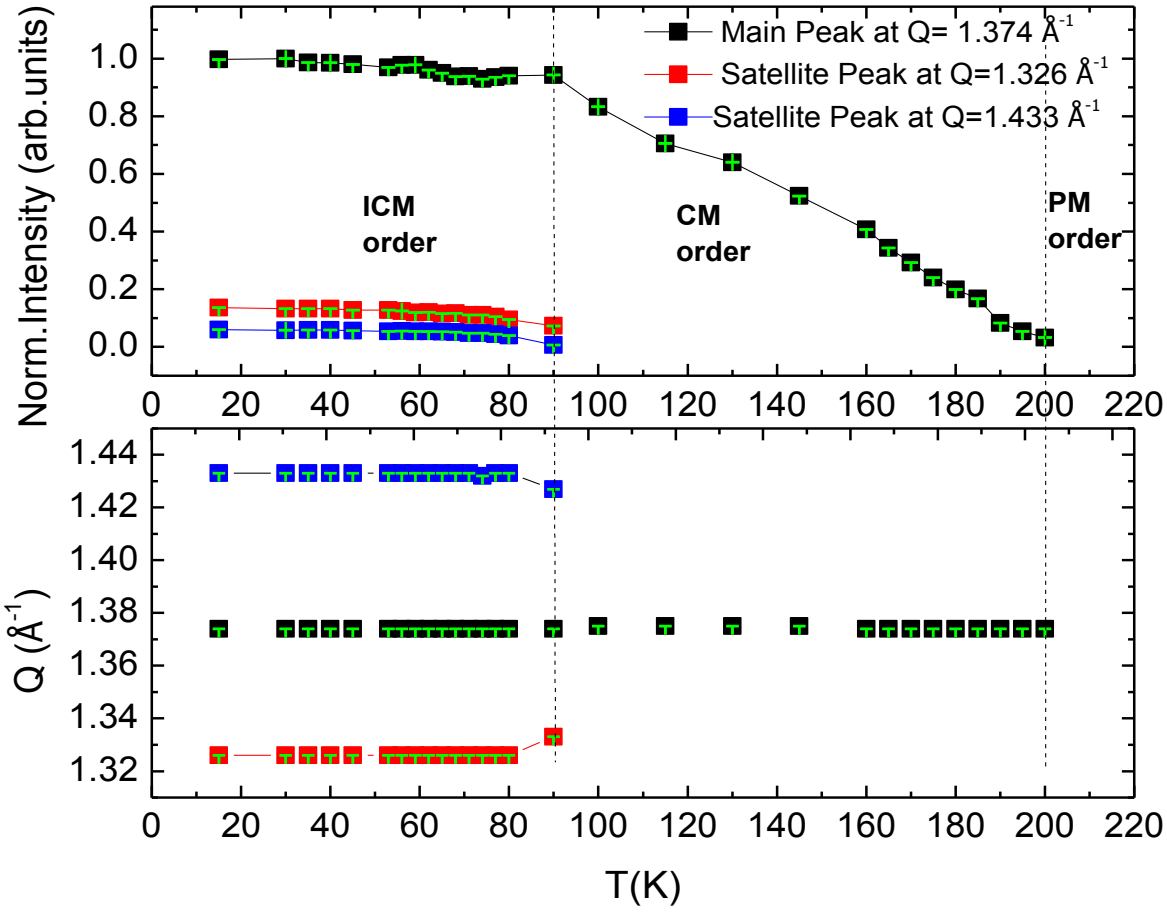

Figure 4.57 Temperature evolution of the normalized intensity of the main magnetic peak at d=4.59 Å and its satellite reflection's at 4.71 Å and 4.39 Å.

Estimation of the critical exponent β for the CM and ICM magnetic transitions.

A common way to describe a magnetic phase transition is by defining its magnetic critical exponents. [126, 221, 222] The critical exponents are strongly related with the dimensionality of the system d, the dimensionality of the order parameter D and the type of interactions: short or long range. These exponents are related to specific physical properties with power laws. For example the specific heat is related with the exponent α with the equation $t^{-\alpha}$,

where t is the reduced temperature t= ($T-T_c/T_c$) (T_c is the critical temperature of the transition).

The intensity of the magnetic peaks versus temperature, is fitted upon the equation[223, 224, 225]

$$I_M=I_o\left(1-\frac{T}{T_N}\right)^{2\beta} \quad \textbf{(4.8)}$$

Where I_M is the intensity of the magnetic peak, T_N is the temperature of the magnetic ordering and the value of the critical exponent β is characteristic of the dimensionality of the spins' interactions.[221] Some typical values for the critical exponent β are: 0.5 according to the Mean Field theory (MF), 0.32 for a 3D Ising and 0.23 for 2D XY magnetic system.[225]

The power law of equation 4.8 was fitted upon the normalized intensity versus temperature of the curves presented in Figure 4.57. The fits for the estimation of the critical exponent β are shown in Figure 4.58. First, the values of 0.5 (MF), 0.32 (3D Ising) and 0.23 (2D XY) were set as fixed parameters in the power law and presented with the purple, orange and grey dashed curves, respectively. The value β=0.5 for the main magnetic peak and T_c= 202 (±1.18) K yielded an acceptable fit (Adj.R- Square=0.949). Moreover, when the fit was done at the same area (175-200 K) and the value of β was freely refined, it derived the value of β= 0.495 (±0.026) which is quite close to 0.5 (the critical temperature was fixed at T_c= 200 K and the Adjustment R-Square was 0.896). The value of β= 0.5 for the critical exponent, derived much better fit than the equivalent analysis with the β= 0.32 and β= 0.23 (see, Appendix C, Table C.1 for details on the fits). According to this analysis we suggest that β-$NaMnO_2$ has a critical exponent of β= 0.5 for the commensurate magnetic transition, a value which is consistent with the predictions of the Mean Field theory.

The same procedure of fits has been followed for the estimation of the β exponents which correspond to the magnetic satellite reflections at the temperature area of 77-90 K. When the values 0.5, 0.32 were applied for the β exponent as fixed parameters for both curves of the satellite peaks, the quality fits were poor in comparison with the fits obtained for the

value of β= 0.23. When β was freely refined and the T_c was set to 90 K, the fit derived the value of β= 0.115 for the satellite at 1.326 $Å^{-1}$ and β= 0.155 for the reflection at 1.433 $Å^{-1}$ with acceptable Adjustment R-Squares.

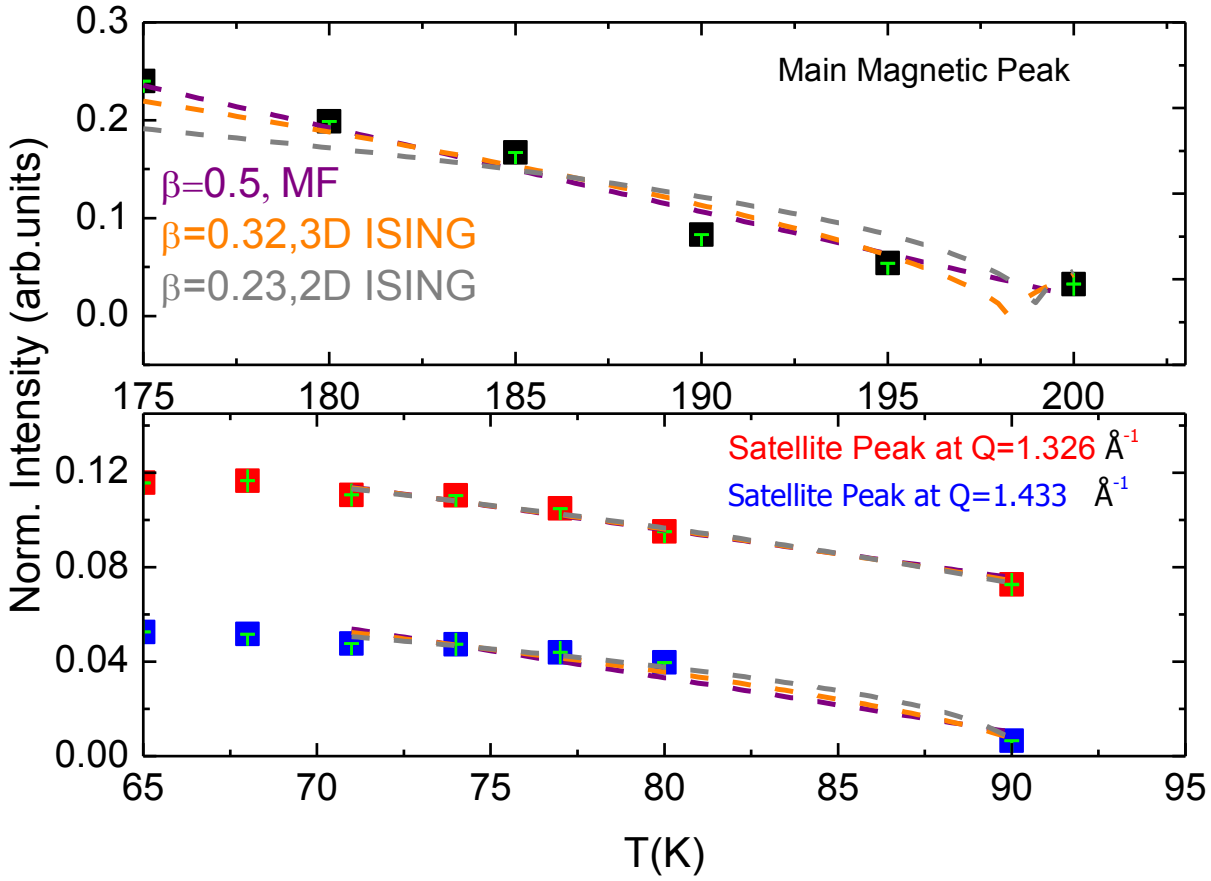

Figure 4.58 Fittings of the main (upper part) and the satellite peaks (lower part) with the power law of equation 4.1 for different values of the critical exponent β. The errors in the estimation of each intensity point are shown with the light green error bars. The values of β: 0.23, 0.32 and 0.5 have been tested for all the curves and shown with the grey, orange and purple color, respectively. The best quality fits yielded the value β= 0.5 for the main curve and β= 0.23 for the satellite peaks at Q=1.326 $Å^{-1}$ and Q=1.433 $Å^{-1}$, respectively.

Although the value of β= 0.155 is within the error to that of a 2D-Heisenberg universality class as found for the magnetic order parameter of other systems as $Fe_{1+x}Te$[226] and the β= 0.115 is quite close to the β= 0.125 which describes the ideal 2D Ising system, we found much better agreement between the experimental curves and the theoretical model applied for the value of β= 0.23 for both satellite reflections. So, we suggest that the β-$NaMnO_2$ behaves as a 2D XY system below the incommensurate transition at 90 K.

4.8 Results and Discussion

In chapter 4 we presented the characterization methods and the results obtained from the investigation of the polycrystalline β-$NaMnO_2$ compound. The novelty in the research of β-$NaMnO_2$ is focused on two major findings: a) the magnetodielectric coupling evident by the appearance of two dielectric anomalies at the temperatures (90 K and 200 K) where magnetic transitions occur, b) the inhomogeneous microstructure of the β-$NaMnO_2$ resulting from the coherent intergrowth of the β-$NaMnO_2$ and the α-$NaMnO_2$ phase, as observed by electron diffraction high resolution transmission electron microscopy and verified by synchrotron XRD data.

The magnetodielectric experiments of the powder samples of β-$NaMnO_2$, turned out to be a challenging task. There were multiple reasons for the encountered difficulty, most important of which were: a) the britlle nature of the pellets b) the history dependence of the obtained results which yields the problem of repeatability, and c) last but not least, the small physical quantities that were measured (pF and nA). Despite these complexities, we proved that the dielectric constant of β-$NaMnO_2$ shows two distinct anomalies, a broad hump at 200 K and a sharp drop at 90 K. According to the neutron powder diffraction data at 200 K, broad magnetic Bragg reflections appear, signaling the onset of an antiferromagnetic commensurate magnetic ordering, whereas at 90 K magnetic satellites emerge around the main magnetic reflections. This provides the first signature of the coupling between the dielectric and magnetic degrees of freedom. Similar behavior has been observed in other magnetoelectric systems such as the $DyMnO_5$. [157] The second sign

arises from the enchancement and the shift towards higher temperatures of the dielectric constant under the effect of external magnetic fields. The low temperature dielectric anomaly is remarkably enchacned when an increasing electric field is applied. Finally, attempts of measuring the polarization loop in the β-$NaMnO_2$ in the temperatures below 90 K resulted in indications of the possible polar character of the compound.

As mentioned before dielectric anomalies appear in the temperatures of the the commensurate transition at 200 K and the incommensurate at 90 K. The dielectric anomaly of the latter is sharper and is greatly affected when external magnetic fields are applied. Analogous findings have been reported for the $DyMn_2O_5$[157] in which colossal magnatodielectric effect has been associated with the commensurate to incommensurate magnetic transition. For the case of $DyMn_2O_5$ the effect is reported to originate from the high sensitivity of the incommensurate state to an external sensitivity.

The magnetodielectric effect has been also observed in β-$NaMnO_2$ samples that have been annealed in oxygen after the completion of the solid state synthesis, in order to produce more firm and stable pellets. X Ray powder diffraction patterns of these samples revealed strong presence of secondary phases, namely those of $Na_{0.7}MnO_2$ and α-$NaMnO_2$. Although HRTEM investigation of the annealed β-$NaMnO_2$ samples has not been carried out yet, it is very likely that high density of planar defects is caused by the existence of the secondary phases, such as antiphase boundaries which could be a factor that influences the strength of its magnetodielectric coupling.[194,227]

Figure 4.30 in section 4.5.3 shows the dielectric constant obtained from the measurements of the α and β-$NaMnO_2$ polymorphs as well as from the β-$NaMnO_2$ samples that have been annealed in oxygen. Two are the characteristics that are usefull to compare with other magnetoelectric systems: the value of the measured dielectric constant and the strength of the dielectric anomalies. The dielectric constant of both α-$NaMnO_2$ and β-$NaMnO_2$ at H=0 T and f=500 kHz, is around ε'~4-5. Other ceramic ABO_2 systems that have been characterized as magnetoelectrics, such as the $CuCrO_2$ and $AgCrO_2$ exhibit comparable values of ε' (ε'~7 for H=0 T and f=100 kHz). [50] Regarding the strength of the dielectric

anomalies and that of the magnetodielectric coupling, we should highlight the difference observed between the annealed and the as made samples. The difference is clearly seen in Figure 4.30 where the sharper dielectric anomaly appears for the annealed β-$NaMnO_2$ in comparison with those of the as made β-$NaMnO_2$ and that of the α-$NaMnO_2$ phase. Moreover, the relative change in the dielectric constant given by the ratio $\Delta\varepsilon'/\varepsilon'_o$ is around 12-14% for the α-$NaMnO_2$ and 25% for the annealed β-$NaMnO_2$.

A critical characteristic of the annealed β-$NaMnO_2$ samples is the existence of secondary phases as seen by the XRPD patterns. That in turn, leads to the formation of microscopic domains which are separated by domain walls. Systems with enchanced density of domain walls have been proved to exhibit remarkable functional properties. Domain wall functionality is linked with properties like multiferroicity,[2, 199] collosal mangetoresistance[200] and ferroelectricity. [197]

Extensive research was undertaken to unravel the complex crystal structure of the β-$NaMnO_2$. The pure β-$NaMnO_2$ crystallizes in the orthorhombic structure, Pnmm, with the following cell parameters a = 6.32 Å, b = 2.85 Å, c = 4.78 Å. The crystal structure of the β-$NaMnO_2$ polymorph is regarded as a derivative of the layered rock salt structure. The cation ordering is promoted by the charge and size difference between the Na and Mn cations.

Electron diffraction and high resolution electron microscopy certified the inhomogeneous microstructure of the β-$NaMnO_2$. High density of planar defects was explained by the presence of the α-$NaMnO_2$ phase. Twin planes are formed by the distorted coordination of the Jahn-Teller active Mn^{+3} cations. The concentration of the twin planes defines the type of the polymorph, ranging from the twin plane free structure of α-$NaMnO_2$ to the β-$NaMnO_2$ with a twin plane every ($NaMnO_2$) plane. The intergrowth of the two phases, is explained by the energetic proximity of the two polymorphs.[10] The similar energies of the two polymoprhs, also explains the considerable complication encountered in the solid state synthesis of an entirely pure β-$NaMnO_2$ compound.

To explain the polymorphism of the $NaMnO_2$ compounds, a superstructure has been proposed. According to the superspace model, the $NaMnO_2$ is considered as modulated (incommensurate) structure, which crystallizes in the monoclinic (3+1)D superspace group X2/m(α0γ)00 where X=[½, ½, ½,½]. The modulation vector of the superstructure is q= ½**a***+γ**c***, where γ is the component that defines the type of the polymorph: γ=0 corresponds to the pure β-$NaMnO_2$, γ=1/2 results in the α-$NaMnO_2$ phase whereas the value of γ=1/6 gives intermediate structure with high density of planar defects[143]. The aforementioned model has been verified for both α- and β- $NaMnO_2$ by refinements of the structure using NPD and XRD synchrotron data.

The first signs of structural irregularities are detected in the XRPD and the NPD patterns. The XRPD patterns show broad peaks and a very weak peak attributed to the 001 Bragg reflection of the α-$NaMnO_2$ compound. The excessive broadening of the β-$NaMnO_2$ is confirmed by the NPD patterns, which also reveal overlapping of many reflections, and asymmetric satellite peaks at long d-spacings. Reasonable Le Bail fit of the NPD patterns is achieved only by the addition of α-$NaMnO_2$ as a secondary phase. These characteristics strongly support the scenario of irregularities in the microstructure which were investigated by TEM.

The magnetism of the β-$NaMnO_2$ has been investigated by measurements of the magnetic susceptibility, Quantum Monte Carlo (QMC) simulations and Neutron Powder Diffraction data. Preliminary analysis of the NPD data suggests the emergence of a commensurate (CM) structure at 200 K. A transition occurs from the commensurate to the incommensurate (ICM) magnetic order at 90 K. The quality of the fits on the magnetic structure is yet low, so the magnetic analysis is an ongoing work.

The triangular lattice of the Mn^{+3} must be characterized by three magnetic interactions, J_1, J_2, J_3. In α-$NaMnO_2$ (γ=1/2 in the modulation vector of the superstructure, Figure 4.39) the nature of magnetic interactions are basically one dimensional (1D) since the strong AFM interaction along b axis (J_1=72 K) is much stronger than the weaker diagonal exchange (J_2=23 K). Pure β-$NaMnO_2$ (γ=0, Figure 4.39) would be a quasi-2D magnet since the

interactions along b (J_1=70 K) and a (J_2=57 K) axis are quite comparable. However, our experimental data correspond to an intermediate microstructure (γ=1/3, Figure 4.39) which shows features of both α and β-$NaMnO_2$ phases. The interaction topology of this β-$NaMnO_2$ structure is characterized as spin ladder since the interactions J_1=74-76 K and J_3=56 K form the spin ladder topology. [143]This analysis has been based on the experimental data of the inverse magnetic susceptibility and relevant QMC simulations. The magnetic susceptibilities of both polymorphs with their relevant model description are presented in Figure 4.59. Comparison of the two theotical curves applied for the β-$NaMnO_2$ sample with γ=1/3 shows that the spin ladder model describes better the magnetic interactions in comparison with the 2D model which corresponds to the β-$NaMnO_2$ phase.

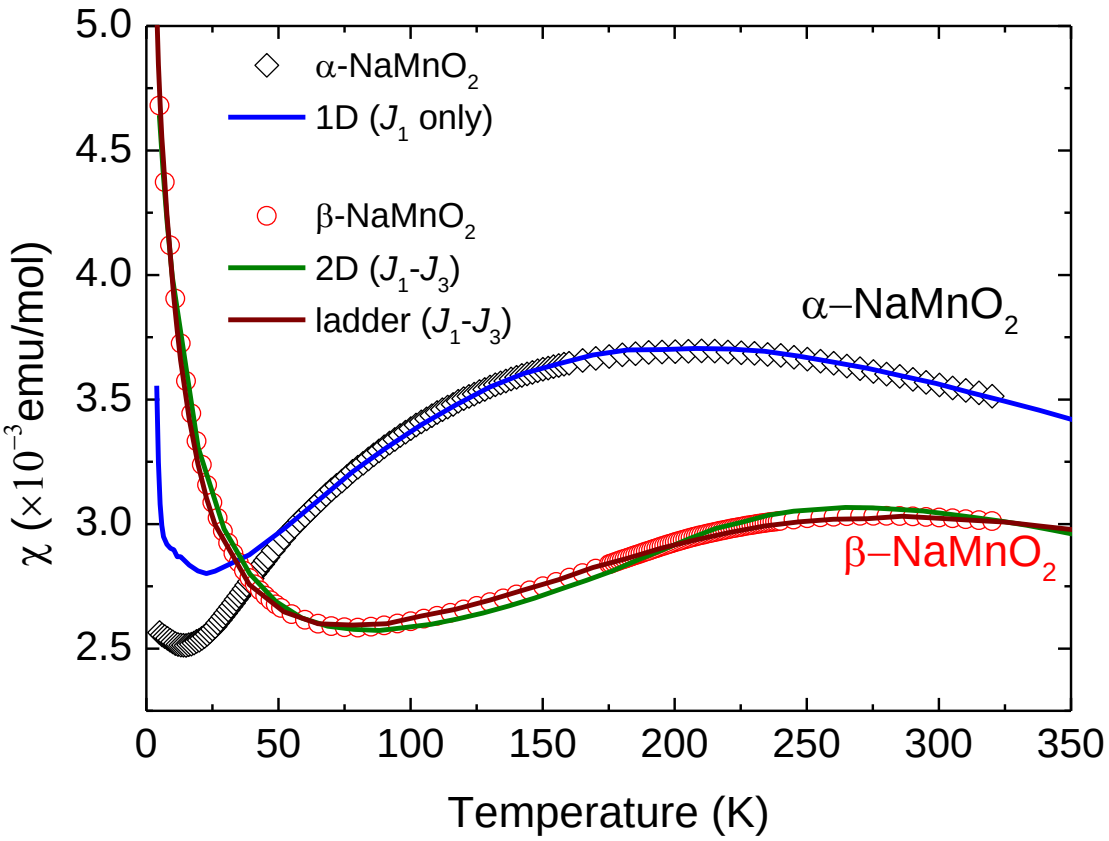

Figure 4.59 Magnetic susceptibilities of α and β $NaMnO_2$ polymorhs shown with the black and red graphs, respectively. Their model description is also shown: 1D model for the α-$NaMnO_2$ (solid blue line), 2D lattice for the pure β-$NaMnO_2$ presented with the solid blue and green line, respectively. The intermediate phase of β-$NaMnO_2$ (γ=1/3) is best described by model of the spin ladder topology which is formed by the J_1-J_3 interactions (see text). Figure reprinted from Reference 143.

4.9 Conclusions

Spin driven magnetodielectric coupling of the polycrystalline β-$NaMnO_2$ compound is proved by measurements of the dielectric constant, under zero and various magnetic magnetic fields. Since dielectric anomalies appear at the temperatures of the magnetic transitions, we suggest that the coupling between the magnetic and electric degrees of freedom is triggered by a commensurate and incommensurate magnetic ordering at 200 K and 90 K, respectively.

Pure β-$NaMnO_2$ crystallizes in the orthorhombic system. The microstructure of the examined samples of β-$NaMnO_2$ is characterized by high concentration of planar defects, attributed to the presence of the monoclinic α-$NaMnO_2$ polymorph. The Jahn-Teller distortion generated by the Mn^{+3}, promotes the formation of twin planes. The driving force behind the interchange between the α-$NaMnO_2$ and β-$NaMnO_2$ is the energetic proximity of the two polymorphs, which also explains well the tendency for the formation of the intermediate $NaMnO_2$ phases. The crystal structure of the $NaMnO_2$ polymorphs is described as a modulated one, with the modulation vector: $q= ½\mathbf{a}^*+\gamma\mathbf{c}^*$, where the value of γ is critical for the development of a particular phase.

The polymorphism of the $NaMnO_2$ compounds affects significantly their magnetism. Specifically, the interaction topology of the Mn^{+3} lattice for $\gamma<1/2$ resembles a coupled two leg spin ladder as compared to geometrically frustrated triangular magnet for $\gamma=1/2$.

To conclude, β-$NaMnO_2$ has proven to be a system worth to investigate from many different aspects. Here, we were succesfull in unravelling the magnetodielectric properties, and the influence of the inhomogeneous microstructure on the magnetic interactions. The findings of this reaseach surely trigger further interest, for a complete crystal and magnetic characterization at the temperature range of 5 K-300 K which would unravel the details of the mechanism that generates the coupling between the magnetic and electric degrees of freedom.

Chapter 5

Crystal and Magnetic Properties of the Birnessite $Na_{0.3}MnO_2 \times 0.2\,H_2O$

5.1 Introduction

A great amount of research has been focused on the fabrication of different crystal structures of various manganese oxides. In previous chapters this thesis has referred to the properties of the α-$NaMnO_2$ and β-$NaMnO_2$, and also to the existence of the $Na_{0.7}MnO_2$ and the $Na_{0.44}MnO_2$[228]. Nevertheless, plenty more manganese oxides exist. Their most frequent type of their structures is shown in Figure 5.1.[229] The common characteristic in their crystal structure is the layers of the MnO_6 edge sharing octahedra which are separated by metal ions (Li, Na) placed between the layers. The interlayer distance varies in each structure ranging from 4.7 Å of the $Li_{1.09}Mn_{0.91}O_2$,[230] 7 Å in the birnessite[79, 137, 231, 232, 233, 234, 235] to the 10 Å in the buserite structure.[236,237]

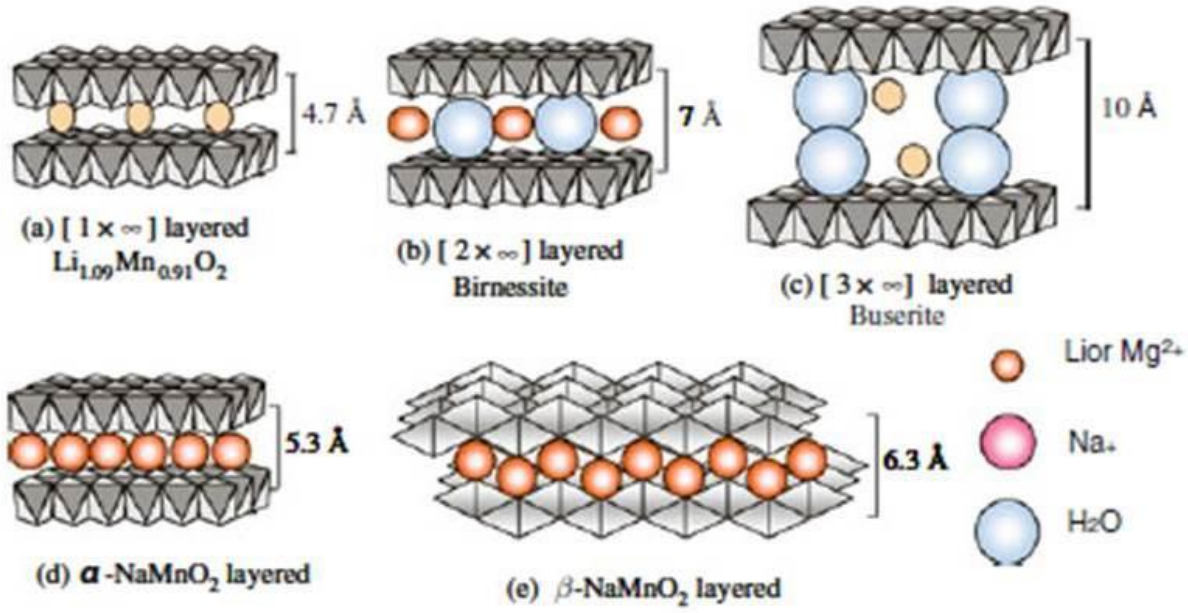

Figure 5.1 Structures of layered manganese oxides. Reprinted from Reference 229.

The layered structure of these manganese oxides has been also studied due to the potential use of these materials as cathode materials in rechargeable batteries. For example, a promising material for the afoerementioned applcations is the $Na_{0.44}MnO_2$,[228] an isostructural system with $Na_4Mn_4Ti_5O_{18}$.[238] $Na_{0.44}MnO_2$ belongs to the family of ABO_2

compounds (A: alkali, B: magnetic cation) and specifically to the layered manganites. It was first identified by Parant in the Na_xMnO_2 phase diagram as the thermodynamical stable high temperature phase for $x \leq 0.5$.[6] $Na_{0.44}MnO_2$ is a mixed Mn^{+3} and Mn^{+4} porous manganite that contains both edge shared octahedral and square pyramidal Mn-O units. The structure of $Na_{0.44}MnO_2$ is characterized by an unusual tunnel structure composed by "S" shaped channel units of MnO_5 and MnO_6 units (Figure 5.2). [228] Due to its peculiar structure, $Na_{0.44}MnO_2$ has received much attention as a potential system for use in lithium ion batteries where the Na ions in the pores are replaced with Li.

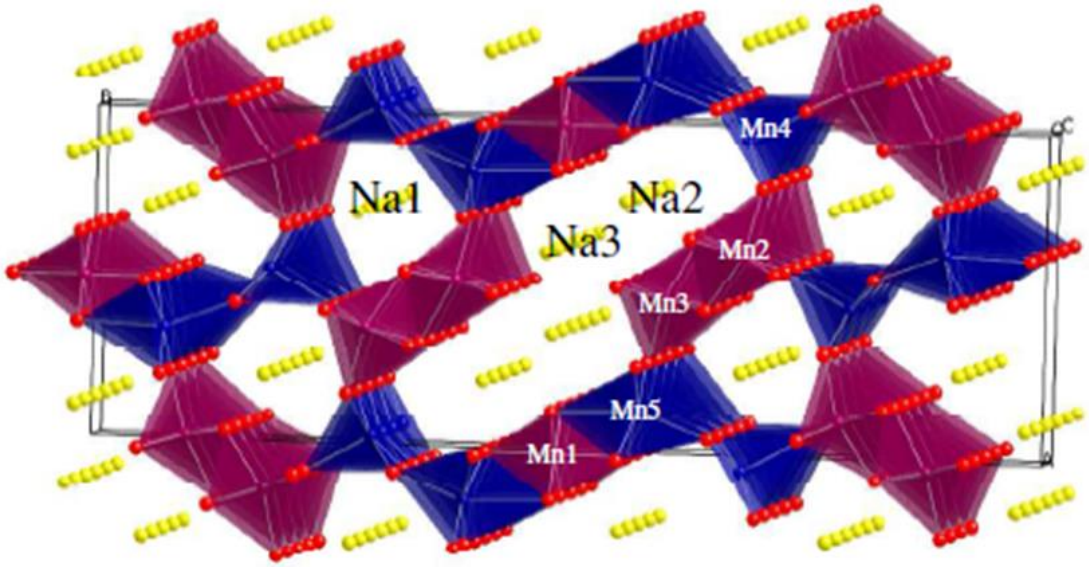

Figure 5.2 Crystal structure of $Na_{0.44}MnO_2$ at 500 K obtained by Rietveld analysis of neutron powder diffraction data.Reprinted from Reference 228.

Although the crystal structure of the birnessite is related with various synthesis protocols has been known for a rather long time, little yet has been reported in the literature regarding the magnetic characterization. [239] In this chapter we characterize the structure and evaluate the magnetic properties of birnessite compound $Na_{0.3}MnO_2 \times 0.2H_2O$ by static and dynamic susceptibility measurements. We show that the interactions between the mixed valence manganese cations, namely the Mn^{+3} and Mn^{+4} are characterized by randomness or frustration which results in the spin glass state of the compound.

5.1.1 The crystal structure

Birnessites are called the hydrated $NaMnO_2$ oxides whose Na/Mn molar ratio is between 0.2-0.7. A ratio higher than 0.7 results to the dehydration of the birnessite and the formation of the α-$NaMnO_2$ occurs.[229]

$Na_{0.3}MnO_2 \times 0.2H_2O$ crystallizes in the triclinic system, space group $P\bar{1}$, with the following cell parameters (see section 5.4.3 on structural analysis): a= 5.53(1) Å, b= 3.11(6) Å, c=7.80(1) Å, α=89.492(13) deg, β=103.136(12) deg, γ=89.929(10) deg. The structure matches with the one reported [13] for the birnessite $Na_{0.3}MnO_2 \times 0.93H_2O$ (cif file obtained from ISCD 260208). Despite the fact that the birnessite has the lower symmetry of a triclinic space group, its crystal structure resembles a lot that of the α-$NaMnO_2$ (Figures 3.1 and 3.2). The major difference though is the expanded c- cell parameter which is expected due to the insertion of the H_2O in the interlayer distance. The enhanced interlayer distance helps the deintercalation or intercalation in the cation exchange reactions.

In the birnessite compounds there are some Mn vacant sites in the MnO_6 octahedral layers. This causes a disruption in the periodicity in the arrangement of the Mn^{+3}/Mn^{+4} cations, thus a probable site disorder. Bond disorder or site disorder causes magnetic frustration (Figures 1.6 and 1.11) which results in the absence of a long range magnetic order. Indeed, the magnetic measurements of the $Na_{0.3}MnO_2 \times 0.2H_2O$ proved the existence of frustration and the emergence of a spin glass state below 29 K.

Figure 5.3 presents the layered structure of the $Na_{0.3}MnO_2 \times 0.2H_2O$. [240] The Mn, O and Na atoms have dark grey, red and purple coloration, whereas the H_2O molecules are represented by the blue spheres.

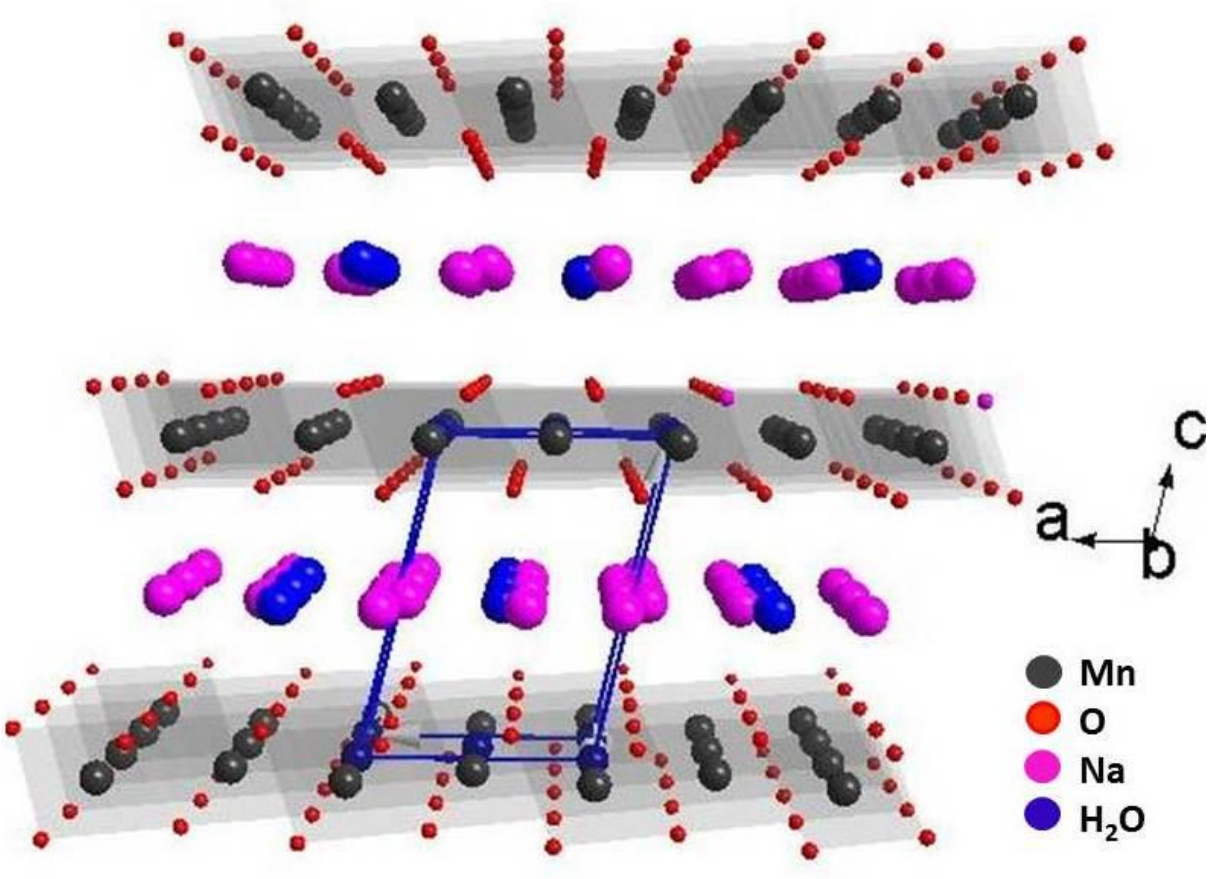

Figure 5.3 The crystal structure of the Na-birnessite (ICSD 260208). The manganese, oxygen, sodium atoms are represented with the black, red and purple spheres. The H_2O molecules in the interlayer distance are shown with the blue spheres. Cell edges are represented with the blue lines.

5.2 Synthesis of the birnessite $Na_{0.3}MnO_2 \times 0.2H_2O$

Many approaches [79, 230, 231, 232, 233, 234, 235] have been reported as suitable for the birnessite compounds such as deinteracalation[233], ion exchange[233] and hydrothermal synthesis[232]. Some examples of these methods include aging of MnO_x gels [235] and oxidation of Mn^{+2} cations with H_2O_2 in a basic medium.[79, 231, 241] Other preparative processes included hydrothermal synthesis with metal ion extraction/ insertion reactions,[232]solid state reaction, melting salt flux process and redox precipitation process[233] as well as reduction of sodium permanganate with sodium iodide in aqueous solutions.[234] The majority of these methods is accomplished by soft chemistry (“*chimie douce”)* routes, namely methods that involve

room temperature preparation of the materials in open reaction vessels. However, some synthesis protocols were found difficult to reproduce while others resulted in two phase compounds. An example of the former is the deintercalation of the Na cations from the host framework of α-$NaMnO_2$ by the use of iodine, which produced a non-stable birnessite-like product characterized by secondary phases; specifically those of the α-$NaMnO_2$ and the $Na_{0.7}MnO_2$ (see Appendix D, Figure D.1).

The synthesis method that was followed in this thesis in order to prepare the $Na_{0.3}MnO_2 \times 0.2H_2O$, is based on the hydration of the parent phase of α-$NaMnO_2$ at ambient conditions in air, for a period of two weeks, by analogy to Abou-El-Sherbini et al [9] report. The difference with the method reported, was the omission of the daily leaching of NaOH with H_2O.

In detail, α-$NaMnO_2$ polycrystalline powder was synthesized as described in paragraph 3.2. After the completion of the α-$NaMnO_2$ synthesis based on the protocol described in section 3.2, the powder remains in room temperature and is exposed to ambient conditions with the purpose to hydrolyze. Initially the α-$NaMnO_2$ powder has brown colour, whereas as the time passes by it reacts with the moisture of the atmosphere it becomes black, due to the oxidation of Mn^{+3} towards Mn^{+4}. Frequent mixing of the powder was undertaken so that all crystallites would become exposed in the atmospheric air. This would promote a homogeneuous compound, while the powder converted from the host framework α-$NaMnO_2$ to the birnessite.

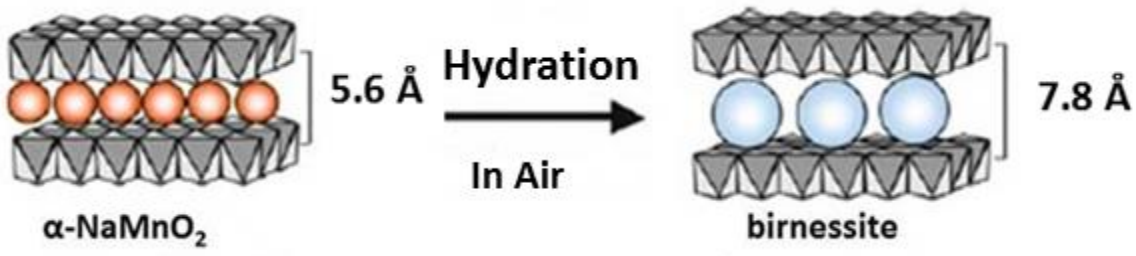

Figure 5.4 A graphical representation of the H_2O insertion in the α-$NaMnO_2$ interlayer space, resulting in the formation of the Na-birnessite and the interlayer distance to 7.8 Å. Reprinted from Reference 227 after adjusting the interlayer distances to the numbers that correspond to the birnessite system that is studied in this thesis.

5.3 Characterization

5.3.1 X Rays Powder Diffraction (XRPD)

The protocol described in the previous paragraph proved to produce a birnessite oxide whose structure is similar with the $Na_{0.3}MnO_2 \times 0.93H_2O$, of mixed manganese valence state Mn^{+3}/Mn^{+4}. The crystal structure of the final product remained stable over a long period of time (more than a year).

The polycrystalline specimens of $Na_{0.3}MnO_2 \times 0.2H_2O$ were found to crystallize upon the triclinic system, space group $P\bar{1}$ with the following cell parameters a=5.53(1) Å, b=3.11 (6), c=7.80(1) Å, α=89.492(13) deg, β=103.136(12) deg, γ=89.929(10) deg.[242] The aforementioned parameters were extracted by the TEM studies.

The crystal structure of the birnessite compound was initially checked by XRD powder diffraction (λ=1.5406 Å), a Le Bail fit obtained from neutron powder diffraction data shown in section 5.5 and by HRTEM presented in paragraph 5.3.4.1. The XRPD pattern is shown in Figure 5.5. The final product exhibits high crystallinity and the characteristic 001 reflection of the birnessite structure at the d-spacing of 7.8 Å (12.455 deg). The shift of the 001 reflection towards lower angles (namely from 16.7 deg of the α-$NaMnO_2$ to 12.455 deg of the birnessite) suggests the expansion of the interlayer distance to 7.8 Å.

The weak peak observed around 16.7 deg is attributed to the α-$NaMnO_2$ powder which was used as precursor, whereas the other two which are pointed out with the black arrows could not be indexed upon the known manganese oxides.

One crucial parameter was to evaluate the changes in the crystal structure of the starting material, the α-$NaMnO_2$ powder, and the time that was needed to hydrolyze into the birnessite compound. For this reason, successive XRPD patterns were collected at specific time intervals, which showed the evolution of the starting α-$NaMnO_2$ powder.

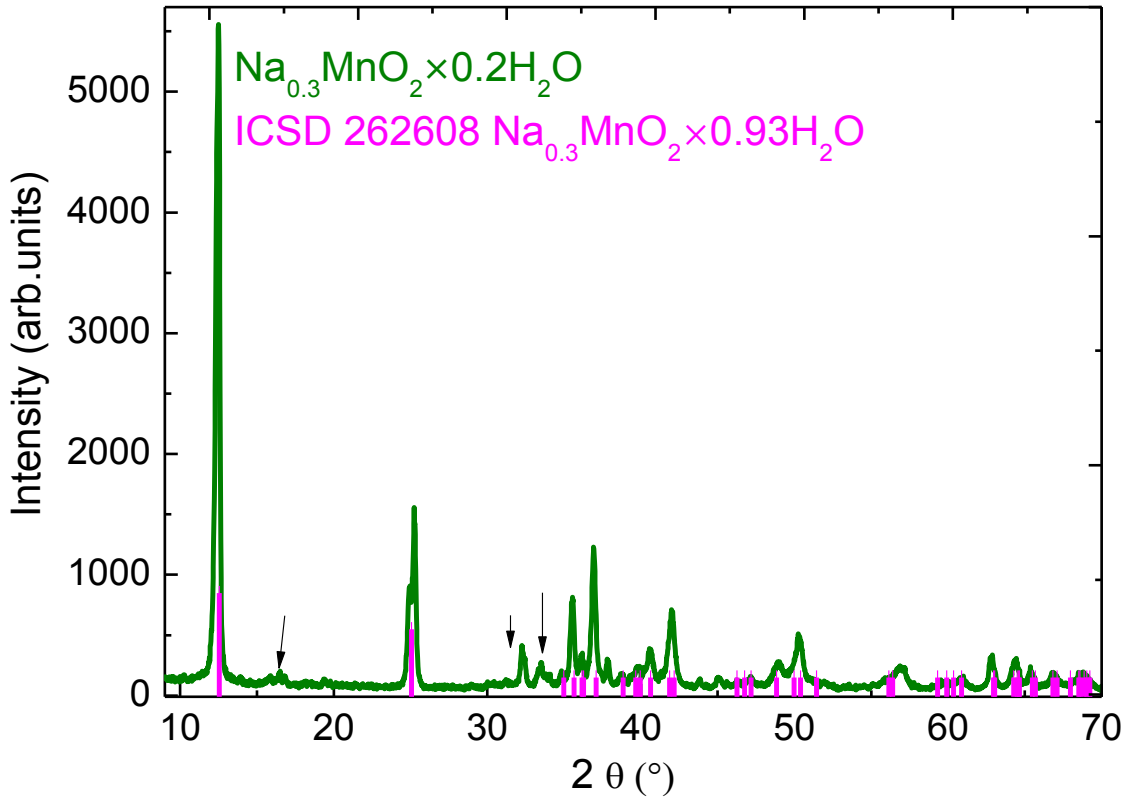

Figure 5.5 X ray powder diffraction (λ=1.5406 Å) of the birnessite $Na_{0.3}MnO_2 \times 0.2H_2O$. The black arrows indicate Bragg reflections attributed to impurities such as the 001 peak of α-$NaMnO_2$ at 16.7 deg. The reflection 001 at 12.5 deg is the one with the highest intensity, indicating the expansion of the structure along the c-axis.

Figure 5.6 presents a narrow 2θ range (12-17°) where the 001 reflections of the birnessite, $Na_{0.7}MnO_2$ and the α-$NaMnO_2$ appear. The first day that the α-$NaMnO_2$ was exposed in the air, a secondary phase appears in the XRPD pattern: the $Na_{0.7}MnO_2$. Actually the intensity of the 001 of the $Na_{0.7}MnO_2$ appears higher than the 001 peak of the α-$NaMnO_2$ phase indicating higher concentration of the $Na_{0.7}MnO_2$ in respect with the α-$NaMnO_2$. The $Na_{0.7}MnO_2$ contribution on the XRPD pattern seems to disappear around the 7th day. On the contrary, the first day the 001 reflection of the birnessite has not emerged yet, but

appears after 4 days. As the days of the exposure to the air increase there is a continuous decrease of the α-$NaMnO_2$ 001 reflection and a rapid increase of the birnessite's 001 Bragg peak. Finally, the interplay between the reflections of the manganese oxides appears to stabilize after two weeks of hydrolysis in air in agreement with the protocol that was reported before.[137]

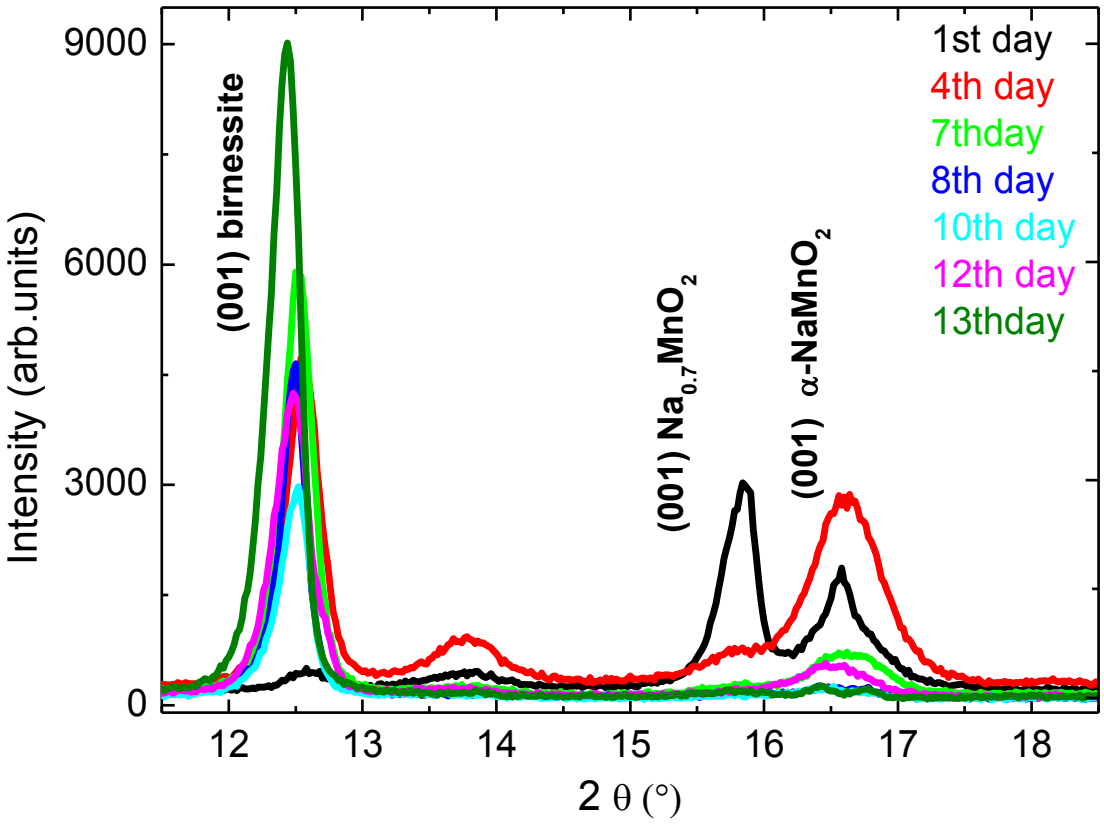

Figure 5.6 X-Ray powder patterns of the as made α-$NaMnO_2$ compound obtained after 1, 4, 7, 8, 10, 12 and 13 days of exposure at ambient conditions. The 001 reflections of the birnessite at 12.45 deg, the $Na_{0.7}MnO_2$ at 15.7 deg and the α-$NaMnO_2$ are also pointed out in the graph.

5.3.2 Inductive Coupled Plasma Optical Emission Spectroscopy (ICP-OES)

The hydration of the α-$NaMnO_2$ in air is expected to result in a compound with reduced amount of Na due to the insertion of the water molecules in the interlayer distance. Thus, the final product should have a chemical formula $Na_xMnO_2 \times zH_2O$ where x<1. Indeed the Na/Mn ratio according to the ICP-OES was found to be 0.7. Therefore the amount of Na according to the ICP is reduced by a 30 % due to the insertion of the H_2O. Concerning the amount of H_2O in the birnessite compound we rely on the TEM analysis which is discussed in paragraph 5.4.3.1.

5.3.3 Thermogravimetric Analysis

Measurements of the weight loss versus temperature were carried out, at the temperature range 25-1000°C. A small quantity (<10 mg) of the birnessite's sample was placed in a alumina pan, and was heated from room temperature to 1000°C with a constant heating rate of 20 °C/min. The results are shown in Figure 5.7. Above 100°C there is a 13% decrease of the weight up to 500°C, which corresponds to the vaporization of the H_2O. Heating upon 500°C results in a 2.5% loss of the compound's weight. The temperature range above 570°C and below 950°C is where the sodium manganese oxides $Na_{0.7}MnO_2$, $Na_{0.44}MnO_2$, α-$NaMnO_2$ and β-$NaMnO_2$ are formed, so the further 2% weight loss probably corresponds to the formation of a mixture of the above phases. The weight seems to stabilize above 1000°C.

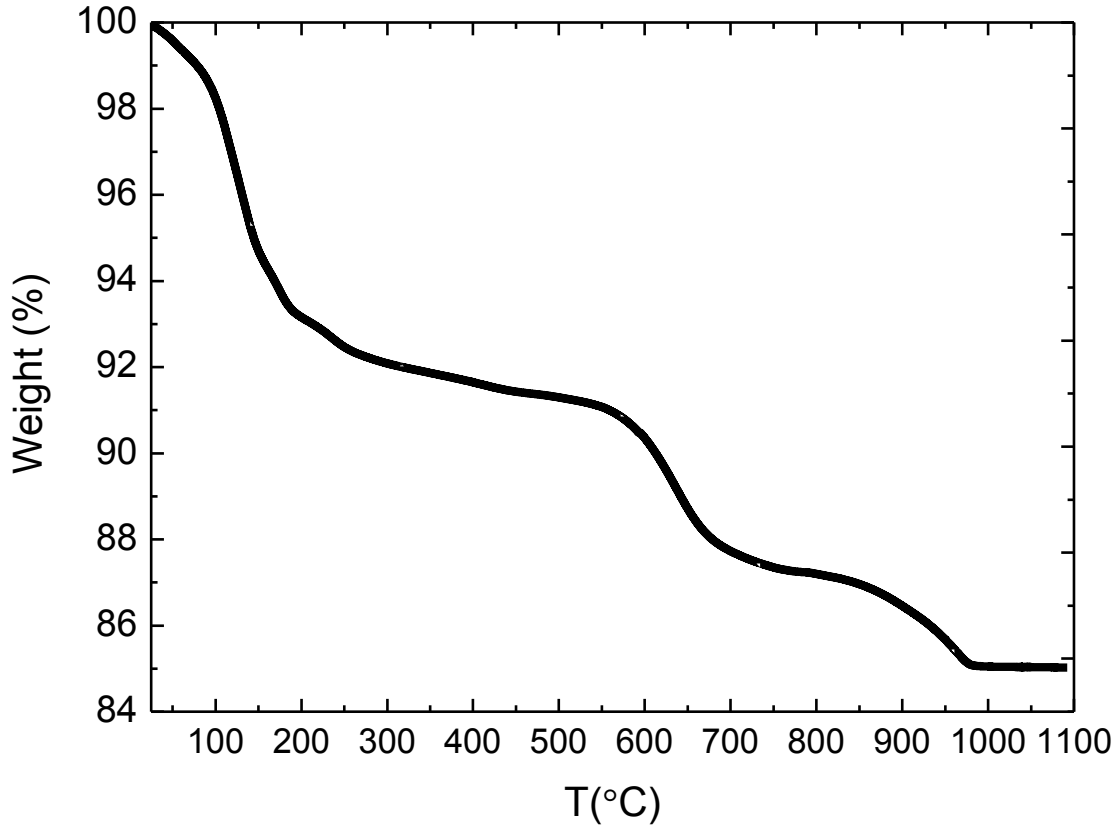

Figure 5.7 Thermogravimetric analysis of the Na-birnessite between the temperature range 100-1100°C.

Immediately after the thermogravimetric experiment was completed, the birnessite's powder was checked by XRPD to compare the paterns before and just after the completion of the heating. The sample that has been heated up to 1000°C exhibits Bragg reflections which are attributed mostly to α-$NaMnO_2$ phase. Reflections from β-$NaMnO_2$ and a few of Mn_3O_4 are also observed, pointing towards a material with at least two secondary phases. Worth noticing that the 001 reflection of the birnessite no longer appears after the heating, strongly suggesting there is no H_2O in the final product.

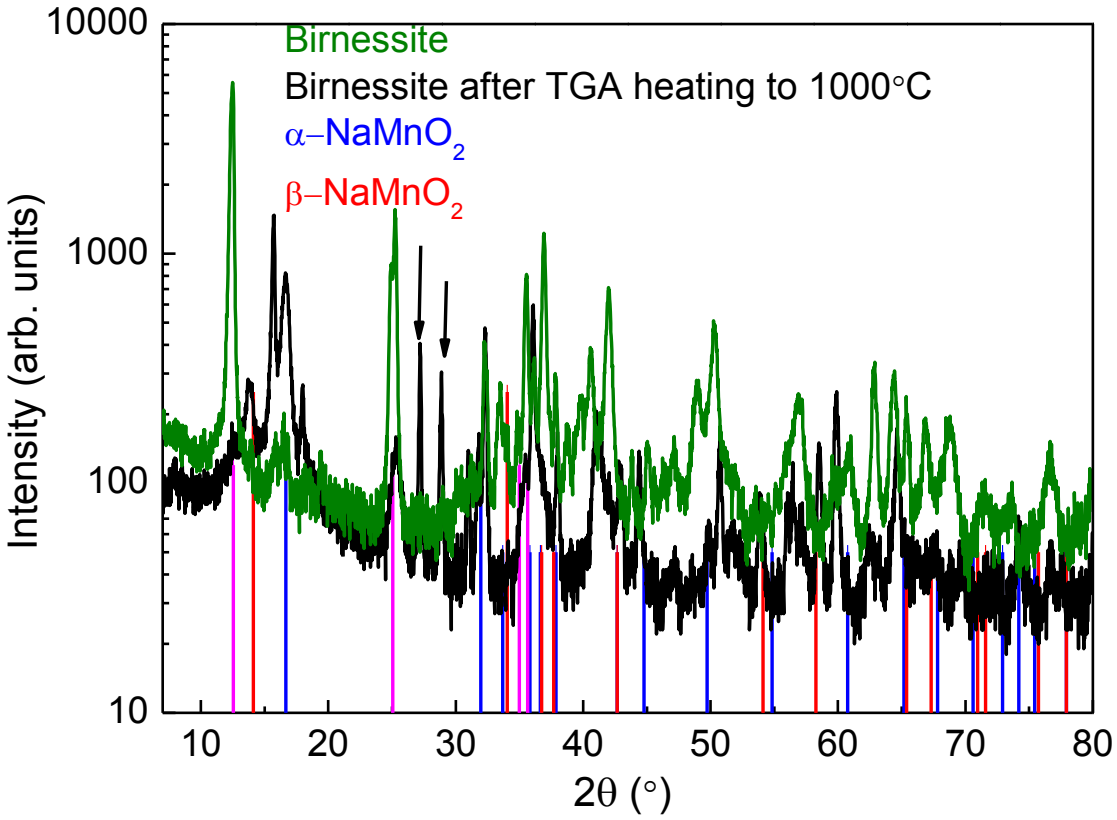

Figure 5.8 Comparison of the XRPD patterns of the birnessite's polycrystalline powder before the TGA heating at 1000°C which is shown with the green graph and after the completion of the TGA experiment (black graph). Indexing has been done upon the α-$NaMnO_2$ (ICSD 16270) and β-$NaMnO_2$ (ICSD 16271) phase shown with the blue and red tick marks, respectively. For reasons of simplicity in the diagram indexing upon the birnessite's cell (ICSD 262208) is shown up to 35 deg. y-axis of intensity is shown in logarithmic scale, for better observation of the weak reflections. The black arrows point at the 25 and 26 deg reflections which are attributed to the Mn_3O_4 oxide.

5.3.4 TEM Studies

HRTEM, EDS and EELS analyses were carried out using a Jeol JEM 2200FS instrument, equipped with an image aberration corrector, an in-column energy filter and a silicon drift detection system for EDS. All the experiments were conducted in Instituto Italiano di Technologia (IIT) in Genova, Italy.

5.3.4.1 HRTEM

High resolution transmission microscopy images were used for the analysis of the crystal structure of the $Na_{0.3}MnO_2 \times 0.2H_2O$. The images reveal the presence of large crystals in the $Na_{0.3}MnO_2 \times 0.2H_2O$ compound. These crystals are composed of smaller ones, whose structure best matched with the one reported for the $Na_{0.3}MnO_2 \times 0.93H_2O$ [242] birnessite. According to the fit from Electron Diffraction (ED) of TEM the compound $Na_{0.3}MnO_2 \times 0.2H_2O$ crystallizes in the triclinic system in the space group $P\bar{1}$, with the following cell parameters: a= 5.53(1) Å, b= 3.11(6) Å, c=7.80(1) Å, α=89.492(13) deg, β=103.136(12) deg, γ=89.929(10) deg.

Figures 5.9 and 5.10 present two different areas of the same $Na_{0.3}MnO_2 \times 0.2H_2O$ sample which have been used for the structural fit. In panel (a) the area from which the fittings took place is presented and in panel (b) the distance between the columns of the atoms is shown to vary from 2.54 Å-3.14 Å.

Stacking faults appear parallel to the $[1\bar{1}2]$ planes. These structural defects are not parallel to the planes in which H_2O molecules are inserted in the structure. The structural modifications could result either form Mn vacancies or from partly inhomogeneous composition of the sample due to some small percentage of non-hydrated α-$NaMnO_2$. An important observation related to this, is that the material is extremely sensitive to the parallel illumination by 200 keV electrons, especially in high magnification. After a few minutes of observation under the HRTEM the crystals collapsed. Taking this into account, one can not exclude that some structural modifications are due to the observation by HRTEM.

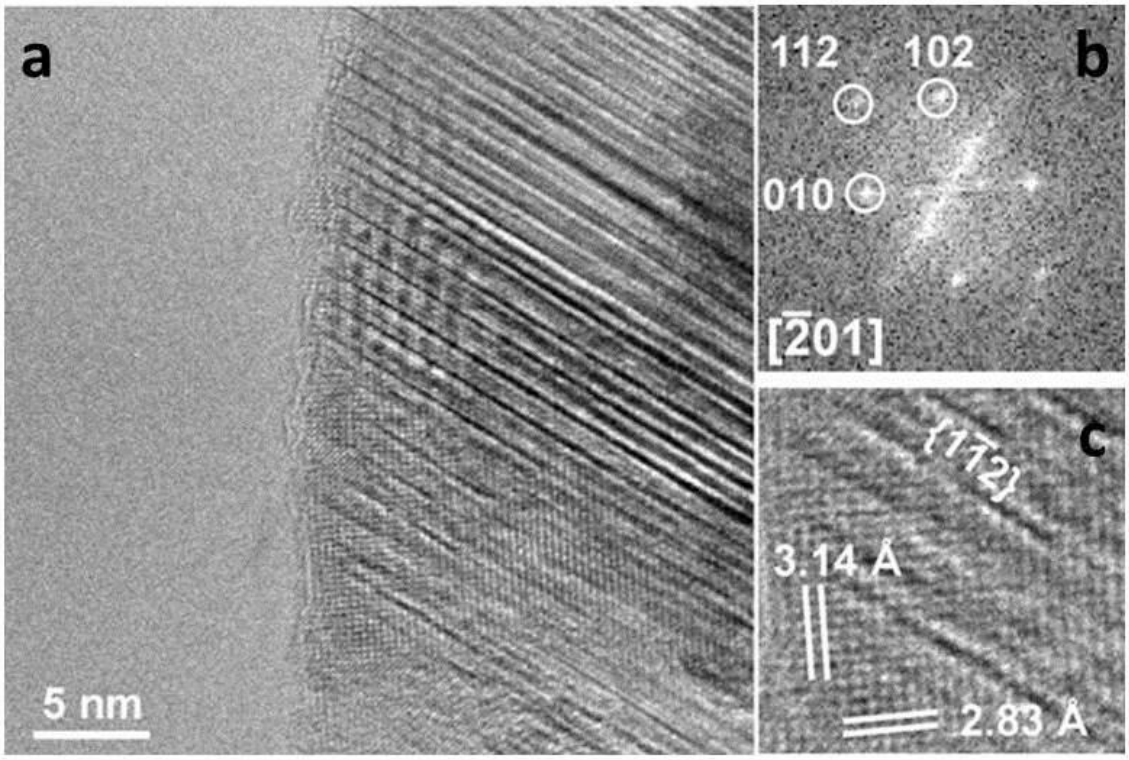

Figure 5.9 HRTEM figure of $Na_{0.3}MnO_2 \times 0.2H_2O$ with 5nm magnification

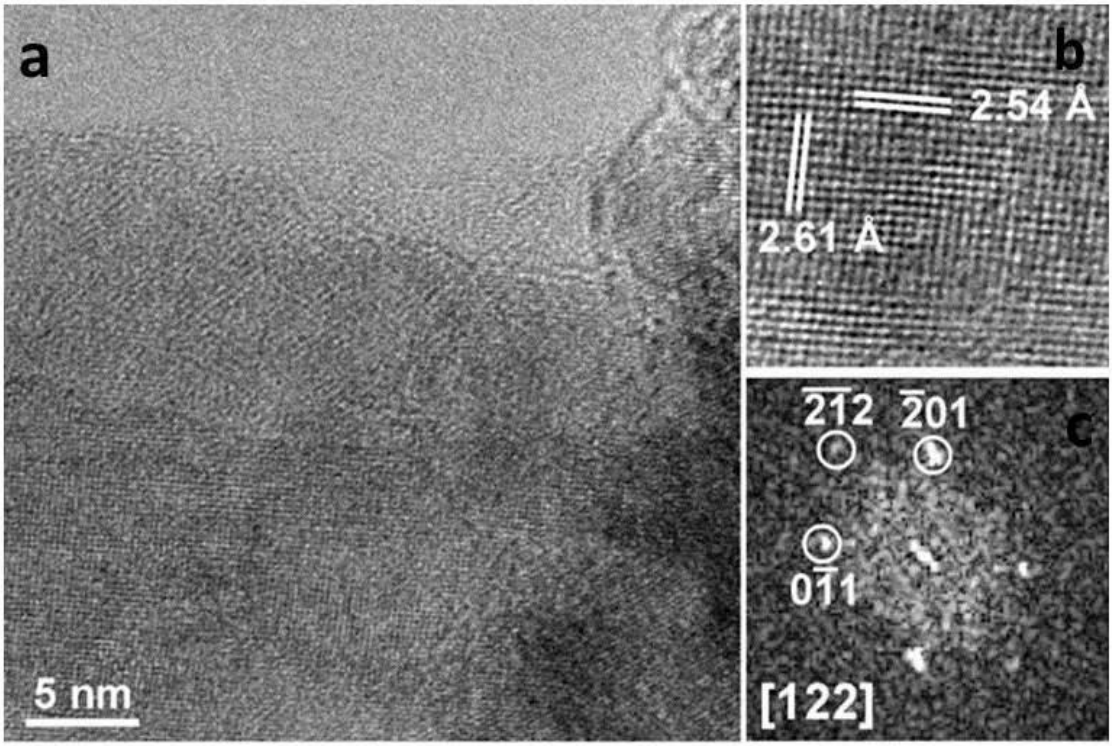

Figure 5.10 A complementary figure of 5nm magnification which was used for the structural fitting of the $Na_{0.3}MnO_2 \times 0.2H_2O$ compound.

5.3.4.2 EDS mapping

Energy dispersive spectroscopy has been used to determine the distribution of the Na, Mn and O atoms in the $Na_{0.3}MnO_2 \times 0.2H_2O$. Two different crystals have been examined which are presented in Figure 5.11 which showed homogenous distribution Na, Mn and O atoms.

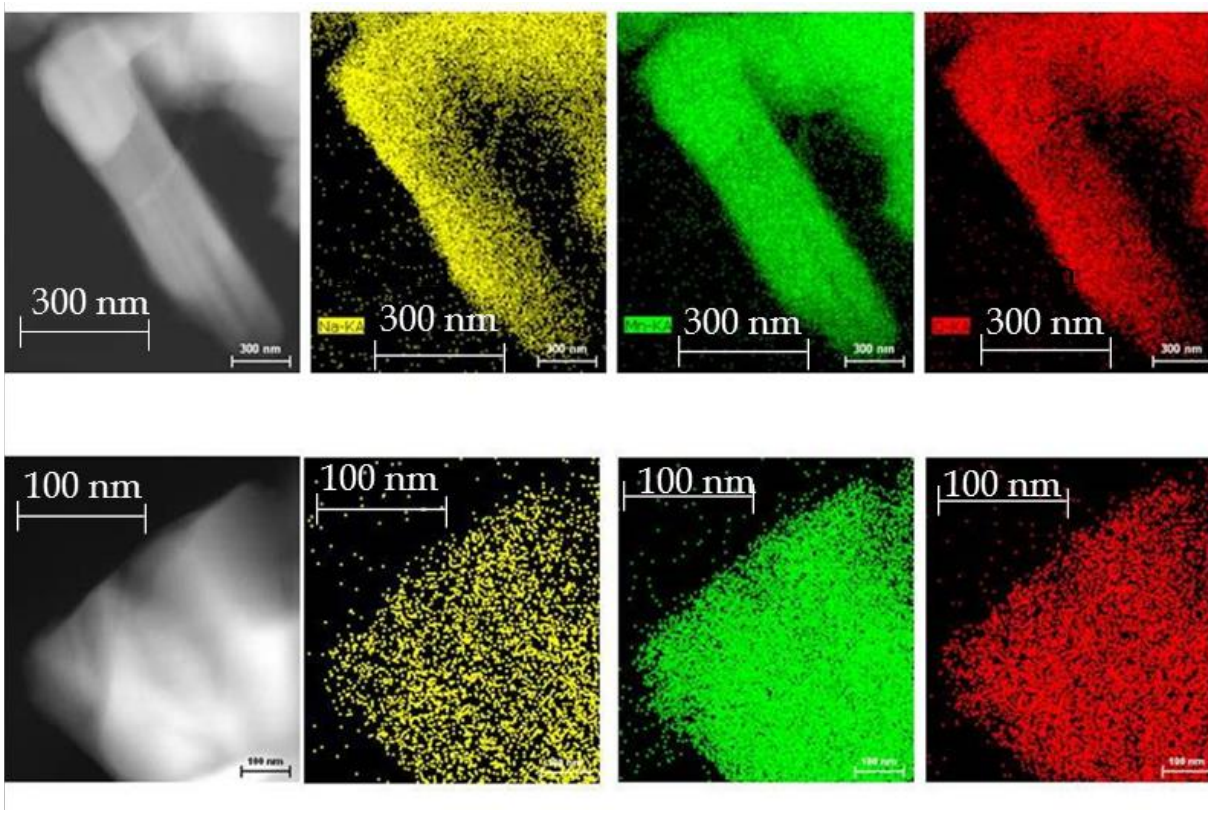

Figure 5.11 EDS mapping of two Na-birnessite crystals shown with 300 nm magnification (upper set of pictures) and 100 nm magnification (bottom part of the figure). The yellow, green and red coloration corresponds to Na, Mn and O atoms, respectively. Both crystals show homogenous distribution of the three elements.

However, these observations have a local character, so since the sample is not 100% homogeneous we can't extract conclusions based only on EDS spectra. In order to quantify the stoichiometry of the birnessite compound EELS studies were carried out which were combined with the EDS spectra.

5.3.4.3 Electron Energy Loss Spectroscopy (EELS)

The transition metal $L_{2,3}$ energy loss spectra of the $Na_{0.3}MnO_2\times0.2H_2O$ was recorded and carefully analyzed based on the white line ratio method[152] (Figure 5.12). According to this method, the integral intensity ratio of the $L_3$and L_2 excitation peaks of a transition metal is correlated to its formal oxidation state [152, 153, 243, 244, 245, 246, 247] The analyses resulted in the average oxidation state of 3.4 for the mixed valence state of the Mn^{+3}/Mn^{+4} cations. It is interesting to point out, that this value is in consistency with the result obtained from the Curie Weiss fit which yielded an effective moment of 3.4 μ_β for the Mn cations (see paragraph 5.4.1.1).

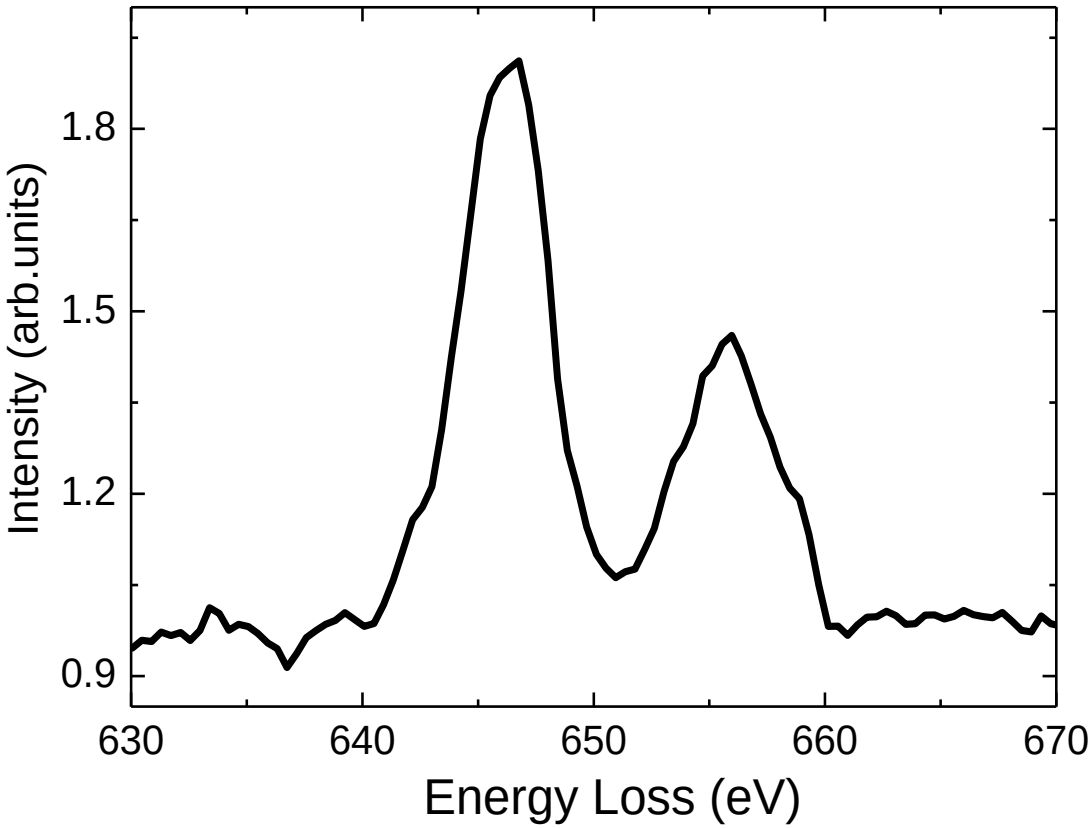

Figure 5.12 L edge energy-loss near-edge structures for the determination of the oxidation state of Mn in the $Na_{0.3}MnO_2\times0.2\,H_2O$ compound.

5.4 Magnetic Properties

The magnetic properties of the $Na_{0.3}MnO_2 \times 0.2H_2O$ revealed that the system undergoes a spin glass transition at low temperatures (T<29 K) in contrast to the long range Neel order (at 45 K) in α-$NaMnO_2$ and the commensurate (~200 K) to incommensurate (~ 90 K) magnetic transition in β-$NaMnO_2$. The origin of a spin glass state, which would help for a better understanding of the 5.4 section experimental results, has already been introduced in paragraphs 1.3.5 and 1.3.6.

5.4.1 Static Magnetic Susceptibility

The static (DC) magnetic susceptibility of the $Na_{0.3}MnO_2 \times 0.2H_2O$ has been measured on a ZFC-FC protocol under 200 Oe external magnetic field. The magnetic properties result from the mixed valent character (Mn^{+3}/Mn^{+4} cations) of the compound. The sample is cooled from room temperature with zero magnetic field (ZFC), to 5 K where 200 Oe field is applied. The magnetization is recorded every 1 K upon heating with a rate of 1 K/min. For the field cool protocol the 200 Oe field is also applied upon cooling the sample.

The results obtained from the aforementioned experiment are shown in Figure 5.13 (a). The striking characteristic is the sharp peak on the ZFC measurement (represented with the blue graph of the open symbols) which occurs at 29 K. Below 29 K there is a large bifurcation between ZFC and FC graphs, since the FC curve increases below the critical temperature whereas there is large drop in the ZFC susceptibility. These are typical signs of a spin glass behavior. The temperature χ_{zfc} maximun is mentioned hereafter as T_{sg} (spin glass temperature).

Worth mentioning here, that the irreversibility of the FC and ZFC provides strong evidence of the spin glass state, however it does not prove it. Certain systems which possess long range magnetic ordering, like ferromagnetic,[248, 249, 250, 251, 252] antiferromagnetic [253] and ferrimagnetic [254] may exhibit a bifurcation between the ZFC-FC χ(T) curves. Moreover, there are also other magnetic systems which show spin glass

features such as superparamagnets, [255, 256] cluster glasses [257, 258] and superconducting oxides.[259]

Still though, many compounds such as the $La_{0.5}Sr_{0.5}CoO_3$,[260] $CuFe_{0.5}V_{0.5}O_2$,[261] $Co_{1-x}Mn_xCl_2 \cdot H_2O$,[262] and most importantly the archetypal spin glass Cu-Mn[30] exhibited both the a sharp maximum in the ZFC susceptibility (χ_{ZFC}) as well as the divergence between the ZFC and FC susceptibilities below the T_{sg}.

When cooling a spin glass from above the freezing temperature (T_{sg}), a qualitative description of the physical picture may be as follows: as the temperature is lowered many of the randomly positioned and freely rotating spins build themselves into locally correlated clusters or domains. The gradual increase of the suscpetibility as the temperature decreases is attributed to the increase of the number and the size of such magnetic domains.[263] Near the transition temperature, T_{sg}, the magnetic units (spins or domains) start to interact with each other over a longer range and the system seeks its ground state configuration. At $T = T_{sg}$ the spins freeze at random directions and the growth of the magnetic domains stops.

The irreversibility of the ZFC-FC curves, is attributed to the effect of the external magnetic field when the sample is polarized above the T_{sg}. In other words, the magnetic ground state of the spin glass is greatly affected when a magnetic field is applied above the T_{sg} of the system. This seems reasonable when taking into account that a spin glass is characterized by bond disorder or frustration, so the magnetic interactions are relatively weak and thus any external perturbation, such as the application of the magnetic field above T_{sg} could affect the interactions of the spins.

Before completing this paragraph on the ZFC-FC measurements, a final comment must be added concerning the stability of the magnetic properties of the $Na_{0.3}MnO_2 \times 0.2H_2O$. Figure 5.13 (b) nicely illustrates this issue by showing the massive difference observed in the ZFC-FC graph measured soon after the sample has been synthesized and 6 months later. The deviation of the ZFC-FC has decreased, when compared to the initial measurement. Critical to clarify that the sample used in both measurements is the same, and the experimental conditions were identical. The XRPD patterns of the sample used for

the static magnetic susceptibility measurements of Figure 5.13 (b) are presented in Appendix D, Figure D.2.

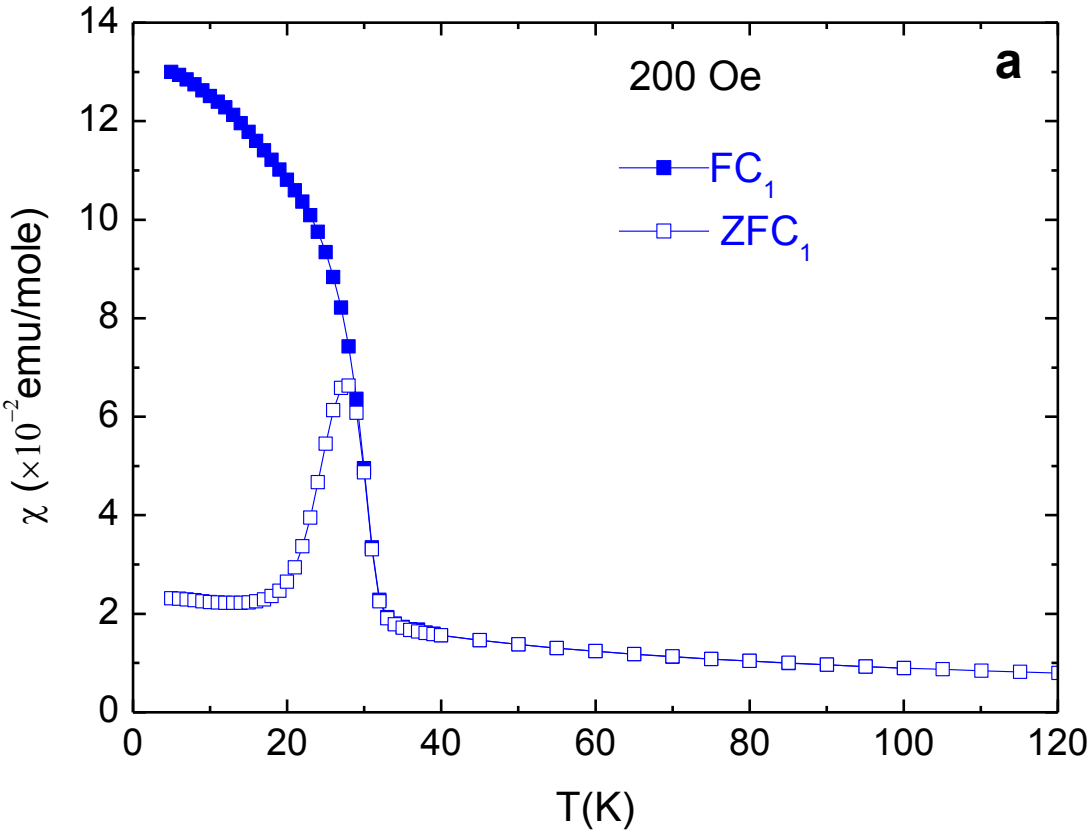

Figure 5.13 (a) The graph showing the ZFC-FC measurement of the $Na_{0.3}Mn \times 0.2H_2O$ from 5-300 K. Note the sharp peak at T_{sg}=29 K on the ZFC and the bifurcation below the T_{sg} between the ZFC and FC graphs

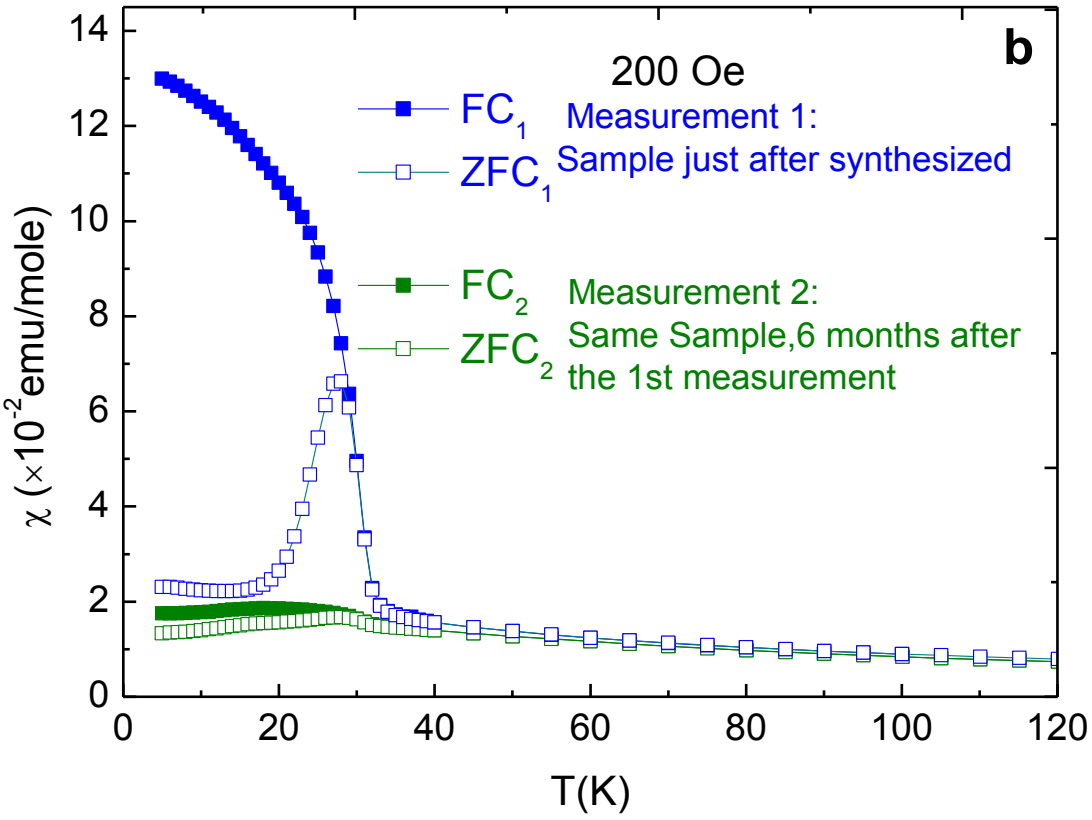

Figure 5.13 (b) ZFC-FC experiments obtained in the sample with a time difference of eight months between the first (ZFC_1, FC_1 shown in blue) and the second (ZFC_2, FC_2 presented in green) measurement. There is a remarkable change in the sharpness of the ZFC peak and the elimination of the bifurcation between the ZFC and FC graphs. The ZFC and FC are presented with the open and closed symbols, respectively.

5.4.1.1 Curie Weiss Fit

The Curie Weiss is a linear fit in the graph of $1/\chi$ versus temperature by which one can calculate the effective moment of the magnetic ion μ_{eff} and the temperature θ_w, (details discussed in section 1.2.5).

The data of the $1/\chi$ are fitted by the equation: $y=a+b\cdot x$ **(5.1)**

The equation that relates the temperature θ_w with the intercept is

$$a=(-3k_\beta/N_A\ \mu_\beta^2)\ \frac{\theta_w}{\mu_{eff}^2} \quad \textbf{(5.2)}$$

And the slope with the effective moment

$$b=(3k_\beta/N_A\ \mu_\beta^2)\frac{1}{\mu_{eff}^2} \quad \textbf{(5.3)}$$

where k_β is the Boltzmann's constant in units of erg/K ($k_\beta=1.3807\cdot10^{-16}$ erg/K), μ_β is the Bohr's magneton in erg/G ($\mu_\beta=9.2741\cdot10^{-21}$ erg/G) and N_A is the Avogadro's number namely $N_A=6.022\cdot10^{23}\,mol^{-1}$.

The Curie Weiss fit of the Na-birnessite is presented in Figure 5.14. The data that have been used are the same with those presented in the ZFC graph of Figure 5.13a. The linear fit yields the values of a=44.472 and b=0.69123, for the intercept and the slope, respectively with an Adjustment R-square of 0.99989. Combining these results with the equations 5.2 and 5.3, the values for the effective moment of the mixed valence Mn^{+3}/Mn^{+4} results in the $\mu_{eff}=3.4\pm1.8\cdot10^{-3}\,\mu_B$ and the temperature $\theta_w=64.28\pm6.8\cdot10^{-3}$ K.

The $\mu_{eff}=3.4\ \mu_B$ is lower than the μ_{eff} of Mn^{+4} (3.87 μ_B) and higher than the formal μ_{eff} of the Mn^{+3} (2.83 μ_B) in a low spin state. The Mn^{3+} in the high spin state (4.90 μ_B) has a high effective moment in comparison to the one calculated for the Na-birnessite. An explanation on the presence of the Mn^{+3} in the low spin state has been reported concerning the Jahn-Teller distortion occurring in the porous manganese oxide octahedral fields.[264] However, in this case the μ_{eff} of the birnessite compound, is the outcome of a mixed valent character, since the Mn^{+3}/Mn^{+4} cations generate competing interactions, and thus magnetic frustration (relevant Figure 1.6).

In order to estimate the relative ratio of Mn^{+3}/Mn^{+4} we take into account the following equations:

$$x\cdot Mn^{+3}+y\cdot Mn^{+4}=3.4 \quad \textbf{(5.4)}$$

where x, y>0 thus $\frac{x}{y}>0$ **(5.5)**

Using the 5.4 and 5.5 relations we get: $\frac{Mn^{+3}}{Mn^{+4}}\approx\frac{2}{5}$ **(5.6)**

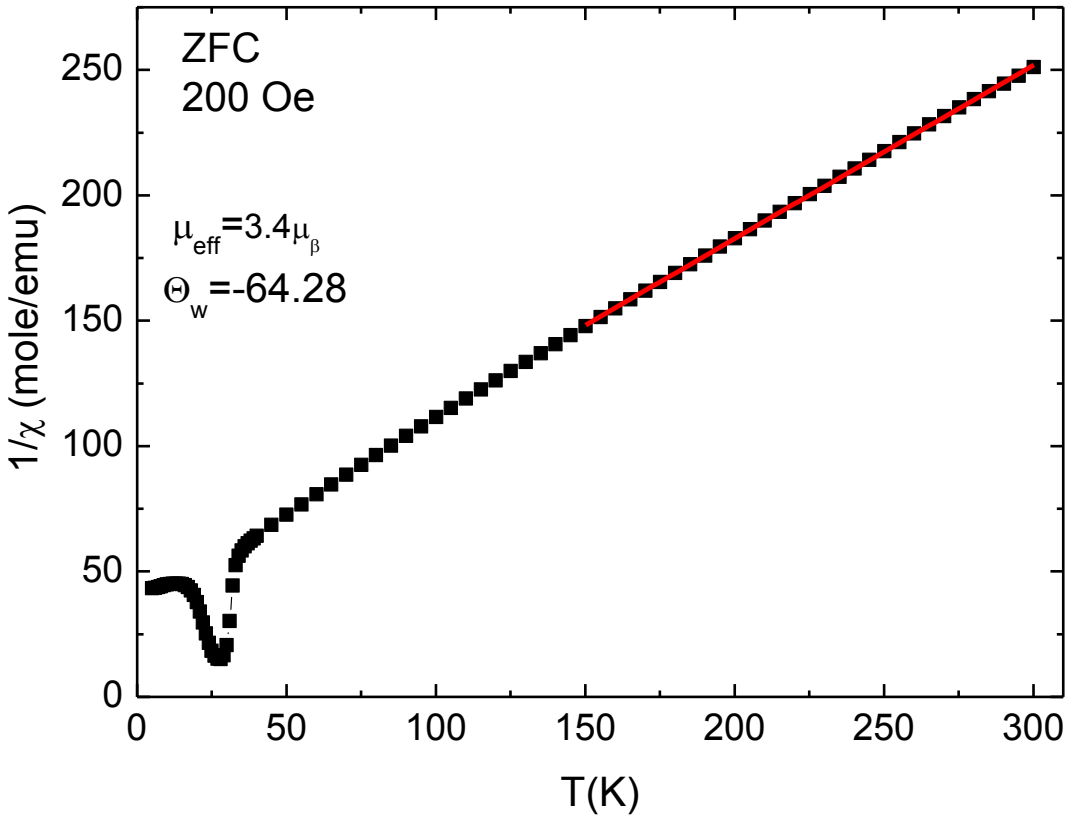

Figure 5.14 The reciprocal susceptibity ($1/\chi$) at the temperature range 150-300 K. The black points correspond to the experimental data, whereas the solid red line above 150 K represents the Curie Weiss fitting. The values of the intercept and the slope result in the calculation of the temperature Θ_w and the effective moment μ_{eff} of the Mn cations.

As mentioned in paragraph 1.3.6, an empirical way to estimate the degree of frustration in a magnetic system is to calculate the ratio $f=-\theta_w/T_N$. According to the above results, for θ_w=-64.28 K and T_N=29 K, f=-(-64.28)/29=2.21. Values of f>1 imply that the system is magnetically frustrated.[18] Nevertheless, the magnetic measurements are very sensitive to the mixed valence ratio.[265] A more reliable method for the determination of the Mn^{+3}/Mn^{+4} would be the EELS spectroscopy.

5.4.1.2 Magnetization versus Magnetic Field M(H)

The magnetization versus magnetic field of the $Na_{0.3}MnO_2 \times 0.2H_2O$ has been measured at 5 K. The sample was zero field cooled from room temperature to 5 K. After the temparture had stabilized at 5 K, the magnetic field was increased from 0-10.000 Oe with steps of 1000 Oe and from 12-50 kOe with steps of 2 kOe.

The result of the measurement is shown in Figure 5.15. No saturation has been observed up to the field 5 T. A small coercive field (H_c=1000 Oe) and a remnant magnetization ($M_R=2\cdot10^{-4}$ emu/gr) are observed. This could be an indication of a ferromagnetic component present in the $Na_{0.3}MnO_2 \times 0.2H_2O$ or it may suggest weak ferromagnetic interactions between the Mn^{+3} and Mn^{+4} cations

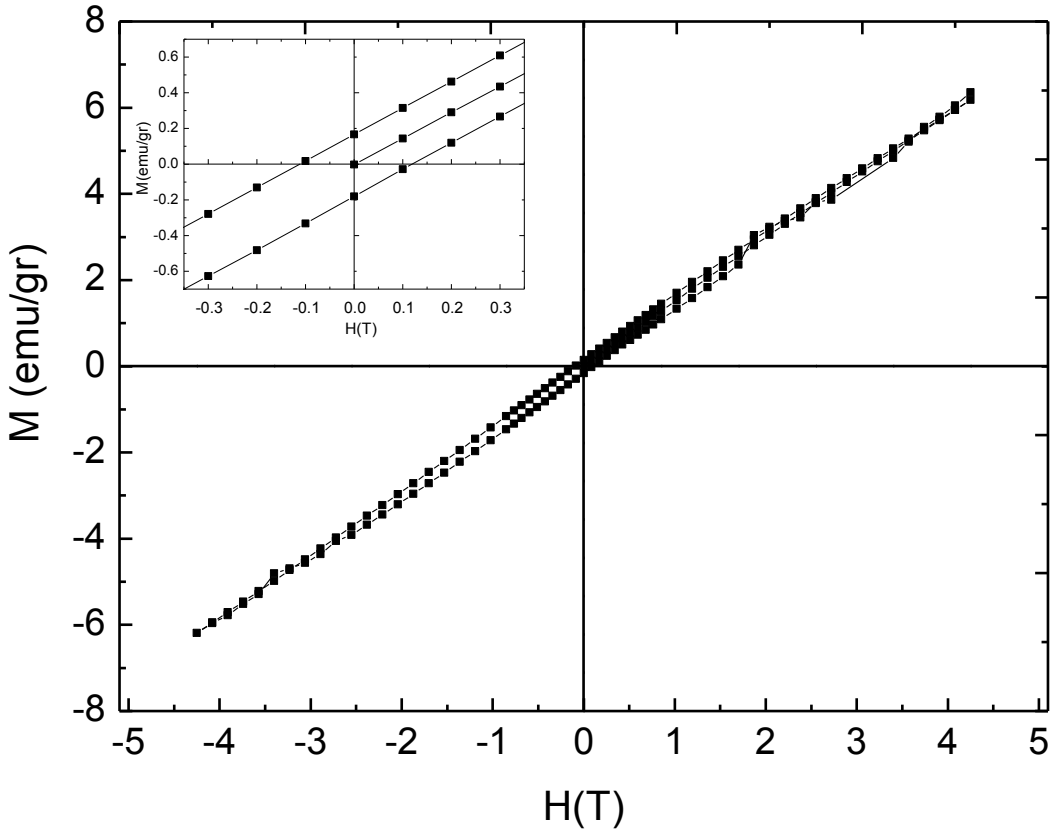

Figure 5.15 Magnetization versus magnetic field of the $Na_{0.3}MnO_2 \times 0.2H_2O$ at 5 K. The inset of the figure shows a detail of the coercive field Hc≅0.1 T.

5.4.1.3 Magnetic Field Dependence of the Spin Glass State.

A typical signature of the glassy state is provided by static measurements of the magnetic susceptibility versus different magnetic fields. In a spin glass as the external magnetic field increases, the sharp cusp in the ZFC susceptibility is expected to smear out, the ZFC-FC divergence becomes less pronounced and the spin glass temperature T_{sg} is shifted. [31] The aforementioned characteristics corroborate the dynamic nature of the spin glass state.

Figure 5.16 presents the ZFC-FC graphs of the Na-birnessite measured at the magnetic fields of 25, 50 , 100, 200, 500, 1000 Oe. Indeed, the sharpness of the transition is wiped out when the field is increased (100-200 Oe) until it becomes almost flat for fields of 500 Oe and 1000 Oe. Similar behavior has been observed in many magnetic systems which undergo a spin glass freezing.[260, 266, 267, 268] The elimination of the peak transition distinguishes a spin glass from the strong geometrically frustrated magnets (Figure 1.6), in which the sharpness of the peak remains intact even under high magnetic fields.[269]

Figure 5.17 shows the temperature dependence of the transition temperature T_{sg} in respect to the applied magnetic field. The T_{sg} is shifted to lower temperatures as the external magnetic field increases. According to the magnetic phase diagram of Figure 5.17, it becomes clear that for small magnetic fields (25-50 Oe) the spin glass transition temperature T_{sg} is around 28-28.5 K, whereas for higher fields (500-1000 Oe) T_{sg} is lowered below 26 K.

The dc field dependence of the spin glass temperature T_{sg} (H) follows the equation

$$T_{sg}(H) \propto 1 - bH^{\delta} \qquad \textbf{(5.7)}$$

in consistency with other spin glasses. [260, 270, 271] The fitted value of the exponent δ is 0.58 as shown in the fit of Figure 5.18, where a line is drawn between the paramagnetic region and the freezing spin state.

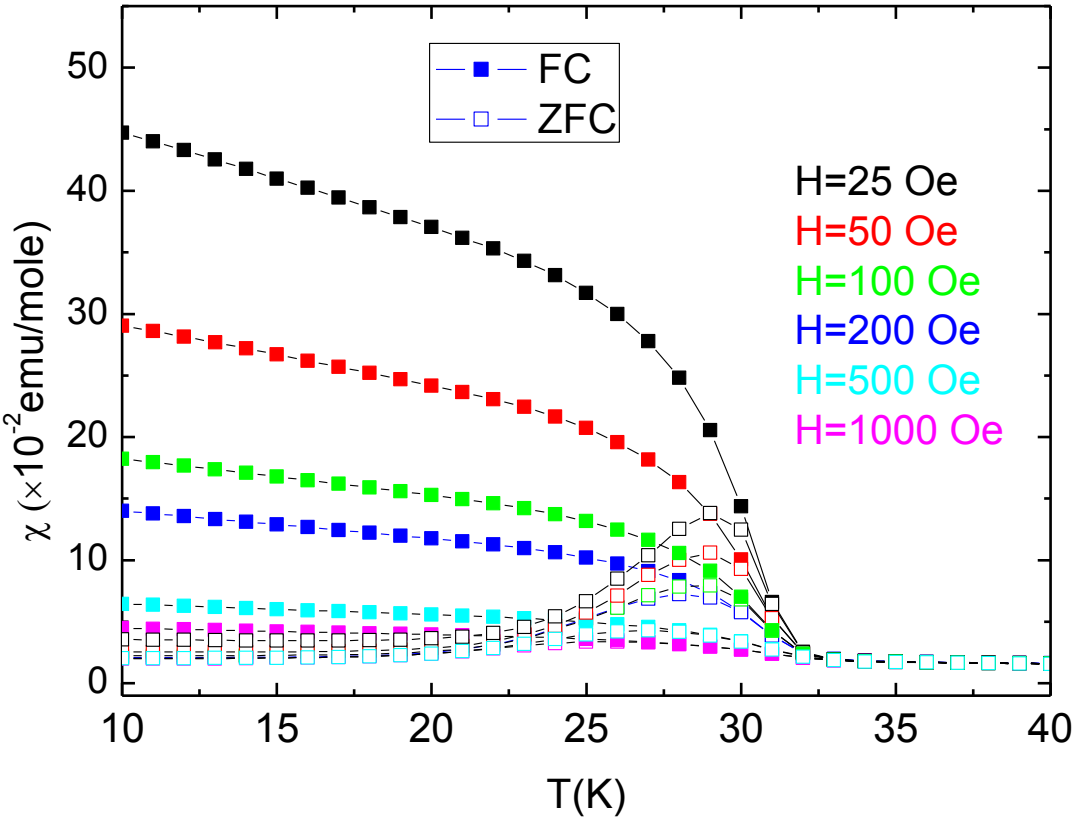

Figure 5.16 Field dependence of magnetic susceptibility as shown from the ZFC-FC measurements of the birnessite measured on dc mode at magnetic fields from 25-1000 Oe, between the temperatures 10-40 K. The sharp cusp at 29 K is eliminated as the external magnetic field is increased.

The justification of the origin of this linear response has caused an intense debate over the last decades.[30, 272] For Ising spin glasses Mean Field Theory (MFT) predicts that $\delta=2/3$. In MFT the transition in a magnetic field for an Ising spin glass (divergent relaxation times) to a paramagnetic phase (finite relaxation times) is separated by the Almeida Thouless (AT) line. The AT line is a ergodic-non ergodic transition with no symmetry change. For Heisenberg systems on the other hand, the dependence of the freezing temperature with the applied magnetic field follows the Gabay Toulouse line.[272] This line separates the

paramagnetic region from the spin glass state and shows a variation of the freezing temperature with the applied magnetic field by a exponent which is 1/2 in contrast to the 2/3 for the Ising systems.[272]

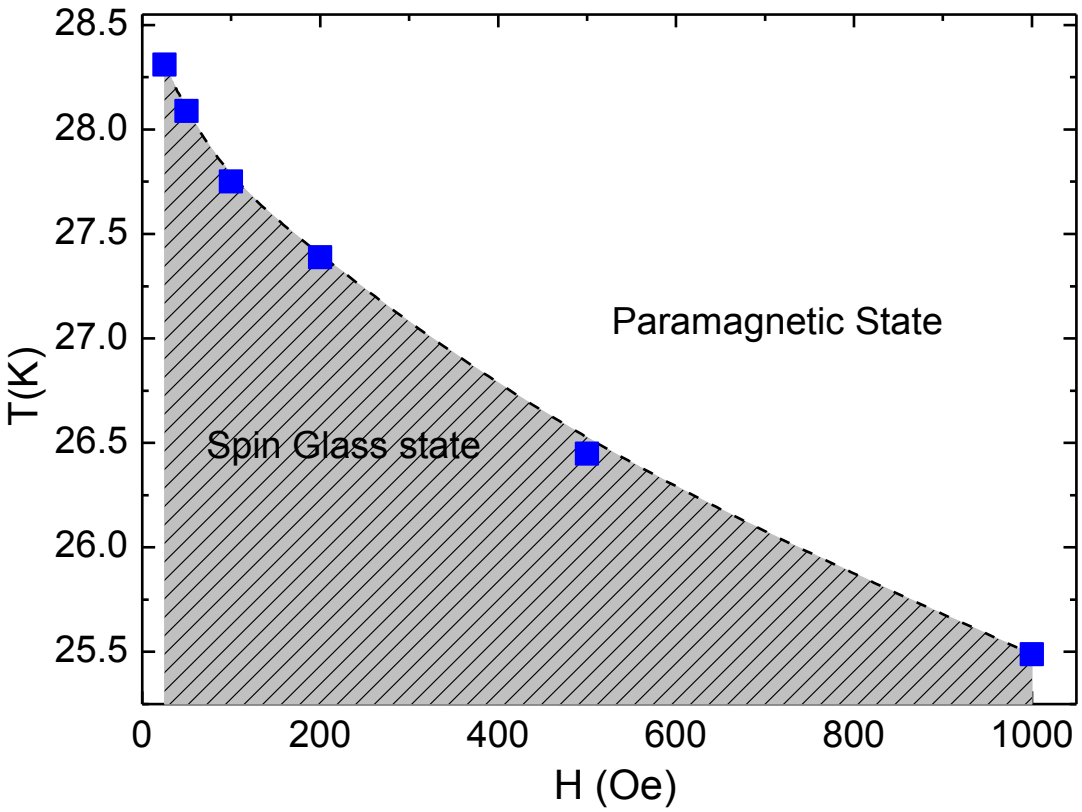

Figure 5.17 Magnetic phase diagram of the Na-birnessite, showing the magnetic field dependence of the spin glass freezing temperature T_{sg}.

The characterization of the $Na_{0.3}MnO_2 \times 0.2H_2O$ as an Ising, XY or Heisenberg spin glass surely requires more experiments and relevant analyses. The strong dependence of the freezing temperature with the magnetic fields provides another indication for the spin glass response, and distinguishes a spin glass from a strongly geometrical frustrated magnetic system.

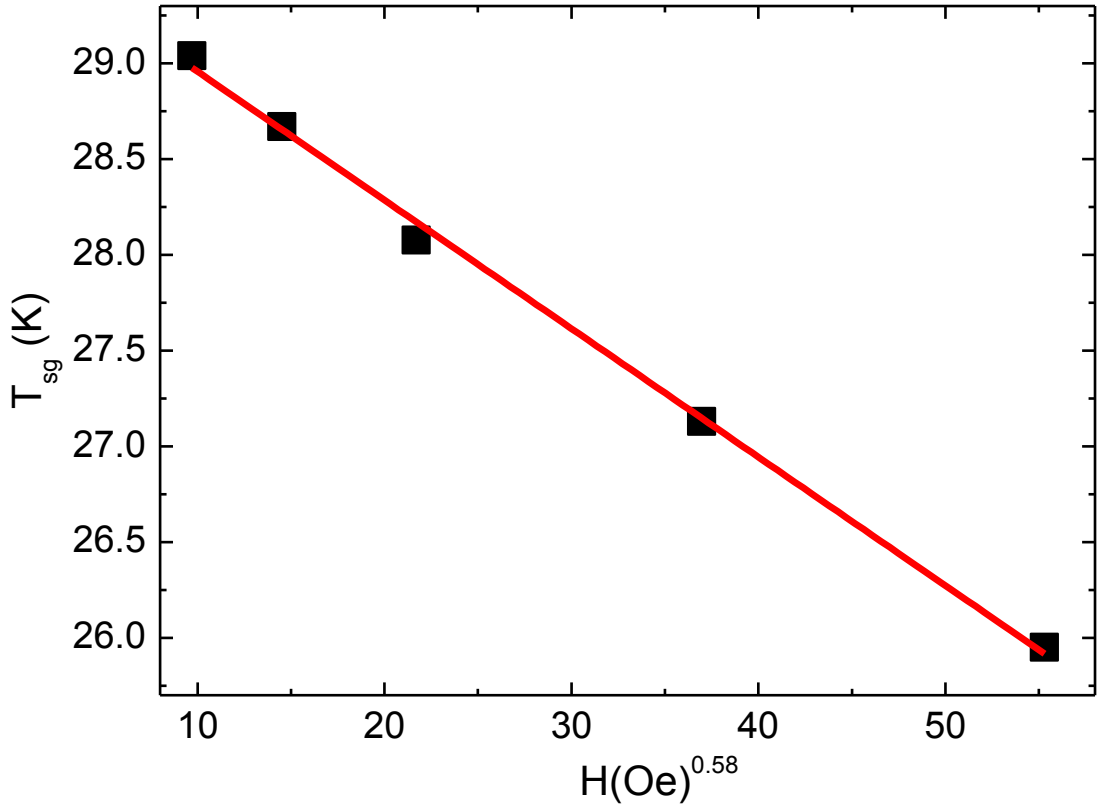

Figure 5.18 The dc dependence of the T_{sg} follows the equation: $T_{sg} \infty 1\text{-}bH^{\delta}$. The superscript δ was calculated equal to 0.58 in good agreement with the Mean Field Theory.

Nevertheless, since a spin glass shares common characteristics with superparamagentic materials the magnetic field dependence of the T_{sg} is still not sufficient to prove the glassy spin state of a material. The critical parameters which are essential in order to manifest that a system undergoes a spin glass transition, and reveal details about this time dependent nature of transition is the measurements of the dynamic susceptibility which are discussed in the following section.

5.4.1.4 Aging of a Spin Glass- Memory Effects and Rejuvenation Experiments

The dynamic properties of a spin glass can also be revealed by its aging properties with the help of relevant experiments in both static and dynamic susceptibility. A system is characterized as spin glass when it undergoes a transition where the spins are frozen below a critical temperature, which is known as freezing or spin glass temperature. The spins freeze in a thermodynamically non equilibrium metastable phase. There are different energy barriers between these metastable states. The effect of aging is realized when the energy barriers change. Specifically, the response to a field variation is logarithmically slow and it depends on the time spent at a temperature below the spin glass transition.[273]

A way to investigate the aging and memory effects in a spin glass system is with the so called rejuvenation experiments.[274, 275, 276] We have carried out these experiments on the static (dc) mode. The protocol that was used is the following: the sample is zero field cooled from 150 K to 10 K with a cooling rate of 2 K/min, then 2 Oe are applied and data are recorded upon heating between 10 -45 K, with a rate of 1 K/min. The sample is cooled down to 10 K, as this temperature is well below the spin glass freezing temperature. This is called the ZFC reference graph. Next, the sample is again heated up to 150 K, zero field cooled to 10 K with the same cooling rate that has been applied before (2 K/min) but during this cooling there is a waiting time of four (4) hours at 25 K. The temperature of 25 K has been chosen since it is lower than the 29 K where the spins of the system freeze. After the waiting time of 4 hours, the sample is further cooled down to 10 K where the field of 2 Oe is applied. Heating occurs with 1 K/min and magnetization is recorded between10-45 K. The data of the reference graph are subtracted from the magnetization of ZFC graph in which the waiting occurred, and their difference is plotted versus temperature.

The goal of the aforementioned experiment is to observe a dip in the temperature where the the waiting time was applied upon cooling the sample. In other words, the sudden decrease of the magnetization at the T_w (where T_w stands for the waiting temperature) would strongly suggest a memory effect for the sample, as it has been observed in other spin glass systems. [274, 275, 276, 277] The critical part is to determine the waiting time, which corresponds

to the characteristic scale of aging in each spin glass and therefore strongly depends upon the dynamic properties of the system.

The result of the aging experiment is presented in Figure 5.19. The plot which represents the difference in the magnetization of the reference graph subtracted from the one which entailed the waiting upon cooling, shows a dip exhibiting memory at the stage of 25 K. Upon further cooling to 10 K, the magnetization merges back to increase until 10 K, just like the reference graph, showing that aging at T=25 K has not influenced the spin frozen state below the waiting temperature[273] ("chaos effect").

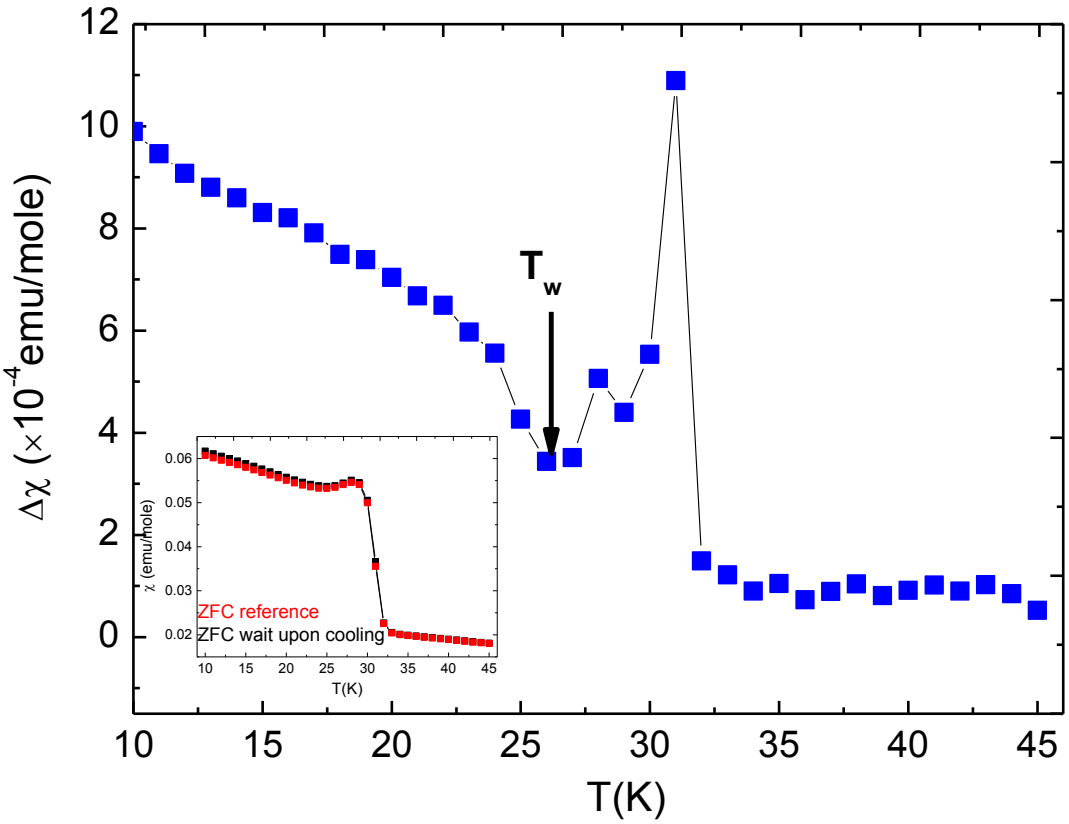

Figure 5.19 Memory effect in the aging of the $Na_{0.3}MnO_2 \times 0.2H_2O$ spin glass. The plot shows the difference in the magnetic susceptibility between an experiment with normal ZFC cooling and another one with a waiting time of 4 hrs at the T_w temperature of 25 K, which are presented in the red and black graph of the inset, respectively. The dip at 25 K reveals the memory effect in this spin glass system.

5.4.2 Dynamic (AC) Susceptibility

5.4.2.1 The Mydosh parameter

Although the dc susceptibility measurements reveal important spin glass features, the signatures of the glassy state are extracted from the dynamic susceptibility experiments. This is reasonable if one takes into account that the transition into the spin glassy state is a dynamic procedure, thus, it is highly dependent on time.

In order to understand better the dynamic process which is engaged in the spin glass transition we have carried out a series of experiments and relevant analysis. Figure 5.20 shows the temperature dependence of the ac susceptibility measured with five different frequencies. The measurements were carried out with a step by step mode with an AC drive field of 3 Oe and a DC field of 0 Oe. The real (χ') and imaginary (χ'') part of the magnetic susceptibility exhibit a sharp peak at 29 K, which is frequency dependent.

Specifically, the peak temperature T_f shifts towards higher temperatures and the height of the susceptibility peak diminishes with increasing frequency. T_f stands for the freezing temperature in analogy with the T_{sg} used for the static (dc) experiments and denotes that the transition temperature depends on the frequency f, where $f=\omega/2\pi$.

A frequency dependent peak in the susceptibility usually reveals a spin glass like state or a superpamagnetic one. According to Mydosh [31] a quantative measure of the frequency shift is obtained by calculating the ratio

$$K= \Delta T_f/[T_f \, \Delta(\log \omega)] \qquad \textbf{(5.8)}$$

which stands for the ratio $\Delta T_f/T_f$ per decade ω, also called as the "*Mydosh parameter*". The quantification of the frequency shift of the transition temperature, offers a good criterion for the distinguishing a canonical spin glass from a superparamagnet. For a spin glass system K is of the order of 0.01 or less, whereas for a superparamagnet K ~ 0.1.

The Mydosh parameter has been calculated from the data of Figure 5.20 for the $Na_{0.3}MnO_2 \times 0.2H_2O$ and was found equal with 0.007 which is in the range for the canonical spin glasses.[277, 278, 279]

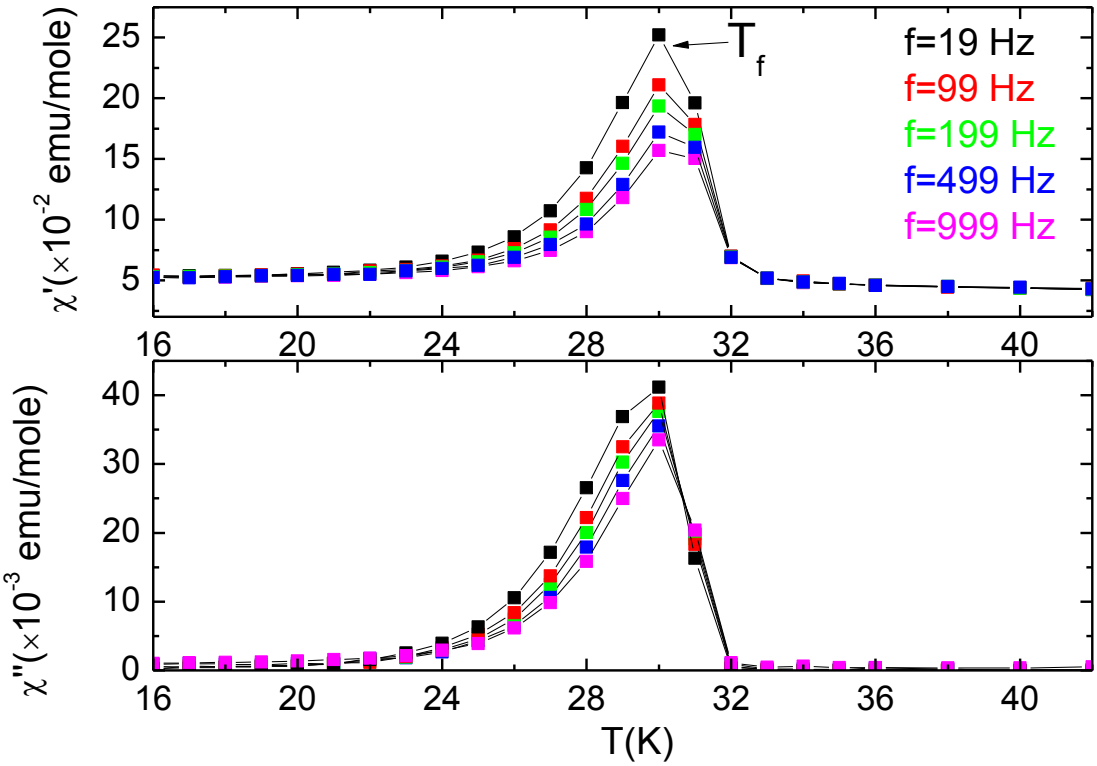

Figure 5.20 Real (χ') and imaginary (χ'') part of the dynamic susceptibility measured at five different frequencies, under the AC drive field of 3 Oe.

At this point it is useful to add a comment concerning the each category of systems ("canonical" spin glasses and "superparmagnets") which exhibit characteristics of the spin glassy state.

The term "canonical spin glass" refers to atomic spin glasses such as the arhectypal CuMn, AuMn systems. In these systems the atomic moments freeze below the transition temperature. The characteristic spin flip time is at the range of 10^{-9}-10^{-13} seconds. Their interactions are usually described by the Vogel Fulcher or the Power Law in contrast with the superparamagnets which are best described by the Arrhenius law (see paragraphs 5.4.2.2 and 5.4.2.3). The interactions for the atomic spin are short or long range RKYY interactions whereas the strength of the interactings moments has amplitudes of some μ_{β}.

[280]According to Mydosh[30] these "good"spin glasses meet three criteria related with the ac susceptibility, the magnetic specific heat and the low temperature magnetization vs field[30] Other magnetic systems which show some of the characteristics of the glassy state without being characterized as spin glasses are the superparamagnets. Superparamagnets are characterized by non interacting single domain particles whose magnetic moments act independently. The magnetic moments are unbstable due to thermal agitation.[247]

5.4.2.2 Phenomenological Desciption of Dynamic Properties in Spin Glasses

The frequency and field dependent nature of the spin glass transition has been the subject of intense debate since the 1970's.[281, 282] As mentioned in the previous paragraph similar spin glass characteristics can be found in magnetic systems with different underlying interactions. Three laws have been proposed to describe the dynamic properties of a spin glass system: the Arrhenius, the Vogel-Fulcher and the Power Law. Each case depends primarily on the type of magnetic particles (atomic spins, clusters or superspins) and the strength of their interaction.

The Arrhenius law describes the interaction mechanisms between weakly or non interacting particles (isolated clusters or superparamagnetic state) and is given by the equation[30]:

$$\tau=\tau_o e^{\frac{E_a}{k\beta T_f}} \qquad \textbf{(5.9)}$$

where E_α is the activation energy determined by the energy needed to exit out of a local potential well, [283] T_f is the shift of the critical temperature with the frequency f and τ_o is the "relaxation" or "attempt" time.[284 283]

An equal expression of equation 5.9 is the

$$\omega=\omega_o e^{\frac{-E_a}{k\beta T_f}} \qquad \textbf{(5.10)}$$

where ω is the driving frequency and T_f is the peak relevant to each frequency.

The strength of the interactions determines the relaxation processes and thus the value of τ_o. A modification of the Arrhenius law is given by the equation

$$\tau=\tau_o e^{\frac{E_a}{k_\beta(T_f-T_0)}} \quad \textbf{(5.11)}$$

where E_α/k_β stands for the activation energy in order to overcome the barrier for the reversal of the magnetization and T_o gives a qualitive estimation for the inter-particle interaction energy.[284] Equation 5.11 is known as the *Vogel Fulcher law* and holds for interactions of moderate strength.

Nowadays it is generally accepted that the dynamic scaling theory best describes the spin glass transition using the Power Law which holds for stronger interactions. According to the dynamic scaling theory,[26] the slowing down of spin dynamics when the freezing point (T_{sg}) is approached from above, can be described by the relation of the correlation time τ with the correlation length ξ according to $\tau \propto \xi^z$, where z is the dynamical scaling exponent. The correlation length, depends upon the temperature according to the $\xi \propto t^{-\nu}$ and so, the evolution of the correlation time near the critical point is given by the power law,

$$\tau = \tau_0 t^{-zv} \quad \textbf{(5.12)}$$

which is equivalent with $$\tau= \tau_o \left[\frac{T_f-T_{sg}}{T_{sg}}\right]^{-zv} \quad \textbf{(5.13)}$$

or the equation $$f=f_o\left[\frac{T_f-T_{sg}}{T_{sg}}\right]^{zv} \quad \textbf{(5.14)}$$

The parameter τ_o corresponds to the time needed for a single spin to undergo a transition from the paramagnetic state to the frozen state of the spin glass and is also known as the relaxation time. The product zv, has acceptable values between 4 and 12 for different spin glasses,[31] for example zv varies from 6-8 for the three dimensional Heisenberg like Ag(Mn) magnetic systems whereas it takes higher values of 10-12 for the Ising $(FeMn)TiO_3$ spin glasses.[25,285,272, 286] The temperature T_f is the one that varies upon frequency changes. In the equilibrium (DC) case, where f=0, T_f reaches T_{sg}. Hence, in the power law fit, the temperature T_{sg} is estimated as if the transition occurred ideally in one temperature. This arises from the need to have one critical temperature (T_{sg}) for each spin glass system which will be frequency independent.

5.4.2.3 Arrhenius Law

Another criterion which rules out the case of superparamagnetism for the $Na_{0.3}MnO_{2\times}0.2H_2O$ is derived from the Arrhenius Law.

In order to use the Arrhenius law in a linear fit, it is more convenient to use equation 5.6 by taking its natural logarithm, which yields the following:

$$In(\tau)=In(\tau_o)+\frac{E_a}{k_\beta}T^{-1} \quad \textbf{(5.15)}$$

Which clearly can be fitted to the simple equation $y=\alpha+bx$,

where x is the reciprocal of the T_f and $In(\tau)$ is calculated by the frequency used as $f=1/\tau$.

According to the data of Figure 5.20 and the aforementioned calculation method, the best fit to the Arrhenius law (Figure 5.21) resulted in completely unreasonable numbers for τ_o and E_a, namely $\tau o=10^{-151}$ sec and $\frac{E_a}{k_\beta}$ =10216 K. The unphysical values of the activation energy barrier and the relaxation time, are attributed to the subtle changes of the T_f with the increasing frequency.[30] This suggests that the system dynamics is not dictated by superparamagnetic blocking of spins.

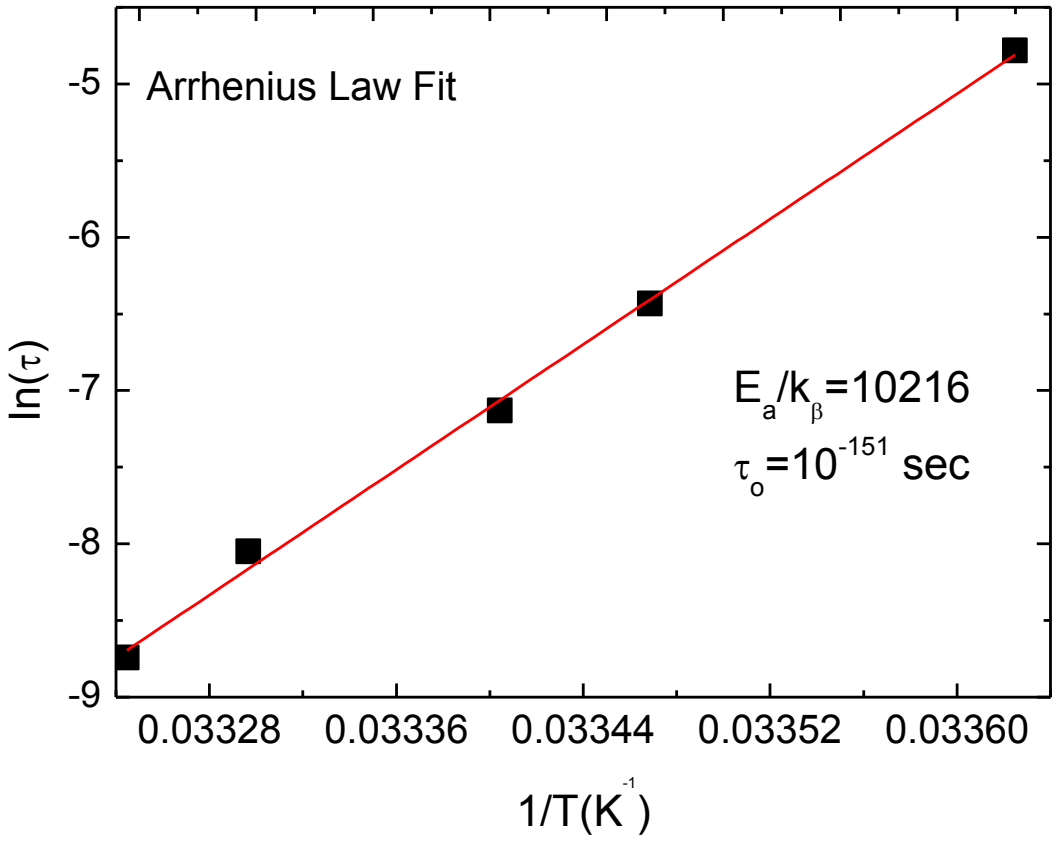

Figure 5.21 The Arrhenius Law fit yields completely unreasonable values for the activation energy and the relaxation time, which excludes the possibility of superparamagnetism for the $Na_{0.3}MnO_2\times0.2H_2O$.

5.4.2.4 Power Law fits: $Na_{0.3}MnO_2\times0.2H_2O$ a canonical spin glass

The data used in the power law fit are shown in Figure 5.22 and were recorded using the "sweep" option in the AC susceptibility measurements. In contrast with the "step by step" (see data of Figure 5.20) in which there is time delay in each temperature step, the sweep mode was chosen as a more appropriate one, since it affects less the thermodynamic and time dependent phenomenon of the spin glass transition.

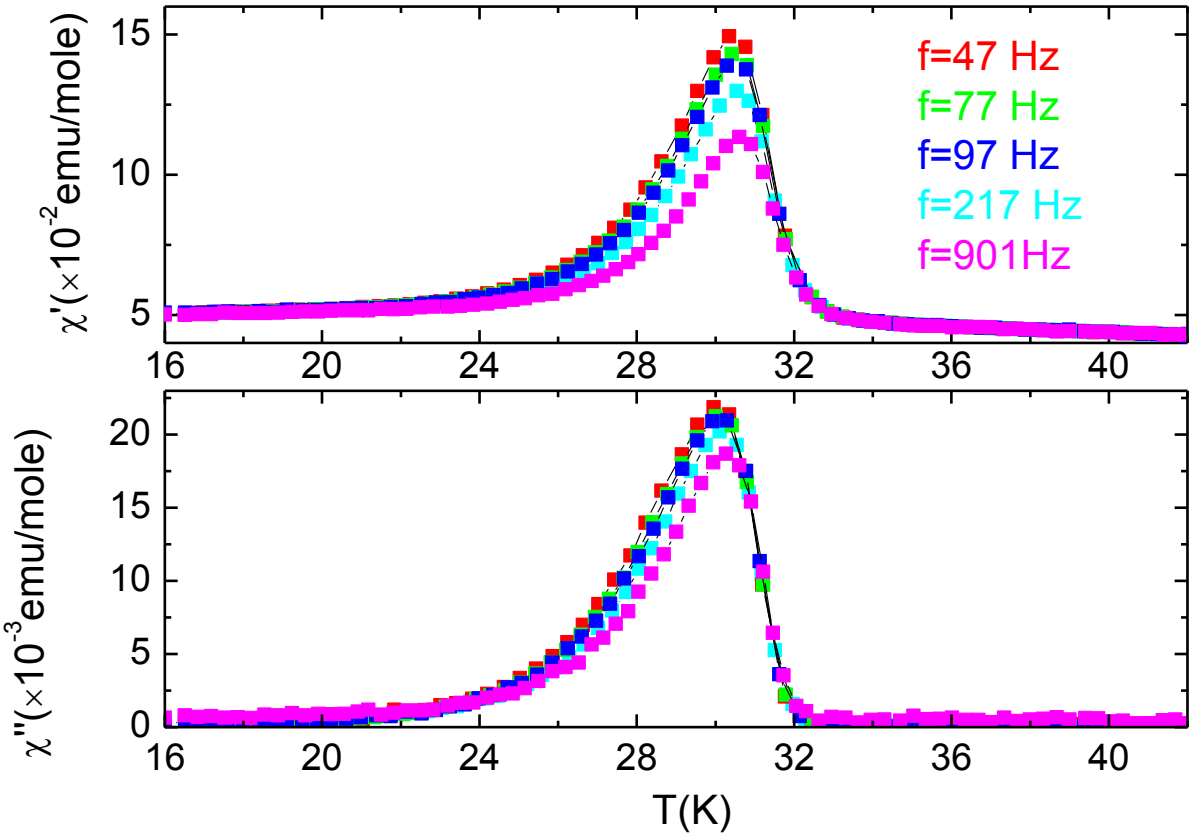

Figure 5.22 Real (χ') and imaginary (χ'') part of imaginary susceptibility versus temperature at 5 different frequencies, measured under 3 Oe AC drive field. The magnitude of both χ' and χ'' are suppressed whereas the T_{sg} is shifted to higher temperatures as the frequency increases.

The fit was done according to the equation [287]

$$\log(f)=\log(f_o)+zv\log\left(\frac{T_f-T_{sg}}{T_{sg}}\right) \qquad \textbf{(5.13)}$$

which is derived from the equation 5.11 and it is presented in Figure 5.23. Details on the method used for the power law fit are presented in Appendix D.

The best fit of the frequency dependence for the $Na_{0.3}MnO_2 \times 0.2H_2O$ yielded the following parameters: T_{sg}=29.64 K, $f_o=3.36\times10^{11}$ Hz which corresponds to $\tau_o=0.275\times10^{-11}$ sec and

zv=5.029(12). The values of τ_o and zv are in consistency with other magnetic systems which have been classified as canonical spin glasses [30, 163, 276] such as the delafossites $CuFe_{0.5}V_{0.5}O_2$ and $CuCr_{0.5}V_{0.5}O_2$ with zv of 6.06, and 9.12[163] respectively. Other examples is the Ising spin glass $Fe_{0.5}Mn_{0.5}TiO_3$ with zv 10.5 and the $CdCr_{1.7}In_{0.3}S_4$, a Heisenberg spin glass with zv 5.[288]

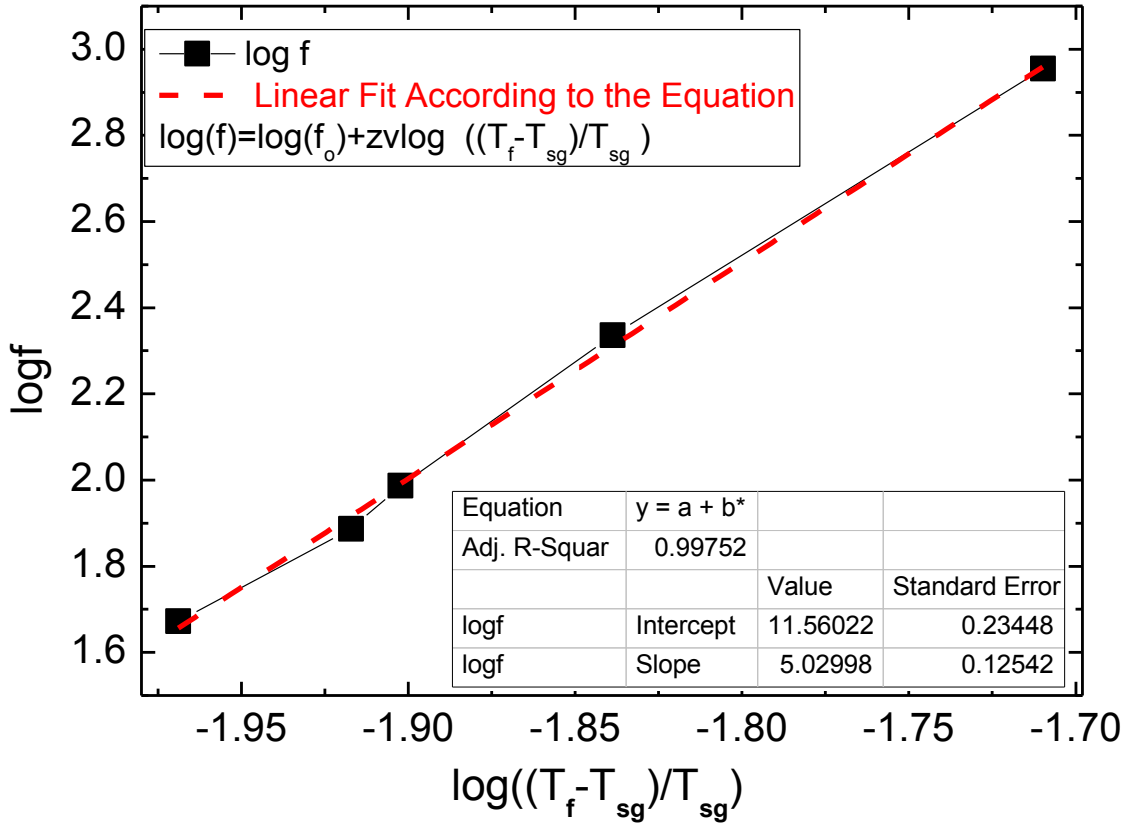

Figure 5.23 Frequency dependence of the freezing temperature in the Na-birnessite in the plot according to the power law. The best fitting is displayed which is based on the data of Figure 5.22, and corresponds to the following parameters: T_{sg}=29.64 K, $\tau_o=10^{-11}$ sec and zv=5.03(12).

5.4.2.5 Field Dependence of the spin glass temperature.

The dependence of the T_f temperature has also been followed upon the application of moderate dc magnetic fields. The dynamic susceptibilities on a ZFC "sweep" mode at the frequencies of 117 Hz and 1217 Hz under the AC drive field of 3 Oe and static (DC) fields H= 25, 50, 100, 200, 250, and 500 Oe, are plotted in Figure 5.24.

In both tested frequencies, as the field increases the sharpness of the peak is decreased and the spin glass temperature is shifted towards lower temperatures. The sharp peak of both χ' and χ'' flattens out and shifts to lower temperatures, when the static magnetic field is increased. These results are in consistency with similar measurements (Figure 5.16) carried out in the static mode under various magnetic fields. These measurements support the spin glass state of the birnessite $Na_{0.3}MnO_2 \times 0.2H_2O$.

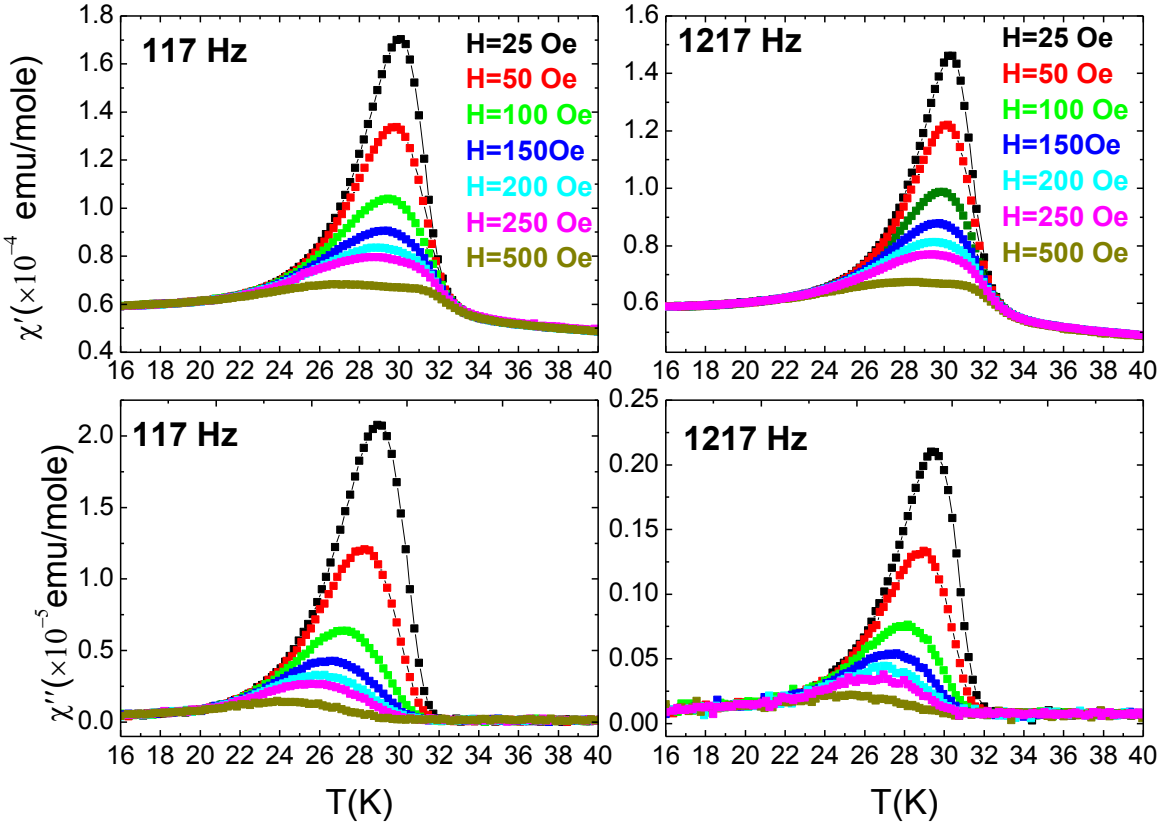

Figure 5.24 Real (χ') and imaginary (χ'') part of the magnetic susceptibility of the $Na_{0.3}MnO_2 \times 0.2H_2O$, measured under 3 Oe drive field measured at 1217 Hz and 117 Hz on a ZFC mode, under various (25-500 Oe) static magnetic fields.

5.5 Neutron Powder Diffraction Data

Neutron powder diffraction data were obtained in the high resolution powder diffractometer BT1, in NCNR-NIST, USA, with the constant wavelength λ=2.0782 Å. Polycrystalline powder $Na_{0.3}MnO_2 \times 0.2H_2O$ of 8 gr was used in the NPD experiment which were mounted in a vanadium can (of 2.4 mm internal diameter).

The goal of this experiment was twofold. First, it was essential to get high resolution data for Rietveld refinements. This would support the indexing and finally the solution of the crystal structure. Scans at different temperatures were taken, namely at 5 K, 20 K, 50 K and 300 K , to check for a possible structural transition due to the spin glass state below 29 K. Secondly, since in a spin-glass the magnetic ordering lacks spatial long-range order, with the NPD experiments one is expected to probe the development of magnetic diffuse scattering at long d-spacings.[289] However, the expected problem of the increased background due to the large incoherent scattering cross section of water protons hindered such observation. Indeed, despite the large quantity of the sample and the intentionally increased duration of each scan (6-7 hrs) which improves the statistics and the intensity of the Bragg reflections, the patterns did exhibit significantly raised background. That in turn, reduced the capability for full profile refinenement of the NPD patterns.

Figure 5.25 shows the NPD patterns obtained at 5 K, 20 K, 50 K and 300 K. One first observes the high background and most importantly the lack of any extra Bragg reflections below the spin freezing transition temperature (29 K) at the patterns of 20 K and 5 K. The absence of the magnetic reflections, is consistent with the spin glass behavior of the $Na_{0.3}MnO_2 \times 0.2H_2O$ below the T_{sg}=29 K.[30, 289] The appearance of a possible diffuse magnetic scattering, even if it existed would be difficult to resolve due to the increased incoherent background.

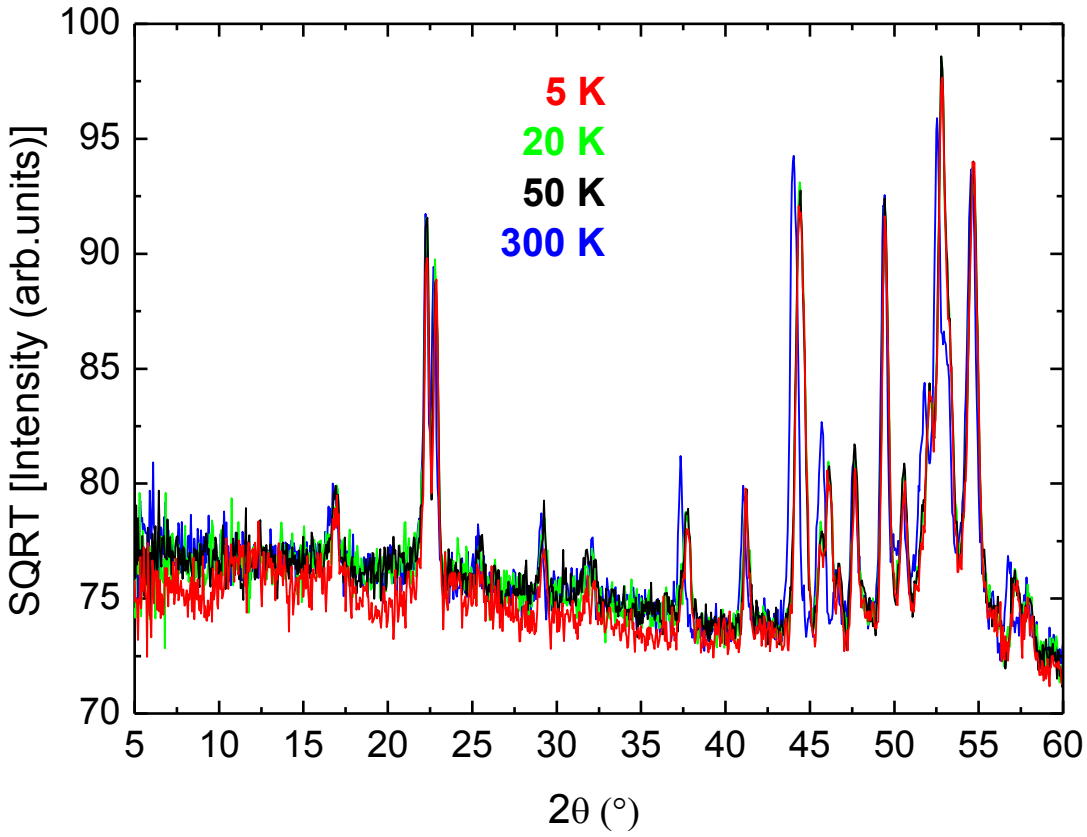

Figure 5.25 Neutron scans obtained at the temperatures of 5 K, 20 K, 50 K and 300 K shown with the red, green, black and blue patterns, respectively. The absence of magnetic reflections at the 5K and 20 K scans, shows that no range magnetic ordering develops below 29 K.

5.6 Results and Discussion

The hydration of the α-$NaMnO_2$ compound resulted in a birnessite compound with different structural charateristics. The $Na_{0.3}MnO_2 \times 0.2H_2O$ crystallizes in the triclinic system, at the space group $P\bar{1}$ with the following cell parameters: a= 5.53(1) Å, b= 3.11(6) Å, c=7.80(1) Å, α=89.492(13)° β=103.136(12)° γ=89.929(10)°. The magnetic properties are generated by the Mn^{+3}/Mn^{+4} cations which exhibit the mean oxidation state of 3.4. The structural difference among the various manganese oxides is generally induced by the

presence of vacancies, the development of planar defects which may give rise to mixed valences cations and specifically induce a variety of Mn^{+3}/Mn^{+4} ratios.

The chemical formula of $Na_{0.3}MnO_2 \times 0.2H_2O$ which is used for the synthesized compound is based on the results and analysis of TEM experiments. It is useful to mention that the comparison of the chemical analysis obtained by the ICP-OES and HRTEM experiments show different results, an issue which should be elucidated. Based on the ICP-OES experiment the Na/Mn ratio was 0.7, whereas the chemical formula of the birnessite according to combined EELS and EDS spectra was found to be $Na_{0.3}MnO_2 \times 0.2H_2O$, meaning that the Na/Mn ratio is 0.3. Moreover, the amount of H_2O as calculated by the TGA experiment is around 13%. This amount is lower in comparison with the results of EELS and EDS analysis.

Concering the inconsistency between the ICP-OES and the TEM results, two are the possible reasons. The first one is related on the lack of good statistics in the ICP-OES experiment. Usually the ICP-OES findings are extracted by at least three measurements, with the relavant statistical errors. In our case, we could perform only one measurement, which decreases the degree of certainty concerning the specific result. The most probable reason though, lies on the fact that the sample was not 100% homogeneous .The ICP-OES and TGA experiments yield results from the entire volume of the sample whereas the observation carried out with TEM has definitely a more local character. Similarly, the TGA and TEM results are different both due to partial inhomegenuity of the sample and also due to the different way by which the results are extracted in these two methods. Nevertheless, we rely on the results obtained from the HRTEM analyses, since the chemical formula $Na_{0.3}MnO_2 \times 0.2H_2O$ described well all the crystals that were examined.

Many birnessite systems have been studied[231, 233], but all the studies were focused on the various preparation methods and their possible technological applications. To our best knowledge, up to now (2014) there are only a few reports which are directed towards the magnetic properties of birnessite compounds. Here for the first time, the glassy state of a birnessite-the $Na_{0.3}MnO_2 \times 0.2H_2O$ has been proven.

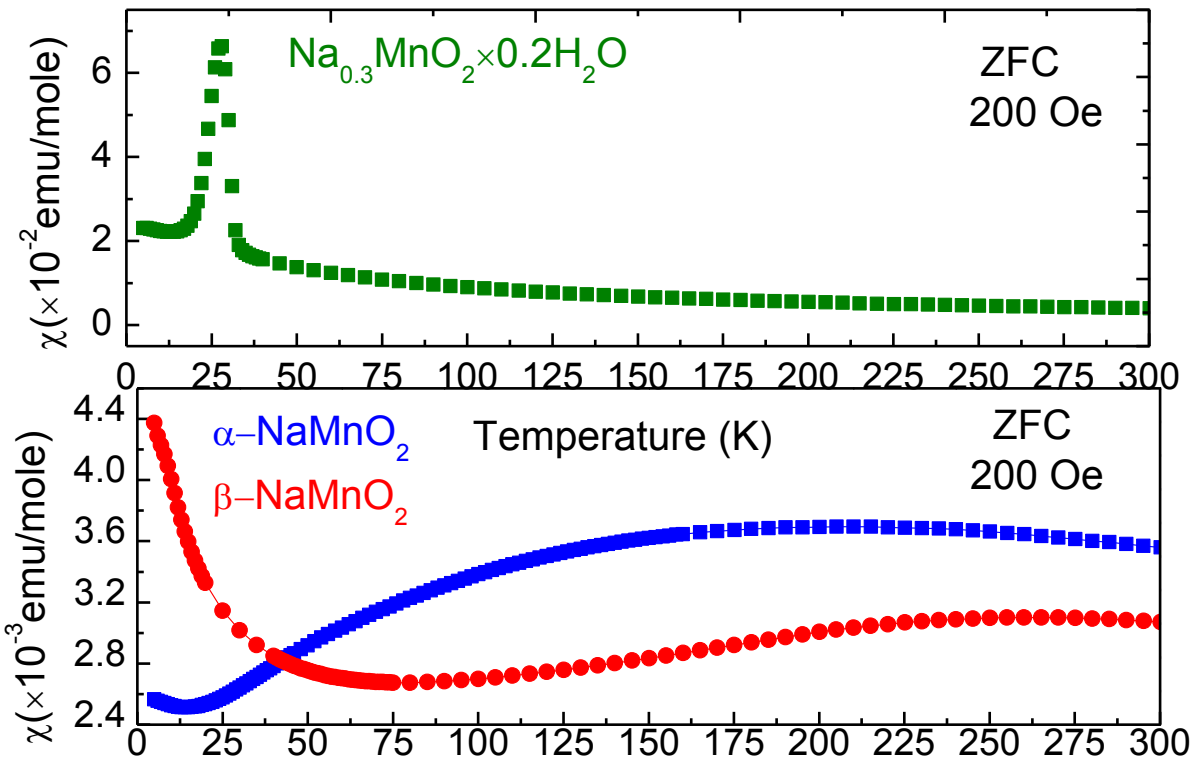

Figure 5.26 Magnetic susceptibility measured on a DC mode at a ZFC measurement at 200 Oe for the α-$NaMnO_2$, β-$NaMnO_2$ and $Na_{0.3}MnO_2 \times 0.2H_2O$ shown with the blue, red and green graphs, respectively.

An extensive research has been carried out concerning the magnetic properties of the $Na_{0.3}MnO_2 \times 0.2H_2O$ compound. Figure 5.26 shows the ZFC measurement on a DC mode under 200 Oe of magnetic field for the birnessite (upper panel of Figure 5.26), and the α-$NaMnO_2$ and β-$NaMnO_2$ compounds (lower panel of Figure 5.26). The low dimensional magnetism of the two antiferromagnets α and β-$NaMnO_2$ has already been discussed in the previous chapters 3 and 4. Here, we aim to highlight the striking difference in the magnetic behavior of the spin glass birnessite and the two antiferromagnets, the $NaMnO_2$ polymorphs. The magnetic susceptibility of both α and β $NaMnO_2$ polymorphs does not

show any obvious sign of magnetic transition. On the contrary, $Na_{0.3}MnO_2\times0.2H_2O$ exhibits a sharp peak at 29 K which marks the onset of a spin glass transition.

The novelty in our studies concerning the $Na_{0.3}MnO_2\times0.2H_2O$ is the investigation of its magnetic properties and especially its characterization as a canonical spin glass below T_{sg}=29 K. The extracted attempt (relaxation) time of $\tau_o=10^{-11}$ sec and the exponent zv=5.026 are typical for atomic spin glasses.[30] Other spin glass systems with comparable zv values are the $Fe_{0.5}Mn_{0.5}TiO_3$ (zv= 10.5) and the $CdCr_{1.7}In_{0.3}S_4$ (zv= 5.286), whereas the relaxation time of $\sim10^{-11}$ is similar with that found for the $SnCFe_3$[290]. The spin glass state is attributed to frustration.

In this section we also consider possible mechanisms which generate the spin frustration in the $Na_{0.3}MnO_2\times0.2H_2O$ compound. In general, bond order or site disorder can cause magnetic frustration. [18] The magnetic properties of the birnessite are generated by the interactions of Mn^{+3} and Mn^{+4} cations. A reasonable thought is that the ratio of the mixed valence cations determines and alters significantly the magnetic properties. Although the presented experimental results can not determine the exact ratio of Mn^{+3}/Mn^{+4}, the calculation of the effective moment to $\mu_{eff}=3.4\ \mu_B$ and the mean oxidation number of 3.4 of the Mn cations are in consistency with the statement that the magnetic properties of birnessite result from the mixed valent Mn cations in the lattice.

Site disorder in the $Na_{0.3}MnO_2\times0.2H_2O$ can be originated by vacancies in the MnO_6 octahedra, which is a general characteristic of the birnessite like compounds. [229] The Mn vacancies, whether attributed to the Mn^{+3} of Mn^{+4} cations, surely would result in a disruption of the periodicity in the magnetic interactions. This can be seen clearly in the planar defects revealed by the TEM experiments (Figures 5.9 and 5.10) of the crystal structure investigations.

On the other hand bond disorder could be motivated by the competition of ferromagnetic and antiferromagnetic interactions either by the Mn^{+3} cations, or by the Mn^{+3} and Mn^{+4}. The replacement of the Mn^{+3} with the Mn^{+4} during the hydration of the α-$NaMnO_2$ probably happens without specific pattern. This resembles the doping of a non magnetic system with randomly distributed magnetic entities.[30] The competing ferromagnetic and

antiferromagnetic interactions due to the coexistence of Mn^{+3} and Mn^{+4} cations at random site distribution may lead to disorder and thus can generate the spin glass state of the $Na_{0.3}MnO_2 \times 0.2H_2O$ compound.

5.7 Conclusions

A new birnessite compound has been synthesized and characterized as a canonical spin glass. The $Na_{0.3}MnO_2 \times 0.2H_2O$ was prepared by hydration of the polycrystalline powder α-$NaMnO_2$. The crystal structure has been probed by XRPD and High Resolution Electron Diffraction. According to the HRTEM analysis the $Na_{0.3}MnO_2 \times 0.2H_2O$ crystallizes in the triclinic, space group $P\bar{1}$. Measurements of the static and dynamic susceptibility reveal the canonical spin glass character of this compound. Characteristic signatures of a glassy magnetic system, such as the irreversibility between the ZFC-FC curves, the calculated Mydosh parameter, the characteristic spin flip time (attempt or relaxation time τ_o), the elimination of the transition when few Oe of magnetic field are applied, the memory effect, all manifest that the system's magnetic moments, undergo a spin freezing state at T_{sg}=29 K. The magnetic properties are attributed to the manganese cations and specifically to the mixed valence of Mn^{+3}/Mn^{+4}, with mean magnetic moment of 3.4 μ_B and oxidation state of ~ 3.4.

Chapter 6: Perspectives

In this chapter we discuss the issues which will shed light on questions concerning the understanding of the α-$NaMnO_2$, β-$NaMnO_2$ and the birnessite $Na_{0.3}MnO_2 \times 0.2H_2O$ physics and technological potential. The α-$NaMnO_2$ is the polymorph that has been studied the most in the recent years in comparison with the β-$NaMnO_2$ and the $Na_{0.3}MnO_2 \times 0.2H_2O$. Currently, the identification of the magnetodielectric coupling at 95 K, and the investigation of its microstructure[143] open new questions and novel fields for research. The information that has been reported from 1971-2014 concerning the β-$NaMnO_2$ is very limited, and related with basic information about its crystal structure. In this thesis we reported a wide range of characterization methods, which could be enriched by continuing the studies on the unusual properties of this complex oxide. The findings reported for the first time in this thesis concerning the preparation, the crystal and magnetic characterization of the birnessite $Na_{0.3}MnO_2 \times 0.2H_2O$ propose the investigation of a new intercalation compound with canonical spin glass magnetic properties. More specifically, the following are some suggestions of what could be done in each oxide to enrich the knowledge on their chemical and physical properties:

1) Magnetic susceptibility measurements on the β-$NaMnO_2$

- From 5 K -320 K, under various magnetic fields ranging from 5 Oe to 7 T: The goal of these measurements would be to check any possible variation in the magnetic susceptibility χ and possibly to observe any anomalies in the χ(T) at the temperatures of the two magnetic orderings: 90 K and 200 K.
- These may be related to a possible spin flop transition, already inferred from preliminary measurements (not presented in the Ph.D thesis) in the region of 4 T-4.5 T. The possibility of such a metamagnetic-like transition could be elucidated from these experiments. [291]

2) Solid State Nuclear Magnetic Resonance (NMR) relaxation experiments on β-$NaMnO_2$. The NMR spectra at temperatures 50 K-300 K would allow us to check for the changes in the Mn^{+3} magnetic ordering at different temperatures, and compare these data with the NPD results.

3) Further investigation on the dielectric properties of β-$NaMnO_2$ and α-$NaMnO_2$

- Measurements of the dielectric constant under various frequencies (20 Hz -1 MHz). The measurements could reveal possible frequency dependence of the observed magnetodielectric anomalies.
- Measurements of the magnetocapacitance. These measurements include scans of the capacitance from negative to positive magnetic fields. The basic information is the strength of the magnetodielectric coupling.
- Pyrocurrent and polarization measurements at low temperatures. The I-V (current versus voltage) loop of Figure 4.31 and the polarization below 70 K shown in Figure 4.33 suggest that β-$NaMnO_2$ is polar below the incommensurate transition temperature (T<90 K). This could be further checked by pyrocurrent (current versus temperature) and polarization measurements. The same procedure can also be followed for the α-$NaMnO_2$ compounds.

4) Low temperature TEM observation of the polymoprhs on β-$NaMnO_2$ and α-$NaMnO_2$ on temperatures 80-280 K. These experiments could inform us about any structural distortions that the system undergoes at 90 K and 200 K where the incommensurate and the commensurate and magnetic ordering develop, respectively. The knowledge of the crystal structure at this temperature range is also critical for the determination of the magnetic structure that the system adopts. Analysis of the magnetic structure and the magnetic symmetry would enlighten the mechanism that generates the magnetodielectric coupling.

5) An intriguing question refers to the the role of the density of the planar defects on the appearance and strength of the magnetodielectric coupling. It would be appealing to address the magnetodielectric response on β-$NaMnO_2$ and α-$NaMnO_2$ with various densities of planar defects, twin planes and thus different modulation vectors.

Furthermore, taking into consideration the appealing potential use of the polymorphs α and β-$NaMnO_2$ as cathode materials in rechargeable batteries, one should also examine the significant impact of the planar defects on the electrochemical potential and the intercalation/deintracalation process of the alkali cations.[143]

6) Another interesting aspect would be to expand this research by synthesizing and characterizing the $Na_{0.7}MnO_2$ oxide. $Na_{0.7}MnO_2$ appeared as a secondary phase in the XRPD patterns of the annealed β-$NaMnO_2$ samples. In these samples the dielectric anomalies were more distinct (Figures 4.27, 4.28, 4.30) and the magnetodielectric coupling was about 25%. The first assumption is related to the high density of the planar defects that a secondary phase induces, regardless if the phase is for example the α-$NaMnO_2$ or the $Na_{0.7}MnO_2$. The second assumption focuses specifically on the role of the $Na_{0.7}MnO_2$ in the appearance of the magnetodielectric coupling. To address this possibility, HRTEM studies would also be of invaluable help, as already stated in the previous (5) suggestion.

7) Optimization of the magnetodielectric measurements setup. An experimental set up, continuously needs adjustments. This is related with possible improvement of the obtained results and foremost with changes which cover the needs and problems of the specific project.

- The efforts would entail the option in the temperature control of using specific ramp rates of temperature (K/min), rather than using temperature steps.
- New method for the mounting of the sample could also be used. The goal is to avoid the minimum mechanical pressure that is applied on the sample, so it requires modifications on sample carrying part of the probe.
- The I-V loop on the β-$NaMnO_2$ showed leakage currents and parasitic capacitance. A good idea would be to try and isolate the source of the problem. A problematic measurement is caused by a specific sample or by the way that the sample is measured (certain specifications of the set up). Someone could try to measure a known, already tested ferroelectric or polar sample at the same temperature region (80 K) which would not be history dependent; this would minimize the factors that affect the final outcome of the measurement. The advantage of knowing in advance the acceptable results makes it easy to spot the differences and decide whether the setup needs to be optimized. If so, possible modifications could entail the use of different wires (with smaller parasitic capacitance), better electric isolation of the sample, and a different grounding.

- Adding more options (software commands in the vi's) on the LabView program. This would enable the user of having more available measurements such as: (a) isothermal frequency scans, (b) isothermal measurements of possible magnetostriction.

8) Regarding the growth of the β-$NaMnO_2$ there are two possible plans.

- The first one would be the attempts for preparing a pure β-$NaMnO_2$ by optimizing the solid state synthesis of the β-$NaMnO_2$. Having tried numerous synthesis protocols we have seen that the best approach, that is to say the sample with the minor secondary phase XRPD peaks, was given by the protocol described in section 4.2. However, in view of new efforts for producing a pure polycrystalline powder of β-$NaMnO_2$, the results of each sample should be checked thoroughly by TEM. The reason for this is the need to detect the differences in the homogeneity of the microstructure and the associated concentration of the planar defects.
- A second plan could involve the synthesis of single crystals of β-$NaMnO_2$ and its characterization with the a series of experiments: neutron and synchrotron diffraction, bulk magnetic susceptibility measurements at various temperatures and magnetic fields, high resolution transmission electron microscopy and magnetodielectric experiments to probe the coupling between the electric and magnetic degrees of freedom. It would be interesting to measure the magnetodielectric strength of the single crystal and compare it with that of the powder.

9) Experiments for the investigation of the spin glass dynamics of the $Na_{0.3}MnO_2 \times 0.2H_2O$. Specifically:

- Neutron spin echo (NSE) experiments for the investigation of the spin glass dynamics.[292]The use of the neutron spin echo technique yields direct, model independent information on spin relaxation in the time domain of 3×10^{-12} to 3×10^{-9} sec. It will be possible to extract information releted to common features of spin glasses such as: (a) the relaxation kinetics which is related to a broad distribution of relaxation time, (b) the absence of momentum dependence in the

relaxation dynamics would indicate that nonexchange type interactions play a fundamental role in the dynamics.

- Muon spin relaxation (μSR) presents a lot of advantages in probing small moment magnetism. Thus, one could utilize this technique for the investigation of the spin dynamics[293] in a complimentary to the NSE time window results.

10) Analysis of the α-$NaMnO_2$ and $CuMnO_2$ neutron powder diffraction experiments carried out on the SPINS (Spin Polarized Inelastic Neutron Spectrometer-NIST, USA). This will allow to draw differences and similarities, e.g extraction of their critical magnetic exponents, between two potentially isostructural systems, where there are indications that also vary in the way that planar defects evolve. These experiments have already taken place and the analysis of the results is an ongoing work.

12) Experiments of magnetic forced microscopy (MFM). Magnetic field-assisted piezoresponse force microscopy has been used as a method for probing [294, 295] the formation of ferroelectric or polar domains in systems which show coupling between the electric and magnetic degrees of freedom. The study of the stress-mediated magnetoelectric coupling by magnetic field-assisted piezoresponse is more common for nanocomposite magnetoelectrics in which two phases are artificially coupled via a mechanical strain. Examples were MFM technique has been used for the characterization of bulk systems is the $ErMnO_3$.[296] In the case of β-$NaMnO_2$ and α-$NaMnO_2$ it would allow us to image the magnetodielectric response of the domains in each compound, under zero and various magnetic fields and assess this against the varying concentration of planar defects amongst the two systems.

APPENDICES

Appendix A

Comparison graphs for the oxides: α-$NaMnO_2$, β-$NaMnO_2$ and $Na_{0.3}MnO_{2\times}0.2H_2O$

Chapters 3, 4 and 5 focused on the experimental results of the three manganese oxides α-$NaMnO_2$, β-$NaMnO_2$ and $Na_{0.3}MnO_2\times0.2H_2O$. In this appendix we present the comparison of some experimental results between the three oxides.

The goal of this comparison is to present some comparative figures which are helpful for the overall understanding of the behavior of these oxides. If we understand and moreover predict the effects that the crystal structure generates, we can control the properties of the materials. This can be achieved by designing the appropriate crystal structure depending on the behavior that is desirable for obtaining specific behavior in each system. Comparative graphs are presented only for experiments that were common among the three manganese oxides and were carried out under identical or comparable conditions.

A.1 The crystal structures of α-$NaMnO_2$, β-$NaMnO_2$ and $Na_{0.3}MnO_2\times0.2H_2O$

The crystal structures of two polymorphs of α-$NaMnO_2$ and β-$NaMnO_2$ are shown in figure A.1. These strutures correspond to the crystallographic data obtained from the cif files created on the structural parameters published when the two polymoprhs were first reported[6]. In the same figure the birnessite's structure is presented. The recent investigation by TEM, conducted for the three oxides is not taken into account.

The main similarity in the three oxides is the layers composed from the MnO_6 octahedra. In the interalayer distance there is one layer of the Na cations in the α-$NaMnO_2$ and two layers of Na^+ for the $NaMnO_2$, H_2O and Na cations for the $Na_{0.3}MnO_2\times0.2H_2O$ birnessite

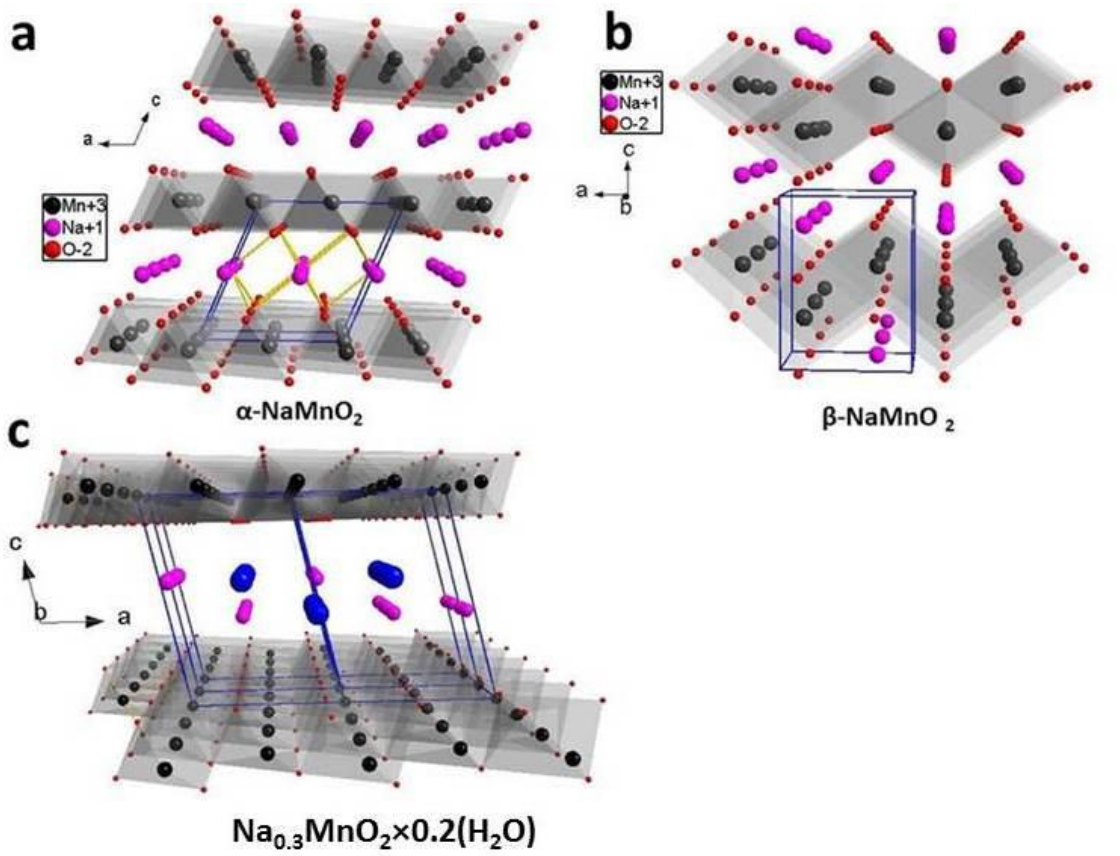

Figure A.1 Crystal Structures of the manganese oxides a) α-$NaMnO_2$ b) β-$NaMnO_2$ and c) the birnessite $Na_{0.3}MnO_2\times0.2H_2O$. The Mn, O and Na atoms are shown with the black, red and purple spheres, respectively. The H_2O molecules in the birnessite's structure are shown with the blue spheres.

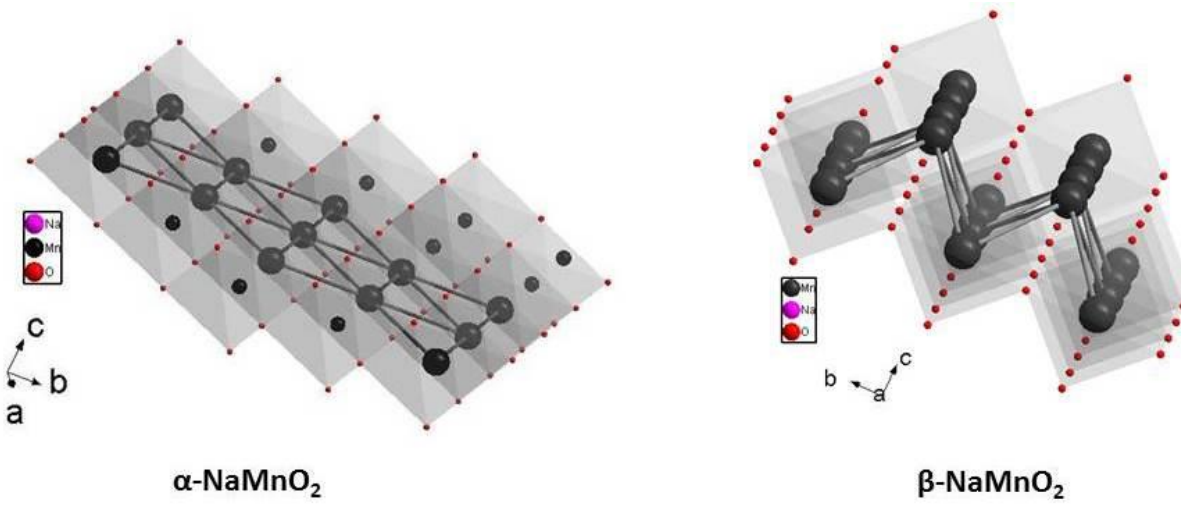

Figure A.2 A projection of the ab plane of the α-$NaMnO_2$ (left) and β-$NaMnO_2$ (right). Note the 1D and 2D arrangement of the Mn cations in α-$NaMnO_2$ and β-$NaMnO_2$, respectively.

Figure A.2 shows the projection of the ab plane on both polymoprhs, to underline the difference in the Mn^{+3} arrangements. In α-$NaMnO_2$ (Figure A.2 left) the Mn^{+3} are organized in a flat one dimensional layer. On the contrary, in β-$NaMnO_2$ the Mn^{+3} map out on a corrugated zig-zag two dimensional layer.

A.2 X Ray Powder Diffraction Patterns

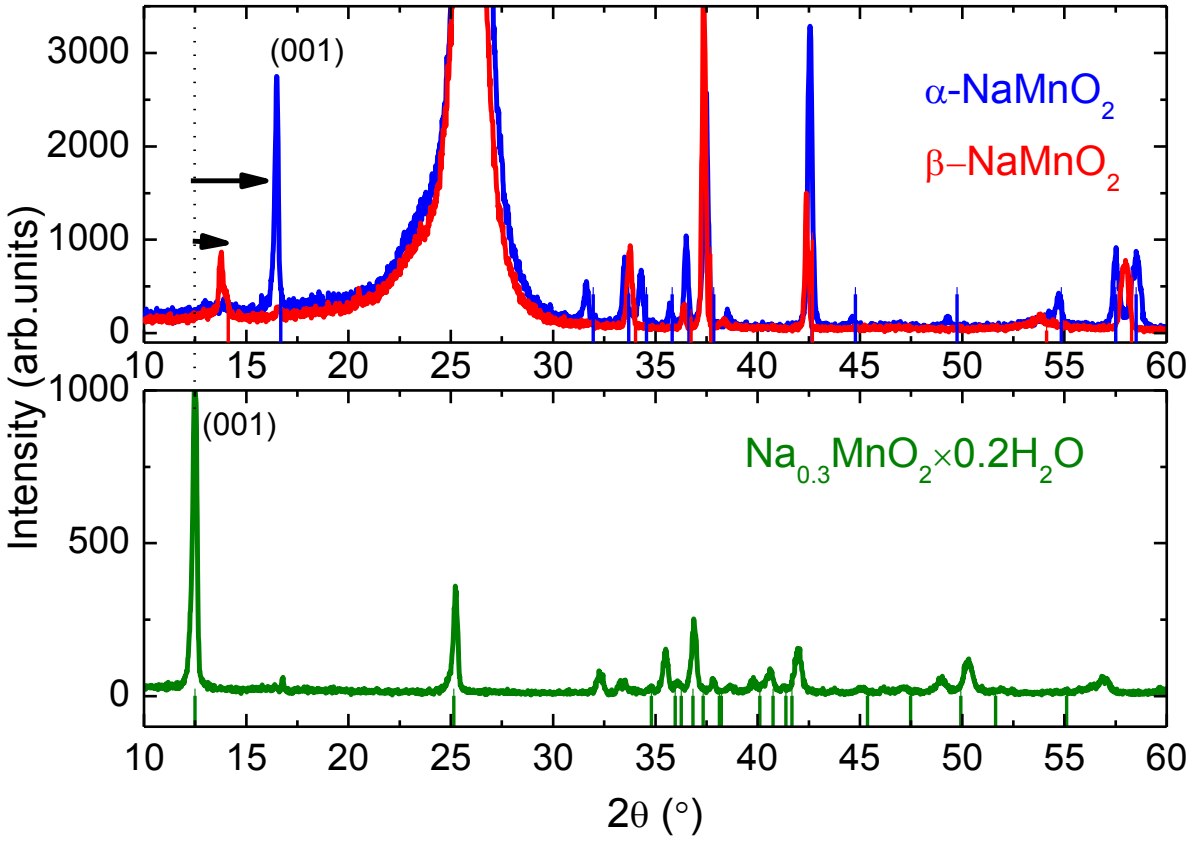

Figure A.3 X rays powder diffraction patterns of the α-$NaMnO_2$, β-$NaMnO_2$ and $Na_{0.3}MnO_2 \times 0.2 H_2O$ shown with red, blue and green graphs, respectively. Note that the broad intense peak between 20-30 deg, is due to the sealing of the samples with the mylar film. The arrows show the difference in the 2 theta angle between the 001 reflection of the birnessite $Na_{0.3}MnO_2 \times 0.2H_2O$ and the (001) reflection of the α-$NaMnO_2$ and the β-$NaMnO_2$.

Figure A.3 shows the XRPD patterns of the α and β-$NaMnO_2$ on the upper layer of the graphs and the birnessite $Na_{0.3}MnO_2 \times 0.2H_2O$ at the bottom. The 001 reflections of the α-$NaMnO_2$ (16.78 deg) and β-$NaMnO_2$ (14.11 deg) are noticeably apart as their c-parameters

differ significanltly, yet many Bragg peaks of the two polymoprhs at angles higher than the 30 deg are quite close. One interesting point arises from the comparison of the XRD graph of α-$NaMnO_2$ with that of the birnessite's. The shift of the 001 reflection from ~16.78 deg to ~12.45 deg corresponds to the increase of the c-parameter of the α-$NaMnO_2$ when it becomes $Na_{0.3}MnO_2 \times 0.2H_2O$ due to the insertion of water in the interlayer distance along the c-axis.

A.3 Magnetic Susceptibility Graphs of the Manganese Oxides

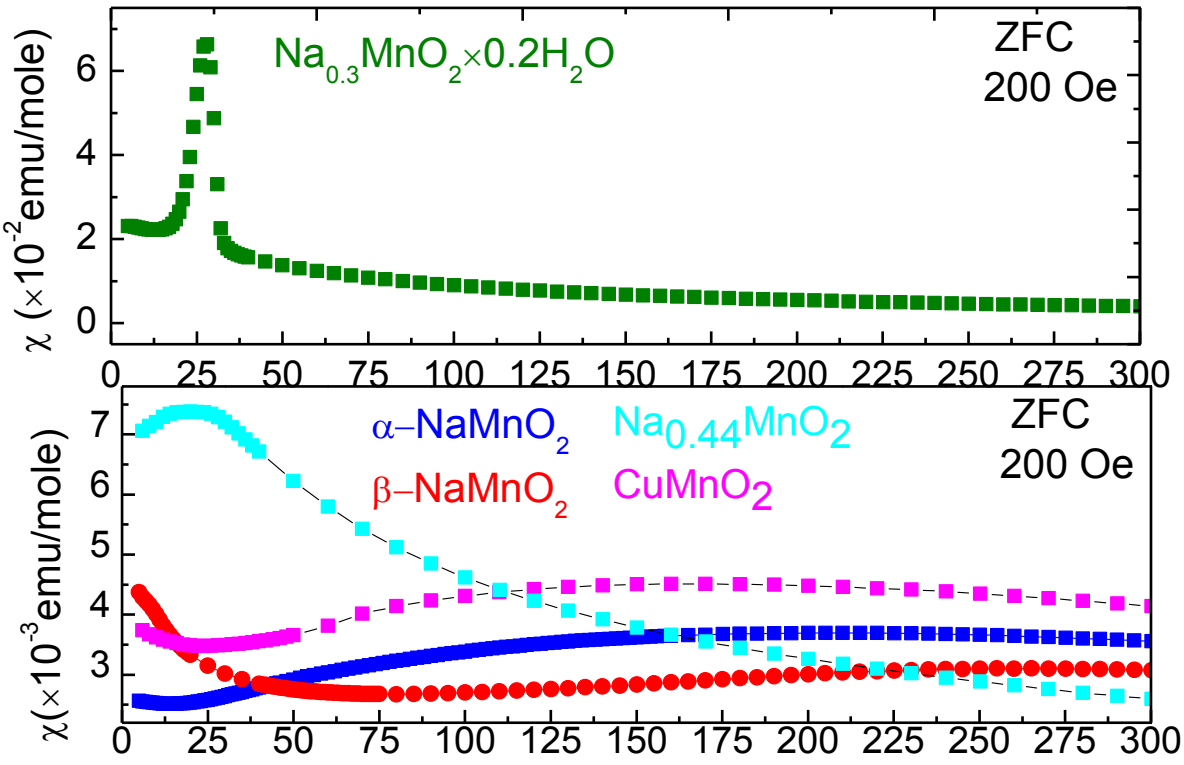

Figure A.4. Measurement of the magnetic susceptibility on a ZFC dc mode under 200 Oe magnetic field for the manganese oxides: α-$NaMnO_2$, β-$NaMnO_2$, $Na_{0.44}MnO_2$ and $CuMnO_2$ presented with the blue, red, cyan and magenta graphs, respectively.

At this point it is interesting to relate the magnetic behavior of the α-$NaMnO_2$, β-$NaMnO_2$ and $Na_{0.3}MnO_2\times0.2H_2O$ with the $Na_{0.44}MnO_2$ [228] as well as with the frustrated antiferromagnet $CuMnO_2$. [297] Figure A.4 presents the magnetic susceptibility of the aforementioned manganese oxides measured under 200 Oe field on a ZFC (dc) mode. At first glance there is a remarkable similirarity on the magnetic susceptibiity of the α-$NaMnO_2$, the β-$NaMnO_2$ and the $CuMnO_2$. Two are the basic common characteristics: the broad hump at high temperatures strongly indicating low dimensional magnetism[151] and the minor contribution from paramagnetic impurities evident by the tail on the magnetic susceptibility at low temperature. The common characteristics of the α-$NaMnO_2$ and β-$NaMnO_2$ have already been discussed in chapters 3 and 4. $CuMnO_2$, has a typical crendnerite structure at room temperature (monoclinic, C2/m) but undergoes a structural phase transition below 65 K (triclinic, $P\bar{1}$), the temperature where it becomes antiferromagnet ($P\bar{1}$, **k** (0, ½, ½)[297]. This behavior is analogous with the α-$NaMnO_2$ phase in which the structural distortion (monoclinic C2/m to triclinic $P\bar{1}$) also occurs at the temperature (45 K) where the antiferromagnetic order emerges. The underlying mechanism of the structural transition in both cases is the magnetoelastic coupling. The magnetic degeneracy (frustration) imposed by the triangular lattice topology is lifted off and long range magnetic order develops in both manganese oxides.

Quite different susceptibility graphs show the $Na_{0.3}MnO_2\times0.2H_2O$ and the $Na_{0.44}MnO_2$ oxides. As it has been presented in chapter 5, $Na_{0.3}MnO_2\times0.2H_2O$ exhibits a spin glass transition at 29 K related with bond disorder among ferromagnetic and antiferromagnetic interactions of the Mn^{+3}/Mn^{+4} cations. Neutron powder diffraction data have not revealed a structural transition at the spin freezing temperature. The tunneled structured $Na_{0.44}MnO_2$ shows also a peak at low temperatures, specifically at 25 K, which is rather broad in comparison with that of the $Na_{0.3}MnO_2\times0.2H_2O$ and has not been correlated [228] with a structural distortion at this temperature region.

Appendix B

Magnetodielectric Measurements Set Up and The LabView Software

The technical details that the experimentalist chooses in order to carry out a measurement have a significant effect on the outcome of each measurement. In experiments where extremely small physical quantities are measured, both the hardware and the software used may affect the reliability of the obtained results.

A LabView Programm has been developed to cover the needs of the magnetodielectric experiments. The major tasks were to measure a) capacitance and dielectric loss versus temperature and under various constant magnetic fields and b) current or charge in respect with one of the following parameters: time, temperature, applied electric field and magnetic field.

B.1 Temperature Control

The first issue that had to be settled effectively was the temperature control. Heating the space of the sample was accomplished by temperature controllers, whereas cooling was achieved by continuous flow of a cryogenic liquid (nitrogen or helium). Controlling the temperature was obtained by providing the necessary power into two heating elements: the resistor which is placed close to the bottom of the cryostat (total resistance 40 Ω) and the resistor at the base of the sample holder (Figure 2.10-total resistance 100 Ω). Close to each heating element there was a Lakeshore sensor which could read temperatures varying from 2 K- 325 K. The temperature controllers (Lakeshore 332 or Lakeshore 340) provide the required electrical power since they function as well-regulated variable DC current sources but also display the temperature that the Lakeshore sensors read. Thus, there are two temperature points to set and control: the first referring to the cryostat's temperature and the second which corresponds to the sample's temperature. These two may slightly vary as the power which is provided in the cryostat's resistor is much higher that the one provided to the resistors of the probe. Moreoever, the cryostat's sensor is closer to the nozzle from where the nitrogen comes out, so less time was needed for the cryostat to cool down in respect with the sample.

The temperature control is built using the LabView software in a way that the temperatures of the cryostat and the sample are not independent. Specifically, first the temperature set

point of the cryostat is reached, when this is reached and stabilized within the allowed limits, the program sets the sample's temperature. This ensures that there are no large thermodynamic deviations between the space of the cryostat and the space of the sample, which could affect the stability of the sample's temperature and its measured physical properties.

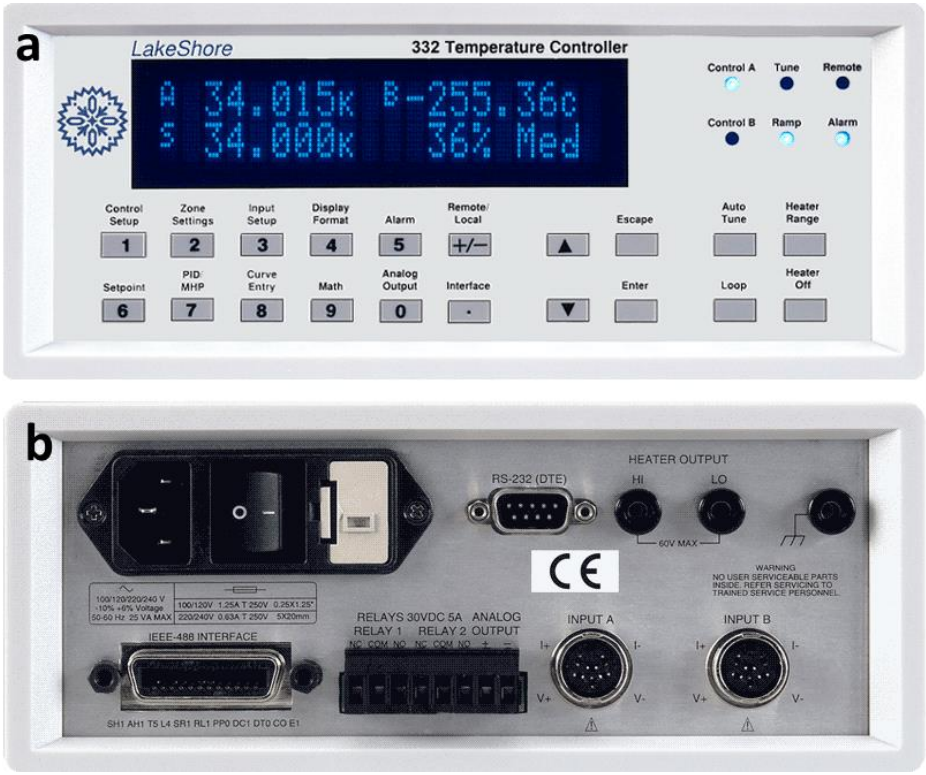

Figure B.1 a) Front panel of Lakeshore 332 Temperature Controller. The first column of numbers displayed refers to the actual temperature (A) whereas below this indication is the temperature set point (S) in units of Kelvin (K). The second column refers to the temperature of the sample and the total percentage of the output electrical power that was provided by the controller. The user may choose which panel will be displayed: the one which refers to the cryostat's temperature (Loop A) or the one which corresponds to the sample's temperature (Loop B).

b) Rear panel of the Lakeshore 332 Temperature Controller. Input A and B are connected with the temperature sensors of the cryostat and the sample, respectively. The heater output

B.2 The LabView Software Program

The software used for the magnetodielectric measurements was based upon a common platform which is called "vi" according to the LabView's definitions. The vi has separate sub-programs which are used for each type of measurement.

There were 4 basic sub-programs: a) the C, D=f(T) for measurements of the capacitance and dielectric loss versus temperature under stable magnetic fields b) the C, D=f(H) used to measure capacitance and dielectric loss isothermally versus magnetic fields from -6.5 T up to 6.5 T, c) the P=f(T) when experiments of current or charge versus time and temperature were required and d) the P=f(H) in order to evaluate charge or current versus magnetic field at a stable temperature.

B.2.1 Measuring the Dielectric Constant and Dielectric Loss

The dielectric constant experiments were carried out with the use of the LCR brigde, the Lakeshore 332 temperature controller, and when magnetic fields were required, the AMI 420 controller of the 7 T superconducting magnet. An example of the experimentalist's interface for these measurements is shown at Figure B.2. This panel is used to measure capacitance and dielectric loss versus temperature. In the following, we discuss in detail the choices and options of the experimentalist.

The "Experiment Parameters" refer to the inputs of each measurement.

- More specifically, the user may insert the initial temperature and the final temperature using the inputs "*Tinitial*"and "*Tfinal*"
- There is also the possibility to define the temperature steps using the choice *"Steps"*. This means that the capacitance values can be recorded every χ K (χ= 1 K, 2 K, 0.5 K, 0.25 K…). We are not able with this program to define the temperature rate (K/min).
- The deviation from the desired temperature point is defined by the number which will be inserted in "*T stabilization error*" tab. For example, if this parameter is set

at 0.15 and the temperature point is 100 K, the accepted values will range from 99.85 K to 100.15 K.

- The program also provides the choice of setting a difference between the samples and the cryostat tempeture set points. This is settled by the input "$\Delta T=T_s-T_c$" where T_s and T_c denote the sample's and the cryostat's temperature, respectively. For positive values of ΔT the cryostat is set to function at lower temperatures, whereas for $\Delta T<0$ the cryostat is settled at higher temperatures in respect with the sample.
- The desired temperature set point should be reached within a reasonable time. If for any reason this does not happen, then the input "*T next step*" gives the choice to pass to the next set point by defining the maximum time (in seconds) within the program is allowed to reach each temperature.
- One can also choose whether to use the "Lakeshore 332" or "Lakeshore 340" by choosing one of the two in the "*Thermometer*" tab.
- The capacitance is converted to the dielectric constant values by the program using the simple equation 2.10 (see paragraph 2.4.2) as long as the user will write the correct values in the "*Sample's Thickness*" and "*Sample's Area*" in meters and square meters, respectively.
- The LCR brigde provides a variety of possible measurements, where pairs of physical quantities are being recorded. The primary parameter of these quantities can be the impendance (Z), the resistance (R), the capacitance (C) and the inductance (L). The function of the LCR Bridge can be specified by the tab "*Imp Type*".
- The measurement is carried out applying one frequency value for each measurement, in the input "*frequency value*"
- The magnet can be charged to a specific magnetic field, specifying the current and the ramp rate by which the magnet is charged. This is done using the tab "*Magnet Parameters"*

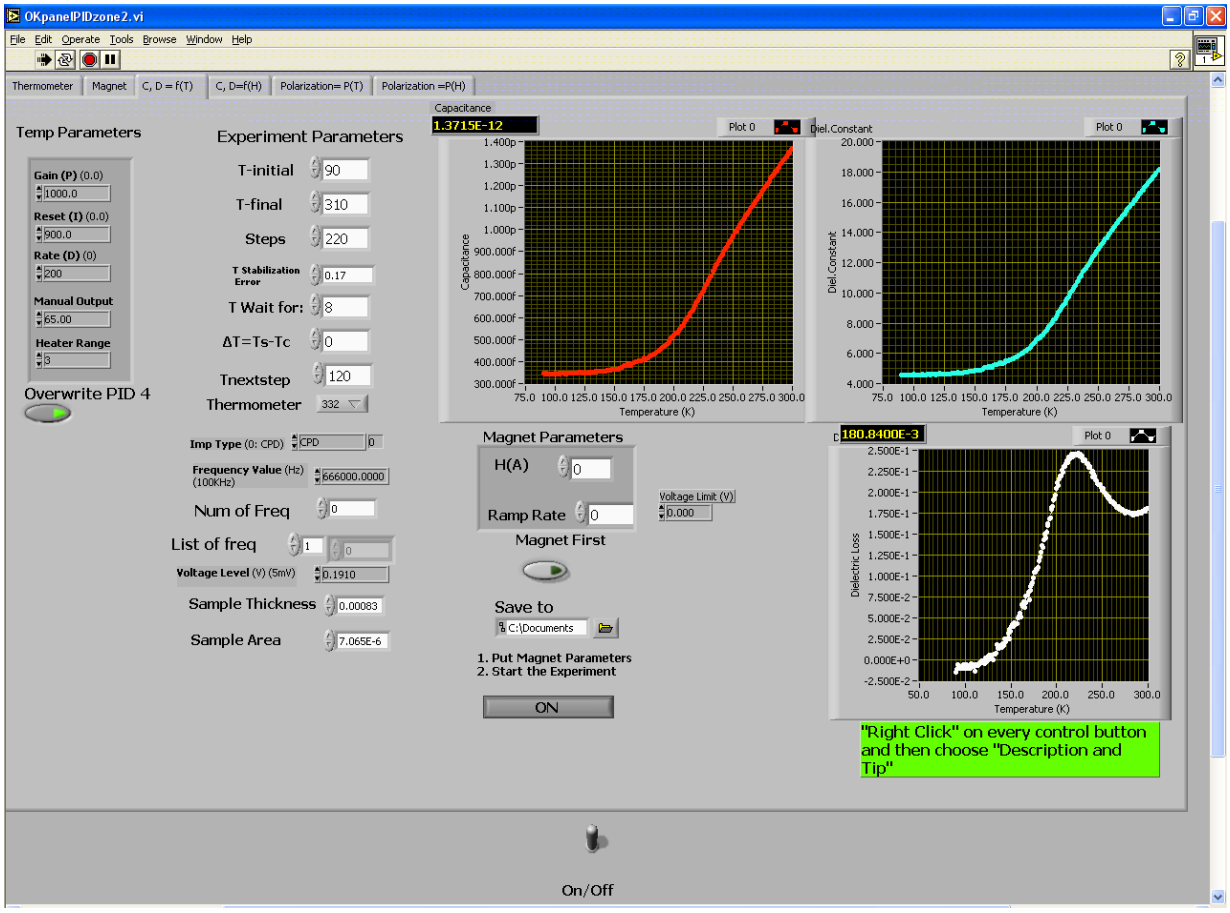

Figure B.2 The interfcace of the LabView vi which allows the user to measure capacitance, dielectric constant and loss, versus temperature as shown in the graphs represented with the red, aqua and white dots, respectively.

- The temperature parameters *Gain(P)*, *Reset (I)*, *Rate (D)* (also known as "PID" values), the *Manual Output* (%) and *Heater Range* define the time within which the temperature point is reached and its deviation of the actual temperature measured. In other words, the PID values determine on a large scale the efficiency of the temperature control. Since the PID values highly depend on the temperature range used (5 K-20 K, 20 K-80 K) the user has also the choice to use the "*Zone Setting*". This ensures that the PID values will change according to the temperature range that the measurement is carried out. Details can be found in the manual of the Lakeshore Temperature Controllers for the 332 and 340 models.

B.2.2 Measuring Capacitance versus Magnetic Field

In many magnetoelectric compounds it is quite useful to estimate the magnetocapacitance, meaning the % change of the capacitance versus the applied magnetic field at different stable temperatures. Usually the experiment is carried out at various temperatures lower than the magnetoelectric transition temperature. The Labview program provides this option. The interface of the program used to measure capacitance versus magnetic field is shown in Figure B.3.

The control of the temperature parameters entails the same settings as those described in the previous paragraph. The difference in this experiment is that the measurement is performed isothermally, so the user needs to define only the temperature and the accepted temperature deviation.

- The magnetic field is set from values ranging between -6.5 T to 6.5 T, using the "H_1" and "H_2" (Figure B.3)
- The number of points between the initial and the final magnetic field taken at each measurement is defined by the *"Steps"*.
- The rate by which the magnetic field is changing is specified in the *"Ramp Rate"*

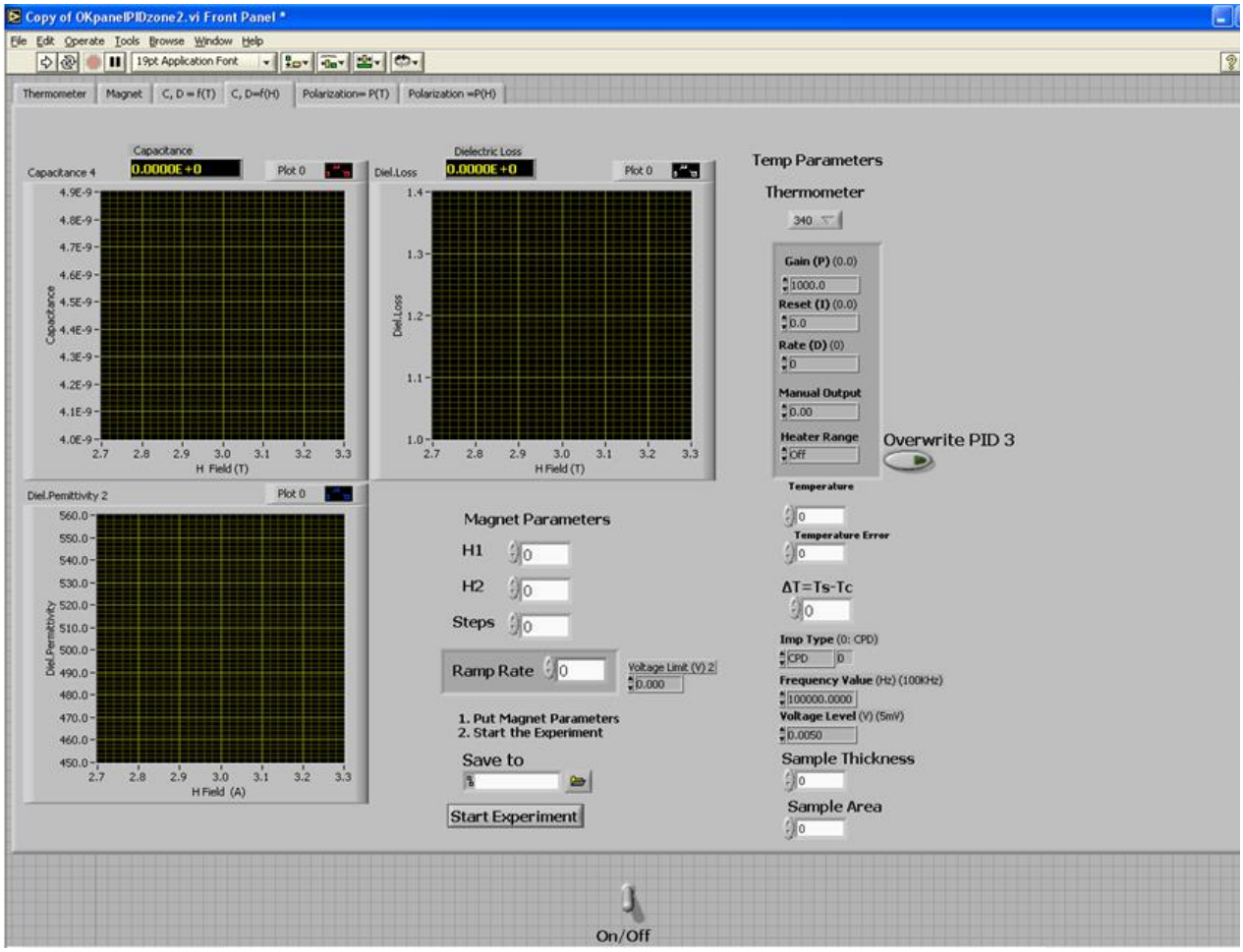

Figure B.3 Interface of the LabView program for the measurement of capacitance, dielectric constant and loss versus magnetic field at a stable temperature.

B.2.3 Measuring Charge or Current (Polarization) versus Temperature

One useful experiment for the detection of possible ferroelectric transition is the measurement of the pyrocurrent or, in other words, the current versus temperature. This measurement is carried out with the help of the Keitley 6517A electrometer. At the LabView program there is the tab of P(T), which is the interface for such meausurements (Figure B.4). The inputs concerning the temperature control and the magnet parameters have the same function as described in the previous paragraph. The new input here is the commands that are related with the Keithley electrometer which are: the "*V-source range*" in order to define the limit of the maximum voltage that might be applied, the "*Output Voltage Value*" to set the applied electric field in the sample and the "*Function"*. If the latter is set to "dc voltage" then the electrometer works as a dc voltage source which can measure current. Baring in mind that we try to measure currents less than nanoAmps, one should be careful with the hardware connections, the triboelectric effects, the electric isolation of the sample, the grounding and any factor which can possibly affect the result of the measurement.

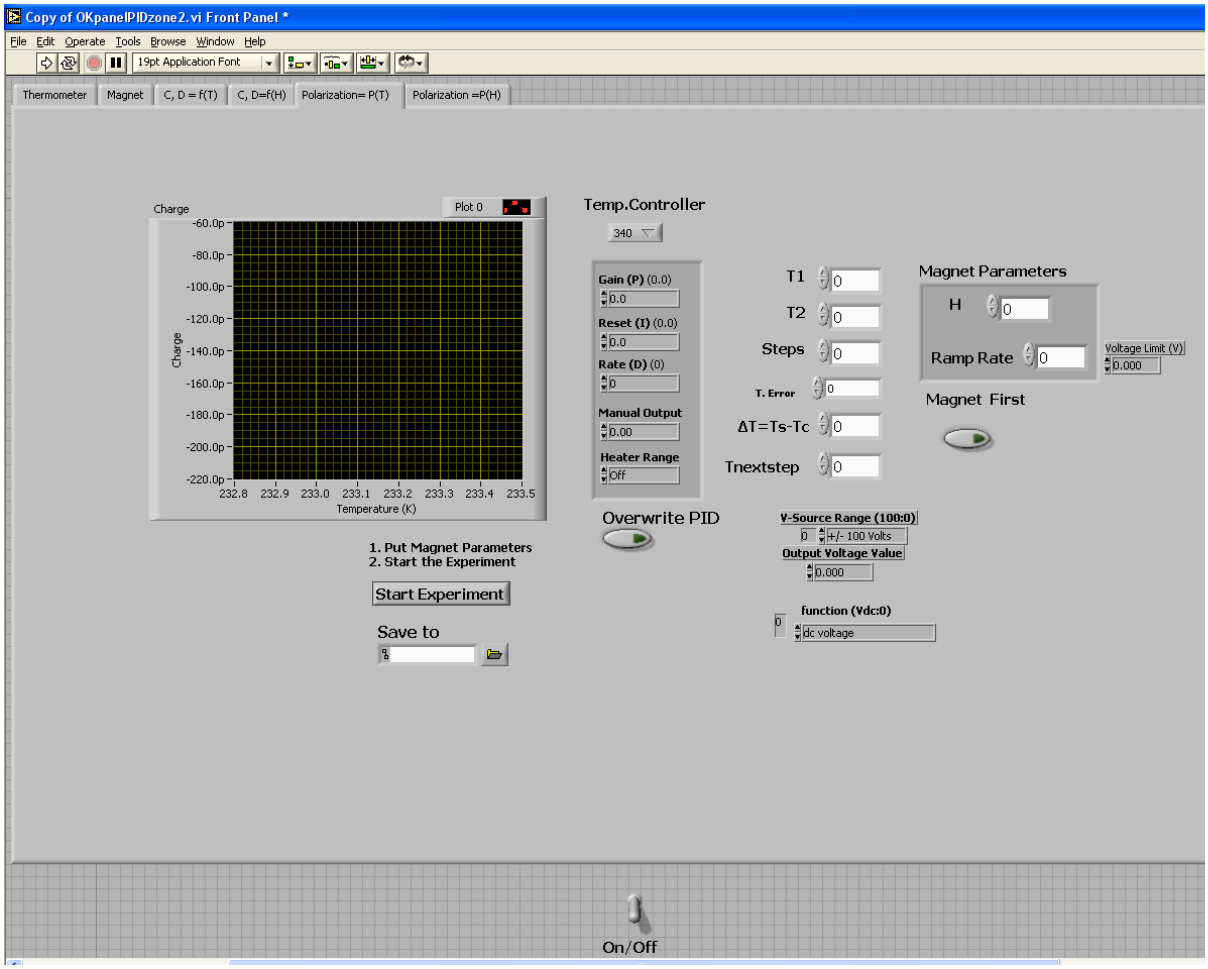

Figure B.4 Interface of the LabView program for the measurement of charge or current versus temperature.

Appendix C
Preliminary Analysis of the Magnetic Structure of β-$NaMnO_2$

The analysis of the magnetic structure of β-$NaMnO_2$ has been done by using the FullProf Suite. The investigation of a magnetic structure requires a complete structural model. Thus, the basic precondition is a Rietveld refinement of the crystal structure which corresponds to the solution of the chemical (nuclear) cell. The Rietveld refinement provides all the structural parameters. The necessary information is the exact peaks' positions of the magnetic reflections and the cell parameters derived from the Rietveld's refinement. These data can be imported in various programs (such as the "Supercell"[298]) in order to calclulate the propagation vector or a number of possible propagation vectors. The propagation vector, the magnetic atoms positions and the space group is inserted again in suitable programs like "Sarah"[299] or BasIreps[300] for the magnetic symmetry analysis. The information obtained from the symmetry analysis is then used in the FullProf program, where the magnetic contribution is imported as a second phase, taking into account only the positions of the magnetic atoms. The first phase is regarded the crystal structure whose parameters are kept stable during the refinement of the magnetic structure.

Since at 100 K there is a magnetic transition from the commensurate to an incommensurate structure the analysis is carried out at 100 K and at 4 K.The fit for the 100 K pattern of the β-$NaMnO_2$ is shown in Figure C.1 and does not include the magnetic contribution.

Based on the structural analysis of Figure C.1 the cell parameters of β-$NaMnO_2$ at 100 K are: a=4.749 (2) Å b=2.855(1) Å c=6.315 (2) Å. The position of the Mn^{+3} is (x, y, z)= (0.25, 0.25, 0.625). The magnetic structure analysis at 100 K of β-$NaMnO_2$ shown in Figure C.1 resulted in the following: β-$NaMnO_2$ is a G- type antiferromagnet (see Figure 1.2c) on the magnetic space group $P\bar{1}$ with the propagation vector of **k** (0.5, 0.5, 0.5).

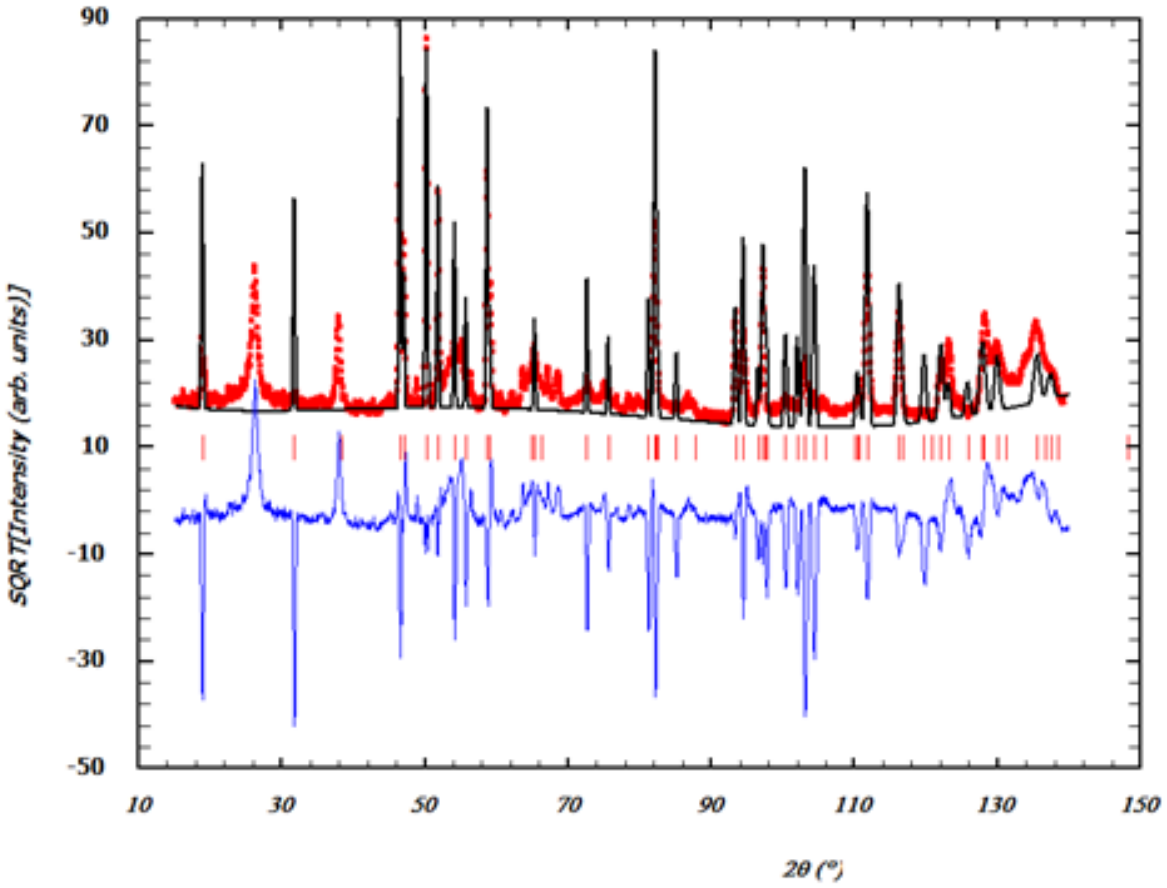

Figure C.1 Crystal structure analysis of β-$NaMnO_2$ at 100K by Rietveld refinement. Note the two magnetic reflections (of the experimental data corresponding to the red graph) which are not calculated yet by the theoretical model.

At 80 K, a magnetic transition is observed since magnetic satellite reflections appear. The satellite peaks appear until 4 K.Rietveld analysis of the 4 K pattern resulted in the following structural parameters: space group Pmmn and a= 4.7450 (2) Å, b=2.8550 (1) Å. The manganese Mn^{+3} positions are: (x, y, z)=(0.25, 0.25, 0.63). Data treatment for the magnetic structure is now based on the search of a propagation vector which will have at least one irrational component of the $\mathbf{k_x, k_y, k_z}$. The magnetic space group remains the $P\bar{1}$ however the propagation vector has changed to **k** (0.5, 0.475±δ, 0.5) where δ=0.0097. The result of the Rietveld refinement is shown in Figures C.2-C.3. The reliability factors (χ^2>50) of the crystal and magnetic analysis indicate that there is much scope of

improvement. This is attributed to the multiple complexity of the crystal structure, which affects the final outcome of the Rietveld refinement. Since we don't have the correct solution for the chemical cell, we also end up with inadequate analysis of the magnetic structure

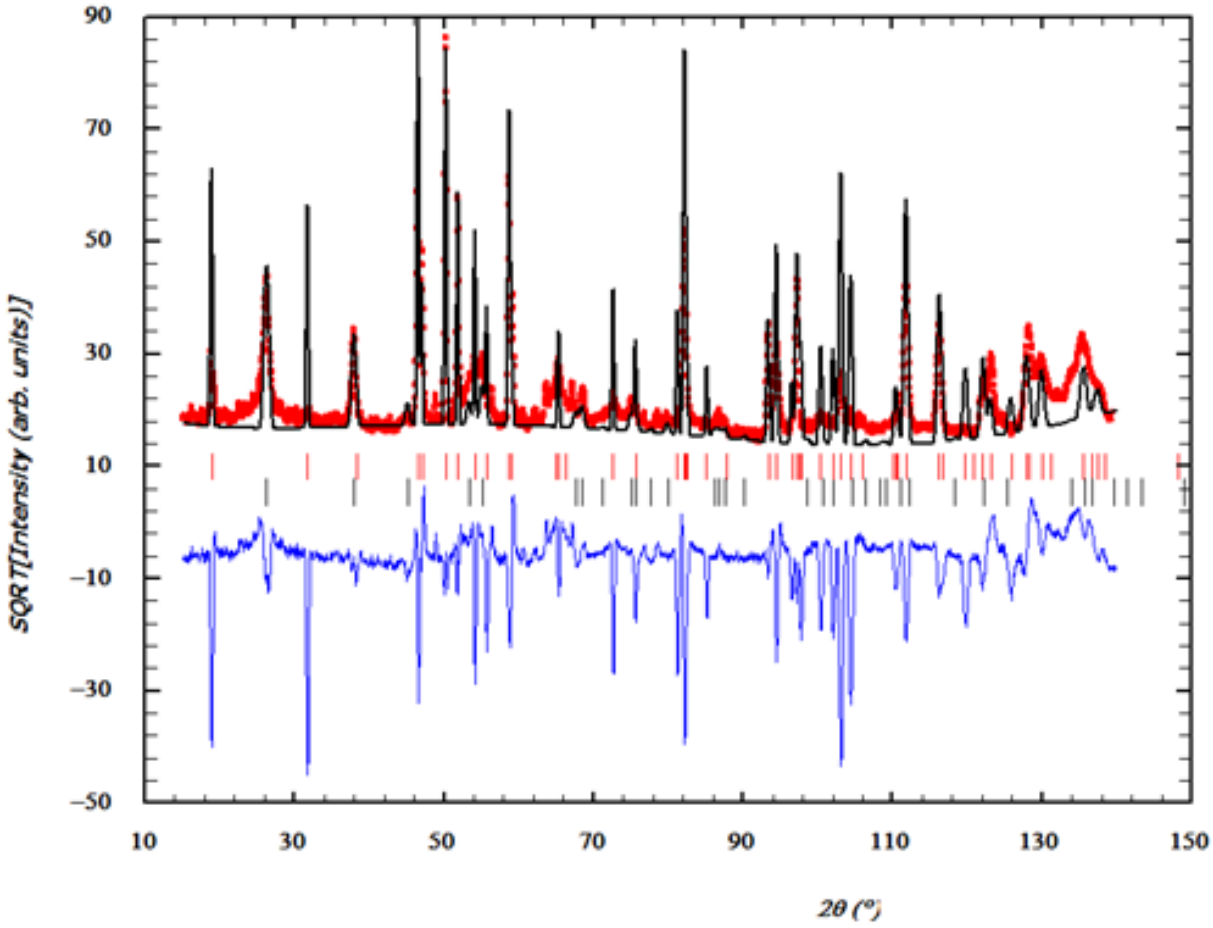

Figure C.2. Two phase Rietveld refinement of β-$NaMnO_2$ NPD data at 100 K. Indexing of the nuclear and magnetic reflections is pointed out with the red and black ticks, respectively.

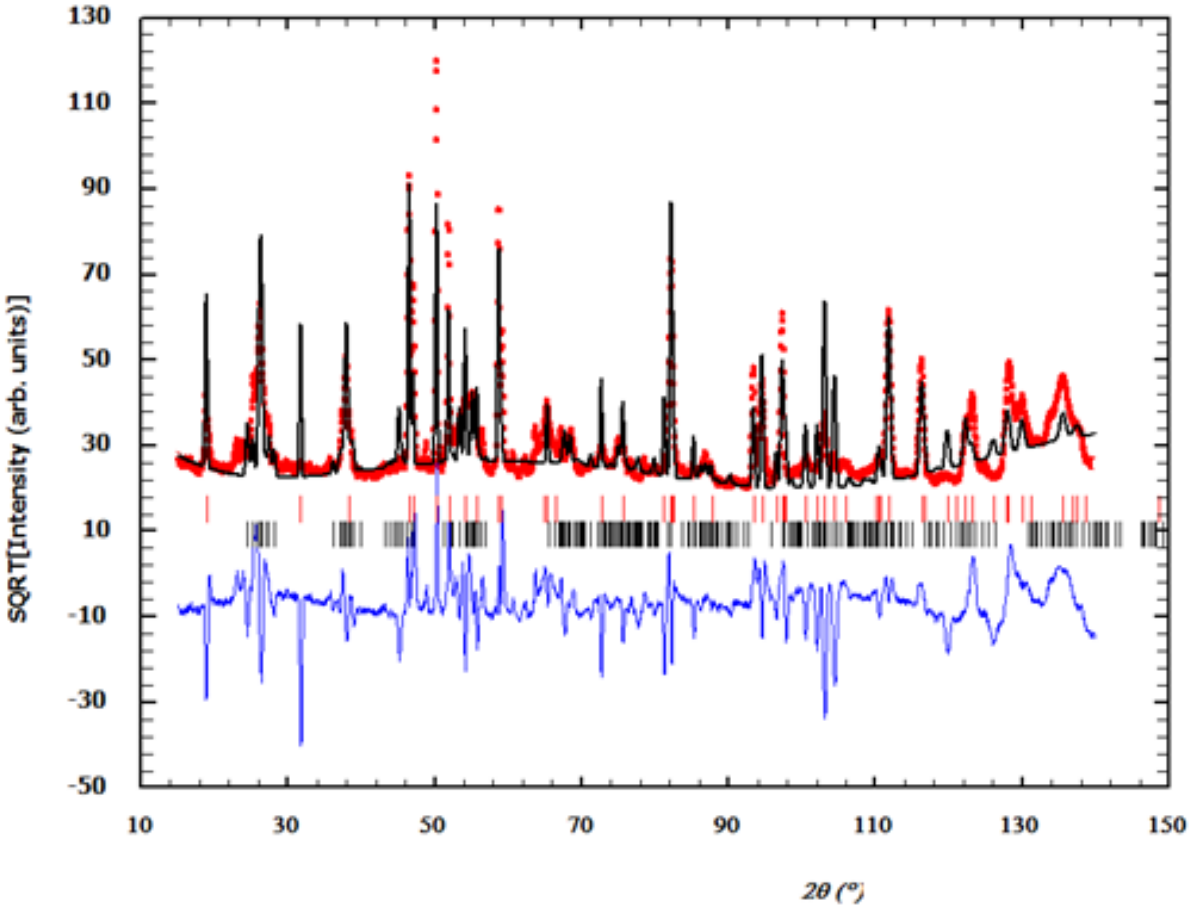

Figure C.3 Rietveld refinement of the 4 K pattern of β-$NaMnO_2$ for the solution of the incommensurate magnetic structure. The red and black graphs correspond to the observed and calculated intensities, respectively. Upper set of ticks marks show the positions of the magnetic peaks whereas the lower set of tick marks (black) indicate the positions of the nuclear peaks.

Methodology used with the DAVE program for the fits of the magnetic peaks

DAVE[301] is software especially designed for the visualization and analysis of inelastic neutron scattering data. All the neutron scans from the temperatures 5-300 K have been analyzed with the aforementioned program. Figures C.4 and C.5 show the 56 K scan as an example of the fits based on the use of Gaussian and the Lorentzian fuctions, respectively.

Figure C.4 shows the magnetic peaks at 56 K fitted with the use of the Gaussian function. The first parameters to set are related with the background. The user can change the "offset" and the slope of the background. The "offset" shows the level line of the background, and has the option to maintain at a fixed value. The slope shows if there is any increase of the background as the temperature of the scans changes. We kept both of these parameters stable. The value of the slope and the offset of the background were extracted by the fitting of the lowest temperature, i.e from the 5 K scan. This ensures that any possible increase in the area of the peaks is attributed strictly to the magnetic reflections.

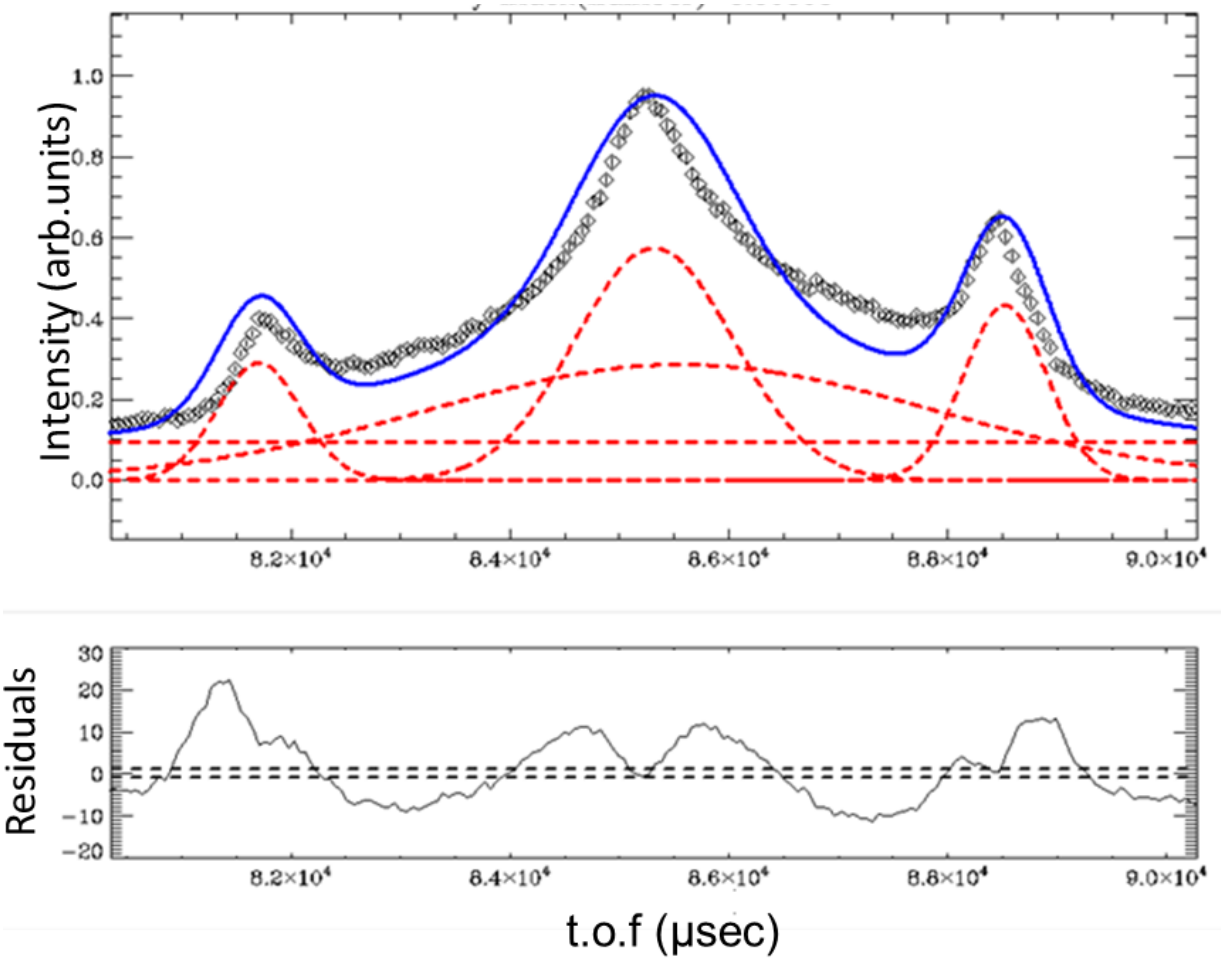

Figure C.4 Fitting with Gaussian functions of the main magnetic peak and its the sattellites at the pattern of 56 K. Y-axis shows the intensity (arbitary units) and the x-axis corresponds to the raw data in time of flight ("tof" in μsec). The upper part of the picture shows the fit where the background and four in total Gaussian functions are used (see text). The lower part shows the residuals which is an illustration for the quality of the fit.

Three magnetic peaks appear, however the group fit of those peaks entailed the use of four in total Gaussians. The reason for this is that the main (commensurate) magnetic peak is unusually wide, and especially when the system enters the incommensurate state, likely indicatingthe development of a short-range spin correlations which give rise to diffuse scattering beneath the central line. So in order to describe this, two Gaussian functions were used instead of one. The first one, being extremely broad, covers the entire Q area (1.30 $Å^{-1}$ < Q < 1.44 $Å^{-1}$). The second one addresses the fit of the central commensurate magnetic peak and the rest two are applied in each of the satellites. The parameters which can be modified by the user concerning the Gaussian function are three: the area, the center and the full width half maximum (FWHM) of each peak. We have set the lower and higher limit stable for each peak. The fit obtained is not satisfactory, since it does exactly describe the shape and width of the magnetic peaks. As the main magnetic peak is exceptionally wide, the Lorentzian function was chosen as a better alternative.

Figure C.5 shows the group fitting of the 56 K scan, which entails the analysis of the background and four in total Lorentzian functions. Specifically two Lorenztians were used for the description of the main magnetic peak, and one function for each one of the satellites. The methodology is similar with the one followed with the previous analysis, meaning that the offset and slope of the background maintained the value extracted from the 5 K run at the entire range of 5 K-300 K. The lower and higher limit of the peaks was also stable. The intensity of the three peaks was extracted and was plotted versus temperature as shown in Figure 4.57. The relevant fittings for the estimation of the critical exponent β are presented in Figure 4.58.

The analyses for the estimation of the critical exponent β of the β-$NaMnO_2$ for the commensurate (100 K<T<200 K) and the incommensurate phase (T<90 K) entailed various trials most important of which are shown in Table C.1 In this table we show the best Adjustment R-Squares according to which the values of β were derived: β=0.5 and β=0.23 for the high and low temperature transition, respectively.

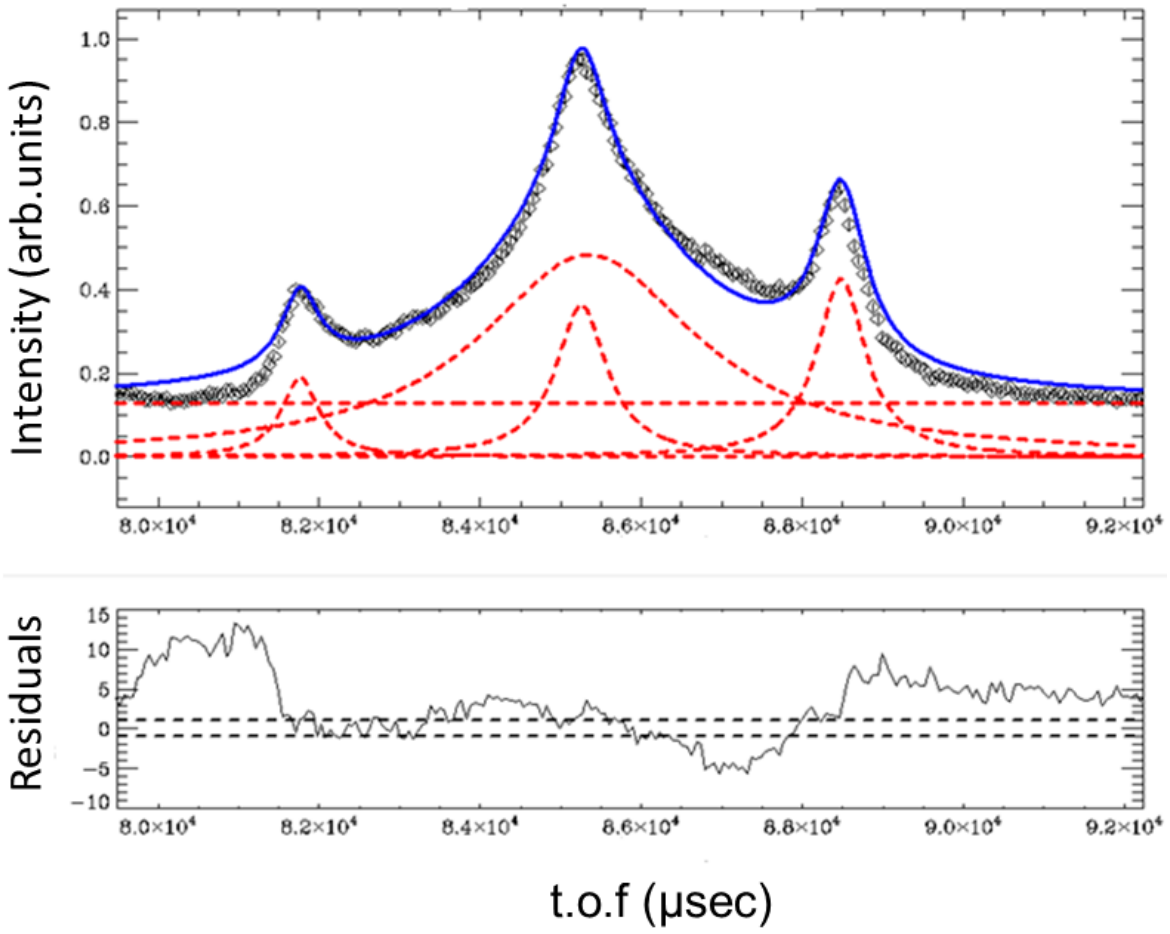

Figure C.5 Fitting with Lorentzian functions of the main magnetic peak and its sattellite reflections at the scan of 56 K. The upper part of the picture shows the fit where the background and four in total Lorentzian functions are used (see text). The lower part shows the residuals which is an indication for the quality of the fit.

Peak	β	Tc	Adj-R-Square
Main Magnetic Peak at Q=1.374 Å^{-1}	0.5	202.39 (±1.41)	0.949
	0.32	198.23 (±0.78)	0.932
	0.23	198.92 (±1.23)	0.792
	0.495 (±0.24)	200 (Fixed)	0.869
Satellite Peak at Q=1.326 Å^{-1}	0.5	125.5 (±7.71)	0.915
	0.32	110.217 (±4.2)	0.932
	0.23	102.04 (±2.68)	0.9425
	0.115	90 (Fixed)	0.718
Satellite Peak at Q=1.433 Å^{-1}	0.5	94.42 (±2.9)	0.889
	0.32	90.95 (±0.75)	0.955
	0.23	90.23 (±0.156)	0.985
	0.145	90 (Fixed)	0.92159

Table C.1. Values of the critical exponent β, the critical temperature T_c that was derived for each fit and the relevant Adjustment R-Square for the fit shown in Figure 4.58.

Appendix D:

Complementary Graphs of Chapter 5

In this Appendix we present some complementary graphs related with the birnessite $Na_{0.3}MnO_2 \times 0.2H_2O$ compound discussed in Chapter 5. Paragraph D1 shows the XRPD pattern of a sample that was prepared with an alternative method of synthesis. Specifically it was synthesized with the use of iodine in order to deinteracalate Na cations. In pararaph D2 we discuss the aging as seen in two XRDP patterns of the same $Na_{0.3}MnO_2 \times 0.2H_2O$ sample measured with a time difference of 6 months . Also in paragraph D3 we present in detail the methodology of the power law analysis presented in the section 5.4.2.4.

D1: XRPD graph of the birnessite synthesized by deintercalation of Na cations.

As already mentioned in 5.2 section the birnessite samples were prepared by hydration of the α-$NaMnO_2$ in air. However, deintercalating Na cations with the use of iodine was also tried. The final product was a well crystallized birnessite, whose XRPD pattern was indexed successfully upon the birnessite of ICSD_262608 crystallographic file (Figure D.1). However, these samples proved to be non –stable (the sample was not stored in the glove box) as secondary peaks appeared just after 24 hours. This is presented in Figure D.1 where one can observe the 001 peak of α-$NaMnO_2$ at 16.6 deg at the graph with the black color. On the contrary, the samples prepared with the hydration of α-$NaMnO_2$ were stable for months. For this reason the deintercalation with iodine was not followed in order to prepare the birnessite samples.

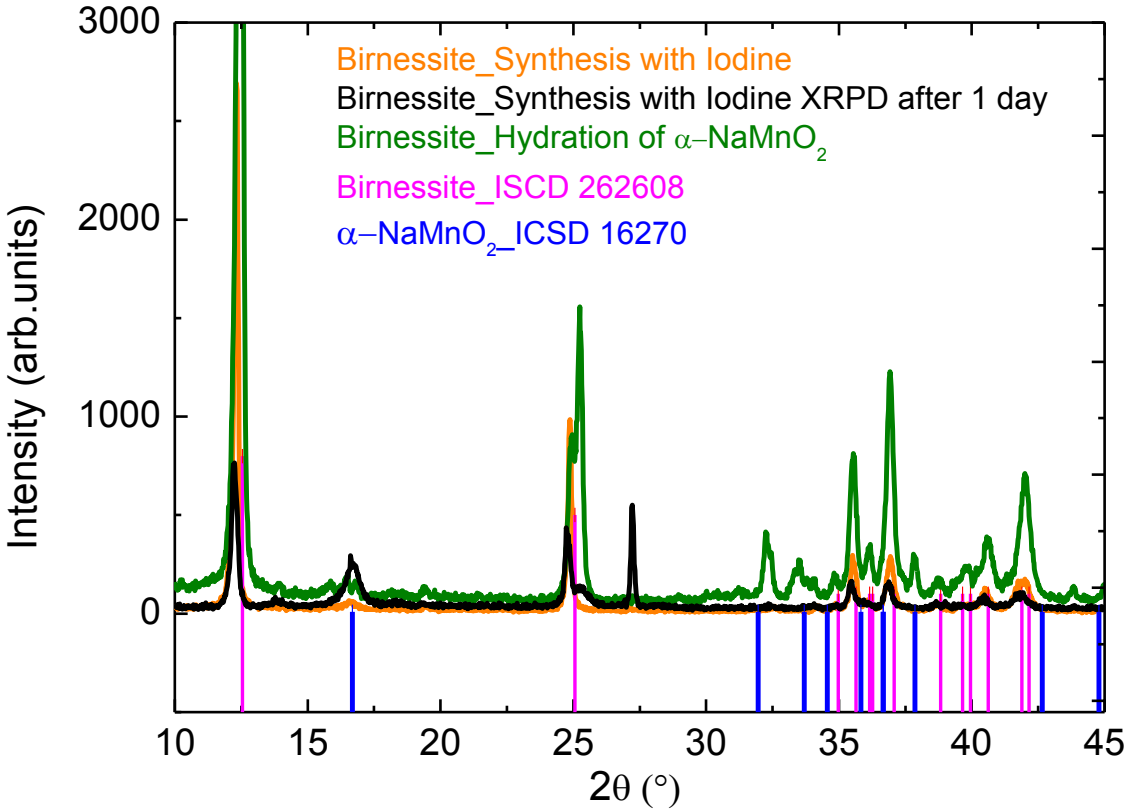

Figure D.1 XRPD patterns of the birnessite which was synthesized by adding iodine in the α-$NaMnO_2$ shown with the orange graph. This sample is compared with the one synthesized with hydration of α-$NaMnO_2$ in air shown with the green graph. The major drawback of the samples synthesized with the use of iodine was the appearance of the secondary phases evident by the 001 peak of α-$NaMnO_2$ as shown in the graph with the black color.

D.2: Aging of the birnessite compound as seen with the XRPD patterns

In section 5.4.1 (Figure 5.13b) we have shown the static magnetic susceptibility measurements of a birnessite (sample's code ib137) which were carried out under the same conditions. The only difference between the susceptibility experiments was that the second one was undertaken 6 months after the first one. Here we show the aging of the same

birnessite sample (ib137) as observed in the XRPD patterns. Similarly, the second XRPD measurement was carried out 6 months after the first one.

The purpose of these XRPD graph (Figure D.2) is to understand the aging effect of the birnessite as observed by the static magnetic susceptibility graphs. The second XRPD pattern is characterized by a shift of the Bragg reflections to the left (lower 2θ angles) and the elimination of the 001 peak of α-$NaMnO_2$ at 16.67 deg. The shift of the 001 peak towards lower angles indicates the change in the stoichiometry of the birnessite most likely due to the insertion of more H_2O in the interlayer distance. These modifications of the crystal structure probably have an effect on the Mn^{+3}/Mn^{+4} ratio of the mixed valence of the compound which affects the magnetic properties as we can observe in Figure 5.13b.

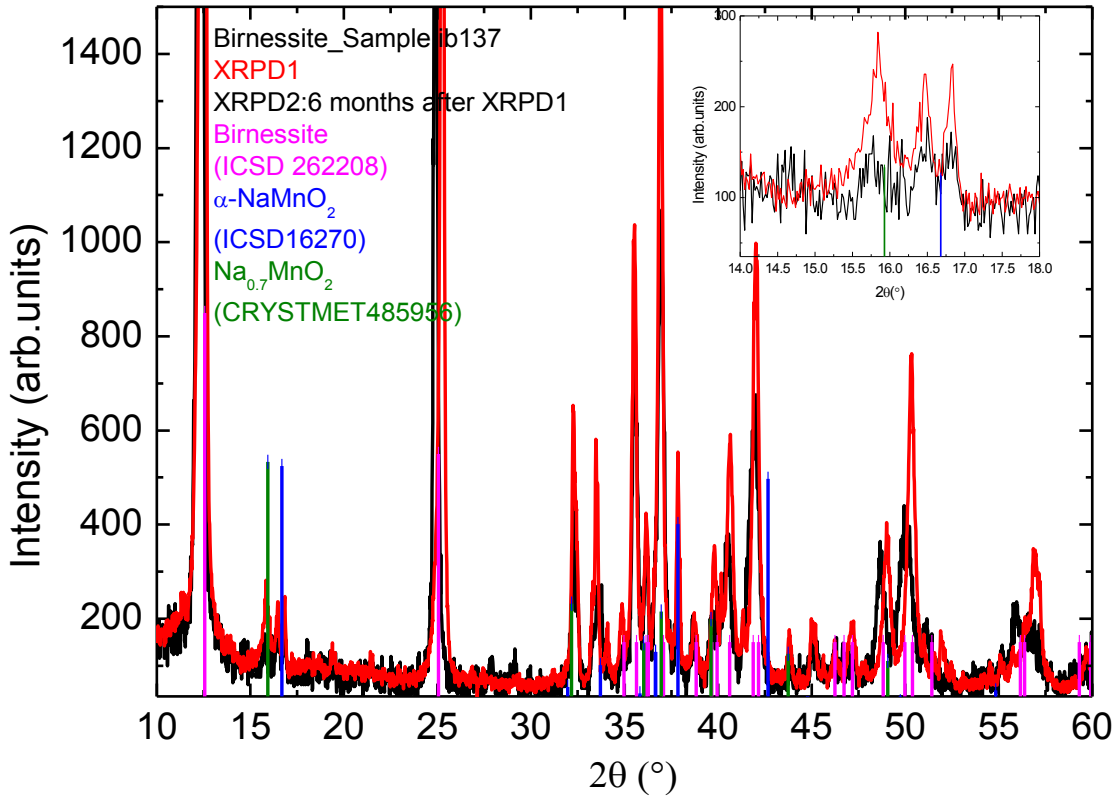

Figure D.2 XRPD graphs of the same samples: the first one shown with the red color was carried out 3 weeks after the sample was synthesized. The second measurement (presented with the black color) was undertaken 6 months after the first one to observe possible aging effects.

D.3 Methodology used for the power law fits presented in chapter 5

All the curves of the primary magnetic susceptibility (χ') shown in Figure 5.22 have been fitted with the Lorentz function in order to estimate the transition temperature T_f obtained at each different frequency. An example of the Lorentz fit is presented in Figure D.3. Various peak functions were used in order to fit the experimental data of each $\chi'_f(T)$ curve. Among these functions were the Gaussian, the Voigt, the Pseudovoigt. The deviations in the estimated T_f obtained by each different fit were small. An example is shown in Table D.1 for the susceptibility peak measured at 77 Hz. The issue of the curves presented in Figure 5.22 which prevents a perfect fit, is their asymmetry.

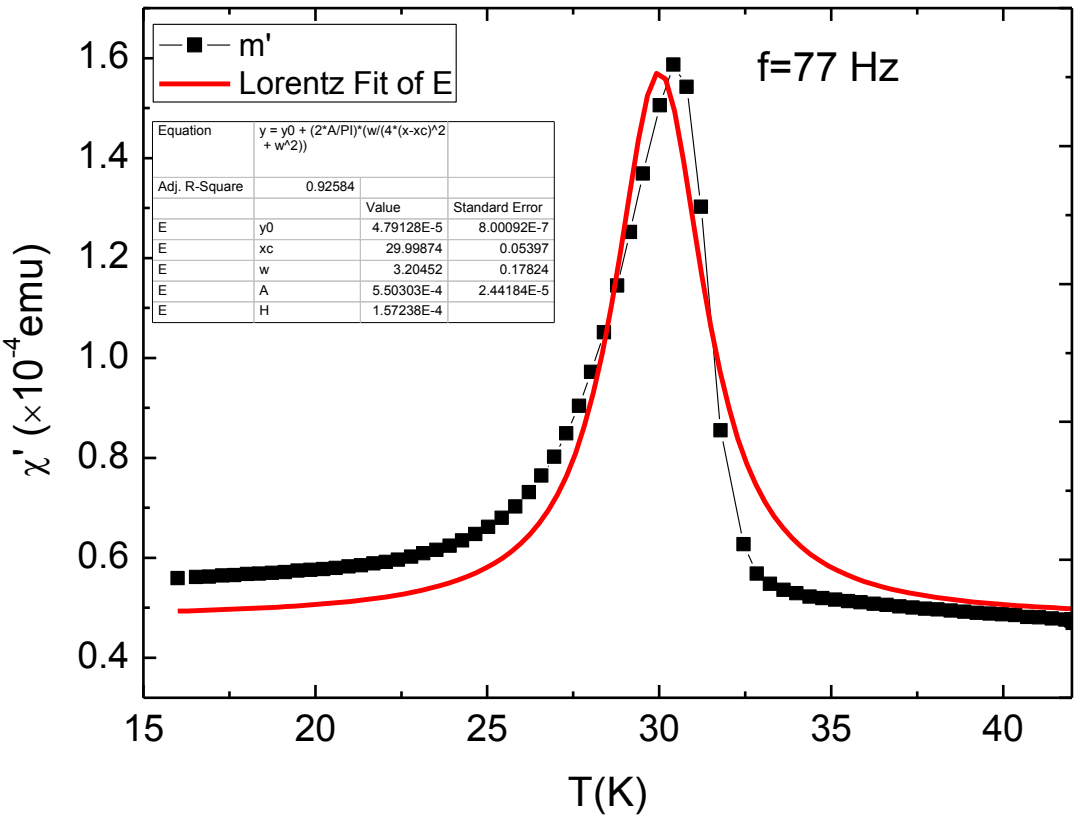

Figure D.3 Lorentz fit of the primary magnetic susceptibility curve measured at f=77 Hz. The adjustment R-square is 0.925, mostly due to the asymmetric shape of the experimental curve which leads to the deviation of the data from the wide bell-shaped Lorentz function

Function	**T_f**	**Adj-R square**
Lorentz	29.998	0.92584
Gauss	29.915	0.91078
Voigt	29.9784	0.92521
PseudoVoigt	29.984	0.92582

Table D.1 The above table presents the various functions used to fit the primary susceptibility peak measured at 77 Hz, shown in Figure D.1, the estimated by each fit T_f and the quality of the fit shown with the adjustment R-square.

Table D.2 shows for each frequency (f) the estimated by the fit temperature T_f. Moreover, the logarithim of each frequency has also been calculated and displayed, as this value is going to appear in the graph, for the power law fit.

One may notice that in Table D.2, the T_{sg} is 29.64 K. Here we discuss the reason that this value was chosen for the T_{sg} temperature. In equation 5.13 there are three parameters that one needs to define: the zv that corresponds to the slope of the linear fit, the intercept $\log(f_o)$ by which the relaxation time τ_o will be calculated and the temperature T_{sg}.

To reduce the complexity of a three parameters linear fit, we follow a method that calculates two parameters: the zv and the $\log(f_o)$.[287] The value of T_{sg} is adjusted in order to get the best linearity in the log(f) versus $\log[(T_f-T_{sg})/T_{sg}]$ plot. The zv and $\tau_o=1/f_o$ are calculated from the parameters of the fitting. We give different values of the T_{sg} we chose the one that gives the higher Adjustment R-square. Some examples of these trials with the T_{sg} values and the calculated parameters are presented in table D.3. Note that very small changes in the T_{sg} cause large deviations in the exponent zv and the relaxation time τ_o. Moreover, values of T_{sg} which resulted in a poor quality fit also gave results with no physical meaning, like the ones corresponding to the T_{sg}=28.85 K. For this value we got the lowest adjustment square and the relaxation time (10^{-21} sec) is unreasonably low for a spin glass system.[30]

Frequency (f) (Hz)	**log(f)**	**T_f (K)**	**log[(Col(T_f)-T_{sg})/T_{sg}]**
			Here T_{sg}=29.64 K
47	1.6721	29.95835	-1.96897
77	1.88649	29.99874	-1.9171
97	1.98677	30.01116	-1.90232
217	2.33646	30.06968	-1.83873
901	2.95472	30.21818	-1.70982

Table D.2 The parameters that were used in order to carry out the linear fit shown in figure 5.18.

The best fit of the frequency dependence for the $Na_{0.3}MnO_2 \times 0.2H_2O$ yielded the following parameters: T_{sg}=29.64 K, $\tau_o = 0.275 \times 10^{-11}$ sec and zv=5.029 (±0.126) and it is presented in Figure 5.23. The values of τo and zv are in consistency with other magnetic systems which have been classified as canonical spin glasses. [30, 163, 276]

T_{sg} (K)	**zv**	**τ_o (sec)**	**Adjustment R-square**
28.85	14.084	10^{-21}	0.99313
29.57	5.848	10^{-12}	0.99727
29.64	**5.029**	**10^{-11}**	**0.99748**
29.67	4.679	10^{-11}	0.99740

Table D.3 Values of the T_{sg} used to calculate the parameters zv, τ_o. The selection of the best T_{sg} was done according to the highest adjustment R-square

D.4 Le Bail Refinement of the 5 K NPD Pattern

The Le Bail refinement for the pattern at 5 K is shown in Figure D.4. The indexing has been done according to the triclinic system, space group $P1^{-}$, and has resulted in the following cell parameters: a=5.191(3) Å, b= 3.149(2) Å, c= 7.624 (6) Å and α= 88.902(8) deg, β= 101.944(6) deg, γ= 89.164 (9) deg. The reliability factors are χ^2=39.1 and R_{wp}=79.2 %.

The Le Bail analysis resulted in cell parameters which showed an increased c-axis (7.6 Å), in comparison with the c-axis (5.8 Å) of the α-$NaMnO_2$ powder, which was used as a precursor for the synthesis of the $Na_{0.3}MnO_2 \times 0.2H_2O$. The indexing of the NPD pattern yields comparable cell parameters with those obtained from the analysis of the TEM studies (paragraph 5.3.4)

However, the quality factors of the Le Bail fit R_{wp}=79% and χ^2=39, suggest that there is much scope of improvement. A few of the observed reflections are not predicted by the theoretical model, there is difference in the intensity between the observed and calculated reflections and also the increased background level, are factors that reduce the reliability of the final outcome. Due to the aforementioned issues the investigation of the NPD pattern with the Rietveld method is excluded.

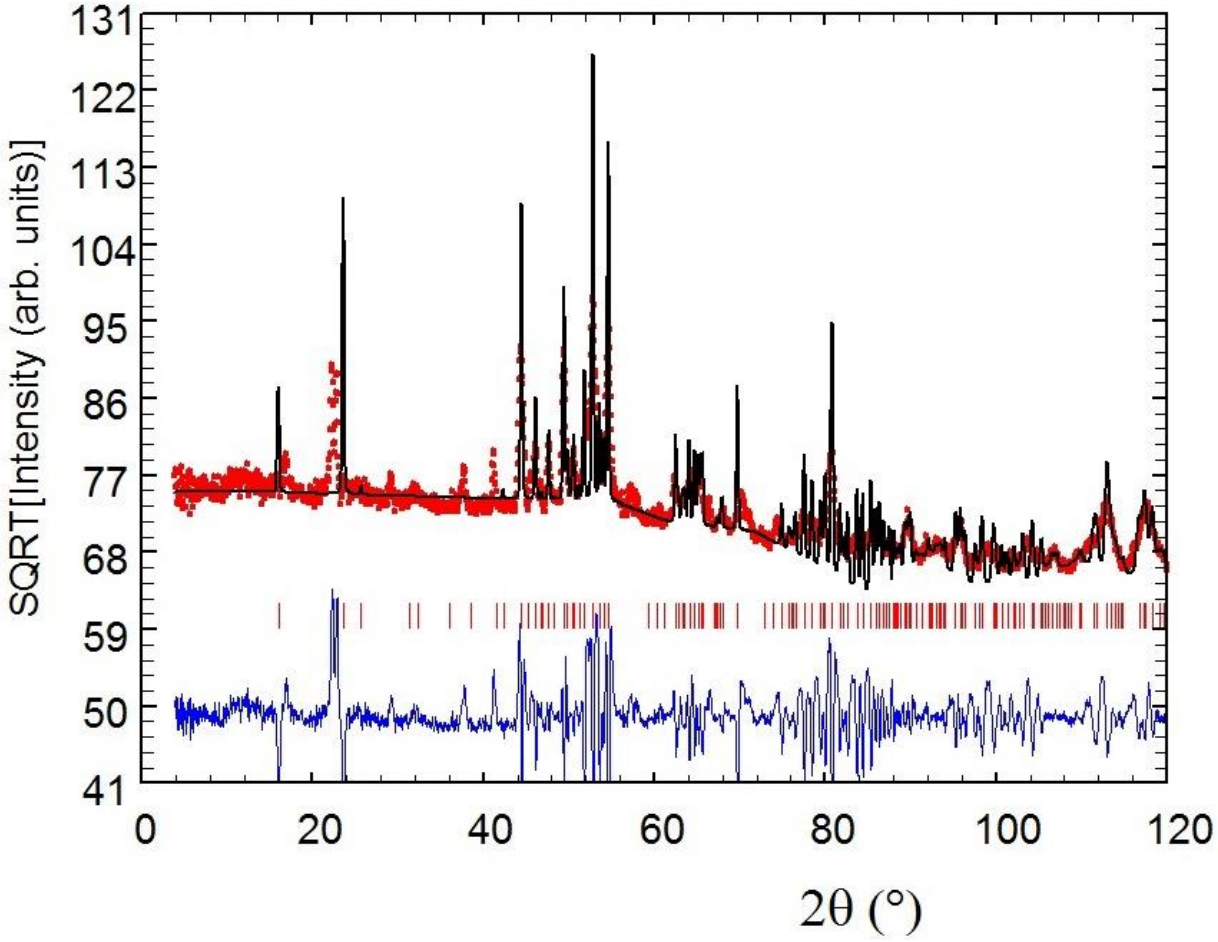

Figure D.4 Le Bail refinement of the NPD pattern obtained at 5 K for the $Na_{0.3}MnO_2 \times 0.2H_2O$.

Appendix E:

Research Training and Professional Development

Conferences and Talks

1) SPIE Photonics West, 1-6 February 2014, San Fransisco, USA. *Poster presented by Ioanna Bakaimi*

"Crystal, Magnetic and Dielectric Studies of the 2D Antiferromagnet: β-$NaMnO_2$" Ioanna Bakaimi, Othon Adamopoulos, Artem Abakumov, Mark A. Green, Alexandros Lappas

2) The Tenth Students Meeting, Processing and Application of Ceramics November 6-9, 2013, Novi Sad, Serbia, 3rd ESR COST MP09. *Oral Presentation by Ioanna Bakaimi*

"Magnetodielectric Coupling in the 2D Antiferromagnet β-$NaMnO_2$*"* I. Bakaimi, O. Adamopoulos, A. Abakumov, M.A. Green,A. Lappas,

3) IIT (Instituto Italiano di Technologia) 28 February 2013, Genova, Italy, *Invited Talk at Dr.Liberato's Manna group by Ioanna Bakaimi*

"Frustrated Magnanese Oxides: the diversity of Crystal Structures Towards Novel Magnetic Behaviors" I.Bakaimi, O. Adamopoulos, C.Stock, M.A Green and A.Lappas

4) TCO (Transparent Conductive Materials) 21-25 October, 2012. Hersonissos, Crete, Greece. *Poster Presentation by Ioanna Bakaimi*

"Growth of β-$NaFeO_2$ Thin Films by Pulsed Laser Deposition" I.Bakaimi, E.L. Papadopoulou, M.A. Green, P. Tzanetakis, A. Lappas

5) 6th International Conference of the Hellenic Crystallographic Association 28-29 September 2012, University of Athens, Greece. *Oral presentation by Ioanna Bakaimi*

"Frustrated Magnanese Oxides: the diversity of Crystal Structures Towards Novel Magnetic Behaviors" I.Bakaimi, O. Adamopoulos, M.Giot, C.Stock, M.A Green, A.Lappas.

6) ACNS-American Conference and Neutron Scattering, June 24 - June 28, 2012 Georgetown, Washinghton DC, USA. *Poster Presentation by Ioanna Bakaimi*: "Order Against Frustration in the Spin-2 Anisotropic Triangular Lattice System α-$NaMnO_2$"

I.Bakaimi, M. Giot, O. Adamopoulos, A. Lappas, C. Stock, L.C. Chapon, J. Taylor , C.M. Brown, M.A. Green

7) Panhellenic Conference on Solid State Physics & Materials Science, Ioannina, 26-29 September 2010. *Oral Presentation by Ioanna Bakaimi and distinction for the best oral presentation titled*:

"Frustration and Induced Magnetodielectric Coupling in $NaMnO_2$ Polymorphs" Ioanna Bakaimi, Othon Adamopoulos, Bohdan Kundys, Mark A. Green, Chris Stock, and Alexandros Lappas

8) Participation in the Panhellenic Conference on Solid State Physics & Materials Science, Heraklion, 21-24 September 2008

9) The European Conference Physics Of Magnetism, June 24-27, 2005 Poznań, Poland, Poster Presentation by M.Kwiecien

"Electronic Structure and Magnetic Properties $Gd_{1-x}Tb_xNi_3$ Compounds"M. Kwiecien and G. Chealkowska and J. Bakaimi

Schools and Workshops

1) *Workshop-training for magnetic structure analysis with the software "Jana2006*":

The 14th Ad Hoc Workshop on Jana 2006, 15-16 October 2012, Institute of Physics Department of Structure Analysis, Prague, Checz Republic

2) *School-training for the crystal and magnetic structure analysis*:

5th ILL Annual School on Neutron Diffraction Data Treatment using the FullProf Suite: FPSchool 2012-23-27 January 2012, Grenoble, France

3) *Workshop-training for crystal structure analysis with the software "Jana2006*"

The 10th Ad Hoc Workshop on Jana 2006, 6-7 December 2011, Institute of Physics Department of Structure Analysis, Prague, Checz Republic

4) "Summer School on Physics of Advanced Materials", July 2003, Thessaloniki, Greece

5) Advanced Physics Summer School', University of Crete, Physics Department, July 2002, Heraklion Crete, Greece

Short Visits and Further Training

1) *15 June2012-15 July 2012*: Guest Researcher at NCNR-NIST in USA (NIST Center for Neutron's Research-National Institutes of Standards and Technology).

Synthesis of Complex Magnetic Oxides, Participation in Neutron Diffraction Experiments, Analysis with Rietveld Method

2) *1 May2011-30June 2011*: Guest Researcher at NCNR-NIST in USA (NIST Center for Neutron's Research-National Institutes of Standards and Technology).

Synthesis of Complex Magnetic Oxides, Participation in Neutron Diffraction Experiments, Analysis with Rietveld Method

3) *31July-30August 2009*: Guest Researcher at NCNR-NIST in USA (NIST Center for Neutron's Research-National Institutes of Standards and Technology).

Synthesis of Complex Magnetic Oxides, Participation in Neutron Diffraction Experiments, Data Analysis with Rietveld Method

Peer-Reviewed Proposals for Neutron Scattering Experiments

1) July 2012*:'Defining Critical Exponents in a-$NaMnO_2$'* Participants: Ioanna Bakaimi, Efrain Rodriguez. Instrument: SPINS triple axis spectrometer at the NCNR, NIST, USA

2) July 2012: "*Elemental composition in the birnessite $Na_xMnO_2(H2O)y$"* Participants :Ioanna Bakaimi, Pawel Zajdel. Instrument: NG7-Prompt Gamma Rays, at the NCNR, NIST, USA

3) July 2012: "*Crystal and Magnetic Structures of the birnessite: $Na_xMnO_2(H_2O)y$*" Participants: Ioanna Bakaimi and Mark Green. Instrument BT1 diffractometer at the NCNR, NIST, USA

4) May 2012: "*Magnetically Driven Ferroelectric Order in the 2D Antiferromagnet b-$NaMnO_2$"* Participants: Ioanna Bakaimi and Alexandros Lappas, Instrument: WISH diffractometer at the I target station 2, ISIS-RAL, Oxford UK,

5) June 2011: *"Spin dynamics in β-$NaMnO_2$"*, Participants: Ioanna Bakaimi, Mark Green. Instrument BT1 diffractometer at the NCNR, NIST, USA

6) March 2010: "*Spin fluctuations in the triangular antiferromagnet beta-$NaMnO_2$*" Participants: Chris Stock, Ioanna Bakaimi, Alexandros Lappas. Instrument: MARI Spectrometer, ISIS-RAL, Oxford UK

7) August 2009: "*Structure and Magnetism of $Na_{0.44}MnO_2$*". Participants: Ioanna Bakaimi, Mark Green, Craig Brown, Instrument DCS (Disc Chopper Spectrometer) at the NCNR, NIST, USA

8) August 2009: "*Crystal Stucture of $Na_{0.44}MnO_2$*" Participants: Ioanna Bakaimi, Mark Green. Instrument BT1 diffractometer at the NCNR, NIST, USA

9) August 2009: "*Magnetic Structure of β-$NaMnO_2$*" Participants: Ioanna Bakaimi, Mark Green. Instrument BT1 diffractometer at the NCNR, NIST, USA

10) August 2009: "*Magnetic Excitations in the β-$NaMnO_2$"* Participants: Ioanna Bakaimi, Mark Green, Craig Brown, Instrument DCS (Disc Chopper Spectrometer) at the NCNR, NIST, USA

11) August 2009: "Crystal Stucture and Magnetic Structure of β-$NaMnO_2$" Participants: Ioanna Bakaimi, Mark Green. Instrument BT1 diffractometer at the NCNR, NIST, USA

Publications

1) Abakumov A., Tsirlin A., **Bakaimi I.**, Van Tendeloo G., and Lappas A., "Multiple twinning as a structure directing mechanism in layered rock-salt-type oxides: $NaMnO_2$ polymorphism, electrochemical behavior and magnetism", Chem.Mater. 2014, 26,3306

Bakaimi I. Abakumov A, Green M.A, Lappas A. "Crystal, Magnetic and Dielectric Studies of the 2D Antiferromagnet: β-$NaMnO_2$" Proc. SPIE 2014, Vol. 8987, 898716 doi: 10.1117/12.2036937

3) Kruk I., Zajdel P., Van Beek W., **Bakaimi I.**, Lappas A., Stock C.,and Green M. A. "Coupled Commensurate Cation and Charge Modulation in the Tunneled Structure, $Na_{0.40(2)}MnO_2$", J. Am. Chem. Soc. 2011, 133, 13950

4) B. Kundys, A. Lappas, M. Viret, V. Kapustianyk, V. Rudyk, S. Semak, Ch. Simon, and **I. Bakaimi** "Multiferroicity and hydrogen-bond ordering in $(C_2H_5NH_3)_2CuCl_4$ featuring dominant ferromagnetic interactions", Phys.Rev. B 2010, 81, 224434

In preparation (2014):

- **Bakaimi I.**, Kundys B., Green M.A., Lappas A. "Magnetodielectric Coupling in $NaMnO_2$ polymorphs"

- **Bakaimi I.**, Brescia R., Green M.A., Manna L., Lappas A., "Crystal and magnetic properties of the spin glass birnessite $Na_{0.3}MnO_2{\times}0.2H_2O$"

References

1. Kimura T. Spiral Magnets as Magnetoelectrics. *Annual Review of Materials Research* 2007, **37:** 387.

2. Khomskii D. Classifying multiferroics: Mechanisms and effects. *Physics* 2009, **2**(20).

3. Kimura T. GT, Shintani H., Ishizaka K.Arima T.Tokura Y. Magnetic control of ferroelectric polarization. *Nature* 2003, **426:** 55.

4. Mostovoy M. Ferroelectricity in Spiral Magnets. *Physical Review Letters* 2006, **96:** 067601.

5. Arima T-h. Spin-Driven Ferroelectricity and Magneto-Electric Effects in Frustrated Magnetic Systems. *Journal of the Physical Society of Japan* 2011, **80:** 052001.

6. Parant JP, Olazcuaga R, Devalette M, Fouassier C, Hagenmuller P. Sur Quelques Nouvelles Phases de Formule Na_xMnO_2 *Journal of Solid State Chemistry* 1971, **3:** 1.

7. Giot M, Chapon L, Androulakis J, Green M, Radaelli P, Lappas A. Magnetoelastic Coupling and Symmetry Breaking in the Frustrated Antiferromagnet α-$NaMnO_2$. *Physical Review Letters* 2007, **99:** 247211.

8. Stock C, Chapon L, Adamopoulos O, Giot M, Lappas A, Taylor JW, *et al.* One-Dimensional Magnetic Fluctuations in the Spin-2 Triangular Lattice α-$NaMnO_2$. *Physical Review Letters* 2009, **103:** 077202.

9. Carlin RL. *Magnetochemistry*. Springer, 1986.

10. Veciana J. *π-Electron Magnetism. From Molecules to Magnetic Materials*. Springer, 2001.

11. Dagotto E, Rice TM. Surprises on the Way from One- to Two Dimensional Quantum Magnets: The Ladder Materials. *Science* 1996, **271:** 618.

12. Ueda YI, M. Magnetic Properties of AV_2O_5. *Journal of Magnetism and Magnetic Materials* 1998, **177-181:** 741.

13. Hiroi ZT, M. Absence of superconductivity in the doped antiferromagnetic spin ladder compound (La,Sr)$CuO_{2.5}$. *Nature* 1995, **377:** 41.

14. Blundell S. *Magnetism in Condensed Matter*. Oxford University Press, 2001.

15. Spaldin NA. *Magnetic Materials. Fundamentals and Applications*. Cambridge University Press 2011.

16. Chaterjii T. *Neutron Scattering from Magnetic Materials*. Elsevier 2006.

17. Moessner R, Ramirez AP. Geometrical Frustration. *Physics Today* 2006, **59:** 24.

18. Ramirez AP. Strongly Geometrically Frustrated Magnets. *Annu Rev Mater Sci* 1994, **24:** 453.

19. Giauque W, Ashley M. Molecular Rotation in Ice at 10°K. Free Energy of Formation and Entropy of Water. *Physical Review* 1933, **43:** 81.

20. Pauling L. The Structure and Entropy of Ice and of Other Crystals with Some Randomness of Atomic Arrangement. *Journal of the American Chemical Society* 1935, **57:** 2680.

21. Bernal JD, Fowler RH. A Theory of Water and Ionic Solution, with Particular Reference to Hydrogen and Hydroxyl Ions. *The Journal of Chemical Physics* 1933, **1:** 515.

22. Haffner H. Frustrated trio mimicked. *Nature* 2010, **465:** 555.

23. Struck J, Olschlager C, Le Targat R, Soltan-Panahi P, Eckardt A, Lewenstein M, *et al*. Quantum simulation of frustrated classical magnetism in triangular optical lattices. *Science* 2011, **333:** 996.

24. Gaulin BD. The texture of frustrated magnets. *Nature materials* 2005, **4:** 296.

25. Mathieu R, Asamitsu A, Kaneko Y, He J, Tokura Y. $Eu_{0.5}Sr_{1.5}MnO_4$: A three-dimensional XY spin glass. *Physical Review B* 2005, **72:** 014436.

26. Lago J, Blundell SJ, Eguia A, Jansen M, Rojo T. Three-dimensional Heisenberg spin-glass behavior in $SrFe_{0.90}Co0._{10}O_{3.0}$. *Physical Review B* 2012, **86:** 064412.

27. Hagemann I, Huang Q, Gao X, Ramirez A, Cava R. Geometric Magnetic Frustration in $Ba_2Sn_2Ga_3ZnCr_7O_{22}$: A Two-Dimensional Spinel Based Kagomé Lattice. *Physical Review Letters* 2001, **86:** 894.

28. MC Queen TM. Frustrated ferroelectricity in niobate pyrochlores. *J Phys: Condens Matter* 2008, **20:** 235210.

29. Balents L. Spin liquids in frustrated magnets. *Nature* 2010, **464:** 199.

30. Mydosh JA. *Spin glasses:an experimental introduction*. Taylor&Francis, 1993.

31. Sanchez-Palencia L, Lewenstein M. Disordered quantum gases under control. *Nature Physics* 2010, **6:** 87.

32. Schmid H. Multi-ferroic magnetoelectrics. *Ferroelectrics* 1994, **162:** 317.

33. Hill N. Why Are There so Few Magnetic Ferroelectrics? *J Phys Chem B* 2000, **104:** 6694.

34. Eerenstein W, Mathur ND, Scott JF. Multiferroic and magnetoelectric materials. *Nature* 2006, **442:** 759.

35. Spaldin NA, Fiebig M. The Renaisanse of Magnetoelectric Multiferroics. *Science* 2008, **309:** 391.

36. Maxwell JC. *A Treatise on Electricity and Magnetism, Volume 1*. Oxford University Press, 1873.

37. Maxwell JC. *A Treatise on Electricity and Magnetism, Volume 2*. Dover Publications: New York, 1891.

38. Roentgen. Ueber die durch Bewegung eines im homogenen electrischne Felde defindlichen Dielectricums hervorgerufene electrodynamische Kraft. *AnnPhysChem* 1888, **35:** 264.

39. Wilson HA. On the Electric Effect of Rotating a Dielectric in a Magnetic Field. *Phil Trans R SocLondA* 1905, **204:** 121.

40. Debye P. Bemerkung zu einigen neue n Versuchen uber einen magneto-elektrischen Richteffekt. *ZPhys* 1926, **36:** 300.

41. Landau L, Lifshitz E. *Electrodynamics of Continuous Media*. Fizmatgiz, Moscow, 1959.

42. Dzyaloshinskii IE. The magnetoelectric effect in antiferromagnets. *SovPhys JETP* 1959, **10:** 628.

43. Astrov. D. On the magneto-electrical effect in antiferromagnets *SovPhys JETP* 1960, **11:** 708.

44. Wang KF, Liu JM, Ren ZF. Multiferroicity: the coupling between magnetic and polarization orders. *Advances in Physics* 2009, **58:** 321.

45. Fiebig M. Revival of the magnetoelectric effect. *Journal of Physics D: Applied Physics* 2005, **38:** R123.

46. Kleemann W. Magnetoelectric Coupling in Disordered Multiferroics. *Ferroelectrics* 2012, **428:** 64.

47. Van Aken BB, Palstra TT, Filippetti A, Spaldin NA. The origin of ferroelectricity in magnetoelectric YMnO3. *Nature materials* 2004, **3:** 164.

48. Hur N, Park S, Sharma PA, Ahn S-J, Guha S, Cheong SW. Electric polarization reversal and memory in a multiferroic material induced by magnetic field. *Nature* 2004, **429:** 392.

49. Lawes G, Harris A, Kimura T, Rogado N, Cava R, Aharony A, *et al.* Magnetically Driven Ferroelectric Order in Ni3V2O8. *Physical Review Letters* 2005, **95:** 087205.

50. Seki S, Onose Y, Tokura Y. Spin-Driven Ferroelectricity in Triangular Lattice Antiferromagnets $ACrO_2$ (A=Cu, Ag, Li, or Na). *Physical Review Letters* 2008, **101:** 067204.

51. Terada N, Khalyavin DD, Manuel P, Tsujimoto Y, Knight K, Radaelli PG, *et al.* Spiral-Spin-Driven Ferroelectricity in a Multiferroic Delafossite $AgFeO_2$. *Physical Review Letters* 2012, **109:** 097203.

52. Johnson RD, Chapon LC, Khalyavin DD, Manuel P, Radaelli PG, Martin C. Giant Improper Ferroelectricity in the Ferroaxial Magnet $CaMn_7O_{12}$. *Physical Review Letters* 2012, **108:** 067201.

53. Kleemann W, Shvartsman VV, Borisov P. Coexistence of Antiferromagnetic and Spin Cluster Glass Order in the Magnetoelectric Relaxor Multiferroic $PbFe_{0.5}Nb_{0.5}O_3$. *Physical Review Letters* 2010, **105:** 257202

54. Shvartsman VV, Bedanta S, Borisov P, Kleemann W. $(Sr,Mn)TiO_3$: A Magnetoelectric Multiglass. *Physical Review Letters* 2008, **101:** 165704.

55. Dzyaloshinskii IE. A thermodynamic theory of 'weak' ferromagnetism of antiferromagnets *J Phys Chem Solids* 1958, **4:** 241.

56. Moriya T. Anisotropic Superexchange Interaction and Weak Ferromagnetism. *Physical Review* 1960, **120**(1)**:** 91.

57. Katsura H, Nagaosa N, Balatsky AV. Spin Current and Magnetoelectric Effect in Noncollinear Magnets. *Physical Review Letters* 2005, **95:** 057205.

58. Mochizuki M, Furukawa N. Theory of Magnetic Switching of Ferroelectricity in Spiral Magnets. *Physical Review letters* 2010, **105:** 187601.

59. Yamasaki Y, Miyasaka S, Kaneko Y, He JP, Arima T, Tokura Y. Magnetic Reversal of the Ferroelectric Polarization in a Multiferroic Spinel Oxide. *Physical Review Letters* 2006, **96:** 207204.

60. Taniguchi K, Abe N, Takenobu T, Iwasa Y, Arima T. Ferroelectric Polarization Flop in a Frustrated Magnet $MnWO_4$ Induced by a Magnetic Field. *Physical Review Letters* 2006, **97:** 097203.

61. Arima T-h. Ferroelectricity Induced by Proper-Screw Type Magnetic Order. *Journal of the Physical Society of Japan* 2007, **76:** 073702.

62. Jia C, Onoda S, Nagaosa N, Han J. Bond electronic polarization induced by spin. *Physical Review B* 2006, **74**(224444).

63. Tokura Y, Seki S. Multiferroics with spiral spin orders. *Adv Mater* 2010, **22:** 1554.

64. Murakawa H, Onose Y, Miyahara S, Furukawa N, Tokura Y. Comprehensive study of the ferroelectricity induced by the spin-dependent d-p hybridization mechanism in $Ba_2XGe_2O_7$ (X = Mn, Co, and Cu). *Physical Review B* 2012, **85:** 174106.

65. Sergienko I, Şen C, Dagotto E. Ferroelectricity in the Magnetic E-Phase of Orthorhombic Perovskites. *Physical Review Letters* 2006, **97:** 227204.

66. Picozzi S, Yamauchi K, Sanyal B, Sergienko I, Dagotto E. Dual Nature of Improper Ferroelectricity in a Magnetoelectric Multiferroic. *Physical Review Letters* 2007, **99**(227201).

67. Damjanovic D. Ferroelectric, dielectric and piezoelectric properties of ferroelectric thin films and ceramics. *Rep Prog Phys* 1998, **61:** 1267.

68. Lawes G, Ramirez AP, Varma CM, M.A. S. Magnetodielectric Effects from Spin Fluctuations in Isostructural Ferromagnetic and Antiferromagnetic Systems. *Physical Review Letters* 2003, **91:** 257208.

69. Seehra MS, Helmick RE. Dielectric anomaly in MnO near the magnetic phase transition. *Physical Review B* 1981, **24:** 5098.

70. Tackett R, Lawes G, Melot B, Grossman M, Toberer E, Seshadri R. Magnetodielectric coupling in Mn_3O_4. *Physical Review B* 2007, **76:** 024409.

71. Muralidharan R, Jang TH, Yang CH, Jeong YH, Koo TY. A Magnetic control of spin reorientation and magnetodielectric effect below the spin compensation temperature in $TmFeO_3$. *Applied Physics Letters* 2007, **90:** 012506.

72. Saito M, Higashinaka R, Maeno Y. Magnetodielectric response of the spin-ice $Dy_2Ti_2O_7$. *Physical Review B* 2005, **72:** 144422.

73. Katsufuji T, Takagi H. Magnetocapacitance and spin fluctuations in the geometrically frustrated magnets $R_2Ti_2O_7$ (R=rare earth). *Physical Review B* 2004, **69:** 064422.

74. Hur N, Park S, Guha S, Borissov A, Kiryukhin V, Cheong SW. Low-field magnetodielectric effect in terbium iron garnets. *Applied Physics Letters* 2005, **87:** 042901.

75. Suzuki T, Aikawa Y, Katsufuji T. Magnetocapacitance in Geometrically Frustrated Magnet $ZnFe_2O_4$. *Journal of the Physical Society of Japan* 2005, **74:** 863.

76. Shapira Y, Yacovitch RD, Nelson DR. Magnetostriction and the two-spin correlation function in MnF_2 *Solid State Communications* 1975, **17:** 175.

77. Bellido N, Martin C, Simon C, Maignan A. Coupled negative magnetocapacitance and magnetic susceptibility in a Kagomé staircase-like compound $Co_3V_2O_8$. *Journal of Physics: Condensed Matter* 2007, **19:** 056001.

78. Lu Y, Wei M, Wang Z, Evans DG, Duan X. Characterization of structure and electrochemical properties of lithium manganese oxides for lithium secondary batteries hydrothermally synthesized from δ-$KxMnO_2$. *Electrochimica Acta* 2004, **49:** 2361.

79. Prieto O, Del Arco M, Rives V. Characterisation of K, Na, and Li birnessites prepared by oxidation with H_2O_2 in a basic medium. Ion exchange properties and study of the calcined products. *Journal of Materials Science* 2003, **38:** 2815.

80. Beznosikov BV, Aleksandrov KS. Predictions of Compounds in the family of Delafossites. *Journal of Structural Chemistry* 2009, **50:** 102.

81. Berthelot R, Pollet M, Doumerc JP, Delmas C. First experimental evidence of a new D4-$AgCoO_2$ delafossite stacking. *Inorganic chemistry* 2011, **50:** 4529.

82. Armstrong AR, Bruce PG. Synthesis of layered $LiMnO_2$ as an electrode for rechargeable lithium batteries. *Nature* 1996, **381:** 499.

83. Oyama N, Tatsuma T, Sato T, Sotomura T. Dimercaptan-polyaniline composite electrodes for lithium batteries with high energy density. *Nature* 1995, **373:** 598.

84. Kawazoe H, Yanagi H, Ueda K, Hosono H. Transparent p-type conducting oxides: Design and fabrication of p-n heterojunctions. *Mrs Bulletin* 2000, **25:** 28.

85. Mekata M, Yaguchi N, Takagi T, Mitsuda S, Yoshizawa H. Magnetic Ordering in delafossite $CuFeO_2$. *Journal of Magnetism and Magnetic Materials* 1992, **104:** 823.

86. Koumoto K, Koduka H, Seo WS. Thermoelectric properties of single crystal $CuAlO_2$ with a layered structure. *Journal of Materials Chemistry* 2001, **11:** 251.

87. Mendels P, Bono D, Bert F, Garlea O, Darie C, Bordet P, *et al.* Oxygen doped S=1/2 Cu delafossites: a muon spin rotation/relaxation study. *Journal of Physics-Condensed Matter* 2004, **16:** S799.

88. Marquardt MA, Ashmore NA, Cann DP. Crystal chemistry and electrical properties of the delafossite structure. *Thin Solid Films* 2006, **496:** 146.

89. Jlaeil F, Elkhouni T, Amami M, Strobel P, Ben Salah A. Structural and physical properties of the (Ca, Mg)-doped delafossite powder $CuGaO_2$. *Materials Research Bulletin* 2013, **48:** 1020.

90. Kimura T, Lashley JC, Ramirez AP. Inversion-symmetry breaking in the noncollinear magnetic phase of the triangular-lattice antiferromagnet $CuFeO_2$. *Physical Review B* 2006, **73:** 220401.

91. Nakajima T, Mitsuda S, Kanetsuki S, Tanaka K, Fujii K, Terada N, *et al.* Electric polarization induced by a proper helical magnetic ordering in a delafossite multiferroic $CuFe_{1-x}Al_xO_2$. *Physical Review B* 2008, **77:** 052401.

92. Hayashi K, Fukatsu R, Nozaki T, Miyazaki Y, Kajitani T. Structural, magnetic, and ferroelectric properties of $CuFe_{1-x}Mn_xO_2$. *Physical Review B* 2013, **87:** 064418.

93. Kundys B, Maignan A, Pelloquin D, Simon C. Magnetoelectric interactions in polycrystalline multiferroic antiferromagnets $CuFe_{1-x}Rh_xO_2$ (x=0.00 and x=0.05). *Solid State Sciences* 2009, **11:** 1035.

94. Inomata A, Kohn K. Pyroelectric effect and possible ferroelectric transition of helimagnetic $GdMn_2O_5$, $TbMn_2O_5$ and YMn_2O_5. *Journal of Physics-Condensed Matter* 1996, **8:** 2673.

95. Ye F, Ren Y, Huang Q, Fernandez-Baca J, Dai P, Lynn J, *et al.* Spontaneous spin-lattice coupling in the geometrically frustrated triangular lattice antiferromagnet $CuFeO_2$. *Physical Review B* 2006, **73:** 220404.

96. Ye F, Fernandez-Baca J, Fishman R, Ren Y, Kang H, Qiu Y, *et al.* Magnetic Interactions in the Geometrically Frustrated Triangular Lattice Antiferromagnet $CuFeO_2$. *Physical Review Letters* 2007, **99:** 157201.

97. Aktas O, Truong KD, Otani T, Balakrishnan G, Clouter MJ, Kimura T, *et al.* Raman scattering study of delafossite magnetoelectric multiferroic compounds: $CuFeO_2$ and $CuCrO_2$. *Journal of physics Condensed matter : an Institute of Physics journal* 2012, **24:** 036003.

98. Quirion G, Plumer M, Petrenko O, Balakrishnan G, Proust C. Magnetic phase diagram of magnetoelectric $CuFeO_2$ in high magnetic fields. *Physical Review B* 2009, **80:** 064420.

99. Smart LE, Moore EA. *Solid State Chemistry*. Taylor and Francis, 2005.

100. Pechrasky V, Zavalij P. *Fundamentals of Powder Diffraction and Structural Characterization of Materials*. Springer, 2008.

101. Hammond C. *The Basics of Crystallography and Diffraction*. Oxford University Press, 2009.

102. Giacovazzo C, Monaco HL, Viterbo D, Scordari F, Gilli G, Zanotti G, *et al. Fundamentals of Crystallography*. Oxford University Press, 2011.

103. Chatterjee SK. *Crystallography and the World of Symmetry.* Springer, 2008.

104. Boss CB, Fredeen KJ. *Concepts, Instrumentation, and Techniques in Inductively Coupled Plasma Optical Emission Spectrometry* Perkin Elmer, 1999.

105. Ghosh S, Prasanna V, Sowjanya B, Alaraja M, Banji D. Inductively Coupled Plasma-Optical Emission Spectroscopy: A Review. *Asian JPharm Ana* 2013, **3:** 24.

106. Fagaly RL. Superconducting quantum interference device instruments and applications. *Review of Scientific Instruments* 2006, **77:** 101101.

107. Josepshon BD. Possible new effects in superconductive tunnelling. *Physics Letters* 1962, **1:** 251.

108. Martien D. *Introduction AC susceptibility*. Quantum Design

109. Moulson AJ, Herbert JM. *Electroceramics Materials, Properties, Applications*. Wiley, 2003.

110. A.S. S. *Domain Structure in Ferroelectrics and Related Materials*. Cambridge International Science Publishing 2006.

111. *Agilent 4284A, Precision LCR Meter, .* Agilent Technologies, 2001.

112. Amorese G. *LCR Impendance Measurement Basics*. Hewlett-Packard Company, 1997.

113. *Agilent Impendance Measurement Handbook, A guide to measurement technology and techniques*. Agilent Technologies, 2009.

114. Kittel C. *Introduction to Solid State Physics*. Wiley, 2004.

115. *Model Keithley 6517A Electrometer, User's Manual*. Keithley Instruments, Inc., 2003.

116. *Low Level Measurements Handbook.Precision DC Current, Voltage, and Resistance Measurements*. Keithley Inc, 2004.

117. Rabe KM. *Physics of Ferroelectrics.A Modern Perspective*. Springer, 2007.

118. von Hippel A. Ferroelectricity, Domain Structure, and Phase Transitions of Barium Titanate. *Reviews of Modern Physics* 1950, **22:** 221.

119. Marshall W, Lovesey SW. *Theory of Thermal Neutron Scattering*. Oxford University Press, 1971.

120. Kisi EH, Howard CJ. *Applications of Neutron Powder Diffraction*. Oxford University Press, 2008.

121. Bacon GE. *Neutron Diffraction*. Oxford University Press, 1975.

122. Squires GL. *Introduction to the Theory of Thermal Neutron Scattering* Cambridge University Press, 1978.

123. Price DL, Skold K. *Methods of Experimental Physics, vol 23, Part A*. Academic Press, London, 1987.

124. Izyumov YA, Ozerov RP. *Magnetic Neutron Diffraction*. Plenum Press, 1970.

125. Shirane G, Saphiro M, Tranquada JM. *Neutron Scaterring with a Triple Axis Spectrometer* Cambridge University Press, 2004.

126. Collins MF. *Magnetic Critical Scattering* Oxford University Press, 1989.

127. Shull CG, Smart JS. Detection of Antiferromagnetism by Neutron Diffraction. *PhysRev* 1949, **76:** 1256.

128. Le Bail A, Duroy H, Fourquet JL. AB-Initio Structure Determination of $LiSbWO_6$ by X-Ray Powder Diffraction. *Materials Research Bulletin* 1988, **23:** 447.

129. Will G. *Powder Diffraction:The Rietveld Method and the Two Stage Method to Determine and Refine Crystal Structures from Powder Diffraction Data*. Springer, 2005.

130. Toby BH. R factors in Rietveld analysis: How good is good enough? *Powder Diffraction* 2006, **21:** 67.

131. Young P. *The Rietveld Method* Oxford University Press, 1991.

132. McCusker LB, Von Dreele RB, Cox DE, Louer D, Scardi P. Rietveld refinement guidelines. *Journal of Applied Crystallography* 1999, **32:** 36.

133. Spence JCH. *High Resolution Electron Microscopy*. Oxford University Press, 2003.

134. Fultz B, Howe JM. *Transmission Electron Microscopy and Diffractometry of Materials*. Springer, 2008.

135. Jansen M, Hoppe R. Knowledge of NaCl Family of Structure-Crystal Structure of $NaMnO_2$. *Zeitschrift Fur Anorganische Und Allgemeine Chemie* 1973, **399:** 163.

136. Abou-El-Sherbini KS, Askar MH, Schollhorn R. Hydrated layered manganese dioxide: III. Role of bismuth oxide on the redox behaviour of hydrated layered manganese dioxides. *Solid State Ionics* 2001, **139:** 121.

137. Abou-El-Sherbini KS, Askar MH, Schollhorn R. Hydrated layered manganese dioxide Part I. Synthesis and characterization of some hydrated layered manganese dioxides from alpha-$NaMnO_2$. *Solid State Ionics* 2002, **150:** 407.

138. Abou-El-Sherbini KS, Askar MH, Schollhorn R. Hydrated layered manganese dioxide Part II. Electrochemical behaviour of some hydrated layered manganese dioxides in alkaline electrolytes. *Solid State Ionics* 2002, **150:** 417.

139. Rahner D, Machill S, Schlorb H, Siury K, Kloss M. Intercalation materials for lithium rechargeable batteries. *Solid State Ionics* 1996, **86:** 891.

140. Tarascon JM, Armand M. Issues and challenges facing rechargeable lithium batteries. *Nature* 2001, **414:** 359.

141. Bruce PG, Scrosati B, Tarascon J-M. Nanomaterials for rechargeable lithium batteries. *Angewandte Chemie-International Edition* 2008, **47:** 2930.

142. Mather GC, Dussarrat C, Etourneau J, West AR. A review of cation-ordered rock salt superstructure oxides. *Journal of Materials Chemistry* 2000, **10:** 2219.

143. Abakumov AM, Tsirlin A, Bakaimi I, Van Tendeloo G, Lappas A. Multiple twinning as a structure directing mechanism in layered rock-salt-type oxides: $NaMnO_2$ polymorphism, electrochemical behavior and magnetism. *Chemistry of Materials* 2014, **26:** 3306.

144. Warren BE. X-Ray Diffraction in Random Layer Lattices. *PhysRev* 1941, **59:** 693.

145. Kresse G, Furthmuller J. Efficient iterative schemes for ab initio total-energy calculations using a plane-wave basis set. *Physical Review B* 1996, **54:** 11169.

146. Perdew JP, Burke K, Ernzerhof M. Generalized gradient approximation made simple. *Physical Review Letters* 1996, **77:** 3865.

147. Franchini C, Podloucky R, Paier J, Marsman M, Kresse G. Ground-state properties of multivalent manganese oxides: Density functional and hybrid density functional calculations. *Physical Review B* 2007, **75:** 195128.

148. Zorko A, El Shawish S, Arcon D, Jaglicic Z, Lappas A, van Tol H, *et al.* Magnetic interactions in alpha-$NaMnO_2$: Quantum spin-2 system on a spatially anisotropic two-dimensional triangular lattice. *Physical Review B* 2008, **77:** 024412.

149. Todo S, Kato K. Cluster algorithms for general-S quantum spin systems. *Physical Review Letters* 2001, **87:** 047203.

150. Albuquerque AF, Alet F, Corboz P, Dayal P, Feiguin A, Fuchs S, *et al.* The ALPS project release 1.3: Open-source software for strongly correlated systems. *Journal of Magnetism and Magnetic Materials* 2007, **310:** 1187.

151. Kahn O. *Molecular Magnetism*. VCH, 1993.

152. Tan H, Verbeeck J, Abakumov A, Van Tendeloo G. Oxidation state and chemical shift investigation in transition metal oxides by EELS. *Ultramicroscopy* 2012, **116:** 24.

153. Riedl T, Gemming T, Wetzig K. Extraction of EELS white-line intensities of manganese compounds: Methods, accuracy, and valence sensitivity. *Ultramicroscopy* 2006, **106:** 284.

154. Freitas R, Mitchell J, Schiffer P. Magnetodielectric consequences of phase separation in the colossal magnetoresistance manganite Pr0.7Ca0.3MnO3. *Physical Review B* 2005, **72**(14).

155. Li PL, Yao XY, Wang KF, Lu CL, Gao F, Liu JM. Steplike magnetocapacitance and dielectric relaxation in spin frustrated $Ca_3Co_2O_6$. *Journal of Applied Physics* 2008, **104:** 054111.

156. Pregelj M, Zorko A, Zaharko O, Kutnjak Z, Jagodič M, Jagličić Z, *et al.* Magnetic phase diagram of the multiferroic $FeTe_2O_5Br$. *Physical Review B* 2010, **82:** 144438.

157. Hur N, Park S, Sharma PA, Guha S, Cheong SW. Colossal Magnetodielectric Effects in $DyMn_2O_5$. *Physical Review Letters* 2004, **93:** 107207.

158. Goto T, Kimura T, Lawes G, Ramirez A-P, Tokura Y. Ferroelectricity and Giant Magnetocapacitance in Perovskite Rare Earth Manganites. *Physical Review Letters* 2004, **92:** 257201.

159. Kornetta O-B, Qi T-F, Ge M, Parkin S, De Long L-E, Schlottmann P, *et al.* Correlated giant dielectric peaks and antiferromagnetic transitions near room temperature in pure and alkali-doped $BaMnO_{3-\delta}$. *J Phys: CondensMatter* 2011, **23:** 435901.

160. Hemberger J, Lunkenheimer P, Fichtl R, Krug von Nidda H-A, Tsurkan V, Loidl A. Relaxor ferroelectricity and colossal magnetocapacitive coupling in ferromagnetic $CdCr_2S_4$. *Nature* 2005, **434:** 364.

161. Lu J, Qiao L-J, Ma X-Q, Chu W-Y. Magnetodielectric effect of $Bi_6Fe_2Ti_3O_{18}$ under ultra low magnetic field. *JPhys:CondensMatter* 2006, **18:** 4801.

162. Kundys B, Martin C, Simon C. Magnetoelectric coupling in polycrystalline FeVO4. *Physical Review B* 2009, **80**(17).

163. Maignan A, Martin C, Singh K, Simon C, Lebedev OI, Turner S. From spin induced ferroelectricity to dipolar glasses: Spinel chromites and mixed delafossites. *Journal of Solid State Chemistry* 2012, **195:** 41.

164. Curecheriu L, Buscaglia M-T, Buscaglia V, Zhao Z, Mitoseriu L. Grain size effect on the nonlinear dielectric properties of barium titanate ceramics. *Applied Physics Letters* 2010, **97:** 242909.

165. Guo Y-Y, Yan Z-B, Zhang N, Cheng WW, Liu J-M. Ferroelectric aging behaviors of $BaTi_{0.995}Mn_{0.005}O_3$ ceramics: grain size effects. *Appl Phys A* 2012, **107:** 243.

166. Hoshina T, Furuta T, Yamazaki T, Takeda H, Tsurumi T. Grain Size Effect on Dielectric Properties of Ba(Zr,Ti)O_3 Ceramics. *Japanese Journal of Applied Physics* 2012, **51:** 09LC04.

167. Zheng P, Zhang JL, Tan YQ, Wang CL. Grain-size effects on dielectric and piezoelectric properties of poled $BaTiO_3$ ceramics. *Acta Materialia* 2012, **60:** 5022.

168. Arlt G, Hennings D, de With G. Dielectric properties of fine grained barium titanate ceramics. *Journal of Applied Physics* 1985, **58:** 1619.

169. Buessem WR, Cross LE, Goswami K. Phenomenological Theory of High Permittivity in Fine Grained Barium Titanate. *J Am Ceram Soc* 1966, **49:** 33.

170. Bell J, Moulson AJ, Cross LE. The Effect of Grain Size on the Permittivity of $BaTiO_3$. *Ferroelectrics* 1984, **54:** 147.

171. Ahmad MM, Yamada K, Meuffels P, Waser R. Aging-induced dielectric relaxation in barium titanate ceramics. *Appl Phys Lett* 2007, **90:** 112902.

172. Zhang L, Ren X. Aging behavior in single-domain Mn-doped BaTiO3 crystals: Implication for a unified microscopic explanation of ferroelectric aging. *Physical Review B* 2006, **73:** 094121.

173. Lambeck PV, Jonker GH. The nature of domain stabilization in ferroelectric perovskites. *J Phys Chem Solids* 1986, **47:** 453.

174. Robels U, Arlt G. Domain wall clamping in ferroelectrics by orientation of defects. *Journal of Applied Physics* 1993, **73:** 3454.

175. Postnikov VS, Pavlov VS, Turkov SK. Internal friction in ferroelectrics due to interaction of domain boundaries and point defects. *J Phys Chem Solids* 1970, **31:** 1785.

176. Carl K, Hardtl KH. Electrical after-effects in Pb(Ti, Zr)O_3 ceramics *Ferroelectrics* 1978, **17:** 473.

177. Schulze WA, Ogino K. Review of literature on aging of dielectrics. *Ferroelectrics* 1988, **87:** 361.

178. Terada N, Khalyavin DD, Perez-Mato JM, Manuel P, Prabhakaran D, Daoud-Aladine A, *et al.* Magnetic and ferroelectric orderings in ferroelectric α-$NaFeO_2$. *Physical Review B* 2014, **89:** 1844421.

179. Elkhouni T, Amami M, Colin CV, Ben Salah A. Structural and Magnetoelectric Interactions of (Ca, Mg)-doped polycrystalline multiferroic $CuFeO_2$. *Materials Research Bulletin* 2014, **53:** 151.

180. Zorko A, Adamopoulos O, Komelj M, Arcon D, Lappas A. Frustration-induced nanometre-scale inhomogeneity in a triangular antiferromagnet. *Nature Communications* 2014, **5:** 4222.

181. Perez-Mato JM, Zakhour-Nakhl M, Weill F, Darriet J. Structure of composites $A_{(1+x)}$ (A ' $B_{x(1-x)}$))O_3 related to the 2H hexagonal perovskite: relation between composition and modulation. *Journal of Materials Chemistry* 1999, **9:** 2795.

182. van Smaalen S. *Incommensurate Crystallography* Oxford Science Publications, 2007.

183. van der Lee A, Evain M, Monconduit L, Brec R, Rouxel J. The Interface-Modulated Structure of $TaSi_{0.360}Te_2$. *Acta Cryst* 1994, **B50:** 119.

184. Petricek V, van der Lee A, Evain M. On the Use of Crenel Functions for Occupationally Modulated Structures. *Acta Cryst* 1995, **A51:** 529.

185. Singh K, Maignan A, Simon C, Hardy V, Pachoud E, Martin C. The spin glass delafossite $CuFe_{0.5}V_{0.5}O_2$: a dipolar glass? *Journal of physics Condensed matter : an Institute of Physics journal* 2011, **23:** 126005.

186. Chu Y-H, Martin LW, Holcomb MB, Ramesh R. Controlling magnetism with multiferroics. *Materials Today* 2007, **10:** 16.

187. Ramesh R, Spaldin NA. Multiferroics: progress and prospects in thin films. *Nature materials* 2007, **6:** 21.

188. Zheng H, Wang J, Lofland SE, Ma Z, Mohaddes-Ardabili L, Zhao T, *et al.* Multiferroic $BaTiO_3$-$CoFe_2O_4$ nanostructures. *Science* 2004, **303:** 661.

189. Zheng H, Straub F, Zhan Q, Yang PL, Hsieh WK, Zavaliche F, *et al.* Self-Assembled Growth of BiFeO3–CoFe2O4 Nanostructures. *Advanced Materials* 2006, **18**(20)**:** 2747-2752.

190. Kleemann W. Disordered Multiferroics. In: Virk HS, Kleemann W (eds). *Ferroics and Multiferroics*, vol. 189, 2012, p 41.

191. Choudhury N, Walizer L, Lisenkov S, Bellaiche L. Geometric frustration in compositionally modulated ferroelectrics. *Nature* 2011, **470**(7335)**:** 513-517.

192. Wang Y, Hu J, Lin Y, Nan C-W. Multiferroic magnetoelectric composite nanostructures. *NPG Asia Materials* 2010, **2:** 61.

193. Maiti RP, Dutta S, Mitra MK, Chakravorty D. Large magnetodielectric effect in nanocrystalline double perovskite Y2FeCrO6. *Journal of Physics D-Applied Physics* 2013, **46:** 415303.

194. Li H, Zheng H, Salamanca-Riba L, Ramesh R, Naumov I, Rabe K. Origin of antiphase domain boundaries and their effect on the dielectric constant of $Ba_{0.5}Sr_{0.5}TiO_3$ films grown on MgO substrates. *Applied Physics Letters* 2002, **81:** 4398.

195. Wei XK, Tagantsev AK, Kvasov A, Roleder K, Jia CL, Setter N. Ferroelectric translational antiphase boundaries in nonpolar materials. *Nature Communications* 2014, **5:** 3031.

196. Catalan G, Seidel J, Ramesh R, Scott JF. Domain wall nanoelectronics. *Reviews of Modern Physics* 2012, **84**(1)**:** 119-156.

197. Schilling A, Bowman RM, Catalan G, Scott JF, Gregg JM. Morphological Control of Polar Orientation in Single-Crystal Ferroelectric Nanowires. *Nano letters* 2007, **7:** 3787.

198. Fu D, Taniguchi H, Itoh M, Mori S. $Pb(Mg_{1/3}Nb_{2/3})O_3$ (PMN) relaxor: dipole glass or nano-domain ferroelectric ? *Advances in Ferroelectrics* 2012, **DOI:10.5772/52139:** 51.

199. Daumont CJM, Mannix D, Venkatesan S, Catalan G, Rubi D, Kooi BJ, *et al.* Epitaxial $TbMnO_3$ thin films on $SrTiO_3$ substrates: a structural study. *J Phys: Condens Matter* 2009, **21:** 182001.

200. Burkhardt MH, Hossain MA, Sarkar S, Chuang Y-D, Gonzalez AGC, Doran A, *et al.* Imaging the First-Order Magnetic Transition in $La_{0:35}Pr_{0:275}Ca_{0:375}MnO_3$. *Physical Review Letters* 2012, **108:** 237202.

201. Velikokhatnyi OI, Chang CC, Kumta PN. Phase stability and electronic structure of $NaMnO_2$. *Journal of the Electrochemical Society* 2003, **150:** A1262.

202. Lawes G, T. K, Varma CM, Subramanian MA, Cava RJ, Ramirez AP. Magnetically tunable dielectric materials. *arxiv:09041974* 2009.

203. Hoppe R, Brachtel G, Jansen M. Knowledge of oxomanganates (III)-$LiMnO_2$ and beta-$NaMnO_2$. *Zeitschrift Fur Anorganische Und Allgemeine Chemie* 1975, **417:** 1.

204. Hirano S, Narita R, Naka S. Hydrothermal Syntheses and Properties of $NaxMnO_2$ Crystals. *Journal of Crystal Growth* 1981, **54:** 595.

205. Kundys B, Martin C, S. C. Magnetoelectric coupling in polycrystalline $FeVO_4$. *Physical Review B* 2009, **80:** 172103.

206. Kolodiazhnyi T, Sakurai H, Vittaykorn N. Spin flop driven magnetoelectric effect in $Co_4Nb_2O_9$. *Applied Physics Letters* 2011, **99:** 132906.

207. Basu T, Iyer KK, Singh K, Sampathkumaran EV. Novel dielectric anomalies due to spin-chains above and below Neel temperature in $Ca_3Co_2O_6$. *Scientific Reports* 2013, **3:** 3104.

208. Basu T, Iyer KK, Singh K, Sampathkumaran EV. Novel dielectric anomalies due to spin chains above and below Neel temperature in $Ca_3Co_2O_6$. *Scientific Reports* 2013, **3:** 3104.

209. Hwang J, Choi ES, Zhou HD, Lu J, Schlottmann P. Magnetoelectric effect in NdCrTiO5. *Physical Review B* 2012, **85:** 024415.

210. Mufti N, Blake GR, Mostovoy M, Riyadi S, Nugroho AA, Palstra TTM. Magnetoelectric coupling in$MnTiO_3$. *physical Review B* 2011, **83**(104416).

211. Fang Y, Wang LY, Song YQ, Tang T, Wang DH, Du YW. Manipulation of magnetic field on dielectric constant and electric polarization in Cr_2WO_6. *Appl Phys Lett* 2014, **104:** 132908.

212. Hwang J, Choi ES, Zhou HD, Xin Y, Lu J, Schlottmann P. Magnetic transitions and magnetodielectric effect in antiferromagnet $SrNdFeO_4$. *Physical Review B* 2012, **85:** 224429.

213. Croguennec L, Deniard P, Brec R, Lecerf A. Nature of the stacking faults in orthorhombic $LiMnO_2$. *Journal of Materials Chemistry* 1997, **7:** 511.

214. Poienar M, Vecchini C, Andre G, Daoud-Aladine A, Margiolaki I, Maignan A, *et al.* Substitution Effect on the Interplane Coupling in Crednerite: the $Cu_{1.04}Mn_{0.96}O_2$ Case. *Chemistry of Materials* 2011, **23:** 85.

215. Singh K, Kundys B, Poienar M, Simon C. Effect of coupled ferroelectric and antiferromagnetic fluctuations on dielectric anomalies in spin induced multiferroics. *Journal of physics Condensed matter : an Institute of Physics journal* 2010, **22**(44)**:** 445901.

216. Salamon MB, Sinha S, Rhyne JJ, Cunningham JE, Erwin RW, Borchers J, *et al.* Long range Incommensurate magnetic order in a Dy-Y multilayer *Physical Review Letters* 1986, **56:** 259.

217. Odisho IH, Aldorry HM. Magnetic Satellites in the incommensurate phase of pure and doped $NiBr_2$. *Journal of Physics-Condensed Matter* 1989, **1:** 6551.

218. Vaknin D, Zarestky JL, Rivera JP, Schmid H. Commensurate-incommensurate magnetic phase transition in magnetoelectric single crystal LiNiPO4. *Physical Review Letters* 2004, **92**(20).

219. Council SaTF. ISIS WISH. 2014 [cited]Available from: http://www.isis.stfc.ac.uk/instruments/wish/wish-6465.html

220. Technology NIoSa. BT1 Diffractometer NCNR NIST. 2014 [cited]Available from: http://www.ncnr.nist.gov/instruments/bt1/

221. Chatterji T. *Neutron Scattering from_Magnetic Materials*: Elsevier, 2007.

222. Cowley RA. *Methods of Experimental Physics*, vol. 23, part c. Academic Press: London, 1987.

223. Li Q, Lynn JW, Gotaas JA. Absolute Measurement of the Ordered Magnetic Moment in Holmium Rich $(Er_{1-x}Ho_x)Rh_4B_4$ *Physical Review B* 1987, **35:** 5008.

224. Nuttall WJ, Perry SC, Stirling WG, Mitchell PW, Kilcoyne SH, Cywinski R. Antiferromagnetic critical phenomena in USb. *Physica B-Condensed Matter* 2002, **315:** 179.

225. Bramwell ST, Holdsworth PCW. Magnetization and universal subcritical behavior in 2-dimensional XY magnets. *Journal of Physics-Condensed Matter* 1993, **5:** L53.

226. Rodríguez EE, Sokolov DA, Green MA, Sobolev O, Rodriguez-Rivera JA, Cao H, *et al.* Magnetic and structural properties near the Lifshitz point in $Fe_{1+x}Te$. *Physical Review B* 2013, **88:** 165110.

227. Wu L, Zhu Y, Park S, Shapiro S, Shirane G, Tafto J. Defect structure of the high-dielectric-constant perovskite $CaCu_3Ti_4O_{12}$. *Physical Review B* 2005, **71:** 014118.

228. Kruk I, Zajdel P, van Beek W, Bakaimi I, Lappas A, Stock C, *et al*. Coupled commensurate cation and charge modulation in the tunneled structure, Na(0.40(2))MnO(2). *Journal of the American Chemical Society* 2011, **133**(35)**:** 13950-13956.

229. Kijima T. *Inorganic and_ Metallic Nanotubular Materials Recent Technologies and Applications Topics in Applied Physics*. Springer, 2010.

230. Rossouw MH, Liles DC, Thackeray MM. Synthesis and structural characterization of a novel layered lithium manganese oxide, $Li_{0.36}Mn_{0.91}O_2$ and its lithiated derivative, $Li_{1.09}Mn_{0.91}O_2$. *Journal of Solid State Chemistry* 1993, **104:** 464.

231. Feng Q, Liu L, Yanagisawa K. Effects of synthesis parameters on the formation of birnessite-type manganese oxides. *Journal of Materials Science Letters* 2000, **19:** 1567.

232. Feng Q, Kanoh H, Miyai Y, Ooi K. Hydrothermal synthesis of lithium and sodium magnanese oxides and their metal ion extraction insertion reactions. *Chemistry of Materials* 1995, **7:** 1226.

233. Feng Q, Kanoh H, Ooi K. Manganese oxide porous crystals. *Journal of Materials Chemistry* 1999, **9:** 319.

234. Jeong YU, Manthiram A. Synthesis of $NaxMnO_{2+\delta}$ by a Reduction of Aqueous Sodium Permanganate with Sodium Iodide. *Journal of Solid State Chemistry* 2001, **156:** 331.

235. Luo J, Suib SL. Preparative parameters, magnesium effects, and anion effects in the crystallization of birnessites. *Journal of Physical Chemistry B* 1997, **101:** 10403.

236. Golden DC, Chen CC, Dixon JB. Transformation of birnessite to buserite, todorokite, and manganite under mild hydrothermal treatment. *Clays and Clay Minerals* 1987, **35:** 271.

237. Luo J, Zhang QH, Huang AM, Giraldo O, Suib SL. Double-aging method for preparation of stabilized Na-buserite and transformations to todorokites incorporated with various metals. *Inorganic chemistry* 1999, **38:** 6106.

238. Mumme WG. The Structure of $Na_4Mn_4Ti_5O_{18}$. *Acta Cryst* 1968, **B24:** 1114.

239. Zhu HT, Luo J, Yang HX, Liang JK, Rao GH, Li JB, *et al.* Birnessite-type MnO_2 Nanowalls and Their Magnetic Properties. *Journal of Physical Chemistry C* 2008, **112:** 17089.

240. Espinal L, Wong-Ng W, Kaduk JA, Allen AJ, Snyder CR, Chiu C, *et al.* Time-dependent CO_2 sorption hysteresis in a one-dimensional microporous octahedral molecular sieve. *Journal of the American Chemical Society* 2012, **134:** 7944.

241. Feng X. Pathways of birnessite formation in alkali medium. *Science in China Series D* 2005, **48**(9)**:** 1438.

242. Espinal L, Wong-Ng W, Kaduk JA, Allen AJ, Snyder CR, Chiu C, *et al.* Time-Dependent CO2 Sorption Hysteresis in a One-Dimensional Microporous Octahedral Molecular Sieve. *Journal of the American Chemical Society* 2012, **134**(18)**:** 7944-7951.

243. van Aken PA, Liebscher B. Quantification of ferrous/ferric ratios in minerals: new evaluation schemes of Fe L-23 electron energy-loss near-edge spectra. *Physics and Chemistry of Minerals* 2002, **29:** 188.

244. Graetz J, Ahn CC, Ouyang H, Rez P, Fultz B. White lines and d-band occupancy for the 3d transition-metal oxides and lithium transition-metal oxides. *Physical Review B* 2004, **69:** 235103.

245. Leapman RD, Grunes LA. Anomalous L3-L2 White-Line Ratios in the 3-D Transition Metals. *Physical Review Letters* 1980, **45:** 397.

246. Riedl T, Gemming T, Gruner W, Acker J, Wetzig K. Determination of manganese valency in $La_{1-x}Sr_xMnO_3$ using ELNES in the (S)TEM. *Micron* 2007, **38:** 224.

247. Bedanta S, Kleemann W. Supermagnetism. *Journal of Physics D-Applied Physics* 2009, **42:** 013001.

248. Greedan JE, Raju NP, Maignan A, Simon C, Pedersen JS, Niraimathi AM, *et al.* Frustrated pyrochlore oxides, $Y_2Mn_2O_7$, $Ho_2Mn_2O_7$, and $Yb_2Mn_2O_7$: Bulk magnetism and magnetic microstructure. *Physical Review B* 1996, **54:** 7189.

249. Maignan A, Varadaraju UV, Millange F, Raveau B. AC susceptibilities and size effect in $Ln_{(0.7)}(Sr,Ca)_{(0.3)}MnO_3$ CMR manganites. *Journal of Magnetism and Magnetic Materials* 1997, **168:** L237.

250. Maignan A, Sundaresan A, Varadaraju UV, Raveau B. Magnetization relaxation and aging in spin-glass $(La,Y)_{(1-x)}Ca_xMnO_3$ (x = 0.25, 0.3 and 0.5) perovskite. *Journal of Magnetism and Magnetic Materials* 1998, **184:** 83.

251. Perez J, Garcia J, Blasco J, Stankiewicz J. Spin-glass behavior and giant magnetoresistance in the $(RE)Ni_{0.3}Co_{0.7}O_3$ (RE = La,Nd,Sm) system. *Physical Review Letters* 1998, **80:** 2401.

252. Troyanchuk IO, Samsonenko NV, Shapovalova EF, Szymczak H, Nabialek A. Synthesis and characterization of $Ln(B_{0.5}Mn_{0.5})O_3$ (Ln-lanthanoid; B=Ni,Co) perovskites. *Materials Research Bulletin* 1997, **32:** 67.

253. Onodera H, Kobayashi H, Yamauchi H, Ohashi M, Yamaguchi Y. Magnetic properties of the single crystalline Dy_3Ni studied by magnetization measurement and Dy-161 Mossbauer spectroscopy. *Journal of Magnetism and Magnetic Materials* 1997, **170:** 201.

254. Nishigori S, Hirooka Y, Ito T. Spin-glass behavior in TbPdIn and DyPdIn. *Journal of Magnetism and Magnetic Materials* 1998, **177:** 137.

255. Giri AK. Magnetic properties of iron-polyethylene nanocomposites prepared by high energy ball milling. *Journal of Applied Physics* 1997, **81:** 1348.

256. Bandaranayake RJ, Lin JY, Jiang HX, Sorensen CM. Synthesis and properties of $Cd_{1-x}Mn_xS$ diluted magnetic semiconductor ultrafine particles. *Journal of Magnetism and Magnetic Materials* 1997, **169:** 289.

257. Ford PJ. Spin glasses. *Contemporary Physics* 1982, **23:** 141.

258. Itoh M, Natori I, Kubota S, Motoya K. Spin-Glass Behavior and Magnetic Phase Diagram of $La_{1-x}Sr_xCoO_3$(($0 \leq x \leq 0.5$) Studied by Magnetization Measurements. *Journal of the Physical Society of Japan* 1994, **63:** 1486.

259. Poole CP, Datta T, Farach HA. *Copper Oxide Superconductors*. Wiley-Interscience, 1988.

260. Nam DNH, Jonason K, Nordblad P, Khiem NV, Phuc NX. Coexistence of ferromagnetic and glassy behavior in the $La_{0.5}Sr_{0.5}CoO_3$ perovskite compound. *Physical Review B* 1999, **59:** 4189.

261. Singh K, Maignan A, Simon C, Hardy V, Pachoud E, Martin C. The spin glass delafossite CuFe0.5V0.5O2: a dipolar glass? *Journal of Physics-Condensed Matter* 2011, **23**(12).

262. DeFotis GC, Coker GS, Jones JW, Branch CS, King HA, Bergman JS, *et al.* Static magnetic properties and relaxation of the insulating spin glass $Co_{1-x}MnxCl_2 \cdot H_2O$ *Physical Review B* 1998, **58:** 12178.

263. Zhou G, Bakker H. Spin-glass behavior of mechanically milled crystalline GdAl2. *Physical Review Letters* 1994, **73**(2)**:** 344-347.

264. Shen XF, Ding YS, Liu J, Han ZH, Budnick JI, Hines WA, *et al.* A magnetic route to measure the average oxidation state of mixed-valent manganese in manganese oxide octahedral molecular sieves (OMS). *Journal of the American Chemical Society* 2005, **127:** 6166.

265. Li L, Pan Y, Chen L, Li G. One-dimensional alpha-MnO_2: Trapping chemistry of tunnel structures, structural stability, and magnetic transitions. *Journal of Solid State Chemistry* 2007, **180:** 2896.

266. Sundaresan A, Maignan A, Raveau B. Spin-glass state and magnetic-field-induced phenomena in distorted $Eu_{0.58}Sr_{0.42}MnO_3$ perovskite. *Physical Review B* 1997, **55:** 5596.

267. Grest GS, Soukoulis CM, Levin K. Irreversibility in Ising and Heisenberg spin glasses (invited). *Journal of Applied Physics* 1984, **55**(6)**:** 1634.

268. Anand VK, Adroja DT, Hillier AD, Taylor J, André G. Signatures of spin-glass behavior in the induced magnetic moment system $PrRuSi_3$. *Physical Review B* 2011, **84**.

269. Binder K. Spin glasses: Experimental facts, theoretical concepts, and open questions. *Reviews of Modern Physics* 1986, **58:** 801.

270. Wang F, Zhang J, Chen Y-f, Wang G-j, Sun J-r, Zhang S-y, *et al.* Spin-glass behavior in $La(Fe_{1-x}Mnx)_{11.4}Si_{1.6}$ compounds. *Physical Review B* 2004, **69:** 094424.

271. Li DX, Nimori S, Shiokawa Y, Tobo A, Onodera H, Haga Y, *et al.* Spin-glass behavior with short-range antiferromagnetic order in Nd2AgIn3. *Applied Physics Letters* 2001, **79**(25)**:** 4183-4185.

272. Fischer KH, Hertz JA. *Spin Glasses*. Cambrigde University Press, 1991.

273. Jonason K, Vincent E, Hammann J, Bouchaud JP, Nordblad P. Memory and chaos effects in spin glasses. *Physical Review Letters* 1998, **81:** 3243.

274. Sasaki M, Jönsson P, Takayama H, Mamiya H. Aging and memory effects in superparamagnets and superspin glasses. *Physical Review B* 2005, **71:** 104405.

275. Suzuki M, Fullem SI, Suzuki IS, Wang L, Zhong C-J. Observation of superspin-glass behavior in Fe_3O_4 nanoparticles. *Physical Review B* 2009, **79:** 024418.

276. Dupuis V, Vincent E, Bouchaud JP, Hammann J, Ito A, Katori H. Aging, rejuvenation, and memory effects in Ising and Heisenberg spin glasses. *Physical Review B* 2001, **64:** 174204.

277. Mulder CAM, Vanduyneveldt AJ, Mydosh JA. Susceptibility of the Cu-Mn Spin Glass-Frequency and Field Dependences. *Physical Review B* 1981, **23:** 1384.

278. Harikrishnan S, Kumar CMN, Bhat HL, Elizabeth S, Roessler UK, Doerr K, *et al.* Investigations on the spin-glass state in Dy(0.5)Sr(0.5)MnO(3) single crystals through structural, magnetic and thermal properties. *Journal of Physics-Condensed Matter* 2008, **20**(27).

279. Siouris IM. The magnetic states of Gd_2CuIn_3. *Journal of Magnetism and Magnetic Materials* 2007, **309:** 222.

280. Parker D, Dupuis V, Ladieu F, Bouchaud JP, Dubois E, Perzynski R, *et al.* Spin glass behavior in an interacting γ-Fe_2O_3 nanoparticle system. 2008, **77:** 104428.

281. Billoire A, Campbell IA. Dynamics in the Sherrington-Kirkpatrick Ising spin glass at and above Tg. *Physical Review B* 2011, **84:** 054442.

282. Fischer KH. Spin Glasses 1. *Physica Status Solidi B-Basic Solid State Physics* 1983, **116:** 357.

283. Saslow W. Scenario for the Vogel-Fulcher "law". *Physical Review B* 1988, **37**(1)**:** 676-678.

284. Kostopoulou A, Brintakis K, Vasilakaki M, Trohidou KN, Douvalis AP, Lascialfari A, *et al.* Assembly-mediated interplay of dipolar interactions and surface spin disorder in colloidal maghemite nanoclusters. *Nanoscale* 2014, **6:** 3764.

285. Levy LP. Critical dynamics of metallic spin glasses *Physical Review B* 1988, **38:** 4963.

286. Gunnarsson K, Svedlindh P, Nordblad P, Lundgren L. Static scaling in a short range Ising spin glass. *Physical Review B* 1991, **43:** 8199.

287. Bréard Y, Hardy V, Raveau B, Maignan A, Lin HJ, Jang LY, *et al.* Spin-glass state induced by cobalt substitution in $CaRuO_3$. *Journal of Physics: Condensed Matter* 2007, **19:** 216212.

288. Li DX, Nimori S, Shiokawa Y, Tobo A, Onodera H, Haga Y, *et al.* Spin-glass behavior with short-range antiferromagnetic order in Nd_2AgIn_3. *Applied Physics Letters* 2001, **79:** 4183.

289. Takahashi M, Sembiring T, Noda Y, Shishido T, Ohshima K-i. Magnetic structures and spin-glass-like behavior in ordered and disordered Pt-rich Pt-Mn alloys. *Physical Review B* 2004, **70:** 014431.

290. Wang BS, Tong P, Sun YP, Zhu XB, Yang ZR, Song WH, *et al.* Observation of spin glass behavior in antiperovskite compound $SnCFe_3$. *Applied Physics Letters* 2010, **97:** 042508.

291. Lappas A, Alexandrakis V, Giapintzakis J, Pomjakushin V, Prassides K, Schenck A. Impurity-induced antiferromagnetic order in the Haldane-gap compound PbNi2-xMgxV2O8 (x=0.24). *Physical Review B* 2002, **66**(1).

292. Mezei F. Neutron Spin Echo Study of Spin Glass Dynamics. *Journal of Applied Physics* 1982, **53:** 7654.

293. Heffner RH, Maclaughlin DE. Comparison of Spin Dynamics Determined by The Muon Spin Relaxation and Neutron Spin-Echo Techniques. *Physical Review B* 1984, **29:** 6048.

294. Caruntu G, Yourdkhani A, Vopsaroiu M, Srinivasan G. Probing the local strain-mediated magnetoelectric coupling in multiferroic nanocomposites by magnetic field-assisted piezoresponse force microscopy. *Nanoscale* 2012, **4:** 3218.

295. Wang Y, Hu J, Lin Y, Nan C-W. Multiferroic magnetoelectric composite nanostructures. *Npg Asia Materials* 2010, **2**(2)**:** 61-68.

296. Geng Y, Das H, Wysocki AL, Wang X, Cheong SW, Mostovoy M, *et al.* Direct visualization of magnetoelectric domains. *Nature materials* 2014, **13:** 163.

297. Vecchini C, Poienar M, Damay F, Adamopoulos O, Daoud-Aladine A, Lappas A, *et al.* Magnetoelastic coupling in the frustrated antiferromagnet $CuMnO_2$. *Physical Review B* 2010, **82:** 094404.

298. http://www.ccp14.ac.uk. [cited]Available from:

299. Wills AS. A new protocol for the determination of magnetic structures using simulated annealing and representational analysis (SARAh). *Physica B* 2000, **276-278:** 680.

300. Carvahal JR. A program for calculating irreducible representation of little groups and basis functions of polar and axial vector properties. *http://www.ccp14.ac.uk/ccp/web-mirrors/plotr/Tutorials&Documents/basireps.pdf;* 2004.

301. NCNR N. Data Analysis and Visualization Enviroment. http://www.ncnr.nist.gov/dave/ 2014 [cited]Available from: